TOPOLOGY OPTIMIZATION OF 3D PRINTED CONCRETE STRUCTURAL WALLS THROUGH ARTIFICIAL INTELLIGENCE TECHNIQUES

ÜÇ BOYUTLU YAZICILAR MARİFETİYLE BETON BİNA İNŞASINDA DUVAR TOPOLOJİSİNİN YAPAY ZEKÂ TEKNİKLERİ İLE OPTİMİZASYONU

ABDULKADİR ÖZALP

DOÇ. DR ALPER ALDEMİR

Supervisor

Submitted to

Graduate School of Science and Engineering of Hacettepe University

as a Partial Fulfilment to the Requirements

for be Award of the Degree of Doctor of Philosophy

in Civil Engineering

2025

ABSTRACT

TOPOLOGY OPTIMIZATION OF 3D PRINTED CONCRETE STRUCTURAL WALLS THROUGH ARTIFICIAL INTELLIGENCE TECHNIQUES

Abdulkadir ÖZALP

Doctor of Philosophy, Department of Civil Engineering

Supervisor: Assoc. Prof. Dr. Alper ALDEMİR

June 2025, 307 pages

Concrete is one of the most widely used building materials worldwide. Various types of concrete, such as self-compacting concrete, high-strength concrete, and chemical-resistant concrete, are used globally to improve the performance of structures. Digital technology applications like 3D printers offer new possibilities for the production of concrete structures. There are many advantages to numerically modeling the 3D concrete printing process. Simulating the printing process allows for predicting the structural behavior of concrete during production, and calculating the potential damage that may occur at this stage. This is important for reducing material waste and preventing wear on the printing machine. With the increasing demand for sustainable product development, scientists have begun to focus on producing hollow structures with high strength and minimum weight. Topology optimization procedures will contribute to the more economical and robust design of structures, providing new contributions to the engineering, architecture, and construction fields. Many researchers have developed

physics-based models to improve the properties of hollow elements printed through 3D printers. However, these formulations require a deep understanding of the production process, which can be very laborious. As an alternative to this method, predictions can be made using only the data obtained. In this context, various artificial intelligence methods can be used.

In the 3D printing process of concrete structures, the design process should be done in the office environment, while the printing process should be done in the construction site. This simultaneous occurrence of the design and printing processes makes it impossible to fully automate the 3D concrete printing process. Additionally, there is no formulation in the literature for the capacity calculation of concrete walls printed through 3D printers and subjected to combined axial and lateral loads (such as design effects occurring during wind loads or seismic demands). To achieve fully automatic 3D concrete printing, in this study, the optimization of wall topology in concrete building construction printed by 3D printers has been realized with artificial intelligence techniques, and automated design tools have been developed using these artificial intelligence models. The dataset required for the artificial intelligence model was obtained through numerical modeling. With this study, the most economical and lightest section topology with the desired strength was determined through the artificial intelligence model without resorting to trial and error, saving material and energy. Additionally, by comparing two different artificial intelligence models, the model with the highest accuracy and the lowest number of parameters was found, reducing the calculation cost. In addition, the pre-trained version of the proposed artificial intelligence-based design tool has been uploaded to permanent storage, and the relevant link has been added in the conclusion section of this study.

Keywords: 3D Concrete Printing, Structural Wall, Topology Optimization, Numerical Modelling, Artificial Intelligence

ÖZET

ÜÇ BOYUTLU YAZICILAR MARİFETİYLE BETON BİNA İNŞASINDA DUVAR TOPOLOJİSİNİN YAPAY ZEKÂ TEKNİKLERI İLE OPTİMİZASYONU

Abdulkadir ÖZALP

Doktora, İnşaat Mühendisliği Bölümü

Tez Danışmanı: Doç. Dr. Alper ALDEMİR

Haziran 2025, 307 sayfa

Beton, dünya çapında en fazla kullanılan yapı malzemelerinden birisidir. Dünya çapında, yapıların performansını iyileştirmek için yüksek dayanımlı beton, kendiliğinden yerleşen beton, kimyasallara karşı dayanıklı beton gibi çeşitli beton türleri kullanılmaktadır. 3 boyutlu yazıcılar gibi dijital teknoloji uygulamaları beton yapıların üretimi için yeni olanaklar sunmaktadır. 3 boyutlu beton basım sürecini nümerik olarak modellemenin birçok avantajı bulunmaktadır. Basım sürecinin simüle edilmesi ile betonun üretim aşamasındaki yapısal davranışı tahmin edilebilmekte ve bu aşamada nasıl bir hasarın meydana gelebileceği hesaplanabilmektedir. Bu durum malzeme israfının azaltılması ve basım makinesinin yıpranmaması açısından önemlidir. Sürdürülebilir ürün geliştirmeye yönelik taleplerin artması ile birlikte bilim adamları odaklarını yüksek mukavemet ve minimum ağırlığa sahip boşluklu yapılar üretmeye kaydırmaya başladılar. Topoloji optimizasyon prosedürleri ile daha verimli sistemlerin üretilmesi yapıların daha ekonomik ve sağlam bir şekilde dizayn edilmesi hususunda mühendislik, mimarlık ve yapı alanlarına yeni katkılar sağlayacaktır. Birçok araştırmacı 3 boyutlu yazıcılar ile

basılan boşluklu elemanların özelliklerini iyileştirmek için fizik tabanlı modeller geliştirmiştir. Fakat, bu formülasyonlar üretim süreci hakkında çok derin bilgi sahibi olmayı gerektirmekte bu da çok zahmetli bir süreç olabilmektedir. Bu yönteme alternatif olarak sadece elde edilen verileri kullanarak tahmin yapılabilir. Bu bağlamda çeşitli yapay zekâ yöntemleri kullanılabilir.

Beton yapıların 3 boyutlu basım sürecinde tasarım işleminin ofis ortamında, basım işleminin ise şantiye ortamında yapılması gerekmektedir. 3 boyutlu basım sürecinde eş zamanlı olmayan bu uygulama 3 boyutlu beton basımı işleminin tam otomatik bir şekilde uygulanmasını imkânsız hale getirmektedir. Ayrıca literatürde, eksenel ve yanal yük etkilerine (rüzgâr yükleri veya sismik talepler sırasında oluşan tasarım etkileri gibi) maruz kalan, 3 boyutlu yazıcılar ile üretilmiş beton duvarların kapasite hesabı için herhangi bir formülasyon bulunmamaktadır. 3 boyutlu beton basımı işleminin tam otomatik bir şekilde uygulanmasını gerçekleştirmek için, bu çalışmada, 3 boyutlu yazıcılar marifetiyle basılan beton bina inşasında duvar topolojisinin yapay zekâ teknikleri ile optimizasyonu gerçekleştirilmiş olup bu yapay zekâ modelleri kullanılarak otomatize edilmiş tasarım araçları geliştirilmiştir. Yapay zekâ modeli için gerekli olan veri seti nümerik modelleme ile elde edilmiştir. Bu çalışma ile deneme yanılma yoluna başvurulmadan yapay zekâ modeli vasıtası ile istenilen dayanıma sahip en ekonomik, en hafif kesit topolojisi belirlenmiş olup malzeme ile enerjiden tasarruf edilmiştir. Ayrıca iki farklı yapay zekâ modeli kıyaslanarak en yüksek doğruluğu veren en düşük parametre sayısına sahip model bulunmuş, böylece hesaplama maliyeti de düşürülmüştür. Buna ek olarak, önerilen yapay zekâ tabanlı tasarım aracının önceden eğitilmiş versiyonu kalıcı bir depolama ortamına yüklenip ilgili bağlantı bu çalışmanın sonuç bölümünde eklenmiştir.

Anahtar Kelimeler: 3 Boyutlu Beton Basımı, Yapısal Duvar, Topoloji Optimizasyonu, Nümerik Modelleme, Yapay Zekâ

ACKNOWLEDGEMENT

I would like to express my deep gratitude to my advisor Assoc. Prof. Dr. Alper ALDEMİR for him guidance and patience during this thesis. In every step, he was very kind and understanding. It was a great chance to study with him.

I owe my sincere thanks to the thesis monitoring committee members, Prof. Dr. Ayşegül ASKAN GÜNDOĞAN and Assoc. Prof. Dr. Mustafa Abdullah SANDIKKAYA for sparing their valuable time to examine this thesis.

I would like to express my deepest and special gratitude to my wife Hande Nur ÖZALP for her great support and encouragement.

Finally, I would like to thank my family for being with me and supporting me throughout my life.

TABLE OF CONTENTS

ABSTRACT i

ÖZET iii

ACKNOWLEDGEMENT v

TABLE OF CONTENTS vi

LIST OF FIGURES viii

LIST OF TABLES xxxi

SYMBOLS AND ABBREVIATIONS xxxii

1. INTRODUCTION 1

2. LITERATURE REVIEW 31

2.1. Studies on Numerical Modeling of Structures Printed Through 3DCP 32

2.2. Studies on Parametric Modeling of Structures Printed Through 3DCP 39

2.3. Studies on Structural Walls Printed Through 3DCP 44

2.4. Studies on TO of Structural Elements Printed Through 3DCP 48

2.5. Studies Using Various AI Methods in the Design and Analysis of Structures Printed Through 3DCP or Optimization of the 3DCP Process 51

3. MATERIALS AND METHODS 62

3.1. Determining the Wall Interior Topologies Used 62

3.2. Modeling of Shear Walls 64

3.2.1. Determination of Geometric Parameters 64

3.2.2. Creation of FE Models 66

3.2.3. Assessment of Results Obtained from FE Analyses 85

3.3. Creating AI Models for Determining the Optimum Interior Topology of Walls 170

3.3.1. Theoretical Knowledge about ML 170

3.3.2. Creating MLP Models 181

3.3.3. Creating CNN Models 210
3.4. Development of AI-Based Design Tools 231
3.5. Calculating the Shear Capacities According to Building Codes/Standards 234
4. RESULTS AND DISCUSSIONS 237
4.1. Comparison of the Values Predicted through the MLP Model and CNN Model 237
4.2. Comparison of the Shear Capacities Predicted by the AI-Based Design Tool with Shear Capacities Calculated through the Formulas in the FEMA 356 280
5. CONCLUSIONS AND RECOMMENDATIONS 291
5.1. Conclusions 292
5.2. Recommendations 294
5.2.1. Practical Recommendations 294
5.2.2. Future Academic Recommendations 294
6. REFERENCES 295
APPENDICIES 305
APPENDIX 1 – Articles Derived from Thesis Work 305
APPENDIX 2 – Thesis Originality Report 306
CURRICULUM VITAE 307

LIST OF FIGURES

Figure 1.1. Areas where AI is applied in Construction 4.0. 1
Figure 1.2. Itaipu Dam, Brasil [5]. 3
Figure 1.3. Central Arizona project pipeline [5]. 3
Figure 1.4. Interior of the sports complex in Rome designed by Pier Luigi Nervi for the 1960 Olympic games [5]. 4
Figure 1.5. Some of the practical real-life applications of extrusion-based 3DCP technology (a) 3D printed multi-storey apartment building; Winsun, (b) the first office building produced with 3DCP technology in Dubai, (c) Europe's first building produced through 3DCP (The BOD), (d) two-storey administrative building in Dubai, (e) 3D Housing 05; Milan, (f) Woven Concrete Benches (XtreeE) [20]. 8
Figure 1.6. Vertico Valeiark project: Parametric design for façade [32]. 15
Figure 1.7. Vertico parametric design made by rotating different parameters (such as height, rotation and radius) [32]. 15
Figure 1.8. The evolution of ML applications in 3DCP [10]. 20
Figure 1.9. Areas where AI, ML, and DL methods are applied, along with the most commonly used algorithms. 26
Figure 1.10. Flow-chart of the main methodology. 29
Figure 1.11. Flow-chart of the proposed holistic approach to achieve fully-automated 3D printed structures. 30
Figure 2.1. Schematic representation of FE model proposed for uniaxial compression test [36]. 33
Figure 2.2. Proposed simulation framework for the members printed through 3DCP (a) proposed macro modeling approach, (b) proposed micro modeling approach [11]. 34
Figure 2.3. 2D stationary computational printing results showing the effect of printing scale on printing results for a cement paste with a yield stress of 350 Pa [17]. 35
Figure 2.4. Proposed FE method strategies (a) voxelization of predefined print part using thick line drawing algorithm, (b) CobraPrint's mesh generation process along a predefined print path [14]. 36
Figure 2.5. General procedure for simulating 3DCP process using lattice model [3]. ... 37

Figure 2.6. Digital design of 3D model of prism-shaped samples with different hollow structures [50]. 38
Figure 2.7. General methodology of the proposed modeling strategy for the simulation of 3DCP [24]. 40
Figure 2.8. Detail of the proposed parametric model [32]..... 40
Figure 2.9. Results of nano clay mixed concrete printed through 3DCP at specified moments (a) numerical results, (b) experimental results [19]. 41
Figure 2.10. Novel computational framework proposed for the 3DCP process [33]. 42
Figure 2.11. Process flow used to model the mechanical properties of structures with honeycomb cellular topology [46]. 43
Figure 2.12. Proposed framework from design stage to production stage [2]. 44
Figure 2.13. FE mesh of a 1 m long straight wall consisting of 25 layers [59]. 45
Figure 2.14. Elastic buckling failure occurring as a result of numerical analysis of a 1m long wall [41]. 46
Figure 2.15. The three essential wall configurations considered are (a) simply supported wall, (b) free wall, (c) fully clamped wall [26]..... 47
Figure 2.16. 210 mm high inclined wall (a) the staircase effect of the appearance on the wall in case of using a rectangular nozzle, (b) the reduction in the staircase effect on the pressed wall in case the recommended nozzle cross-section is used [21]. 48
Figure 2.17. A flowchart about the implementation of the proposed strategy [30]..... 50
Figure 2.18. Setup used for the topology optimization of a simply supported beam subjected to uniformly distributed load [29]..... 50
Figure 2.19. ML techniques used in 3DCP [51]. 52
Figure 2.20. U-Net neural network [53]. 53
Figure 2.21. Transition from traditional to industrialized construction [1]. 54
Figure 2.22. Demonstration of the proposed methodology together with optimization methods [52]. 55
Figure 2.23. Number of publications on applications of AI in the field of CEM between 1997 and 2020 [54]. 56
Figure 2.24. Proposed CNN architecture [43]. 57
Figure 2.25. Workflow used for AI-based performance prediction of 3D printed concrete, considering steam curing conditions and anisotropy [40]. 58
Figure 2.26. ANNMOGOA flow chart [56]. 60

Figure 2.27. The mean square error values obtained during training (a) for the conventional ANN, (b) for the CNN [58]. 61
Figure 3.1. The three-dimensional views of the wall interior topologies used are (a) solid topology, (b) hollow topology, (c) cellular topology, (d) lattice topology, (e) truss topology, (f) triangular - 1 topology, (g) triangular - 2 topology, (h) arch topology, (i) elliptic topology. 63
Figure 3.2. The two-dimensional views of the wall interior topologies used are (a) solid topology, (b) hollow topology, (c) cellular topology, (d) lattice topology, (e) truss topology, (f) triangular - 1 topology, (g) triangular - 2 topology, (h) arch topology, (i) elliptic topology. 64
Figure 3.3. Comparison of masonry wall and 3D-printed concrete wall in different dimensions. 69
Figure 3.4. FE approach with detailed micro modeling [65]. 70
Figure 3.5. FE approach with detailed macro modeling [65]. 70
Figure 3.6. Macro model and some micro models for masonry structures [66]. 71
Figure 3.7. Linear solid (brick) element [69]. 72
Figure 3.8. Representation of the linear solid element with natural coordinates [69]. ...72
Figure 3.9. Stress-strain curve of the concrete used in 3DCP [23]. 74
Figure 3.10. M-C (red line) and D-P (blue line) yield criteria [28]. 75
Figure 3.11. M-C and D-P yield criteria on the stress plane [70]. 75
Figure 3.12. The displacement convergence graph for a wall with a solid topology, measuring 1000 mm in length, 200 mm in width, and 3000 mm in height. 80
Figure 3.13. The mesh system automatically generated as a result of the convergence study for a wall with a solid topology, measuring 1000 mm in length, 200 mm in width, and 3000 mm in height. 80
Figure 3.14. Fixed support boundary conditions applied to shear walls. 81
Figure 3.15. Load types applied to shear walls. 82
Figure 3.16. The analysis method used in numerical analyses. 83
Figure 3.17. The details of the analysis method used in numerical analyses. 84
Figure 3.18. Some of the pushover curves created according to the result of the numerical analyses for walls with solid topology. 86
Figure 3.19. Some of the pushover curves created according to the result of the numerical analyses for walls with solid topology. 87

Figure 3.20. Some of the pushover curves created according to the result of the numerical analyses for walls with solid topology..... 88
Figure 3.21. Some of the pushover curves created according to the result of the numerical analyses for walls with solid topology..... 89
Figure 3.22. Some of the pushover curves created according to the result of the numerical analyses for walls with solid topology..... 90
Figure 3.23. Some of the pushover curves created according to the result of the numerical analyses for walls with solid topology..... 91
Figure 3.24. Some of the pushover curves created according to the result of the numerical analyses for walls with solid topology..... 92
Figure 3.25. Some of the pushover curves created according to the result of the numerical analyses for walls with solid topology..... 93
Figure 3.26. Some of the pushover curves created according to the result of the numerical analyses for walls with solid topology..... 94
Figure 3.27. Some of the pushover curves created according to the result of the numerical analyses for walls with arch topology..... 95
Figure 3.28. Some of the pushover curves created according to the result of the numerical analyses for walls with arch topology..... 96
Figure 3.29. Some of the pushover curves created according to the result of the numerical analyses for walls with arch topology..... 97
Figure 3.30. Some of the pushover curves created according to the result of the numerical analyses for walls with arch topology..... 98
Figure 3.31. Some of the pushover curves created according to the result of the numerical analyses for walls with arch topology..... 99
Figure 3.32. Some of the pushover curves created according to the result of the numerical analyses for walls with arch topology..... 100
Figure 3.33. Some of the pushover curves created according to the result of the numerical analyses for walls with arch topology..... 101
Figure 3.34. Some of the pushover curves created according to the result of the numerical analyses for walls with arch topology..... 102
Figure 3.35. Some of the pushover curves created according to the result of the numerical analyses for walls with arch topology..... 103
Figure 3.36. Some of the pushover curves created according to the result of the numerical analyses for walls with cellular topology. 104

Figure 3.37. Some of the pushover curves created according to the result of the numerical analyses for walls with cellular topology. 105
Figure 3.38. Some of the pushover curves created according to the result of the numerical analyses for walls with cellular topology. 106
Figure 3.39. Some of the pushover curves created according to the result of the numerical analyses for walls with cellular topology. 107
Figure 3.40. Some of the pushover curves created according to the result of the numerical analyses for walls with cellular topology. 108
Figure 3.41. Some of the pushover curves created according to the result of the numerical analyses for walls with cellular topology. 109
Figure 3.42. Some of the pushover curves created according to the result of the numerical analyses for walls with cellular topology. 110
Figure 3.43. Some of the pushover curves created according to the result of the numerical analyses for walls with cellular topology. 111
Figure 3.44. Some of the pushover curves created according to the result of the numerical analyses for walls with cellular topology. 112
Figure 3.45. Some of the pushover curves created according to the result of the numerical analyses for walls with elliptic topology. 113
Figure 3.46. Some of the pushover curves created according to the result of the numerical analyses for walls with elliptic topology. 114
Figure 3.47. Some of the pushover curves created according to the result of the numerical analyses for walls with elliptic topology. 115
Figure 3.48. Some of the pushover curves created according to the result of the numerical analyses for walls with elliptic topology. 116
Figure 3.49. Some of the pushover curves created according to the result of the numerical analyses for walls with elliptic topology. 117
Figure 3.50. Some of the pushover curves created according to the result of the numerical analyses for walls with elliptic topology. 118
Figure 3.51. Some of the pushover curves created according to the result of the numerical analyses for walls with elliptic topology. 119
Figure 3.52. Some of the pushover curves created according to the result of the numerical analyses for walls with elliptic topology. 120
Figure 3.53. Some of the pushover curves created according to the result of the numerical analyses for walls with elliptic topology. 121

Figure 3.54. Some of the pushover curves created according to the result of the numerical analyses for walls with hollow topology. 122
Figure 3.55. Some of the pushover curves created according to the result of the numerical analyses for walls with hollow topology. 123
Figure 3.56. Some of the pushover curves created according to the result of the numerical analyses for walls with hollow topology. 124
Figure 3.57. Some of the pushover curves created according to the result of the numerical analyses for walls with hollow topology. 125
Figure 3.58. Some of the pushover curves created according to the result of the numerical analyses for walls with hollow topology. 126
Figure 3.59. Some of the pushover curves created according to the result of the numerical analyses for walls with hollow topology. 127
Figure 3.60. Some of the pushover curves created according to the result of the numerical analyses for walls with hollow topology. 128
Figure 3.61. Some of the pushover curves created according to the result of the numerical analyses for walls with hollow topology. 129
Figure 3.62. Some of the pushover curves created according to the result of the numerical analyses for walls with hollow topology. 130
Figure 3.63. Some of the pushover curves created according to the result of the numerical analyses for walls with lattice topology..... 131
Figure 3.64. Some of the pushover curves created according to the result of the numerical analyses for walls with lattice topology..... 132
Figure 3.65. Some of the pushover curves created according to the result of the numerical analyses for walls with lattice topology..... 133
Figure 3.66. Some of the pushover curves created according to the result of the numerical analyses for walls with lattice topology..... 134
Figure 3.67. Some of the pushover curves created according to the result of the numerical analyses for walls with lattice topology..... 135
Figure 3.68. Some of the pushover curves created according to the result of the numerical analyses for walls with lattice topology..... 136
Figure 3.69. Some of the pushover curves created according to the result of the numerical analyses for walls with lattice topology..... 137
Figure 3.70. Some of the pushover curves created according to the result of the numerical analyses for walls with lattice topology..... 138

Figure 3.71. Some of the pushover curves created according to the result of the numerical analyses for walls with lattice topology. 139
Figure 3.72. Some of the pushover curves created according to the result of the numerical analyses for walls with triangular-1 topology. 140
Figure 3.73. Some of the pushover curves created according to the result of the numerical analyses for walls with triangular-1 topology. 141
Figure 3.74. Some of the pushover curves created according to the result of the numerical analyses for walls with triangular-1 topology. 142
Figure 3.75. Some of the pushover curves created according to the result of the numerical analyses for walls with triangular-1 topology. 143
Figure 3.76. Some of the pushover curves created according to the result of the numerical analyses for walls with triangular-1 topology. 144
Figure 3.77. Some of the pushover curves created according to the result of the numerical analyses for walls with triangular-1 topology. 145
Figure 3.78. Some of the pushover curves created according to the result of the numerical analyses for walls with triangular-1 topology. 146
Figure 3.79. Some of the pushover curves created according to the result of the numerical analyses for walls with triangular-1 topology. 147
Figure 3.80. Some of the pushover curves created according to the result of the numerical analyses for walls with triangular-1 topology. 148
Figure 3.81. Some of the pushover curves created according to the result of the numerical analyses for walls with triangular-2 topology. 149
Figure 3.82. Some of the pushover curves created according to the result of the numerical analyses for walls with triangular-2 topology. 150
Figure 3.83. Some of the pushover curves created according to the result of the numerical analyses for walls with triangular-2 topology. 151
Figure 3.84. Some of the pushover curves created according to the result of the numerical analyses for walls with triangular-2 topology. 152
Figure 3.85. Some of the pushover curves created according to the result of the numerical analyses for walls with triangular-2 topology. 153
Figure 3.86. Some of the pushover curves created according to the result of the numerical analyses for walls with triangular-2 topology. 154
Figure 3.87. Some of the pushover curves created according to the result of the numerical analyses for walls with triangular-2 topology. 155

Figure 3.88. Some of the pushover curves created according to the result of the numerical analyses for walls with triangular-2 topology..... 156
Figure 3.89. Some of the pushover curves created according to the result of the numerical analyses for walls with triangular-2 topology..... 157
Figure 3.90. Some of the pushover curves created according to the result of the numerical analyses for walls with truss topology. 158
Figure 3.91. Some of the pushover curves created according to the result of the numerical analyses for walls with truss topology. 159
Figure 3.92. Some of the pushover curves created according to the result of the numerical analyses for walls with truss topology. 160
Figure 3.93. Some of the pushover curves created according to the result of the numerical analyses for walls with truss topology. 161
Figure 3.94. Some of the pushover curves created according to the result of the numerical analyses for walls with truss topology. 162
Figure 3.95. Some of the pushover curves created according to the result of the numerical analyses for walls with truss topology. 163
Figure 3.96. Some of the pushover curves created according to the result of the numerical analyses for walls with truss topology. 164
Figure 3.97. Some of the pushover curves created according to the result of the numerical analyses for walls with truss topology. 165
Figure 3.98. Some of the pushover curves created according to the result of the numerical analyses for walls with truss topology. 166
Figure 3.99. The load-displacement curve of the 3D-printed concrete shear wall with lattice internal topology. 167
Figure 3.100. Local damage region of a wall with a length of 1000 mm, width of 400 mm, thickness of 10 mm, height of 3000 mm, and cellular interior hollow topology.. 167
Figure 3.101. Flowchart of the procedure for FE models..... 169
Figure 3.102. SWOT analysis for applications of ML in the 3DCP field [10]..... 171
Figure 3.103. Possible solutions for problems that may arise from the use of ML in the field of 3DCP [55]. 172
Figure 3.104. Categorization of ML [1]. 175
Figure 3.105. Schematic representation of a MLP and a single neuron. 176
Figure 3.106. Workflow for conventional learning and deep learning [58]. 180
Figure 3.107. A typical CNN architecture. 180

Figure 3.108. Activation functions (a) Tanh activation function, (b) Sigmoid activation function, (c) ReLU activation function [84].....183
Figure 3.109. Adam optimizer algorithm [86]. 187
Figure 3.110. Comparison of different optimizers for the process of training multilayer neural networks with MNIST images [86].....188
Figure 3.111. The architectures of MLP models created for the displacement capacities of walls with an arch topology are as follows (a) model created using bias value, (b) model created without using bias value. 191
Figure 3.112. The architectures of MLP models created for the shear capacities of walls with an arch topology are as follows (a) model created using bias value, (b) model created without using bias value. 191
Figure 3.113. The architectures of MLP models created for the displacement capacities of walls with a cellular topology are as follows (a) model created using bias value, (b) model created without using bias value.....192
Figure 3.114. The architectures of MLP models created for the shear capacities of walls with a cellular topology are as follows (a) model created using bias value, (b) model created without using bias value. 192
Figure 3.115. The architectures of MLP models created for the displacement capacities of walls with an elliptic topology are as follows (a) model created using bias value, (b) model created without using bias value.....193
Figure 3.116. The architectures of MLP models created for the shear capacities of walls with an elliptic topology are as follows (a) model created using bias value, (b) model created without using bias value. 193
Figure 3.117. The architectures of MLP models created for the displacement capacities of walls with a hollow topology are as follows (a) model created using bias value, (b) model created without using bias value.....194
Figure 3.118. The architectures of MLP models created for the displacement capacities of walls with a hollow topology are as follows (a) model created using bias value, (b) model created without using bias value.....194
Figure 3.119. The architectures of MLP models created for the displacement capacities of walls with a lattice topology are as follows (a) model created using bias value, (b) model created without using bias value. 195

Figure 3.120. The architectures of MLP models created for the shear capacities of walls with a lattice topology are as follows (a) model created using bias value, (b) model created without using bias value. 195
Figure 3.121. The architectures of MLP models created for the displacement capacities of walls with a solid topology are as follows (a) model created using bias value, (b) model created without using bias value. 196
Figure 3.122. The architectures of MLP models created for the shear capacities of walls with a solid topology are as follows (a) model created using bias value, (b) model created without using bias value. 196
Figure 3.123. The architectures of MLP models created for the displacement capacities of walls with a triangular-1 topology are as follows (a) model created using bias value, (b) model created without using bias value..... 197
Figure 3.124. The architectures of MLP models created for the shear capacities of walls with a triangular-1 topology are as follows (a) model created using bias value, (b) model created without using bias value. 197
Figure 3.125. The architectures of MLP models created for the displacement capacities of walls with a triangular-2 topology are as follows (a) model created using bias value, (b) model created without using bias value..... 198
Figure 3.126. The architectures of MLP models created for the shear capacities of walls with a triangular-2 topology are as follows (a) model created using bias value, (b) model created without using bias value. 198
Figure 3.127. The architectures of MLP models created for the displacement capacities of walls with a truss topology are as follows (a) model created using bias value, (b) model created without using bias value. 199
Figure 3.128. The architectures of MLP models created for the shear capacities of walls with a truss topology are as follows (a) model created using bias value, (b) model created without using bias value. 199
Figure 3.129. The learning curves of the MLP models created for the displacement capacities of walls with an arch topology are as follows (a) plot for the model created using bias value, (b) plot for the model created without using bias value..... 200
Figure 3.130. The learning curves of the MLP models created for the shear capacities of walls with an arch topology are as follows (a) plot for the model created using bias value, (b) plot for the model created without using bias value. 200

Figure 3.131. The learning curves of the MLP models created for the displacement capacities of walls with a cellular topology are as follows (a) plot for the model created using bias value, (b) plot for the model created without using bias value. 201
Figure 3.132. The learning curves of the MLP models created for the shear capacities of walls with a cellular topology are as follows (a) plot for the model created using bias value, (b) plot for the model created without using bias value. 201
Figure 3.133. The learning curves of the MLP models created for the displacement capacities of walls with an elliptic topology are as follows (a) plot for the model created using bias value, (b) plot for the model created without using bias value. 202
Figure 3.134. The learning curves of the MLP models created for the shear capacities of walls with an elliptic topology are as follows (a) plot for the model created using bias value, (b) plot for the model created without using bias value. 202
Figure 3.135. The learning curves of the MLP models created for the displacement capacities of walls with a hollow topology are as follows (a) plot for the model created using bias value, (b) plot for the model created without using bias value. 203
Figure 3.136. The learning curves of the MLP models created for the shear capacities of walls with a hollow topology are as follows (a) plot for the model created using bias value, (b) plot for the model created without using bias value. 203
Figure 3.137. The learning curves of the MLP models created for the displacement capacities of walls with a lattice topology are as follows (a) plot for the model created using bias value, (b) plot for the model created without using bias value. 204
Figure 3.138. The learning curves of the MLP models created for the shear capacities of walls with a lattice topology are as follows (a) plot for the model created using bias value, (b) plot for the model created without using bias value. 204
Figure 3.139. The learning curves of the MLP models created for the displacement capacities of walls with a solid topology are as follows (a) plot for the model created using bias value, (b) plot for the model created without using bias value. 205
Figure 3.140. The learning curves of the MLP models created for the shear capacities of walls with a solid topology are as follows (a) plot for the model created using bias value, (b) plot for the model created without using bias value. 205

Figure 3.141. The learning curves of the MLP models created for the displacement capacities of walls with a triangular-1 topology are as follows (a) plot for the model created using bias value, (b) plot for the model created without using bias value. 206
Figure 3.142. The learning curves of the MLP models created for the shear capacities of walls with a triangular-1 topology are as follows (a) plot for the model created using bias value, (b) plot for the model created without using bias value. 206
Figure 3.143. The learning curves of the MLP models created for the displacement capacities of walls with a triangular-2 topology are as follows (a) plot for the model created using bias value, (b) plot for the model created without using bias value. 207
Figure 3.144. The learning curves of the MLP models created for the shear capacities of walls with a triangular-2 topology are as follows (a) plot for the model created using bias value, (b) plot for the model created without using bias value. 207
Figure 3.145. The learning curves of the MLP models created for the displacement capacities of walls with a truss topology are as follows (a) plot for the model created using bias value, (b) plot for the model created without using bias value..... 208
Figure 3.146. The learning curves of the MLP models created for the shear capacities of walls with a truss topology are as follows (a) plot for the model created using bias value, (b) plot for the model created without using bias value..... 208
Figure 3.147. The architectures of CNN models created for the displacement capacities of walls with an arch topology are as follows (a) model created using bias value, (b) model created without using bias value..... 212
Figure 3.148. The architectures of CNN models created for the shear capacities of walls with an arch topology are as follows (a) model created using bias value, (b) model created without using bias value..... 212
Figure 3.149. The architectures of CNN models created for the displacement capacities of walls with a cellular topology are as follows (a) model created using bias value, (b) model created without using bias value. 213
Figure 3.150. The architectures of CNN models created for the shear capacities of walls with a cellular topology are as follows (a) model created using bias value, (b) model created without using bias value..... 213

Figure 3.151. The architectures of CNN models created for the displacement capacities of walls with an elliptic topology are as follows (a) model created using bias value, (b) model created without using bias value. 214
Figure 3.152. The architectures of CNN models created for the shear capacities of walls with an elliptic topology are as follows (a) model created using bias value, (b) model created without using bias value. 214
Figure 3.153. The architectures of CNN models created for the displacement capacities of walls with a hollow topology are as follows (a) model created using bias value, (b) model created without using bias value. 215
Figure 3.154. The architectures of CNN models created for the displacement capacities of walls with a hollow topology are as follows (a) model created using bias value, (b) model created without using bias value. 215
Figure 3.155. The architectures of CNN models created for the displacement capacities of walls with a lattice topology are as follows (a) model created using bias value, (b) model created without using bias value. 216
Figure 3.156. The architectures of CNN models created for the shear capacities of walls with a lattice topology are as follows (a) model created using bias value, (b) model created without using bias value. 216
Figure 3.157. The architectures of CNN models created for the displacement capacities of walls with a solid topology are as follows (a) model created using bias value, (b) model created without using bias value. 217
Figure 3.158. The architectures of CNN models created for the shear capacities of walls with a solid topology are as follows (a) model created using bias value, (b) model created without using bias value. 217
Figure 3.159. The architectures of CNN models created for the displacement capacities of walls with a triangular-1 topology are as follows (a) model created using bias value, (b) model created without using bias value. 218
Figure 3.160. The architectures of CNN models created for the shear capacities of walls with a triangular-1 topology are as follows (a) model created using bias value, (b) model created without using bias value. 218
Figure 3.161. The architectures of CNN models created for the displacement capacities of walls with a triangular-2 topology are as follows (a) model created using bias value, (b) model created without using bias value. 219

Figure 3.162. The architectures of CNN models created for the shear capacities of walls with a triangular-2 topology are as follows (a) model created using bias value, (b) model created without using bias value. 219
Figure 3.163. The architectures of CNN models created for the displacement capacities of walls with a truss topology are as follows (a) model created using bias value, (b) model created without using bias value. 220
Figure 3.164. The architectures of CNN models created for the shear capacities of walls with a truss topology are as follows (a) model created using bias value, (b) model created without using bias value. 220
Figure 3.165. The learning curves of the CNN models created for the displacement capacities of walls with an arch topology are as follows (a) plot for the model created using bias value, (b) plot for the model created without using bias value. 221
Figure 3.166. The learning curves of the CNN models created for the shear capacities of walls with an arch topology are as follows (a) plot for the model created using bias value, (b) plot for the model created without using bias value. 221
Figure 3.167. The learning curves of the CNN models created for the displacement capacities of walls with a cellular topology are as follows (a) plot for the model created using bias value, (b) plot for the model created without using bias value. 222
Figure 3.168. The learning curves of the CNN models created for the shear capacities of walls with a cellular topology are as follows (a) plot for the model created using bias value, (b) plot for the model created without using bias value. 222
Figure 3.169. The learning curves of the CNN models created for the displacement capacities of walls with an elliptic topology are as follows (a) plot for the model created using bias value, (b) plot for the model created without using bias value. 223
Figure 3.170. The learning curves of the CNN models created for the shear capacities of walls with an elliptic topology are as follows (a) plot for the model created using bias value, (b) plot for the model created without using bias value. 223
Figure 3.171. The learning curves of the CNN models created for the displacement capacities of walls with a hollow topology are as follows (a) plot for the model created using bias value, (b) plot for the model created without using bias value. 224

Figure 3.172. The learning curves of the CNN models created for the shear capacities of walls with a hollow topology are as follows (a) plot for the model created using bias value, (b) plot for the model created without using bias value. 224
Figure 3.173. The learning curves of the CNN models created for the displacement capacities of walls with a lattice topology are as follows (a) plot for the model created using bias value, (b) plot for the model created without using bias value. 225
Figure 3.174. The learning curves of the CNN models created for the shear capacities of walls with a lattice topology are as follows (a) plot for the model created using bias value, (b) plot for the model created without using bias value. 225
Figure 3.175. The learning curves of the CNN models created for the displacement capacities of walls with a solid topology are as follows (a) plot for the model created using bias value, (b) plot for the model created without using bias value. 226
Figure 3.176. The learning curves of the CNN models created for the shear capacities of walls with a solid topology are as follows (a) plot for the model created using bias value, (b) plot for the model created without using bias value. 226
Figure 3.177. The learning curves of the CNN models created for the displacement capacities of walls with a triangular-1 topology are as follows (a) plot for the model created using bias value, (b) plot for the model created without using bias value. 227
Figure 3.178. The learning curves of the CNN models created for the shear capacities of walls with a triangular-1 topology are as follows (a) plot for the model created using bias value, (b) plot for the model created without using bias value. 227
Figure 3.179. The learning curves of the CNN models created for the displacement capacities of walls with a triangular-2 topology are as follows (a) plot for the model created using bias value, (b) plot for the model created without using bias value. 228
Figure 3.180. The learning curves of the CNN models created for the shear capacities of walls with a triangular-2 topology are as follows (a) plot for the model created using bias value, (b) plot for the model created without using bias value. 228
Figure 3.181. The learning curves of the CNN models created for the displacement capacities of walls with a truss topology are as follows (a) plot for the model created using bias value, (b) plot for the model created without using bias value. 229

Figure 3.182. The learning curves of the CNN models created for the shear capacities of walls with a truss topology are as follows (a) plot for the model created using bias value, (b) plot for the model created without using bias value. 229
Figure 3.183. The main screen includes different wall interior topologies (a) the main screen of the software developed for shear capacity prediction, (b) the main screen of the software developed for displacement capacity prediction. 232
Figure 3.184. The input screen includes the parameters of the wall for which capacity estimation will be performed (a) input screen of the software developed for shear capacity prediction, (b) input screen of the software developed for displacement capacity prediction. 233
Figure 3.185. The output screen displays the prediction made using pre-trained AI models (a) output screen of the program developed for shear capacity estimation, (b) output screen of the program developed for displacement capacity estimation. 233
Figure 3.186. Schematic representation of a typical unreinforced masonry structure under earthquake load [88]. 234
Figure 3.187. Failure modes of unreinforced in-plane masonry walls (a) rocking failure, (b) sliding failure, (c) diagonal tension failure [88] 235
Figure 4.1. The scatter plots for the displacement capacity data of walls with arch topology are as follows (a) plot for the training dataset of the CNN model with bias, (b) plot for the test dataset of the CNN model with bias, (c) plot for the training dataset of the CNN model without bias, (d) plot for the test dataset of the CNN model without bias. 238
Figure 4.2. The scatter plots for the displacement capacity data of walls with arch topology are as follows (a) plot for the training dataset of the MLP model with bias, (b) plot for the test dataset of the MLP model with bias, (c) plot for the training dataset of the MLP model without bias, (d) plot for the test dataset of the MLP model without bias. 239
Figure 4.3. The scatter plots for the shear capacity data of walls with arch topology are as follows (a) plot for the training dataset of the CNN model with bias, (b) plot for the test dataset of the CNN model with bias, (c) plot for the training dataset of the CNN model without bias, (d) plot for the test dataset of the CNN model without bias. 240
Figure 4.4. The scatter plots for the shear capacity data of walls with arch topology are as follows (a) plot for the training dataset of the MLP model with bias, (b) plot for the

test dataset of the MLP model with bias, (c) plot for the training dataset of the MLP model without bias, (d) plot for the test dataset of the MLP model without bias. 241
Figure 4.5. The scatter plots for the displacement capacity data of walls with cellular topology are as follows (a) plot for the training dataset of the CNN model with bias, (b) plot for the test dataset of the CNN model with bias, (c) plot for the training dataset of the CNN model without bias, (d) plot for the test dataset of the CNN model without bias. 242
Figure 4.6. The scatter plots for the displacement capacity data of walls with cellular topology are as follows (a) plot for the training dataset of the MLP model with bias, (b) plot for the test dataset of the MLP model with bias, (c) plot for the training dataset of the MLP model without bias, (d) plot for the test dataset of the MLP model without bias. 243
Figure 4.7. The scatter plots for the shear capacity data of walls with cellular topology are as follows (a) plot for the training dataset of the CNN model with bias, (b) plot for the test dataset of the CNN model with bias, (c) plot for the training dataset of the CNN model without bias, (d) plot for the test dataset of the CNN model without bias. 244
Figure 4.8. The scatter plots for the shear capacity data of walls with cellular topology are as follows (a) plot for the training dataset of the MLP model with bias, (b) plot for the test dataset of the MLP model with bias, (c) plot for the training dataset of the MLP model without bias, (d) plot for the test dataset of the MLP model without bias. 245
Figure 4.9. The scatter plots for the displacement capacity data of walls with elliptic topology are as follows (a) plot for the training dataset of the CNN model with bias, (b) plot for the test dataset of the CNN model with bias, (c) plot for the training dataset of the CNN model without bias, (d) plot for the test dataset of the CNN model without bias. 246
Figure 4.10. The scatter plots for the displacement capacity data of walls with elliptic topology are as follows (a) plot for the training dataset of the MLP model with bias, (b) plot for the test dataset of the MLP model with bias, (c) plot for the training dataset of the MLP model without bias, (d) plot for the test dataset of the MLP model without bias. 247
Figure 4.11. The scatter plots for the shear capacity data of walls with elliptic topology are as follows (a) plot for the training dataset of the CNN model with bias, (b) plot

for the test dataset of the CNN model with bias, (c) plot for the training dataset of the CNN model without bias, (d) plot for the test dataset of the CNN model without bias. 248
Figure 4.12. The scatter plots for the shear capacity data of walls with elliptic topology are as follows (a) plot for the training dataset of the MLP model with bias, (b) plot for the test dataset of the MLP model with bias, (c) plot for the training dataset of the MLP model without bias, (d) plot for the test dataset of the MLP model without bias. 249
Figure 4.13. The scatter plots for the displacement capacity data of walls with hollow topology are as follows (a) plot for the training dataset of the CNN model with bias, (b) plot for the test dataset of the CNN model with bias, (c) plot for the training dataset of the CNN model without bias, (d) plot for the test dataset of the CNN model without bias. 250
Figure 4.14. The scatter plots for the displacement capacity data of walls with hollow topology are as follows (a) plot for the training dataset of the MLP model with bias, (b) plot for the test dataset of the MLP model with bias, (c) plot for the training dataset of the MLP model without bias, (d) plot for the test dataset of the MLP model without bias. 251
Figure 4.15. The scatter plots for the shear capacity data of walls with hollow topology are as follows (a) plot for the training dataset of the CNN model with bias, (b) plot for the test dataset of the CNN model with bias, (c) plot for the training dataset of the CNN model without bias, (d) plot for the test dataset of the CNN model without bias. 252
Figure 4.16. The scatter plots for the shear capacity data of walls with hollow topology are as follows (a) plot for the training dataset of the MLP model with bias, (b) plot for the test dataset of the MLP model with bias, (c) plot for the training dataset of the MLP model without bias, (d) plot for the test dataset of the MLP model without bias. 253
Figure 4.17. The scatter plots for the displacement capacity data of walls with lattice topology are as follows (a) plot for the training dataset of the CNN model with bias, (b) plot for the test dataset of the CNN model with bias, (c) plot for the training dataset of the CNN model without bias, (d) plot for the test dataset of the CNN model without bias. 254

Figure 4.18. The scatter plots for the displacement capacity data of walls with lattice topology are as follows (a) plot for the training dataset of the MLP model with bias, (b) plot for the test dataset of the MLP model with bias, (c) plot for the training dataset of the MLP model without bias, (d) plot for the test dataset of the MLP model without bias. 255
Figure 4.19. The scatter plots for the shear capacity data of walls with lattice topology are as follows (a) plot for the training dataset of the CNN model with bias, (b) plot for the test dataset of the CNN model with bias, (c) plot for the training dataset of the CNN model without bias, (d) plot for the test dataset of the CNN model without bias. 256
Figure 4.20. The scatter plots for the shear capacity data of walls with lattice topology are as follows (a) plot for the training dataset of the MLP model with bias, (b) plot for the test dataset of the MLP model with bias, (c) plot for the training dataset of the MLP model without bias, (d) plot for the test dataset of the MLP model without bias. 257
Figure 4.21. The scatter plots for the displacement capacity data of walls with solid topology are as follows (a) plot for the training dataset of the CNN model with bias, (b) plot for the test dataset of the CNN model with bias, (c) plot for the training dataset of the CNN model without bias, (d) plot for the test dataset of the CNN model without bias. 258
Figure 4.22. The scatter plots for the displacement capacity data of walls with solid topology are as follows (a) plot for the training dataset of the MLP model with bias, (b) plot for the test dataset of the MLP model with bias, (c) plot for the training dataset of the MLP model without bias, (d) plot for the test dataset of the MLP model without bias. 259
Figure 4.23. The scatter plots for the shear capacity data of walls with solid topology are as follows (a) plot for the training dataset of the CNN model with bias, (b) plot for the test dataset of the CNN model with bias, (c) plot for the training dataset of the CNN model without bias, (d) plot for the test dataset of the CNN model without bias. 260
Figure 4.24. The scatter plots for the shear capacity data of walls with solid topology are as follows (a) plot for the training dataset of the MLP model with bias, (b) plot for the test dataset of the MLP model with bias, (c) plot for the training dataset of the

MLP model without bias, (d) plot for the test dataset of the MLP model without bias. 261
Figure 4.25. The scatter plots for the displacement capacity data of walls with triangular-1 topology are as follows (a) plot for the training dataset of the CNN model with bias, (b) plot for the test dataset of the CNN model with bias, (c) plot for the training dataset of the CNN model without bias, (d) plot for the test dataset of the CNN model without bias. 262
Figure 4.26. The scatter plots for the displacement capacity data of walls with triangular-1 topology are as follows (a) plot for the training dataset of the MLP model with bias, (b) plot for the test dataset of the MLP model with bias, (c) plot for the training dataset of the MLP model without bias, (d) plot for the test dataset of the MLP model without bias. 263
Figure 4.27. The scatter plots for the shear capacity data of walls with triangular-1 topology are as follows (a) plot for the training dataset of the CNN model with bias, (b) plot for the test dataset of the CNN model with bias, (c) plot for the training dataset of the CNN model without bias, (d) plot for the test dataset of the CNN model without bias. 264
Figure 4.28. The scatter plots for the shear capacity data of walls with triangular-1 topology are as follows (a) plot for the training dataset of the MLP model with bias, (b) plot for the test dataset of the MLP model with bias, (c) plot for the training dataset of the MLP model without bias, (d) plot for the test dataset of the MLP model without bias. 265
Figure 4.29. The scatter plots for the displacement capacity data of walls with triangular-2 topology are as follows (a) plot for the training dataset of the CNN model with bias, (b) plot for the test dataset of the CNN model with bias, (c) plot for the training dataset of the CNN model without bias, (d) plot for the test dataset of the CNN model without bias. 266
Figure 4.30. The scatter plots for the displacement capacity data of walls with triangular-2 topology are as follows (a) plot for the training dataset of the MLP model with bias, (b) plot for the test dataset of the MLP model with bias, (c) plot for the training dataset of the MLP model without bias, (d) plot for the test dataset of the MLP model without bias. 267
Figure 4.31. The scatter plots for the shear capacity data of walls with triangular-2 topology are as follows (a) plot for the training dataset of the CNN model with bias,

(b) plot for the test dataset of the CNN model with bias, (c) plot for the training dataset of the CNN model without bias, (d) plot for the test dataset of the CNN model without bias. 268
Figure 4.32. The scatter plots for the shear capacity data of walls with triangular-2 topology are as follows (a) plot for the training dataset of the MLP model with bias, (b) plot for the test dataset of the MLP model with bias, (c) plot for the training dataset of the MLP model without bias, (d) plot for the test dataset of the MLP model without bias. 269
Figure 4.33. The scatter plots for the displacement capacity data of walls with truss topology are as follows (a) plot for the training dataset of the CNN model with bias, (b) plot for the test dataset of the CNN model with bias, (c) plot for the training dataset of the CNN model without bias, (d) plot for the test dataset of the CNN model without bias. 270
Figure 4.34. The scatter plots for the displacement capacity data of walls with truss topology are as follows (a) plot for the training dataset of the MLP model with bias, (b) plot for the test dataset of the MLP model with bias, (c) plot for the training dataset of the MLP model without bias, (d) plot for the test dataset of the MLP model without bias. 271
Figure 4.35. The scatter plots for the shear capacity data of walls with truss topology are as follows (a) plot for the training dataset of the CNN model with bias, (b) plot for the test dataset of the CNN model with bias, (c) plot for the training dataset of the CNN model without bias, (d) plot for the test dataset of the CNN model without bias. 272
Figure 4.36. The scatter plots for the shear capacity data of walls with truss topology are as follows (a) plot for the training dataset of the MLP model with bias, (b) plot for the test dataset of the MLP model with bias, (c) plot for the training dataset of the MLP model without bias, (d) plot for the test dataset of the MLP model without bias. 273
Figure 4.37. The scatter plots for the shear capacity of walls with arch topology are as follows (a) plot for the shear capacity in case of the rocking failure, (b) plot for the shear capacity in case of the sliding failure, (c) plot for the shear capacity in case of the diagonal tension failure, (d) plot for the minimum shear capacity of three failure modes, (e) plot for the shear capacity predicted through AI-based design tool....281

Figure 4.38. The scatter plots for the shear capacity of walls with cellular topology are as follows (a) plot for the shear capacity in case of the rocking failure, (b) plot for the shear capacity in case of the sliding failure, (c) plot for the shear capacity in case of the diagonal tension failure, (d) plot for the minimum shear capacity of three failure modes, (e) plot for the shear capacity predicted through AI-based design tool. .. 282
Figure 4.39. The scatter plots for the shear capacity of walls with elliptic topology are as follows (a) plot for the shear capacity in case of the rocking failure, (b) plot for the shear capacity in case of the sliding failure, (c) plot for the shear capacity in case of the diagonal tension failure, (d) plot for the minimum shear capacity of three failure modes, (e) plot for the shear capacity predicted through AI-based design tool. .. 283
Figure 4.40. The scatter plots for the shear capacity of walls with hollow topology are as follows (a) plot for the shear capacity in case of the rocking failure, (b) plot for the shear capacity in case of the sliding failure, (c) plot for the shear capacity in case of the diagonal tension failure, (d) plot for the minimum shear capacity of three failure modes, (e) plot for the shear capacity predicted through AI-based design tool. .. 284
Figure 4.41. The scatter plots for the shear capacity of walls with lattice topology are as follows (a) plot for the shear capacity in case of the rocking failure, (b) plot for the shear capacity in case of the sliding failure, (c) plot for the shear capacity in case of the diagonal tension failure, (d) plot for the minimum shear capacity of three failure modes, (e) plot for the shear capacity predicted through AI-based design tool. .. 285
Figure 4.42. The scatter plots for the shear capacity of walls with solid topology are as follows (a) plot for the shear capacity in case of the rocking failure, (b) plot for the shear capacity in case of the sliding failure, (c) plot for the shear capacity in case of the diagonal tension failure, (d) plot for the minimum shear capacity of three failure modes, (e) plot for the shear capacity predicted through AI-based design tool. .. 286
Figure 4.43. The scatter plots for the shear capacity of walls with triangular-1 topology are as follows (a) plot for the shear capacity in case of the rocking failure, (b) plot for the shear capacity in case of the sliding failure, (c) plot for the shear capacity in case of the diagonal tension failure, (d) plot for the minimum shear capacity of three failure modes, (e) plot for the shear capacity predicted through AI-based design tool. 287
Figure 4.44. The scatter plots for the shear capacity of walls with triangular-2 topology are as follows (a) plot for the shear capacity in case of the rocking failure, (b) plot for the shear capacity in case of the sliding failure, (c) plot for the shear capacity in

case of the diagonal tension failure, (d) plot for the minimum shear capacity of three failure modes, (e) plot for the shear capacity predicted through AI-based design tool. 288
Figure 4.45. The scatter plots for the shear capacity of walls with truss topology are as follows (a) plot for the shear capacity in case of the rocking failure, (b) plot for the shear capacity in case of the sliding failure, (c) plot for the shear capacity in case of the diagonal tension failure, (d) plot for the minimum shear capacity of three failure modes, (e) plot for the shear capacity predicted through AI-based design tool....289

LIST OF TABLES

Table 1.1. Various application areas including AM of ML. 22

Table 1.2. The most commonly utilized ML and DL algorithms in the construction and building sector. 23

Table 3.1. Geometric parameters. 65

Table 3.2. Material parameters. 79

Table 3.3. Results of the displacement convergence study for a wall with solid topology, measuring 1000 mm in length, 200 mm in width, and 3000 mm in height. 80

Table 3.4. Percentage of linear pushover curves based on solidity ratio. 85

Table 3.5. Parameters used in MLP models and the value ranges of these parameters. 189

Table 3.6. Optimum parameter values of MLP models. 190

Table 3.7. Error values for MLP models. 209

Table 3.8. Optimum parameter values of CNN models. 211

Table 3.9. Error values for CNN models. 230

Table 4.1. Correlation coefficients obtained as a result of regression and correlation analyses. 274

Table 4.2. Determination coefficients obtained as a result of regression and correlation analyses. 275

Table 4.3. The number of parameters that the created models have, in case the optimum parameters are selected. 277

Table 4.4. Correlation and determination coefficients obtained as a result of regression and correlation analyses. 290

SYMBOLS AND ABBREVIATIONS

Symbols

A	Cross-sectional area of the wall
a	Regression constant
b	Bias
$\boldsymbol{b}$	Bias vector
b_{uv}	Regression coefficient of u to v
c	Cohesion for Mohr-Coulomb yield criterion
E	Modulus of elasticity
E_{cj}	Elasticity modulus of "j" daily concrete
f_c	Characteristic compressive strength of concrete
f_{cj}	Characteristic cylinder compressive strength of "j" daily concrete
f_t	Characteristic tensile strength of concrete
$f(x)$	Nonlinear activation function
g	ReLU activation function
$\boldsymbol{h}$	Feature vector of hidden layer
H_{eff}	Effective height of the wall
H_j	Output value from hidden layer j
h_w	Height of the wall
I'_1	First invariant of the effective stress tensor
I_i	Input value of input layer neuron i
J_2	Second invariant of the stress deviator tensor
k	Axial load ratio
K_j	Threshold value of hidden layer neuron j
L	Length of the wall

L_1	Loss function for L1 regularization
$max\{s(i)\}$	Maximum value in the dataset
$min\{s(i)\}$	Minimum value in the dataset
n	Number of variables in the X and Y series
N_1	First shape function of the linear brick element
N_2	Second shape function of the linear brick element
N_3	Third shape function of the linear brick element
N_4	Fourth shape function of the linear brick element
N_5	Fifth shape function of the linear brick element
N_6	Sixth shape function of the linear brick element
N_7	Seventh shape function of the linear brick element
N_8	Eighth shape function of the linear brick element
n_l	Number of connections in the lth layer response
P	Vertical compressive force on the wall
p	Axial pressure
R^2_{xy}	Coefficient of determination
r_i	Specific input data
r_{min}	The smallest input data
r_{max}	The largest input data
r_{xy}	Coefficient of correlation
$\widehat{U}$	Estimated value of assumed dependent variable
U	Assumed dependent variable
V	Assumed independent variable
V_{be}	Shear capacity for rocking failure
V_{dt}	Shear capacity for diagonal tension failure
V_u	Shear capacity for sliding failure

$\boldsymbol{w}$	Weight vector
w	Weight
$w_i x_i$	Weighted input from input layer neuron i
w_{ji}	Weight value used in calculating the value in hidden layer neuron j from input layer neuron I
w_l	Matrix of size d*n in the lth layer, where d is the number of filters in layer l
$\overline{X}$	Average of the variables in the X series
X_i	Variable value in the X series
$\overline{Y}$	Average of the variables in the Y series
$\hat{y}$	Predicted output
Y_i	Variable value in the Y series
α	Regularization parameter
β	Factor equal to 0.5 for fixed-free cantilever wall, or equal to 1.0 for fixed-fixed wall
δ_u	Ultimate displacement that the wall can undergo
ϕ	Angle of internal friction for Mohr-Coulomb yield criterion
γ	Friction coefficient
η	Natural coordinate of the linear brick element which corresponds to y direction
κ	Cohesion for Drucker–Prager yield criterion
λ	Angle of internal friction for Drucker–Prager yield criterion
μ	Natural coordinate of the linear brick element which corresponds to z direction
ν	Poisson's ratio
θ	Capacity reduction factor depending on aspect ratio
σ	Axial compressive strength

σ'_1	Major principal effective stress
σ'_2	Intermediate principal effective stress
σ'_3	Minor principal effective stress
ξ	Natural coordinate of the linear brick element which corresponds to x direction

Abbreviations

3DCP	Three-dimensional Concrete Printing
AEC	Architectural, Engineering, and Construction
AI	Artificial Intelligence
AM	Additive Manufacturing
ANN	Artificial Neural Networks
AR	Augmented Reality
BESO	Bi-directional Evolutionary Structural Optimization
BIM	Building Information Modeling
CAGR	Computer-controlled Placement Annual Growth Rate
CEM	Construction Engineering and Management
CI	Computational Intelligence
CNC	Computer Numeric Control
CNN	Convolutional Neural Networks
Cobot	Collaborative Robot
Conv Layer	Convolutional Layer
D-P	Drucker-Prager
DL	Deep Learning
ESO	Evolutionary Structural Optimization
FC Layer	Fully Connected Layer
FE	Finite Element
FE	Finite Element
FEMA	Federal Emergency Management Agency
FFBP	Feedforward Backpropagation
FNN	Feedforward Neural Networks
GP	Genetic Programming

GPU	Graphics Processing Unit
IoT	Internet of Things
M-C	Mohr-Coulomb
MAE	Mean Absolute Error
MAPE	Mean Absolute Percentage Error
ML	Machine Learning
MLP	Multilayer Perceptron
MOGOA	Multi-objective Grasshopper Optimization Algorithm
MSE	Mean Squared Error
ReLU	Rectified Linear Unit
TO	Topology Optimization
TS	Turkish Standard
TSC	Turkish Seismic Design Code for Buildings
TPMS	Triply Periodic Minimal Surface
SVM	Support Vector Machine
SWOT	Strengths, Weaknesses, Opportunities, and Threats

1. INTRODUCTION

Industry 4.0 represents the shift from conventional manufacturing practices to self-sufficient, intelligent systems that leverage cutting-edge digital technologies, marking what is referred to as the fourth industrial revolution. Similarly, the concept of Construction 4.0 considers the use of state-of-the-art cyber-physical systems, industrial manufacturing systems, and digital information processing technologies to redefine the design, operation, construction, and maintenance of building infrastructure and infrastructure, taking into account circularity [1]. Industrial manufacturing systems include prefabrication and off-site construction, 3D printing and assembly, cyber-physical systems such as robots, Internet of Things (IoT), collaborative robots (Cobots), and actuators, while digital information processing technologies include Building Information Modeling (BIM), artificial intelligence (AI), machine learning (ML), deep learning (DL), big data and data analysis, cloud computing, blockchain, digital twins, and augmented reality (AR). The application areas of artificial intelligence in the construction Industry 4.0 are given in Figure 1.1 [1].



Figure 1.1. Areas where AI is applied in Construction 4.0.

The construction sector, due to its wide scope and important support to other sectors, is a venture that practically carries great value in terms of creating facilities or assets. Due to increasing urbanization in several countries, the construction industry is anticipated to account for 13% of the global gross domestic product. As an example, in 2020, Saudi Arabia's construction and building industry had a gross domestic product of 2.62 trillion Saudi Riyals [2]. The construction industry in Saudi Arabia ranks as the second largest sector, following the oil industry. Therefore, the significance of the construction sector requires consideration of its environmental impacts and efficiency. Even modest improvements in the operational efficiency of the construction industry will have a substantial positive impact on both the world's population and economy [2]. In recent years, the construction sector has slowly begun to shift towards digital production processes [3]. Digital technology is bringing about a radical change in the construction sector, changing the rules of the game. In the last thirty years, digitalization has brought about clear changes in how human resources are utilized in the industry, prompting businesses to revise themselves in this regard [2]. The construction sector has lagged in terms of digitalization and productivity compared to most industrial organizations. Unlike many other sectors, digital technologies in the building and construction sector are just beginning to bring about fundamental changes [2].

The construction sector extensively utilizes concrete as the primary building material [1,4,5]. One field of study where a lot of new developments are seen is concrete technology [6]. Concrete is generally obtained by mixing Portland cement with sand, gravel, and water. The current global consumption of concrete is approximately 11 billion metric tons per year [5]. There are three main reasons for the widespread use of concrete. First, concrete has excellent water resistance. Concrete is the perfect material for buildings intended to store, control, and move water since it can survive the impacts of water without suffering significant damage, unlike wood or standard steel [5]. Today, the use of normal concrete in canal linings, dams, and pavements is a common practice in almost every part of the world. One of these applications, the Itaipu Dam, is shown in Figure 1.2 [5].



Figure 1.2. Itaipu Dam, Brasil [5].

Piles, foundations, bridge piers, pavements, columns, beams, roofs, external walls, and pipes, which are frequently exposed to moisture, are often constructed with reinforced concrete and prestressed concrete. An example of such an application is shown in Figure 1.3, which depicts the pipeline of the Central Arizona project [5].

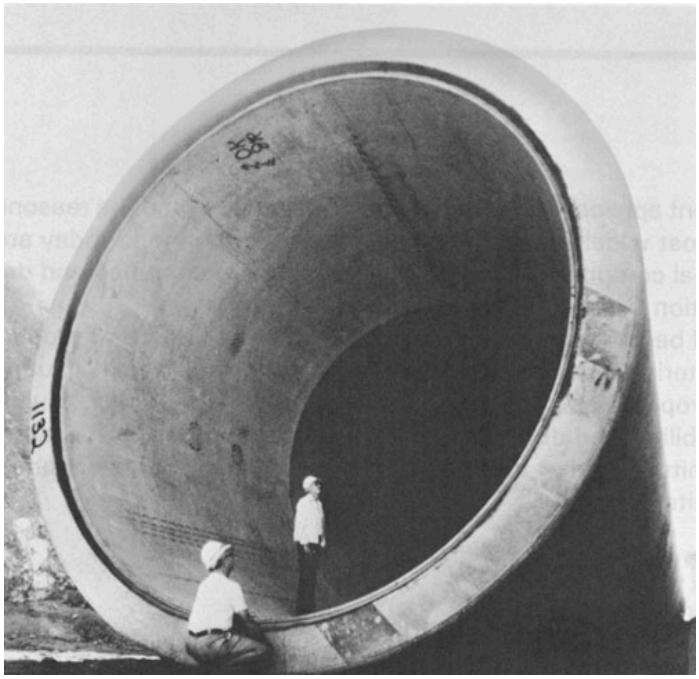

Figure 1.3. Central Arizona project pipeline [5].

The ease with which structural concrete components may be constructed in a variety of sizes and shapes, as illustrated in Figure 1.4, is the second reason for the widespread usage of concrete. This is because fresh concrete has a plastic consistency that allows it to be placed in the formwork, which is the mold for the material. After a few hours, when the concrete has hardened and solidified, the formwork can be removed for reuse [5].



Figure 1.4. Interior of the sports complex in Rome designed by Pier Luigi Nervi for the 1960 Olympic games [5].

The fact that concrete is typically the most affordable and readily available material is the third reason it is the most widely utilized material in the construction industry. Three readily available and reasonably priced fundamental materials are utilized to produce concrete: water, aggregate, and Portland cement. These materials are found all around the world. Depending on the transportation costs of its components, the price of concrete can range up to 75 to 100 US dollars per cubic meter in some geographical regions, while in other regions it can drop to 60 to 70 US dollars per cubic meter [5].

Some of the reasons for preferring concrete over steel as a building material are maintenance, fire resistance, and resistance to cyclic loading. The construction material is not corrosive, does not require any surface treatment and its strength continues to increase over time; so it requires very little maintenance. Concrete's fire resistance may

be the most important part of the safety of buildings, and it is also where concrete's advantages are most evident. The fatigue strength of steel structures is greatly affected by sudden changes in geometry, such as transitions from local stress zones in welded connections, corroded areas, and thin to thick frame connections [5]. For all these reasons, concrete has been preferred as the building material in this study.

Concrete is, in principle, a composite material composed of a binder medium with embedded particles or aggregates. In hydraulic concrete, the binder consists of a blend of hydraulic cement and water. Aggregate is a granular material used in the binder medium to manufacture concrete or mortar, including gravel, crushed stone, sand, construction and demolition waste, or crushed blast furnace slag. On the other hand, there's a mixture of sand, cement, and water in the mortar. Mortar resembles concrete without coarse aggregates. Cement, a finely ground dry material, does not possess binding properties on its own but gains binding properties as a result of hydration which is chemical reaction between water and cement minerals. If the products formed as a result of hydration exhibit stable behavior in a watery environment, the cement is called hydraulic cement. Hydraulic cement, as defined above in the concrete description, does not include the fourth component, which is a commonly used chemical admixture in modern concrete mixtures. Chemical admixtures are substances, distinct from aggregates, cement, and water, that are incorporated into a concrete mix either during the mixing process or at the time of mixing [5].

Depending on the application and performance requirements, different types of concrete are manufactured day after day. Based on the unit weights, concrete types may be grouped into three major categories. Depending on the application and performance requirements, different types of concrete are manufactured day after day. Based on the unit weights, concrete types may be grouped into three major categories. Concrete made with natural sand and gravel or crushed stone aggregates, usually having a density of approximately 2400 kg/m^3, is referred to as normal-weight concrete. The most common use in the construction industry is this type of cement [5]. The unit weight of concrete can be decreased by utilizing aggregates with low density, either naturally occurring or treated through pyroprocessing, for situations where a higher strength-to-weight ratio is needed.

Concrete with a density of around 1800 kg/m³ or less is known as lightweight concrete [5]. On the other hand, heavyweight concrete, which is used for radiation shielding, is produced using high-density aggregates and typically has a density exceeding 3200 kg/m³. In Europe and other countries, the classification of cement and concrete types according to their strengths is also common [5]. In this respect, concrete may be broadly classified on the basis of compression strength in three main categories. These are; high strength concrete, ordinary strong concrete, and lower strength concrete. The term low-strength concrete is used for concretes which have a compressive strength lower than 20 MPa, the term normal-strength concrete is utilized for concretes which have a compressive strength between 20 MPa and 40 MPa, and the term high-strength concrete is utilized for concretes which have a compressive strength higher than 40 MPa [5]. The term normal-strength concrete is also used for ordinary or normal concretes, which are the most commonly used in the construction sector. High-strength concretes are used in special applications [5]. In addition to these, there are many other concrete types such as expansive cement concrete, fiber-reinforced concrete, latex-modified concrete, cellular concrete, self-compacting concrete, and self-curing concrete [5,6]. New types of concrete can improve the performance of structures [4]. Despite all these developments, requirements that are of great importance to the construction sector, such as labor productivity, shortage of skilled workers, high energy consumption, shortened construction time, and reduced costs, are still not adequately met [4,7].

In this period characterized by global trends such as rapid urbanization, digitalization, and climate change, the construction sector needs to transform to meet the increasing demand for infrastructure while also reducing the environmental impact caused by practices in this sector [8]. Therefore, in recent years, the construction sector has gradually started to shift towards digital production processes [3]. To enhance the digital transformation process in the construction sector, there has been rapid progress in technology for process, control, material, and fresh concrete analysis in the field of three-dimensional concrete printing (3DCP), a type of additive manufacturing (AM) [3,8–11]. Due to its potential to meet the expectations of full automation in the construction sector, rapidly advancing 3DCP technology has gained a significant place that can set new horizons in the building sector [11–13]. This technology is also one of the current focal points within the scope of the term "Construction 4.0," which is used to express the

digitalization of the construction sector [14]. Automated production technologies like 3DCP have attracted significant interest in academia and industry, with many researchers worldwide working in this field [3]. In the past decade, there has been an increase in research on large-scale commercial applications of 3DCP in addition to the technology itself [3,15–18]. The growing number of large-scale commercial and residential infrastructure projects completed successfully in recent years has shown an increased interest and trend toward this technology [3,11,13,14,17]. At present, numerous research teams are exploring this technology to create innovative materials, models, and architectural designs that are beyond the scope of conventional construction methods [8,17,19]. This field has become increasingly important and popular today [3,14,17]. Recently, various studies have been published on concrete mix design and the properties of printed concrete materials using 3DCP [17]. The advancements in 3D concrete printing have enabled the evolution of design features, leading to the creation of houses, columns with organic-inspired forms, walls with tailored insulation properties, and even bridges [15]. Some practical applications of extrusion-based 3DCP technology are shown in Figure 1.5 [20]. In addition to all these, AM technology is also used in the polymer, metal, electronic, food, automotive, medical, security, and aerospace sectors [12,21]. This layer-by-layer production process is superior to traditional production methods in many aspects [16]. Various regions worldwide, including the United Kingdom, China, the Middle East, and the United States, are promoting the adoption of 3DCP technology through regulations and public initiatives [20].



(a) (b)

(c) (d)

(e) (f)

Figure 1.5. Some of the practical real-life applications of extrusion-based 3DCP technology (a) 3D printed multi-storey apartment building; Winsun, (b) the first office building produced with 3DCP technology in Dubai, (c) Europe's first building produced through 3DCP (The BOD), (d) two-storey administrative building in Dubai, (e) 3D Housing 05; Milan, (f) Woven Concrete Benches (XtreeE) [20].

With Industry 4.0, new methods are needed to address current issues in the architecture, engineering, and construction (AEC) industry, such as high energy consumption and

carbon dioxide emissions [22,23]. AM in the concrete construction industry was first extensively explored by Pegna and has since attracted considerable interest, as it became possible to produce structural elements in the desired geometry [24]. 3D printing, as a developing technology in automated construction, has introduced substantial transformations and new possibilities within the AEC sector [23,25]. Although 3D printers were invented in the 1980s, their potential use in construction was only recognized recently [22,25]. This technology, which allows shaping concrete without using traditional molds, has been developed over the past twenty years [20]. 3D printers were first used in the construction industry to propose contour crafting, using concrete as a special ink to create surfaces of desired shapes and construct buildings in a computer-controlled, layered manner [21,23]. Contour crafting is presently the most efficient technique for 3D construction. Subsequently, an optimized form of contour crafting was proposed, which, despite still relying on cement extrusion, enables much better control of both internal and external geometries, with a smaller deposition resolution in concrete printing technology [23]. The 3D printing technology for construction first emerged in the United States and, after decades of development, the most research and application reports in this sector are now prepared in the United States and China. Additionally, new 3D building printing technologies are being developed and implemented in Europe [10]. Although 3DCP in construction is a relatively new research area, it has been largely confirmed that this new construction technology offers significant advantages in terms of customization, construction speed, and mold savings [23]. Many researchers suggest that this technology should be used in larger construction projects and emphasize that it is a necessary technology for the Construction 4.0 field [25].

In a recent market assessment conducted by Allied Market Research, it is estimated that the global market share of 3DCP is approximately $310.9 million. According to the computer-controlled placement annual growth rate (CAGR) of 106.5% for 3D-printed cementitious mortars between 2020 and 2027, it is projected that the value of projects using extrusion-based 3DCP technology will reach $40.6 million by 2027 [11].

This AM technology is able to convert digital data from a computer model into a physical product [3]. 3D printing techniques can be divided into four main production processes:

molding techniques, subtractive manufacturing, hybrid methods, and additive methods (rapid prototyping) [22]. Subtractive manufacturing concerns cutting technologies where unwanted parts of objects are removed utilizing CNC (Computer Numeric Control) machines or analogous tools. Molding techniques include reshaping objects without adding or subtracting material. Hybrid techniques combine the best features of additive and subtractive manufacturing techniques [22]. AM, on the other hand, refers to the technique of constructing objects by sequentially layering materials based on 3D model data, unlike subtractive production methods such as traditional machining techniques that cause material removal [12,22,26]. Recently, the combination of cementitious materials and digital fabrication techniques has led to the improvement of innovative production processes for producing concrete-like products, structures, or objects [12]. Currently, technologies based on extrusion or particle bed approaches are actively being developed in this field [24]. These include layered extrusion (concrete printing, contour crafting, freeform construction), slip-forming, binder jetting (D-shape), and dynamic smart casting [12,26]. However, the most referenced term in this field is 3DCP, which is a production process based on extrusion [24]. 3D printing refers to obtaining a final model printed with AM techniques from a digital 3D model [9,20,26,27]. This process is also referred to as "digital manufacturing" or "automatic construction" due to the automation of the final printing process [20]. 3DCP uses digital data to fabricate the final product by utilizing the layer-by-layer addition technique to create functional building and structural components using the robotic concrete deposition process [20,27,28]. So, 3DCP refers to the technology that utilizes a robotic concrete printing process to produce functional building and structural components [28]. In this process, the product is a copy of a 3D model from which machine control operations are derived, similar to traditional AM processes [11]. With this technology, manufacturing can be done as desired using a 3D printer that can be automatically controlled, eliminating the need for molds as in traditional production techniques [9]. The 3DCP system typically consists of a mechanism (often a gantry system or an industrial 6-axis robotic arm) for precise positioning control of the concrete or cementitious mixture and pumping system [14,28]. The first step of the 3DCP process is the transportation of freshly mixed cementitious mortar from the pump to the nozzle, followed by the extrusion of the single filament material from the moving nozzle. After completing a single-layer print, the nozzle is raised to a certain height, and the printing process continues by extruding a new filament onto the previous layer. Finally, the concrete structure is produced through the layer-by-layer deposition method [18].

With the growing need for constructing intricate structures, digital fabrication methods like 3DCP have become increasingly vital [19]. 3DCP addresses safety and construction time requirements, while also cutting costs and fulfilling aesthetic demands [19,29]. It can precisely place materials in sequential layers in certain volumes through computer-controlled positioning [29]. Additionally, concerning the fabrication of concrete structures, some solutions have been proposed recently that utilize calculation and digital production, such as concrete shells cast onto textile molds to confine waste generated during production or printed space frame insulation walls that carry some of the weight of the concrete used in traditional building systems. These solutions emphasize manufacturing consciousness and material understanding in the design process. The 3D printing of materials such as concrete or cement can be shown as an excellent example of an object being produced as a result of the manufacturing process [15].

The 3DCP technology, due to its optimized material usage, provides extensive aesthetic possibilities for cost-effective, effortless, and rapid production of geometrically complex parts [4,19,29,30]. The construction industry utilizes more than 50% of the world's raw materials and accounts for 40% of the world's total energy consumption [6]. 3DCP allows the construction of structures in desired geometries, enabling the production of hollow, lighter structural components, or shell elements in desired geometries and thicknesses [2,3,6,8,9,12,14,18,22,25,26,30–34]. As a result, more durable structures can be built using less material and consuming less energy [3,6,10,22,26,27,32,35]. Compared to traditional production methods, 3DCP also leads to lower CO2 emissions and higher productivity [6,11,35]. This method, which falls under Construction 4.0, also enables better quality control and cost reduction through process and material optimization [2,9,14,15,18,20,22,25,26,28,30,31,35]. As it fully automates the extrusion-based production process, the 3DCP technique does not require mold use and requires much less labor compared to traditional methods [2,8–10,18,21,22,28,29,31,33,36,37]. Some other advantages of 3DCP include shorter construction times, the ability to build safe structures, ensuring safety on the construction site, and the ability to print in desired locations [2,8,9,12,14,15,19,29,35,36,38,39]. The construction sector, which has seen a significant increase in the number of people but a depletion of natural resources, accounts for 35% of all solid waste worldwide [15]. As the amount of waste material in the

construction sector will decrease thanks to 3DCP, this technology is also environmentally friendly [6,10,15,25,27]. With this technology, production can also be carried out with recycled waste materials, which is crucial for sustainability [6,40]. Additionally, with 3DCP, it is possible to build personalized structures, reconstruct structures after disasters, and even produce in very harsh environmental conditions [10]. For all these reasons, 3DCP has significant potential to improve the concrete construction phase compared to traditional production methods [24,41]. Therefore, this study focuses on 3D printing technology as a production technique.

In today's world, the most commonly used method in 3DCP is the trial-and-error method, which requires more time and cost for the development of the final product [3,14,20,36]. Most of the printing parameters are generally determined through a series of experiments using the trial-and-error method. However, the uncertainty remains as to whether the parameters determined by this method are optimal. In addition, experiments for large structures, which are encountered especially in engineering and architectural applications in daily life, use a lot of resources [3].

While experimental and theoretical studies form the basis of engineering research, numerical tools, and finite element (FE) analysis have played an important role in design, analysis, and predictions in the field of construction engineering in recent years [42]. Suitable structural analysis methods should be developed to make the production process more economical by overcoming the time loss and cost increase due to finding the optimum printing process and material mixture for the construction of structural elements using the trial-and-error method. However, in numerical models, material properties and loading characteristics, which have a variable nature, must also be properly modeled [41]. The numerical modeling of 3DCP processes is a developing and highly new research area with many problems and difficulties in mind, and studies in this area are still limited [11,24]. The primary challenges in numerically modeling these structures stem from the intricate characteristics and time-dependent properties of cement-based materials, which are complex, multi-scale, and evolve over time [17]. Another issue is the unique structure of concrete printed with 3D printers and the limited experimental data available on this subject. Therefore, studies are ongoing to create an optimal numerical and analytical

model for the 3DCP process [41]. Research on the numerical assessment and simulation of the mechanical performance of 3D-printed concrete elements after hardening is relatively scarce in the literature [11].

Numerical modeling of the 3DCP process offers several advantages [24]. Firstly, simulation of the printing process allows for predicting the structural behavior of concrete during the production stage and can anticipate when and how premature failure might occur [18,20,24,36]. This allows users to adjust printing settings, change materials, and modify geometry (especially in large overhangs) [20,24]. This is crucial for saving material and time, reducing wear on the machine, and minimizing setup time for the printing system. Additionally, through numerical simulation, it is possible to optimize the printing process for speed to maximize productivity. Therefore, by numerically modeling the printing process, optimal printing settings, material properties, or optimal geometry can be predetermined [24]. The printed structure may undergo excessive deformation compared to the originally designed geometry and become unusable. The second advantage of numerically modeling the 3DCP process is its ability to predict and potentially compensate for this deviation by changing appropriate parameters [24]. Thus, numerical analysis can also calculate deformations in the printed structure [18,20,24]. These adjustments are crucial for the successful printing of thin shell elements (subjected to axial loading) that are sensitive to geometric imperfections [28]. Finally, compared to experimental methods, numerical modeling is a cheaper, faster, and more easily controllable method [3]. With numerical modeling strategies developed specifically for elements printed through 3DCP, it is possible to structurally verify components without the need for large-scale destructive testing on the structure [11]. Consequently, structures can be produced more quickly and cost-effectively without trial and error [3,14,20,34,36,43,44]. Many studies on concrete elements printed through 3DCP consist of experimental studies [17]. However, it is suggested that for the use of AI techniques in the 3DCP field, the required data set should be produced not with numerous experiments but with numerical simulation [45]. For all these reasons, the data sets used in this study were obtained through numerical modeling.

Parametric design is one method to optimize the 3DCP process [32]. Many researchers in the 3DCP field use parametric modeling to create innovative and ambitious designs. Numerical models developed using parametric tools can be used to investigate material properties required for predefined geometries and printing settings. Thus, materials scientists can use preliminary test results to control the printability of a structure based on material characterization and use a suitable ML approach to find the most suitable material properties [24]. Although parametric design is more widely used and better known in other fields, its potential to transform the construction industry is gradually gaining attention. This method enables designers to adjust parameter values and create tailored versions of a predefined component. Design parameterization has many advantages. Thanks to parametric design, designers can easily change the design geometry with minimal effort and quickly customize the geometry of an element to meet customer requirements [32]. Additionally, geometric parameters (such as width, height, and thickness) can be used to optimize the design, as shown in Figures 1.6 and 1.7, by reducing the time required to obtain data necessary to make technical decisions and optimizing the design based on any need (aesthetics, functionality, or cost) [18,32,44,46]. The literature shows that adjusting input parameters (both machine and geometry-related) can improve the properties of the printed element [18,46]. Another advantage of parametric modeling is its ability to create a numerical model without the need for extensive manual modeling. Thus, automating the preprocessing step for numerical analysis and simulating the structural behavior of a randomly shaped object during printing is possible [24]. This method also provides the ability to find suitable material properties for a specific printed object at a desired printing speed or vice versa [19,24]. With parametric design, the printing process can be simulated and improved before physical experiments, thereby reducing material waste resulting from experiments. Additionally, various high-level programming languages such as C#, Python, or VB can be used in parametric modeling in addition to various computer-aided design or FE analysis programs [24]. Therefore, numerical analyses within the scope of this study were conducted using parametric modeling.



Figure 1.6. Vertico Valeiark project: Parametric design for façade [32].



Figure 1.7. Vertico parametric design made by rotating different parameters (such as height, rotation and radius) [32].

Considering the architectural design freedom that can affect the performance of structures produced through 3DCP, very few studies have been conducted on the capacity of large-scale concrete structural elements [4]. There is growing interest not just in modeling the printing process while the concrete is still fresh, but also in analyzing the mechanical performance of 3D-printed concrete structures once they have fully hardened [18]. Therefore, in this study, the capacities of hardened concrete elements have been considered.

Over the last decade, AM has identified a broad range of applications in different fields including the aerospace and automotive industries (car, satellite, and aircraft components), food industry (pizza, chocolate, meat), biomedical engineering (tissue scaffolds, prostheses, dental implants, bioprinting of organs), consumer goods industry (sports equipment, toys, electronics), civil engineering and architectural (structural elements, bridges, houses), weapon industry (weapon prototyping), pharmacokinetics (drug delivery devices), and fine arts and design (sculptures, paintings) [17]. Building walls are the most common application of 3DCP technology, as can be seen from the BOD building built by COBOD in Denmark, the Dubai Municipality building built by ApisCore in the United Arab Emirates, and Studio 2030 built by CyBe in Saudi Arabia [2]. Therefore, in the numerical analyses within the scope of this study, the shear and displacement capacity of shear walls printed through 3DCP is addressed. The examples given above are just a few of the possible systems that can be constructed through 3DCP, and it is also possible to construct different systems with 3DCP technology [2].

Key factors that significantly impact the drift capacity of walls include the axial load ratio, shear span, and the size of the walls [47]. As the axial load ratio increases in shear walls, both the initial stiffness and effective stiffness increase [48]. Shear walls exhibit sudden brittle failure when they are subjected to lateral reversed-cyclic loads under a high axial load ratio, thus losing their vertical load-bearing capacities [49]. Therefore, the axial load ratio is crucial for the shear and displacement capacity of shear walls and has been considered as a parameter in this study.

With the increasing demand for sustainable product development, scientists have started to focus on producing hollow structures with high strength and minimum weight [46]. Three-dimensional printing technology can be used to produce structures with random geometry and hollow interior topologies [46,50]. The development of new hollow concrete wall types can minimize the weight of the structure through smart design and topology optimization (TO) [50]. In particular, 3D-printed concrete hollow structures will have sustainable structural strength while being lighter [46,50]. Therefore, hollow structures designed with smart architecture have gained significant interest in the

construction sector due to their unique and superior properties, which cannot be achieved with traditionally designed solid structures. For example, structures designed with a honeycomb-like interior topology are used for damping purposes - to absorb energy and for easy packaging. Truss core sandwich panels have much higher bending strength, bending stiffness, and impact resistance compared to solid panels of the same mass. Hollow structural elements should be preferred for the construction of large lightweight structures [50]. Therefore, in this study, the capacities of shear walls with solid topology as well as shear walls with hollow topology have been calculated and compared.

The mechanical and functional properties mentioned above of hollow structures largely depend on the architectural and topological design of these structures [50]. Load-bearing walls are one of the most important parts of buildings printed through 3D printers [4]. However, there is no standard or optimum geometry for modeling these elements [3,4,6,7,11,24,41]. There is also not enough research in the literature on the numerical analysis of members with complex geometric shapes printed through 3DCP [11]. A comprehensive approach should be developed to systematically evaluate the mechanical strengths of different geometric configurations to select a hollow structure with optimum geometry [8,50]. Due to the geometric design freedom provided by 3DCP, optimizing the flow, design, calculations, and simulation of the concrete element printing process has become an important issue [32,33,46].

TO is a field that seeks to find the optimal architectural design layout under specified conditions [29,30]. Within this field, a mathematical approach is developed to improve the spatial distribution of a predefined material in the production stage, aiming to minimize the amount of material used, based on specific load and boundary conditions [2]. Producing more efficient structural elements through TO methods will not only lead to more robust designs but also contribute to the more economical design of structures in the fields of engineering, construction, and architecture [11]. The integration of 3DCP and TO enables the production of structurally efficient components with less material and cost, without the need for expensive molds and excessive labor [12,18,29,30,33]. Using less material with this method will also reduce the construction industry's negative impact on the environment [29]. Through the development of a parametric model during

optimization, FE models can be created in detail without the need for manual modeling [24]. Furthermore, 3DCP, due to the design freedom it provides, is highly compatible with TO, which limits the application of traditional methods [28–30]. Looking at the literature, it can be seen that adjusting both the geometry of the element to be printed and the input parameters related to the machine and the printing process appropriately can improve the properties of the printed structural element [46].

The application of TO in the construction industry is not a new concept. In the literature, TO has been utilized to increase structural efficiency by reducing material usage and enhancing structural rigidity [2,28,29]. Recently, comprehensive studies have been initiated to facilitate the integration of 3DCP and TO [18,30]. One of the significant examples of TO in architecture is the D-Shape printer, developed by Enrico Dini to realize the works of architect Andrea Morgante using a revolutionary construction method based on 3D printing technology. Another important project is the pedestrian bridge developed by Ghent University, which integrates TO and 3DCP [2]. In large-scale construction projects, combining 3DCP with TO facilitates the creation of structurally efficient buildings with striking and innovative designs [29,30]. Moreover, TO is highly effective in computational models, demonstrating its ability to provide reliable results [28]. For all these reasons, this study focuses on the topological optimization of various wall sections produced with 3DCP.

Many researchers have developed physics-based models to improve the properties of hollow members printed through 3D printers. However, these formulations require a deep understanding of the production process, which can be very laborious. As an alternative to this method, predictions can be made using only the acquired data. Data-driven approaches to modeling physical events are highly appreciated due to their significant and increasing successes [43,51]. The most recent studies in the construction field regarding these approaches are related to design and TO [43]. Most optimization applications are primarily carried out utilizing optimization algorithms like second-order cone optimization, linear programming, and metaheuristic optimization algorithms, as part of ML/DL optimization processes, mainly used in feature prediction. In the field of

material optimization, ML/DL has been commonly used in studies focusing on environmental impact, cost, and strength [1].

Mathematical techniques covering a wide range of problems have been used to solve numerous issues in the field of science and technology. In spite of their excellent performance, mathematical processes are still confronted with considerable difficulties to in overcoming optimization problems. The use of mathematical algorithms appears to be the most appropriate solution, given the growing complexity of optimization problems. Metaheuristic algorithms are algorithms designed and inspired by nature. There are a lot of algorithms replicating phenomena, like social behavior, competition between humans, or natural responses [52]. Their most important feature is the ability to escape from local optimal points. Swarm-based algorithms simulate species-specific social features such as the division of labor in food collection or pattern formation. Evolutionary algorithms simulate natural evolution, including selecting the most suitable individuals for reproduction to ensure the continuation of species [52]. The evolution from Construction 4.0 to Construction 5.0 in the future will close the gaps in Construction 4.0 and integrate the intelligence factor that has been lacking in the construction industry so far. This approach will allow us to merge the capabilities of precise, accurate, and smart machines with human creativity and skill. Furthermore, embracing AI in a human-centered way will offer personalized solutions and environmentally friendly production. With the increasing integration of AI into Construction 5.0, smart, human-centered design, production, and maintenance will emerge. In the future, customers will have access to more customized designs through 3D printing technology [1]. AI and ML are frequently used in new studies initiated to tackle the complex relationship between print quality and process parameters in 3DCP through regression analysis and pattern recognition. Applying ML to cementitious materials is not a new field, and it has been used in the literature for the prediction of microstructure development, cement phase analysis, concrete mix design, and estimation of fresh and hardened properties [17]. AI techniques have recently been used in structural optimization, mechanical analysis, and structural health monitoring fields as well [53]. The evolution of ML applications in 3DCP over time is shown in Figure 1.8 [10]. As can be seen from this figure, research and applications in this field, especially after 2010, have been further developed, and

scientific studies have gradually entered a period of rapid development [10,21,51]. Thus, the use of AI techniques in 3DCP technology is increasing [21,51,52,54].

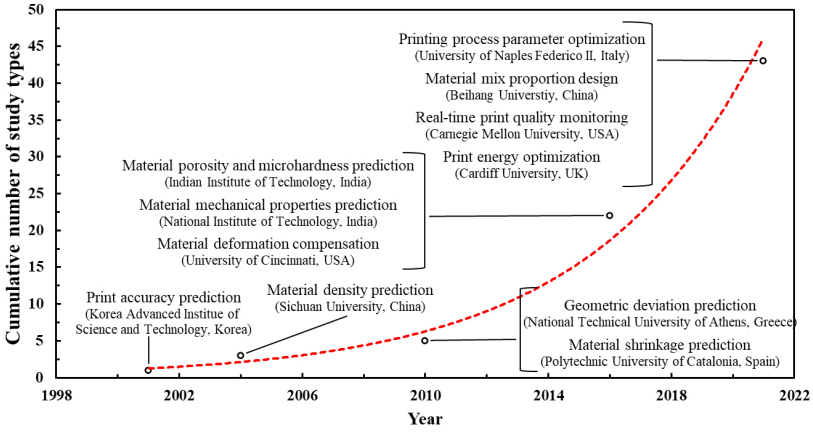

Figure 1.8. The evolution of ML applications in 3DCP [10].

Simulating and forecasting the entire 3D printing process and the performance of the printed material using physics-based models is nearly unfeasible [17]. With the ML approach, optimal material parameters and geometric parameters can be found without the need for preliminary experimental studies and simulation test results [1,20,54]. ML can learn new things from the available data by applying certain algorithms and managing the data. After the algorithm has sufficiently learned from the available data, it is termed a 'model' and used to generate predictions [55]. Therefore, data-driven models are largely of interest [17,51]. Statistics fundamentally focuses on making inferences about a population using a sample from that population, while the fundamental goal of ML is to identify predictive patterns in data that can be generalized [1]. Many numerical models are expensive in terms of computational cost because they require a detailed and fine mesh generation process [18,43,53]. However, a well-designed ML model can make intelligent decisions by accurately calculating the importance of input features [1,53]. Moreover, the current research trend in the scientific community is to automatically adjust knowledge-based intelligence (i.e., ML and DL) to achieve more reliable decisions, thus integrating these methods into the industry at a higher level [54]. Through AI, a large amount of data can be generated and systematically analyzed, facilitating the development of novel architectural and structural designs. This technology enhances safety in construction and operations, lowers energy consumption during production,

speeds up construction processes to minimize project duration, reduces costs, decreases labor requirements, and promotes sustainability [1,10,40,51,55,56]. ML-based models can efficiently establish relationships that include features extracted from inputs and outputs, without requiring significant human intervention and fracture mechanics knowledge [40,45,53]. Alongside data gathered from research and laboratory experiments, substantial volumes of data are also collected from the routine operations within the manufacturing sector. The gathered data stands out not only because of its quantity but also due to its distinct variations and diversity when compared to typical data sets [55]. Analyzing a very large number of data and recognizing patterns with computer programs using rule-based approaches is not possible with human hands or other traditional methods [1,55]. With the development of data collection and storage systems, data-driven ML techniques have gained wide application in digital manufacturing systems for finding hidden information and creating overly complex connections [10,45]. With the use of the correct data set, ML models can learn hidden patterns in quality assurance, process improvement, and system development to improve decision-making [10,57]. Therefore, AI's ability to process large amounts of data, create large-scale statistical models and recognize models provides significant facilitation in the processing of digitized data in the Construction 4.0 field [1,51].

ML has a wide range of applications in AM. These applications are shown in Table 1.1 [55]. ML algorithms have also started to be integrated into 3DCP processes and are changing the future of intelligent and digital manufacturing [1]. One of the benefits of AI that offers more optimized solutions in 3DCP is increasing levels of automation, using more advanced robots to manufacture and design structures according to desired shapes [1,18]. Additionally, with this method, 3DCP simulation can be performed with a limited amount of data [18]. ML techniques can also predict the behaviors of members printed through 3DCP technology, both in their fresh state and in their hardened state (such as fracture behavior) [40,51,53]. Furthermore, ML and DL are widely used in the construction industry for various purposes like durability assessment and system reliability, structural damage diagnosis and identification, structural strength estimation, and structural health monitoring studies for frames, dams, buildings, bridges, tunnels, metros, and other types of structures, and this approach has been very successful in these areas [1,40,51,54]. In addition, AI methods are widely used in areas such as fatigue

analysis, buckling analysis, and strength and performance prediction of structural elements [1,51]. In recent years, advancements in computational power through high-performance graphics processing units (GPUs), improvements in ML and DL algorithms, and the availability of ML and DL libraries and software for popular programming languages have made many of these applications feasible [1]. Utilizing ML, a subfield of AI, and its subfield DL, within the framework of Construction 4.0 allows for research in various domains, including architectural design, visualization, structural design and analysis, material optimization, offsite production and automation, progress tracking, construction management, safety measures, building management, health monitoring of structures, intelligent operations, lifecycle assessment, durability of buildings, and circular economy practices [1,18,43]. Although ML is widely used in 3DCP technology, more research is needed on integrating ML into 3DCP [10].

Table 1.1. Various application areas including AM of ML.

Algorithm	Application
Forward propagation	Creating a biomimetic rod using 3D printing with excellent resistance to buckling.
Bayesian optimization	Designing soft ionic polymer metal composite actuators for use in soft robotics.
Hierarchical clustering through SVM	Recommendations for design features in the conceptual design stage.
Induction rule, decision tree, and Naïve Bayes	Constructing the optimal relationship between the risks of deformation and the quality of the part to be manufactured using electron beam melting.
CNN	Forecasting mechanical characteristics and creating new microstructural patterns.
	Studying the maximum stress and its relationship with the layers underneath.
	Utilized for coarse-graining, which involves designing and analyzing materials without requiring complete microstructural data.

SVM including attitude signals	Fault diagnosis.
Offline DNN	Enhancement of the fundamental failure mechanisms in the AM process.
Deep CNN	Automated detection of defects in layer printing.
CNN and linear model	Predicting mechanical properties using limited training datasets.
SVM and hierarchical clustering	For assistance in recommending design features, enabling design freedom associated with additive manufacturing.
Self-organizing map of ANN	Adjusting the microhardness and microstructure using mechanistic modeling.
Linear regression model and CNN	Optimizing the printing orientation considering build time and part mass.
Feedforward ANN	Adjusting the geometry of the STL file based on the simulated defects generated.
ANN including a fully connected layer, LSTM cells, and a fully connected linear output layer	Decrease in the length of time it takes to compute from hours to milliseconds.
Resilient backpropagation method on ANN	Predicting layer thickness, raster angle, orientation, width, and air gap.
ANN	Predicting laser power, hatch spacing, scanning speed, layer thickness, and powder temperature.
CNN and linear SVM	Evaluating discontinuities like incomplete fusion, cracks, porosity, or inclusions.

Table 1.2. The most commonly utilized ML and DL algorithms in the construction and building sector.

ML Algorithm	Description

Logistic regression	This technique is a supervised algorithm mainly applied in binary classification, offering probability estimates for the different classification categories.
SVMs	The SVM algorithm is used for classification and outlier detection, but it is mainly employed for classification. In order to determine the data points, it's looking for an optimum hyperplane in a N-dimensional space.
Linear regression	This method is a supervised approach that identifies the linear line that best fits the provided data.
K-nearest neighbors	This method is applicable to both classification and regression tasks. Based on the neighboring data points in the dataset, it will calculate the probability of a particular data point belonging to this category.
Decision trees	Decision trees represent another supervised ML approach suitable for both regression and classification problems. This technique builds a tree-structured model that uses simple decision rules to predict the class or value.
Random forests	This algorithm involves an ensemble of decision trees, designed to produce more precise and consistent outcomes by aggregating the results of multiple trees.

Since 2006, researchers have demonstrated the success of DL in many application areas such as speech recognition, computer vision, image feature coding, handwriting recognition, semantic classification, robotics, and information retrieval [58]. With DL techniques, results can be obtained much faster compared to traditional analysis methods (such as the FE method), which have high computational costs. Using DL, results can be obtained by bypassing traditional numerical simulation methods [43]. Therefore, numerous researchers in construction and structural fields have explored DL algorithms [1,55]. Table 1.2 provides an overview of commonly employed ML and DL algorithms in these areas, along with brief descriptions [1].

ML methods can be divided into many categories. One of the most common methods used to categorize ML models is by evaluating the level of supervision they obtain during

the training phase. In this context, ML models can be classified into three classes: supervised, unsupervised, and reinforced learning [53]. DL is an extended version of supervised learning [58]. The two most commonly used tasks for supervised learning are classification and regression [53].

In today's forecasting analysis, the application of various ML algorithms that can learn from large data from different sources and predict new inputs is increasing [54]. The areas where AI, ML, and DL methods are applied, along with the most commonly used algorithms, are given in Figure 1.9 [1]. In particular, the ensemble model, along with artificial neural networks (ANN) and support vector machines (SVM), are increasingly employed [46,54]. In addition, in many studies in the 3DCP field, various computational intelligence (CI) methods like genetic programming (GP), fuzzy logic, and DL methods have also been used [1]. Nonetheless, in machine learning, artificial neural networks (ANN) are the most frequently utilized algorithms and are constantly evolving thanks to the accessibility of large datasets and computational power [45]. A review of the literature reveals that ANN has been frequently used in recent years in studies in the field of civil engineering [52]. Research employing artificial neural networks primarily concentrates on predicting the mechanical characteristics of concrete, including tensile strength, compressive strength, and modulus of elasticity [1,51,56]. Studies have shown that ANN performs very well in regression problems [56]. In recent years, studies have also begun on the properties of recycled concrete aggregates, fiber-reinforced polymers, and permeable pavements, as well as their effects on the durability of concrete (chloride penetration, sulfate attack, carbonation depth) [1]. ANN, one of the most effective AI algorithms, can also be used to solve multi-parameter nonlinear problems [27]. ANN can be used at every stage of 3DCP technology, including model design, printing process, material selection, and evaluation and characterization of the printed component [45]. Among the varieties of ANN, multilayer perceptron (MLP) and convolutional neural networks (CNN) can be used to adjust the optimum printing parameters and minimize printing errors [10,45,58]. MLPs have a wide range of applications in civil engineering. Researchers have used ANN in various areas such as regression of material properties, structural analysis, and failure or damage of materials [43]. A comparison of the efficiency of ANN and CNN in optimizing 3D printing features for efficiency is also seen in the literature. In this study, a classification problem rather than a regression problem is

addressed. Another comparison study is the comparison of traditional ANN with CNN for optimizing 3DCP properties for the tensile strength of the exoskeleton of a sample [58]. Additionally, ANN can also predict the final surface quality of a product printed with 3DCP [18].

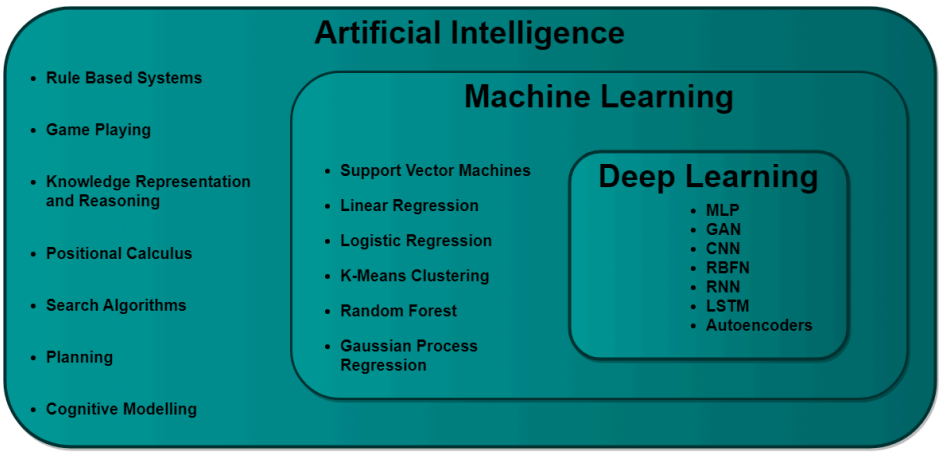

Figure 1.9. Areas where AI, ML, and DL methods are applied, along with the most commonly used algorithms.

DL is typically accomplished by using a stack of layers called a neural network. CNN, a stack of layers, is a widely used technique in DL today due to the increasing computational power of computers. Because of the existence of long computational paths, DL algorithms are generally more useful than ML algorithms in problems involving high-dimensional data such as videos, images, and audio [1]. In other words, more sophisticated structures are required to design networks with higher accuracy [56]. The popularity of DL is due to two main reasons: reducing hardware costs and increasing the computational capacity of processors (e.g., GPUs). CNN is a powerful technique that can be used for solving various complex problems through DL [58].

CNN models can be used instead of traditional numerical analysis methods. Many recent studies have shown that CNN can be used to predict the mechanical behaviors of heterogeneous materials. In the literature, it can be seen that CNN is used for determining the stress-crack width curve and crack pattern for this purpose. CNN provides successful results with low errors in this field [53]. However, CNN is mostly used for classification problems on visual data, which is mostly two-dimensional [1,58]. In addition, CNN can be specifically used for optimizing performance in the design of self-learning algorithms

for 3D printing materials, optimizing 3DCP properties, predicting the stiffness and toughness of composite materials, and predicting the stress distribution in steel plates with varying loading types and boundary conditions [10,43,51,58]. In some cases, ANN algorithms can work faster than CNN algorithms, but CNN algorithms can achieve higher accuracy. CNN, and thus DL, have a higher potential for solving problems requiring complex calculations compared to traditional ANN [58]. MLP and CNN algorithms were used in this study to create the network necessary to design 3D-printed concrete walls due to the success of MLP and CNN algorithms in predicting the capacity of structural members (Figure 1.9) [50].

In 3DCP, the design of each wall should be done correctly, taking into account wind intensity at the construction area, seismic hazards at the construction site, and potential dynamic and dead loads on the wall. Therefore, the construction of all structures printed through 3D printers starts with completing the design of these structures in an office environment. Nonetheless, this method greatly limits the ability of 3DCP technology to achieve full automation in manufacturing. Therefore, in this study, a new method has been proposed for fully automating the 3DCP process from the design stage to the construction stage. The initial stage of this proposed method is the development of an automated structural design tool. In this context, an AI-based design tool has been developed by optimizing the 3D-printed concrete wall topology with AI techniques to realize the design of concrete structures printed by 3D printers on-site. The dataset required for the AI model was obtained through numerical modeling. Numerical analyses were performed using the same parameters for various wall topologies. In these analyses, parameters such as wall thickness, wall length, thickness of elements for hollow walls, wall height, axial load ratio, tensile strength, compressive strength, elasticity modulus, internal friction angle, and cohesion were used. The walls were subjected to nonlinear static analysis under axial pressure, and the load-carrying capacity of each wall was determined. The obtained data were used as a dataset in MLP and CNN models, which are two different AI techniques. After creating a dataset through finite element analyses, optimum hyperparameter values for AI models were calculated using pre-determined value ranges. Subsequently, correlation and regression analyses were performed by using actual values and predicted values through artificial intelligence models to determine the most efficient model. As a next step, two AI-based design tools were developed in

executable format for predicting both displacement and shear capacity using the Python programming language. Most efficient AI models were employed in these design tools. Finally, the predicted shear capacity values obtained through the AI-based design tool were compared with the calculated shear capacity values according to building codes or standards to demonstrate the efficiency of the developed AI-based design tool. A flowchart of the main methodology is given in Figure 1.10.

This study aims to automatically determine the most cost-effective and lightweight cross-section design that meets the required strength using an AI-driven design tool, avoiding trial and error, while also conserving materials and energy. The proposed design tool allows all design calculations to be performed on a computer controlling the 3D concrete printer. After these design calculations, the structure can be printed automatically at the construction site (Figure 1.11). This holistic approach to 3D printing can eliminate the need for manpower in the design and construction stages.

In addition to all these, it is also aimed to find the model with the highest accuracy and the lowest number of parameters by comparing two different AI models and reducing the computation cost. As can be seen from Tables 1.1, and 1.2, CNN, a DL method, has never been used in regression tasks in the 3DCP field before. One of the innovative aspects of this study and its contributions to the literature is the use of CNN, a DL method, for regression problems in the 3DCP field.

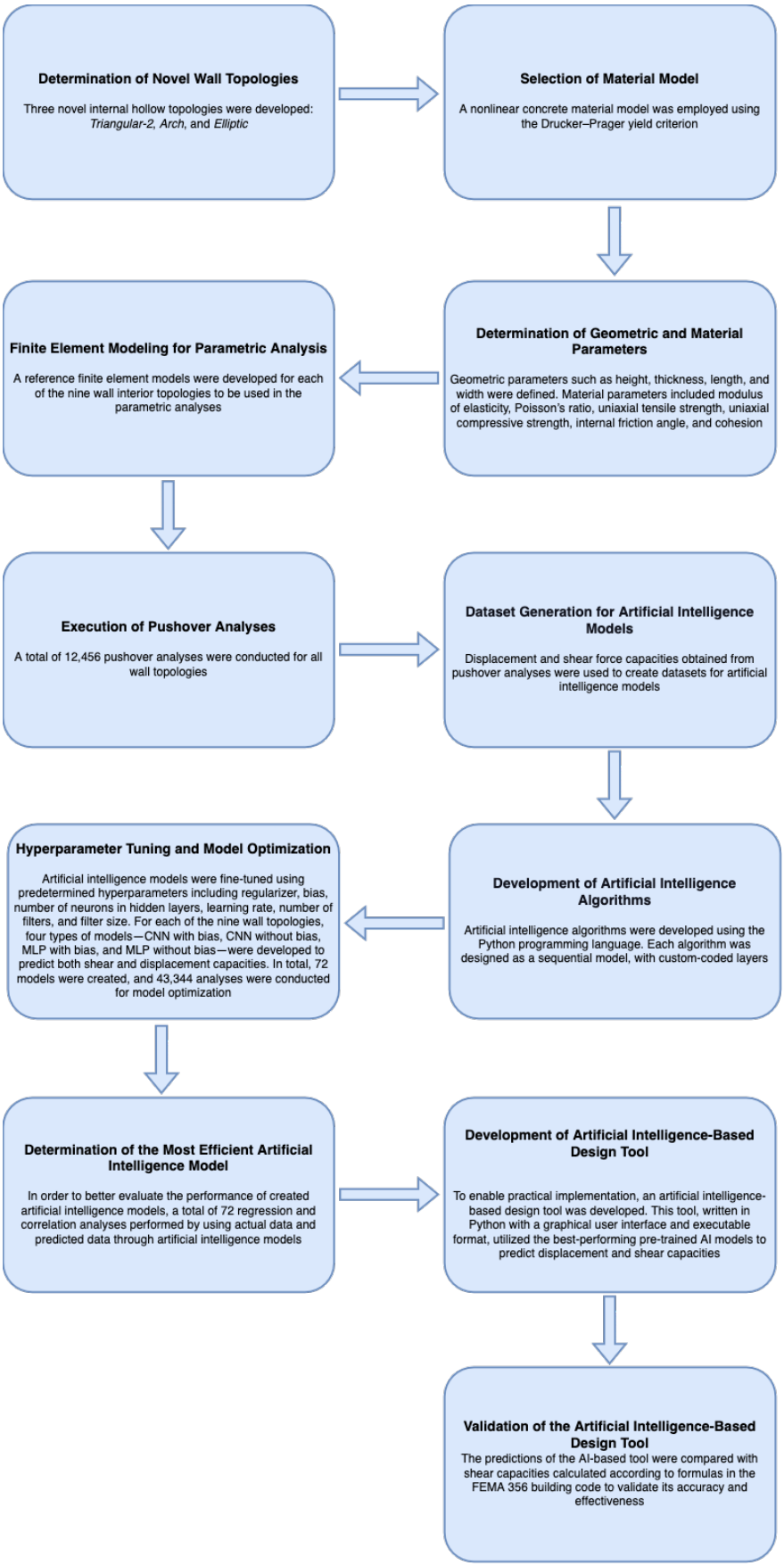

Figure 1.10. Flow-chart of the main methodology.

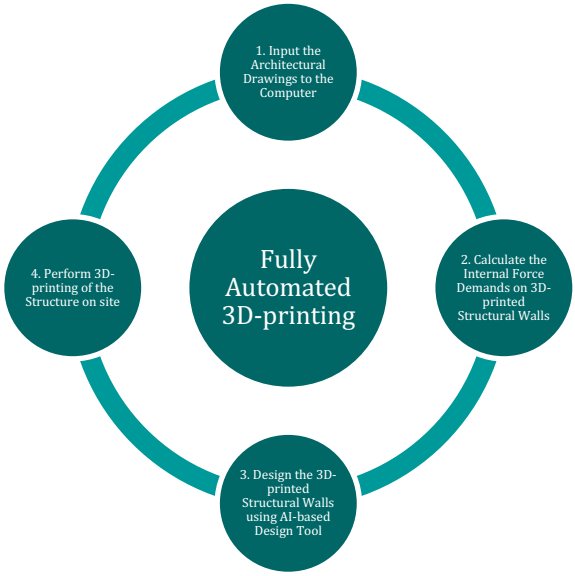

Figure 1.11. Flow-chart of the proposed holistic approach to achieve fully-automated 3D printed structures.

2. LITERATURE REVIEW

Integration between 3DCP and TO, i.e., optimization of wall cross-section, enables the production of structurally efficient components in terms of material and cost without requiring expensive molds and excessive labor [12,18,29,30,32]. Recently, AI techniques have been utilized in mechanical analysis, structural health monitoring, structural optimization, cement phase analysis, concrete mix design, prediction of microstructure development, and estimation of fresh and hardened features of structural elements and materials [17,53]. The use of AI techniques in 3DCP technology is rapidly increasing over time [21,51,52,54].

In summary, simulating and predicting the entire performance of the 3D printing process and the printed material with physics-based models is almost impossible [17]. However, with the ML approach, optimal material parameters and geometric parameters can be found without the need for preliminary experimental studies and simulation test results [1,20,54]. Many numerical models are computationally expensive due to the need for a detailed and precise meshing process [18,43,53]. However, a well-designed ML model can make intelligent decisions by accurately calculating the importance of input features [1,53]. With the help of AI, it is possible to create innovative architectural and structural designs, reduce the amount of energy required for production, increase construction safety and operational security, shorten production time by increasing construction speed, reduce the required labor force, reduce costs, and increase sustainability by generating a large amount of data and systematically analyzing this data [1,10,40,51,55,56]. ML-based models do not necessitate considerable human intervention or knowledge about fracture mechanics but can establish a relationship that includes properties obtained from inputs and outputs [40,45,53]. The ability of ML to recognize patterns in the model, process large amounts of data, and create large-scale statistical models provides a significant advantage in processing digitalized data in the Construction 4.0 field [1,51].

Since 2006, researchers have proven the success of DL and ML in various application areas such as computer vision, image processing, speech recognition, semantic

classification, information retrieval, handwriting recognition, and robotics [58]. Through DL techniques, results can be obtained in a shorter time compared to traditional analysis methods (e.g., FE method) with very high computational costs [43]. Therefore, DL methods have been addressed by many researchers in the construction field [1,55].

In this study, the MLP and CNN algorithms were used to create the necessary network for the design of 3D-printed concrete walls. This is because MLP and CNN algorithms are good methods for estimating the capacities of structural elements [50]. To the best of the authors' knowledge, as can also be seen from Table 1.1, CNN (i.e., a DL method) has never been used in the literature for regression tasks in the 3DCP area. Therefore, one of the novelties and contributions of this study to the literature is the use of CNN for a regression task in the 3DCP area.

2.1. Studies on Numerical Modeling of Structures Printed Through 3DCP

Khan and Koç (2022) conducted a study on numerical modeling and simulation for extrusion-based 3DCP. They focused on addressing the challenges faced in numerical modeling and highlighted the potential of understanding the basic physics underlying this subject. The current approach in 3DCP is often based on the trial and error method, which leads to higher costs and longer manufacturing time. This research explores how numerical tools can enhance the design process for 3DCP, identifies limitations and challenges, and outlines future research directions. In order to take into consideration printing parameters, material properties and geometry of printed structures, a number of different analytical and numerical models were proposed in the literature. These models aim to predict product performance and rheological responses, and optimize printing parameters, ultimately providing a more efficient and cost-effective solution. Analytical models are suitable for simple shapes like straight or inclined walls but fall short for complex structures, where numerical methods are essential. The review of existing literature indicates a lag in computational technology development for 3DCP in the construction industry. Predicting the performance of 3D-printed concrete structures becomes challenging for complex geometries, varying process parameters, or when using multiple materials. The complexity arises from the involvement of multiphysics phenomena in each subprocess, limiting the applicability of developed numerical models

to specific ranges of processes. A roadmap to integrating different subprocesses into a single computer model, which covers from material mixing to completion of buildability, has been proposed by the study. This integrated approach aims to overcome the current limitations and advance the field of 3DCP in construction.

Liu et al. (2022) undertook a study employing the Drucker-Prager (D-P) material model to assess the viability of constructing early-age structures using 3DCP. One of the challenges faced when printing structures with 3DCP at early ages is the risk of collapse due to poor buildability, which can disrupt the printing process. To address this, the researchers developed an FE model that integrates the D-P model to accurately simulate the buildability of 3DCP structures in their early stages, incorporating the essential material properties of concrete (Figure 2.1). The D-P model's hardening rule, flow, and yield criterion were compared against those of the Mohr-Coulomb (M-C) model. To describe the mechanical properties of freshly printed 3D concrete structures, a nonlinear stress-strain relationship was utilized. The simulation results were calibrated and validated through hollow cylinder tests, straight wall printing tests, and uniaxial compression tests. The predicted maximum stress from the uniaxial compression tests and the elastic buckling characteristics of straight walls aligned with the experimental findings. The D-P model demonstrated a 13.8% reduction in predicted error for the plastic failure of hollow cylinders when compared to the M-C model. In conclusion, the study highlighted and discussed the viability of using the D-P model for these applications.

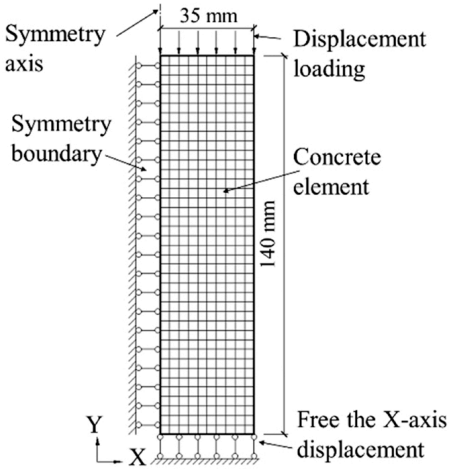

Figure 2.1. Schematic representation of FE model proposed for uniaxial compression test [36].

Heever et al. (2022) focused their research on numerical modeling strategies tailored for reinforced concrete elements produced using 3DCP. The advent of extrusion-based 3DCP has ushered in a new epoch for reinforced concrete structures, due to significant developments in control, process, material, and fresh-state analysis technologies. Despite these advancements, there has been a notable gap in the numerical analysis for intricate geometric forms manufactured through 3DCP technology. This study presents two distinct FE modeling methodologies for the numerical assessment of 3D-printed concrete structural elements (Figure 2.2). These models are specifically developed to predict the structural capacity in the hardened state and failure mechanisms of singly and doubly reinforced concrete deep beams under varying loading conditions. The proposed FE modeling strategies undergo validation through experimental assessment of reinforced 3D-printed concrete deep beams. By drawing parallels between masonry and 3DCP structures, the groundwork is laid for the presented FE modeling strategies. The paper offers succinct descriptions of the respective modeling approaches, modifications to the material model specifications, and application areas of 3DCP.

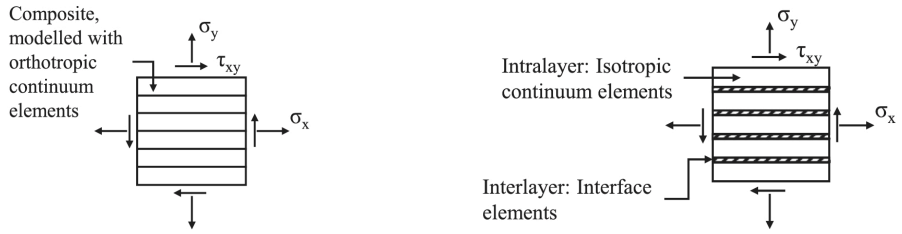

Figure 2.2. Proposed simulation framework for the members printed through 3DCP (a) proposed macro modeling approach, (b) proposed micro modeling approach [11].

Remarkably, the suggested input parameters demonstrate strong alignment with the experimentally determined configurations, with all simulations indicating a load-bearing capacity within 14% of the experimental outcomes. Not only is the load-displacement response deemed suitable, but the cracking patterns predicted numerically also instill confidence in the suggested numerical simulation techniques. Additionally, it is

demonstrated that simplifying the hollow beam geometry with fiber reinforcement to a 2D plane stress model yields sufficient agreement while considerably reducing the computational cost needed to simulate the anisotropic printed composites' nonlinear response.

Khan et al. (2020) worked on 3D printing for creating concrete structures. In this article, recent advancements in 3DCP, its application in the construction industry, historical context, and improvements in equipment, materials, and computer modeling are presented. The authors showcase several sample projects and discuss the challenges and opportunities associated with 3DCP (Figure 2.3). One significant challenge is developing ink formulations using local and on-site materials, which remains an ongoing area of development. Furthermore, research is ongoing regarding the utilization of 3D printers in large-scale construction applications. This article is a valuable resource for both experienced researchers and newcomers in the 3DCP field, as well as for those involved in transitioning 3DCP technology from research to practical implementation.

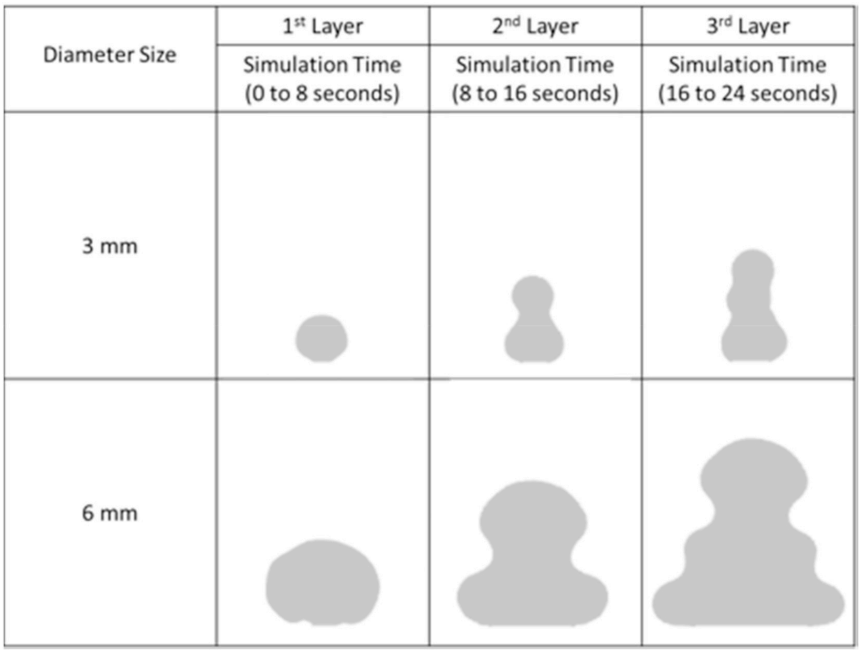

Figure 2.3. 2D stationary computational printing results showing the effect of printing scale on printing results for a cement paste with a yield stress of 350 Pa [17].

Vantgyhem et al. (2020) conducted a study that focused on developing finite element modeling techniques for simulating 3DCP. Their research introduced two distinct strategies utilizing the FE method to replicate the 3DCP processes. These models were designed to anticipate the structural behavior during the printing process while the concrete is still in its fresh state, aiming to determine the maximum overhang angle and optimal printing speed to prevent printing errors. Both FE analyses involved solving multiple static implicit steps, with finite element sets being added incrementally until failure was observed. The primary difference between the two methods lay in how the 3D model was discretized. The first method utilized voxelization in order to approximate the 3D shape, but the second approach constructed FEs by defining toolpaths and sweeping them along the paths (Figure 2.4). To evaluate the effectiveness of both strategies, a case study was presented, demonstrating that both models were in good agreement and produced similar structural responses. The article also addressed the limitations and future challenges of these models, highlighting the need for further research. It concluded that FE-based models could effectively simulate complex prints, providing valuable insights for enhancing printing strategies, such as optimal printing speed, overhang angle, layer height, thickness, and infill patterns. By mitigating printing errors, this approach could lead to significant time, resource, and cost savings. Future research will concentrate on validating the proposed numerical models and comparing them with experimental tests.

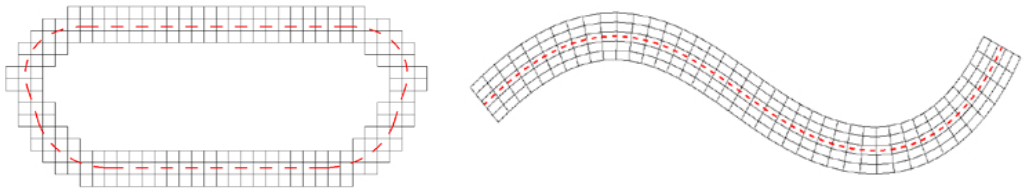

(a) (b)

Figure 2.4. Proposed FE method strategies (a) voxelization of predefined print part using thick line drawing algorithm, (b) CobraPrint's mesh generation process along a predefined print path [14].

Chang et al. (2021) developed a discrete lattice model to evaluate the constructability of 3D-printed concrete (Figure 2.5). Their investigation employed this model to examine the 3DCP procedure and establish the maximum feasible printing height. The model

integrates numerous variables, including structural failure, printing velocity, time-dependent rigidity and strength, localized harm, uneven gravitational load, and spatial diversity of the printed entity. It is capable of replicating plastic collapse failure modes documented in prior studies.

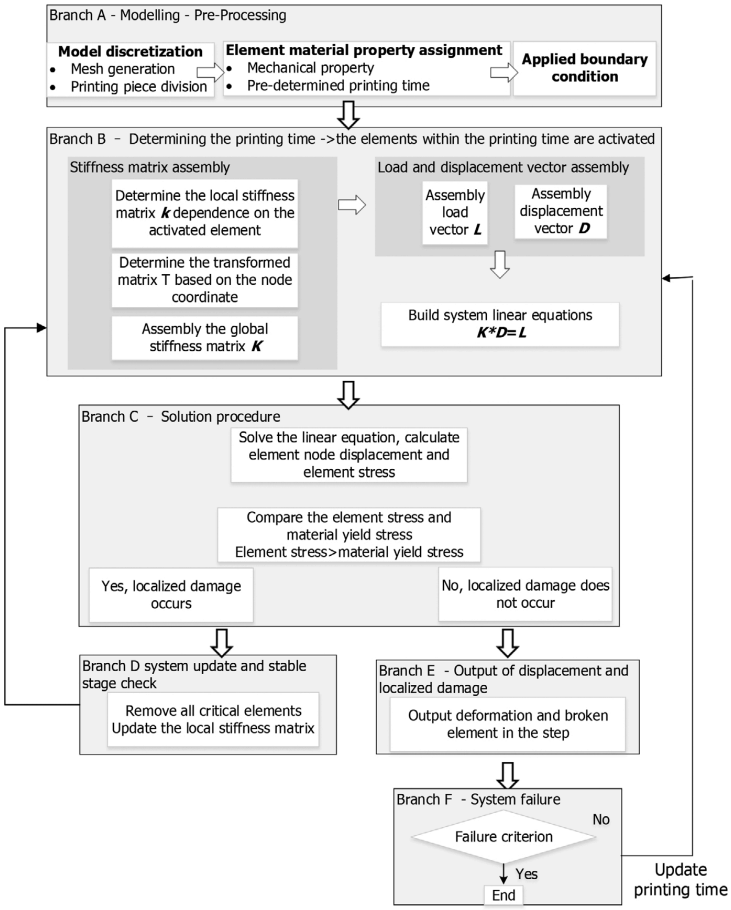

Figure 2.5. General procedure for simulating 3DCP process using lattice model [3].

This study enhances 3DCP modeling in multiple aspects. Firstly, it introduces a new failure criterion to improve the forecast of the critical printing height. Secondly, it employs an element birth method to mimic uninterrupted printing and assess the influence of uneven gravitational load. Thirdly, it represents structural variability by incorporating irregularities in mesh generation and contemplating Gaussian distributions for material traits. The model is utilized for parametric investigations on material diversity and uneven gravitational load to evaluate their impacts on critical printing height and failure-deformation response. Validation is conducted by contrasting the model with two 3D

printing trials from existing literature. The lattice model effectively replicates failure-deformation modes for a cylinder with a hollow topology and a square wall layout. For the square configuration, there exists a 10% inconsistency in the forecasted printing height when compared to empirical data, while the model demonstrates good correspondence with empirical data for the cylinder structure concerning radial deformation and associated height. The article examines possible reasons for these quantitative deviations.

Wang et al. (2020) investigated the mechanical properties of lightweight concrete structures with hollow sections created through 3D printing. The combination of 3DCP and lightweight cement-based materials has the potential to revolutionize construction by enabling the production of intricate hollow structures. Five different concrete mixtures were prepared with varying ratios of lightweight ceramsite sand to silica sand to assess their suitability for extrusion-based 3D printing. The ceramsite sands underwent a coating process with polyvinyl alcohol to reduce shrinkage caused by water absorption and micro-cracking. A suitable cement-based material was selected by fine-tuning its fresh properties to match the requirements of the continuous printing process. Beam and cube elements were designed with four distinct hollow structure types and were 3D printed using the refined lightweight mixture (Figure 2.6).

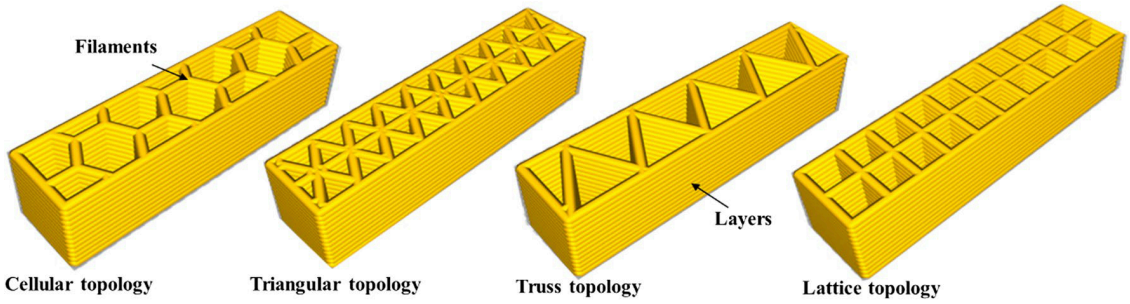

Figure 2.6. Digital design of 3D model of prism-shaped samples with different hollow structures [50].

These internal structures included truss-like, cellular-shaped, lattice-shaped (with a square topology), and grid-shaped (with a triangular topology) configurations. The printed samples' mechanical strength was assessed using compressive tests for cubes and

four-point bending tests for beams. Results indicated that the lattice-shaped topology within a rectangular hollow prism exhibited the highest mechanical resistance to compression, but the truss-shaped prism structure displayed superior bending properties. Furthermore, stress distribution and failure processes were analyzed using the FE method.

2.2. Studies on Parametric Modeling of Structures Printed Through 3DCP

Ooms et al. (2021) introduced a parametric modeling approach to simulate the 3D printed elements with intricate geometries numerically. They presented a numerical model for simulating the structural behavior of fresh concrete in 3D printing (Figure 2.7). Achieving precise control over the additive manufacturing process requires the meticulous definition of material properties and layer interactions, which involves creating finite element meshes layer by layer. To streamline this process, they developed a parametric tool that enables the creation of FE models without the need for extensive manual modeling. The primary benefit of the tool is its capacity to automate the initial preprocessing step for numerical analysis and to model the structural behavior of a randomly shaped element as it is being printed. Additionally, it enables the identification of suitable material properties for a particular printing object at a designated printing speed, and conversely. This capability enables the virtual simulation and optimization of the printing process before physical experimentation, thereby reducing material waste. Overall, the developed tool can enhance efficiency and material usage in the complete workflow for 3DCP. The models generated with the tool underwent assessment and validation against numerical and experimental data from existing literature. Finally, an instance of a geometrically intricate printing object was showcased to demonstrate the capability of the tool.

Aramburu et al. (2023) investigated the parametric modeling of 3D-printed segmented reinforced concrete beams exposed to bending moments. 3DCP is an increasingly important technology for producing lightweight components and intricate free-form structures. Nevertheless, for this technology to develop fully, a number of issues need to be addressed, e.g. the placement of reinforcement members that can withstand stress from tension, the production of large structures, and the design of joint systems among segments.

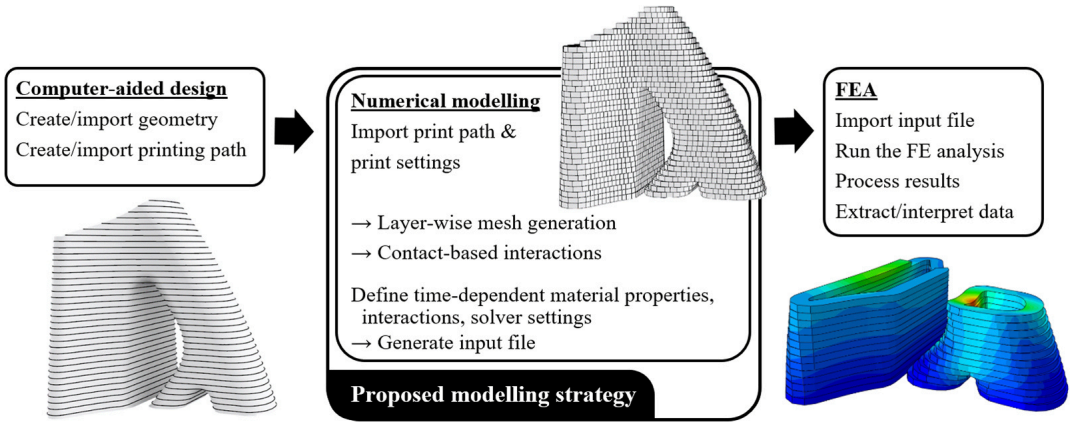

Figure 2.7. General methodology of the proposed modeling strategy for the simulation of 3DCP [24].

The research presents a novel approach and parametric model for simulating the behavior of segmented reinforced concrete beams fabricated using 3DCP and tested under three-point bending (Figure 2.8). This approach accounts for the entire beam geometry and incorporates considerations such as material age, segments with different materials and reinforcement, and the interface between rebar and concrete adhesion in the segments. It is strengthened by a set of programmed routines that integrate commercial design software with FE analysis programs. This approach requires only one human interaction with the initial routine to estimate the structural element's performance in the three-point bending test. Finally, the proposed method's validity was confirmed by comparing its results with those obtained from experimental tests.

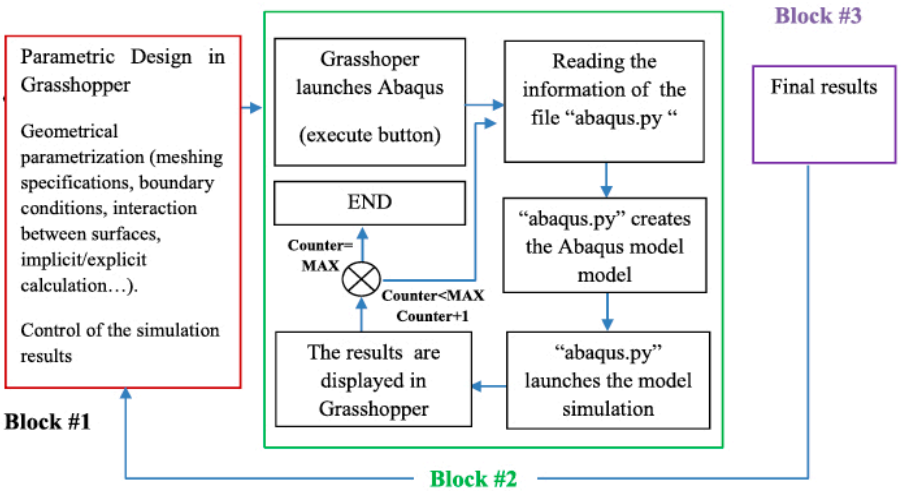

Figure 2.8. Detail of the proposed parametric model [32].

Nguyen-Van et al. (2022) examined the modeling of thin-walled structures produced through 3D printing. Structures produced through 3DCP typically fail due to either green strength (plastic collapse) or instability (elastic buckling) mechanisms. Their research utilized a numerical model for the 3DCP process to simulate these two failure mechanisms, incorporating the mechanical properties of two printable mixes at an early age as input data. The precision of the FE modeling was confirmed through comparison with 3DCP experiments on a hollow cylinder geometry (Figure 2.9). This numerical analysis accurately anticipated failure modes and deformation throughout the 3DCP. This numerical simulation effectively predicted failure modes and deformation during the 3DCP process. Furthermore, the FE model was employed to validate a free-standing thin wall printed with 3DCP. Sensitivity and parametric analyses were also conducted to explore how printing process parameters, such as extrusion width, printing speed, and different mesh sizes, impact buildability capability.

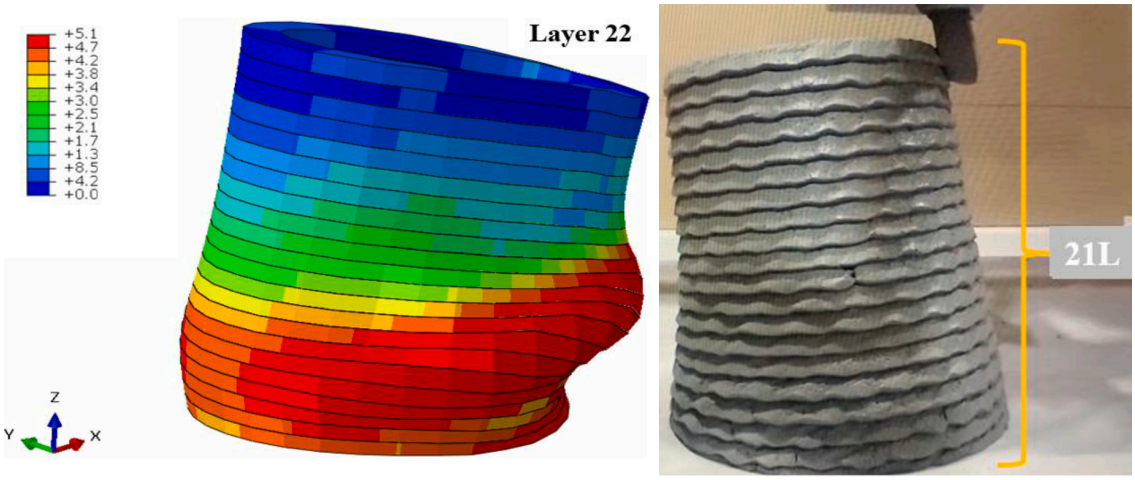

(a) (b)

Figure 2.9. Results of nano clay mixed concrete printed through 3DCP at specified moments (a) numerical results, (b) experimental results [19].

Nguyen-Van et al. (2021) have explored modeling and digital design computation for 3DCP. They introduced a computational framework for a novel 3DCP process aimed at analyzing the failure modes and layer-wise buildability of intricate triply periodic minimal surfaces (TPMS) like Gyroid and Primitive blocks (Figure 2.10). In this framework, a toolpath dataset derived from G-code serves as the source of input, obtained

from a virtual model generated by 3D printing slicing software. Validation of the framework was carried out using experimental data from printing a hollow cylindrical specimen with a nano-clay cement mixture. The framework accurately predicted several collapse modes for the printed cylinder with hollow topology, showing good agreement with experimental results. Furthermore, they simulated the 3DCP process for TPMS blocks using the chosen printing material from the experiment. The numerical analysis revealed that the Gyroid structure exhibits lower buildability compared to the Primitive structure. Additionally, sensitivity and parametric analyses were conducted to examine the impact of printing speed on vertical deformation and buildability during the concrete printing process.

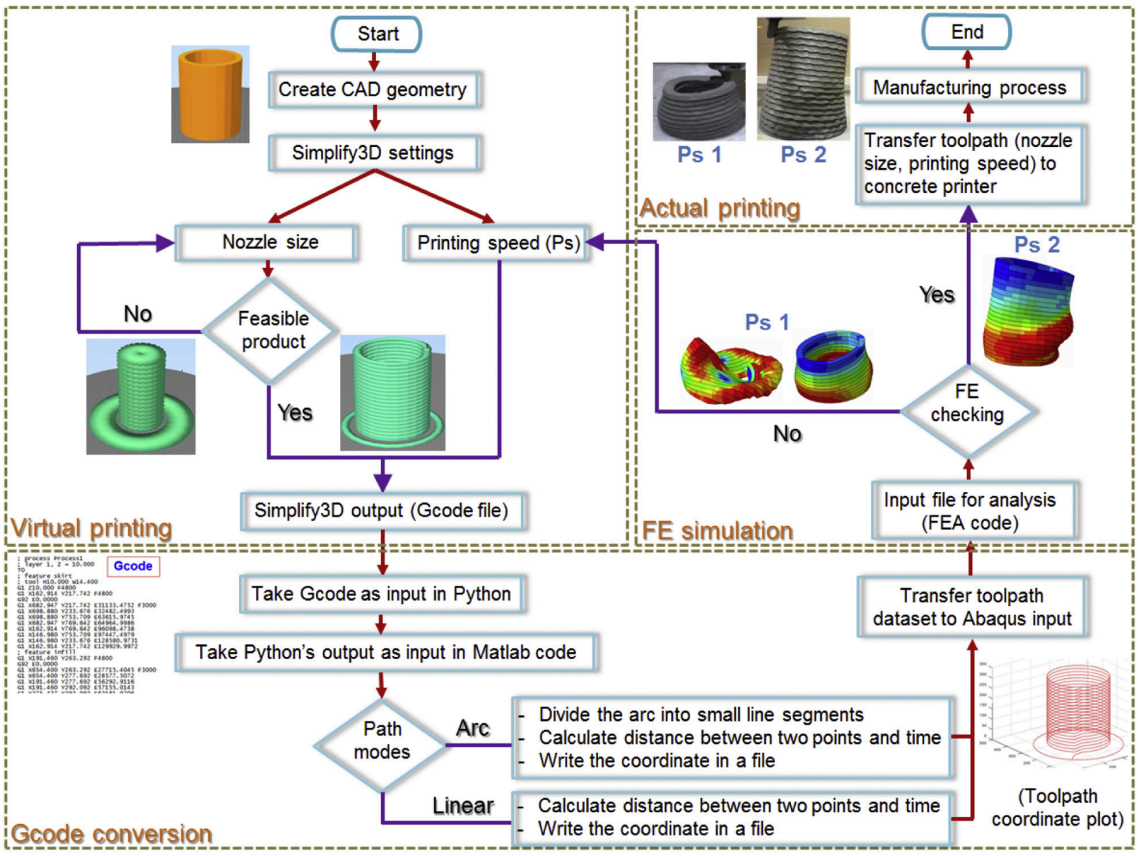

Figure 2.10. Novel computational framework proposed for the 3DCP process [33].

Panda et al. (2018) conducted a study that focused on numerical and experimental modeling of the mechanical properties of structures featuring a honeycomb topology fabricated via 3DCP. Initially, they conducted experimental research to analyze the impact of design parameters such as wall thickness and cell size on the mechanical

properties (modulus of elasticity - stiffness and yield strength) of structures with a honeycomb topology produced utilizing the fused deposition modeling process. Later, they utilized CI-based numerical modeling methods, including automatic neural network search, GP, and response surface regression. These methods were used to develop models for the two mechanical properties, and their performances were compared (Figure 2.11). Statistical analysis demonstrated that the automatic neural network search model exhibited the best performance, followed by the response surface regression and GP models. The experimental results were validated through 3D and 2D surface analyses conducted on the models formulated using automatic neural network search.

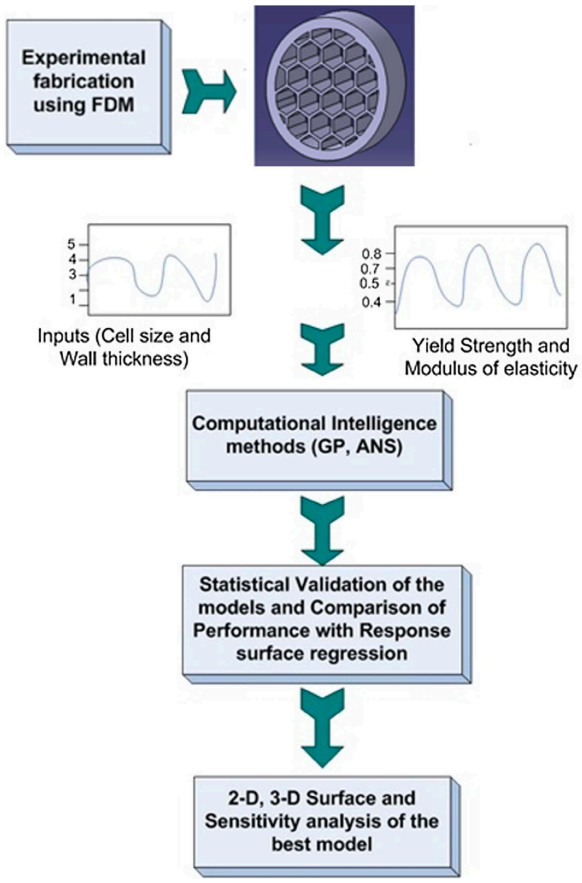

Figure 2.11. Process flow used to model the mechanical properties of structures with honeycomb cellular topology [46].

Alabbasi et al. (2023) have focused on advancing the robotic 3DCP for structural members of housing projects in Saudi Arabia. Their study introduces and validates a comprehensive design-to-manufacturing framework aimed at enhancing the efficiency of

manufacturing reinforced concrete elements using 3DCP technology in the Kingdom of Saudi Arabia. The study proposes an algorithmic framework for customizing a typical Saudi Arabian house through robotic 3DCP tools and techniques, FE analysis, TO, and parametric modeling (Figure 2.12). The framework's validation included manufacturing optimized reinforced concrete columns and testing these members' structural performance in accordance with the Saudi Building Code (SBC 304). The study discusses the pros and cons of the suggested framework and compares it with traditional construction methods in Saudi Arabia. It also emphasizes the importance of mass customization in the Saudi Arabian construction industry.

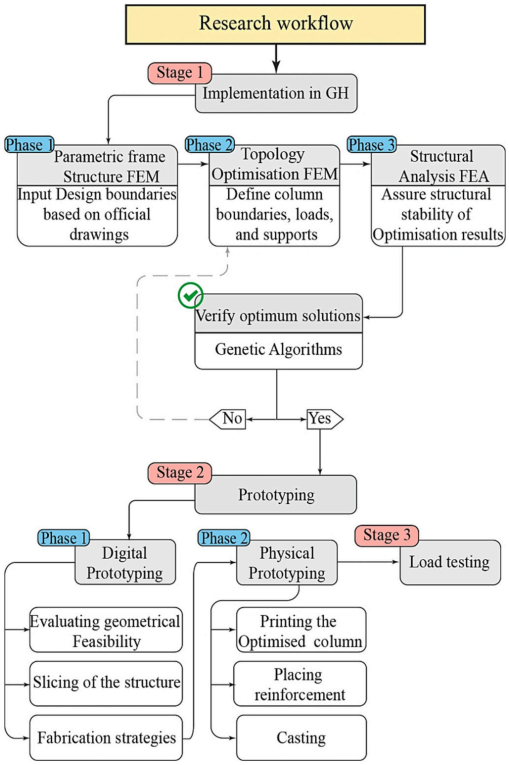

Figure 2.12. Proposed framework from design stage to production stage [2].

2.3. Studies on Structural Walls Printed Through 3DCP

Nedjar (2021) has developed a method involving geometrically nonlinear increments for modeling 3DCP. The paper introduces a framework for modeling where constitutive relationships are expressed incrementally, a method well-suited for aging concretes undergoing hydration. Given the deformable nature of fresh concrete in 3D printing, it is crucial to account for geometric nonlinearities. The kinematics must be appropriately

adjusted to ensure a theoretically robust formulation. To achieve this, the study adopts a multiplicative split for the deformation gradient into its known part at a previous time and the relative deformation gradient. This approach leads to an intermediate configuration where incremental constitutive relationships can be defined before being transformed back to the reference configuration for the Lagrangian formulation, eliminating the need for back mapping. The article provides model examples for clarification, and a series of simulations demonstrate the efficiency of the proposed framework (Figure 2.13).

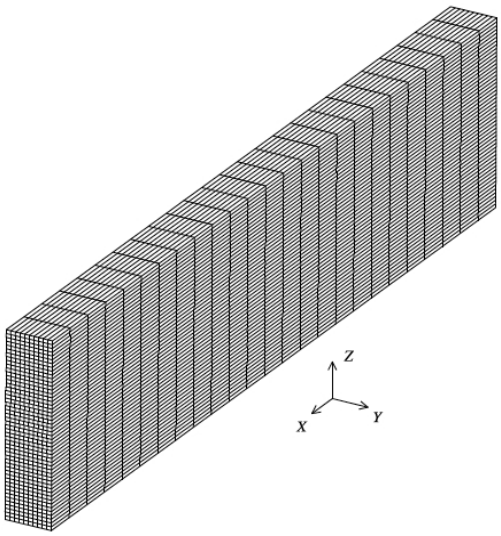

Figure 2.13. FE mesh of a 1 m long straight wall consisting of 25 layers [59].

Wolfs et al. (2019) conducted research on the triaxial compression testing of early-age concrete to facilitate numerical modeling relevant to 3DCP. Understanding the structural behavior is critical for comprehending potential failure mechanisms during the printing process. Therefore, it is crucial to ascertain material properties through experimental tests for early-age concrete. The researchers developed a specialized setup for triaxial compression testing to characterize all parameters necessary for evaluating material failure, including yielding and elastic buckling, according to the M-C criterion. Results from these triaxial tests were compared with simultaneous ultrasonic wave transmission and unconfined axial compression tests to investigate their relationship. The results showed that the triaxial compression test is effective for determining material properties through a series of experiments. These experimental results were then applied to the structural analysis of 3D-printed walls of different lengths using finite FE modeling

(Figure 2.14). The walls were 3D-printed until failure occurred during compression testing, and these results were compared to numerical predictions. The numerical model accurately forecasted the critical height and failure mode for smaller objects. There is potential to enhance the quantitative alignment between critical height and compression test results for larger objects or extended printing processes. Additionally, the article explores two possible explanations for the discrepancies observed in the findings.

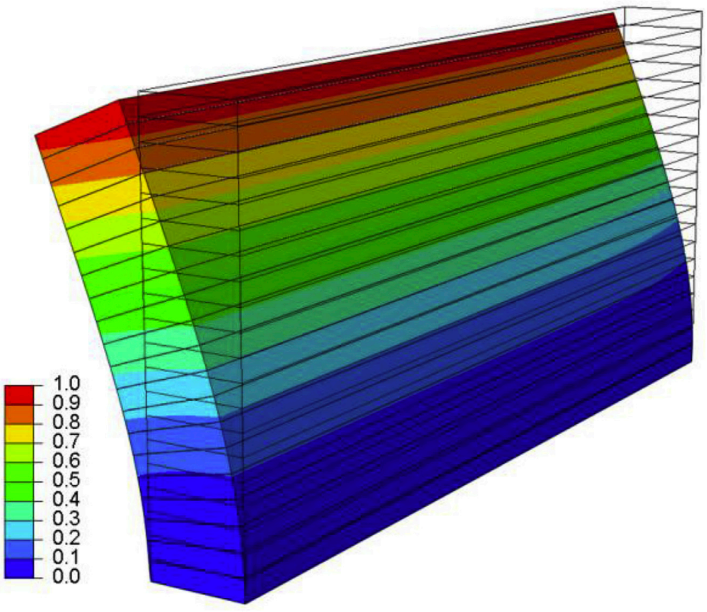

Figure 2.14. Elastic buckling failure occurring as a result of numerical analysis of a 1m long wall [41].

Suiker (2018) conducted a study focusing on the theoretical and experimental analysis mechanical behavior of walls in 3DCP, along with the design tool development for these structures. The research introduces a mathematical model to analyze and enhance the mechanical performance of 3D-printed structural walls. This model addresses two primary failure mechanisms: plastic collapse and elastic buckling. It incorporates key process parameters like the printing speed, curing characteristics of the printing material, geometric properties of the printed object, presence of imperfections, heterogeneous strength and stiffness properties, and non-uniform dead load loading. The study primarily explores the sensitivity to plastic collapse and elastic buckling for three fundamental configurations: i) simply supported wall, ii) free wall, and iii) fully clamped wall (Figure 2.15). These structures are printed in either a linear or exponential decrease in the curing

process. For a rectangular wall section, design charts and collapse mechanism maps have been developed for these essential configurations, providing a practical tool for analyzing any wall structure across a wide printing parameter range. The simply supported wall defines a lower limit for the buckling length of the wall, indicating the global buckling of an entire wall structure, and the fully clamped wall sets an upper limit, representing the local buckling of a single wall. The critical buckling lengths identified by these boundaries can be further refined based on the critical wall length for plastic collapse. An expression has been derived for the non-uniform rotational stiffness provided by the supporting structure of a buckling wall, enabling the accurate prediction of critical buckling length and the associated buckling mode for any wall configuration, as illustrated with a rectangular wall section. Furthermore, the study shows that as deflection increases in the existence of imperfections, the buckling response asymptotically approaches the bifurcation buckling length of a straight wall. The calculated buckling responses for both a free-standing wall and a wall structure that has a rectangular layout closely align with the experimental findings of 3D-printed concrete walls. Consequently, the model can be utilized to systematically examine the impacts of individual printing parameters on the mechanical performance of specific wall structures, facilitating the optimization of printing time and material usage. It can also serve as a validation tool for FE models of 3D-printed wall structures under particular process conditions.

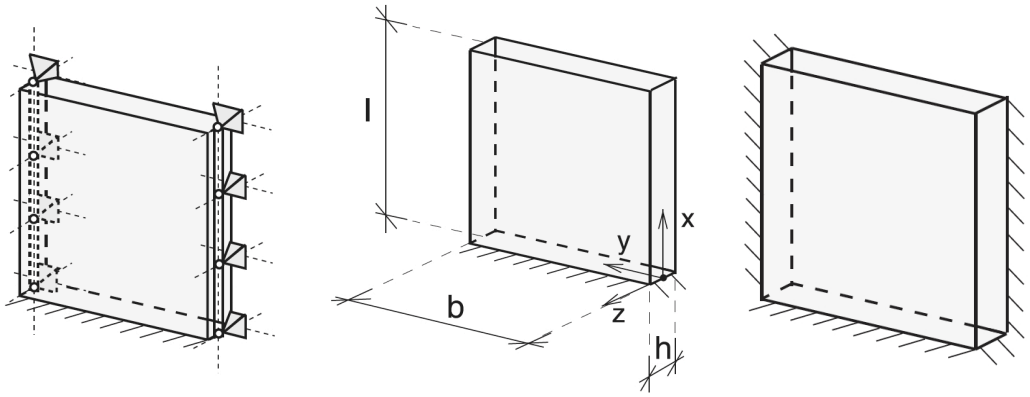

(a) (b) (c)

Figure 2.15. The three essential wall configurations considered are (a) simply supported wall, (b) free wall, (c) fully clamped wall [26].

Lao et al. (2020) focused on enhancing the surface finish quality in extrusion-based 3DCP by employing machine learning-based control over extrudate geometry. In 3D printing, the layering of each extruded line can lead to visible lines or marks at the interfaces between layers, affecting the surface finish quality and potentially the strength of the bond between layers. The study utilized an ANN model to establish a correlation between extrudate formation and printing parameters, using data obtained from 3DCP experiments. The trained model's performance was validated experimentally, demonstrating good conformity between the predicted extrudate geometry and the actual extrudate geometry. Later, the model was used to identify suitable nozzle shapes for producing the desired extrudate geometries. The identified nozzle shapes led to significant improvements in the surface finish of 3D printed objects, including inclined walls, vertical walls, and curved sections (Figure 2.16).



(a) (b)

Figure 2.16. 210 mm high inclined wall (a) the staircase effect of the appearance on the wall in case of using a rectangular nozzle, (b) the reduction in the staircase effect on the pressed wall in case the recommended nozzle cross-section is used [21].

2.4. Studies on TO of Structural Elements Printed Through 3DCP

Nguyen-Van et al. (2023) have focused on modeling the 3DCP process, specifically in terms of material and structural simulation. They highlight the development of several printable materials, 3DCP techniques, and computational design tools to meet durability,

mechanical, and structural requirements. By integrating numerical simulation approaches and parametric design, 3DCP can further optimize construction and realize complex designs. This study presents the latest advancements in modeling and design optimization tools for 3DCP, aiming to provide a current overview of these developments. It proposes a comprehensive framework that considers multiple factors to simulate and model concrete printing. The study discusses modeling and simulation strategies for 3DCP in various contexts, including the properties of fresh and hardened concrete, as well as recent advances in ML applications in 3DCP. Additionally, it summarizes and discusses the design of the printing toolpath, which is crucial in the design optimization stage of 3DCP and involves algorithm development. Lastly, the study covers recent developments and applications of TO in 3DCP.

Bi et al. (2022) have focused on optimizing the topology for 3DCP while considering several manufacturing constraints. This study addresses several constraints inherent in 3DCP by using the bi-directional evolutionary structural optimization (BESO) framework. Firstly, it introduces a layer-based sensitivity scheme to enable the creation of self-supporting designs in the specified printing direction. After, a new continuous extrusion constraint is applied to facilitate uninterrupted printing. Thirdly, the optimization accounts for the anisotropy in the 3DCP process by using a transversely isotropic material model. Fourthly, it proposes area partitioning to aid modular construction, allowing every segment to be associated with a specific printing direction. Lastly, the algorithm's effectiveness is shown through TO applied to a chair design (Figure 2.17)

Vantyghem et al. (2020) have investigated the 3DCP for a post-tensioned concrete beam designed using TO. This study focuses on the digital design and fabricating of a post-tensioned concrete beam, combining two innovative technologies: 3DCP for manufacturing optimized shapes and TO for simulation-based design (Figure 2.18). While this work does not represent the first concrete structure printed through 3DCP, it is the initial demonstration of merging topology optimization with 3D concrete extrusion printing to reduce material consumption, thus enabling the creation of efficient structures.

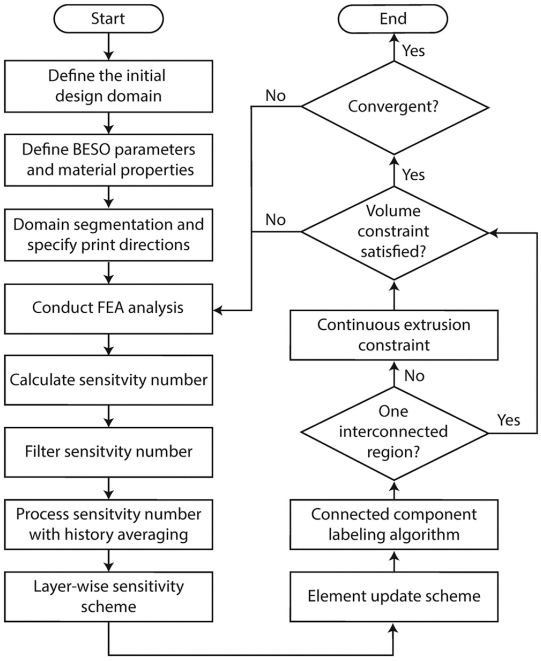

Figure 2.17. A flowchart about the implementation of the proposed strategy [30].

Since an optimization procedure tailored for post-tensioned concrete structures was previously only available in 2D, additional post-design processes were required, including a 3D FE analysis. Following the 3DCP process (including printing and assembly), the beam's structural performance was validated experimentally using digital image correlation, and its shape was compared with the numerical results. This article also delves into the manufacturing challenges encountered, such as printing setup, assembly, and reinforcement integration.

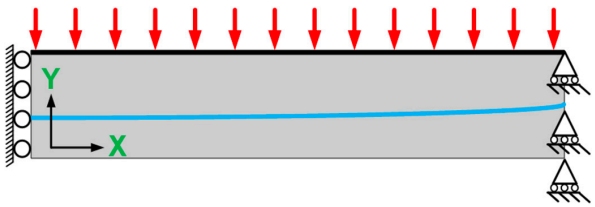

Figure 2.18. Setup used for the topology optimization of a simply supported beam subjected to uniformly distributed load [29].

Asprone et al. (2018) have explored the technological and design aspects of 3D printing reinforced concrete elements. This study proposes a novel approach to manufacturing

reinforced concrete elements using 3DCP technology. The method involves dividing a reinforced concrete element into separate concrete segments, which are individually printed and then assembled with a steel reinforcement system to create a unified element. This approach aims to streamline the production of structurally optimized reinforced concrete elements with complex shapes, ultimately reducing concrete usage and creating lighter structures. The article includes a case study detailing the material characterization and manufacturing process of a straight reinforced concrete beam measuring 3.00 m in length. It also presents the results of a full-scale three-point bending test conducted on this beam. Furthermore, the article examines the production of a reinforced concrete beam with a variable cross-section and free-form shape to showcase the potential of this method.

2.5. Studies Using Various AI Methods in the Design and Analysis of Structures Printed Through 3DCP or Optimization of the 3DCP Process

Goh et al. (2021) have examined the applications, potential, and difficulties of ML in 3DCP. ML has been used to enhance the entire design and production process in several engineering and manufacturing domains, especially in the context of Industry 4.0. This article first introduces a variety of ML approaches (Figure 2.19). After, their applications in a range of engineering and manufacturing domains are explored, including 3D printing design, material and process optimization, on-site monitoring, cloud services, and cybersecurity. Furthermore, prospective uses of machine learning in domains including tissue engineering, biomedical engineering, architecture, and construction are emphasized. The application of ML in engineering and manufacturing faces several obstacles, such as qualification criteria, data collection methods, and processing expenses. In the authors' opinion, the on-site monitoring of AM operations has greatly benefited from machine learning's object detection capacity. Sharing AM data will hasten the integration of ML into the AM domain, as ML requires a huge dataset. To make data sharing simple, standards for shared data are required. The development of more potent computer chips and improved methods for data collecting will lead to broader adoption of ML in AM.

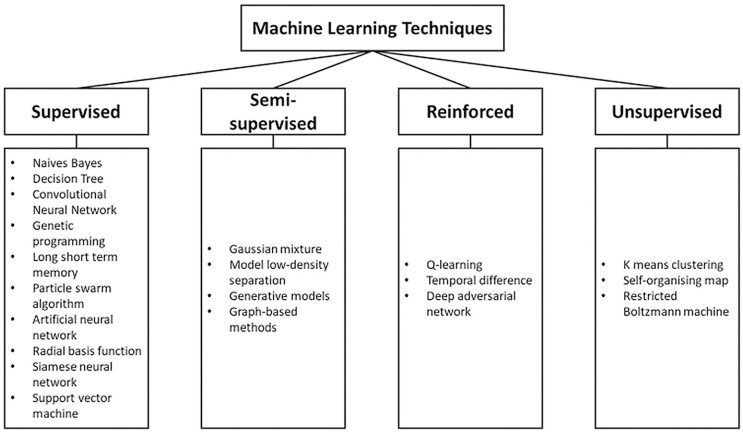

Figure 2.19. ML techniques used in 3DCP [51].

Chang et al. (2022) conducted research focused on enhancing the predictability of stress-crack width graphs and crack patterns within air-void structures found in 3D-printed concrete. This innovative approach involves the utilization of a CNN tailored for this purpose. In the realm of extrusion-based 3DCP, this technique is particularly relevant due to the complex microstructures of the materials involved, characterized by high porosity and pronounced anisotropy. The inherent challenges of analyzing fracture in these void-laden structures, including material heterogeneity and rapid crack propagation, often result in high computational costs. To address these challenges, the study proposes a novel methodology based on CNNs for fracture analysis utilizing air-void structures. The researchers employed a lattice fracture model to construct a dataset comprising input air-void structures and corresponding fracture details, such as crack patterns and crack width graphs. The core of the methodology involves the introduction of a U-net CNN, which integrates principal component analysis and CNN techniques to predict stress-crack width curves (Figure 2.20). Notably, the CNN model's predictions exhibited a high degree of agreement with lattice numerical analyses, achieving an Intersection over Union of 0.85 for crack pattern prediction and an R2 value of 0.75 for stress-crack width curve prediction. These promising results suggest that CNN models can effectively replace traditional numerical analyses in this context. To elucidate the efficacy of the suggested CNN models in fracture analysis of air-void systems, the study provides feature maps utilized during convolutional or non-convolutional operations. These maps offer insights into why the CNN models excel in this application. Furthermore, the research discusses the potential for generalization of the model using techniques like fine-tuning and transfer learning to accommodate various pore information that reflects diverse microstructures.

This adaptability enhances the model's versatility in analyzing fracture in 3D printed materials. In a bid to explore new avenues for CNN models in fractures analysis of 3D-printed materials, microstructures extracted from XCT are examined. This investigation showcases the broader applications of CNN models in this field.

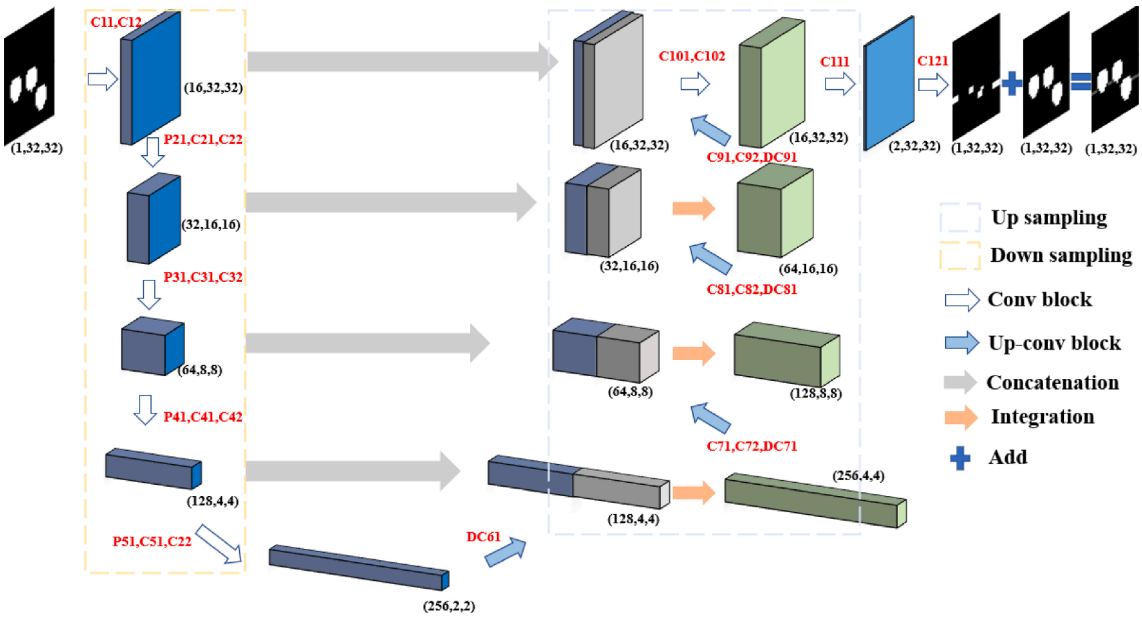

Figure 2.20. U-Net neural network [53].

Baduge et al. (2022) have conducted an assessment of computer vision and AI applications in the realm of Construction 4.0. Their focus lies on the utilization of ML and DL methods within this context. This article presents a thorough examination of AI, ML, and DL applications within the construction industry, encompassing a wide array of areas such as architectural design, material optimization, structural analysis, construction management, offsite manufacturing, progress monitoring, safety protocols, smart operations, health monitoring, building management, durability assessments, life cycle analysis, and circular economy integration. The article offers a unique perspective by detailing the implementation of AI/DL/ML technologies from the conceptualization phase through the design, construction, operation, and maintenance stages, and finally, to the end of the building's life cycle (Figure 2.21). Furthermore, it delves into data collection strategies employing smart vision and sensors, preprocessing techniques for data cleaning, and data storage methodologies essential for model development. In addition to outlining the applications of AI/DL/ML in various construction phases, the

article addresses challenges encountered during model development and provides strategies to overcome these obstacles. It also discusses future trends in these areas and presents potential research avenues for further exploration.

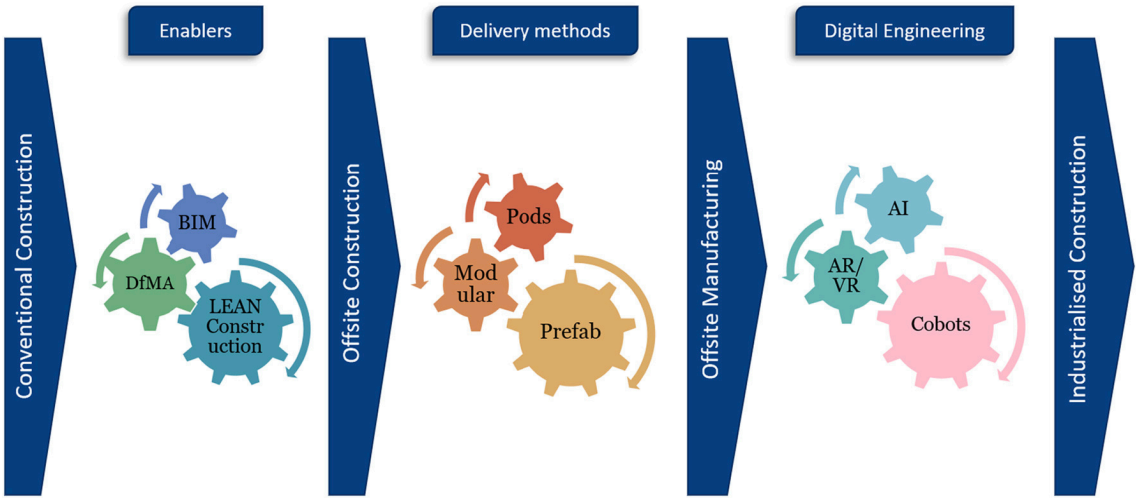

Figure 2.21. Transition from traditional to industrialized construction [1].

Sergis and Ouellet-Plamondon (2022) conducted research focused on automating the mixture design process for 3D-printed concrete structures using optimization methods. While 3D printing technology offers significant advantages in terms of customization potential in construction, it also poses challenges in mixture design. As the complexity of materials used in the mixture design increases, so does the workload in the development process, growing exponentially. In this article, optimization methods were employed to automate the development of mortar mixtures (Figure 2.22). The primary objectives included achieving buildability, workability, and increased compressive strength. To achieve these goals, a total of eight factors were examined, comprising three qualitative factors and five quantitative factors. These factors included types of sand, cement, and superplasticizer, as well as the sand-cement ratio, water-cement ratio, and dosages of additives. Initially, a D-optimal set comprising 18 mixtures was created to significantly decrease the number of experiments needed. Feedforward neural networks (FNN) were then used to predict the properties of new mixtures. Genetic algorithms were used to adjust each network's hyperparameters to improve the accuracy of the model. Finally, a Pareto optimization algorithm was used to control the materials and dosages, simultaneously optimizing the values of the three main objectives. After five iterations,

the suggested multi-objective technique produced enhanced mixtures that satisfied all three criteria and produced twenty-one more mixtures. These findings show that this technology can produce mixture compositions with improved attributes that follow an ideal trend while also reducing the necessary workload.

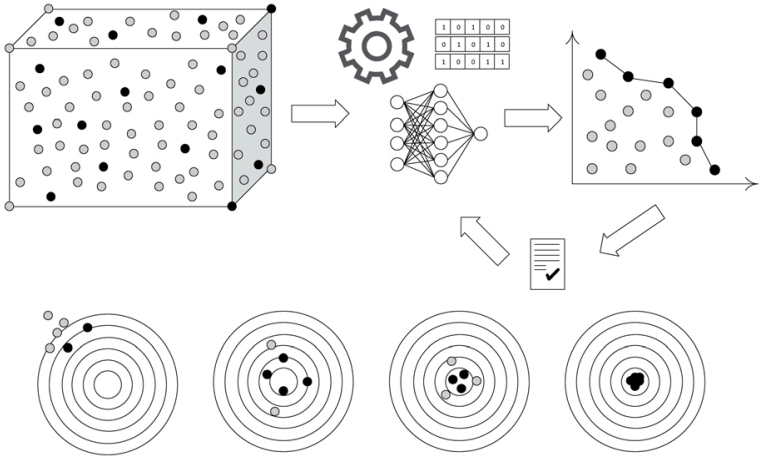

Figure 2.22. Demonstration of the proposed methodology together with optimization methods [52].

Pan and Zhang (2021) conducted an in-depth examination of the impact of AI on structural engineering and management, highlighting upcoming trends. Construction engineering and management (CEM) is quickly evolving as AI becomes more widely embraced, leading to a significant digital transformation in this field. As AI-based solutions take center stage in current CEM research, it becomes crucial to gain a comprehensive understanding of this subject. This article undertakes a systematic review, employing both qualitative and scientometric analyses, to present the current state of AI integration in CEM and to dispute future research directions. The authors first conducted a scientometric study to analyze 4,473 journal articles published between 1997 and 2020, focusing on keywords, journals, and clusters. The study revealed a notable increase in relevant articles over the last decade, with keywords such as BIM and digital twins gaining popularity (Figure 2.23). Following this, the article briefly outlines emerging AI trends in automation, risk mitigation, enhanced efficiency, computer vision, and digitalization, showcasing their potential applications in CEM. Six key research areas are highlighted to underscore the benefits of AI in CEM, including information representation and reasoning, computer vision, information fusion, intelligent optimization, natural

language processing, and process mining. These areas aim to enable data-centric modeling, prediction, and optimization throughout the entire life cycle of complex projects. Moreover, the article points out six future research directions, including smart robotics, Artificial Intelligence of Things (AIoT), cloud-based virtual and augmented reality (cloud VR/AR), digital twins, blockchain, and 4D printing. These directions are expected to further streamline automation and enhance the utilization of AI in CEM.

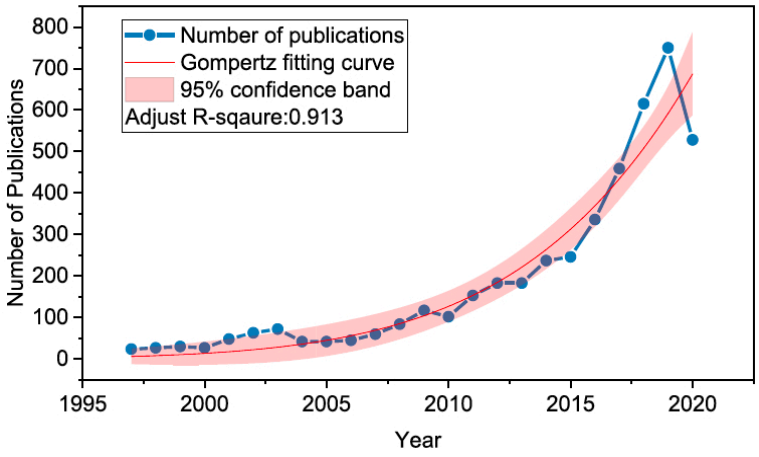

Figure 2.23. Number of publications on applications of AI in the field of CEM between 1997 and 2020 [54].

Raza et al. (2022) conducted a thorough examination of ML applications in AM. This comprehensive review delves into the diverse applications of ML techniques across various facets of AM. These applications span from the initial stages of material selection and alloy development to the optimization of AM process parameters. ML plays a crucial role in training data to establish correlations between the AM process, resulting structure, material properties, and the detection of defects in printed objects. The review also discusses the sequential stages of the ML process in AM, encompassing data collection, model selection, population generation, training, and application. Furthermore, the review identifies specific challenges hindering the long-term integration of ML in AM and proposes potential solutions to address these challenges.

Bolandi et al. (2022) conducted research on estimating high-resolution stress distribution in structural components, aiming to bridge the gap between FE analysis and DL. DL

methodologies have the capability to deliver results significantly faster than traditional runtime analysis, offering substantial advantages for real-time structural assessment tasks. In this investigation, CNN was utilized to forecast high-resolution stress distributions in steel plates subjected to varying boundary and loading conditions (Figure 2.24). The CNN architecture was developed and trained to anticipate stress contours based on geometric features, boundary conditions, and applied loads. A comparative analysis was performed with FE analysis simulations conducted using a partial differential equation solver. The trained DL model achieved an absolute peak error of 0.46% and a mean absolute error of 0.9% for the von Mises stress distribution, indicating its efficacy in predicting stress distributions. This study showcases the applicability and potential of employing DL techniques as alternatives to FE analysis for stress analysis applications.

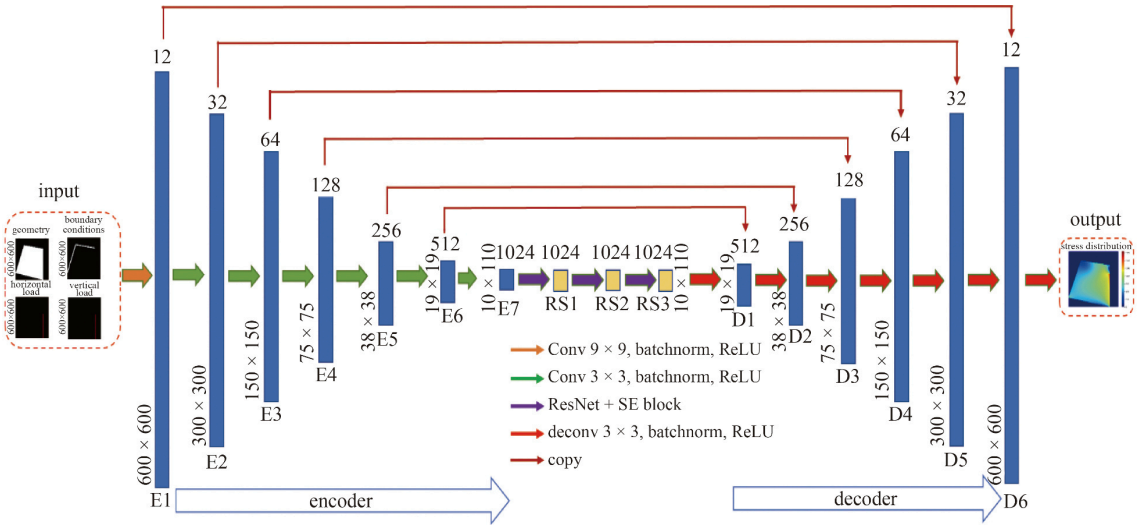

Figure 2.24. Proposed CNN architecture [43].

Mahmood et al. (2020) performed research on ANN algorithms in the context of 3DCP. Their work highlights the recent recognition that ML techniques can effectively establish relationships between process parameters and printed part properties, eliminating the need for developing and solving complex physical models to identify patterns and establish specific relationships. Their study provides a comprehensive overview of the evolution of ANN applications in the 3DCP field. It also discusses the challenges

associated with implementing ANN in 3DCP and proposes potential solutions. Lastly, the study offers predictions on future trends regarding the use of ANN in 3DCP.

Yao et al. (2023) performed a study on the prediction of 3D-printed concrete's performance using AI, focusing on anisotropy and steam curing. Despite the lack of systematic research on the mechanical impact of 3DCP, this study aimed to explore how several steam curing conditions (sustained temperature, including heating rate and retention capacity) affect the properties of 3D printed concrete materials (Figure 2.25). Through a comprehensive test that included macroscopic and microscopic analyses, the study investigated the performance properties of 3D-printed concrete materials at different curing ages. The research also aimed to determine the optimal steam curing conditions for achieving compressive strength in different directions and to evaluate the anisotropy of the mechanical features of printed materials under different curing settings. This study contributes to the theoretical understanding of how steam curing conditions impact printed parts. Moreover, the experimental results were utilized to develop two ML models, utilizing the beetle antenna search technique. These models were designed to anticipate the mechanical performance of steam cured concrete based on test data. The beetle antenna search algorithm was employed to automatically discover the optimal hyperparameters of the ML models, enabling the rapid generation of accurate predictive models.

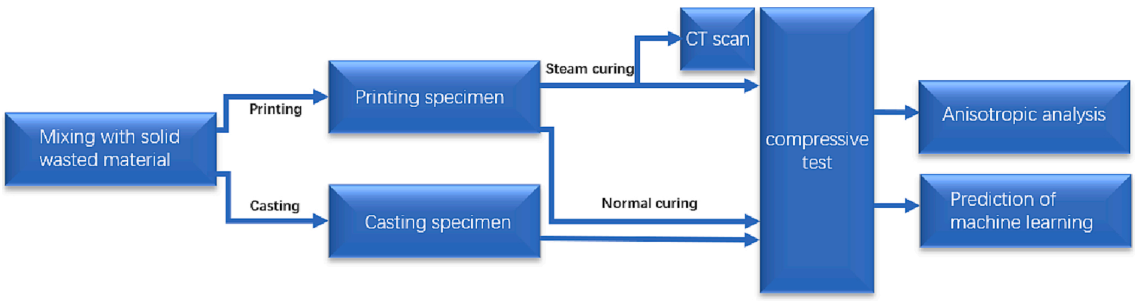

Figure 2.25. Workflow used for AI-based performance prediction of 3D printed concrete, considering steam curing conditions and anisotropy [40].

Geng et al. (2023) conducted a thorough examination of the utilization of ML in 3DCP and the associated expectations. This study serves to offer an overview, condensation,

analysis, and presentation of the advancements in ML applications within 3D printing in the construction domain. The article also addresses current obstacles and future research trajectories. Initially, it introduces the categorization and operational principles of both 3D printing and ML technologies. Subsequently, it delves into the current application landscape of ML in 3D printing within the construction sector, specifically focusing on material design, printing process management, and construction component quality assurance. Building upon this foundation, the article outlines the future possibilities and challenges that ML faces in the construction sector's 3D printing domain. It aims to serve as a guide for achieving enhanced efficiency, intelligence, and sustainability in construction engineering, with a particular emphasis on enhancing interlayer bonding, real-time monitoring, and anisotropic behavior control.

Izadgoshasb and colleagues (2021) undertook a study on predicting the compressive strength of cement mortar that had been 3D printed into structural components using ML techniques. The main objective of their study was to assess and forecast the compressive strength of 3D-printed concrete through the application of various algorithms. Their investigation employed both the ANN and multi-objective grasshopper optimization algorithm (MOGOA). Given that the efficacy of an ML model hinges on the volume of data available, which is relatively limited in the context of 3DCP, the researchers devised an integrated approach, the ANN-MOGOA, which combined both methodologies to predict the compressive strength of 3D-printed concrete (Figure 2.26). Encouraging results were achieved during the iterative process of their study.

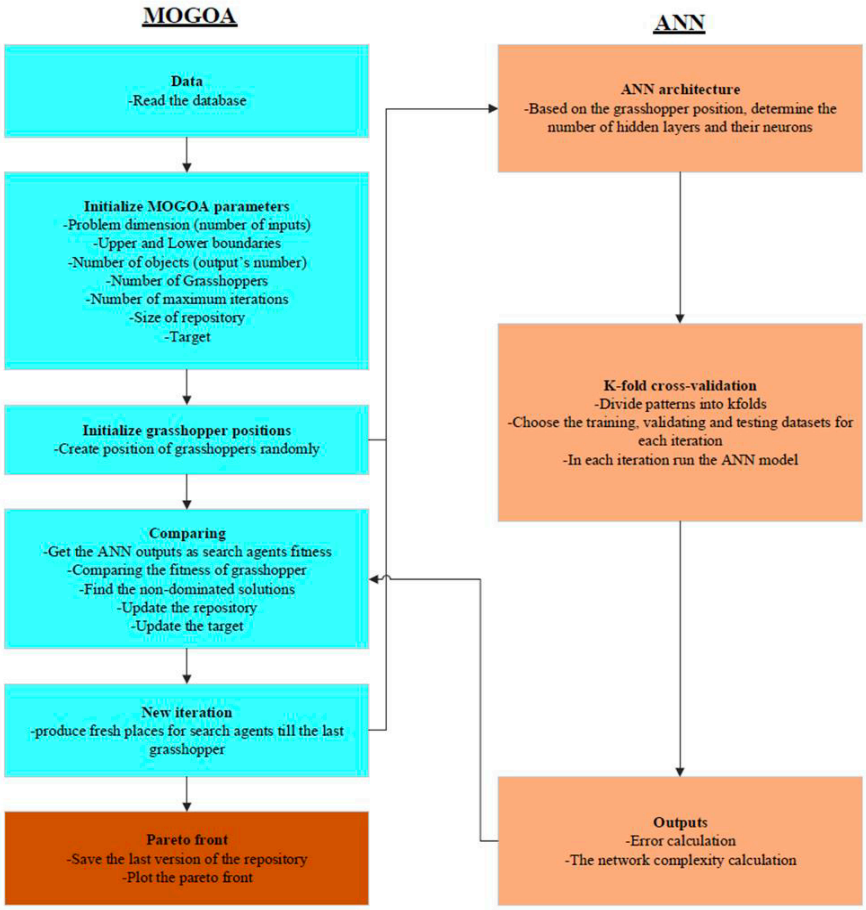

Figure 2.26. ANNMOGOA flow chart [56].

Rojek et al. (2021) conducted a study comparing traditional ANN with DL in optimizing material properties for 3D printing. The performance of 3D printed objects is often constrained by the increasing variety of materials available and the need to optimize numerous process variables. This research aimed to compare the effectiveness of two approaches – traditional ANN and CNN within the framework of DL – in optimizing 3D printing properties to maximize the tensile strength of a skeleton specimen (Figure 2.27). In comparison to the traditional ANN method, the DL-based approach significantly accelerated computation speed by up to 1.5 times while maintaining printing quality. Additionally, it enhanced overall quality, reduced mean squared error (MSE), and enabled the identification of a broader range of printing parameters that were previously only determined by trial and error. These findings underscore the effectiveness of DL as a versatile tool for planning and optimizing material features in the 3D printing process. Future studies should focus on developing cost-effective and computationally efficient

solutions for multitasking and multi-material additive manufacturing to further enhance the practical implementation of DL in 3DCP.

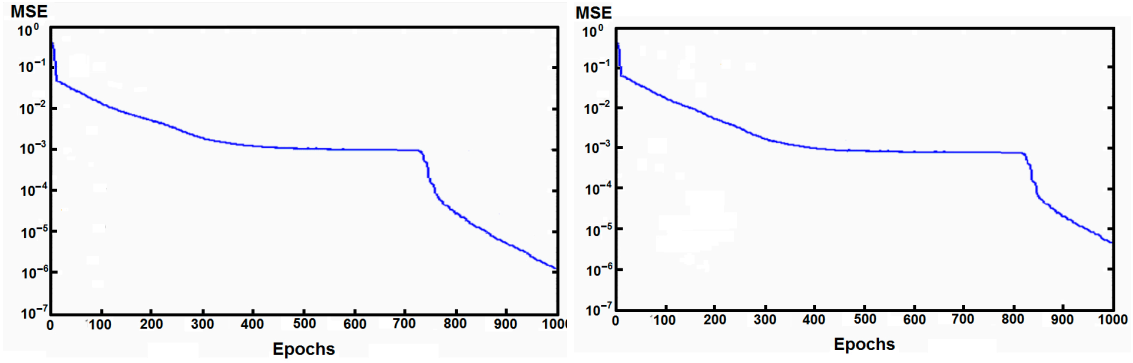

(a) (b)

Figure 2.27. The mean square error values obtained during training (a) for the conventional ANN, (b) for the CNN [58].

3. MATERIALS AND METHODS

3.1. Determining the Wall Interior Topologies Used

TO is an area focused on finding the most efficient structural layout based on predefined design criteria. Introduced in the 1980s, TO has evolved into various methods, including the homogenization method, the level set method, the penalization method with solid isotropic material, the moving morphable component method, evolutionary structural optimization (ESO), BESO, and the moving morphable void method [30]. In addition to these methods, specially developed approaches such as the density-based approach, where the structural topology is represented by a density value that can vary between 0 (void) and 1 (material) at certain points in the design domain, are also used [14]. In addition, it is now a commonly used approach to build architecture with specific objectives such as the highest rigidity for certain volumes or mass constraints by using code-based algorithms or commercial design software packages [33]. To develop an efficient structural system, TO often uses a voxel-based 3D model. The term voxel refers to representing a pixel in 3D. A voxel 3D model is the representation of volume, not a set of borders [2]. With this optimization method, the density of a strong region is reduced while the density of a weak region is increased, resulting in a more efficient material distribution. This optimization method will be even more successful if performed through parametric analysis using any computer software [2]. Several studies in the literature have explored the potential for constructing optimized structures using cement-based materials [2,12,30]. With TO, it is possible to optimize structures printed through 3DCP cement-based elements according to various material and geometric properties, achieving more economical and sustainable designs [17,28].

The subject of producing structures with optimized geometries inspired by nature using 3DCP has been gaining increasing attention worldwide since bio-inspired structures began to exhibit superior mechanical performance [37]. In the literature, various studies have been conducted on structures produced by taking inspiration from nature, such as Bouligand structures, cell-shaped structures, and lattice-shaped structures with square topology [37,50]. In addition to these, studies have also been conducted on ordinary interior topologies, such as solid topology, hollow topology, truss-like structures, and triangular grid-shaped structures [4,24,33,41,50,59]. Through optimization with different

wall topologies, structures with higher strength and more economical structures can be obtained compared to elements produced with traditional topologies [33].

In this study, novel wall topologies are proposed in addition to the most commonly used wall topologies printed through 3DCP according to the literature and practice. The topology types used by considering the literature and application are solid topology, hollow topology, cellular topology, square-shaped lattice topology, triangular-shaped grid topology, and truss topology [4,24,33,41,50,59]. These topologies are shown in Figures 3.1 and 3.2. The proposed novel topologies are arch topology, elliptical topology, and triangular topology. These topologies are also shown in Figures 3.1 and 3.2.

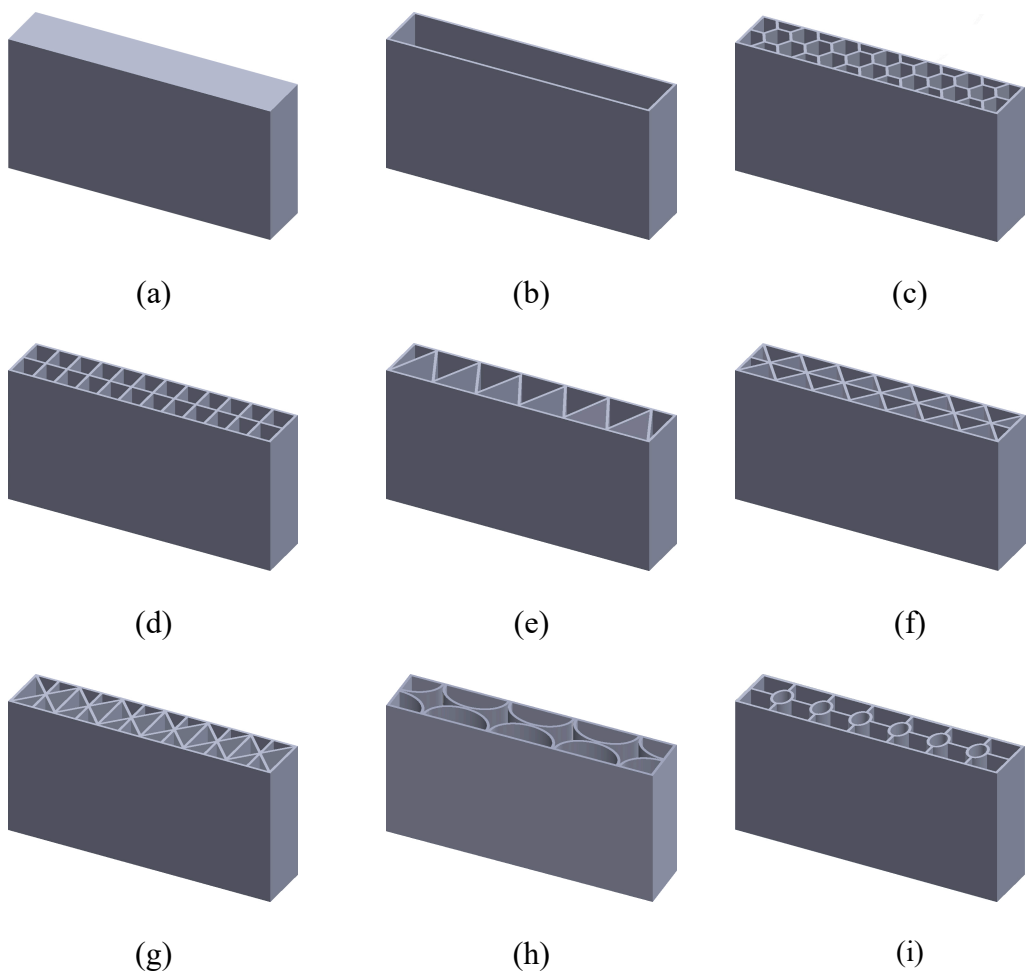

Figure 3.1. The three-dimensional views of the wall interior topologies used are (a) solid topology, (b) hollow topology, (c) cellular topology, (d) lattice topology, (e) truss topology, (f) triangular - 1 topology, (g) triangular - 2 topology, (h) arch topology, (i) elliptic topology.

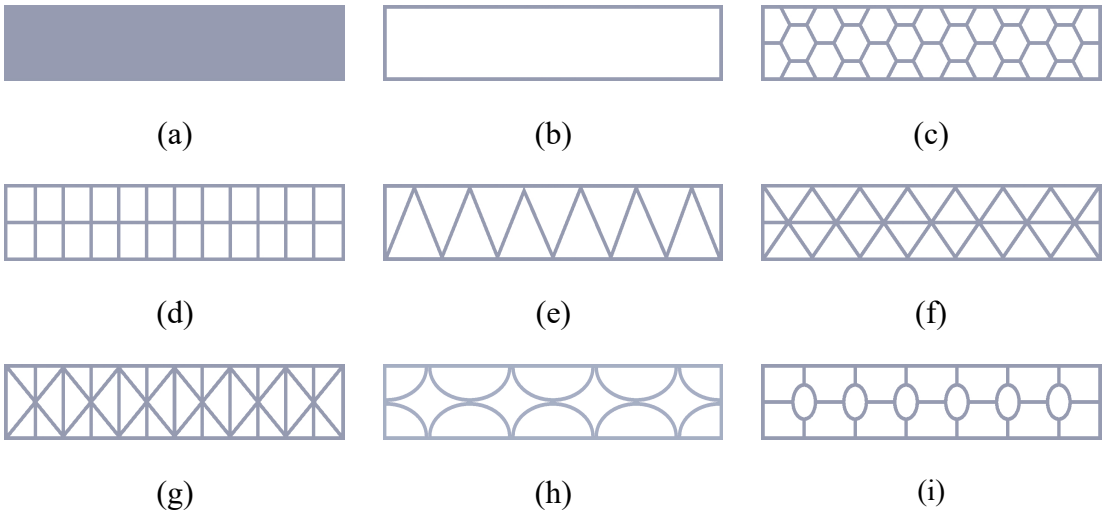

Figure 3.2. The two-dimensional views of the wall interior topologies used are (a) solid topology, (b) hollow topology, (c) cellular topology, (d) lattice topology, (e) truss topology, (f) triangular - 1 topology, (g) triangular - 2 topology, (h) arch topology, (i) elliptic topology.

3.2. Modeling of Shear Walls

3.2.1. Determination of Geometric Parameters

Parametric modeling software can be used to handle complex shapes and create machine instructions necessary for 3DCP [24]. By applying various values to predefined variables, parametric design creates dynamic relationships between parameters and their applications to generate a geometry that may be continually updated. The parametric model offers a framework for calculation and design; both processes can be modified through a parameter table. Therefore, after the model is adjusted, it does not require the use of additional computer-aided design or FE analysis software to check the results of different models based on calculation purposes or parameterized geometries [32].

Recently, innovative approaches have been developed to combine parametric modeling with 3DCP technology for use in the construction field [32]. Parametric modeling has been used in various fields in 3DCP technology such as simulating the performance of segmented reinforced concrete beams subjected to a 3-point bending test, detecting the printability of the printed object and vertical deformation in it, simulating the structure produced with an FE model, and the effect of design parameters (wall thickness and cell

size) of a wall with a honeycomb-like cellular topology on its mechanical properties such as elasticity modulus and yield strength [2,32,33,35,46]. In this study, parametric modeling was used to create numerical models for all wall geometries because it can handle complex shapes and be used to create machine instructions necessary for 3DCP [24].

An appropriate design tool requires a correct capacity estimation formulation or an integrated network with AI. Capacity estimation formulation can be derived using an analytical formulation based on various tests or using nonlinear regression. However, in the literature for the 3DCP field, there are limited mechanical tests on small-scale wall samples due to the 3DCP technology being an evolving field in the construction sector. Also, the fully automated 3DCP network created only requires a computer and does not need an explicit formulation for capacity estimation. Therefore, in this study, ML networks were created to estimate the capacity of 3D-printed concrete walls. However, these networks require a large database to perform training, validation, and testing operations. Due to the limited experimental data in this regard, a numerical database was created. For this purpose, nine different wall topologies (Figure 3.2) were selected to optimize the amount of concrete and printing time.

Table 3.1. Geometric parameters.

Parameter	Values (mm)
Length of the wall	1000 – 3000 – 6000 – 8000
Width of the wall	200 – 300 – 400
Thickness of the wall	10 – 30 – 50 – 70
Height of the wall	3000 – 3250 – 3500

In this study, considering the literature review, length parameters of 1000-3000-6000 mm, width parameters of 200-300-400 mm, wall thickness parameters of 10-30-50-70 mm, and height parameters of 3000-3250-3500 mm were used [2–4,11,19,24,26,32,36,38,44,46,50,59]. The geometric parameters used in this study are shown in Table 3.1.

3.2.2. Creation of FE Models

The importance of predicting the final mechanical performance of a printed structure has increased with the widespread adoption of 3DCP applications, which are more durable, larger, and more practical [20].

Due to the unique nature of 3DCP and the limited availability of experimental data in this field, studies continue to focus on developing an appropriate analytical or numerical model to simulate 3DCP [11,23,41]. Therefore, there is no universally accepted structural model for 3DCP [8,23]. Consequently, while some studies on numerically modeling structures printed through 3DCP find a good agreement between numerical analysis results and experimental results, others do not [4,13,14,19,20,23,32,33,35,37,41,44,50,60,61]. Thus, it is possible to achieve highly successful results with an appropriate numerical model. Furthermore, there are very few studies that combine experimental and numerical research to develop functional models for examining the mechanical behaviors of structures with hollow topologies printed through 3DCP [11,46]. For these reasons, in this study, numerical models were created based on assumptions made considering the literature and existing regulations.

Considering the architectural design freedom that can affect the performance of the structure, very few studies have been conducted on the capacity of large-scale structural members printed through 3DCP [4]. Structural design is typically performed using analytical models derived from fundamental principles, relying on regulations or standards, or through computer simulations like finite element analysis [1].

Due to the limited capacity of the human mind to grasp complex events and behaviors around it in a single operation, all systems continue to be a subject of research for engineers through the process of dividing them into easily understood individual components or elements and then reconstructing the original system from such components to examine the behavior of the system. The use of a finite number of well-defined components in many cases leads to an appropriate approximation [62]. These types of problems are referred to as discrete problems. In other kinds of problems, the

subdivision process can continue indefinitely, and a mathematical solution can only be achieved by considering infinitesimal increments. This results in differential equations or equivalent expressions, which are composed of an infinite number of elements. These types of systems are referred to as continuous systems. Overall, the emergence of digital computers has made it straightforward to solve discrete problems, even when they involve numerous elements [62]. As all computers are constrained by their capacity, continuous problems have to be solved in the form of simple mathematics operations. Existing mathematical methods for exact solutions generally limit themselves to oversimplified situations. To overcome the types of continuum problems encountered in real life, various discretization methods have been proposed by scientists, engineers, and mathematicians [62]. All of these methods include approaches that approach the real continuous solution in the limit as the number of discrete variables increases. The discretization of continuous problems has been considered in different ways by engineers and mathematicians. Engineers generally approach problems more intuitively compared to mathematicians, creating an analogy between real discrete elements and finite divisions of a continuum field at nodal points, leading to the term "finite element" in the light of the "direct analogy" point of view in the field of engineering [62]. Over time, significant progress has been made in this field, and today, approaches based entirely on mathematics and the "direct analogy" approach can be used together. The FE method is a general discretization procedure for continuous solid mechanics problems expressed in mathematical terms [62].

The FE method is the most popular choice for simulating both fresh and hardened cement-based materials [20,44]. This method has been used in many studies in the 3DCP field [1,2,8,9,12–14,18–20,22,23,25,29,30,32,33,35–39,41–44,59–61,63]. Some of these studies focus on detecting defects during the printing process and determining the type of structural damage, obtaining stress-strain curves and determining crack patterns, evaluating the structural performance of hollow structures, reinforced concrete beams, and shell structures, modeling the elastoplastic material behavior, simulating the constructability of fresh concrete, establishing the relationship between printing path and bearing capacity, among others [12,18,19,36,37,44,61]. The FE method has provided successful results in many of these studies [19,44]. It allows the numerical verification of the analytical model created [35]. It can also simulate the constructability of fresh cement

[36]. Although analytical models are theoretically good at predicting damage to structures with complex geometries, they are not practical. However, with numerical modeling methods like the FE method, it is possible to achieve very successful results both theoretically and practically [61]. For all these reasons, numerical modeling in this study was done using the FE method.

After many years of research, a standardized approach has been established for analyzing discrete problems. A civil engineer focusing on structures begins by estimating the force-displacement relationships for each structural component and then attempts to piece together the entire structure using a clear procedure that ensures local equilibrium at each "node" or connection point. The resulting equations are solvable to calculate unknown displacements [62]. The flowchart used for FE applications is as follows [43,62]:

- Modeling the geometry and its components,
- Determination of boundary conditions, material properties, and loading characteristics,
- Implementation of the mesh generation strategy for the geometry [43,62].

In this study, FE analyses were performed using the ANSYS software, taking into account other studies conducted on walls printed through 3DCP [4,64].

Both structures printed through 3DCP and masonry structures consist of discrete elements (bricks and fibers) bonded together to form a composite structure, along with obvious similarities arising from the layered nature of both types of structures [11,15]. Masonry walls and walls printed through 3DCP are compared in different sizes in Figure 3.3 [2]. The knowledge and experience gained over centuries regarding the design and analysis of masonry structures can undoubtedly be used for the design of structures printed through 3DCP as well. Indeed, these similarities have been addressed in many studies in the literature [11]. Some of these studies have addressed domes, vaults, and cantilevers printed through 3DCP, some have proposed a potential connection between computational modeling strategies, some have confirmed the applicability of an anisotropic macro modeling approach adapted from masonry structures, some have

established an analogy between proven accuracy numerical simulation strategies for masonry structures and adapted this analogy to fit the material properties of members printed through 3DCP, some have established an analogy between masonry structures and structures printed through 3DCP, and the modeling strategies used for masonry structures have also been used for the design and analysis of structures printed through 3DCP [8,11]. Additionally, the techniques used for masonry structures are also used in the technology, process, and material fields of 3DCP [2]. Therefore, in this study, shear walls printed with 3DCP are modeled similarly to masonry walls.

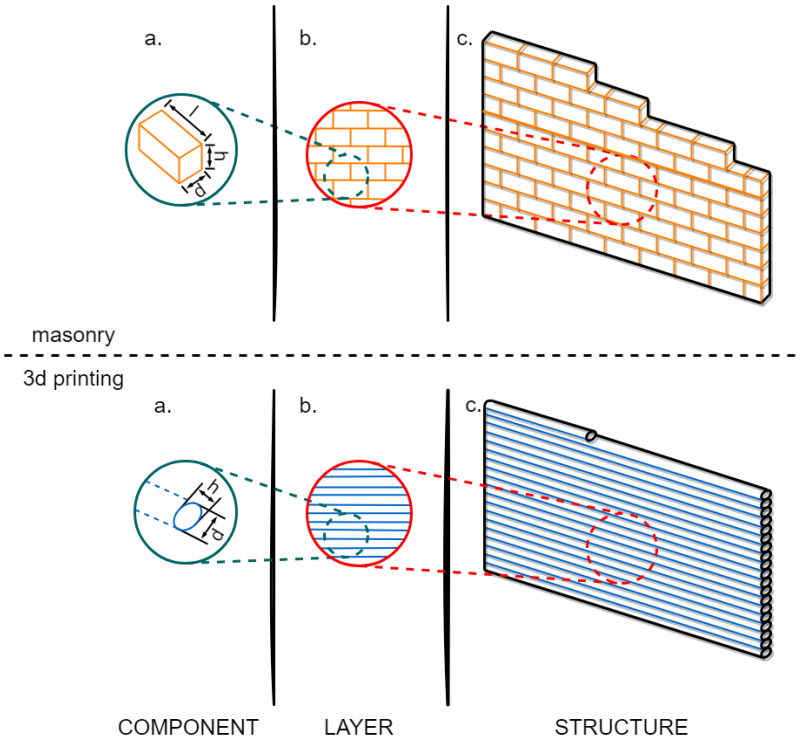

Figure 3.3. Comparison of masonry wall and 3D-printed concrete wall in different dimensions.

In the modeling of composite structures using the FE method, two different modeling approaches are used depending on the required level of detail and accuracy: macro modeling and micro modeling [65,66].

In the micro model approach, the simulation can be further detailed [65]. In this detailing, the structure elements or units and mortar are modeled as continuous elements, and the

structure element-mortar interface is modeled as a discontinuous element [65–67]. The detailed micro modeling shown in Figure 3.4 can provide more accurate results. However, the computational cost increases significantly with this method. Therefore, the application of this approach is limited to modeling structures on a relatively small scale [65].

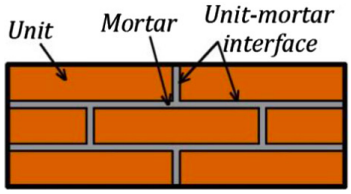

Figure 3.4. FE approach with detailed micro modeling [65].

In the macro model approach shown in Figure 3.5, the masonry structure elements (units) are assumed to be homogeneous and isotropic or anisotropic, with no distinction between them and the mortar. The material properties are derived from the typical characteristics of a masonry structure component, and it is modeled in a series of continuum elements [65–67]. This approach is applied to studies where relatively large and more complicated masonry structures are modeled, and the global behavior is examined [65,67]. Therefore, in this study, the macro modeling approach was used to create the necessary large database (12456 analyses collected for nine different wall topologies). Macro and micro model approaches are compared in Figure 3.6 [66].

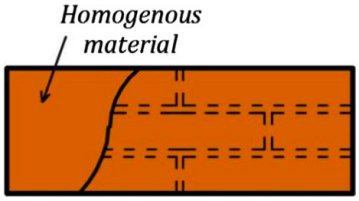

Figure 3.5. FE approach with detailed macro modeling [65].

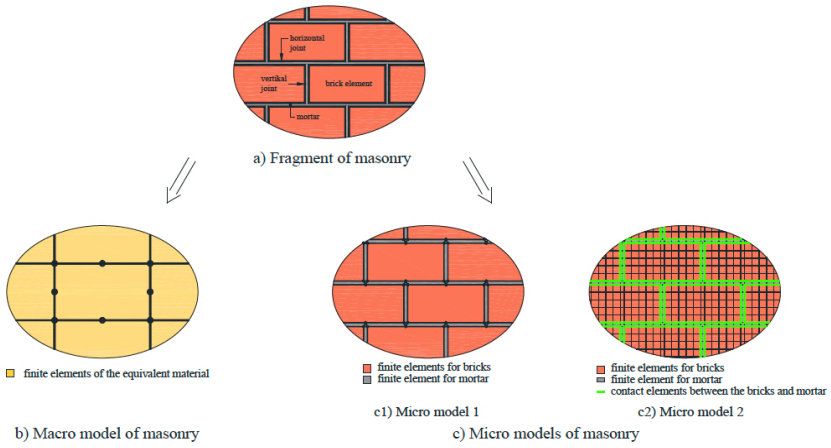

Figure 3.6. Macro model and some micro models for masonry structures [66].

Both numerical modeling approaches yield good results; however, due to their wide practical applications, macro modeling is more advantageous. With macro modeling, large finite elements can be used for the simulation of stack structures, reducing the number of unknowns and shortening the analysis time. Additionally, the macro modeling approach simplifies the analysis significantly, making it possible to analyze more complex structures [66]. The micro modeling approach, on the other hand, requires relatively smaller FEs and contact elements, leading to an increase in the number of unknowns and the analysis time. The combination of numerical integration order and discretization with a large number of small FEs causes the calculated stiffness of the structure to deviate significantly from the actual stiffness. This problem is particularly common in the dynamic analysis of structures due to known issues with numerical algorithms for time integration [66].

Taking into account the literature review, this study uses an eight-node linear solid element type for FE simulation [11,13,14,19,23,24,33,36,37,59,64]. In ANSYS, the eight-node linear solid element type is represented by the SOLID65 element type[68]. Therefore, the SOLID65 element type is selected as the FE type in ANSYS.

The linear solid (brick) element is a three-dimensional FE with both local and global coordinates. This element is characterized by a linear shape function in each of the x, y, and z axes [69]. The element is also referred to as a trilinear hexahedron. The linear solid

element has a Poisson's ratio (ν) and a modulus of elasticity (E). All linear solid elements have eight nodes with three degrees of freedom each, as shown in Figure 3.7 [69].

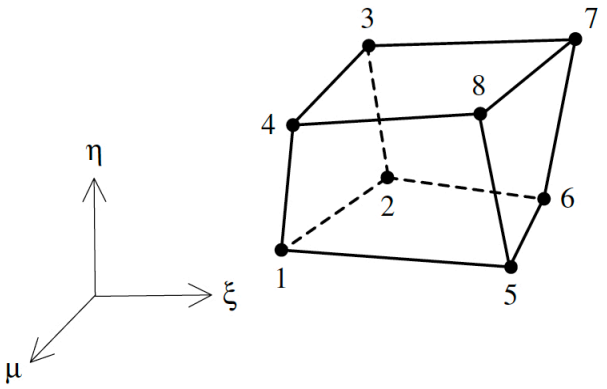

Figure 3.7. Linear solid (brick) element [69].

It is also possible to express this element as a hexahedron, using natural coordinates ξ, η, and μ, as shown in Figure 3.8 [69].

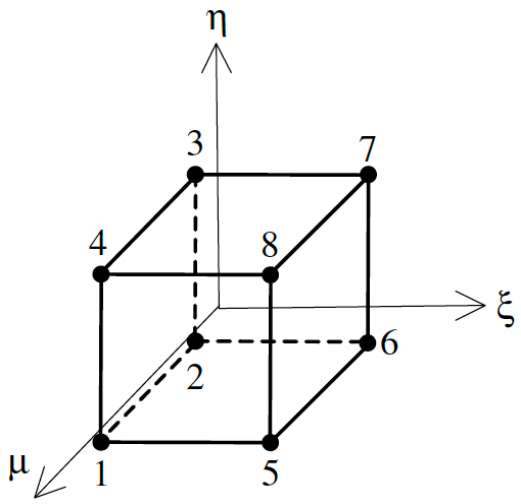

Figure 3.8. Representation of the linear solid element with natural coordinates [69].

The following equations present eight shape functions for this element based on the natural coordinates η, ξ, and μ [69].

$$N_1 = \frac{(1-\eta)(1-\xi)(1+\mu)}{8} \tag{3.1}$$

$$N_2 = \frac{(1-\eta)(1-\xi)(1+\mu)}{8} \tag{3.2}$$

$$N_3 = \frac{(1-\eta)(1-\xi)(1+\mu)}{8} \tag{3.3}$$

$$N_4 = \frac{(1-\eta)(1-\xi)(1+\mu)}{8} \tag{3.4}$$

$$N_5 = \frac{(1-\eta)(1-\xi)(1+\mu)}{8} \tag{3.5}$$

$$N_6 = \frac{(1-\eta)(1-\xi)(1+\mu)}{8} \tag{3.6}$$

$$N_7 = \frac{(1-\eta)(1-\xi)(1+\mu)}{8} \tag{3.7}$$

$$N_8 = \frac{(1-\eta)(1-\xi)(1+\mu)}{8} \tag{3.8}$$

The fundamental advantage of brick-type elements in numerical modeling is that the nodes have a structured order, simplifying the process of mesh generation based on the printing path [24].

Currently, there is no standard or regulation regarding the modeling of concrete used in 3DCP [11,22,25]. For practical use in structural analysis models of 3DCP, it can be assumed that this material exhibits linear elastic behavior before yielding

[13,18,20,41,44]. Additionally, in TO studies, nonlinear material behavior is generally ignored [18]. After being deposited, concrete primarily remains in a static condition, where its elastic-plastic behavior is more significant than its viscous-plastic behavior during yielding. Consequently, solid mechanics methods are better suited for assessing the constructability of elements created using 3DCP [20,36]. In the literature, it is observed that in many studies in the field of 3DCP, a material model exhibiting linear elastic behavior before yielding and nonlinear behavior after yielding is selected [16,18,20,22,23,28,32,36]. Therefore, in this study, a concrete material model exhibiting nonlinear behavior was used (Figure 3.9) [23].

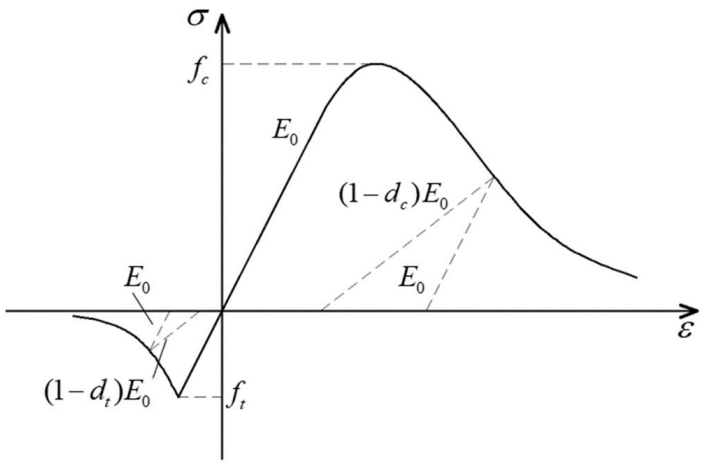

Figure 3.9. Stress-strain curve of the concrete used in 3DCP [23].

The material yield criterion plays a vital role in the FE analysis of 3DCP. The most commonly utilized yield criteria are von Mises, Rankine, Tresca, D-P, and M-C yield criteria [36]. Von Mises and Tresca are single-parameter criteria focused solely on shear stress, and they are unable to characterize the shear strength of early-age concrete when normal stress increases. In addition, the Rankine criterion is generally used to model tensile failure in brittle materials, which do not behave the same way as early-age concrete. Similarly to the M-C criterion, the D-P criterion also considers the effect of normal stress on shear stress [36]. Nonetheless, the M-C criterion features a hexagonal yield surface in the principal plane, leading to challenges in achieving numerical solutions. In contrast, the D-P criterion has a conical yield surface, providing a smoother alternative that helps to circumvent these issues [36]. These two yield criteria are shown

on the stress plane in Figures 3.10 and 3.11 [28,70]. In the M-C model, the material exhibits perfect plasticity after yielding, which does not sufficiently reflect the behavior of the concrete material used in 3DCP. The D-P model, on the other hand, can successfully describe the hardening process and peak stresses of concrete materials. Therefore, using the D-P model as the material model in 3DCP is appropriate [36]. Therefore, in this study, the D-P criterion is used as the yield criterion for nonlinear concrete material.

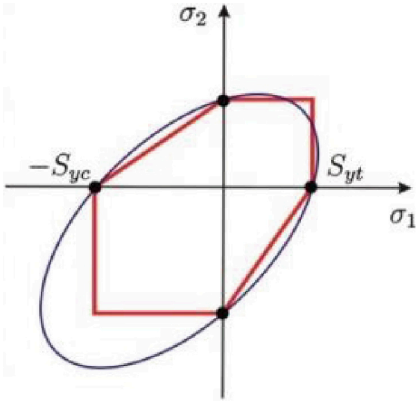

Figure 3.10. M-C (red line) and D-P (blue line) yield criteria [28].

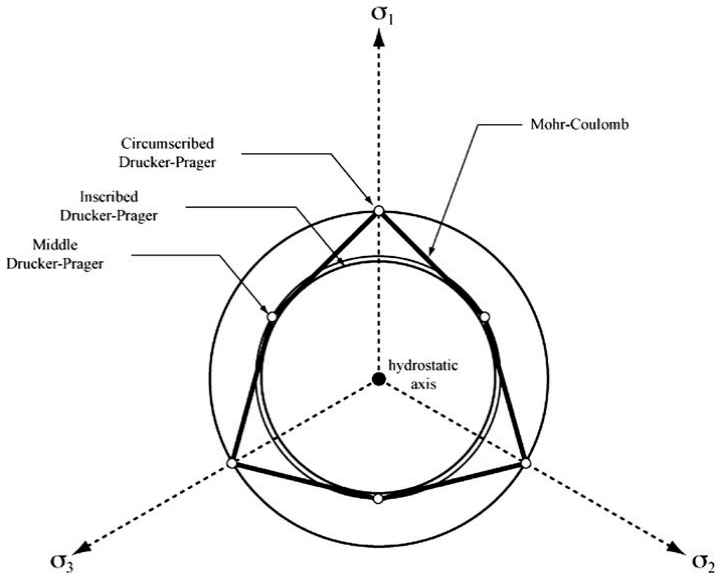

Figure 3.11. M-C and D-P yield criteria on the stress plane [70].

The D-P yield criterion is a three-dimensional, pressure-dependent model designed to determine the stress level at which a material attains its maximum strength. It relies on the premise of a linear relationship between octahedral shear stress and octahedral normal stress at the point of failure. This criterion can be represented by the following equation [70].

$$\sqrt{J_2} = \lambda I_1' + \kappa \tag{3.9}$$

where, κ and λ are cohesion and internal friction angle for the D-P model respectively, $I_1^{'}$ represents the first invariant of the stress deviator, J_2 refers to the second invariant of the stress deviator tensor, as defined as in Equations 3.10, 3.11, 3.12 and 3.13 [70,71].

$$I_1' = \sigma_1' + \sigma_2' + \sigma_3' \tag{3.10}$$

$$J_2 = \frac{1}{6}[(\sigma_1' - \sigma_2')^2 + (\sigma_1' - \sigma_3')^2 + (\sigma_3' - \sigma_1')^2] \tag{3.11}$$

$$\lambda = \frac{2\ sin\phi}{\sqrt{3}(3 - sin\phi)} \tag{3.12}$$

$$\kappa = \frac{6c\ cos\phi}{\sqrt{3}(3 - sin\phi)} \tag{3.13}$$

where, $\sigma_1^{'}$, $\sigma_2^{'}$, and $\sigma_3^{'}$ are effective principal stresses, φ is the internal friction angle, and c is the cohesion for the M-C model [70,71]. Characteristic strengths for the case of compressive failure and uniaxial tensile failure of concrete can be calculated through formulas given in Equations 3.14 and 3.15 according to the M-C criterion [71].

$$f_t = \frac{2c\ cos\phi}{1 + sin\phi} \tag{3.14}$$

$$f_c = \frac{2c\ cos\phi}{1 - sin\phi} \tag{3.15}$$

where, f_c represents the characteristic compressive strength of concrete and f_t represents the characteristic tensile strength of concrete [71]. If f_c and f_t present, the cohesion and the internal friction angle for D-P yield criteria can also be expressed by Equations 3.16 and 3.17 [70,71].

$$\kappa = \frac{2f_c f_t}{\sqrt{3}(f_c + f_t)} \tag{3.16}$$

$$\lambda = \frac{f_c - f_t}{\sqrt{3}(f_c + f_t)} \tag{3.17}$$

Since the behaviors of structures printed through 3DCP are not fully understood, research is ongoing to investigate these behaviors and compare them with those of traditional concrete structures [9]. In the literature, it is observed that a nonlinear material model and the D-P yield criterion are combined for the concrete material used in 3DCP [9,23,24,28,36,42,60].

Generally, an isotropic and homogeneous material model is utilized in the analytical modeling of 3DCP. Isotropic materials exhibit the same properties in all directions. It is observed in the literature that an isotropic material model is used in 3DCP [20,42]. Therefore, an isotropic material model is also used in this study.

Taking into account the literature review, the density, modulus of elasticity, uniaxial compressive strength, Poisson's ratio, uniaxial tensile strength, cohesion, and internal

friction angle of the material were used for the material model [2–4,12–14,16,19,22–26,28–30,33–39,41,42,44,46,50,59,60,63,64]. For the uniaxial compressive strength values, commonly used values of 20, 30, and 40 MPa were used [2,4,12,22,23,25,29,33,50]. A Poisson's ratio of 0.2 was selected [14,23,29,37,42,60]. There is no standard or code available that addresses the modeling of the concrete used in 3DCP [11,22,25]. Due to the unique characteristics of this automated production procedure and the use of anomalous cement-based composites, compliance with existing structural codes poses a significant constraint on the adoption of large-scale concrete structure manufacturing methods [11]. Therefore, designers and regulatory authorities do not have a standardized protocol to refer to for designs in the 3DCP field [11,22,25]. Consequently, existing building standards and codes related to traditional manufacturing and construction techniques have been adopted in the literature [11]. Some of these standards include ACI 380, CEB-FIP Model Code 1990, Saudi Building Code (SBC 304), EN 1992-1-1:2004, AS1170, and AS3600 [2,8,23,25,64]. It can thus be understood that there is no specific standard within existing concrete structure standards that can be strictly defined for 3DCP. Therefore, in this study, cohesion and internal friction angle were calculated according to Equations 3.16 and 3.17, and the modulus of elasticity (E) and characteristic tensile strength (f_t) values were calculated according to Equations 3.18 and 3.19 adapted from the TS (Turkish Standard) 500 standard [72].

$$E_{cj} = 3250\sqrt{f_{cj}} + 14000\ (MPa) \tag{3.18}$$

$$f_t = 0.35\sqrt{f_c}\ (MPa) \tag{3.19}$$

where, E_{cj} represents the elasticity modulus of "j" daily concrete, f_{cj} represents the characteristic cylinder compressive strength of "j" daily concrete, f_t represents the characteristic axial tensile strength of concrete, and f_c represents the characteristic axial compressive strength of concrete. Taking into account the literature review, the material density value was selected as 2400 kg/m³ [4,23,29]. The material parameters used are summarized in Table 3.2.

Table 3.2. Material parameters.

Parameter	Values
Modulus of elasticity (MPa)	28534 – 31800 – 34555
Poisson's ratio	0.2
Characteristic compressive strength (MPa)	20 – 30 – 40
Characteristic tensile strength (MPa)	1.565 – 1.917 – 2.214
Cohesion (MPa)	1.676 – 2.081 – 2.422
Internal friction angle (Degree)	28.278 – 29.106 – 29.611
Density (kg/m^3)	2400

To obtain the data in the dataset to be used in AI algorithms, a lot of analysis is required, and different walls with different topologies will be used in the analysis. Therefore, the optimum mesh size and optimum mesh method for each model have been automatically determined by ANSYS to achieve a convergence of 10% in force and displacement [19,33,37]. Thus, numerical accuracy is ensured, and analyses are completed in a shorter time, saving computational costs [33,37]. In this study, FE analysis was performed on a total of 12456 walls for nine different interior hollow topologies. The results of one of the convergence studies conducted in this thesis are shown in Figure 3.12 and Table 3.3. The convergence graph shown in Figure 3.12 belongs to a wall with a solid topology with dimensions of 1000 mm in length, 200 mm in width, and 3000 mm in height. The term 'Elements' in Table 3.3 represents the number of FEs generated, while the term 'Nodes' represents the number of nodes resulting from the generated FEs. The mesh system automatically created by ANSYS to achieve a convergence of 10% in force and displacement for this wall is shown in Figure 3.13.

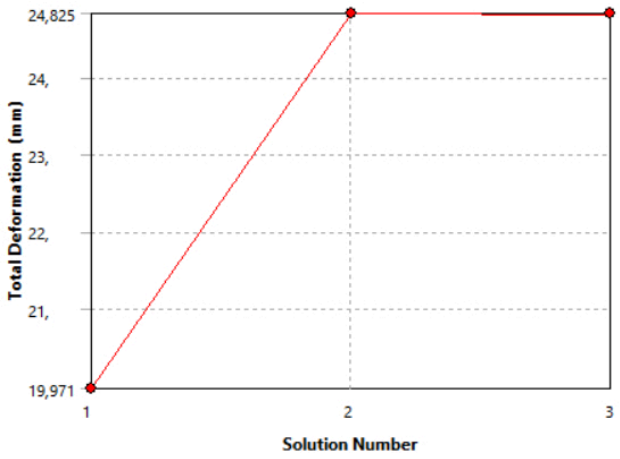

Figure 3.12. The displacement convergence graph for a wall with a solid topology, measuring 1000 mm in length, 200 mm in width, and 3000 mm in height.

Table 3.3. Results of the displacement convergence study for a wall with solid topology, measuring 1000 mm in length, 200 mm in width, and 3000 mm in height.

Step	Total Deformation (mm)	Change (%)	Nodes	Elements
1	11.689	-	926	114
2	17.715	40.985	8779	5322
3	19.365	8.9025	14604	9304

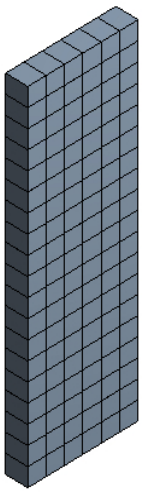

Figure 3.13. The mesh system automatically generated as a result of the convergence study for a wall with a solid topology, measuring 1000 mm in length, 200 mm in width, and 3000 mm in height.

Considering the literature review, fixed support boundary conditions were implemented at the bottom of the wall for all degrees of freedom [3,4,19,23,33,36,41,64]. The applied boundary conditions are shown in Figure 3.14.

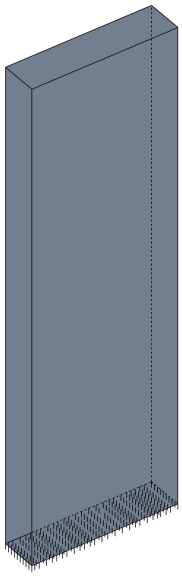

Figure 3.14. Fixed support boundary conditions applied to shear walls.

During the 3DCP process, two common failure modes are usually identified in the material: plastic collapse and elastic buckling, which can occur due to either local or global instability [16,19,20,44,59,61]. Plastic collapse occurs when stresses from gravity reach the yield stress, while elastic buckling collapse occurs due to geometric instability in the collapse [20,44]. Therefore, buckling is a crucial phenomenon in walls printed through 3DCP both during production and after the concrete has hardened [14,26,34,59]. This aspect has been considered in many studies [14–16,19,20,24,26,33–36,41,44,59,61].

Additionally, in walls printed through 3DCP, after the concrete has hardened, the axial loads on the wall result in a confining effect of hydrostatic pressure. An increase in the confining effect causes an increase in material stiffness, especially for older specimens. For large-scale structures, the confining effect has a much more significant impact on strength and stiffness behavior [41]. Various studies in the literature have applied axial loads to structures printed through 3DCP [2,18,24,35,36,41,61]. In this study, the capacity of walls with different topologies, dimensions, and material properties was calculated. To

ensure the exact collapse of the wall, the planned axial loads were calculated by multiplying the cross-sectional area of the wall by the characteristic compressive strength of the concrete. As the numerical analysis focused on determining the shear capacity of each wall, lateral forces were applied alongside the axial pressure (Figure 3.15). The intensity of the applied lateral loads was adjusted to induce shear failure in the walls.

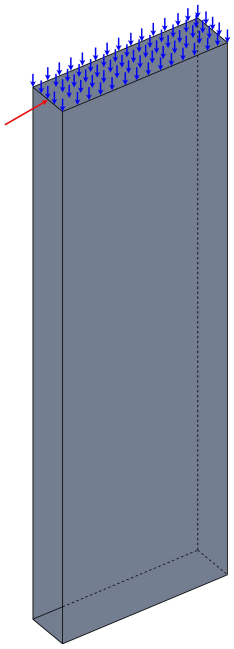

Figure 3.15. Load types applied to shear walls.

Shear walls lose their vertical load-carrying capacities by exhibiting brittle failure under lateral loads at high pressures [49]. In many studies in the literature and in many existing regulations, the axial load and flexural capacity are taken into account using the axial load ratio [47–49]. For concrete shear walls, this value is typically in the range of 0-0.2 [49]. Therefore, in this study, axial load ratio values of 0.01, 0.05, 0.1, and 0.2 were selected, and the ultimate axial loads were calculated and applied according to the following formula (Equation 3.20).

$$p = f_c * A * k \tag{3.20}$$

where, p represents the axial pressure, A denotes the cross-sectional area of the wall, and k represents the axial load ratio.

The type of analysis to be performed in the numerical simulation of 3DCP depends on the assumption being made. If contact-based interactions are considered, dynamic analysis should be used. However, if the structure is to be modeled with macro modeling, i.e., if contact-based interactions are not considered, static analysis will be sufficient [24]. For the consideration of material nonlinearity and geometric nonlinearity, nonlinear analysis should be performed [11,73]. Therefore, in many studies in the literature, nonlinear static analysis has been used when analyzing shear walls produced through 3DCP or traditional methods [2,8,9,11,18,20,24,33,36,42,64,67,74–77]. In this study, nonlinear static analysis was selected as the analysis method to account for nonlinear material properties, since a nonlinear material model was used (Figure 3.16, Figure 3.17). Second-order moments (P-Δ effects) were also considered in the analyses to obtain realistic capacities of the walls [2,74]. During these analyses, the lateral loads acting on the walls were applied using the displacement-controlled technique [2]. In this technique, the loads are applied to the structure until a displacement that could cause failure in the structure occurs, and the results obtained can be used to calculate the performance level, capacity, and structural ductility of the structure [74,77].

Details of "Static Structural (A5)"	
Definition	
Physics Type	Structural
Analysis Type	Static Structural
Solver Target	Mechanical APDL
Options	
Environment Temperature	22, °C
Generate Input Only	No

Figure 3.16. The analysis method used in numerical analyses.

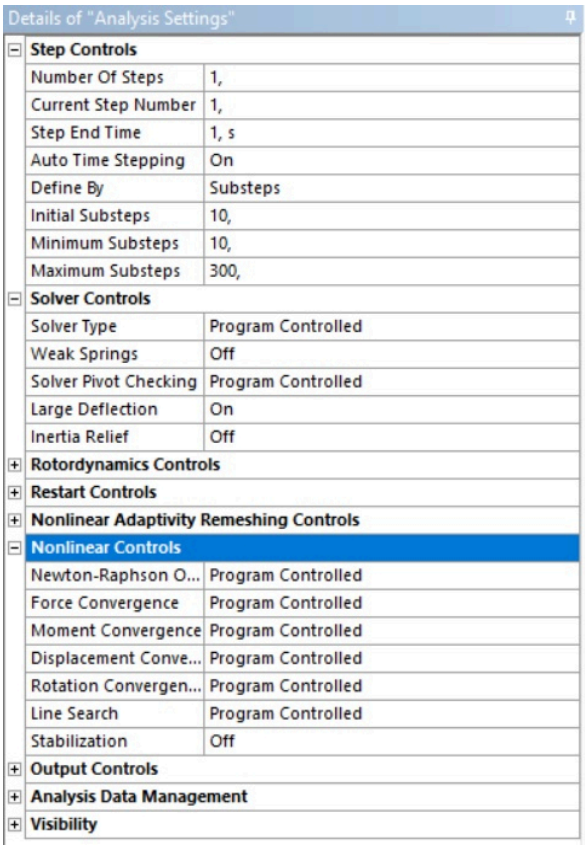

Figure 3.17. The details of the analysis method used in numerical analyses.

Nonlinear analysis is generally performed through an iterative process. Investigating nonlinear behavior encompasses the plastic analysis and buckling of structures. A key challenge in nonlinear analysis is solving systems of nonlinear equations [73]. As loading conditions vary over time, the stiffness of the structure may increase or decrease, potentially leading to a more stable or unstable equilibrium path, while the structure might be undergoing the loading or unloading phase. These occurrences are marked by the presence of critical points, such as limit points and snap-back points, in the load-displacement curves [73].

The solution process can be executed through various approaches. The essential requirement for any method is its capacity to address numerical challenges associated with different types of behavior. In practical nonlinear analysis, external forces are applied gradually. Typically, solving the set of nonlinear equations is accomplished using incremental or iterative techniques, such as the predictor-corrector method [73]. This is achieved by solving the equations for a series of load or displacement parameter values.

The solution corresponding to a specific value of the parameter is used to calculate an appropriate approach (predictor) for displacements at a different value of the parameter. This approach then serves as the initial estimate for displacements in a corrective iterative process [73].

3.2.3. Assessment of Results Obtained from FE Analyses

In this study, the nonlinear static pushover curves obtained from the numerical analyses are shown in Figures 3.18 to 3.98. As can be understood from these curves, as the width, length, thickness, and height values of the walls increase, the base shear force increases, while the maximum displacement values decrease. In other words, as the width, length, thickness, and height values increase, the walls exhibit more brittle behavior. This means a decrease in ductility, which is the ability of the elements to undergo plastic deformation. Some walls with hollow topology have bilinear graphs. However, this is not an abnormal situation because such cases are encountered in the literature, as shown in Figure 3.99 [4,24].

Moreover, as the wall topology transitions from hollow to solid, i.e., as the solidity ratio of the wall interior topology increases, the pushover curves also transition from linear to nonlinear form (Table 3.4). In addition, local damage zones are observed in the pushover graphs of walls with hollow interior topology. These local damage zones have been observed at the top corners of the walls, where the lateral load is applied (Figure 3.100).

Table 3.4. Percentage of linear pushover curves based on solidity ratio.

Solidity Ratio (%)	Percentage of Linear Pushover Curves (%)
5-10	73
10-20	68
20-40	67
40-60	59
60-80	54
80-100	37

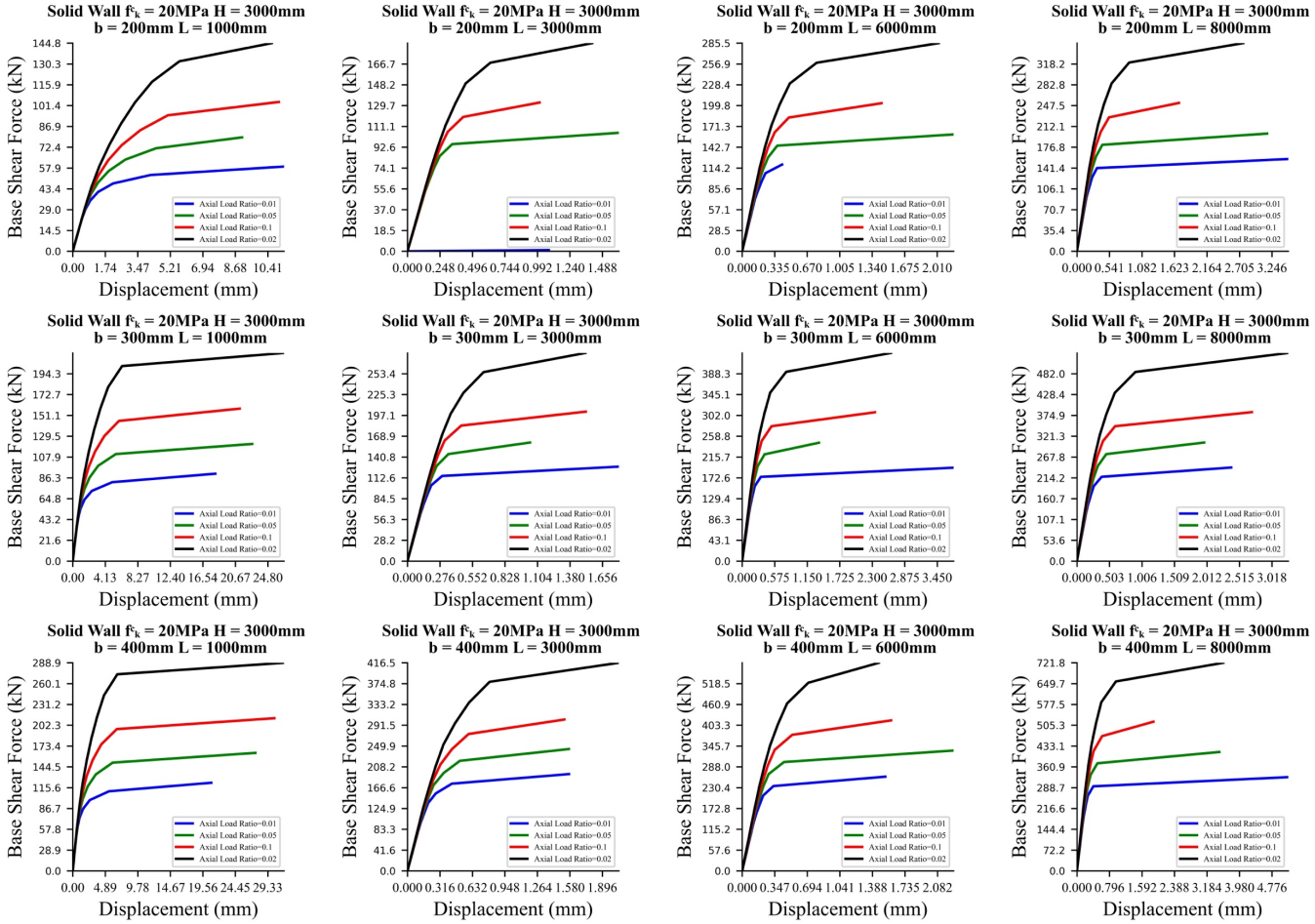

Figure 3.18. Some of the pushover curves created according to the result of the numerical analyses for walls with solid topology.

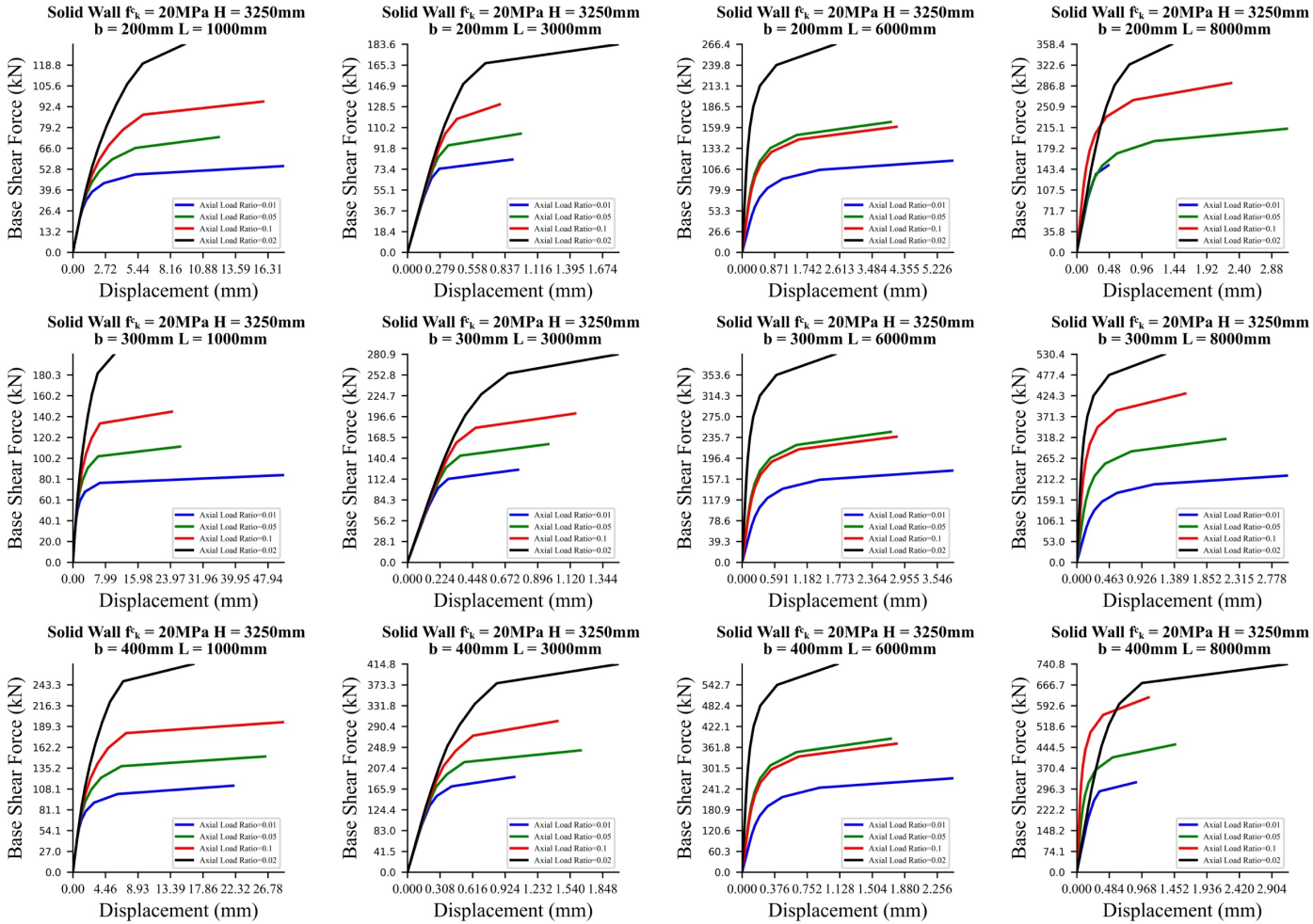

Figure 3.19. Some of the pushover curves created according to the result of the numerical analyses for walls with solid topology.

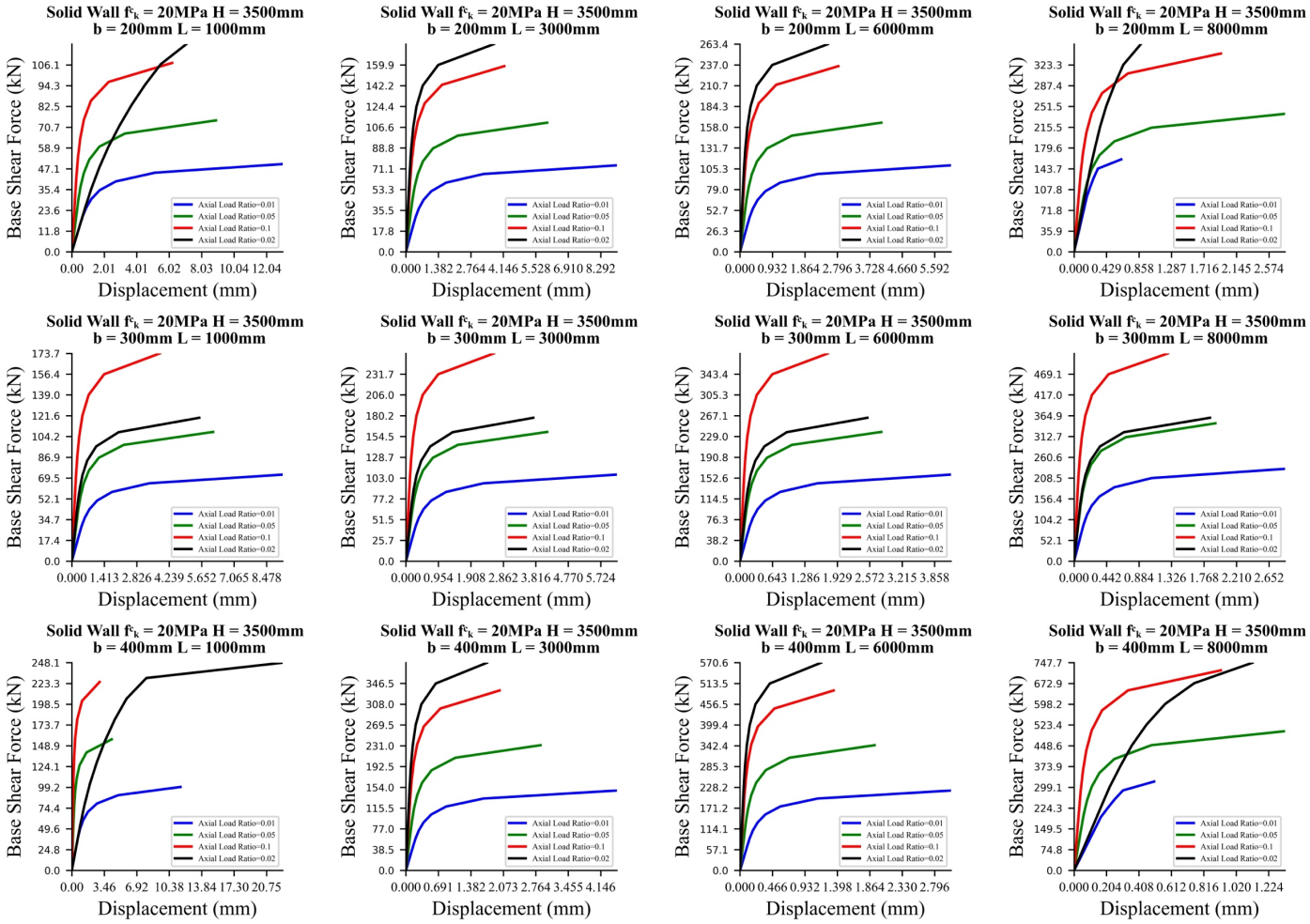

Figure 3.20. Some of the pushover curves created according to the result of the numerical analyses for walls with solid topology.

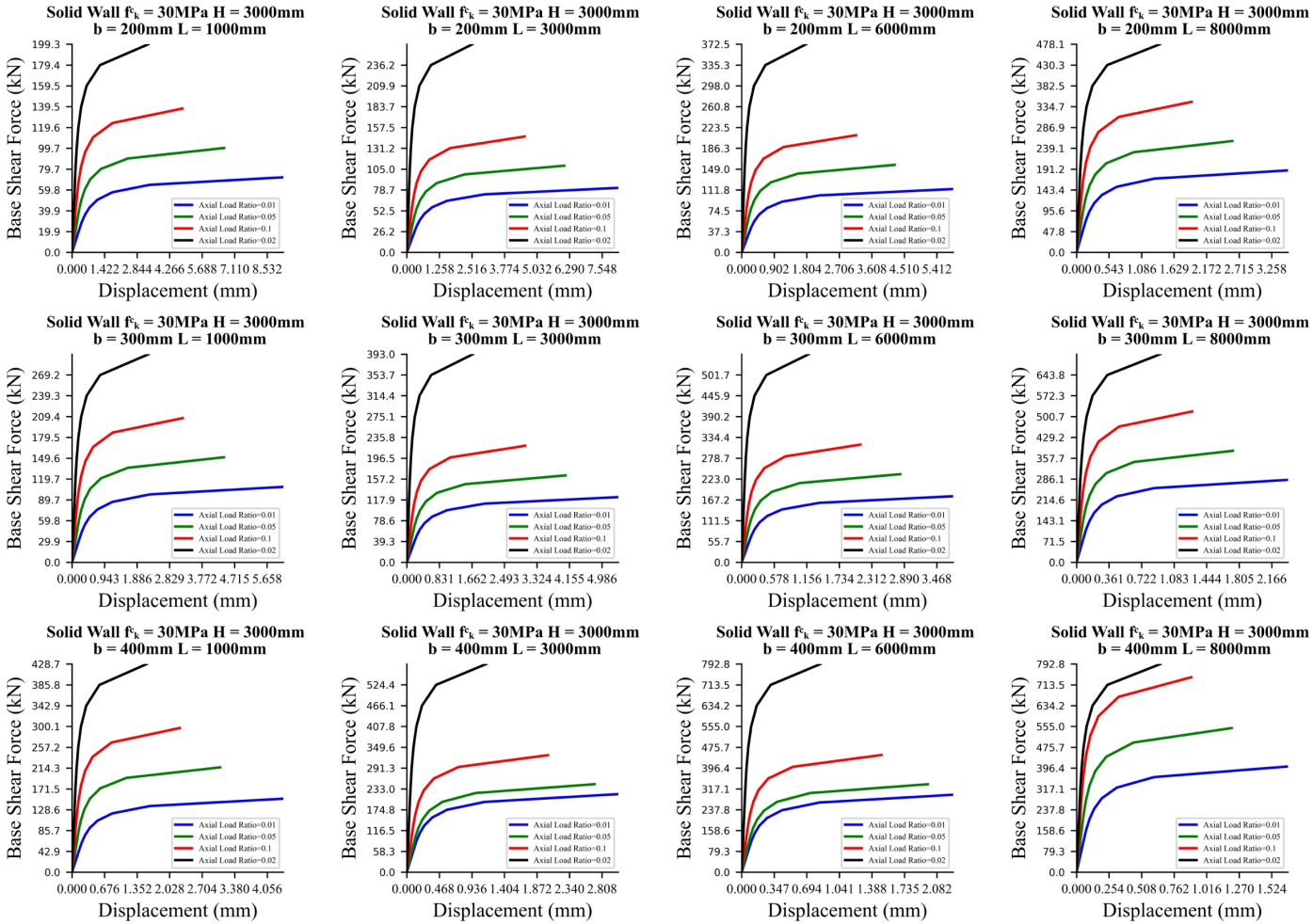

Figure 3.21. Some of the pushover curves created according to the result of the numerical analyses for walls with solid topology.

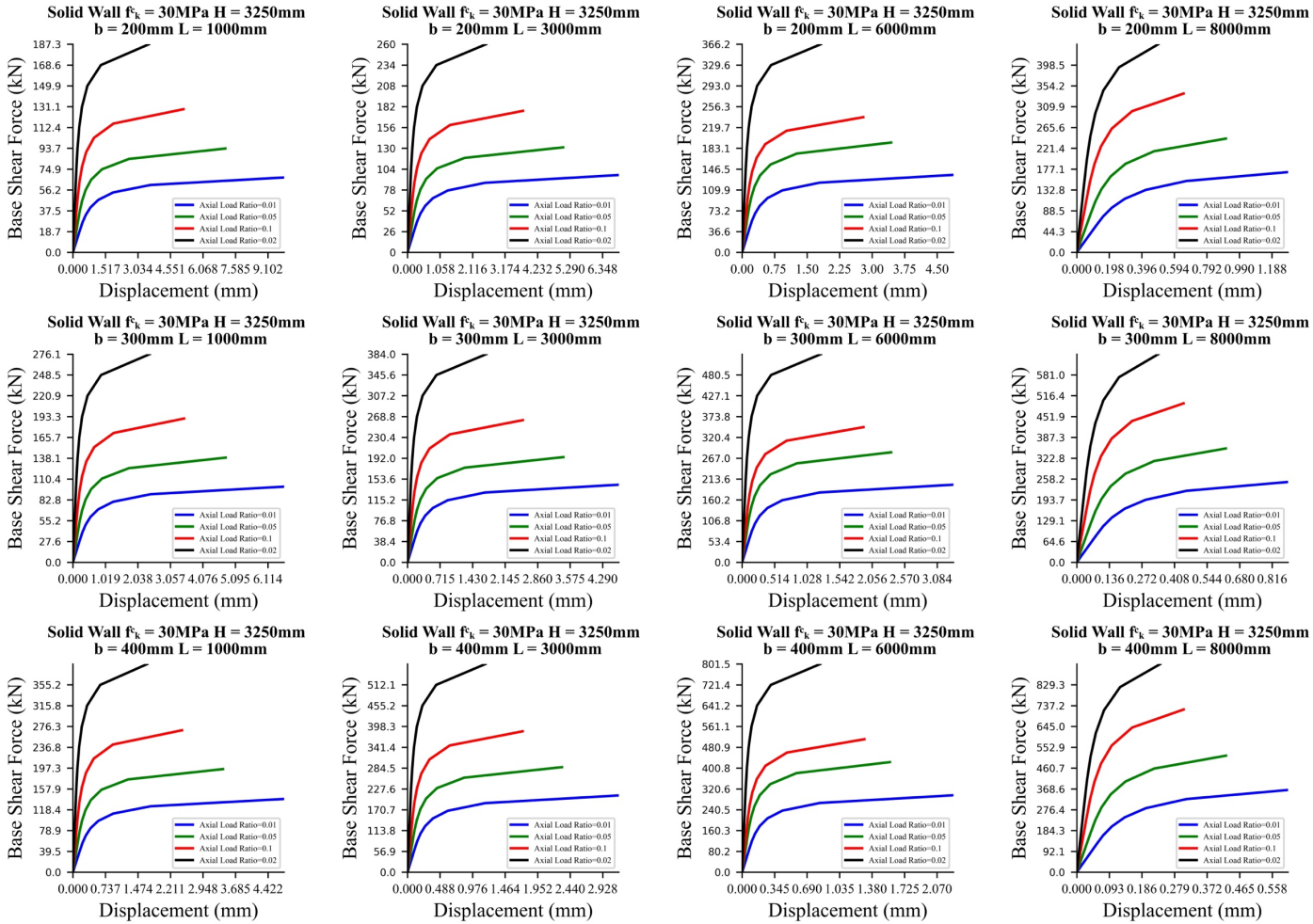

Figure 3.22. Some of the pushover curves created according to the result of the numerical analyses for walls with solid topology.

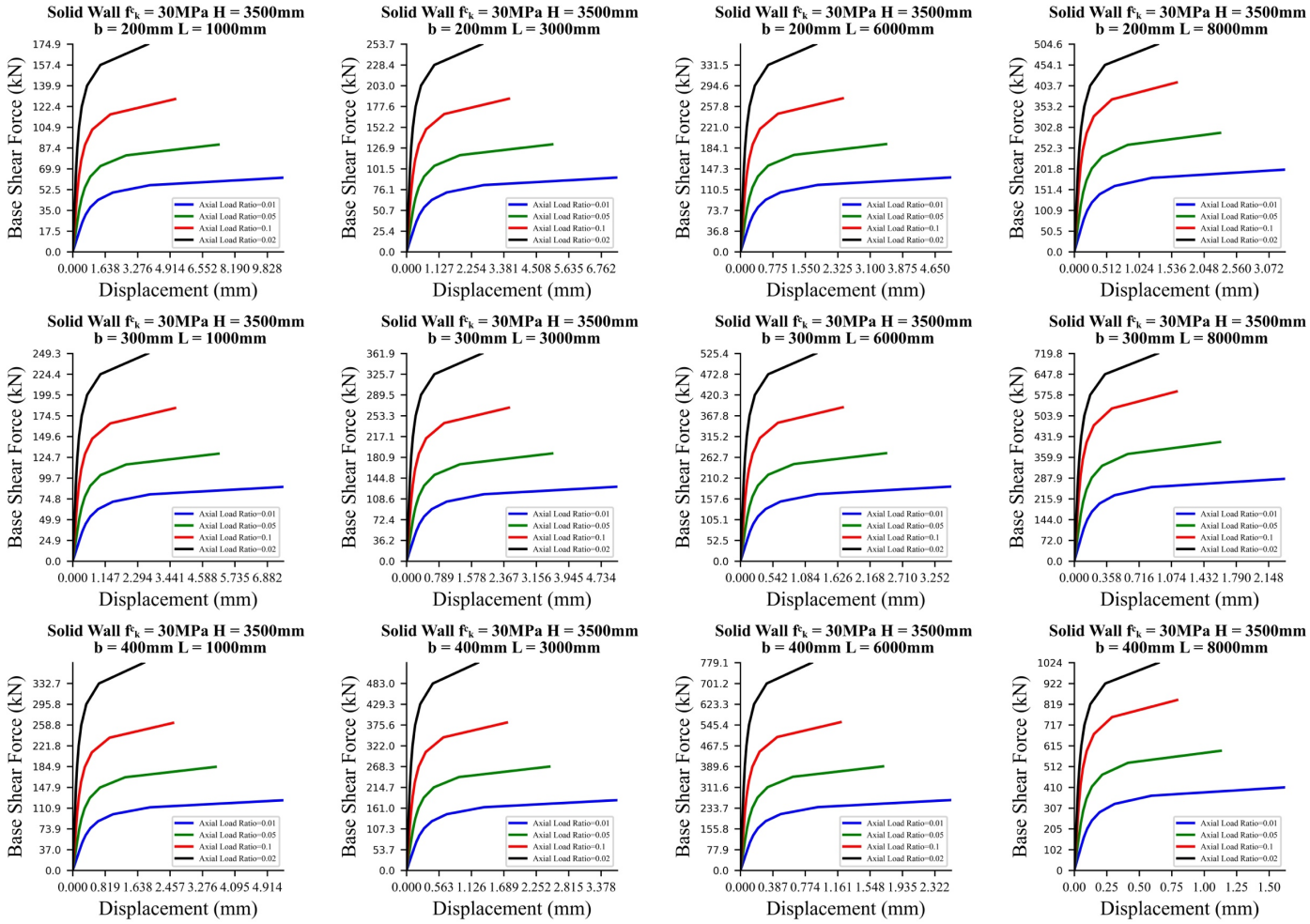

Figure 3.23. Some of the pushover curves created according to the result of the numerical analyses for walls with solid topology.

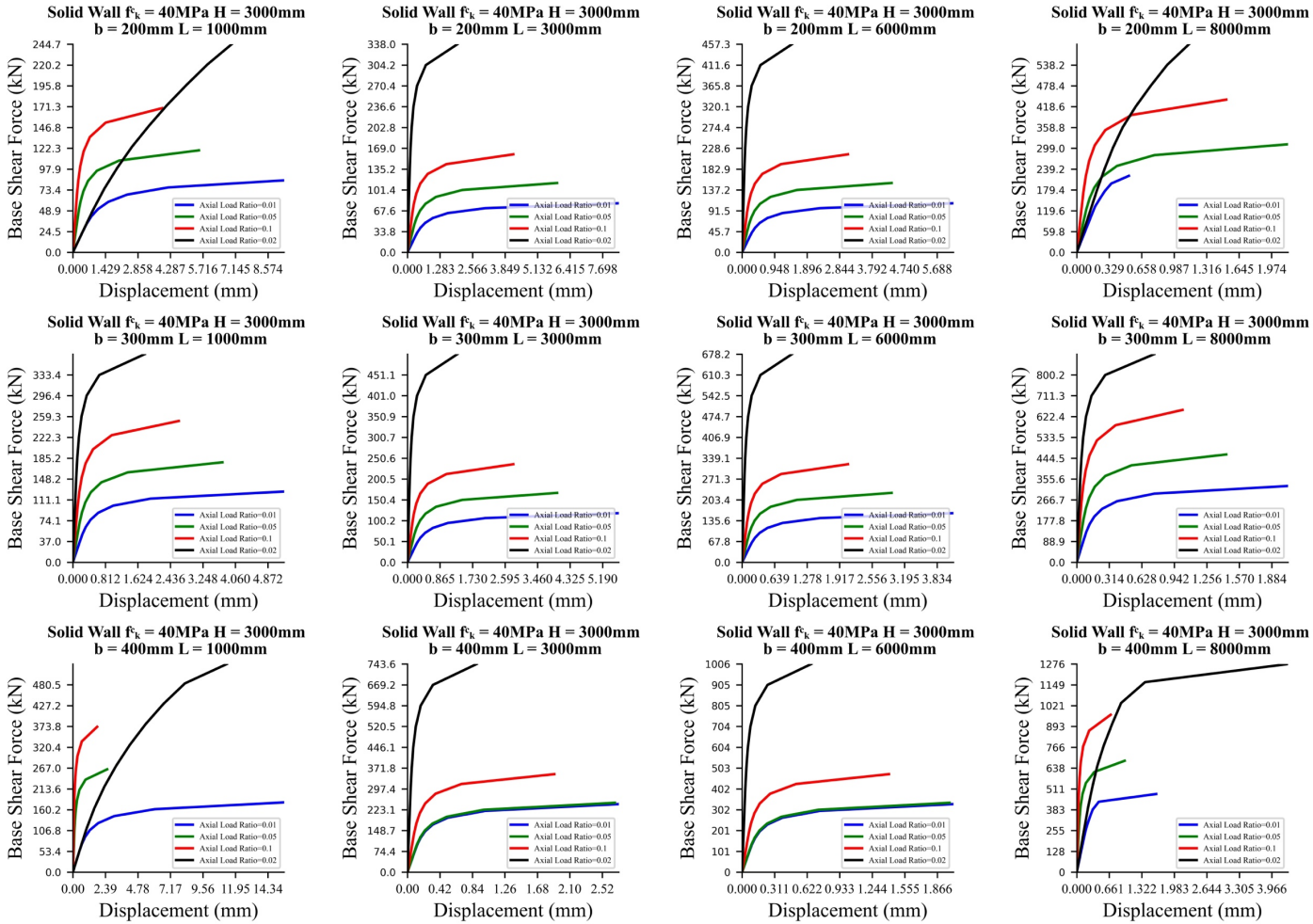

Figure 3.24. Some of the pushover curves created according to the result of the numerical analyses for walls with solid topology.

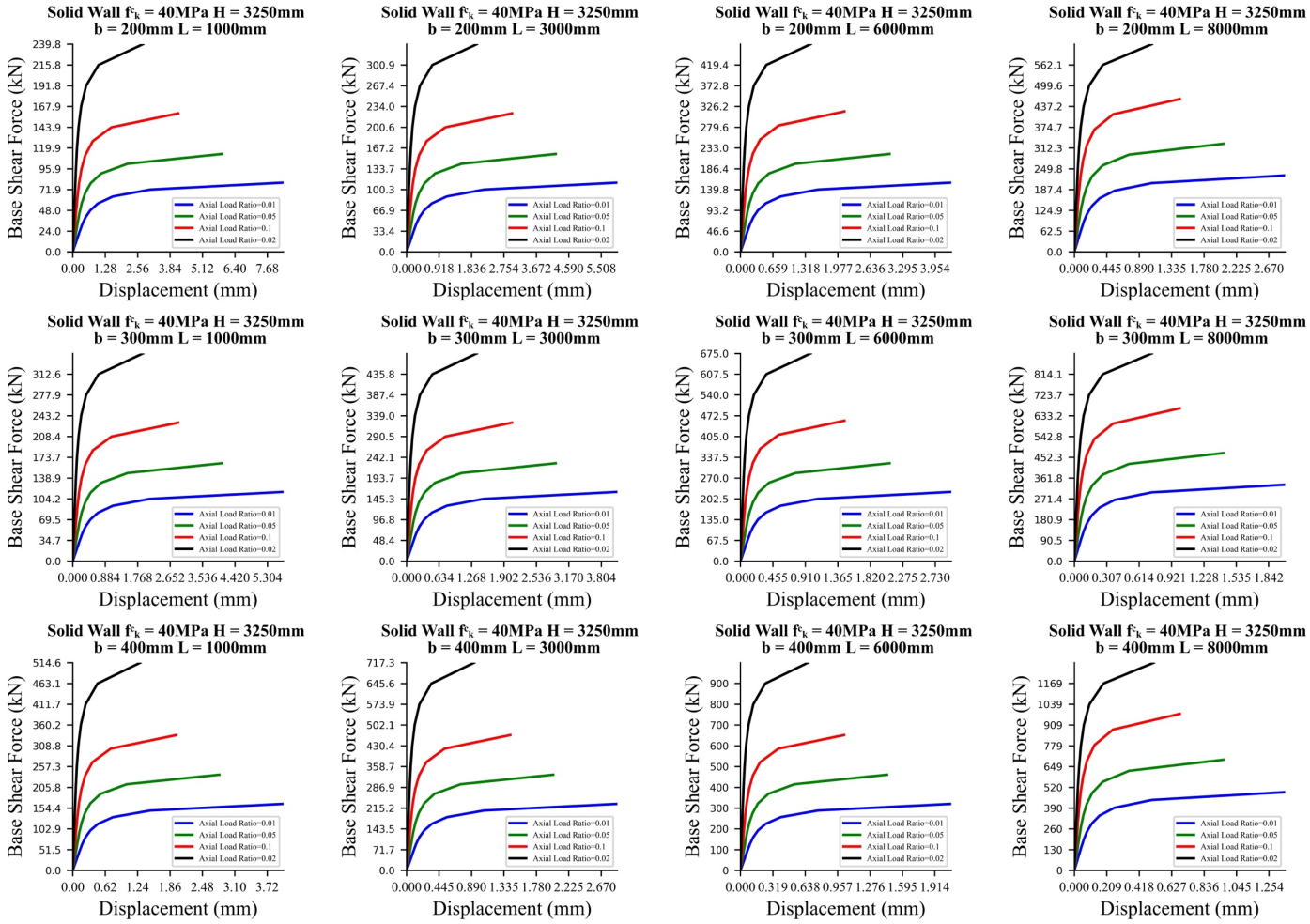

Figure 3.25. Some of the pushover curves created according to the result of the numerical analyses for walls with solid topology.

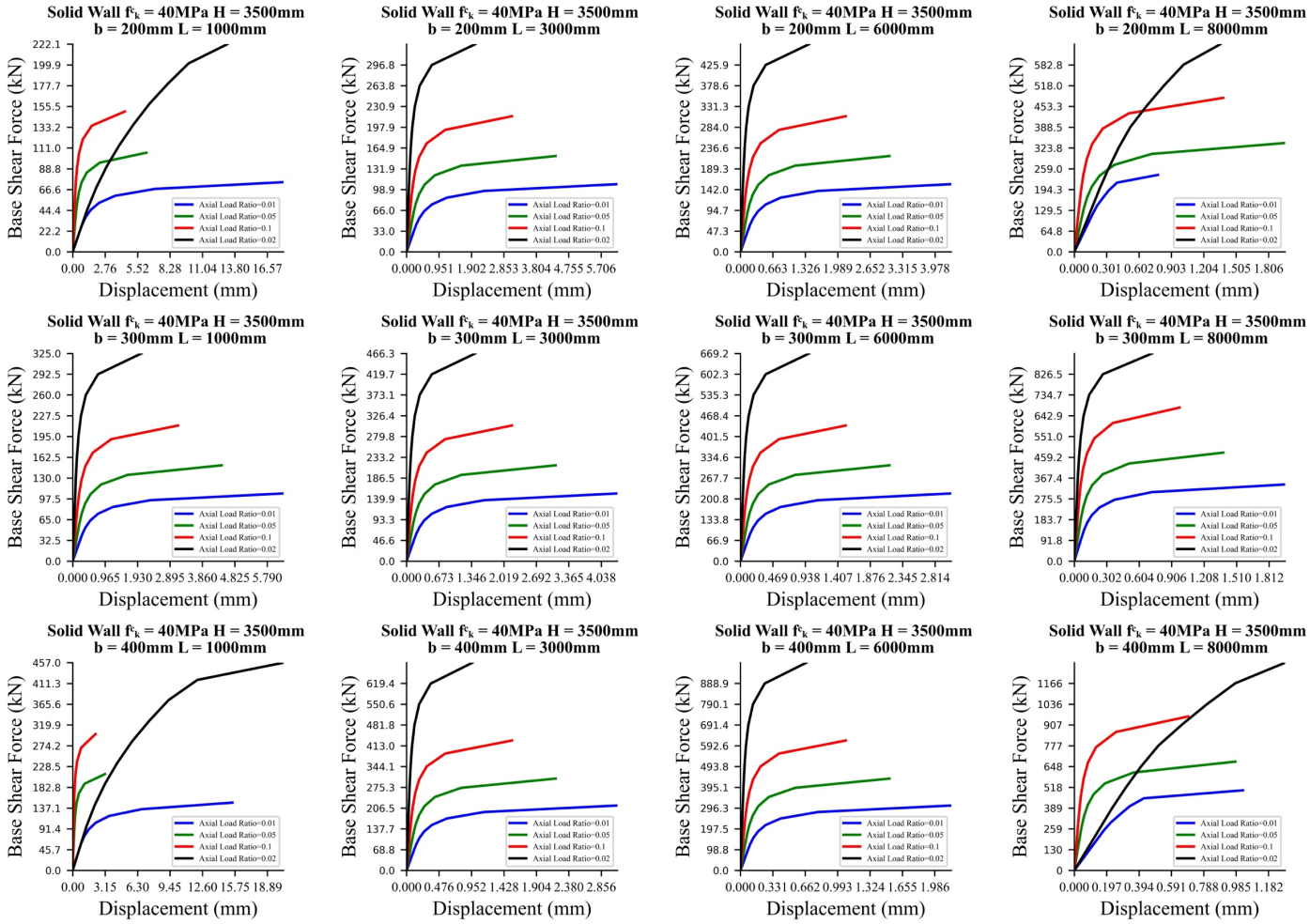

Figure 3.26. Some of the pushover curves created according to the result of the numerical analyses for walls with solid topology.

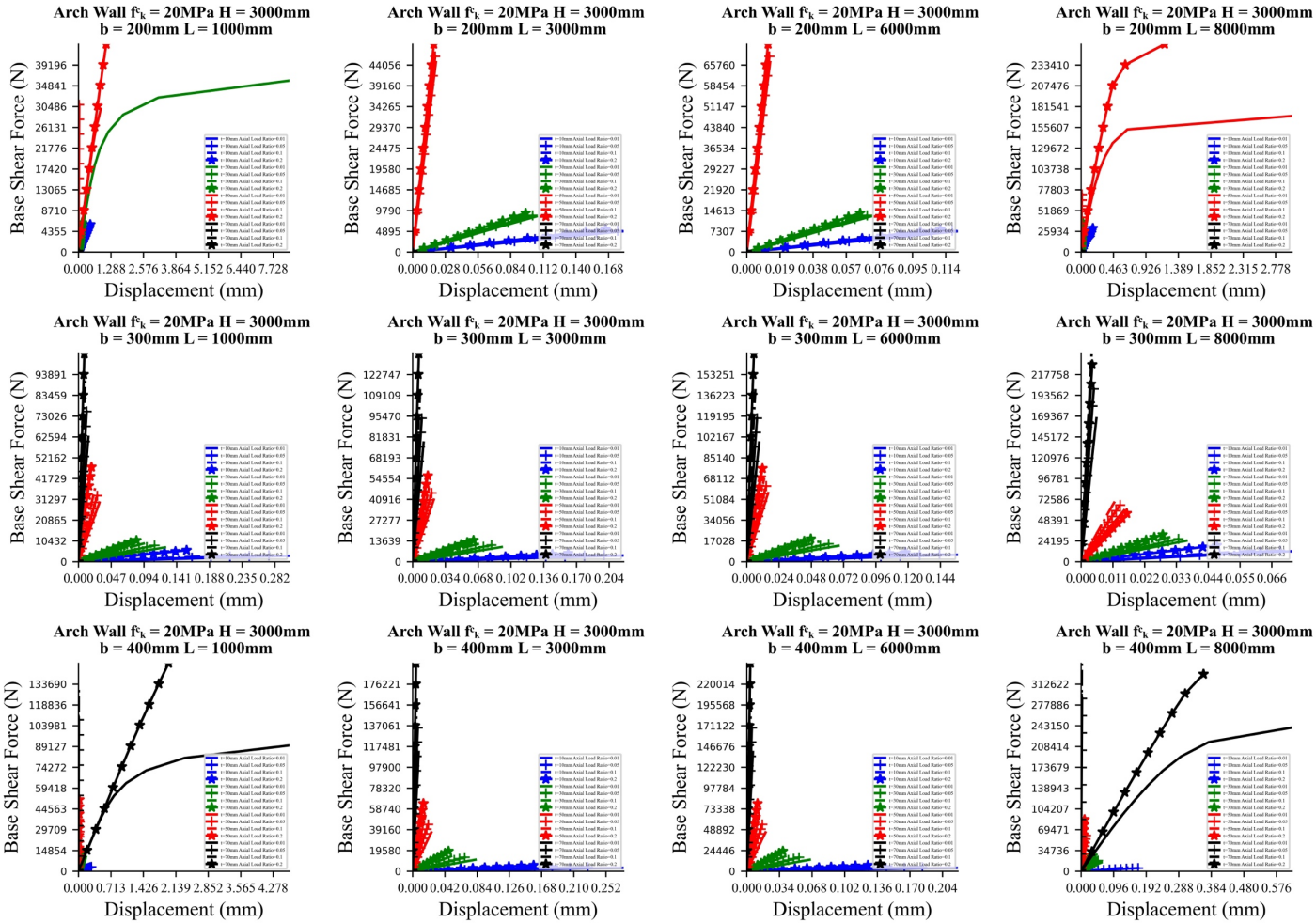

Figure 3.27. Some of the pushover curves created according to the result of the numerical analyses for walls with arch topology.

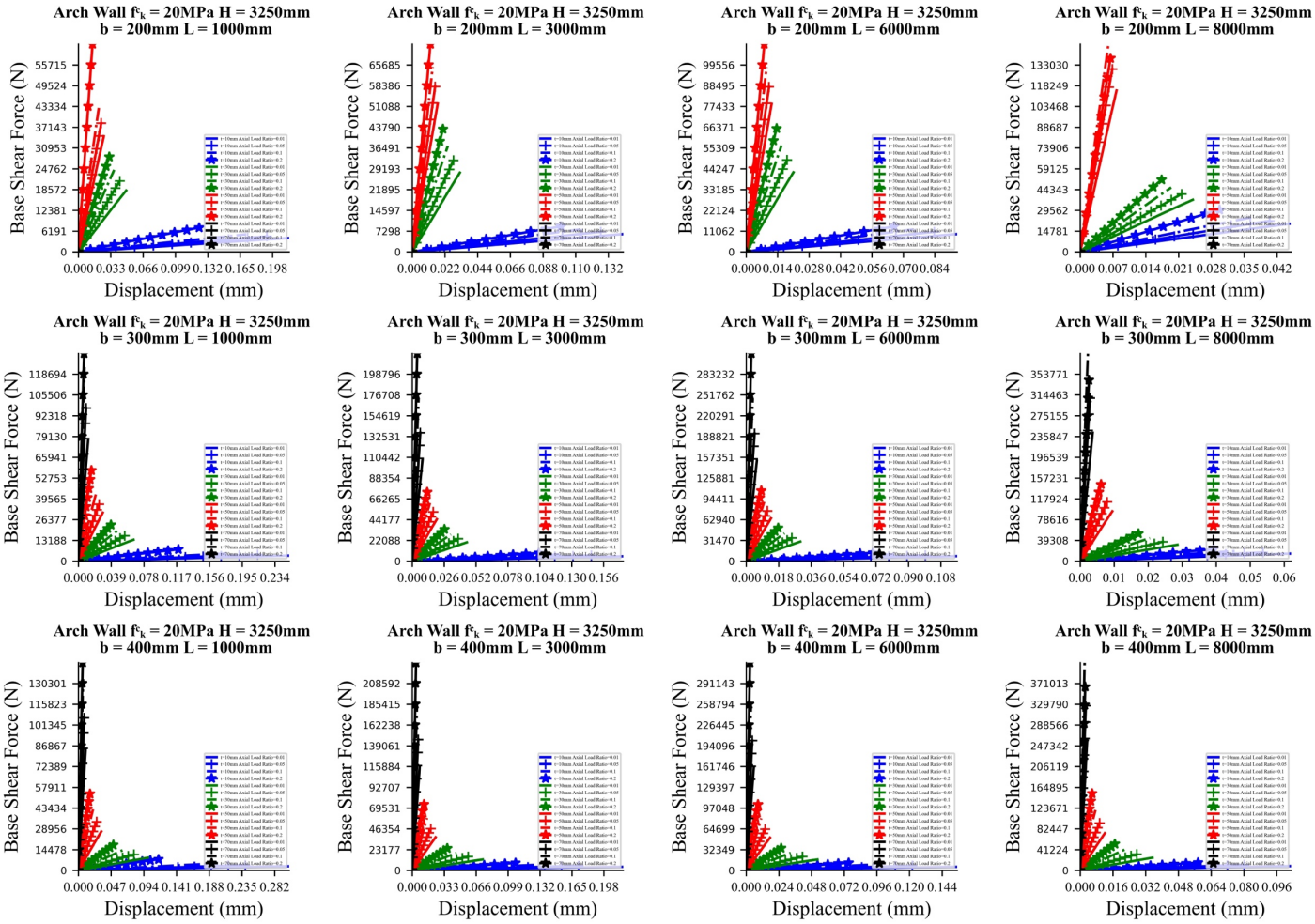

Figure 3.28. Some of the pushover curves created according to the result of the numerical analyses for walls with arch topology.

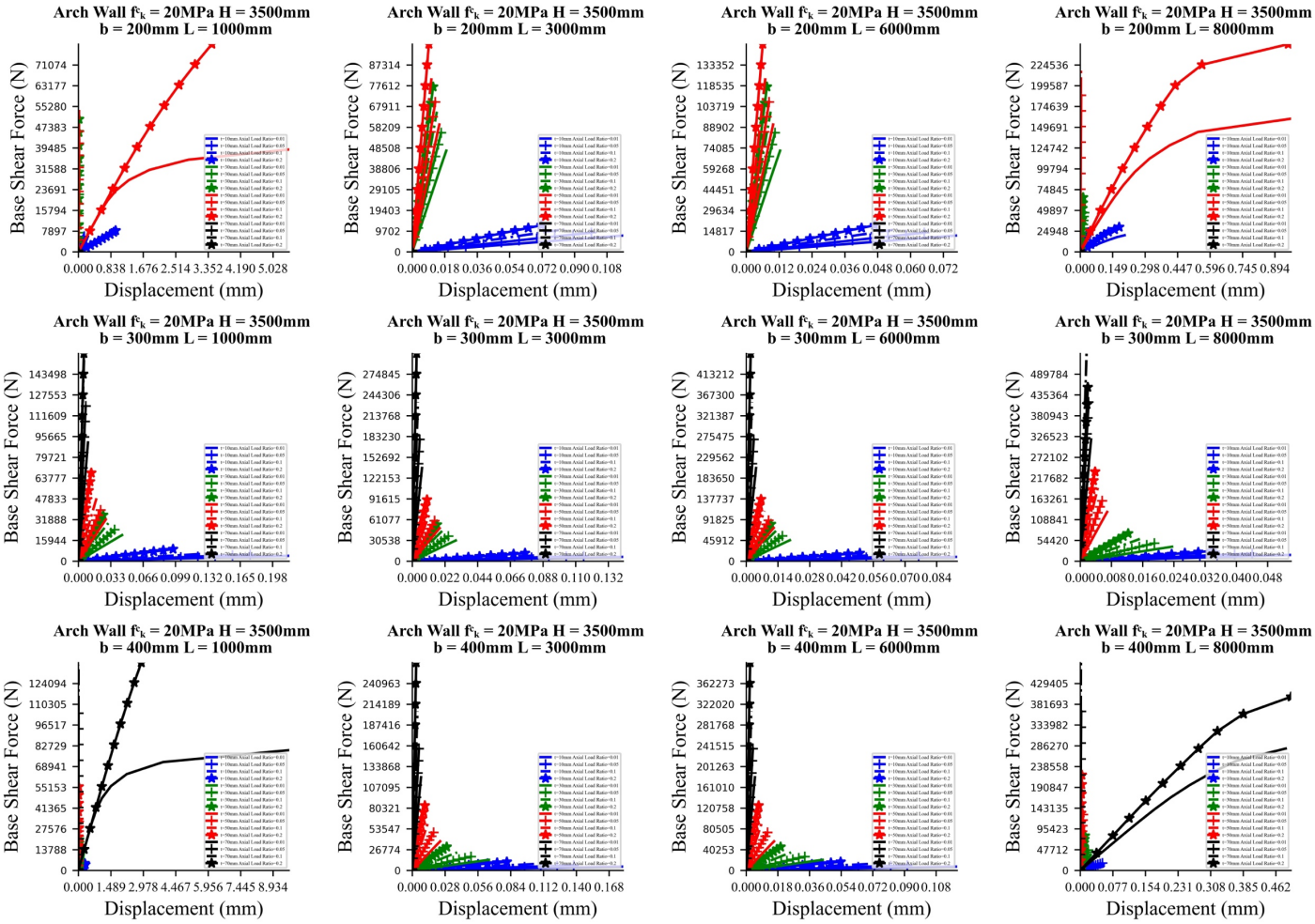

Figure 3.29. Some of the pushover curves created according to the result of the numerical analyses for walls with arch topology.

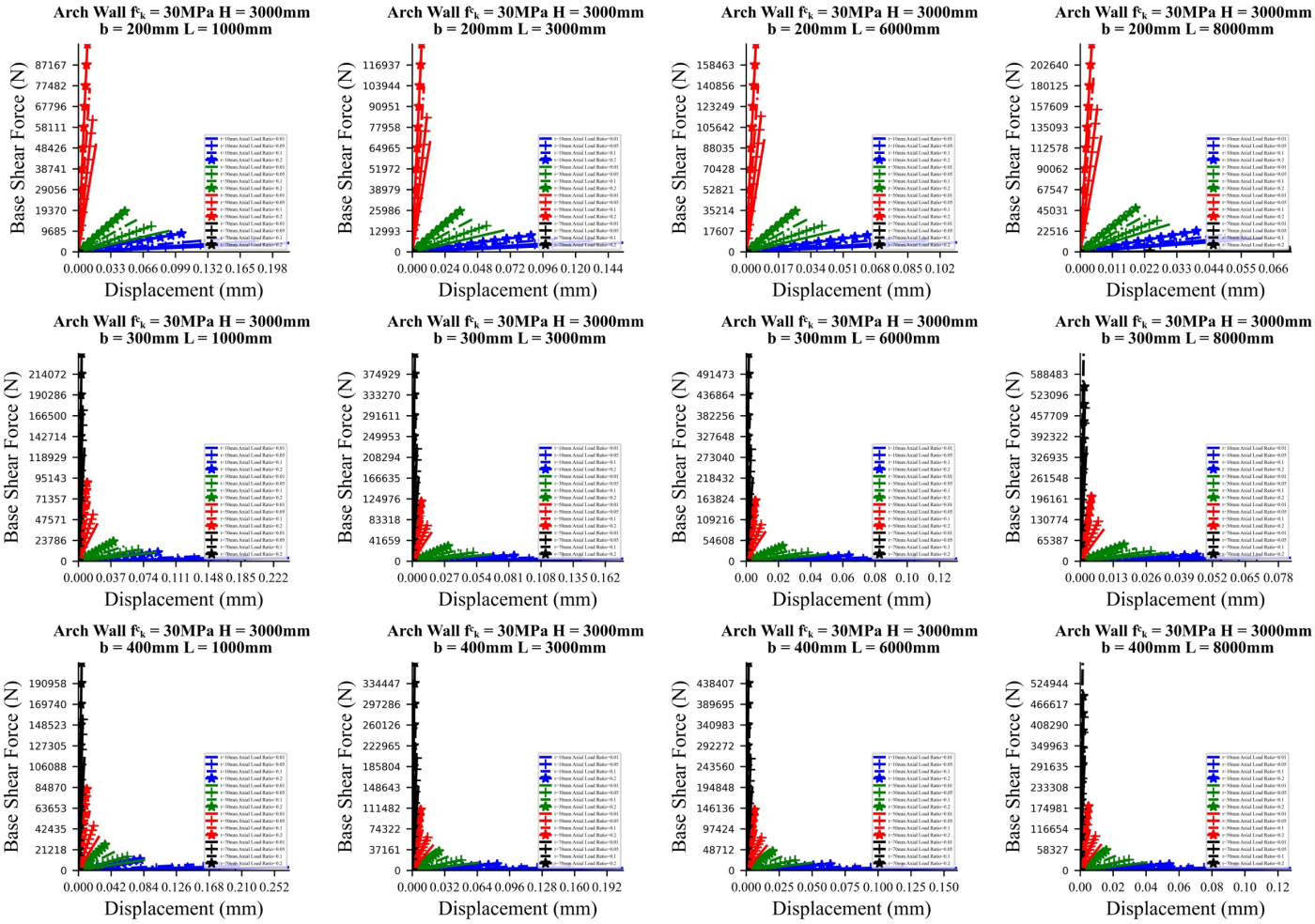

Figure 3.30. Some of the pushover curves created according to the result of the numerical analyses for walls with arch topology.

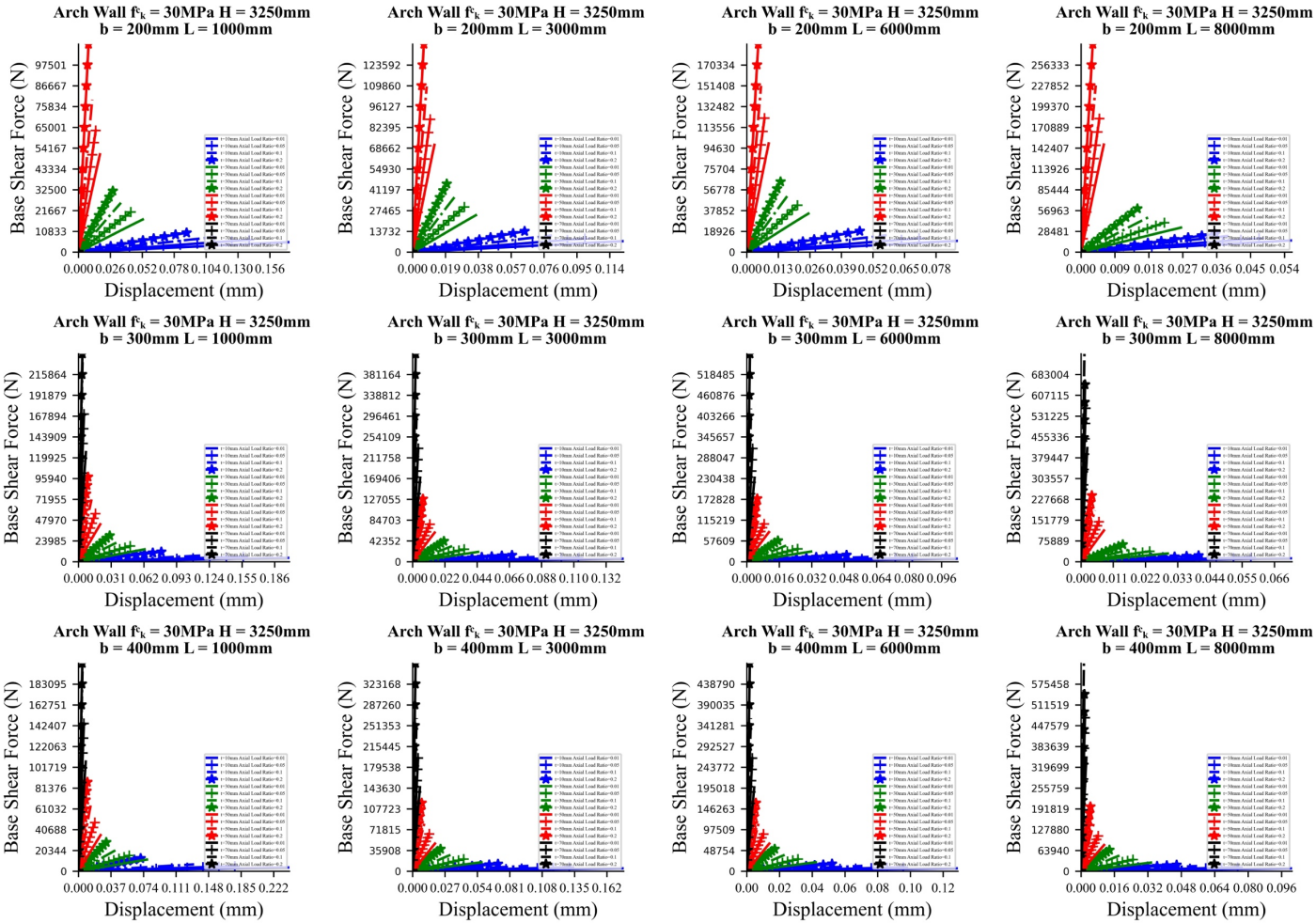

Figure 3.31. Some of the pushover curves created according to the result of the numerical analyses for walls with arch topology.

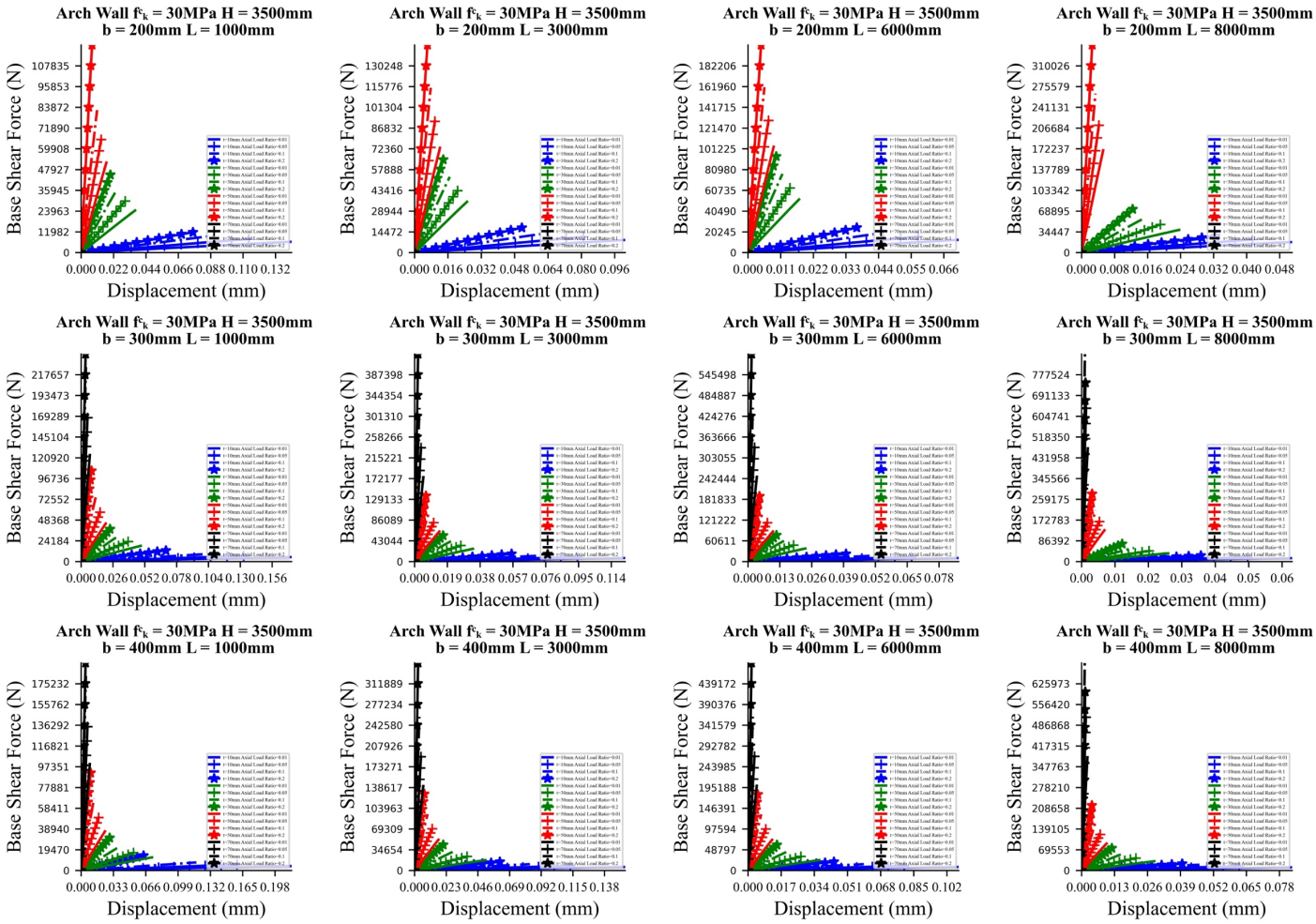

Figure 3.32. Some of the pushover curves created according to the result of the numerical analyses for walls with arch topology.

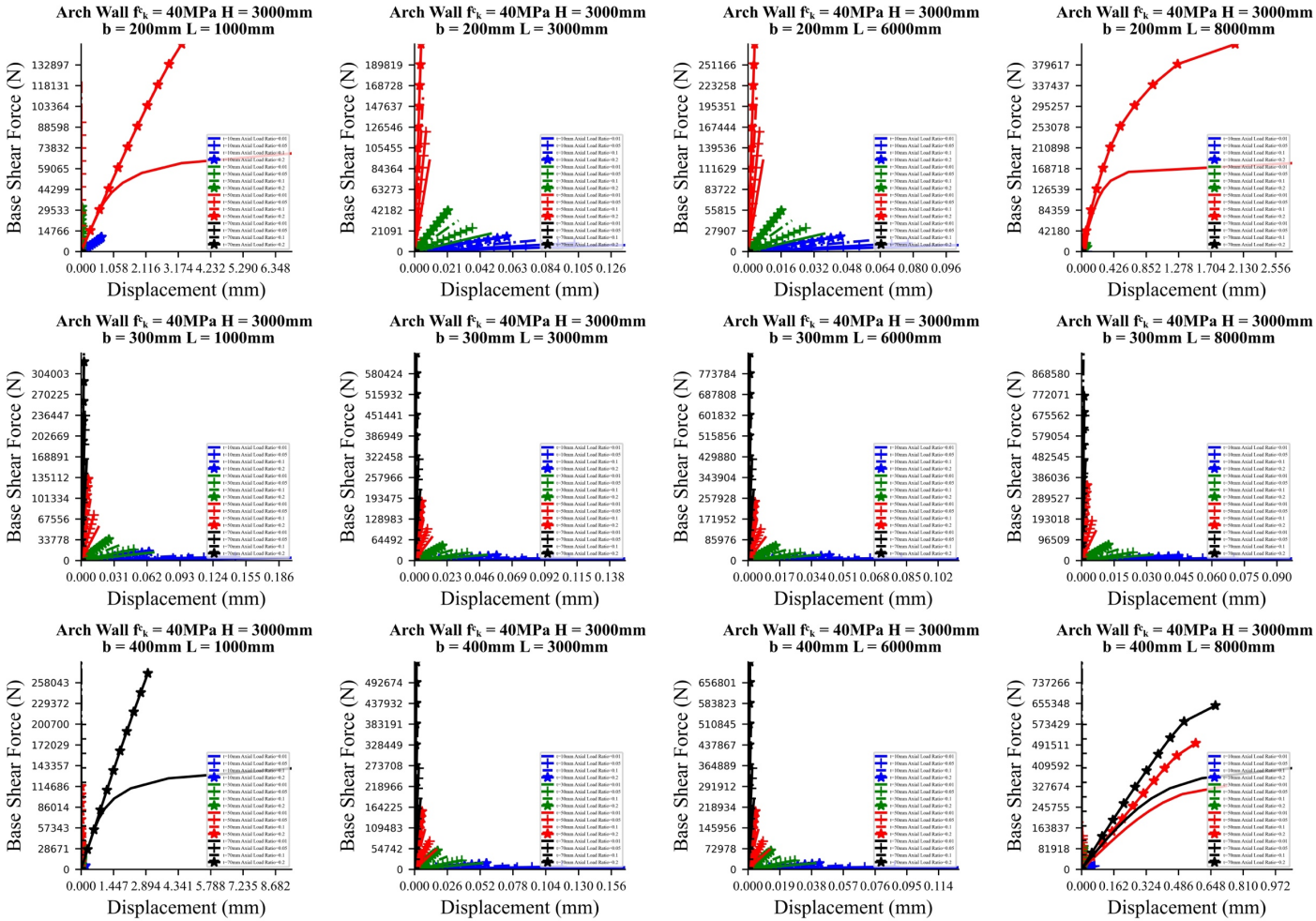

Figure 3.33. Some of the pushover curves created according to the result of the numerical analyses for walls with arch topology.

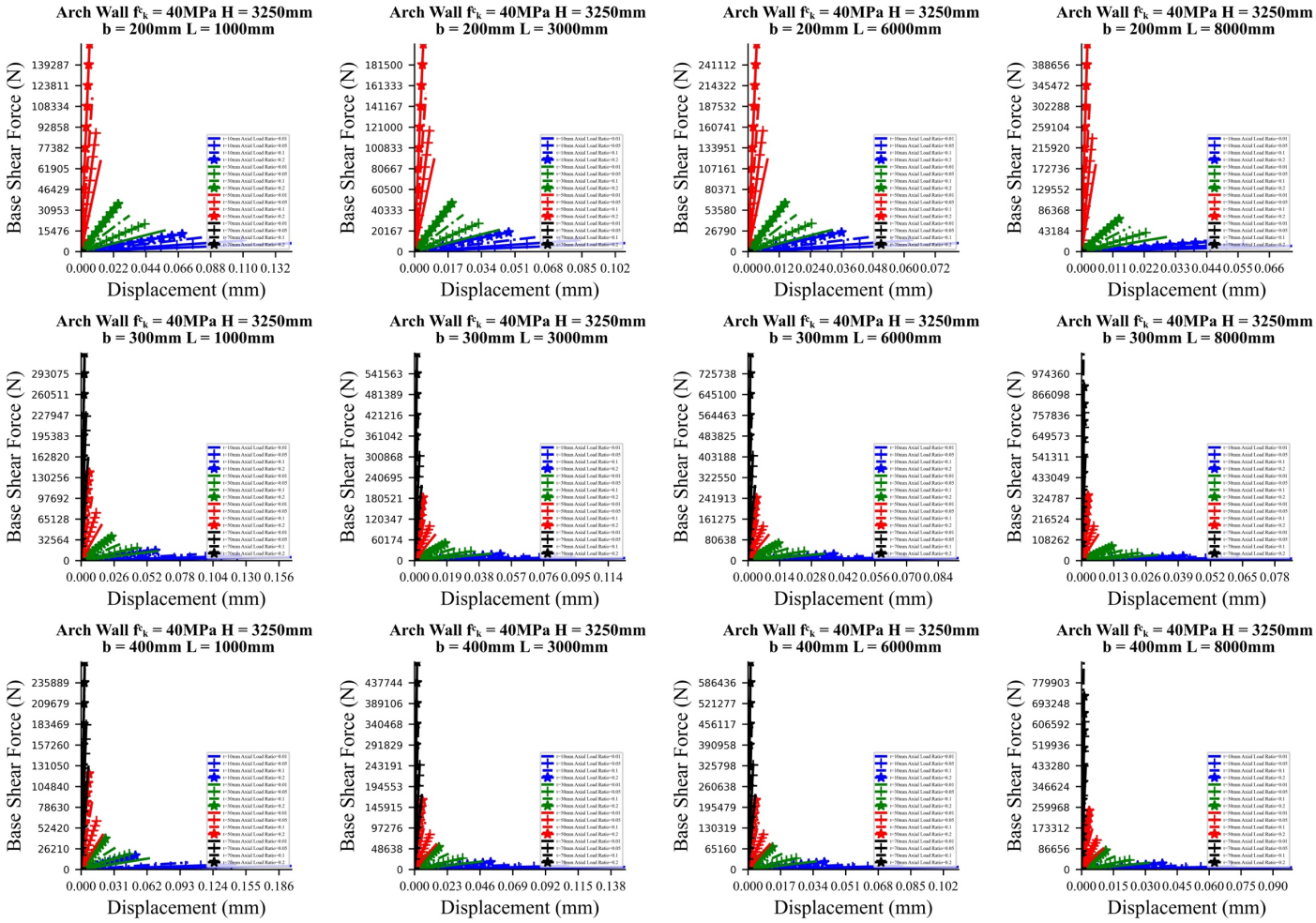

Figure 3.34. Some of the pushover curves created according to the result of the numerical analyses for walls with arch topology.

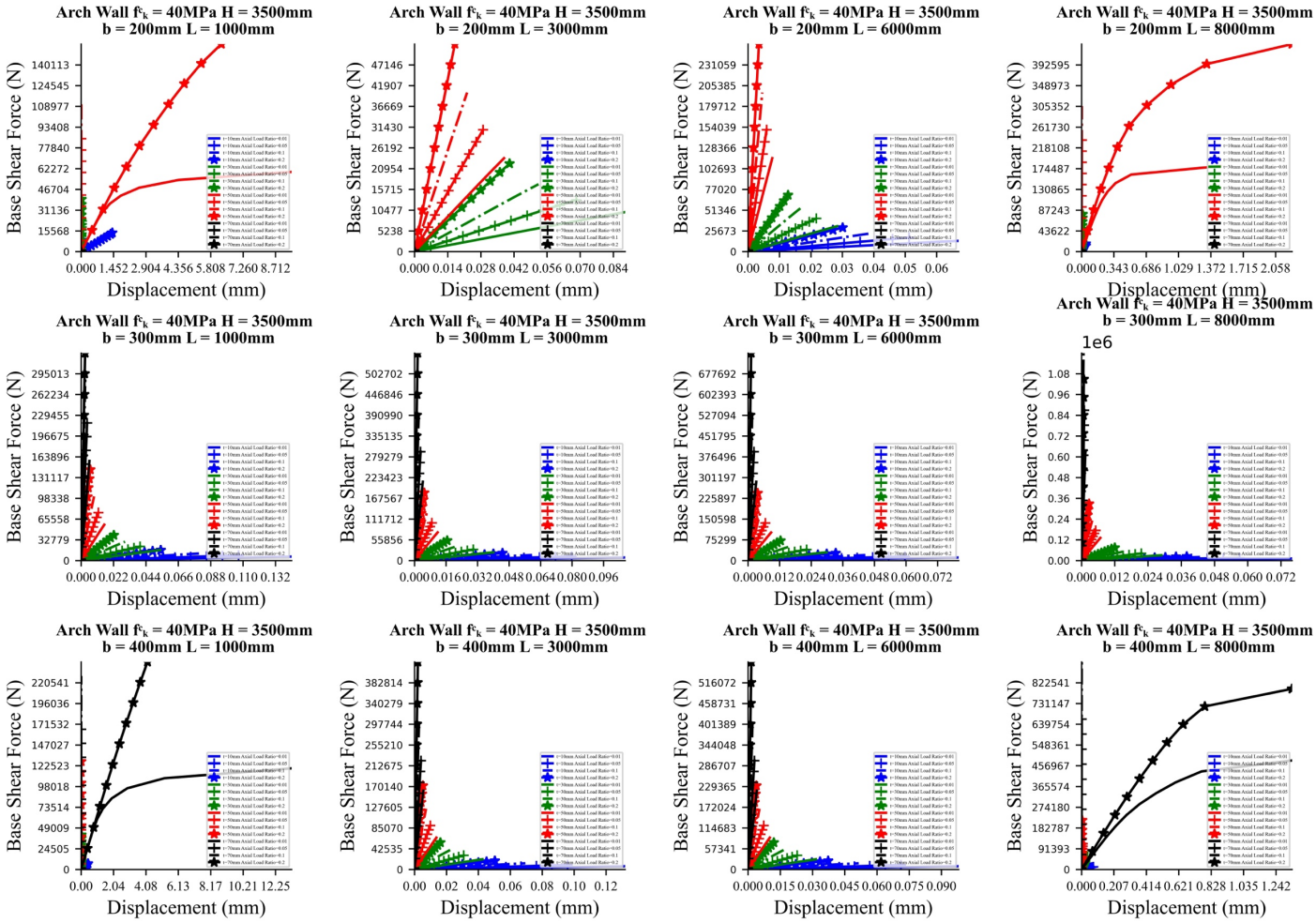

Figure 3.35. Some of the pushover curves created according to the result of the numerical analyses for walls with arch topology.

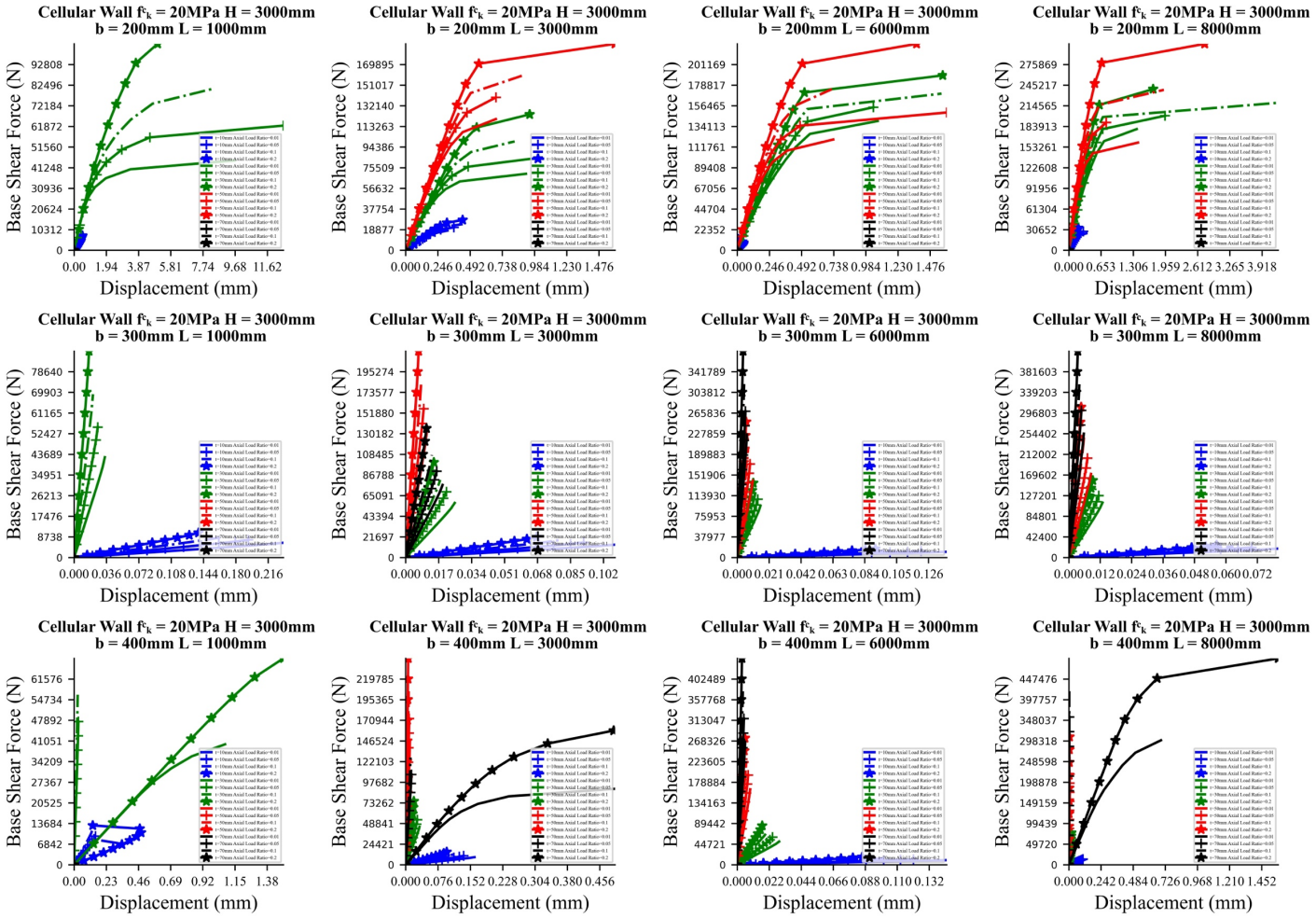

Figure 3.36. Some of the pushover curves created according to the result of the numerical analyses for walls with cellular topology.

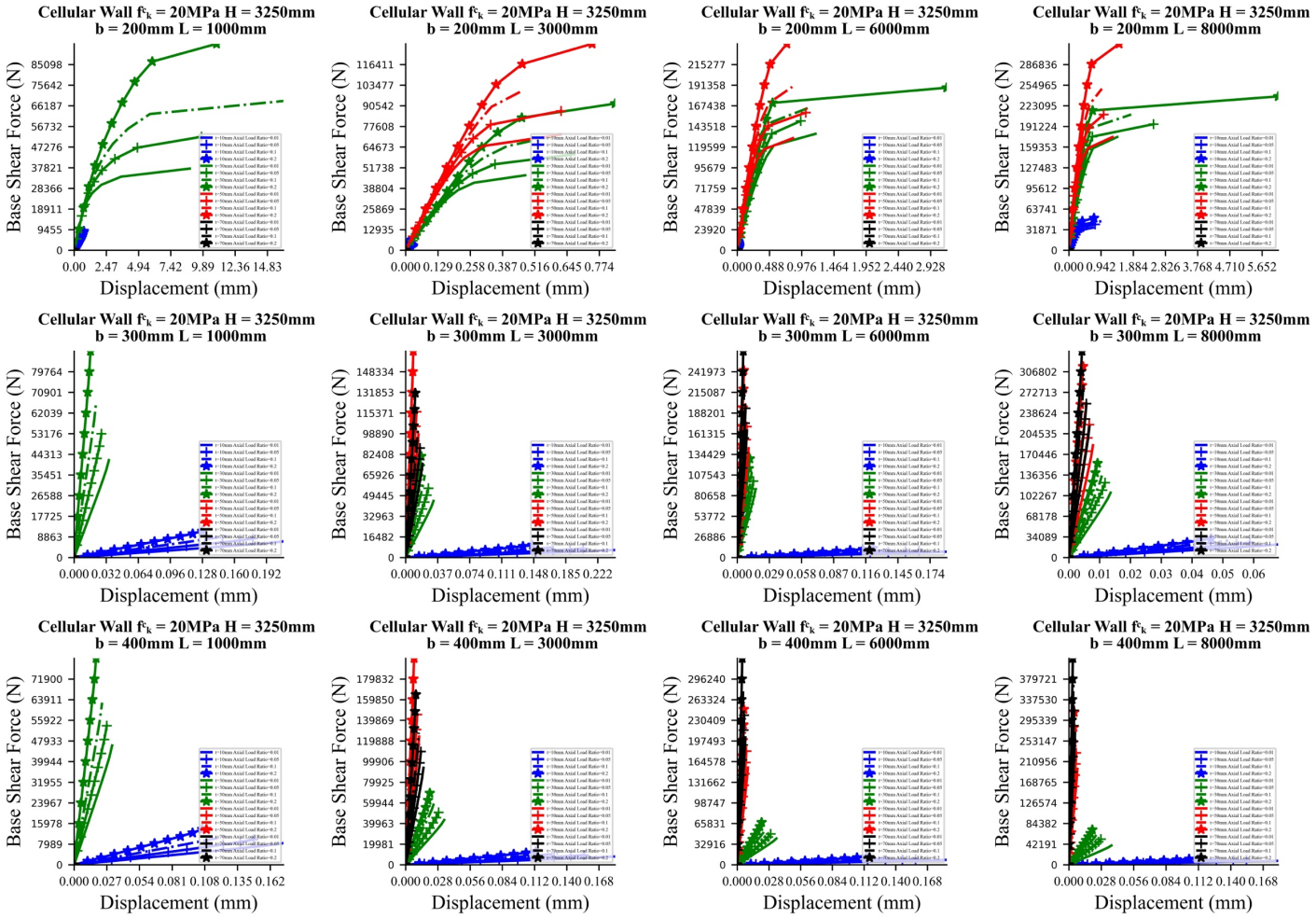

Figure 3.37. Some of the pushover curves created according to the result of the numerical analyses for walls with cellular topology.

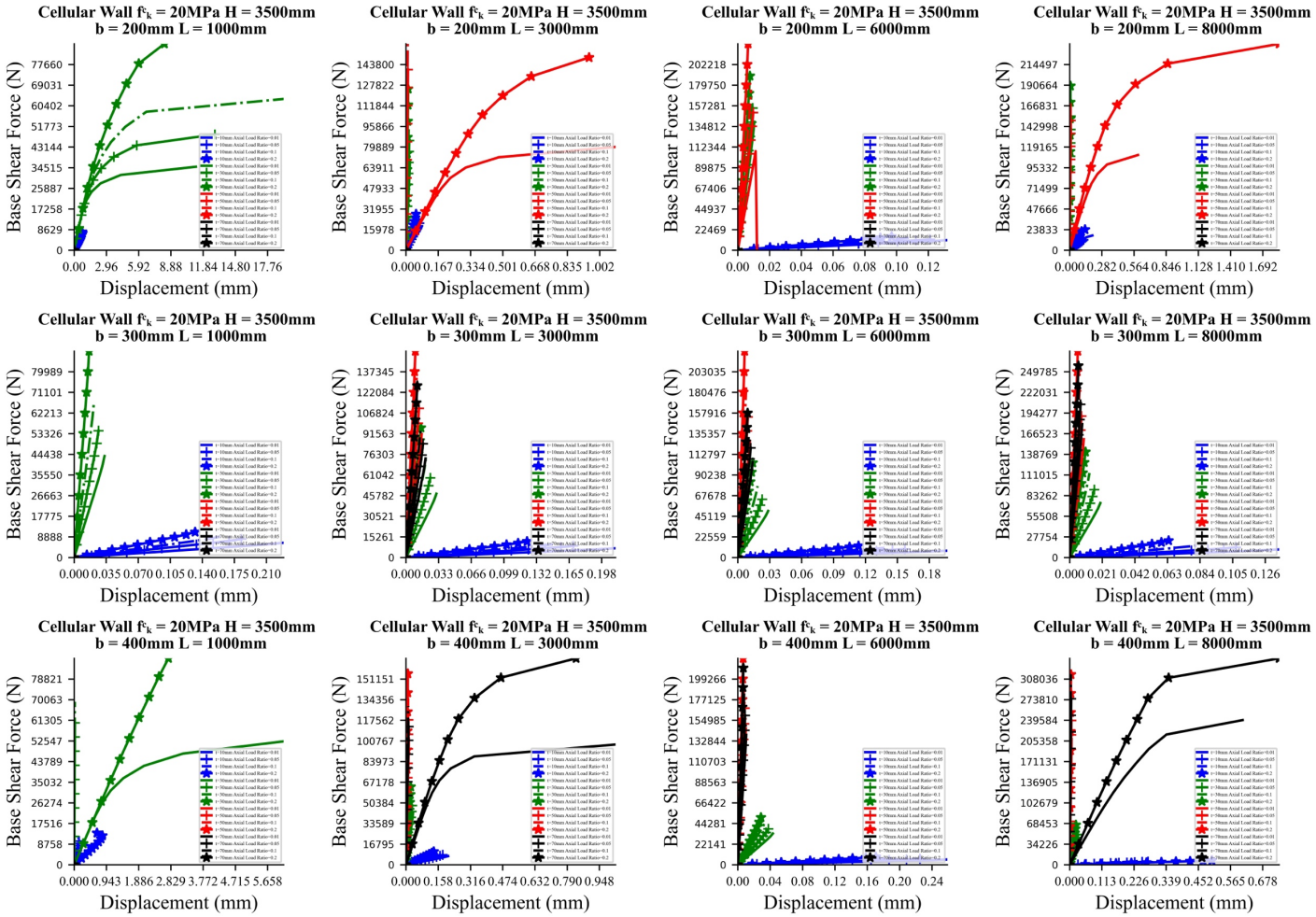

Figure 3.38. Some of the pushover curves created according to the result of the numerical analyses for walls with cellular topology.

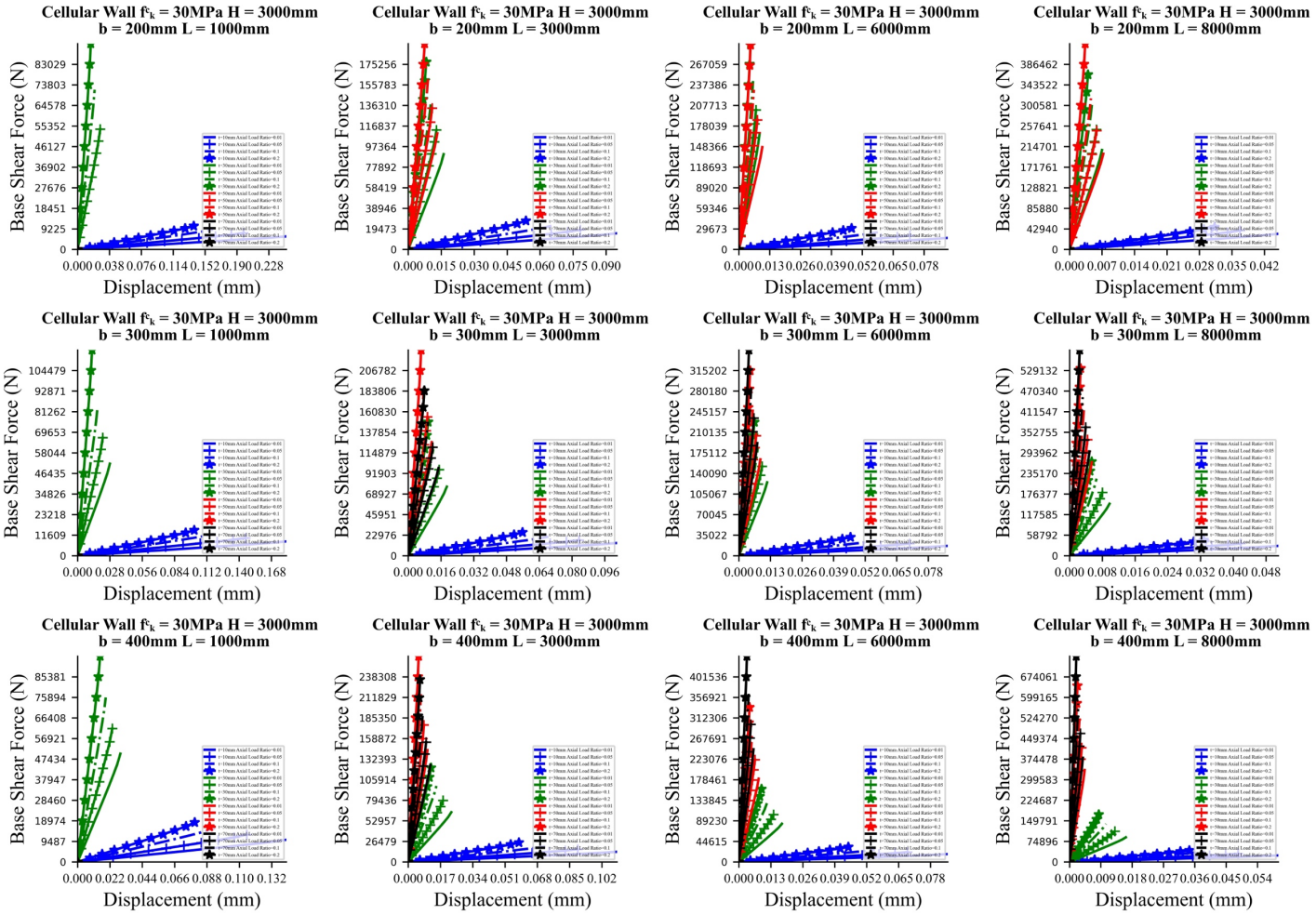

Figure 3.39. Some of the pushover curves created according to the result of the numerical analyses for walls with cellular topology.

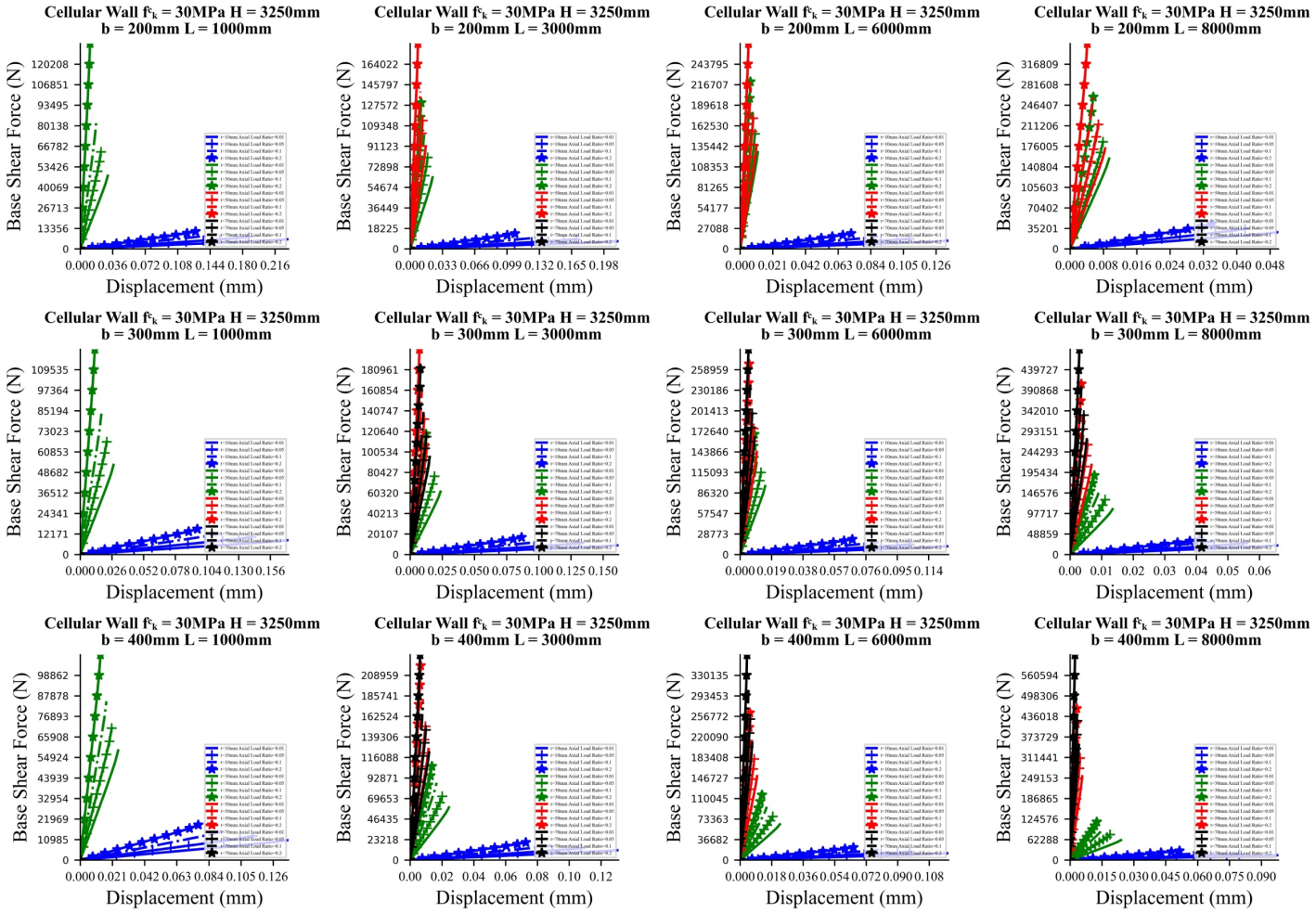

Figure 3.40. Some of the pushover curves created according to the result of the numerical analyses for walls with cellular topology.

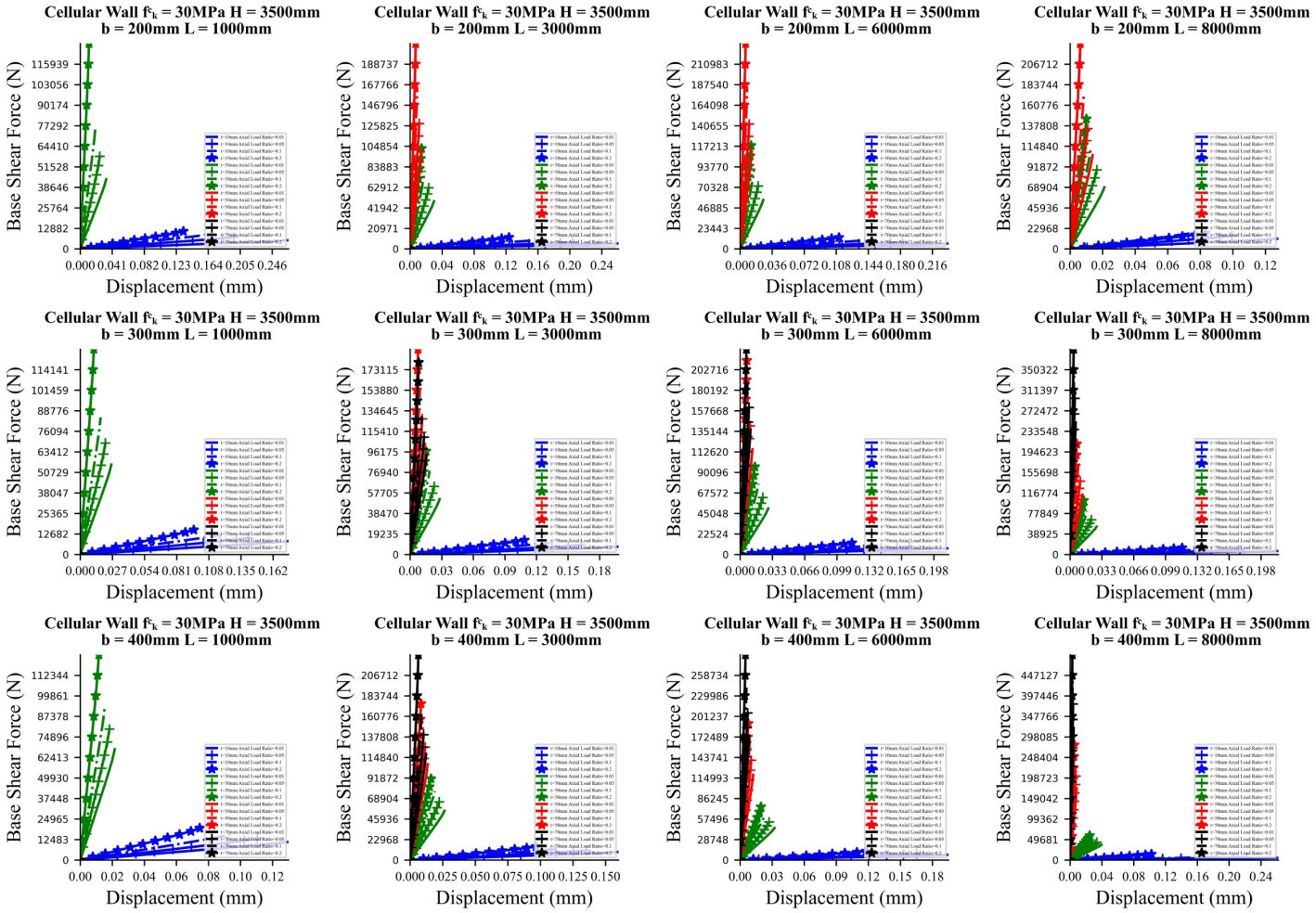

Figure 3.41. Some of the pushover curves created according to the result of the numerical analyses for walls with cellular topology.

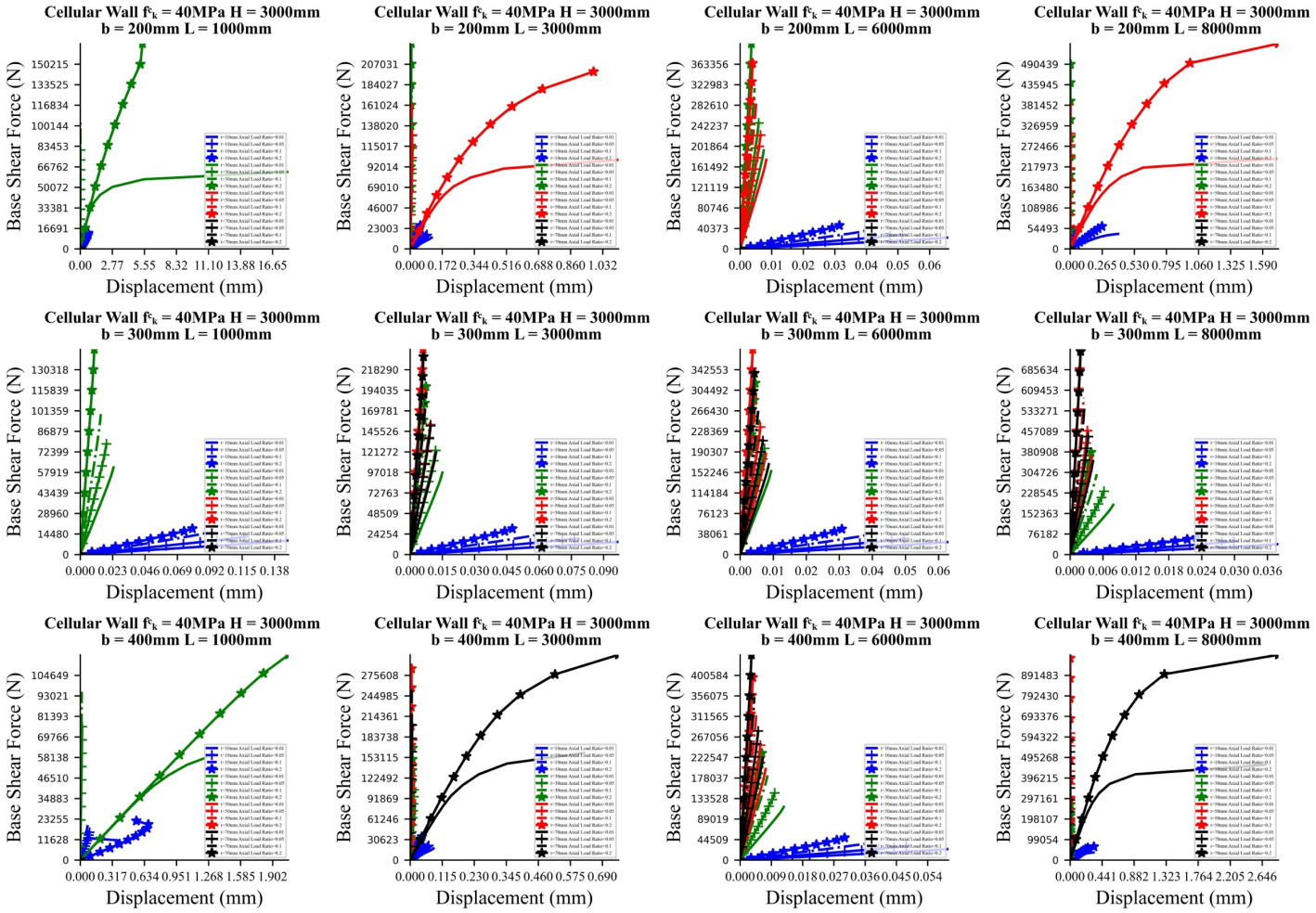

Figure 3.42. Some of the pushover curves created according to the result of the numerical analyses for walls with cellular topology.

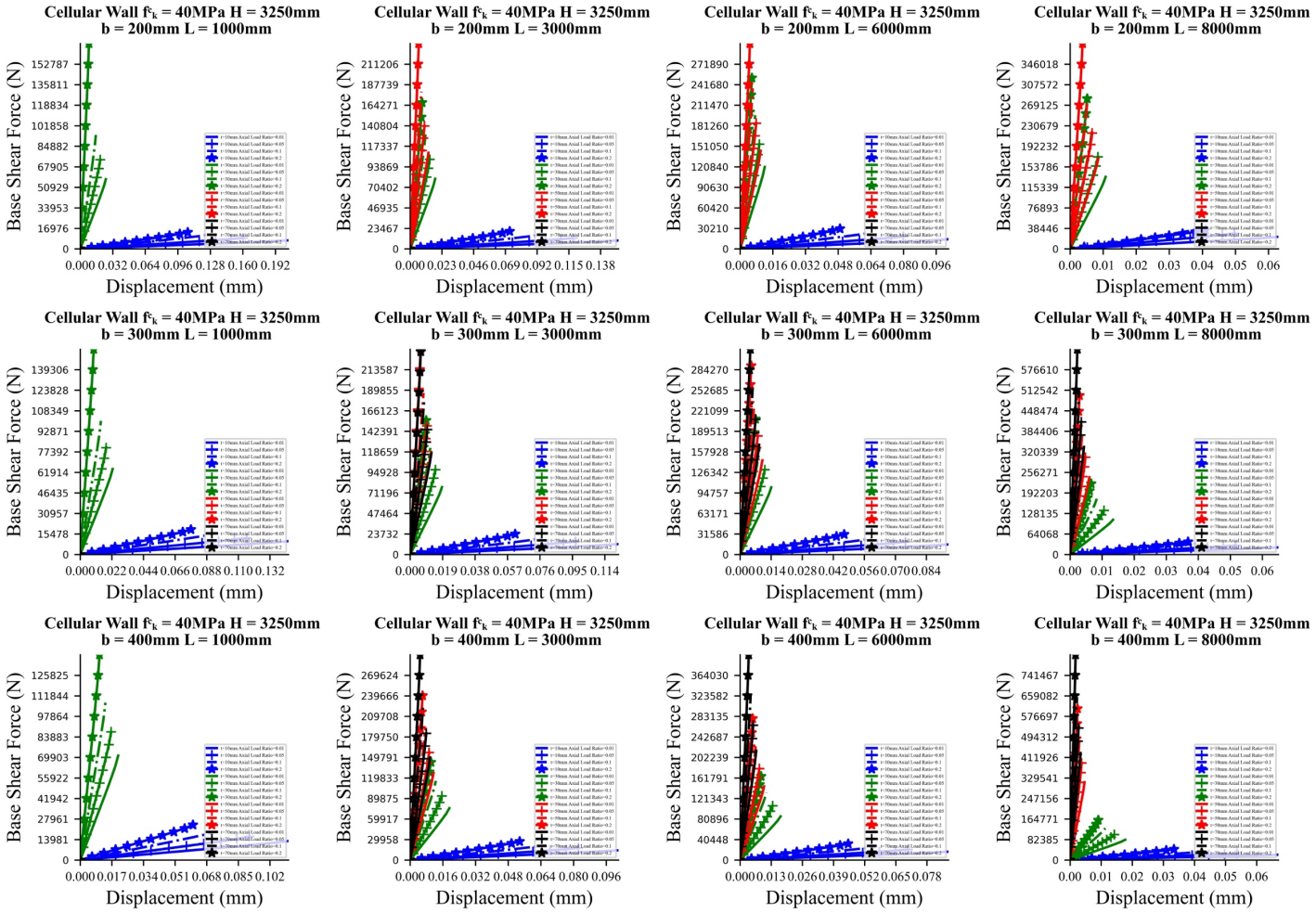

Figure 3.43. Some of the pushover curves created according to the result of the numerical analyses for walls with cellular topology.

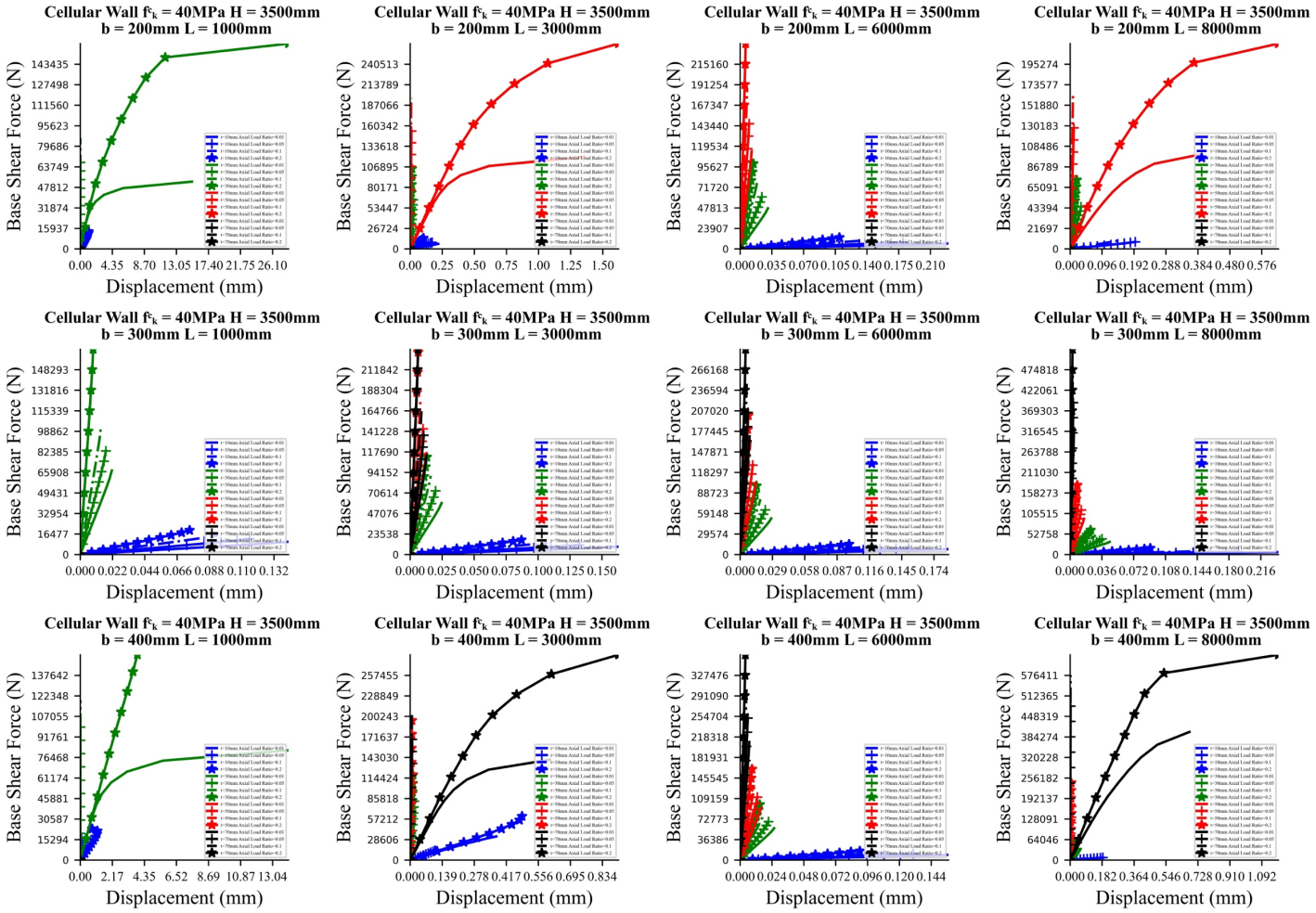

Figure 3.44. Some of the pushover curves created according to the result of the numerical analyses for walls with cellular topology.

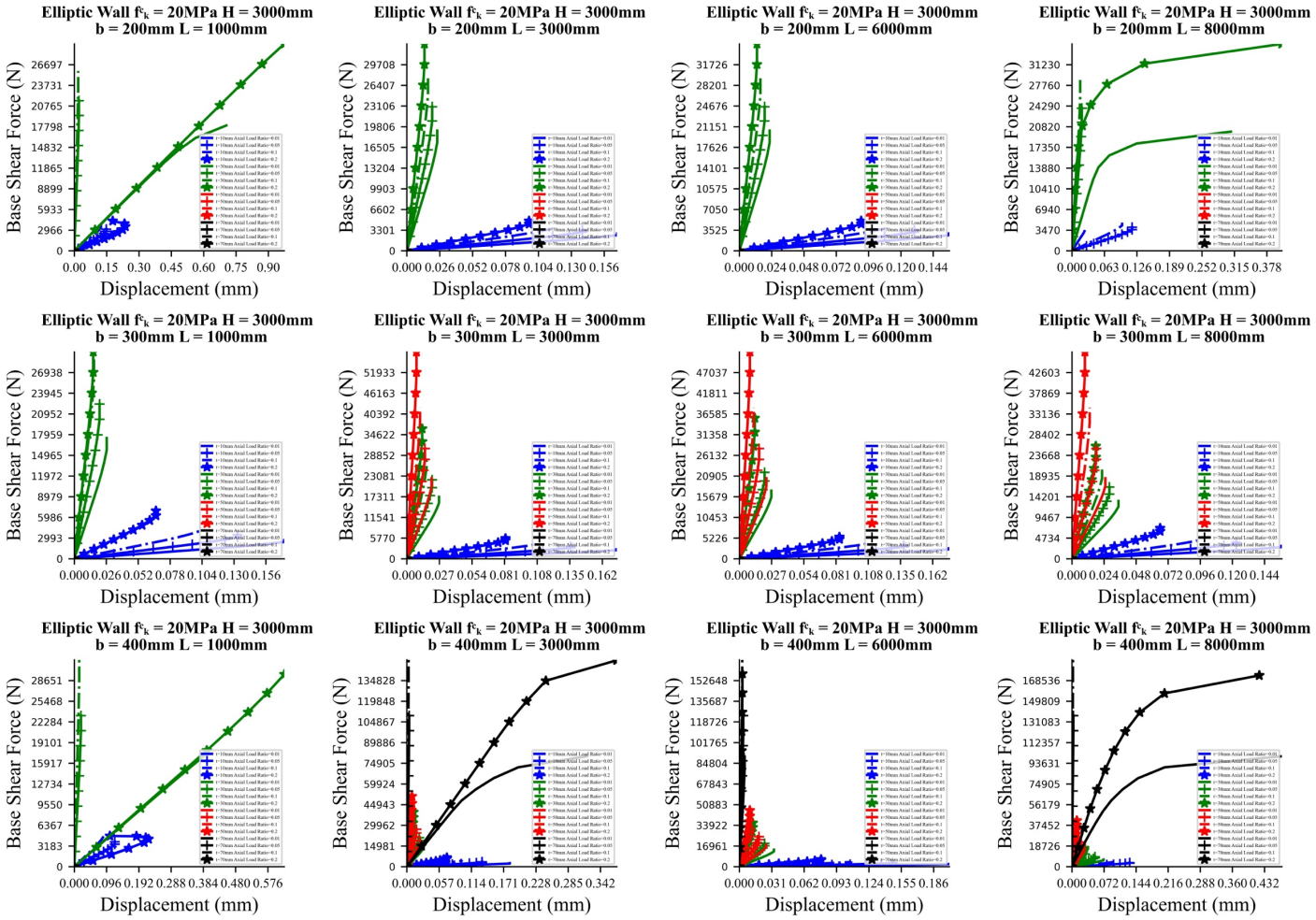

Figure 3.45. Some of the pushover curves created according to the result of the numerical analyses for walls with elliptic topology.

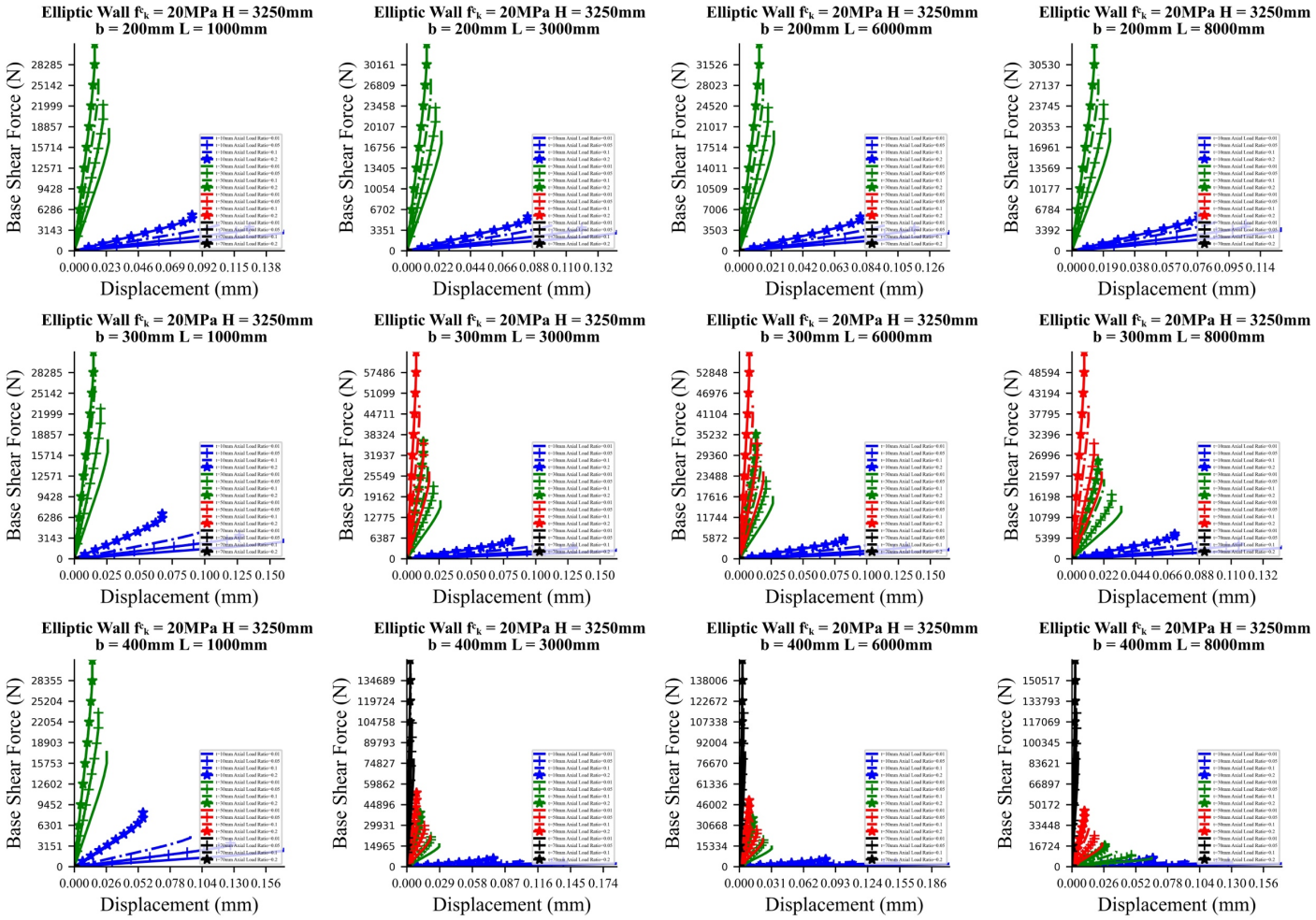

Figure 3.46. Some of the pushover curves created according to the result of the numerical analyses for walls with elliptic topology.

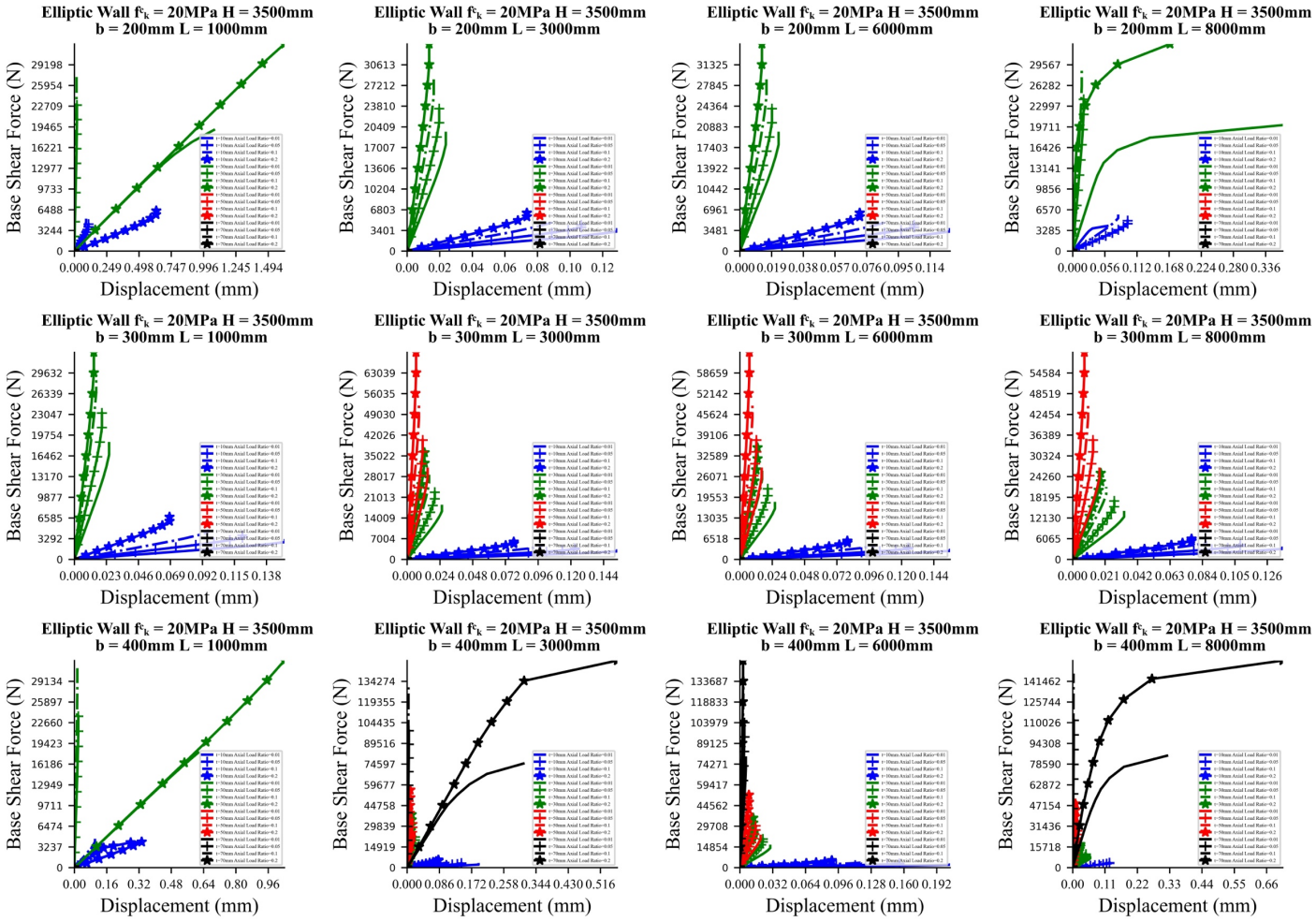

Figure 3.47. Some of the pushover curves created according to the result of the numerical analyses for walls with elliptic topology.

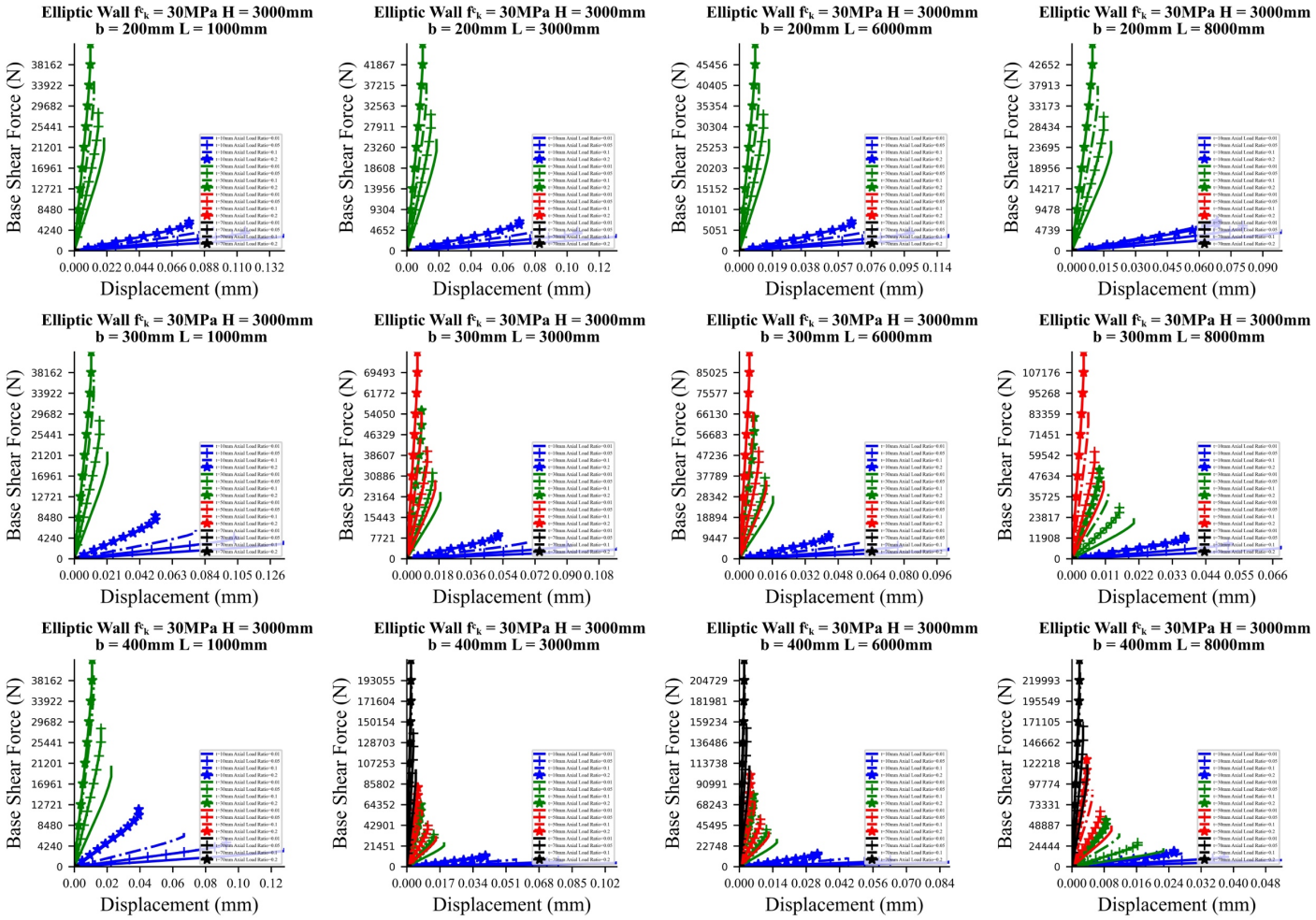

Figure 3.48. Some of the pushover curves created according to the result of the numerical analyses for walls with elliptic topology.

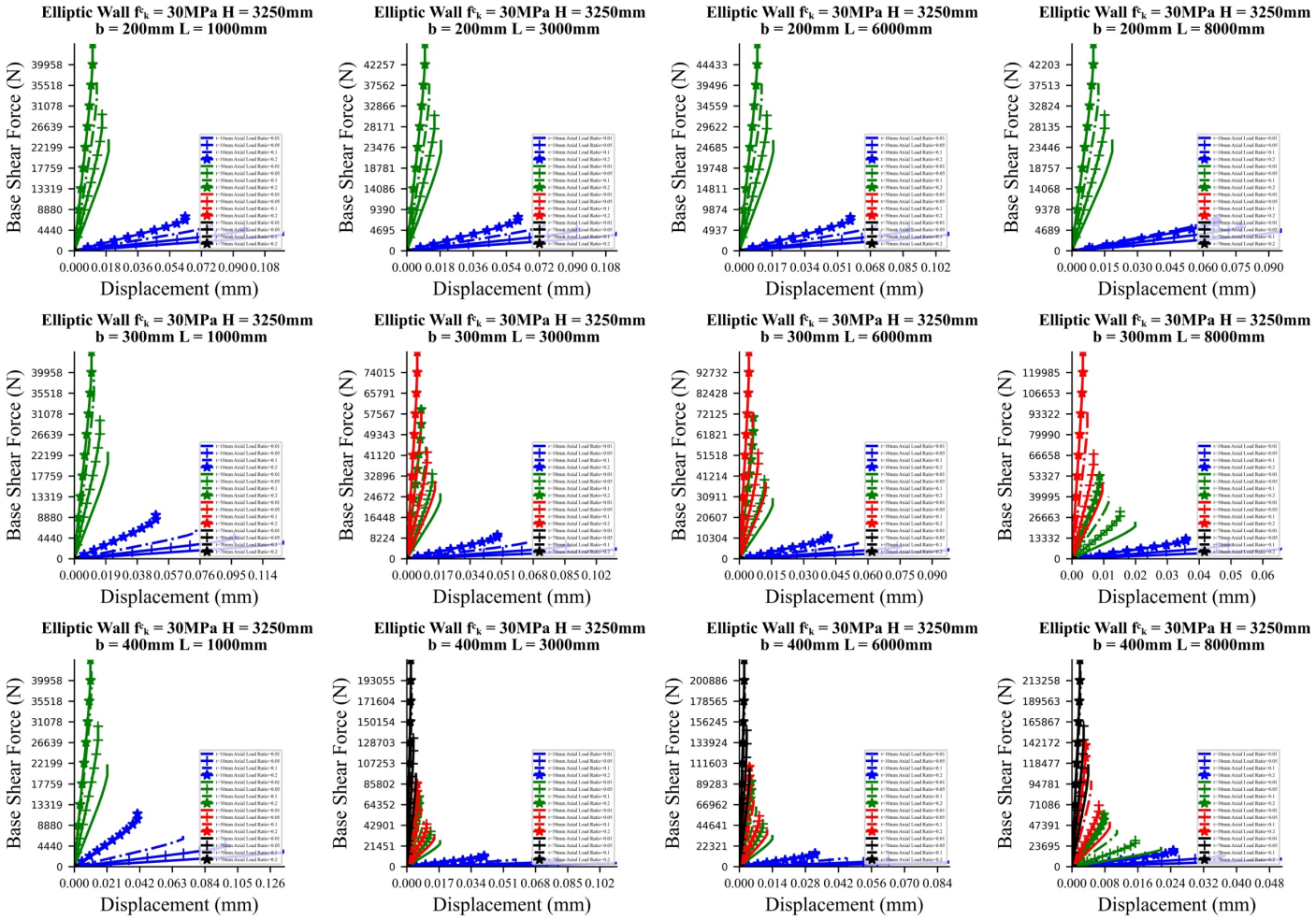

Figure 3.49. Some of the pushover curves created according to the result of the numerical analyses for walls with elliptic topology.

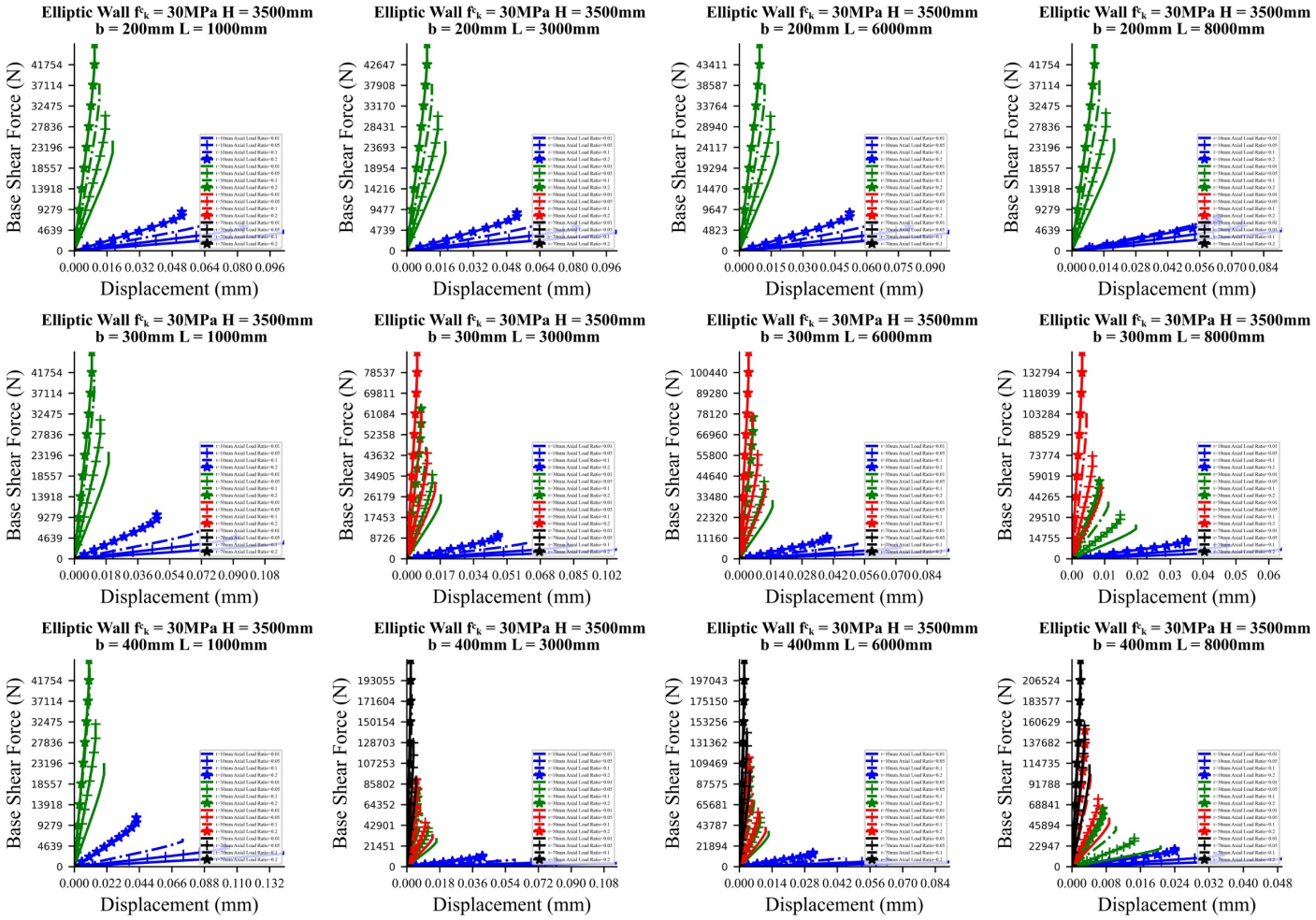

Figure 3.50. Some of the pushover curves created according to the result of the numerical analyses for walls with elliptic topology.

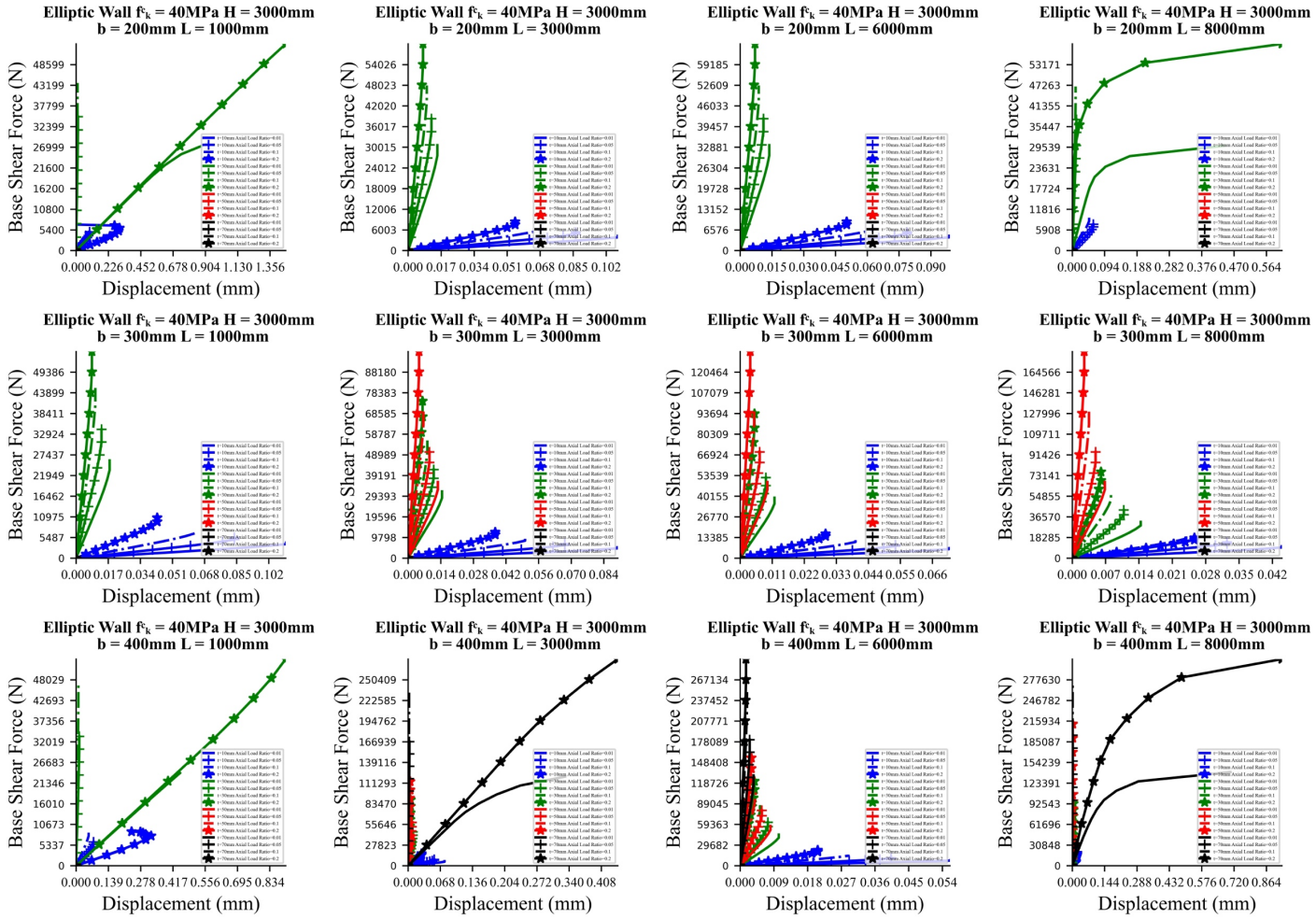

Figure 3.51. Some of the pushover curves created according to the result of the numerical analyses for walls with elliptic topology.

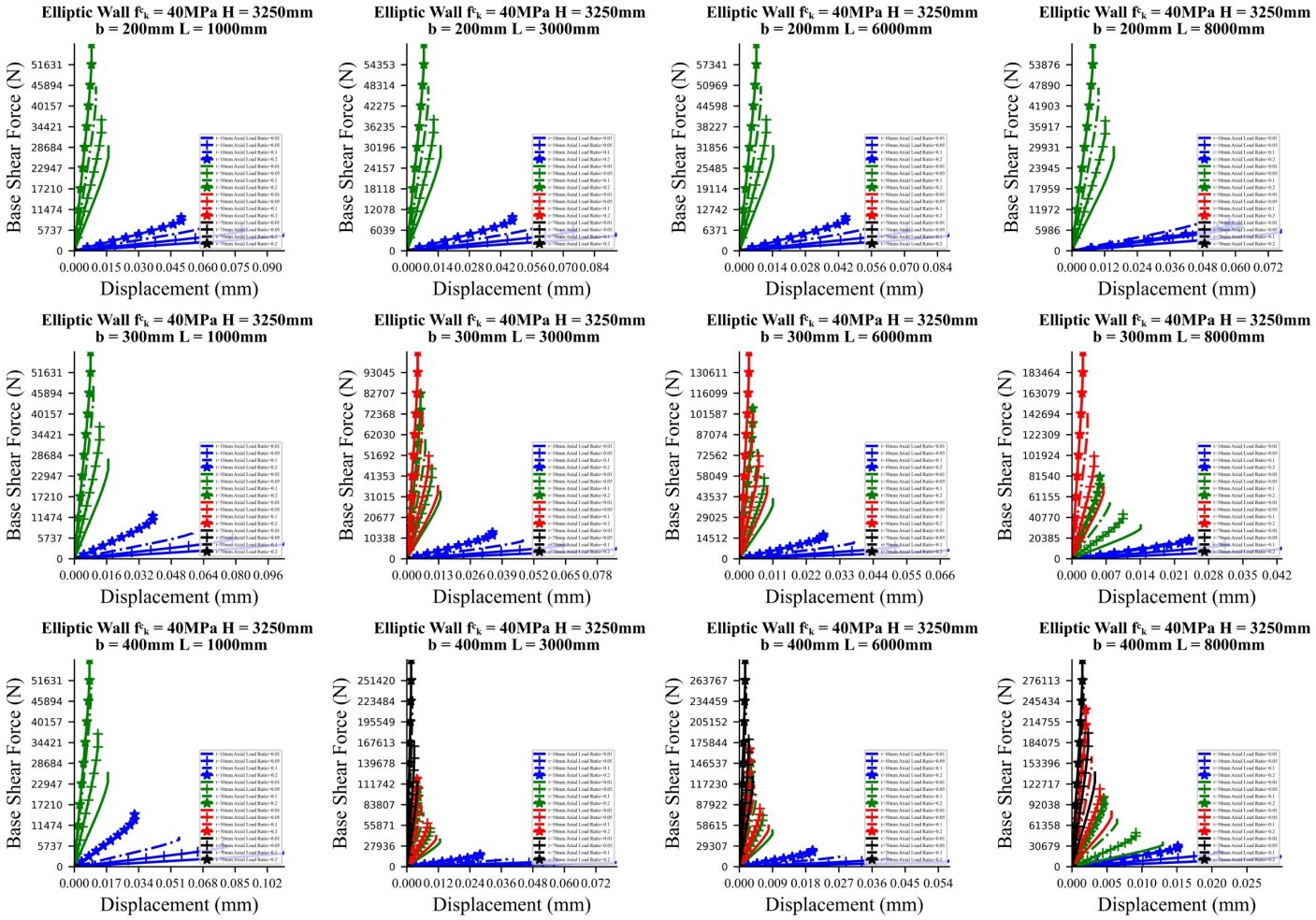

Figure 3.52. Some of the pushover curves created according to the result of the numerical analyses for walls with elliptic topology.

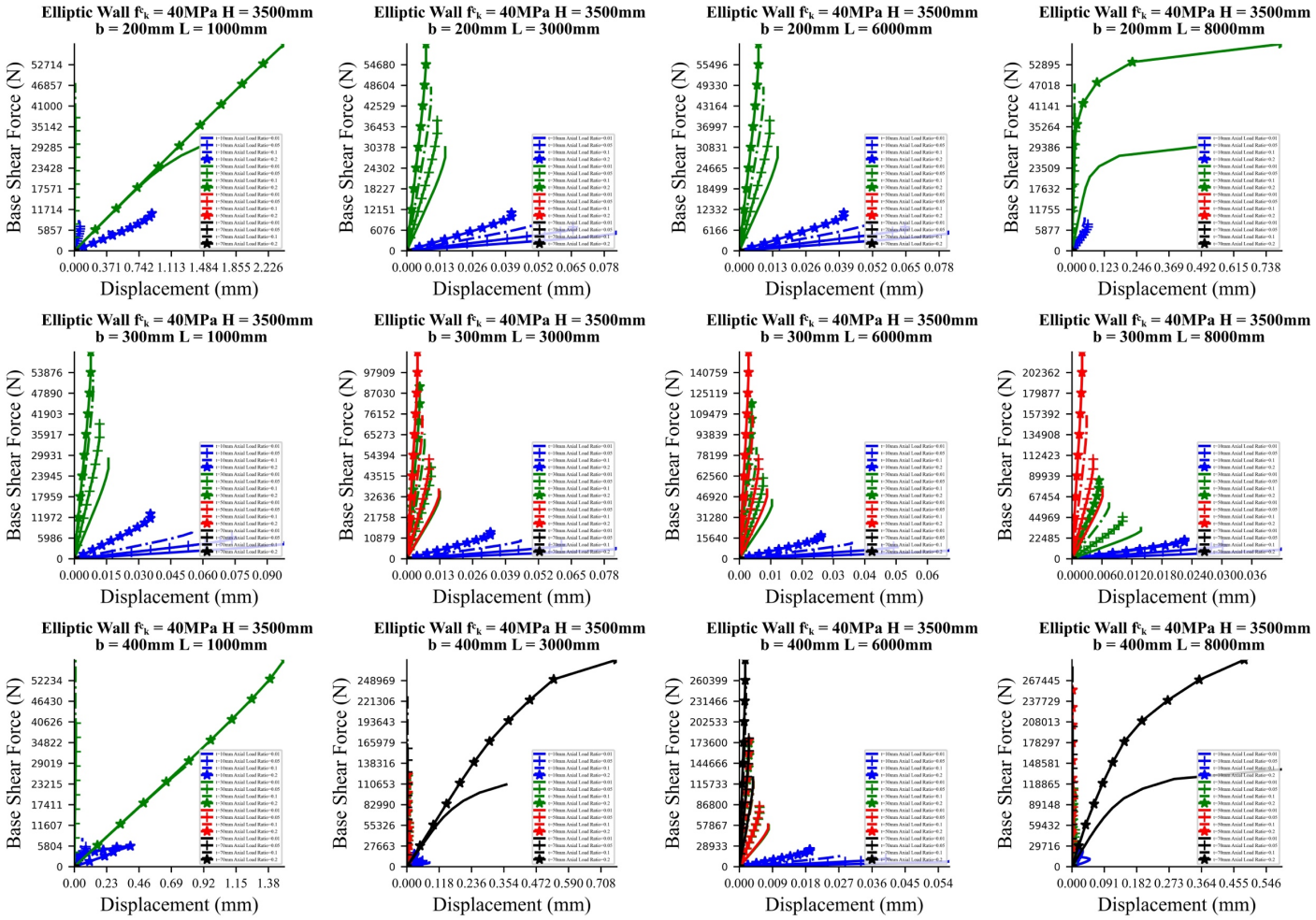

Figure 3.53. Some of the pushover curves created according to the result of the numerical analyses for walls with elliptic topology.

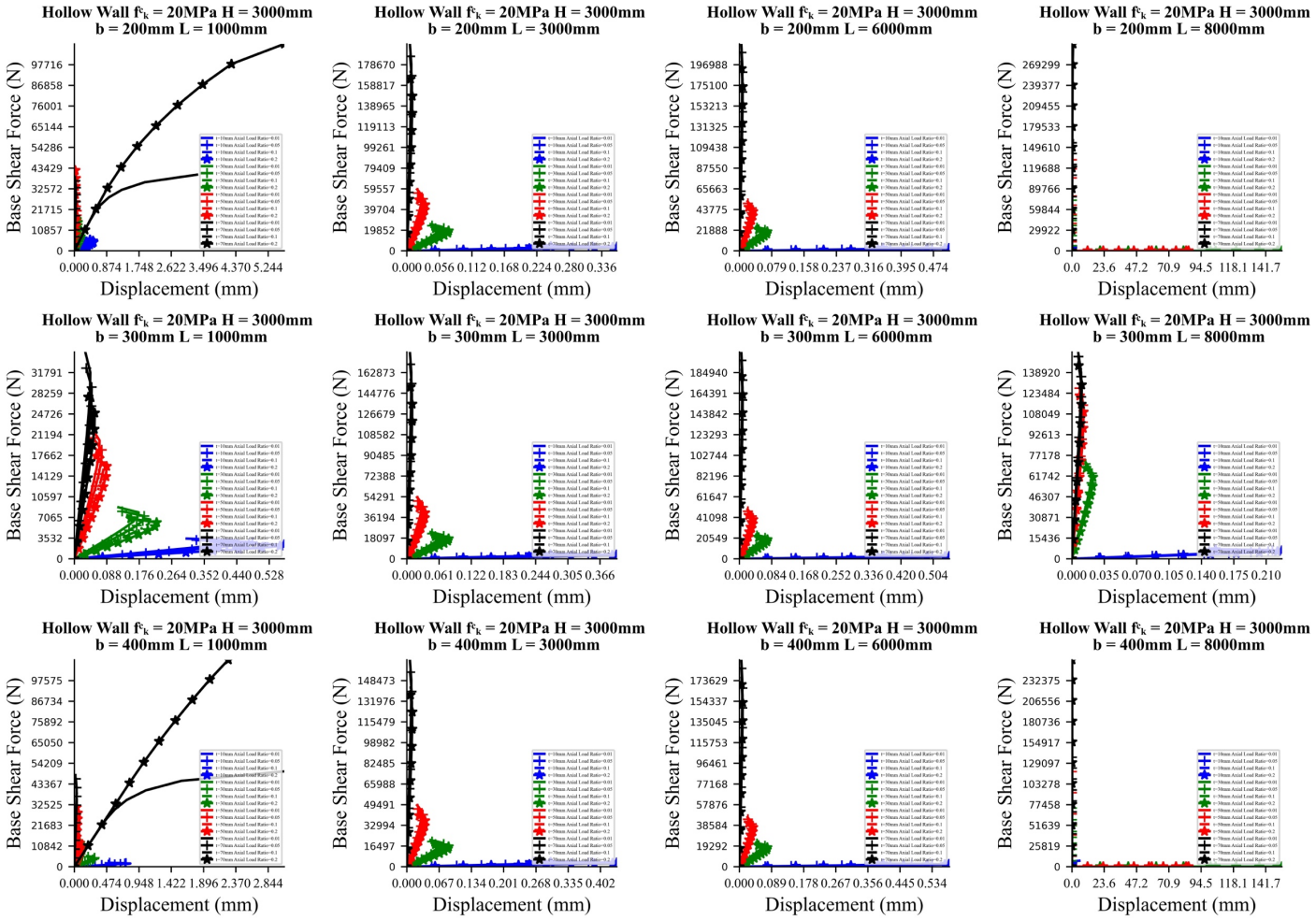

Figure 3.54. Some of the pushover curves created according to the result of the numerical analyses for walls with hollow topology.

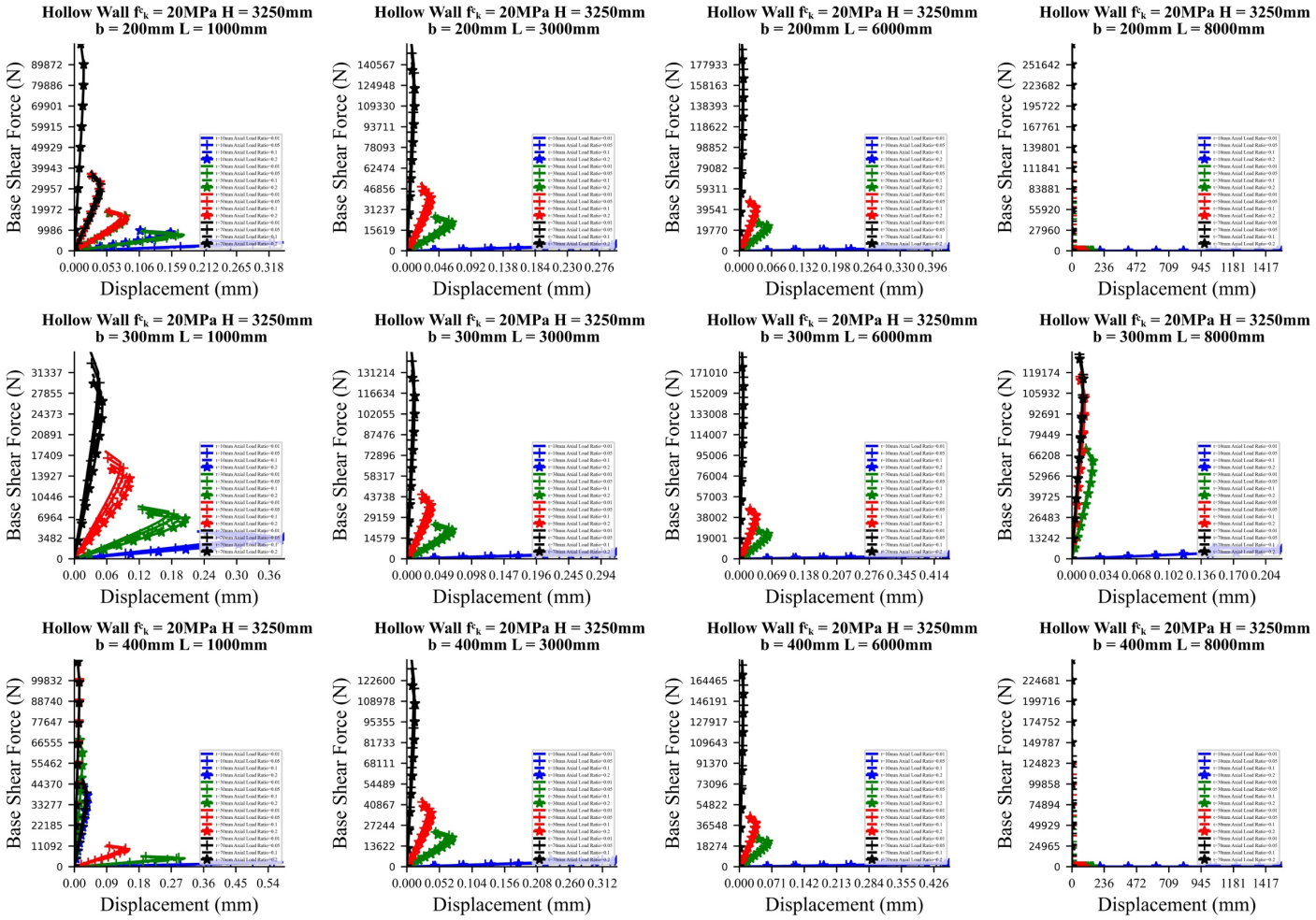

Figure 3.55. Some of the pushover curves created according to the result of the numerical analyses for walls with hollow topology.

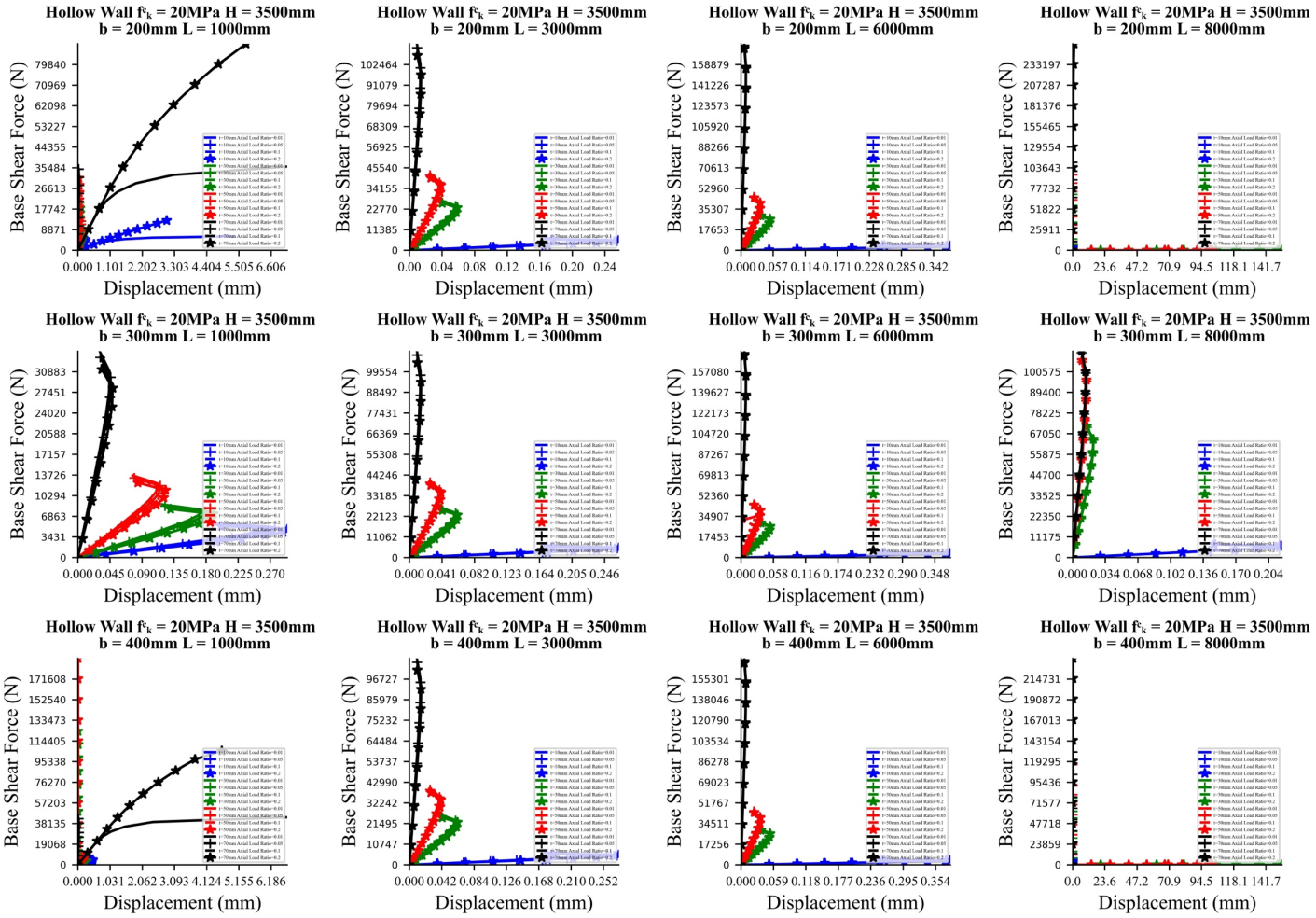

Figure 3.56. Some of the pushover curves created according to the result of the numerical analyses for walls with hollow topology.

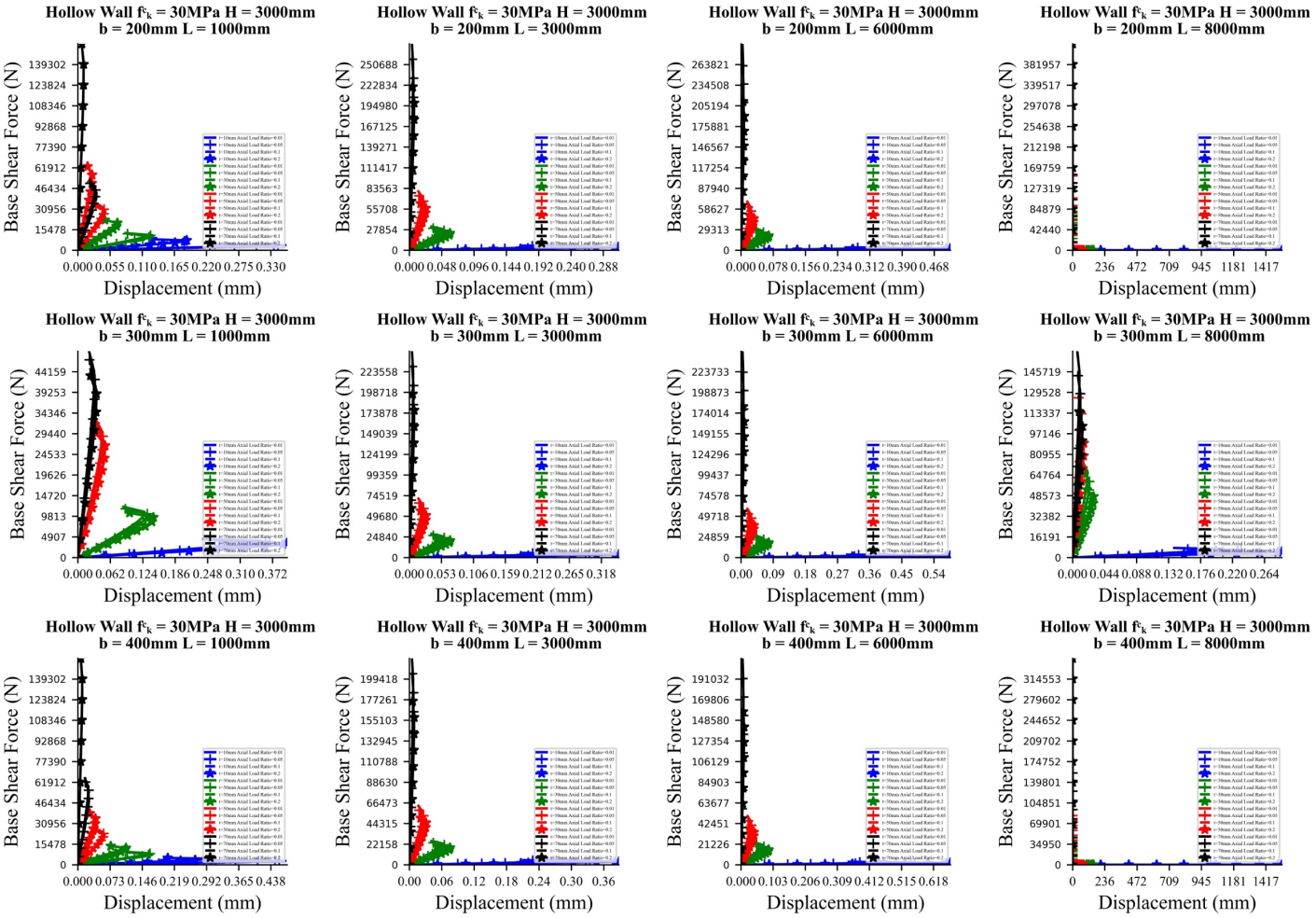

Figure 3.57. Some of the pushover curves created according to the result of the numerical analyses for walls with hollow topology.

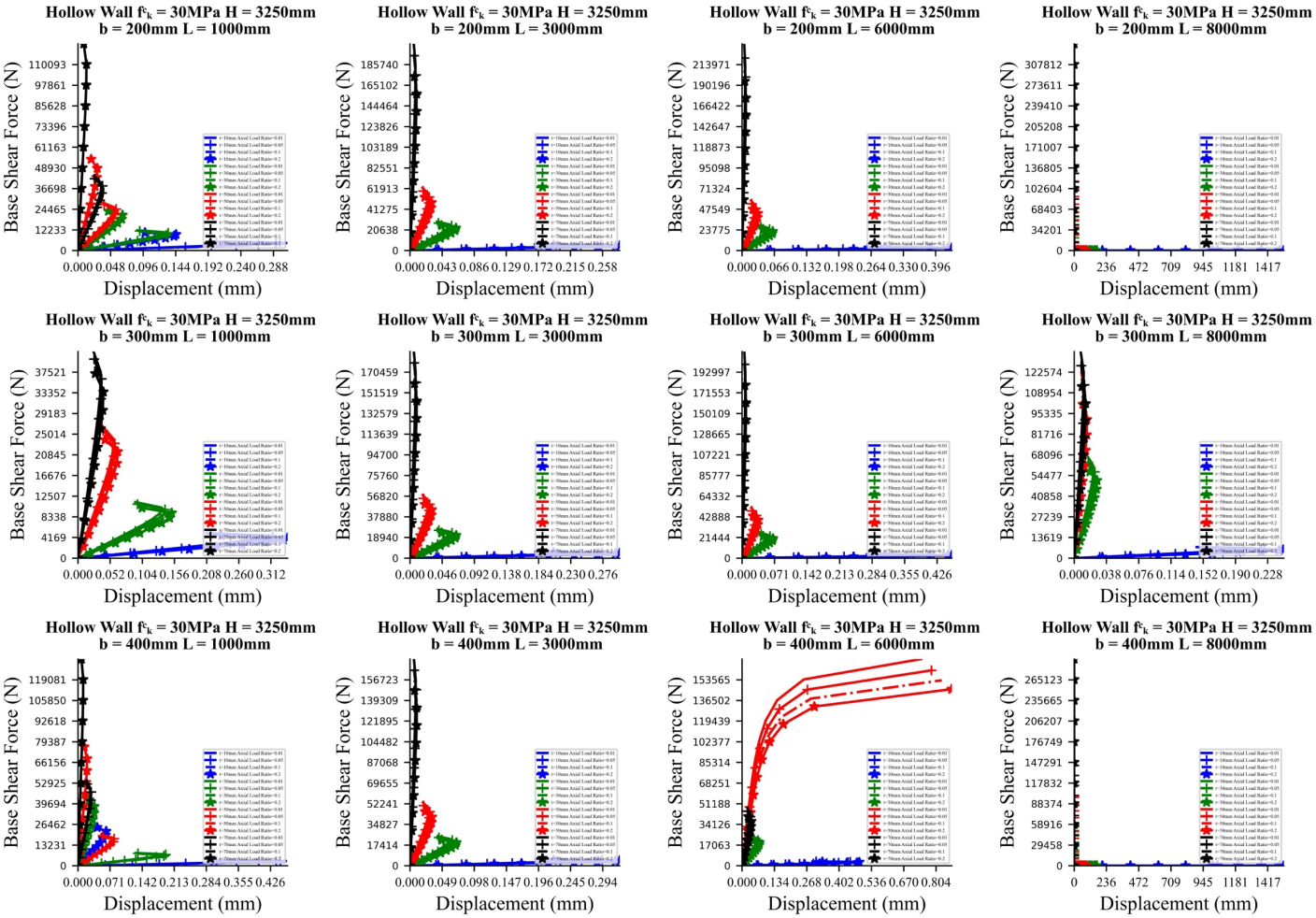

Figure 3.58. Some of the pushover curves created according to the result of the numerical analyses for walls with hollow topology.

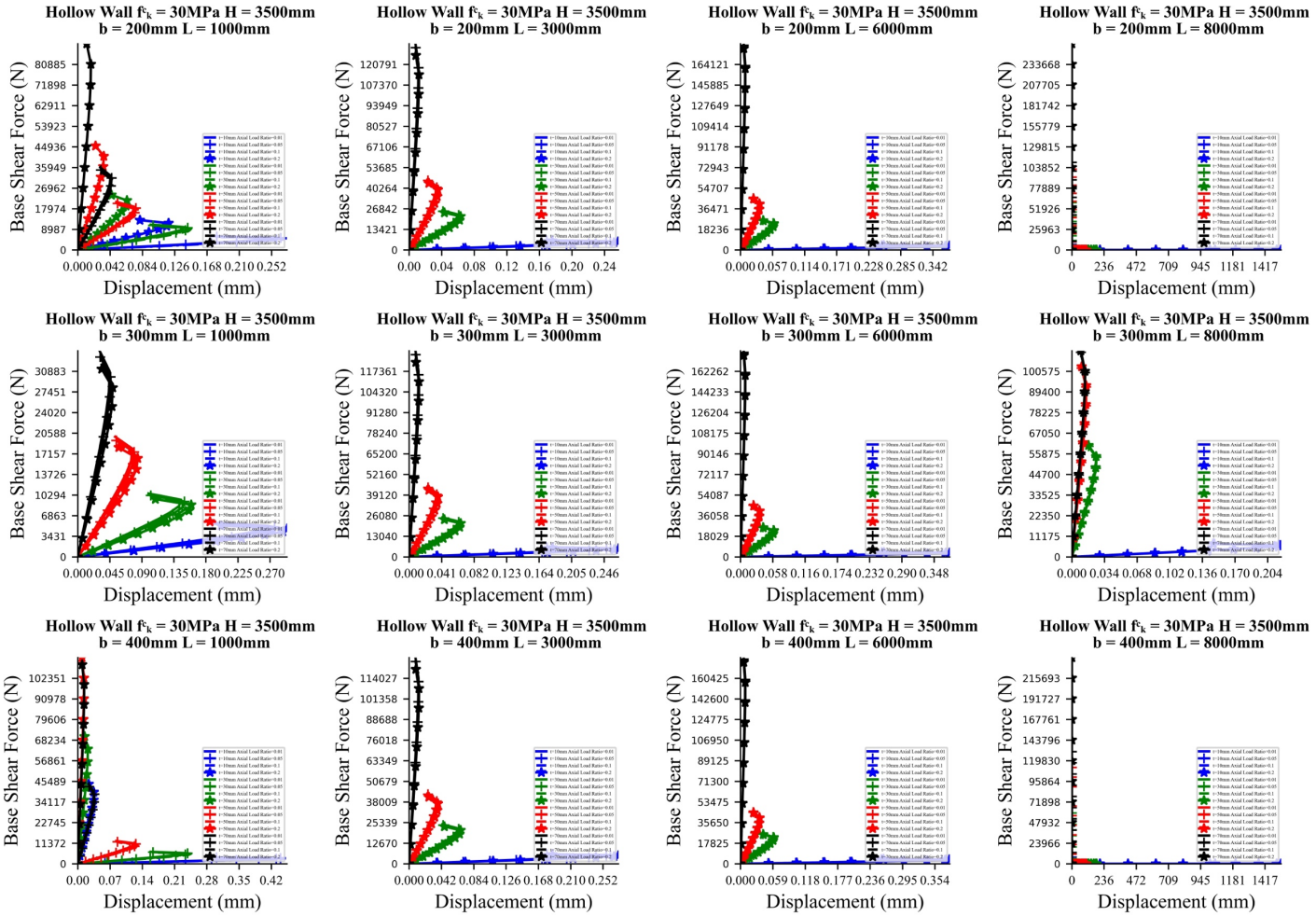

Figure 3.59. Some of the pushover curves created according to the result of the numerical analyses for walls with hollow topology.

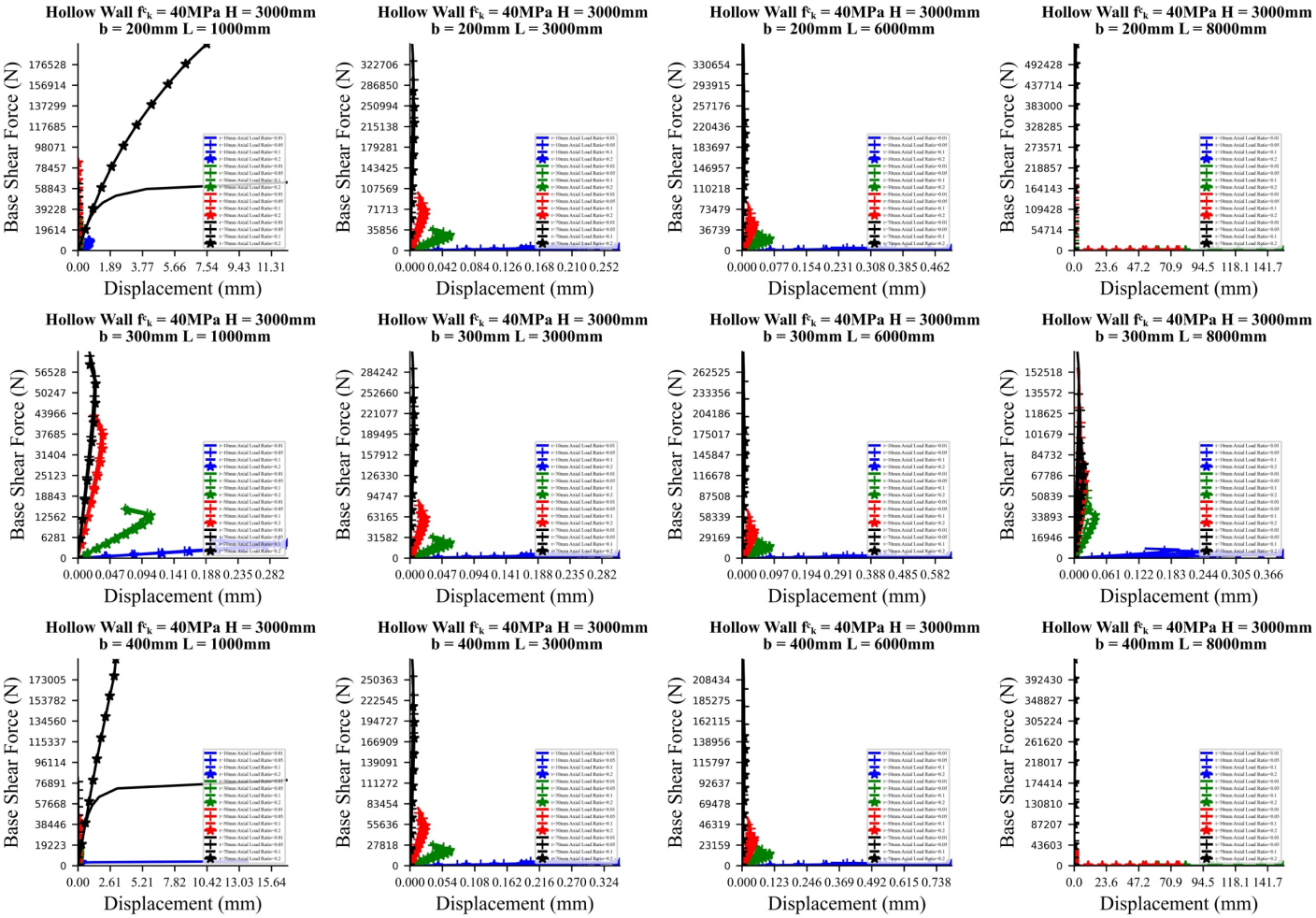

Figure 3.60. Some of the pushover curves created according to the result of the numerical analyses for walls with hollow topology.

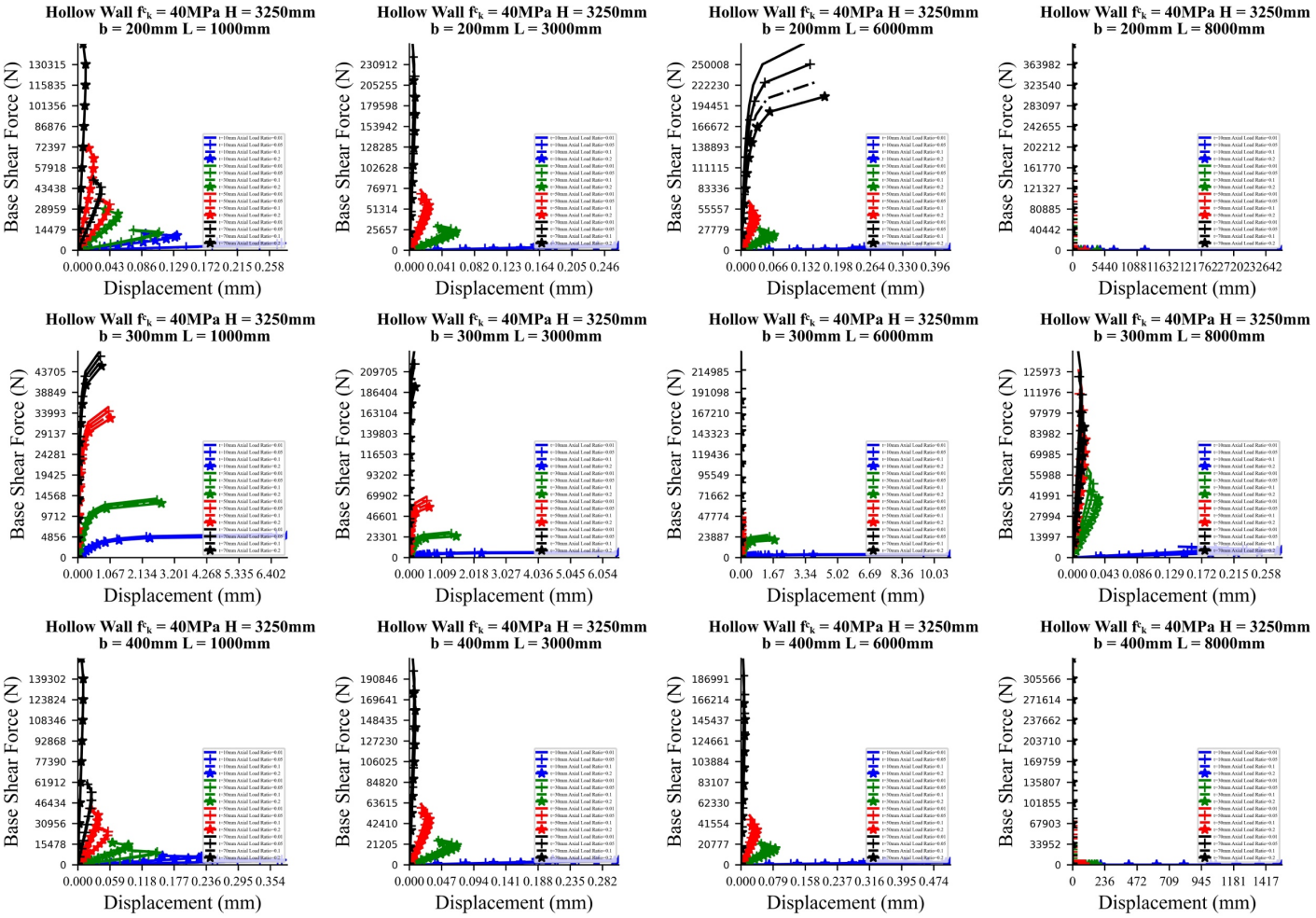

Figure 3.61. Some of the pushover curves created according to the result of the numerical analyses for walls with hollow topology.

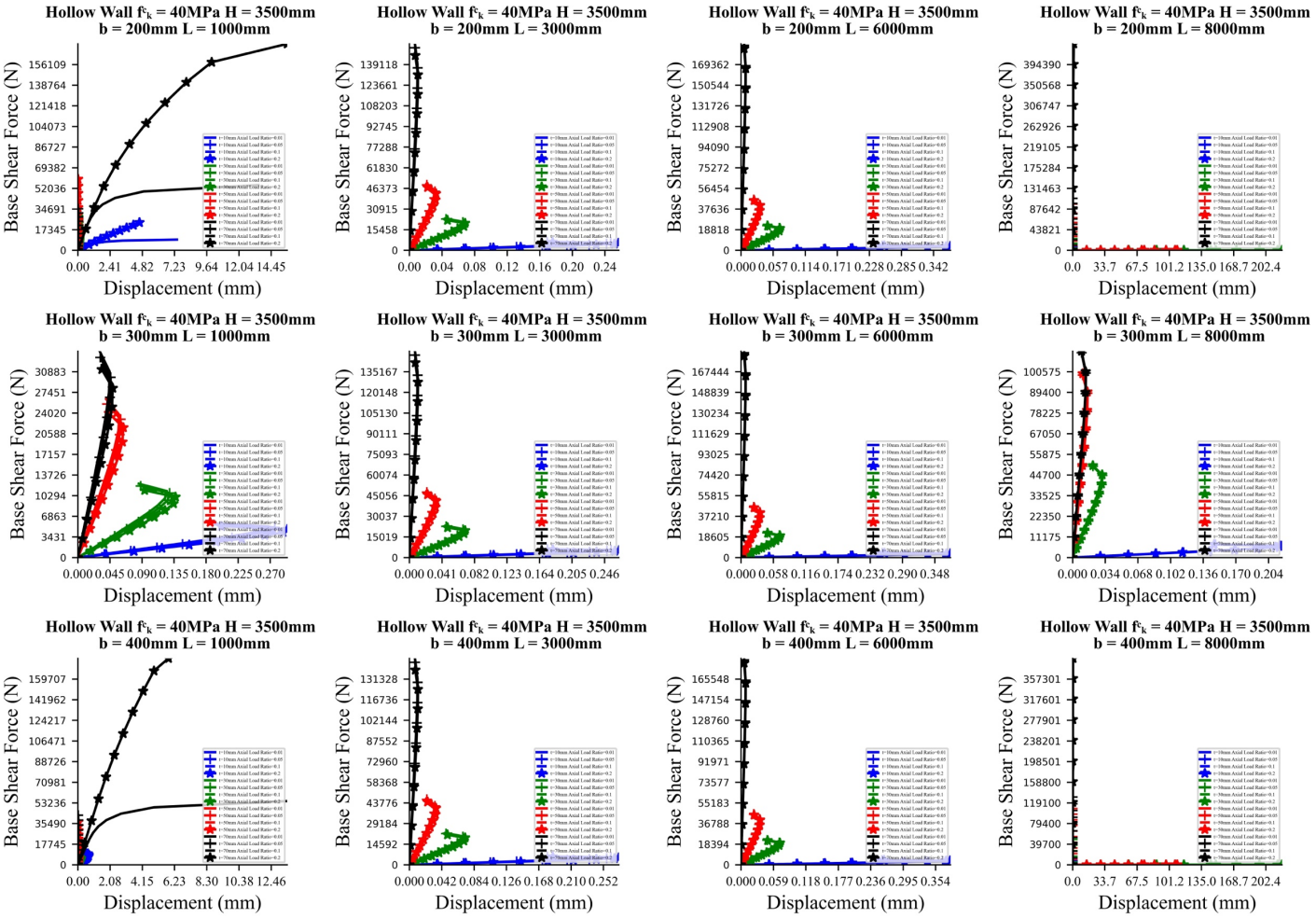

Figure 3.62. Some of the pushover curves created according to the result of the numerical analyses for walls with hollow topology.

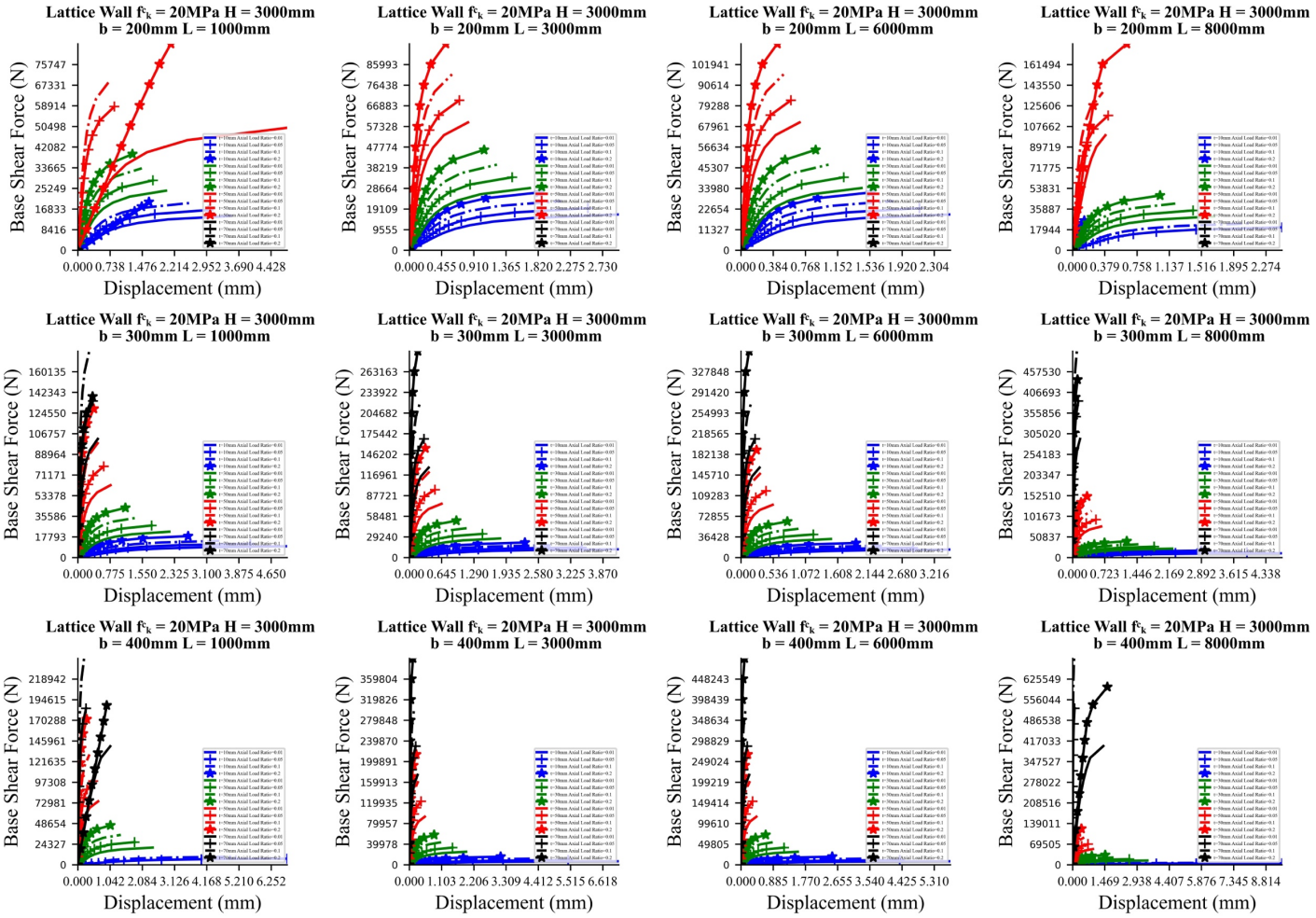

Figure 3.63. Some of the pushover curves created according to the result of the numerical analyses for walls with lattice topology.

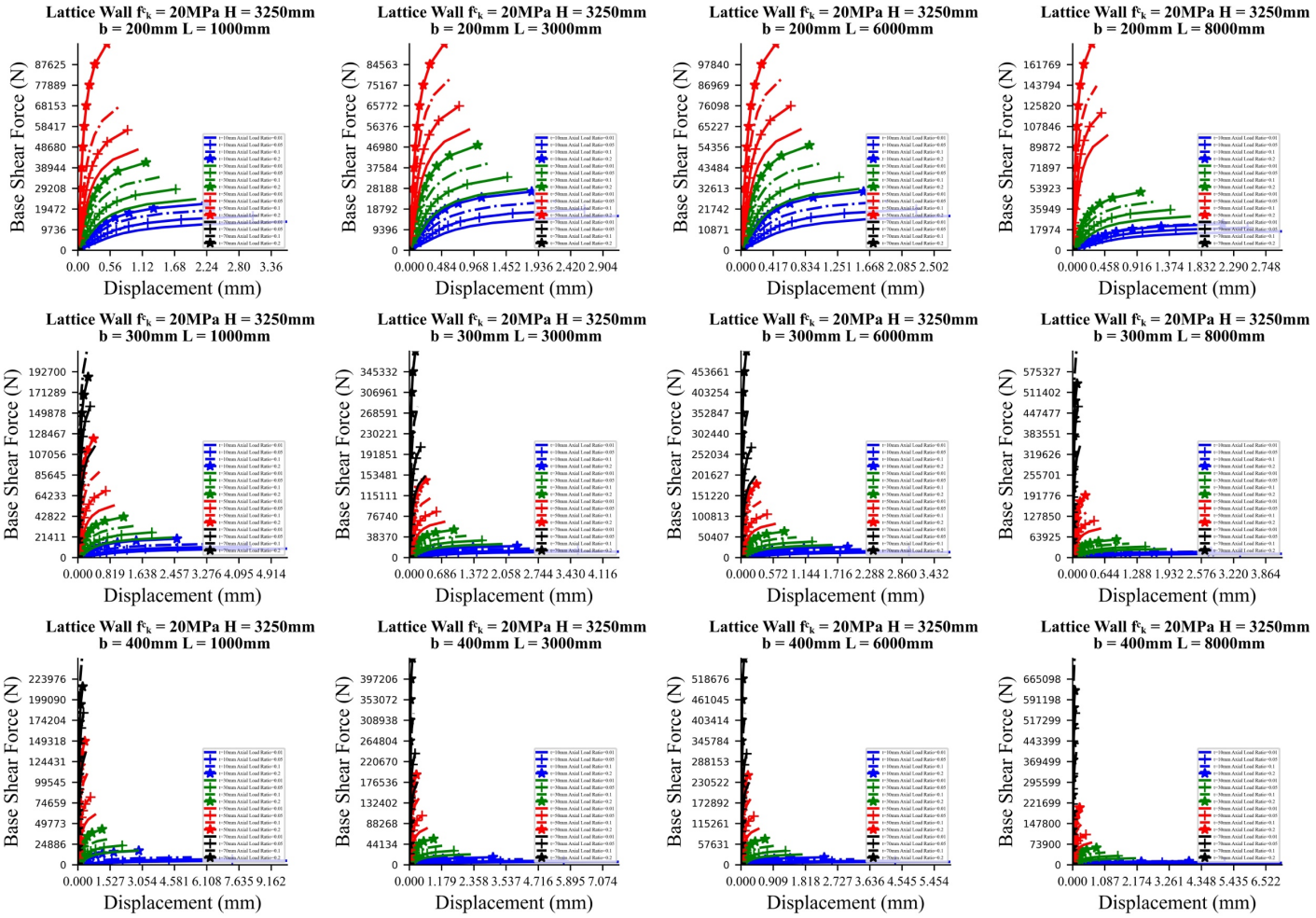

Figure 3.64. Some of the pushover curves created according to the result of the numerical analyses for walls with lattice topology.

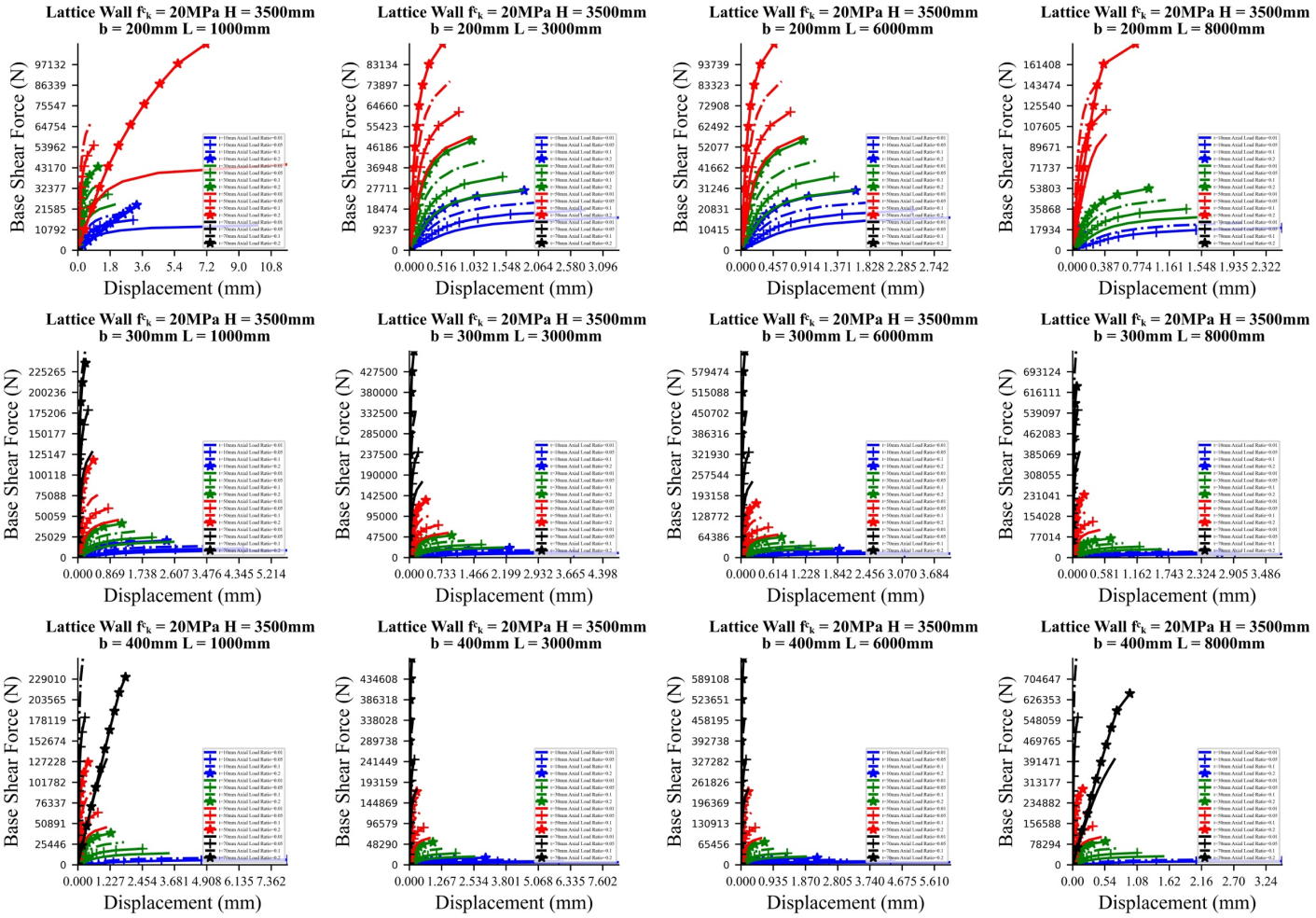

Figure 3.65. Some of the pushover curves created according to the result of the numerical analyses for walls with lattice topology.

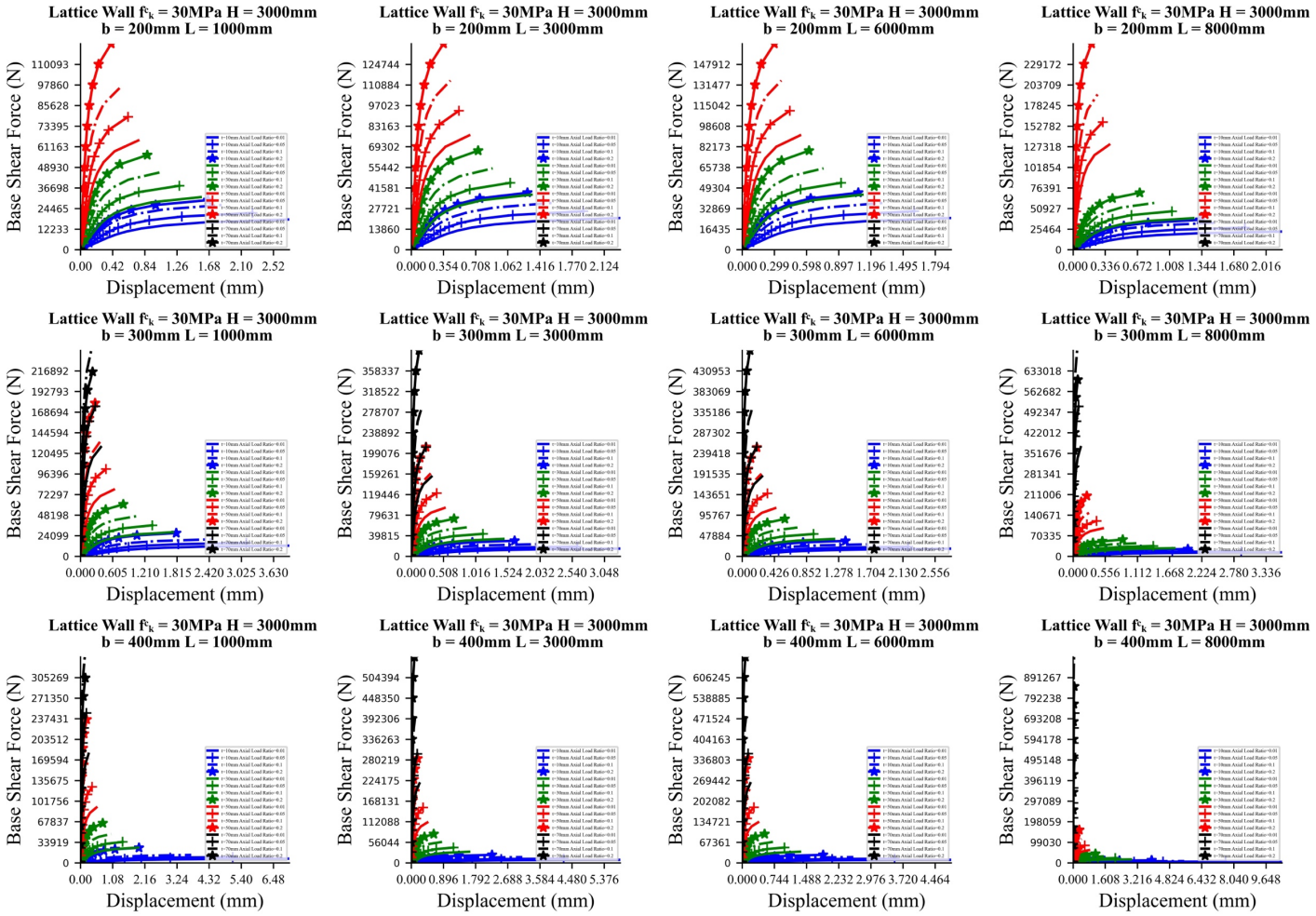

Figure 3.66. Some of the pushover curves created according to the result of the numerical analyses for walls with lattice topology.

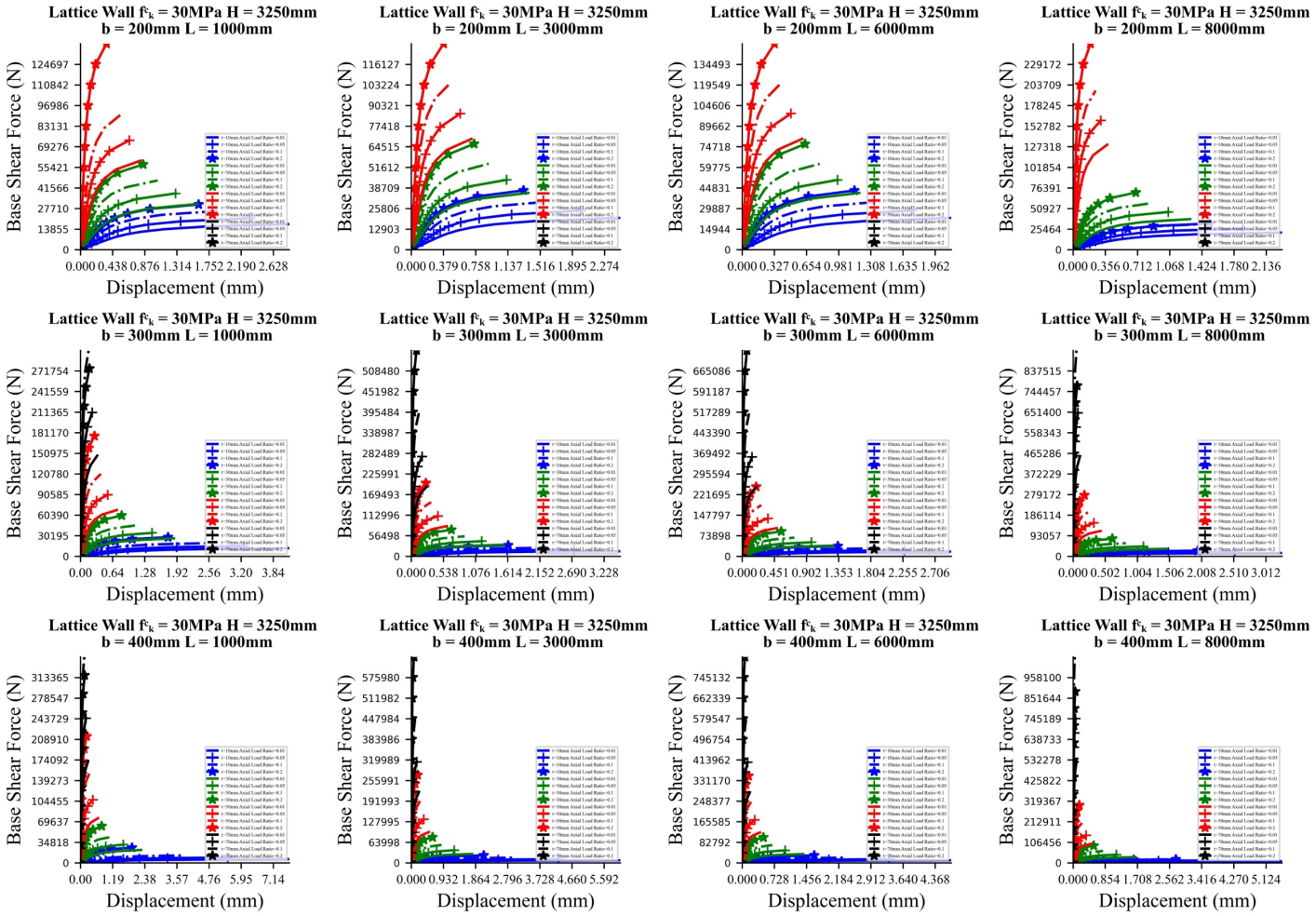

Figure 3.67. Some of the pushover curves created according to the result of the numerical analyses for walls with lattice topology.

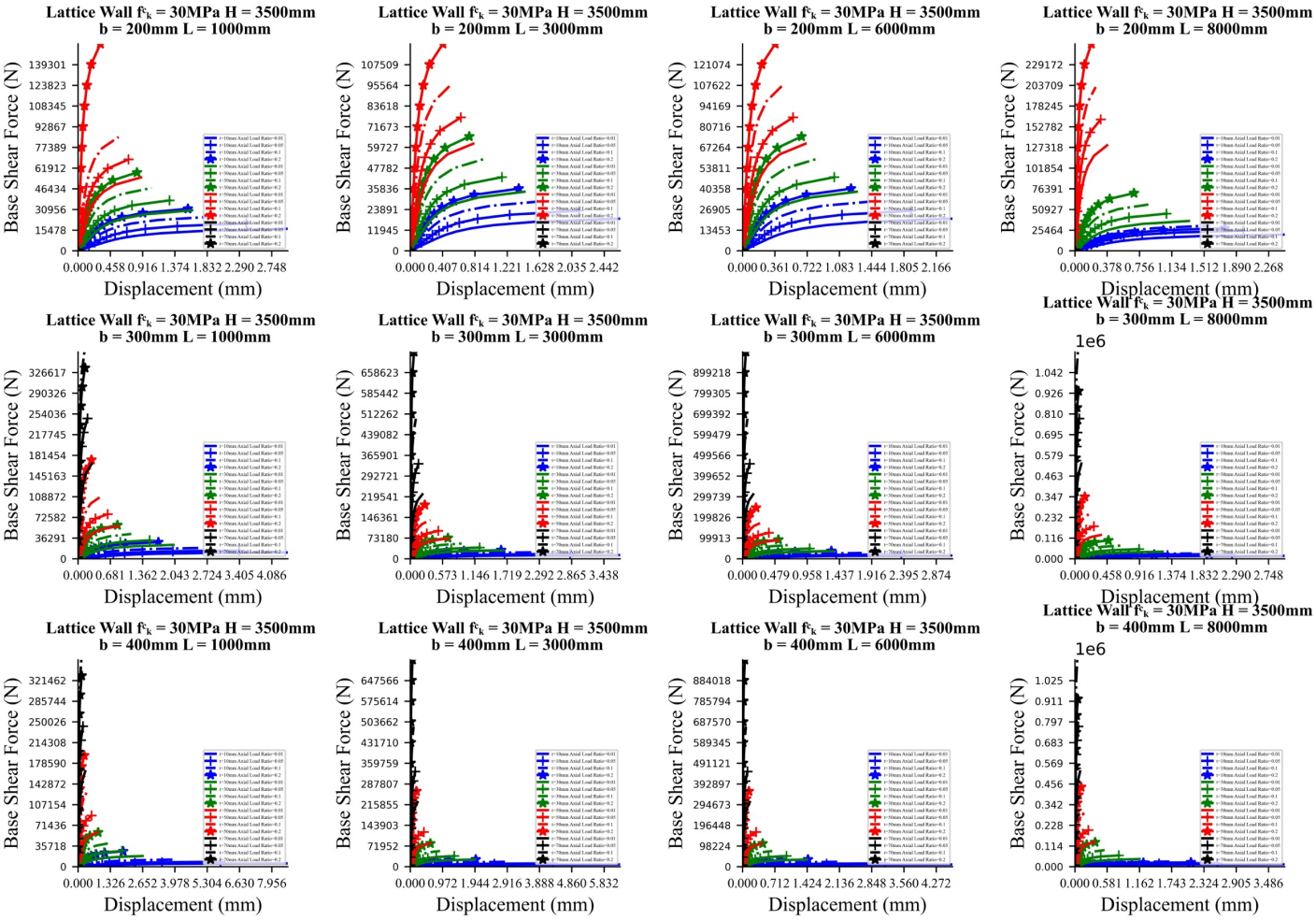

Figure 3.68. Some of the pushover curves created according to the result of the numerical analyses for walls with lattice topology.

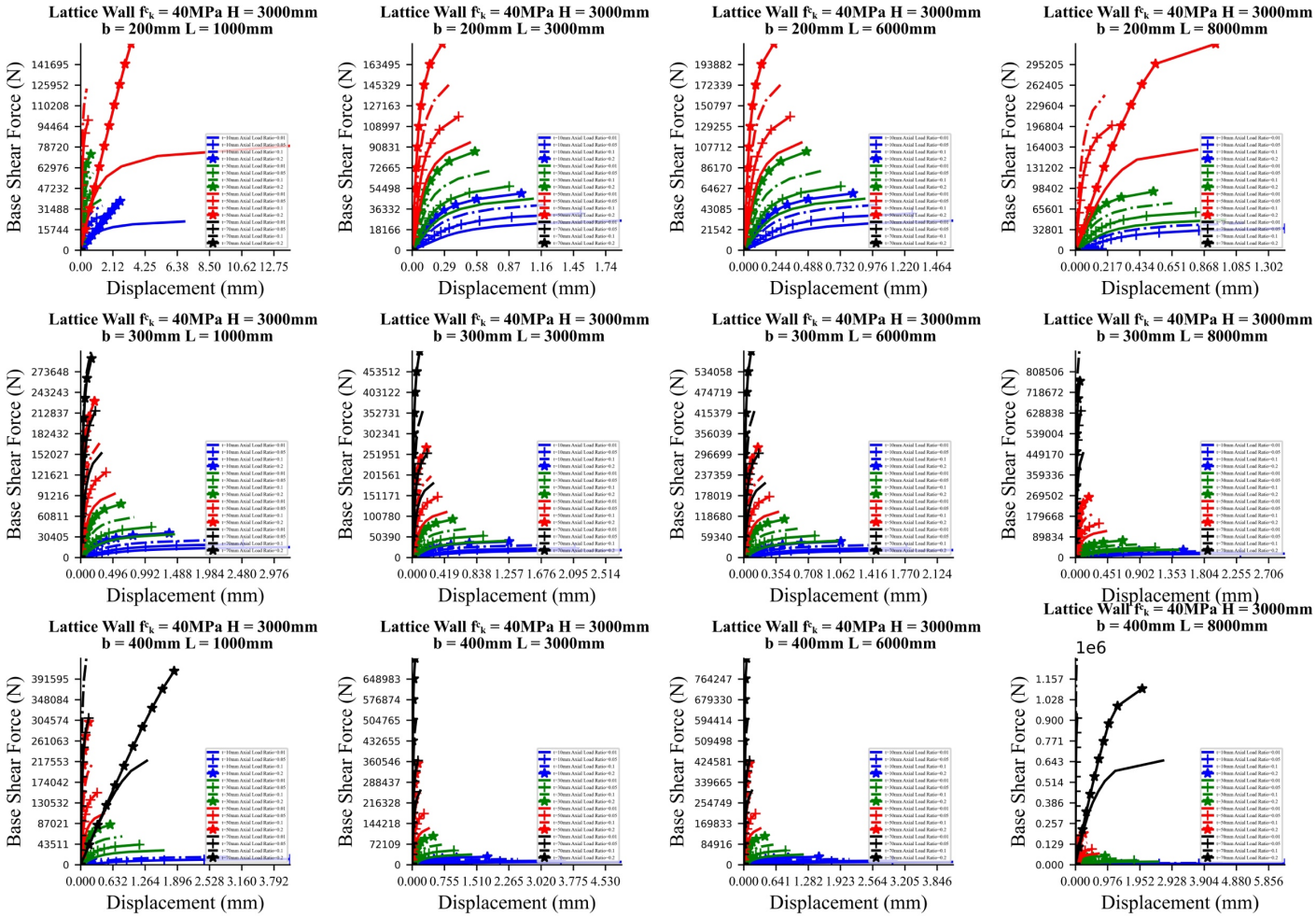

Figure 3.69. Some of the pushover curves created according to the result of the numerical analyses for walls with lattice topology.

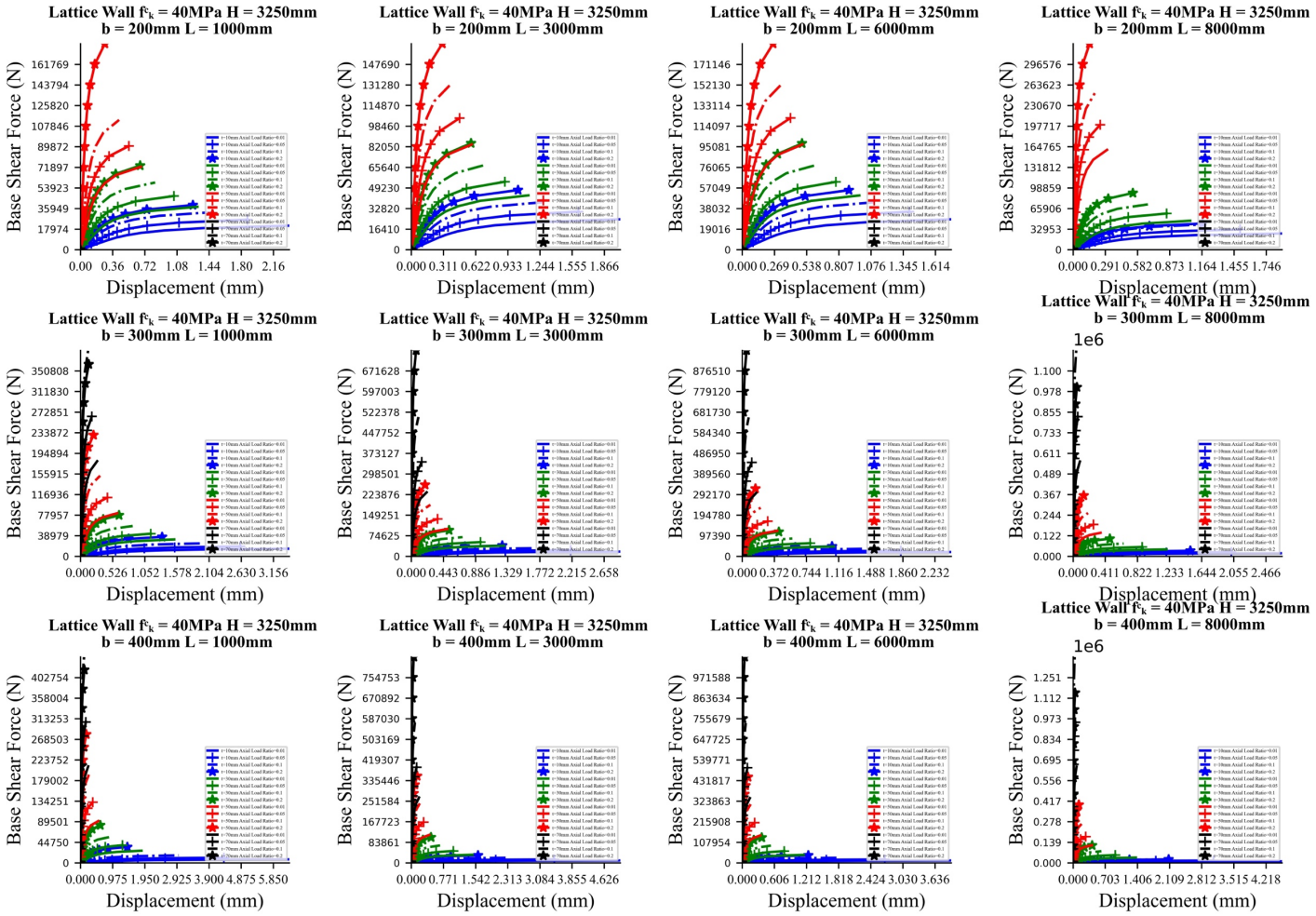

Figure 3.70. Some of the pushover curves created according to the result of the numerical analyses for walls with lattice topology.

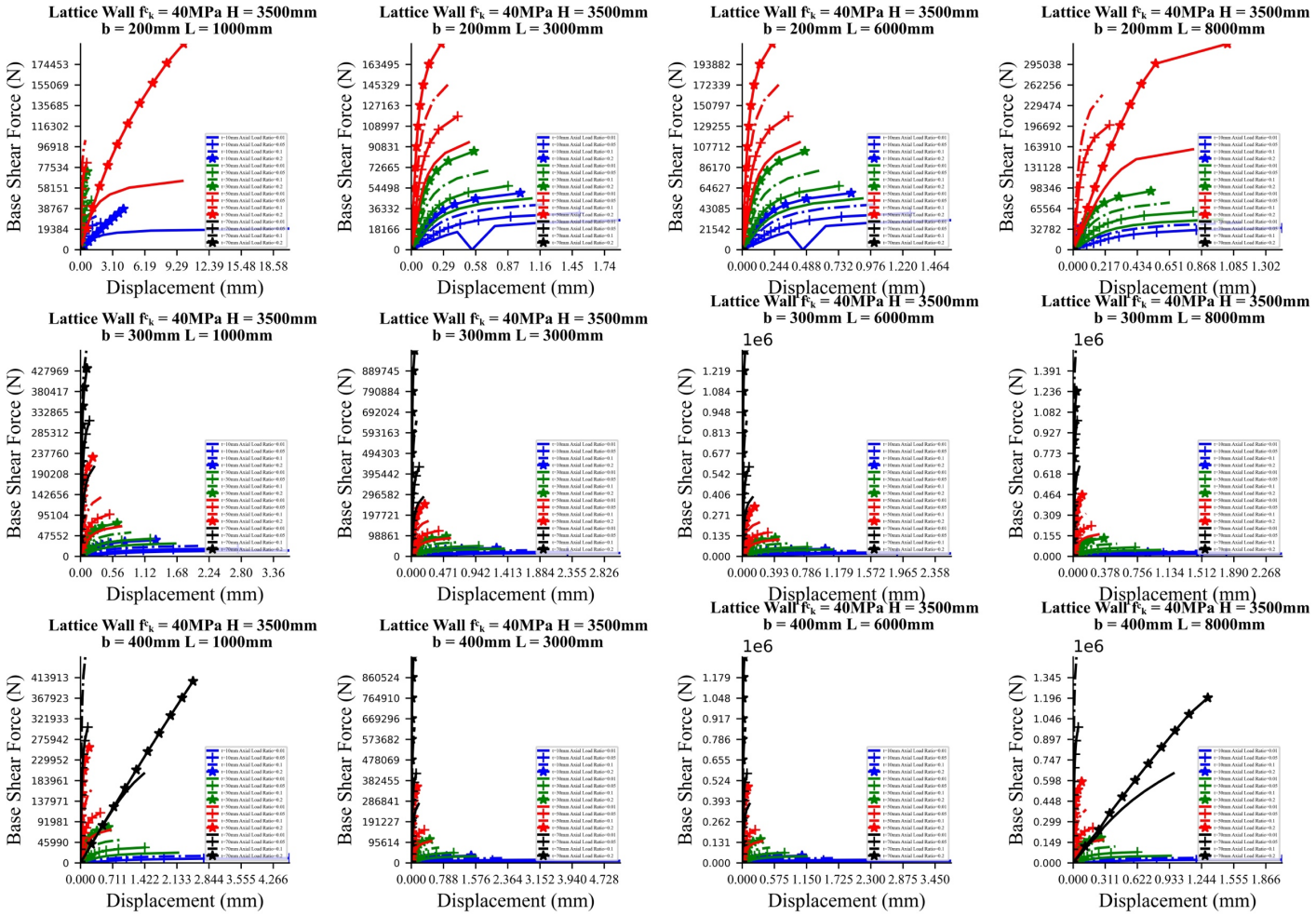

Figure 3.71. Some of the pushover curves created according to the result of the numerical analyses for walls with lattice topology.

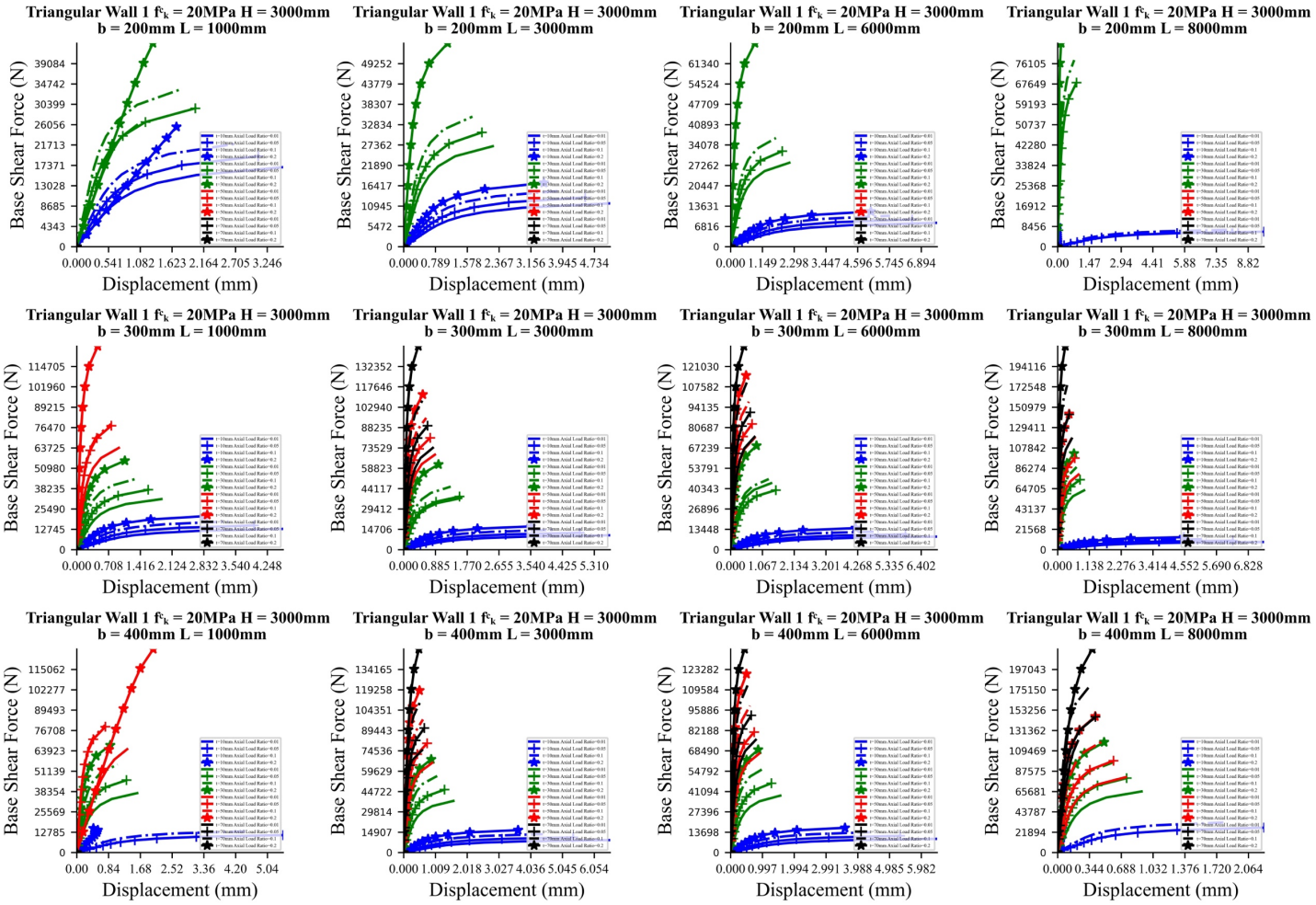

Figure 3.72. Some of the pushover curves created according to the result of the numerical analyses for walls with triangular-1 topology.

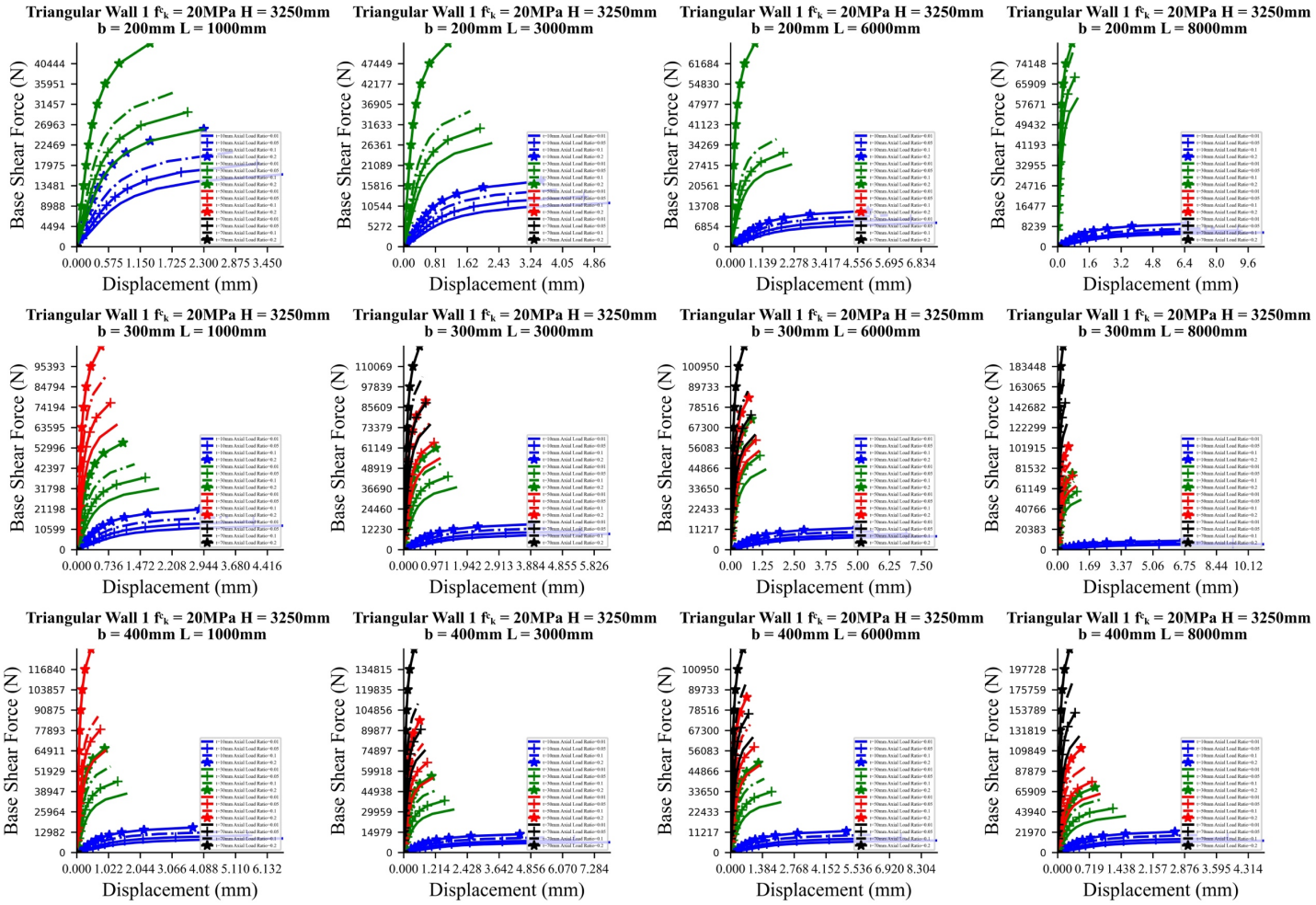

Figure 3.73. Some of the pushover curves created according to the result of the numerical analyses for walls with triangular-1 topology.

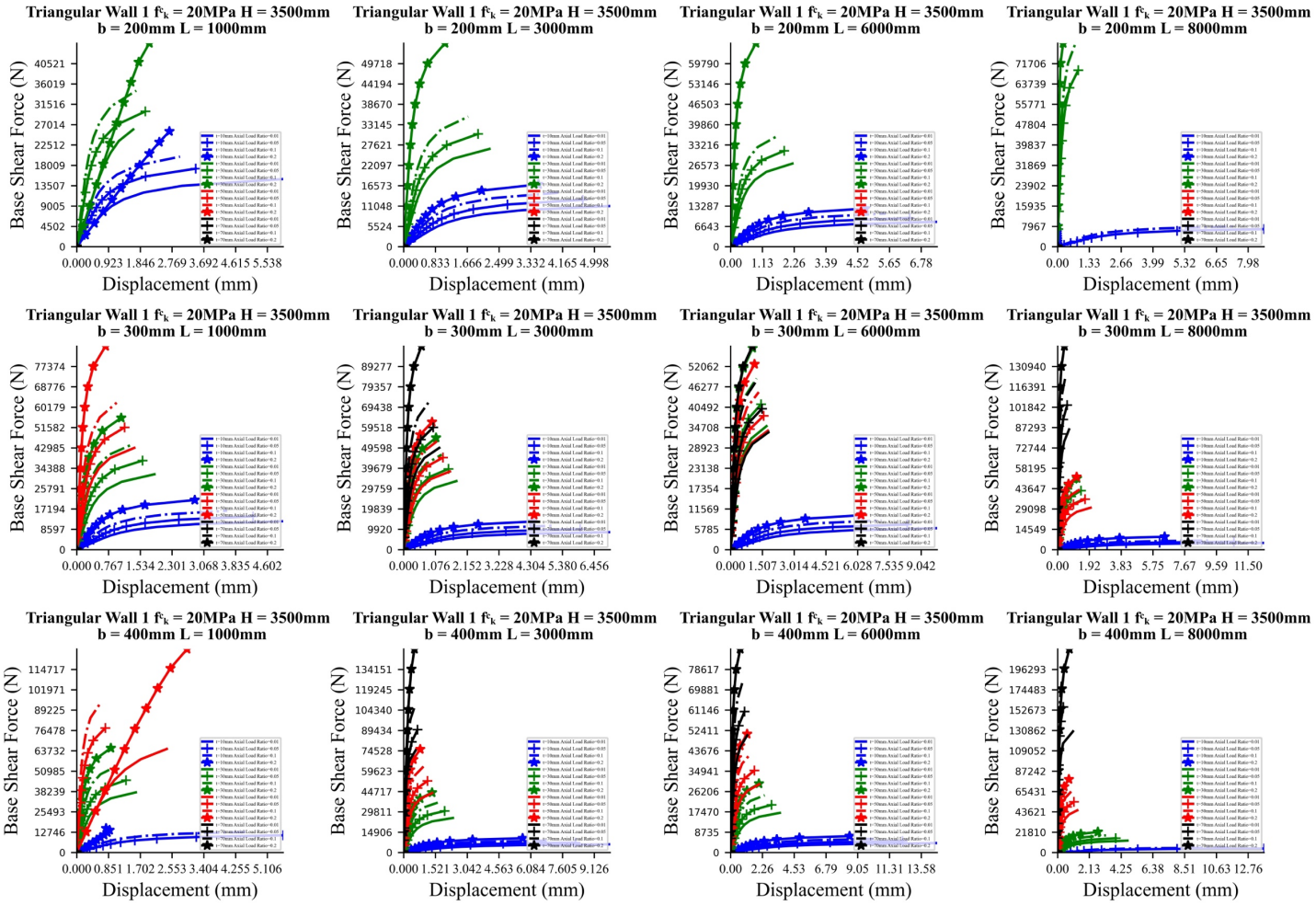

Figure 3.74. Some of the pushover curves created according to the result of the numerical analyses for walls with triangular-1 topology.

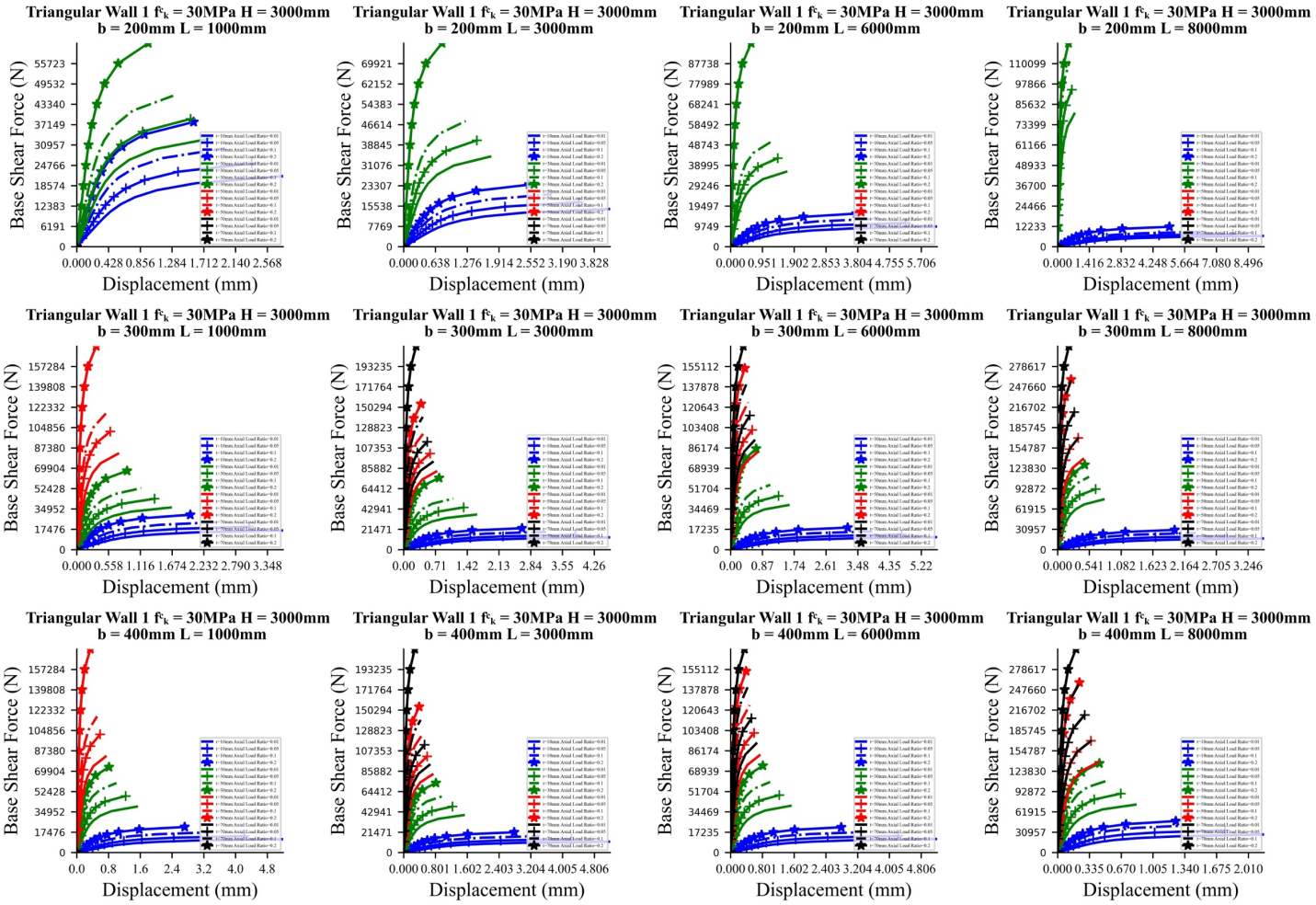

Figure 3.75. Some of the pushover curves created according to the result of the numerical analyses for walls with triangular-1 topology.

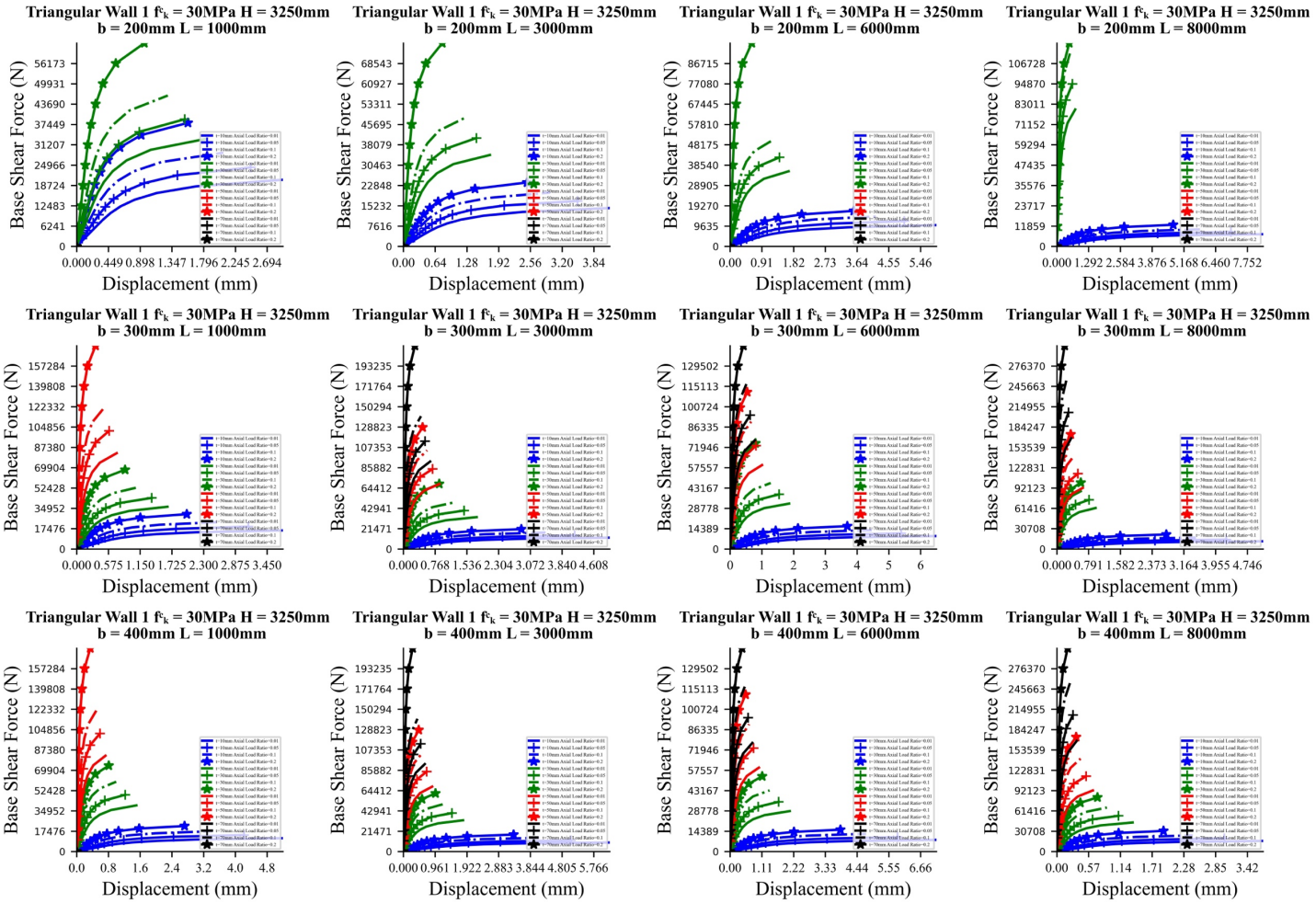

Figure 3.76. Some of the pushover curves created according to the result of the numerical analyses for walls with triangular-1 topology.

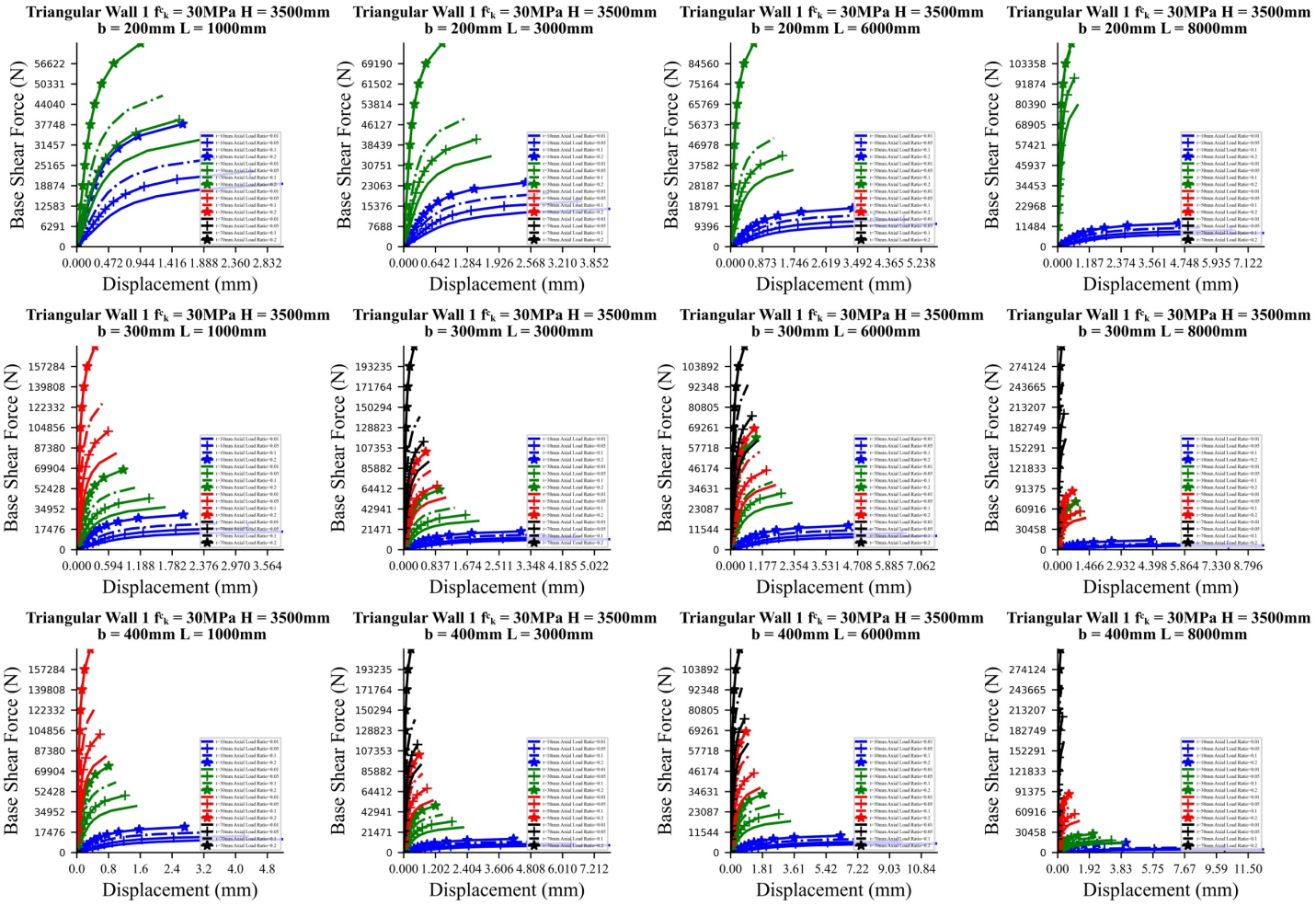

Figure 3.77. Some of the pushover curves created according to the result of the numerical analyses for walls with triangular-1 topology.

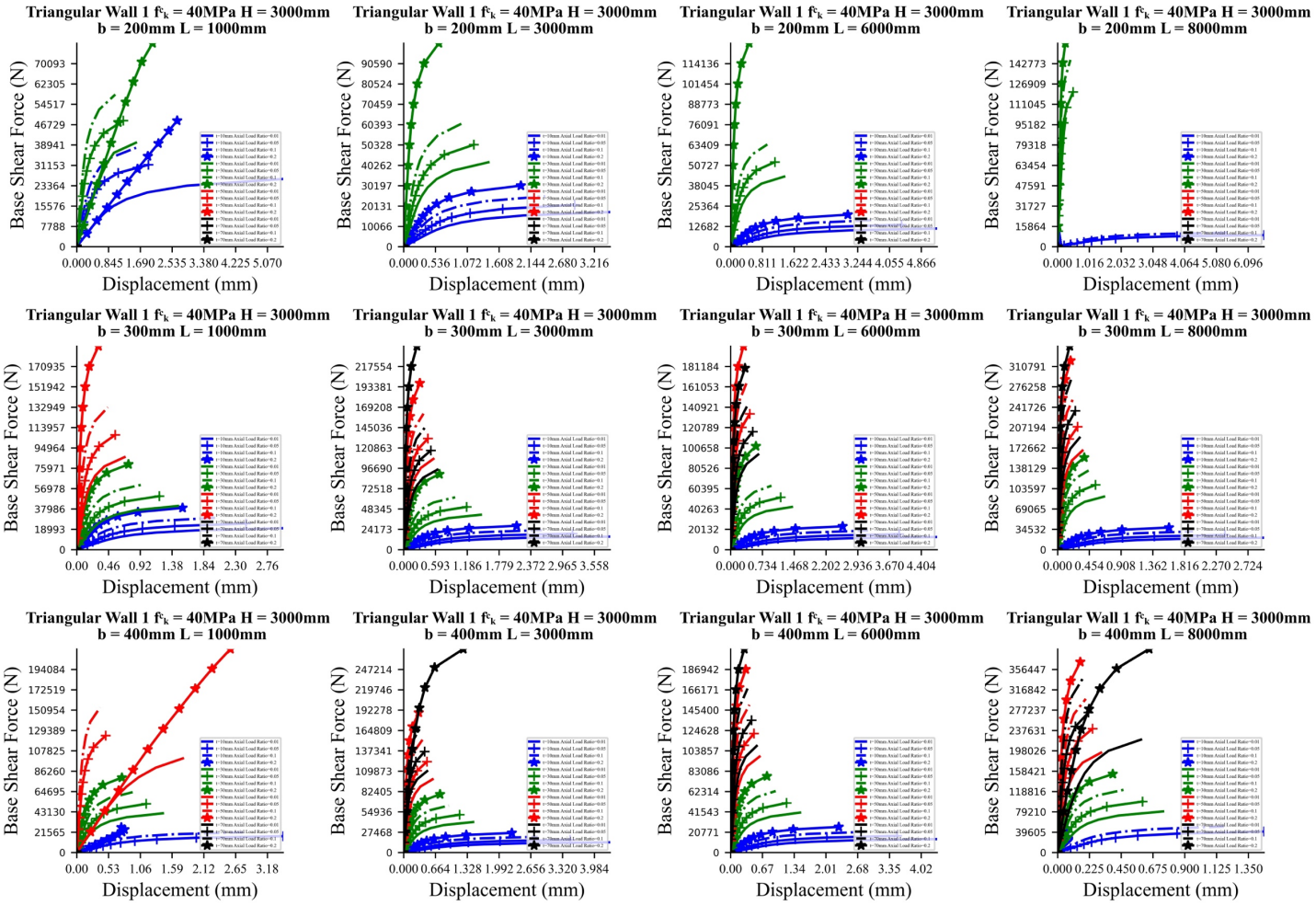

Figure 3.78. Some of the pushover curves created according to the result of the numerical analyses for walls with triangular-1 topology.

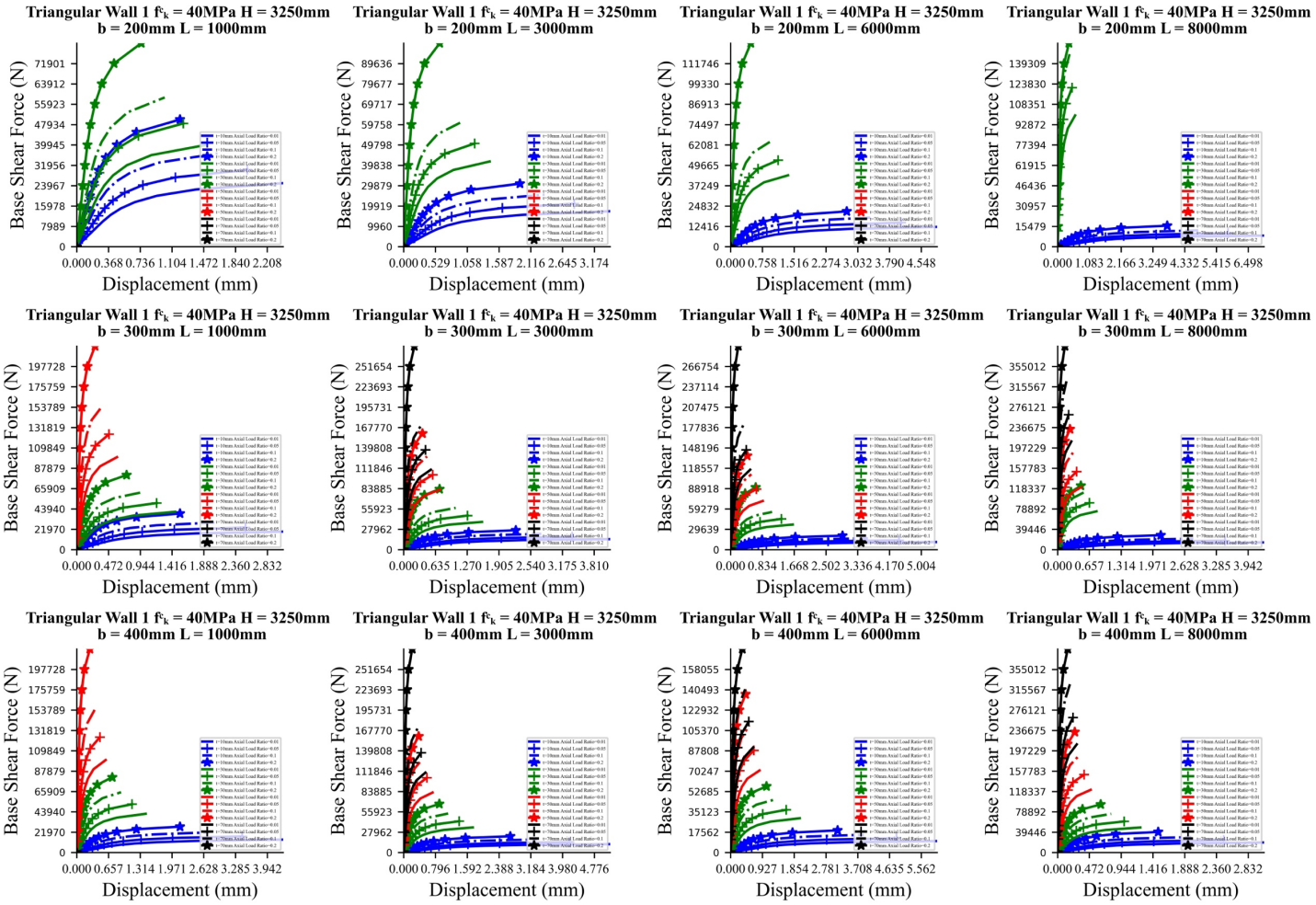

Figure 3.79. Some of the pushover curves created according to the result of the numerical analyses for walls with triangular-1 topology.

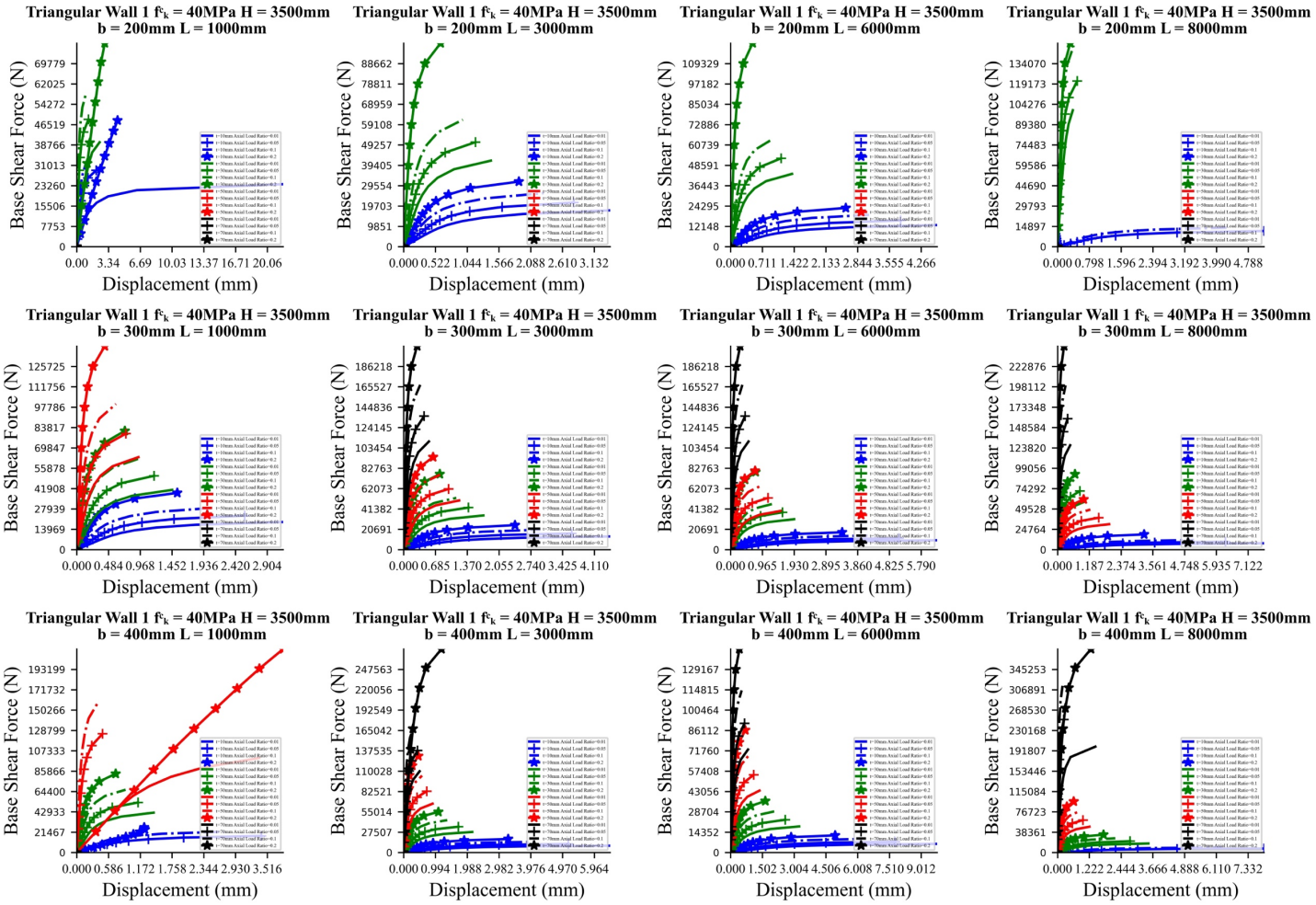

Figure 3.80. Some of the pushover curves created according to the result of the numerical analyses for walls with triangular-1 topology.

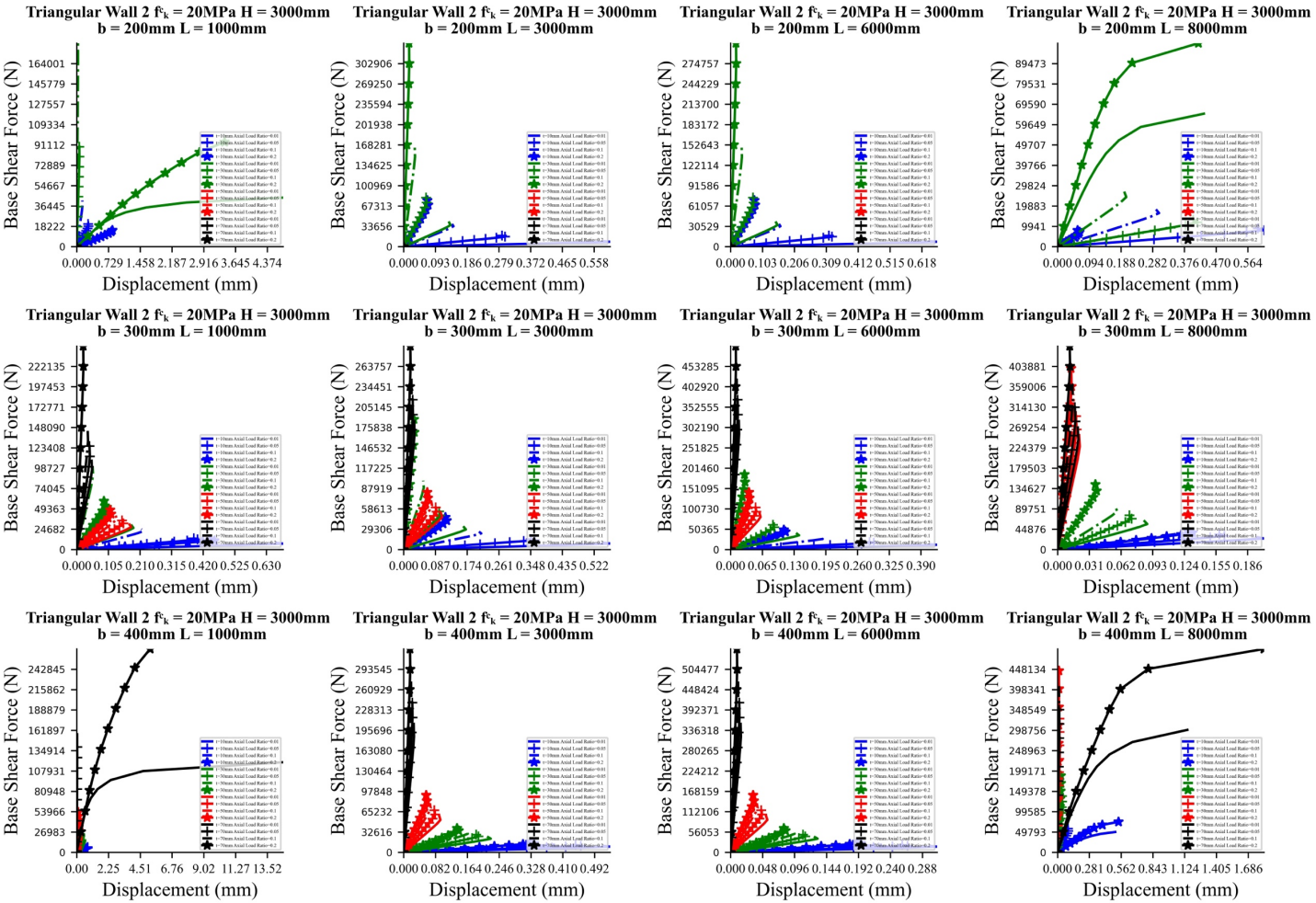

Figure 3.81. Some of the pushover curves created according to the result of the numerical analyses for walls with triangular-2 topology.

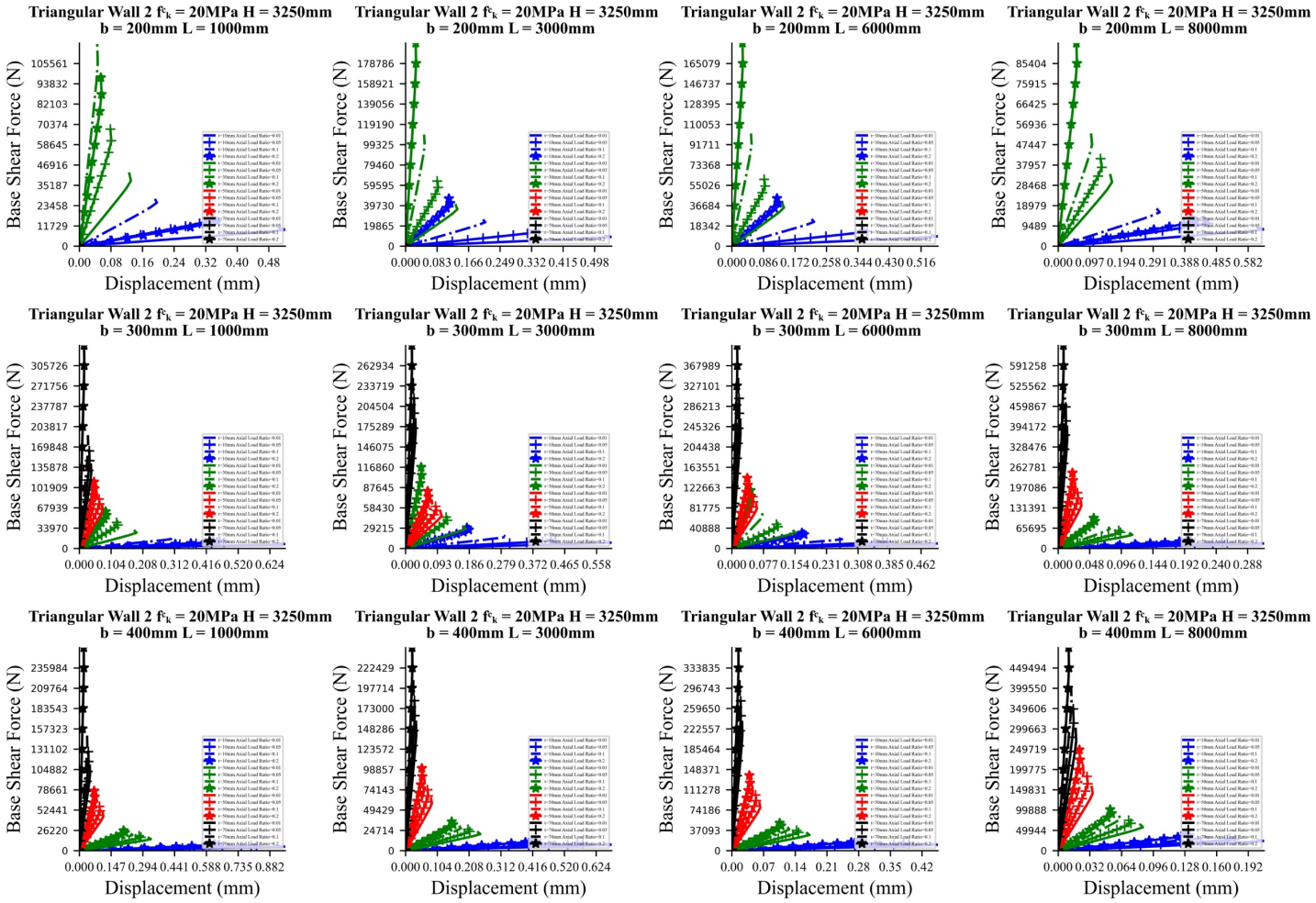

Figure 3.82. Some of the pushover curves created according to the result of the numerical analyses for walls with triangular-2 topology.

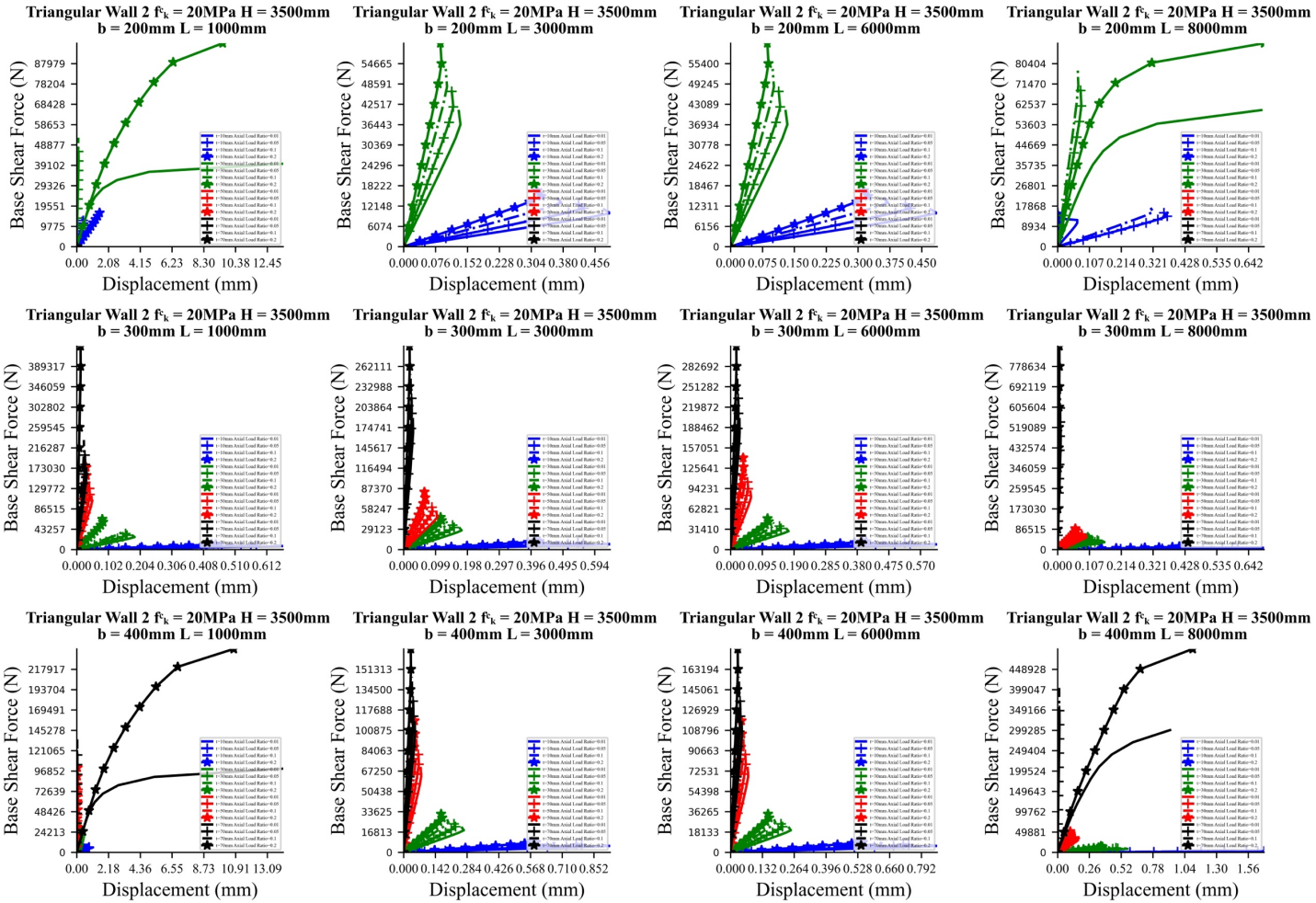

Figure 3.83. Some of the pushover curves created according to the result of the numerical analyses for walls with triangular-2 topology.

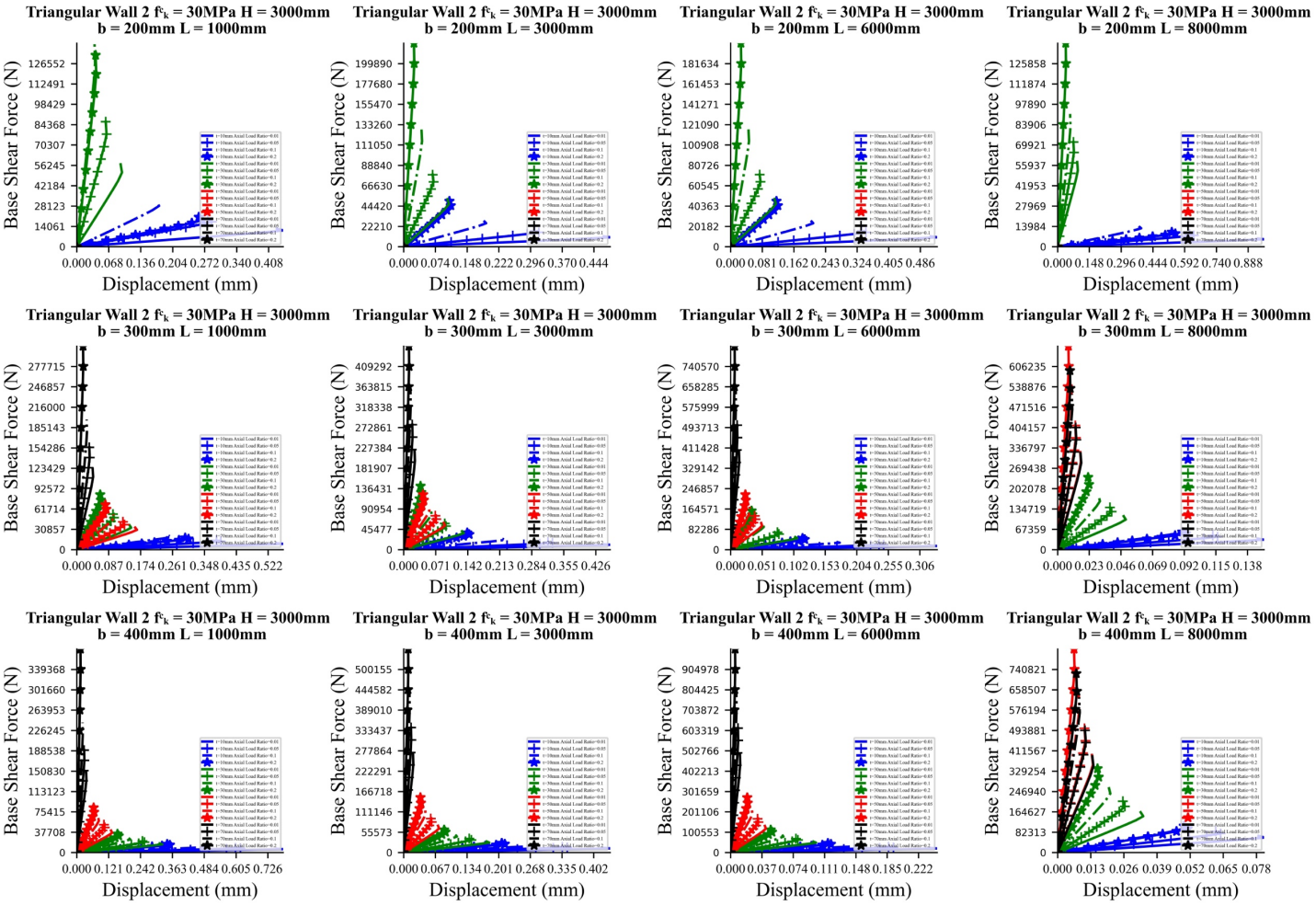

Figure 3.84. Some of the pushover curves created according to the result of the numerical analyses for walls with triangular-2 topology.

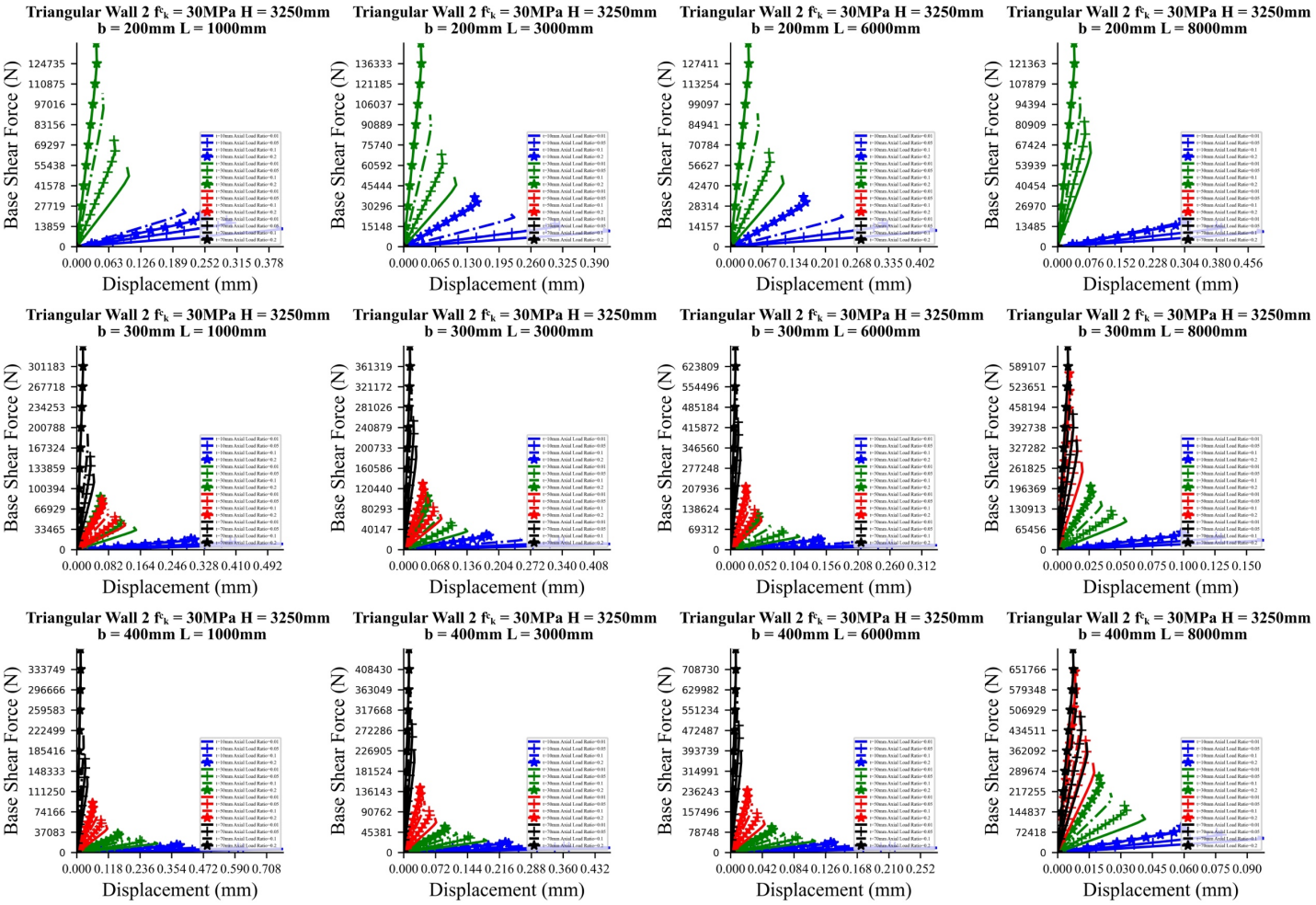

Figure 3.85. Some of the pushover curves created according to the result of the numerical analyses for walls with triangular-2 topology.

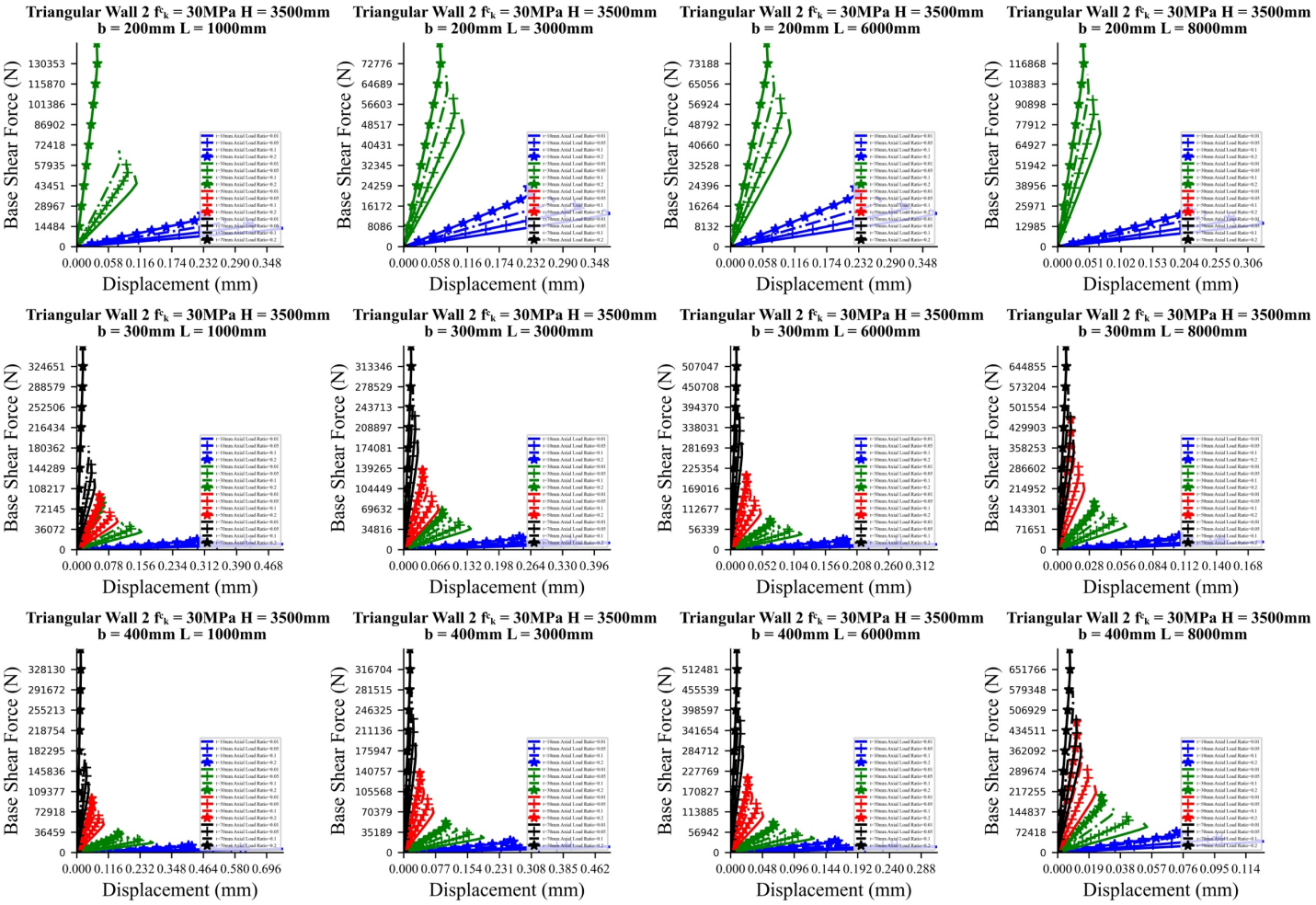

Figure 3.86. Some of the pushover curves created according to the result of the numerical analyses for walls with triangular-2 topology.

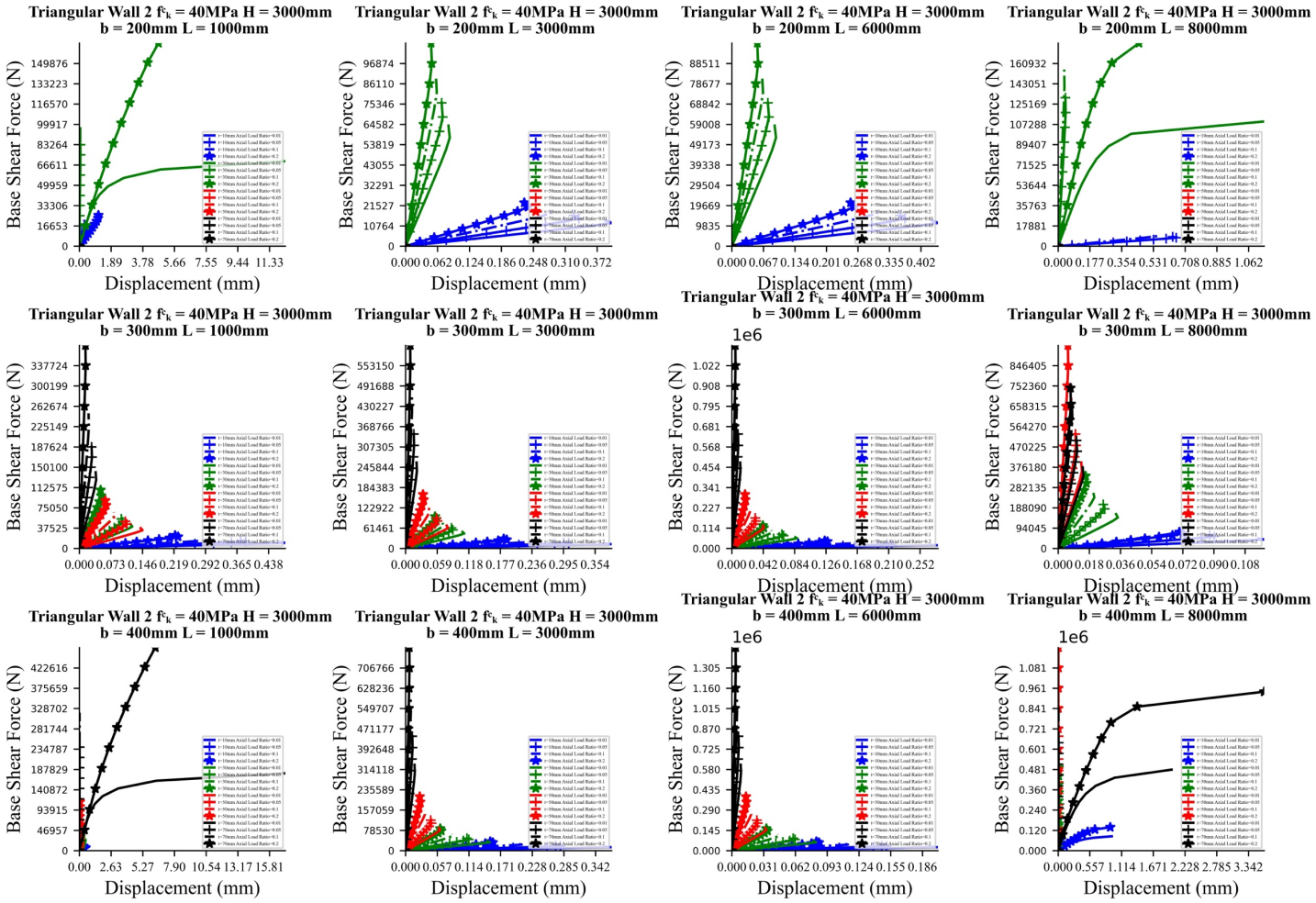

Figure 3.87. Some of the pushover curves created according to the result of the numerical analyses for walls with triangular-2 topology.

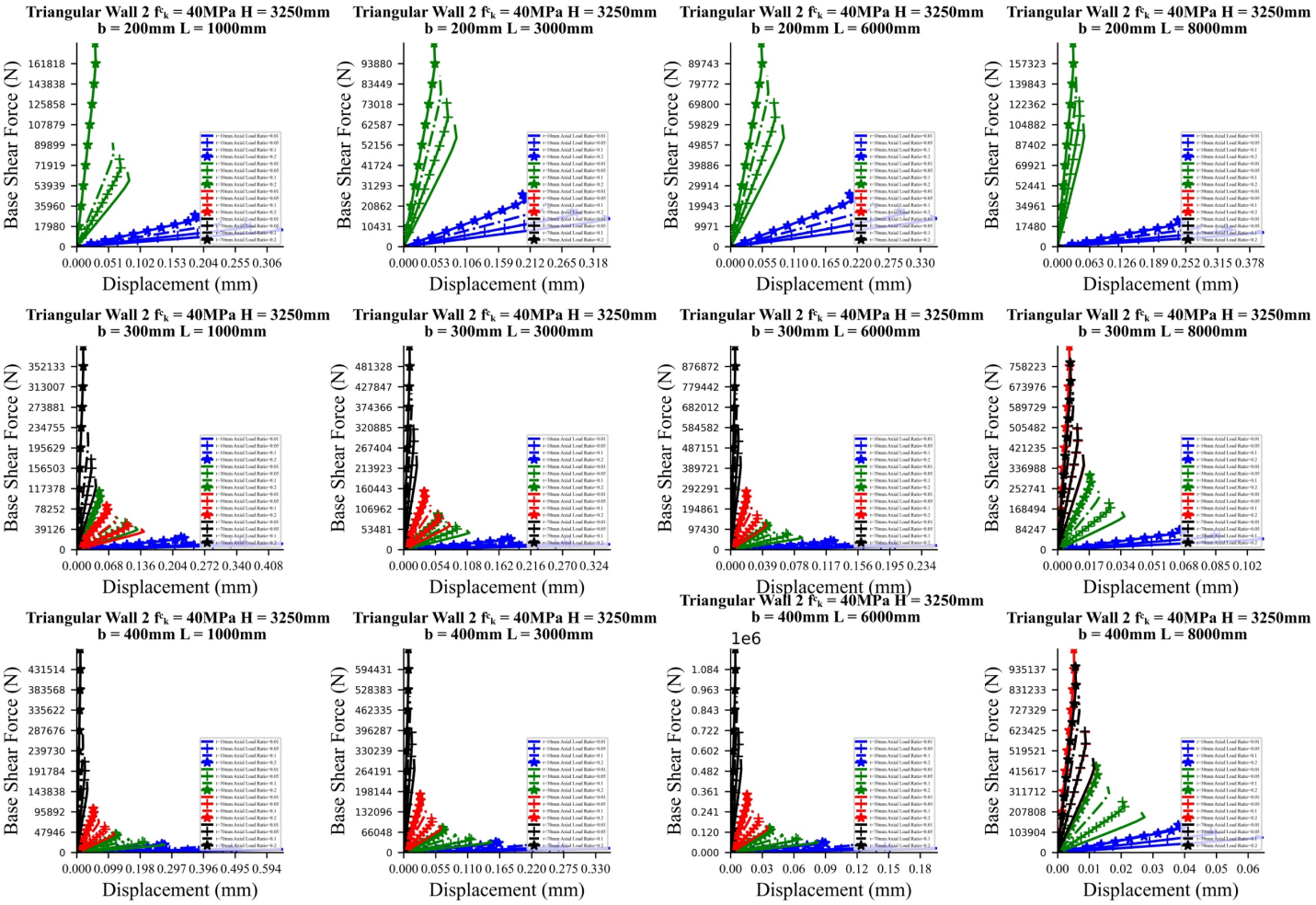

Figure 3.88. Some of the pushover curves created according to the result of the numerical analyses for walls with triangular-2 topology.

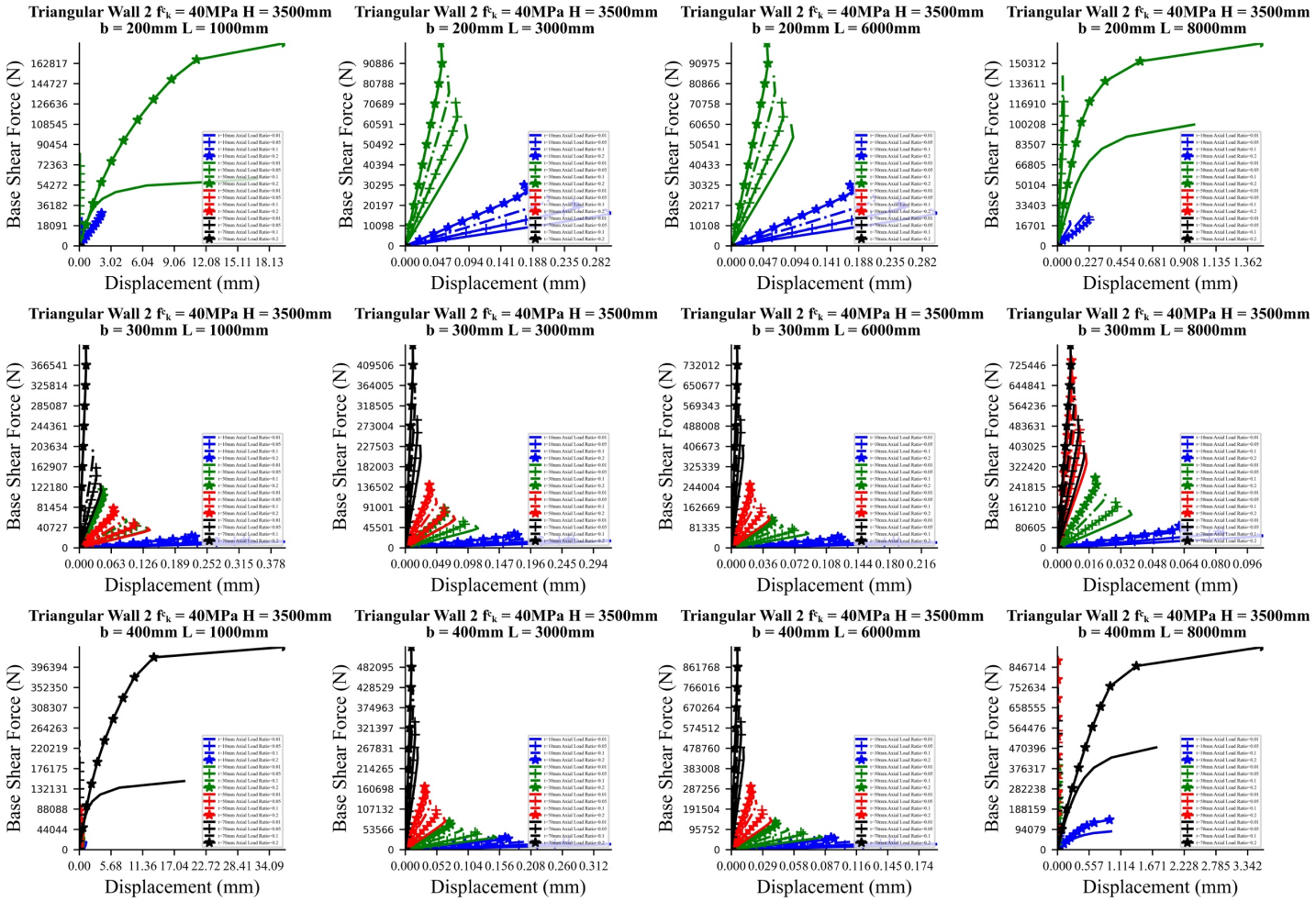

Figure 3.89. Some of the pushover curves created according to the result of the numerical analyses for walls with triangular-2 topology.

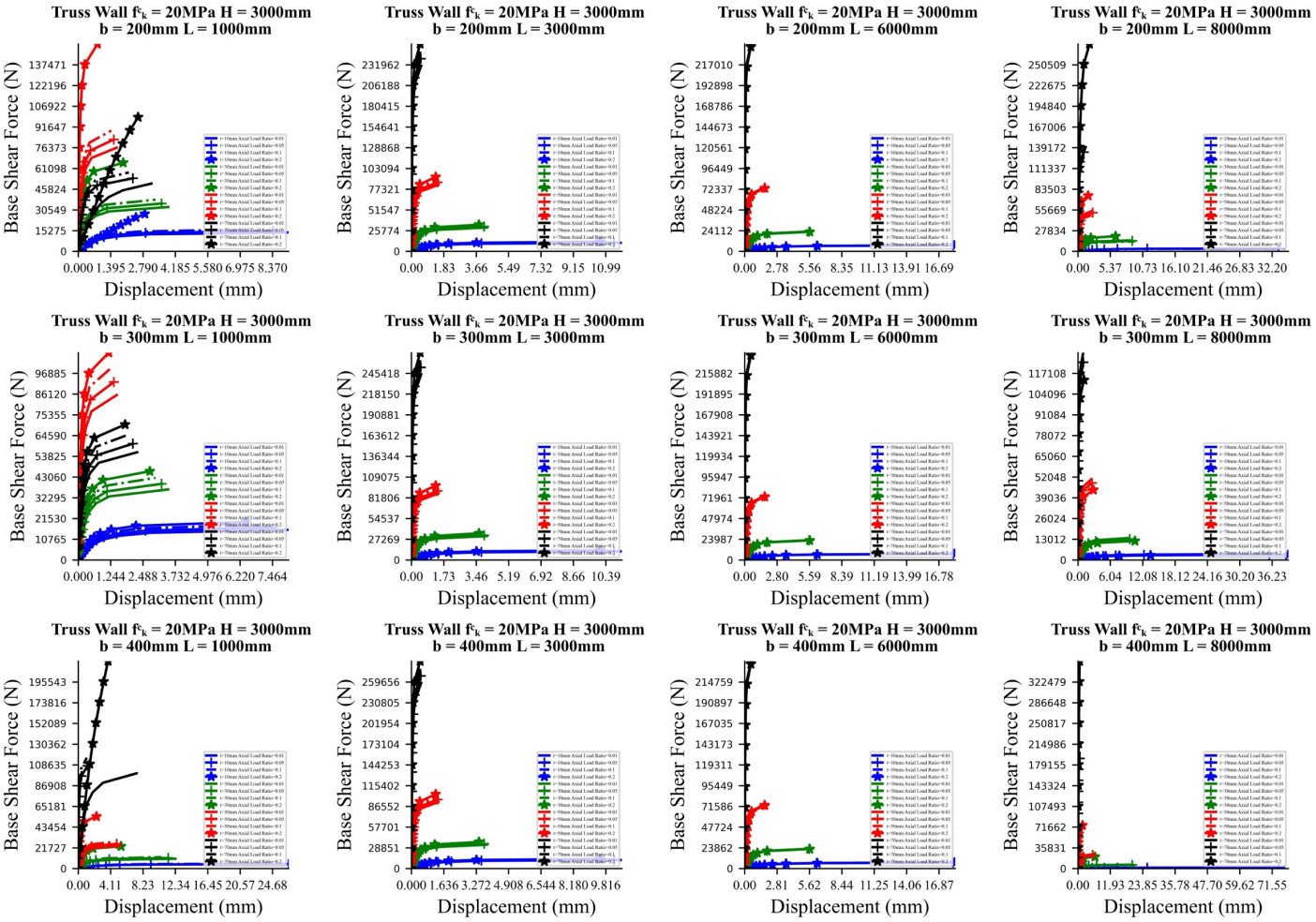

Figure 3.90. Some of the pushover curves created according to the result of the numerical analyses for walls with truss topology.

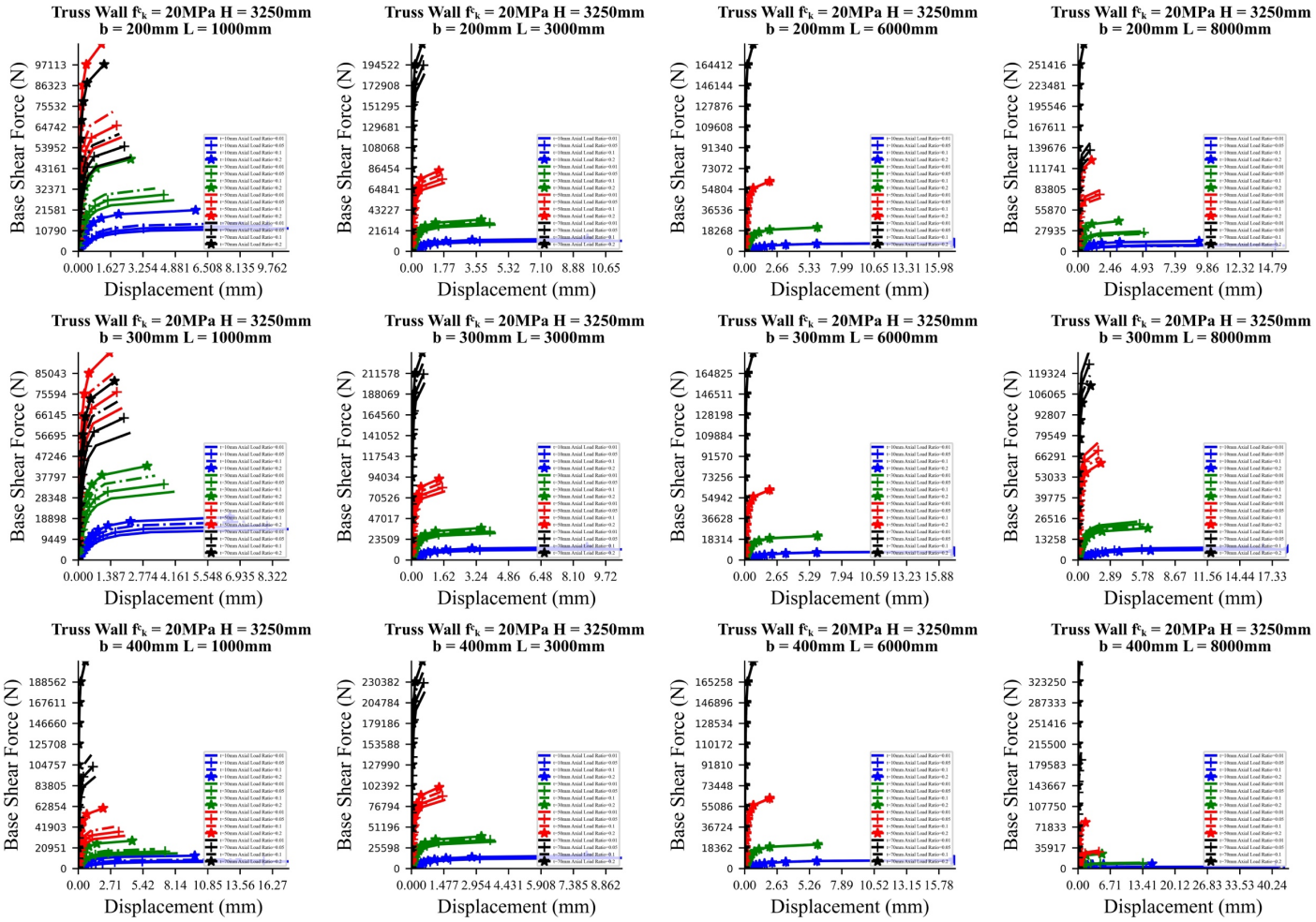

Figure 3.91. Some of the pushover curves created according to the result of the numerical analyses for walls with truss topology.

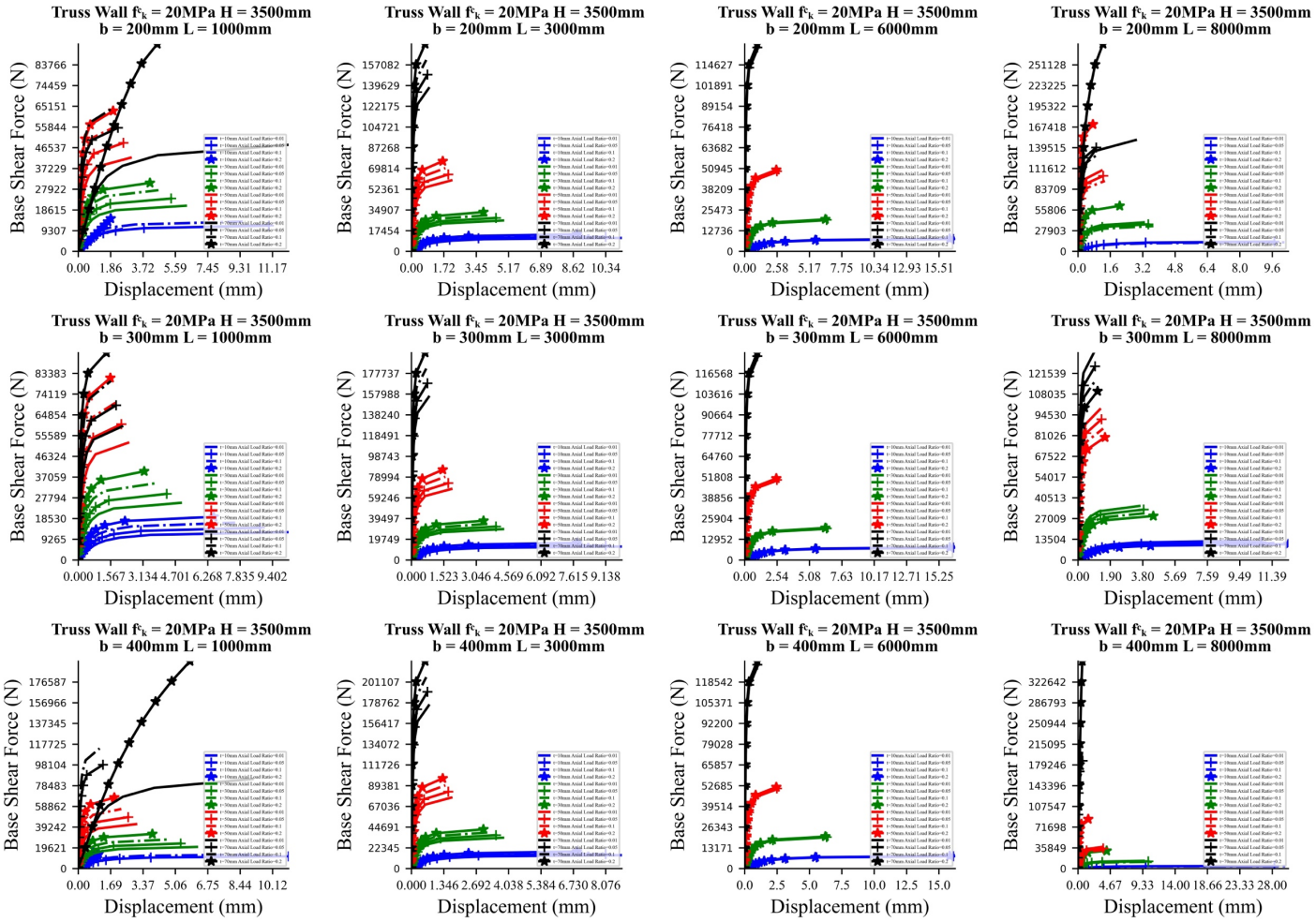

Figure 3.92. Some of the pushover curves created according to the result of the numerical analyses for walls with truss topology.

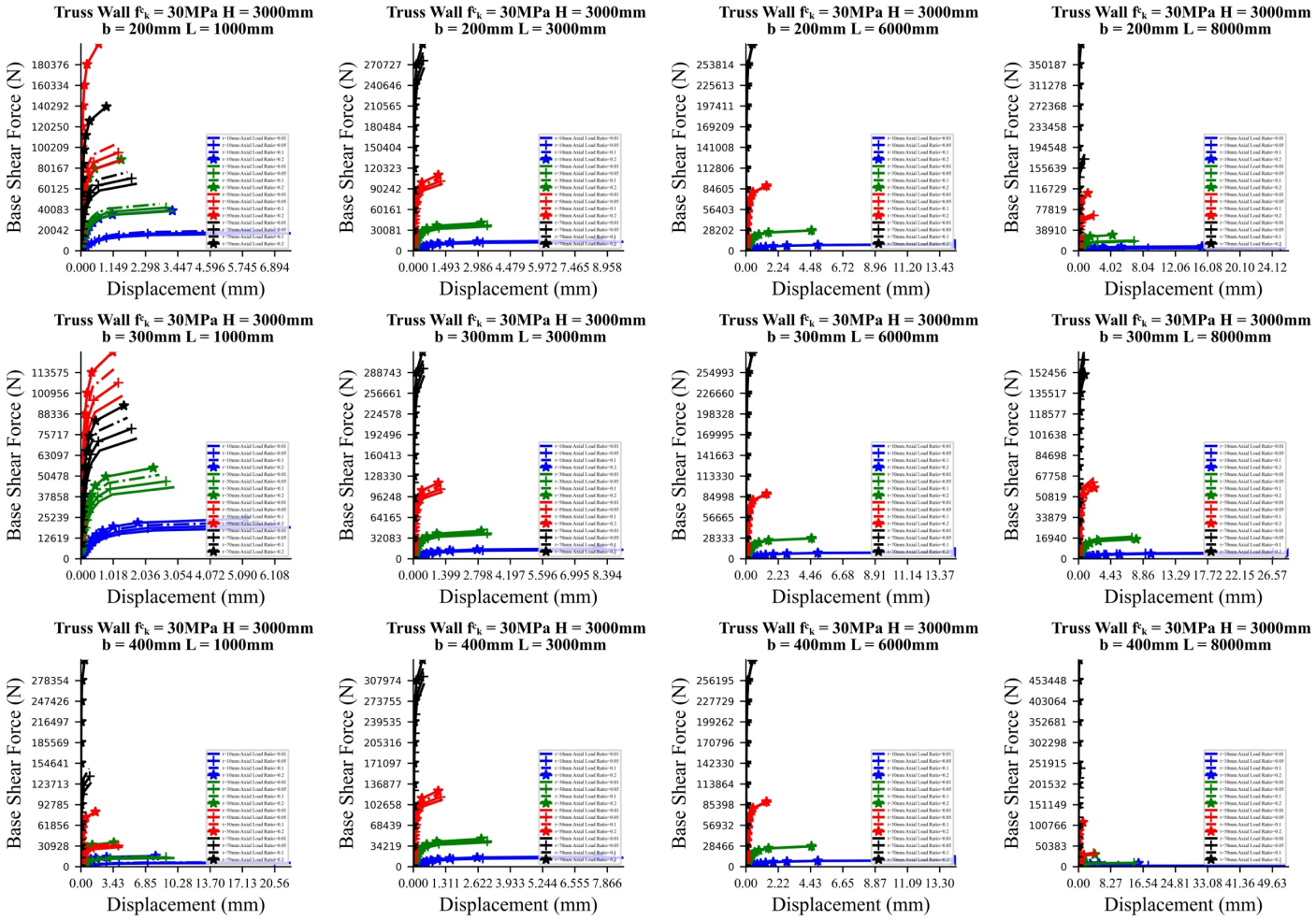

Figure 3.93. Some of the pushover curves created according to the result of the numerical analyses for walls with truss topology.

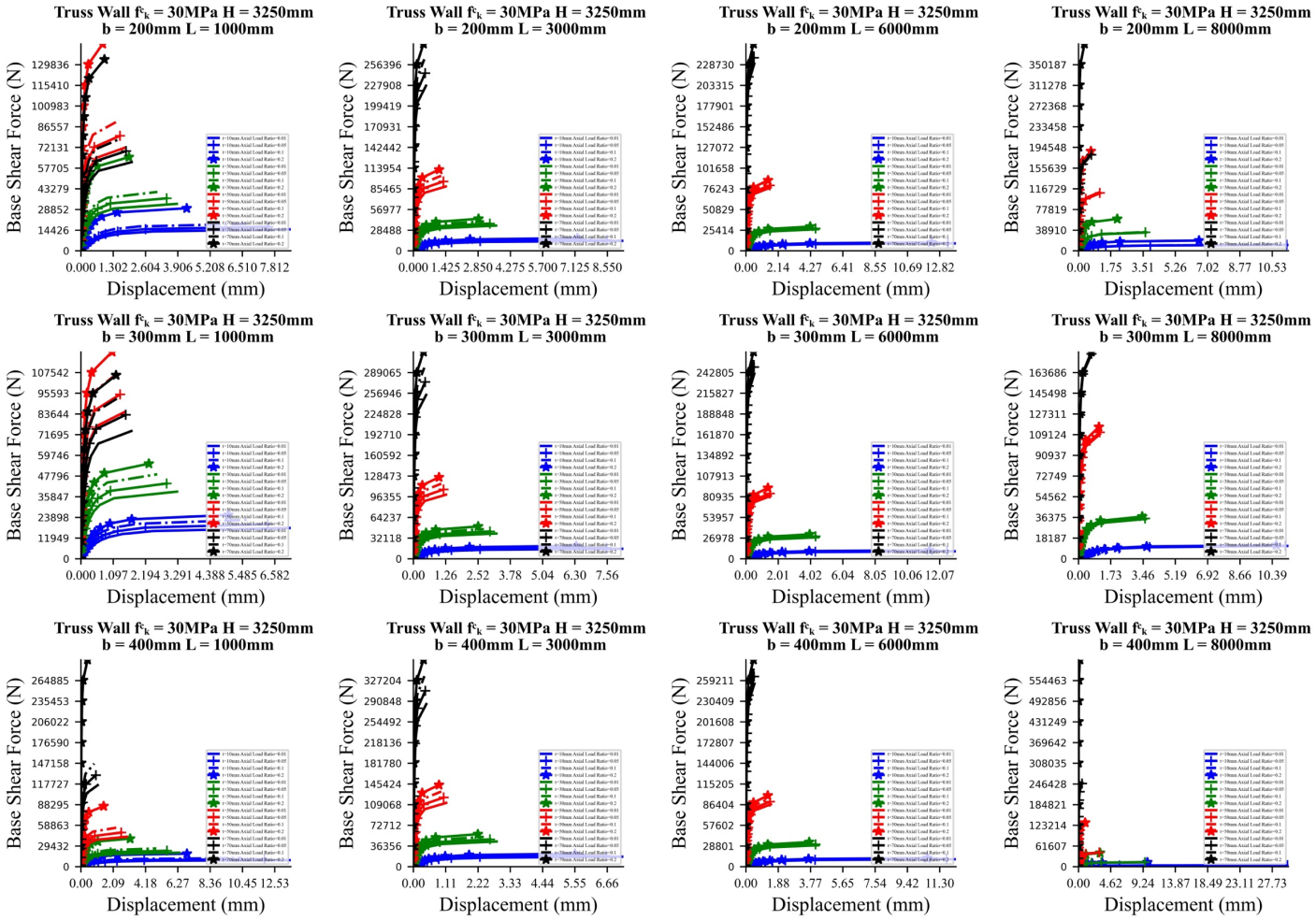

Figure 3.94. Some of the pushover curves created according to the result of the numerical analyses for walls with truss topology.

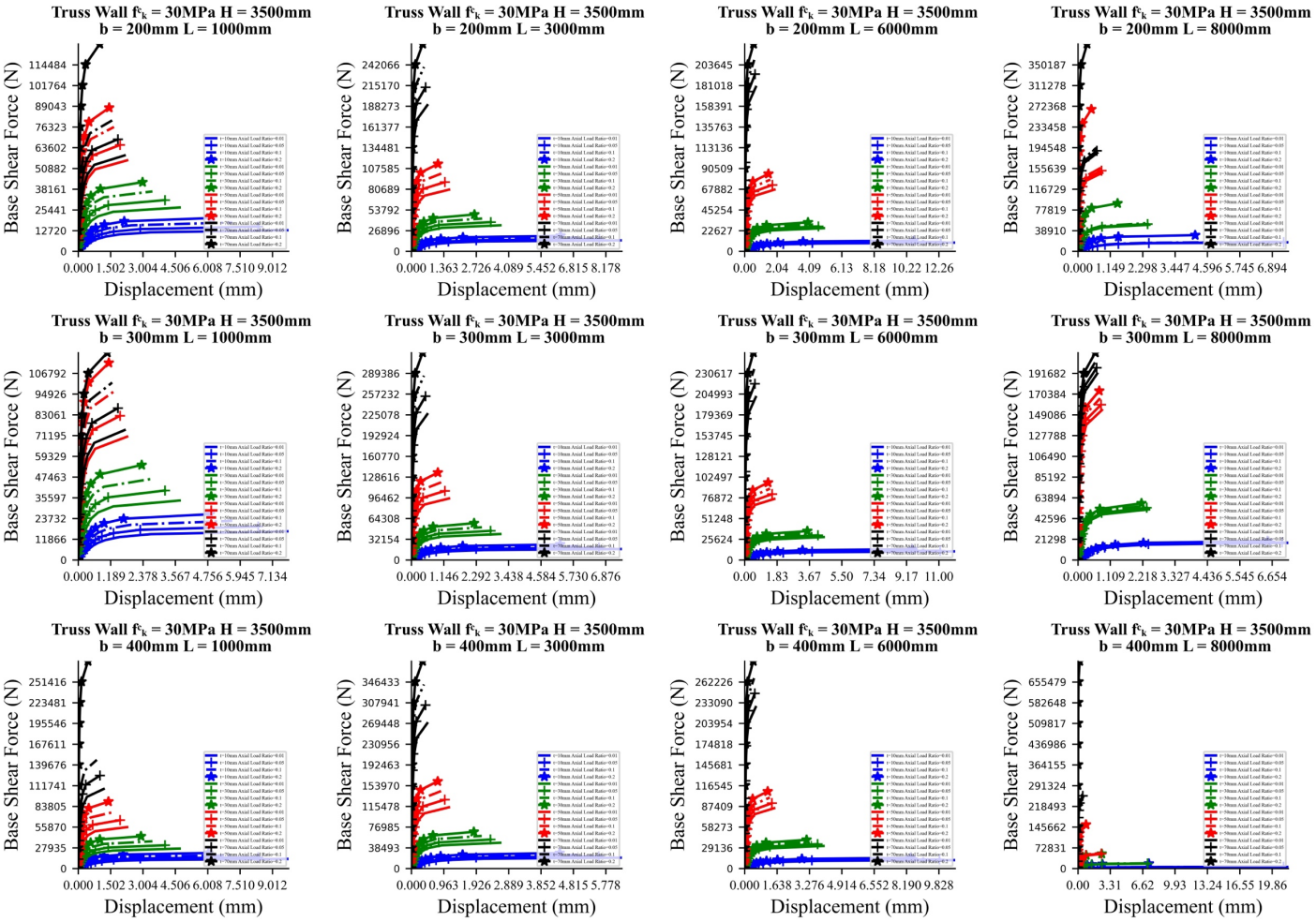

Figure 3.95. Some of the pushover curves created according to the result of the numerical analyses for walls with truss topology.

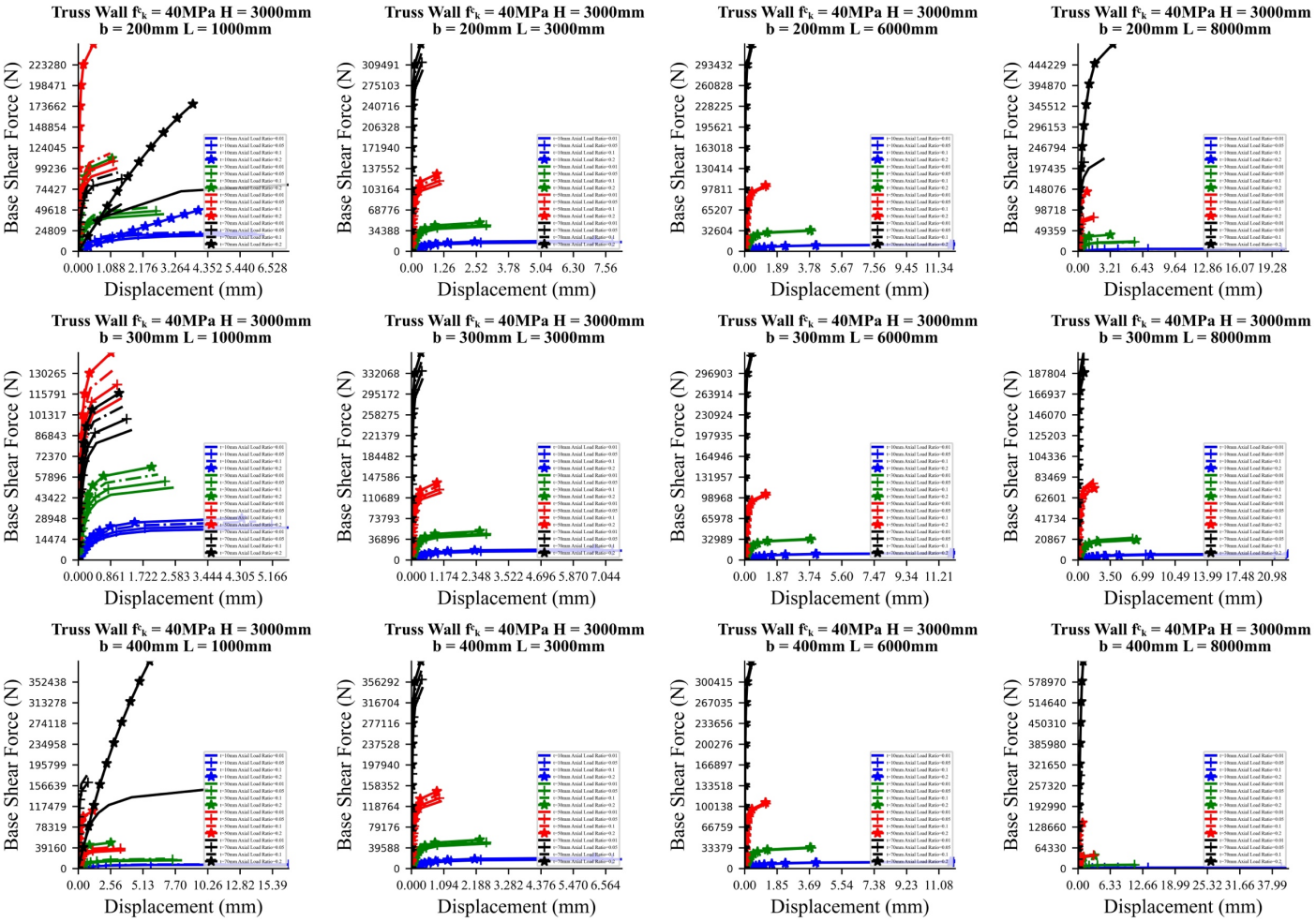

Figure 3.96. Some of the pushover curves created according to the result of the numerical analyses for walls with truss topology.

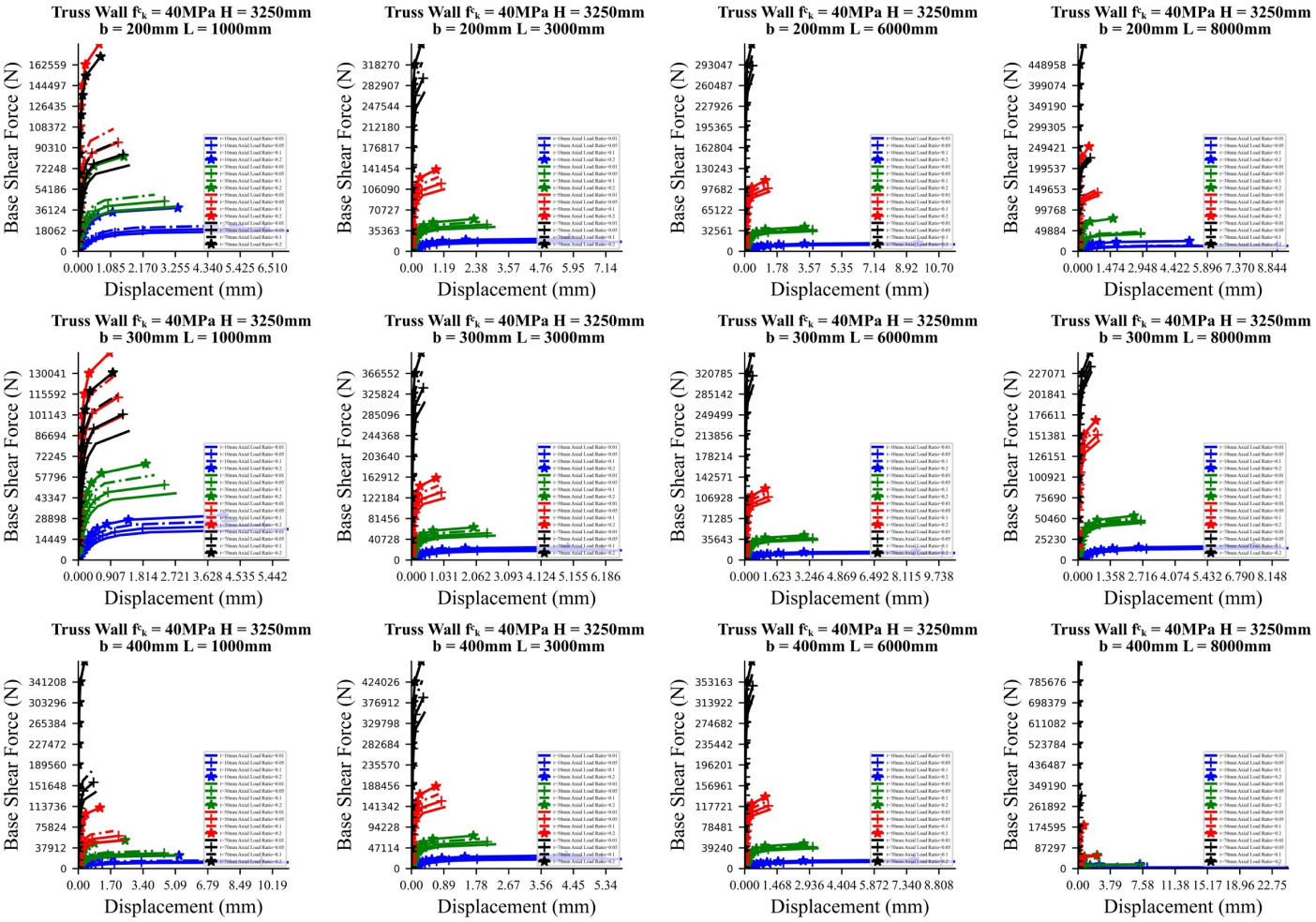

Figure 3.97. Some of the pushover curves created according to the result of the numerical analyses for walls with truss topology.

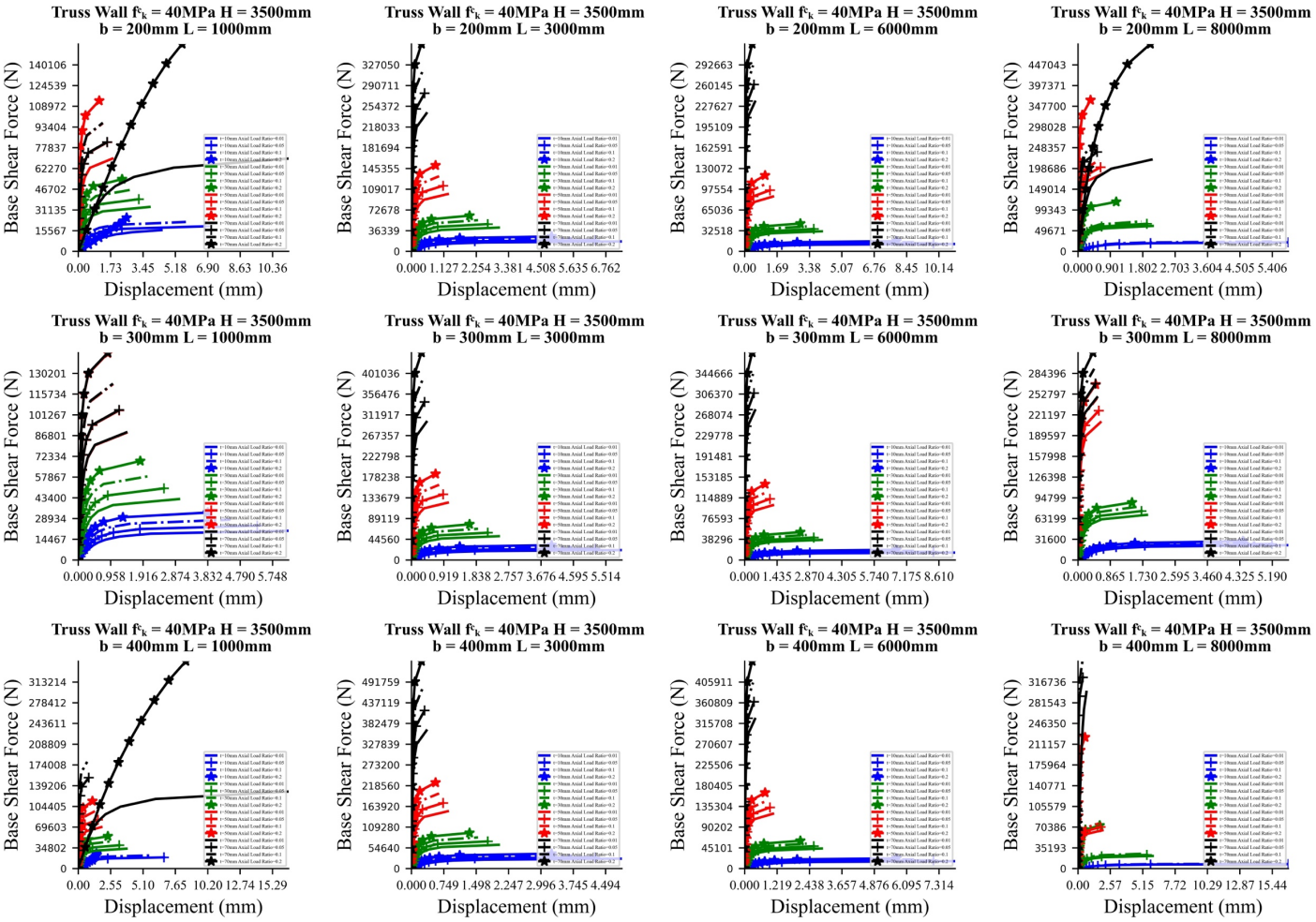

Figure 3.98. Some of the pushover curves created according to the result of the numerical analyses for walls with truss topology.

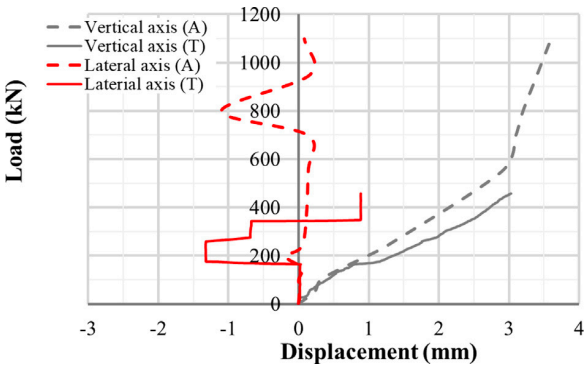

Figure 3.99. The load-displacement curve of the 3D-printed concrete shear wall with lattice internal topology.

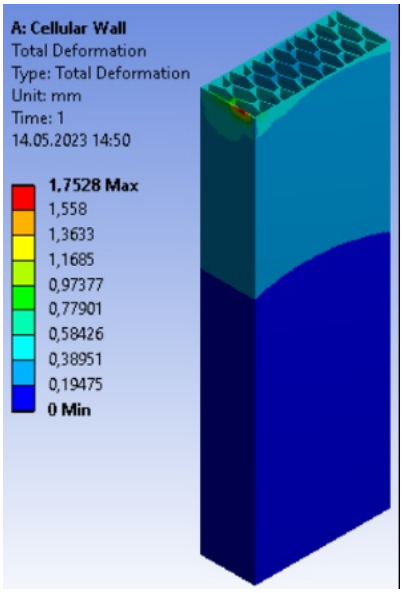

Figure 3.100. Local damage region of a wall with a length of 1000 mm, width of 400 mm, thickness of 10 mm, height of 3000 mm, and cellular interior hollow topology.

For the values of 20 MPa compressive strength, 0.2 axial load ratio, 3000 mm height, 1000 mm length, 200 mm width, and 10 mm thickness, it can be seen that walls with triangular-2 topology, one of the proposed novel topologies, have higher shear strength and maximum displacement compared to walls with cellular, elliptical, arch, and hollow topology. Similarly, walls with arch topology, one of the proposed novel topologies, have higher shear strength and maximum displacement compared to walls with elliptical and hollow topology. When all values are kept the same and only the thickness is increased

to 30 mm, it can be seen that walls with triangular-2 topology have higher shear strength and maximum displacement compared to walls with triangular-1, lattice, elliptical, arch, and hollow topology. Similarly, walls with elliptical topology have higher shear strength and maximum displacement compared to walls with arch and hollow topology. In addition, it was observed that the cross-sectional areas of walls with solid topology are the highest, followed by walls with triangular-1 and triangular-2 topologies. The cross-sectional areas of these two topologies are very close to each other. These walls are followed by walls with cellular topology. After walls with cellular topology, walls with lattice, arch, and elliptical topologies have the highest cross-sectional areas. The cross-sectional areas of these three topologies are also very close to each other. Walls with truss topology followed these walls, and the walls with the least cross-sectional area were hollow. It can be understood from this that the proposed novel wall interior topologies can perform better than other interior topologies used in the literature depending on geometric properties, material properties, and axial load ratio.

The deformation capacity for masonry walls is generally defined as a certain maximum displacement capacity [47,78]. Since walls printed through 3DCP have a similar structure to masonry walls, in this study, the realism of the results obtained with FE simulation was controlled considering the drift ratios. The drift ratio is obtained by dividing the lateral displacement by the wall height, as shown in Equation 3.21 [47,78,79].

$$\delta_u / h_w \tag{3.21}$$

where, δ_u represents the ultimate displacement that the wall can undergo, while h_w represents the height of the wall [78]. Current regulations suggest different empirical models considering factors such as failure mode, aspect ratio, axial load ratio, and normalized shear span for the lateral displacement capacity of masonry walls [47]. The limit drift ratio for shear failure in the case of 'Significant Damage' is 0.4% [47,78,79]. Therefore, in this study, the results were compared considering a drift ratio of 0.4%. As a result of the numerical analyses in this study, it was observed that 6.5% of walls with solid topology, 1% of walls with triangular-1 topology, 1% of walls with triangular-2 topology, 0.6% of walls with cellular topology, 0.6% of walls with lattice topology, 0.5%

of walls with elliptic topology, 0.5% of walls with arch topology, 7.6% of walls with truss topology, and 3.5% of walls with hollow topology exceeded the 0.4 limit shear displacement ratio. This difference in drift ratios is due to the lack of a specific standard or procedure for modeling members printed through 3DCP, resulting in the creation of a single modeling procedure by making certain assumptions for elements with different topologies. However, the majority of modeled walls do not exceed the 0.4% drift ratio, indicating that the results obtained are reasonable.

The flowchart of the procedures related to the FE model created in this study is given in Figure 3.101.

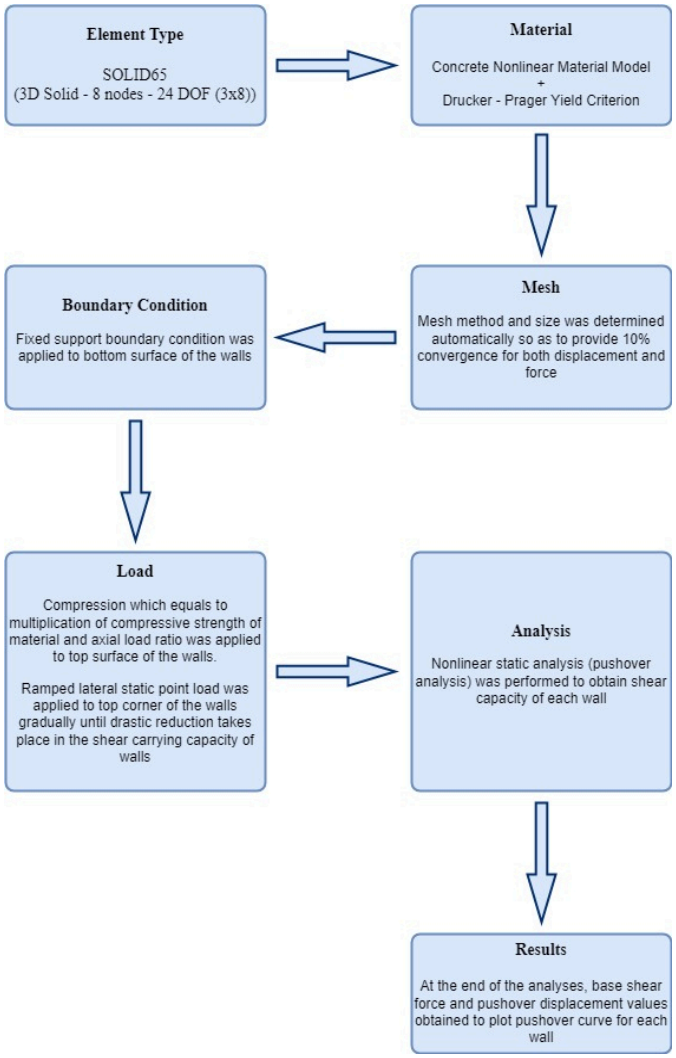

Figure 3.101. Flowchart of the procedure for FE models.

The flowchart of the procedures related to the FE model created in this study is given in Figure 3.101.

3.3. Creating AI Models for Determining the Optimum Interior Topology of Walls

3.3.1. Theoretical Knowledge about ML

The concept of AI, which originated in the 1940s, involves developing intelligent machines or computer programs to emulate human intelligence [46,56]. The human brain is much more adept at solving new problems and processing information compared to traditional computers, but it operates at a slower speed [56]. AI is a technology that develops theories, methods, techniques, and applications to further expand human intelligence. It is a highly comprehensive field consisting of various components such as ML and computer vision. The primary goal of AI is to enable machines to perform complex tasks that have historically required human intelligence [57].

ML is a subfield of AI where a computer builds a model using input data that it observes from a specific dataset and can be utilized to solve various problems [1,21,56]. The concept of ML sets it apart from traditional programming, where rules are written in a computer language without gaining knowledge from the data [1]. ML utilizes data to develop predictive models for making predictions with data that has not been seen before, in contrast to conventional programming [1,21,56]. Developing a rule-based program can be very challenging for certain issues because of the complexity of the code. In these situations, ML can be utilized as long as there is sufficient data accessible for the specific problem [1,56]. ML is a highly effective method and is widely used in the literature [55,56]. An ML model with high accuracy can be obtained with a small number of training data [51]. This method has various advantages and disadvantages. The SWOT (strengths, weaknesses, opportunities, and threats) analysis of ML is given in Figure 3.102 [10].

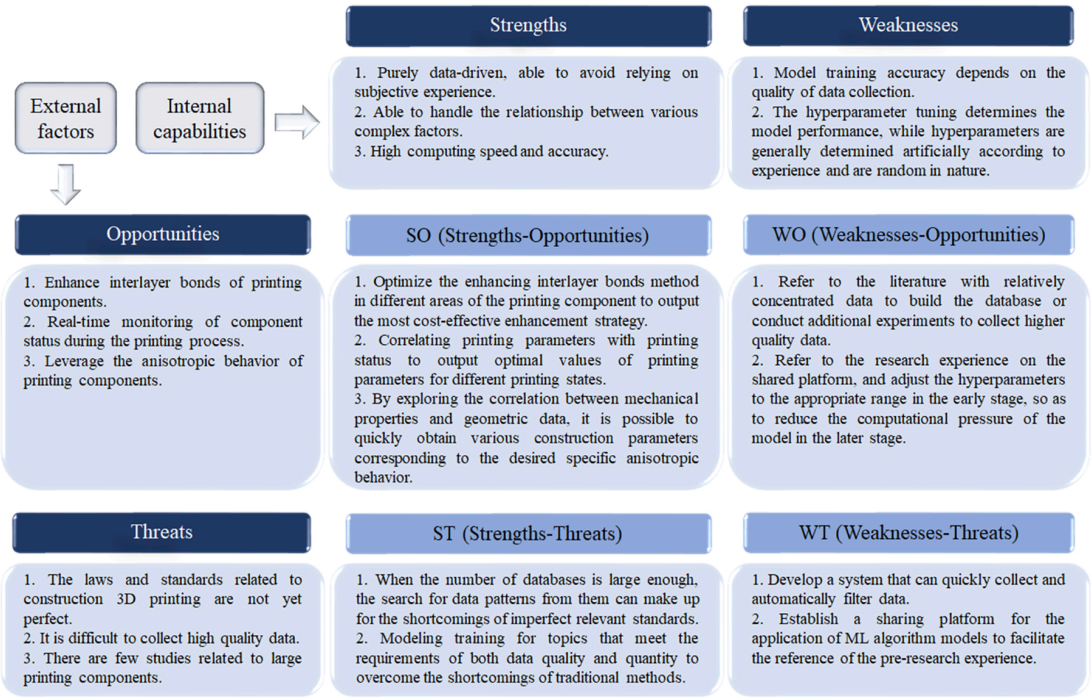

Figure 3.102. SWOT analysis for applications of ML in the 3DCP field [10].

Besides the many advantages of ML, there are various challenges such as high computation cost, data processing, data acquisition, gathering standardized data, labeling, dataset size, and fitting the data to appropriate ML modeling procedures. It has been proven that ML-based numerical simulations are more accurate and efficient than physics-based numerical simulations. Efficient data sharing is the key to the success of ML algorithms. Despite the enormous increase in the number of individuals researching new processes and materials, there are still no specific standards for data collection and preprocessing integrated with ML protocols [55]. Data collection is crucial for training ML models to obtain accurate and effective results. For the 3DCP process, training data can be obtained either through experiments or through simulation results. The two methods present their own difficulties, since simulations may produce inaccurate results, while experiments can be a costly and time-consuming approach. However, these problems are not unsolvable. Possible solutions to these problems are given in Figure 3.103 [55].

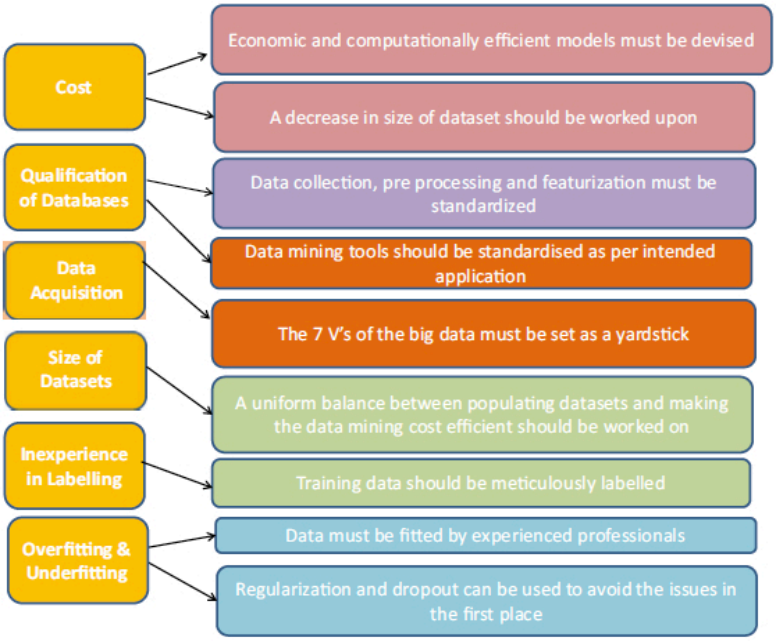

Figure 3.103. Possible solutions for problems that may arise from the use of ML in the field of 3DCP [55].

DL falls under the category of ML and can be defined as an ML method with multiple layers of adaptable and simple computing components. DL can be considered as the study of ANN and other related ML algorithms that consist of multiple hidden layers [1]. In other words, unlike traditional learning methods, DL refers to supervised or unsupervised techniques using ML techniques to automatically learn the hierarchical representation in deep architectures created to classify intelligent patterns [55,58].

A common reason for the algorithm's prediction being weak in ML techniques is underfitting or overfitting the problem. When the neural network algorithm attempts to fit every data point in the training set, it results in overfitting. Consequently, a model that has been overtrained is highly susceptible to noise or outliers [55]. This is because in the case of overfitting, the noise in the training data is captured, and these noisy data are also learned [51]. Underfitting, on the other hand, means that the artificial neural network algorithm cannot extract a meaningful relationship among the available data in the training dataset [55]. The model fails to fit the training data in the case of underfitting, indicating that it is unable to establish a meaningful relationship between the data and the model [51].

The accuracy of predictions made with AI algorithms and the efficiency of these algorithms can be measured by conducting correlation analysis using real values and predicted values. Correlation analysis is a very adaptable data analysis method due to its broad applicability. Simple correlation analysis can be used when the dependent variable, which is a quantitative variable, is to be treated as a function of or related to the independent variables which can be any factor in question [80]. The use of correlation analysis is applicable in practical prediction scenarios where the aim is to predict a result using previously collected data. When data for two quantitative variables is gathered from a sample group or other entities, the connection between the variables can be visually represented using a scatterplot [80]. To reveal this relationship between the two variables, it is necessary to calculate the quantity called the correlation coefficient, which expresses these relationships numerically and interprets them. The correlation coefficient measures the linear relationship between two variables and is calculated according to Equation 3.22, where r_{xy} represents the correlation coefficient, X_i and Y_i represent the variable values in the X and Y series, $\overline{X}$ and $\overline{Y}$ represent the averages of the variables in the X and Y series, and n represents the number of variables in the X and Y series [80].

$$r_{xy} = \frac{\sum_{i=1}^{n}(X_i - \bar{X})(Y_i - \bar{Y})}{\sqrt{\sum_{i=1}^{n}(X_i - \bar{X})^2(Y_i - \bar{Y})^2}} \tag{3.22}$$

The correlation coefficient's sign shows the relationship's direction, and its magnitude shows the relationship's strength. The correlation coefficient ranges from -1 to +1 [80]. A perfect linear relationship between two variables is indicated by a value of -1 or +1. If the value of r exceeds 0.8, it suggests a strong relationship between the two variables, while a value lower than 0.5 indicates a weak relationship. A value of 0 suggests that there is no relationship between the two variables [80].

Scatter plots allow for the visual examination of the form of the relationship between two variables. These relationships can be well defined by a straight line indicating a rectilinear (negative or positive) relationship [80]. This linear relationship between variables can be expressed through regression analysis. Regression analysis is the process of expressing

the relationship between two variables, one dependent and the other independent, with a functional (mathematical) equation. Regression analysis enables the estimation of the dependent variable assumed from known (independent) variables [80]. Thus, by conducting a regression analysis using actual values, a straight line (regression line) representing the linear relationship between the actual and predicted variables can be drawn, and the efficiency of the algorithm can be evaluated by comparing the predicted values obtained through the AI algorithm with the values on this line.

In regression analysis, if the number of independent variables is one, it is called a "Simple Regression Model", and if it is two or more, it is called a "Multiple Regression Model". If a model is to be built based on the linear relationship between variables, it is called a "Linear Regression Model" [80]. The mathematical expression of the simple linear regression model between the assumed independent variable V and the assumed dependent variable U is given in Equation 3.23. The estimated U value is denoted by $\widehat{U}$ in this equation, while a represents the regression constant, and b_{uv} represents the regression coefficient of y to x [80].

$$\widehat{U} = a + b_{uv} * V \tag{3.23}$$

The coefficient of determination, R^2_{xy}, calculated during regression analysis, is the most effective measure of how well experimental data aligns with the regression line [80]. This value represents the ratio of the variance in the response variable that the predictor variable in the regression model can account for, and it equals the square of the correlation coefficient, r_{xy}. The R^2_{xy} value ranges from 0 to 1. A value of 1 for R^2_{xy} suggests a highly robust relationship between predictor variables and the response variable, demonstrating a perfect fit of the data to a linear curve. The more data points there are, the more reliable the R^2_{xy} value is [80].

In this study, the efficiency of predictions made through AI models was evaluated by considering the correlation coefficients between real data in both the training and test

datasets and the predicted data, as well as the determination coefficients calculated by considering the regression lines created using actual data.

The categorization of ML methods can be done in various ways. The predominant approach for classifying ML models is based on the level of supervision they undergo during the training process [1]. Following this classification method, ML is segmented into three primary categories: supervised, unsupervised, and reinforcement learning, as illustrated in Figure 3.104 [1,10,51].

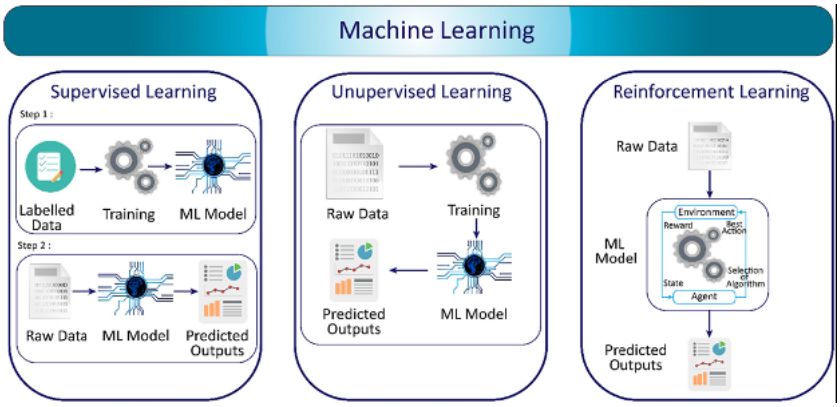

Figure 3.104. Categorization of ML [1].

In supervised learning, the dataset contains predictors and outcomes known as labels [1,51]. To begin with, a supervised ML model is trained using a labeled dataset, as depicted in step 1 of Figure 3.104. Subsequently, the trained ML model can be utilized to make predictions for unseen data [1,51,81]. Classification and regression are two widely used supervised tasks [1,81]. Since the problem addressed in this study is a regression problem, supervised learning methods will be used. Some of the most commonly used supervised learning algorithms include Naive Bayes, GP, decision tree, particle swarm optimization, long short-term memory, radial basis function, logistic regression, linear regression, k-Nearest Neighbors, neural networks, and SVMs [1,10,51].

Unlabeled datasets are utilized in unsupervised learning to identify concealed patterns or inherent structures within the data [1,51]. Tasks commonly tackled using unsupervised

learning encompass clustering, visualization, anomaly detection, and dimensionality reduction [1]. Some of the most commonly used unsupervised learning algorithms include k-means clustering, restricted Boltzmann machines, and self-organizing maps [10,51].

Reinforcement learning involves training an ML model by punishing undesired behaviors and rewarding desired behaviors. The reinforcement learning agent, a learning system, observes the environment and takes actions that result in either reward or punishment [1,51]. The objective here is to determine the optimal strategy, known as the 'policy,' by maximizing rewards over time [1]. Some of the most commonly used reinforcement learning algorithms include Q-learning, temporal difference, and deep adversarial networks [10,51].

ANN, a subfield of supervised ML, and one of the AI techniques are designed to mimic biological neural networks with interconnected neurons to imitate a higher-dimensional space to produce a general solution for problems [46,55,56]. ANN is developed inspired by the human learning process [46,55]. With this method, it is possible to develop a model based on direct prediction by providing suitable training data [21].

FNN, also known as MLP, is a widely used ML algorithm that only has forward information flow without any feedback, as shown in Figure 3.105 [1,21]. The circles in this architecture represent neurons [1].

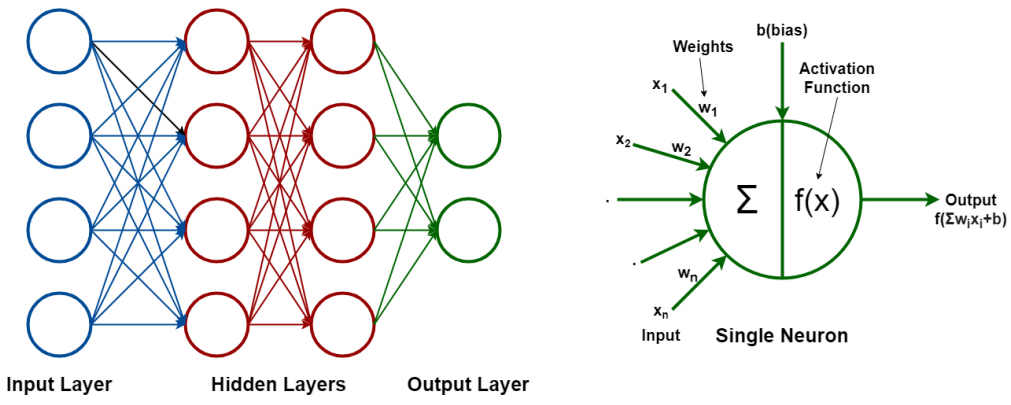

Figure 3.105. Schematic representation of a MLP and a single neuron.

In MLP, the most common method used to perform tasks similar to those carried out by the human brain, using data collected from previous experiences, is feedforward backpropagation (FFBP). Due to its ease of implementation and predictive abilities, FFBP has been the most commonly used method in previous studies for training ANN [27,52,56].

MLP consists of layers composed of interconnected neurons [1,21,27,56,58]. Two nodes adjacent to each layer are called a link and are directly connected [27,55]. In FFBPs, the input layer is fed with input data, and the data is transferred from neurons to other neurons through hidden layers [1,27,55,56]. Finally, the output layer produces a result [1,21,55,56]. All neurons in the following layer are linked to every neuron in the preceding layer through separate connections [21,27,55,56].

The input layer contains a neuron for each input variable [27,46,55,56,58]. The number of neurons in the hidden layer is determined based on the training algorithm [27,46,52,55,58]. Each neuron in the hidden layer receives input from the previous hidden layer, computes the weighted input ($w_i x_i$) by adding the bias term (b), and transfers the result through the nonlinear activation function f(x) as shown in Figure 3.105 [1,21,27,52,55,56,58]. The input I_i of input layer neuron i, the weight value w_{ji} used in calculating the value in hidden layer neuron j from input layer neuron i, and the threshold value K_j of hidden layer neuron j can be selected, and the output value H_j from hidden layer neuron j can be calculated as in Equations 3.24 and 3.25 [27].

$$H_j = f\left(\sum_i w_{ji} I_i + K_j\right) \tag{3.24}$$

$$f(x) = \frac{1}{1 + \exp(-x)} \tag{3.25}$$

where, f generally refers to Sigmoid function.

MLP can have one or more hidden layers [1,21,58]. The number of hidden layers and neurons determines the accuracy of MLP. As the complexity of the network increases, so does the accuracy [56]. MLP with multiple hidden layers are considered DL algorithms [1].

The number of neurons in the output layer is equivalent to the number of outputs [21,27,46,55,58]. Since each data type has a different complexity, the network selected for each output can be different [46,52]. The activation function in the neurons of the hidden and output layers plays an important role in predicting correct values [46,56]. Depending on the application, various nonlinear activation functions such as ReLU (Rectified Linear Unit), Softmax, Sigmoid, and Tanh can be used [1,58].

During the training of an ANN, a dataset is used to train the network. In this training process, the outputs from the output layer are evaluated by comparing them with the actual expected values, and then the error is computed [1,52,58]. To calculate errors, many methods such as binary cross-entropy, mean absolute error (MAE), and MSE are available [1]. The sum of errors for the complete training set, along with any regularization to prevent overfitting, is used to calculate the error function. The objective is to minimize the error function by modifying the neural network weights through a technique known as backpropagation [1,52].

Backpropagation calculates the gradient between the weights and the error [1,27,52]. The fundamental principle of this method is to use the steepest gradient descent approach to achieve approximation [27].

The optimization algorithms such as Adam, Adadelta, NAdam, and Gradient Descent calculate the weights that minimize the error based on the gradient between the error and the weights [1]. To adjust these weights, the same dataset is processed multiple times, resulting in a trained model with minimized error. The weights of trained models are adjusted for each input data for each neuron, and these weights are proportional to the relevance of the input data for the output results [1,52]. A test dataset is used to calibrate

the network, prevent overtraining, and measure the performance of the neural network algorithm [58]. Finally, the model is used to predict the output using new data [1,52].

Looking at the literature, it is seen that MLP is used as an ML model in many studies in the field of 3DCP [46,56]. Therefore, in this study, an MLP model was used as an ML model. FNN is used for predicting new features in the MLP model. FNN is used for predicting new features in the MLP model. The performance of any algorithm generally varies depending on the problem solved [52]. In some studies, an MLP model consisting of three layers, input layer, hidden layer, and output layer, has been used, and these models have achieved high accuracy results [21,27,45,46]. In some studies, different numbers of hidden layers and neurons have been used through trial and error to evaluate the performance of different neural network models [21]. Values ranging from 1 to 100 for the number of neurons in the hidden layer have been used [27]. The most important factors affecting the performance of ANN are generally the number of hidden layers, the number of neurons, the activation function, and the error function [27,45]. In the studies mentioned above, yielding strength prediction, compressive strength prediction, and extrudate formation have been associated with printing parameters. The results have shown that high-accuracy results can be obtained using only one hidden layer [21,27,45,46,56].

Convolutional Neural Network (CNN), a supervised deep learning method, is a unique type of artificial neural network that can be used to process data with a grid-like topology [1]. CNN is also a feedforward neural network [58].

CNN is commonly used in classification problems using image data and computer vision applications. CNN architectures basically include three different types of layers: convolutional layer (Conv layer), pooling layer, and fully connected layer (FC layer) [1]. The Conv layer, which is the main element of the CNN architecture, consists of a series of learning filters. In the hidden layers of CNN, convolution, and linking functions are generally used instead of normal activation functions, as shown in Figure 3.106 [58]. In a typical CNN, after the Conv layer, another Conv layer or pooling layer is used, and finally, an FC layer is used, as shown in Figure 3.107 [1].

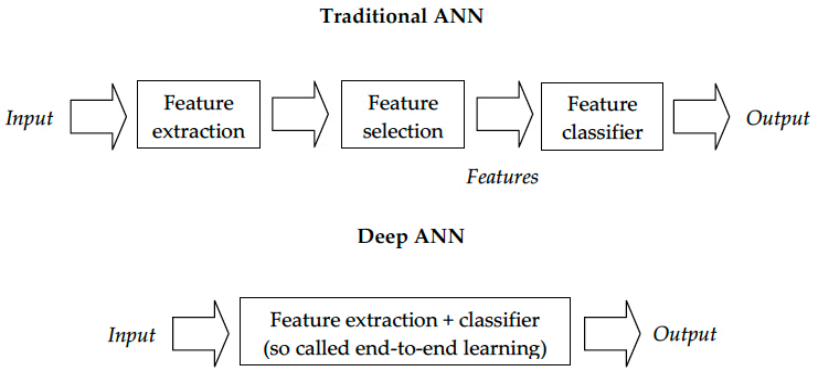

Figure 3.106. Workflow for conventional learning and deep learning [58].

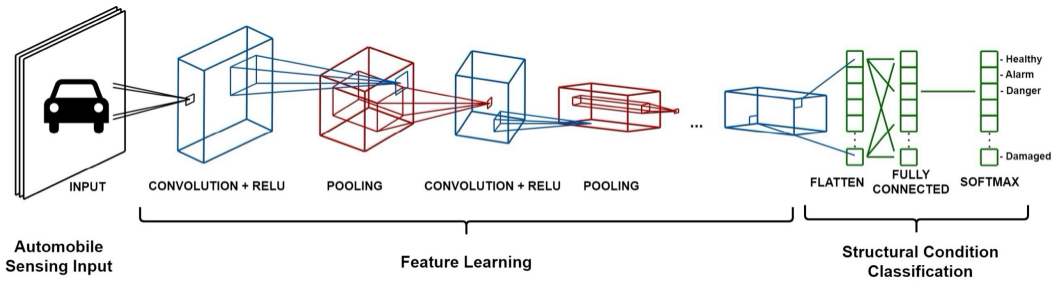

Figure 3.107. A typical CNN architecture.

In comparison to ML algorithms, DL algorithms are more useful for problems involving high-dimensional data such as images, sound, and videos, as they require more complex computations [1]. A review of the literature reveals that in many studies in the 3DCP field, CNN is used as a DL model [1,43,53,81]. Some of these studies focus on fracture analysis and segmentation of polyvinyl alcohol fibers in strain-hardening cementitious composites. In these studies, image data, which is a two-dimensional data type, is used [53,81]. The results of these studies indicate that after dimensionality reduction, the CNN can learn more efficiently in this lower-dimensional space. Thus, using the same CNN architecture, higher accuracy can be achieved with the same training data [53]. However, in none of the previous studies on regression problems in the 3DCP field, CNN models have been used. Therefore, in this study, a novel approach was developed using a one-dimensional CNN model as a DL model. Since automatic design is a regression problem with only one-dimensional space, the dimensionality of the CNN algorithm has been reduced to 1D to provide more efficient learning in this space.

3.3.2. Creating MLP Models

In this study, MLP models with three layers, namely the input layer, hidden layer, and output layer, were used, taking into account the literature review [21,27,45,46]. Indeed, MLP architectures with multiple hidden layers are considered within the scope of DL models [1]. Considering the literature reviews, the FFBP method was used to train MLP models [27,52,56].

Specifically, data sparsity and bias are highly important for the validity and performance of ML models [18]. It is possible to explain the bias term more elaborately using the linear regression model in Equation 3.26 [82].

$$\hat{y} = \boldsymbol{w}^t x + b \tag{3.26}$$

where, ŷ represents the output value predicted by our model, the expression w represents the weight vector, the expression x represents the input matrix, and the expression b represents the intercept term. According to this equation, there is a linear relationship between the parameters and the predictions, but an affine function is used to obtain predictions from features [82]. This extension to affine functions means that the graph of the model's predictions still appears as a straight line but does not necessarily pass through the origin. The intercept term b is generally referred to as the bias parameter of the affine transformation. This terminology derives from the perspective that the output of the transformation is biased when there is no input [82]. For this reason, the bias term has a significant impact on the performance of ML algorithms [18]. Therefore, in this study, two MLP and CNN models were used for each wall topology, one biased and the other unbiased, for displacement and shear strength data. In MLP, bias values are added to the input layer and the hidden layer, while in CNN, the bias value is added to the Conv layer and the FC layer.

Taking into account the literature reviews, all ML algorithms were implemented using the high-level programming language Python with the TensorFlow and Keras libraries [24,30,32,33,35,53,63,81]. All model architectures, including the selection and

arrangement of layers, activation functions, optimizers, and training procedures, were designed and implemented manually by the author. No pre-built models or automated model-generation tools were used. This approach ensured full control over the model behavior and structure, reflecting a hands-on understanding of deep learning principles rather than reliance on out-of-the-box solutions.

Considering the literature reviews, the data partitioning process was automatically performed, and the data were divided into training and validation sets according to a 4:5 (0.2) standard split ratio, with the number of data points in the test dataset being the same as the number of data points in the validation dataset [21,40,43,46,51,52,81]. The validation data not used for training the network are used to check if the network calculation accuracy for these data is similar to the accuracy of the training data [81]. The test dataset allows for the unbiased evaluation of the final model designed according to the training dataset [82].

When noisy data is considered and included in the learning process, overfitting occurs. Normalizing input parameters before using them for ML models is important as it allows for faster learning of ML and ensures that inputs are in a unique range [45,51,55]. Also, when using multiple input types with varying ranges or scales, all data should be normalized to prevent network error from increasing due to some weights associated with certain inputs being updated much faster than others [1,51,56]. The normalization process is generally performed according to Equation 3.27, such that input values are in the [0, 1] range [51]. Equation 3.27 was used for normalization in this study as well.

$$\frac{r_i - r_{min}}{r_{max} - r_{min}} \tag{3.27}$$

where, r_i denotes a specific input data, r_{min} denotes the smallest input data, and r_{max} denotes the largest input data.

The activation function plays an important role in ensuring nonlinearity in ML networks. In ANN, Sigmoid or Tanh activation functions are commonly used. However, such nonlinearity often leads to high computation costs by limiting the output with highly complex functions, as well as causing problems such as vanishing gradients or exploding gradients [53]. Therefore, these types of activation functions are not suitable for CNN, where high computational capacity is required [53]. To overcome this problem, the ReLU activation function, which does not limit the output, is used after each Conv layer [8,53,83]. The ReLU activation function accelerates the convergence rate of neural network calculations, produces better results compared to traditional activation functions such as Sigmoid, and prevents vanishing or exploding gradient problems [81,83]. Additionally, training rectifier networks is easier compared to traditional Sigmoid-like activation networks [83]. For all these reasons, and because the same activation function will be used in MLP and CNN within the scope of this study, the ReLU activation function has been selected. Commonly used activation functions are shown in Figure 3.108 [84].

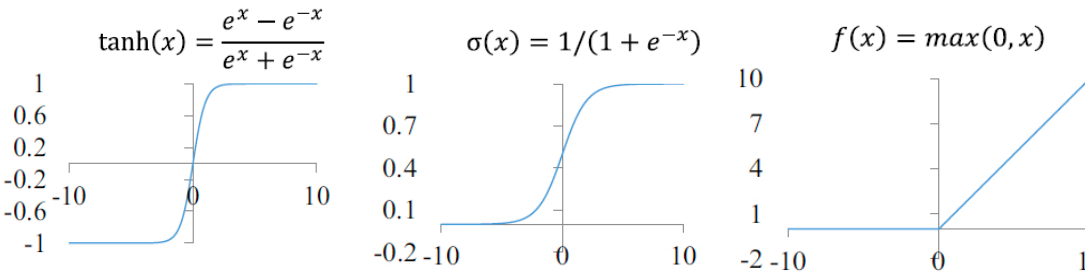

(a) (b) (c)

Figure 3.108. Activation functions (a) Tanh activation function, (b) Sigmoid activation function, (c) ReLU activation function [84].

Regularizers should be used to prevent the overfitting of networks [18,81]. Thus, a model more suitable for general use can be created [83].

One of the goals of DL algorithms is to analyze the factors that explain the variations in the data. A dense representation is quite complex because almost every change in the input changes most of the inputs in the representation vector. Conversely, a sparse and resilient representation can maintain non-zero feature sets with minor input alterations

[85]. Therefore, data sparsity is extremely important for the validity and performance of machine learning models [18]. The representation of information in a high-dimensional space makes sparse representations more likely to be linearly separable or separable with less nonlinear machinery. This can also reflect the original data format. For example, in applications related to text, the original raw data is already very sparse [85]. Dense-distributed representations are potentially more efficient than completely local ones. The efficiency of sparse representations is still higher because the power of the exponent is the number of non-zero features [85]. As can be understood from above, sparse representations, especially for ML algorithms with many depths, are quite suitable [18,81,85].

Another problem can arise due to the unbounded behavior of activations. Regularizers can also be used to prevent this problem [85]. The L1 regularizer provides both sparsity and prevents potential numerical problems that may arise from the unbounded behavior of activation. Therefore, in some studies in the literature, the L1 regularizer has been used to penalize activation values [85]. For all these reasons, in this study, the L1 regularizer expressed in Equation 3.28 has been used as a regularizer [82]. Regularizers have been added to the input layer and hidden layer in MLP, and the Conv layer and FC layer in CNN.

$$L_1 = (wx + b - y)^2 + \alpha|w| \tag{3.28}$$

It is possible to derive a method that considers the rectifier nonlinearity, especially with weight initializers. Thus, the training of very deep rectified models from the beginning is feasible and allows for the exploration of network architectures that are deeper or wider. A poor initialization can hinder the learning of a system with high nonlinearity [83].

Unlike Sigmoid-like traditional activation functions, the ReLU activation function is not symmetric. Therefore, the average response of ReLU is not always smaller than zero. Additionally, assuming that the inputs/weights follow symmetric distributions, the

responses' distributions may still be asymmetric because of the nature of the ReLU function [83].

The weights used in CNN today are predominantly randomly initialized from Gaussian distributions. With constant standard deviations, convergence of very deep models is very difficult. To overcome this problem, some researchers have pre-trained a model with eight Conv layers to initialize more complex models. Nevertheless, more training time is needed for this approach, and it may result in achieving a poorer local optimum [83]. Glorot and Bengio have proposed the utilization of a properly scaled uniform distribution for initialization. This initialization method is called "Xavier" initialization. The basic idea of this method is based on the assumption that activations are linear [83]. However, this assumption is not valid for ReLU. While the convergence of extremely deep models is not possible with the Xavier initializer, the He initializer allows this. The fundamental difference between the He initializer and the Xavier initializer is the consideration of rectifier nonlinearities in the He initializer [1,83]. Only the linear case has been considered in the derivative in the Xavier initializer. In this method, the result can be obtained through Equation 3.29 which can be applied as a zero-mean Gaussian distribution with a standard deviation of $\sqrt{1/n_l}$ [83].

$$n_l Var[w_l] = 1 \tag{3.29}$$

In this equation, the term n_l denotes the number of connections in the lth layer response, while the term w_l represents a matrix of size d*n in the lth layer, where d is the filters' number in layer l and each column of w_l represents the weight of the filters in layer l. The He initializer, on the other hand, yields a result obtained using Equation 3.30, which is a zero-mean Gaussian distribution with a standard deviation of $\sqrt{2/n_l}$, where n_l is the connections' number for layer l [83].

$$\frac{1}{2} n_l Var[w_l] = 1, \forall 1 \tag{3.30}$$

When the depth of the layer is L, the standard deviation value in the Xavier initializer becomes $1/\sqrt{2}^{L}$ times the standard deviation value in the He initializer. Therefore, the He initializer begins to reduce the error earlier compared to the Xavier initializer. Additionally, the Xavier method disrupts the learning process by causing the vanishing gradient problem in the training of overly deep models [83]. Therefore, it would be appropriate to use the He initializer, which takes into account the nonlinearity with the ReLU activation function [1,83]. For this reason, in this study, the He initializer is used as the weight initializer.

Rectified linear units are typically used in an affine transformation, as shown in Equation 3.31 [82].

$$\boldsymbol{h} = g(\boldsymbol{w}^T\boldsymbol{x} + \boldsymbol{b}) \tag{3.31}$$

where, **x** denotes the input matrix, **b** denotes the bias vector, g denotes the ReLU activation function, **w** denotes the weights of the linear transformation, and **h** denotes the feature vector in the hidden layer. As mentioned in the literature, when initializing the parameters of an affine transformation, setting all elements of the bias vector **b** to a small, positive value such as 0.1 can be a good practice. The use of this technique often results in the rectified linear units being active for the majority of inputs in the training set at the beginning, which enables the derivatives to make progress [82]. Therefore, in this study, bias values were initialized using a small, positive constant.

Most DL algorithms involve some form of optimization. Optimization refers to the task of minimizing or maximizing some f(x) functions by changing x. Most optimization problems are generally expressed in terms of minimizing f(x) [82]. This method is an incremental and iterative update procedure necessary for the correct training of the network [81].

Adam is a type of adaptive learning rate optimization algorithm, and this algorithm is shown in Figure 3.109 [82,86]. The name "Adam" is derived from the expression "adaptive moments". Adam is generally considered robust in hyperparameter selection. However, sometimes it is necessary to change the learning rate from its default value [82]. As shown in Figure 3.110, the Adam optimizer is faster and converges much more quickly compared to other optimizers [86]. Additionally, this method can also overcome problems such as vanishing learning rates, vanishing gradients, and high variance [82]. The Adam optimization algorithm has also been used in studies in the literature [53,81,87].

Data: $\eta_t := \frac{\eta}{\sqrt{t}}$ as step size, $\beta_1, \beta_2 \in (0,1)$ as decay rates for the moment estimates, $\beta_{1,t} := \beta_1 \lambda^{t-1}$ with $\lambda \in (0,1)$, $\epsilon > 0$, $e(w(t))$ as a convex differentiable error function and $w(0)$ as the initial weight vector.

Set $m_0 = 0$ as initial 1st moment vector

Set $v_0 = 0$ as initial 2nd moment vector

Set $t = 0$ as initial time stamp

while $w(t)$ *not converged* **do**

$t = t + 1$

$g_t = \nabla_w e(w(t-1))$

$m_t = \beta_{1,t} m_{t-1} + (1 - \beta_{1,t}) g_t$

$v_t = \beta_2 v_{t-1} + (1 - \beta_2) g_t^2$

$\hat{m}_t = \frac{m_t}{(1-\beta_1^t)}$

$\hat{v}_t = \frac{v_t}{(1-\beta_2^t)}$

$w(t) = w(t-1) - \eta_t \frac{\hat{m}_t}{(\sqrt{\hat{v}_t} + \epsilon)}$

end

return $w(t)$

Figure 3.109. Adam optimizer algorithm [86].

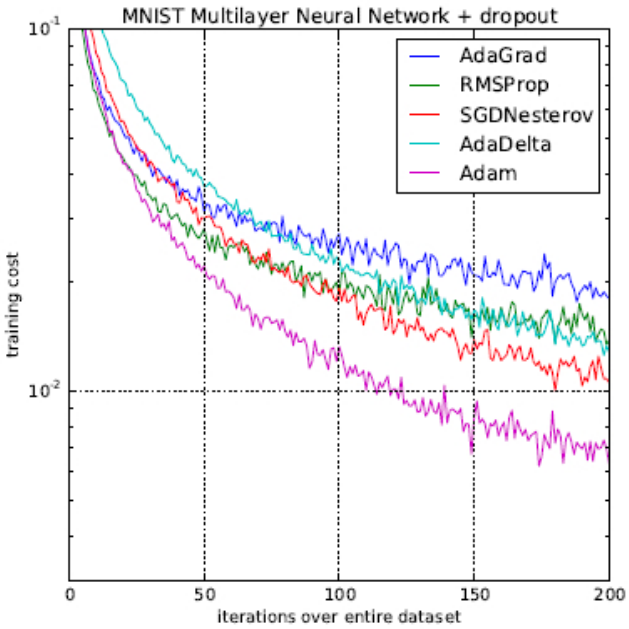

Figure 3.110. Comparison of different optimizers for the process of training multilayer neural networks with MNIST images [86].

The most commonly used error functions are MSE, MAE, and mean bias error. In the literature, it can be seen that in studies conducted in the field of 3DCP and using ANN, the mean absolute percentage error (MAPE) function expressed in Equation 3.32 is used as the error function, and quite successful results are obtained [43,46,56]. Therefore, in this study, the MAPE error function is also used.

$$MAPE = \frac{MAE}{max\{s(i)\} - min\{s(i)\}} * 100 \tag{3.32}$$

where, max{s(i)} represents the maximum value in the dataset, min{s(i)} represents the minimum value in the dataset.

Considering the literature review, the batch size value was chosen as 64 [53,81].

"Epoch", in the incremental-iterative time-stepping procedure applied during the training and validation of a neural network, denotes a specific time instant. When the entire

training dataset and validation dataset have been passed through the network once, it is assumed that an individual epoch has been completed [81]. In this study, the number of epochs was selected as 10,000 to achieve a high level of accuracy and significant convergence.

ML models generally demonstrate excellent performance in prediction problems, including regression tasks [40,56]. However, some fundamental adjustments of hyperparameters, such as the number of neurons in the hidden layer, regularization, bias, and learning rate, still need to be made [40,53,56]. Considering the literature reviews, the ranges of hyperparameter values for the MLP model were selected as shown in Table 3.5, and the optimal hyperparameter values were found through trial and error using the Keras library [1,56–58]. In this table, the term Reg-1 denotes the regularizer added to the input layer, Reg-2 denotes the regularizer added to the hidden layer, Bias-1 denotes the bias added to the input layer, and Bias-2 denotes the bias added to the hidden layer.

Table 3.5. Parameters used in MLP models and the value ranges of these parameters.

Parameter	Values
Reg-1	0 – 0.00001 – 0.00005 – 0.0001 – 0.0005 – 0.001 – 0.015
Reg-2	0 – 0.00001 – 0.00005 – 0.0001 – 0.0005 – 0.001 – 0.015
Bias-1	0 – 0.025 – 0.05 – 0.1 – 0.15 – 0.2 – 0.25
Bias-2	0 – 0.025 – 0.05 – 0.1 – 0.15 – 0.2 – 0.25
Number of neurons in the hidden layer	Increasing by 32 increments between 16 and 4096
Learning rate	0.0001 – 0.0005 – 0.001 – 0.005 – 0.01 – 0.02 – 0.05

Optimum parameter values of the MLP models used are given in Table 3.6.

Table 3.6. Optimum parameter values of MLP models.

	Parameter	Arch Wall		Cellular Wall		Elliptic Wall		Hollow Wall		Lattice Wall		Solid Wall		Triangular Wall - 1		Triangular Wall - 2		Truss Wall	
		MLP with bias	MLP without bias	MLP with bias	MLP without bias	MLP with bias	MLP without bias	MLP with bias	MLP without bias	MLP with bias	MLP without bias	MLP with bias	MLP without bias	MLP with bias	MLP without bias	MLP with bias	MLP without bias	MLP with bias	MLP without bias
Displacement capacity	Reg-1	0.001	0.0005	0.001	0.001	0.00000	0.00005	0.00001	0.00005	0.0001	0.001	0.0005	0.00000	0.001	0.0001	0.0015	0.0001	0.001	0.00001
	Reg-2	0.00001	0.001	0.0001	0.00005	0.0001	0.00001	0.001	0.0005	0.00005	0.00005	0.0001	0.0015	0.0001	0.00005	0.00000	0.0005	0.001	0.00000
	Bias-1	0.1	-	0.15	-	0.25	-	0.2	-	0.2	-	0.025	-	0.2	-	0.5	-	0.2	-
	Bias-2	0.1	-	0.02	-	0.000	-	0.1	-	0.1	-	0.1	-	0.1	-	0.025	-	0.025	-
	Number of neurons in the hidden layer	592	16	48	208	2320	48	656	400	2320	48	720	2544	752	3376	752	624	496	208
	Learning rate	0.01	0.02	0.005	0.005	0.005	0.01	0.01	0.001	0.01	0.01	0.02	0.01	0.005	0.005	0.005	0.001	0.01	0.01
Shear Capacity	Reg-1	0.00005	0.00005	0.0015	0.00000	0.00001	0.00005	0.00005	0.00000	0.001	0.0001	0.00000	0.00000	0.00000	0.00001	0.0001	0.0015	0.0015	0.00000
	Reg-2	0.00000	0.00000	0.00000	0.00000	0.00000	0.00000	0.00000	0.00000	0.00000	0.00000	0.00000	0.00000	0.00000	0.00000	0.00000	0.00000	0.00001	0.00000
	Bias-1	0.2	-	0.025	-	0.25	-	0.000	-	0.5	-	0.25	-	0.1	-	0.5	-	0.15	-
	Bias-2	0.000	-	0.5	-	0.02	-	0.5	-	0.1	-	0.5	-	0.1	-	0.2	-	0.000	-
	Number of neurons in the hidden layer	3568	3056	3120	1712	3824	2896	3824	3952	3344	4080	3024	3216	2960	3792	3440	2864	2928	3984
	Learning rate	0.02	0.05	0.05	0.05	0.02	0.05	0.05	0.02	0.05	0.05	0.05	0.05	0.05	0.05	0.05	0.05	0.02	0.05

As can be seen from Table 3.6, different optimum parameter values are used for different models, and there is no exact ratio or relationship between these values. This situation arises from the fact that the optimum AI models generally vary depending on the dataset. The architectures of the MLP models created considering the parameters in Table 3.6 are shown in Figures 3.111-3.128.

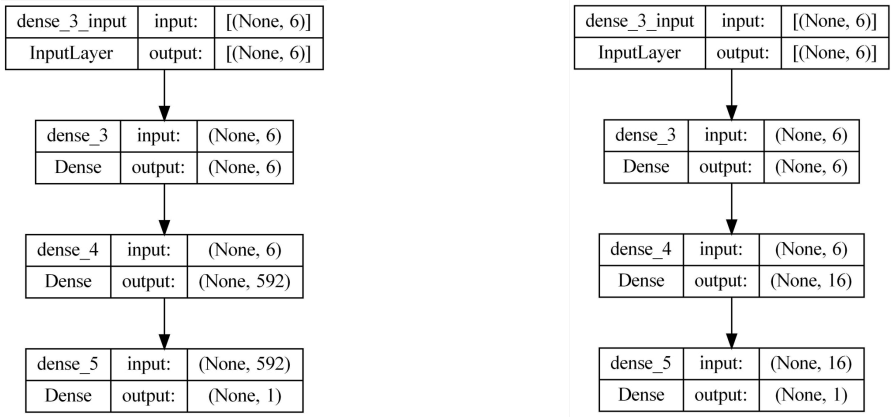

(a) (b)

Figure 3.111. The architectures of MLP models created for the displacement capacities of walls with an arch topology are as follows (a) model created using bias value, (b) model created without using bias value.

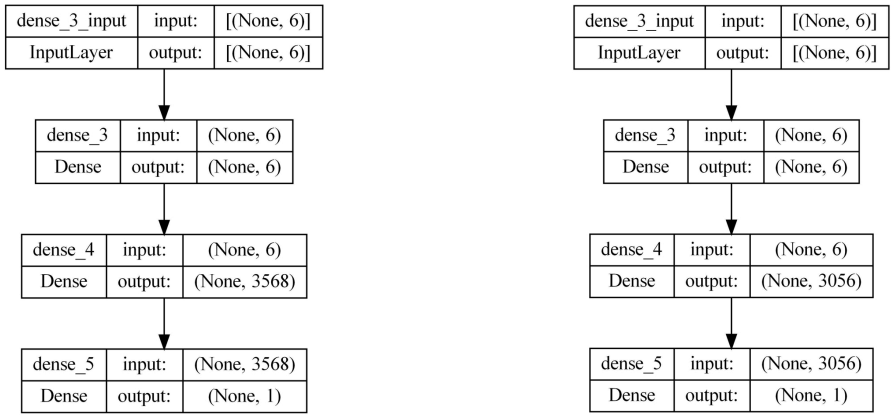

(a) (b)

Figure 3.112. The architectures of MLP models created for the shear capacities of walls with an arch topology are as follows (a) model created using bias value, (b) model created without using bias value.

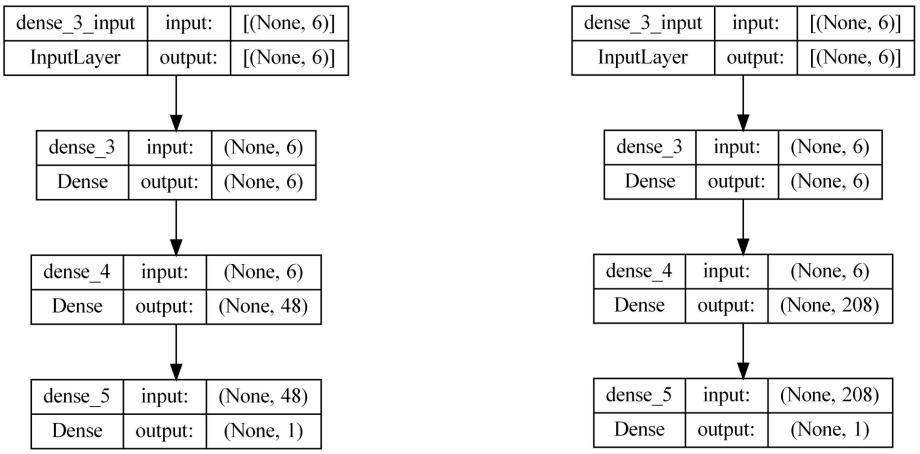

(a) (b)

Figure 3.113. The architectures of MLP models created for the displacement capacities of walls with a cellular topology are as follows (a) model created using bias value, (b) model created without using bias value.

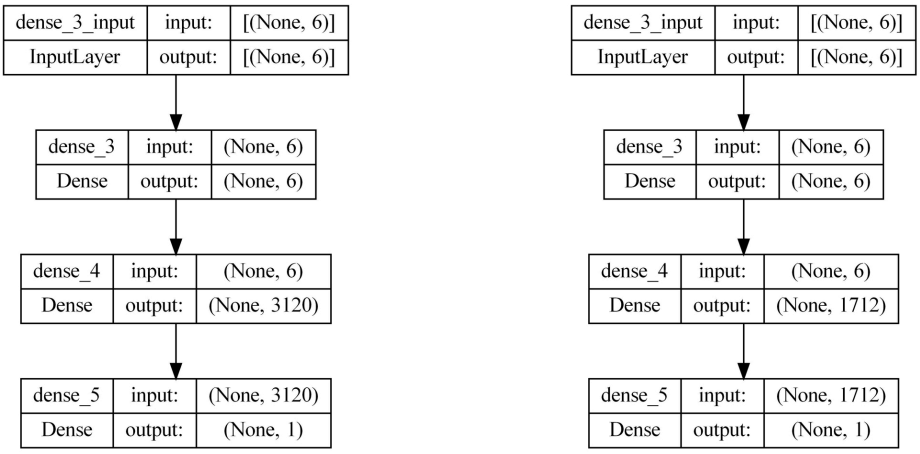

(a) (b)

Figure 3.114. The architectures of MLP models created for the shear capacities of walls with a cellular topology are as follows (a) model created using bias value, (b) model created without using bias value.

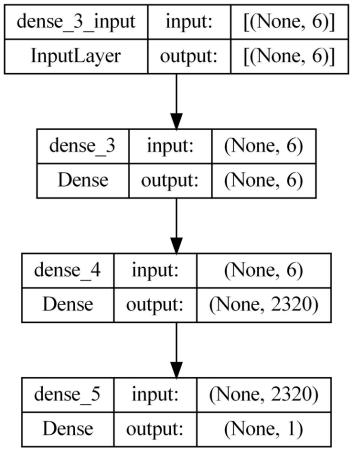

(a)

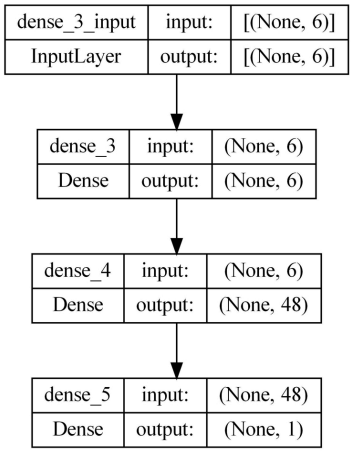

(b)

Figure 3.115. The architectures of MLP models created for the displacement capacities of walls with an elliptic topology are as follows (a) model created using bias value, (b) model created without using bias value.

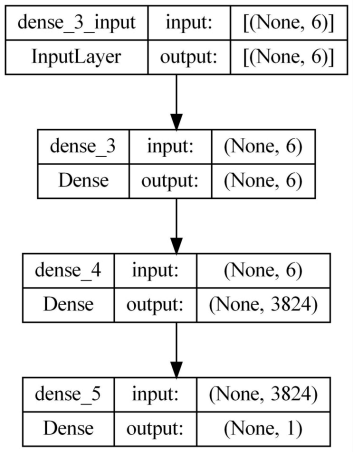

(a)

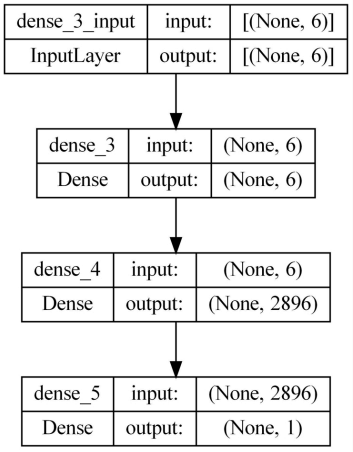

(b)

Figure 3.116. The architectures of MLP models created for the shear capacities of walls with an elliptic topology are as follows (a) model created using bias value, (b) model created without using bias value.

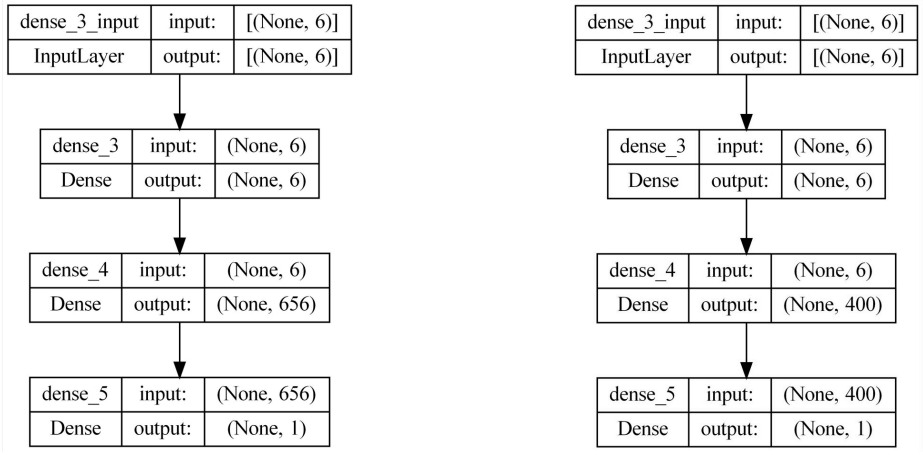

(a) (b)

Figure 3.117. The architectures of MLP models created for the displacement capacities of walls with a hollow topology are as follows (a) model created using bias value, (b) model created without using bias value.

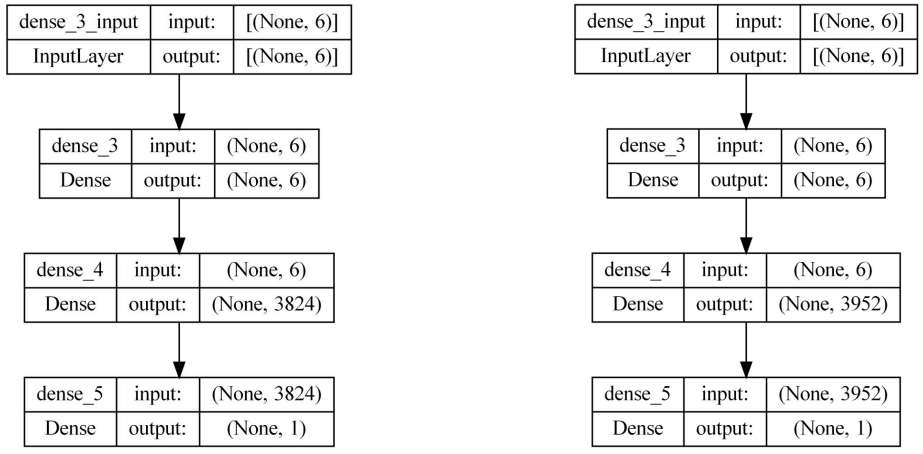

(a) (b)

Figure 3.118. The architectures of MLP models created for the shear capacities of walls with a hollow topology are as follows (a) model created using bias value, (b) model created without using bias value.

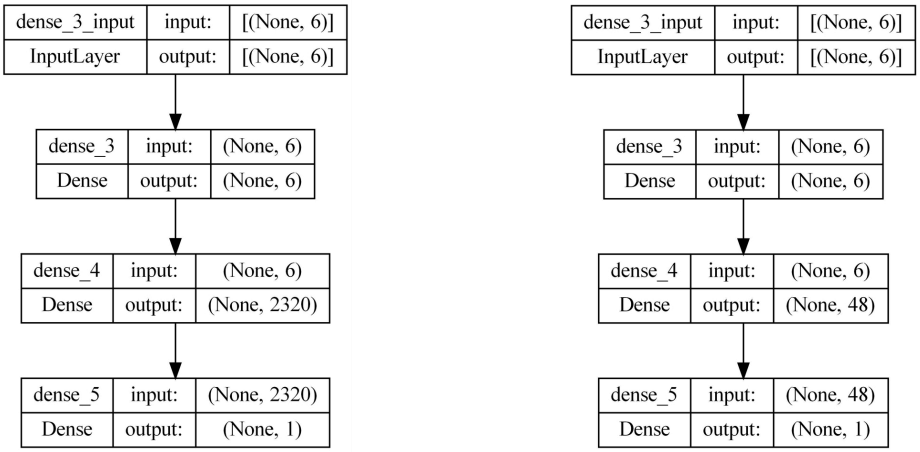

(a) (b)

Figure 3.119. The architectures of MLP models created for the displacement capacities of walls with a lattice topology are as follows (a) model created using bias value, (b) model created without using bias value.

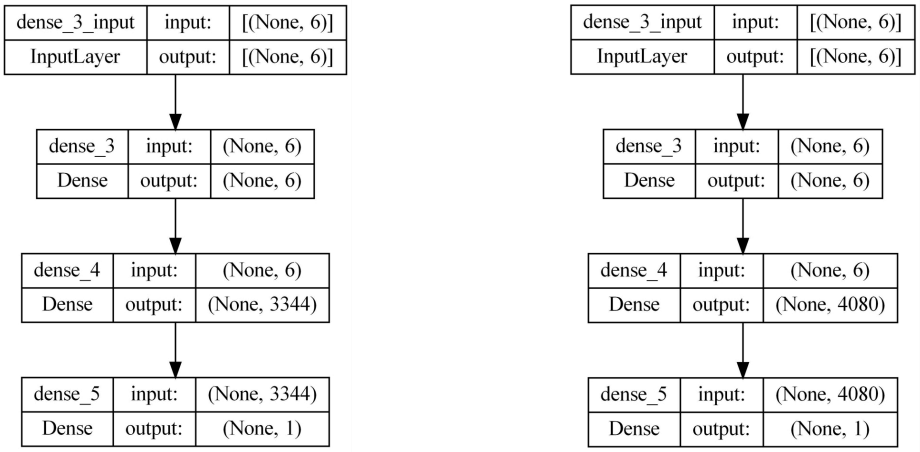

(a) (b)

Figure 3.120. The architectures of MLP models created for the shear capacities of walls with a lattice topology are as follows (a) model created using bias value, (b) model created without using bias value.

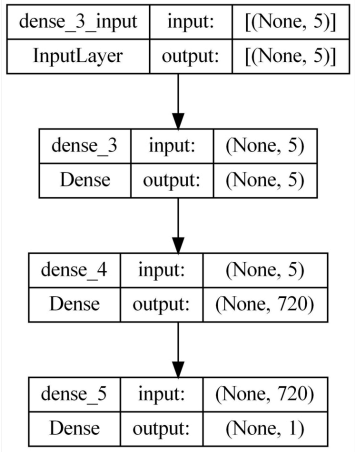

(a)

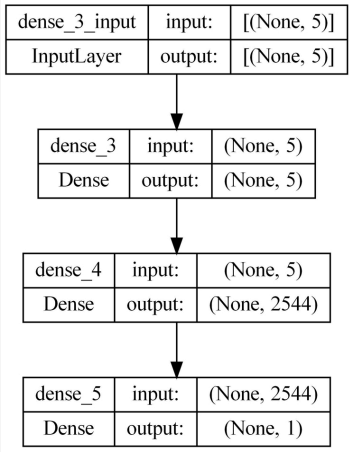

(b)

Figure 3.121. The architectures of MLP models created for the displacement capacities of walls with a solid topology are as follows (a) model created using bias value, (b) model created without using bias value.

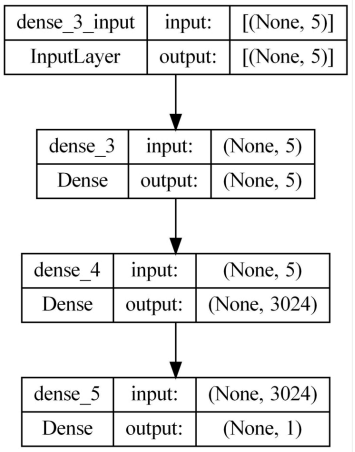

(a)

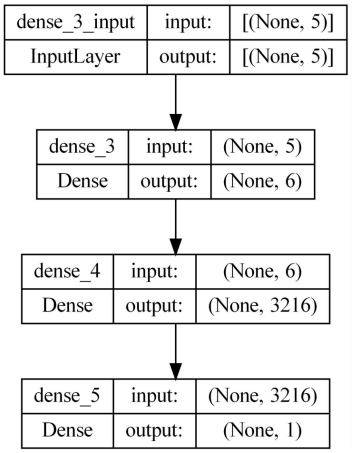

(b)

Figure 3.122. The architectures of MLP models created for the shear capacities of walls with a solid topology are as follows (a) model created using bias value, (b) model created without using bias value.

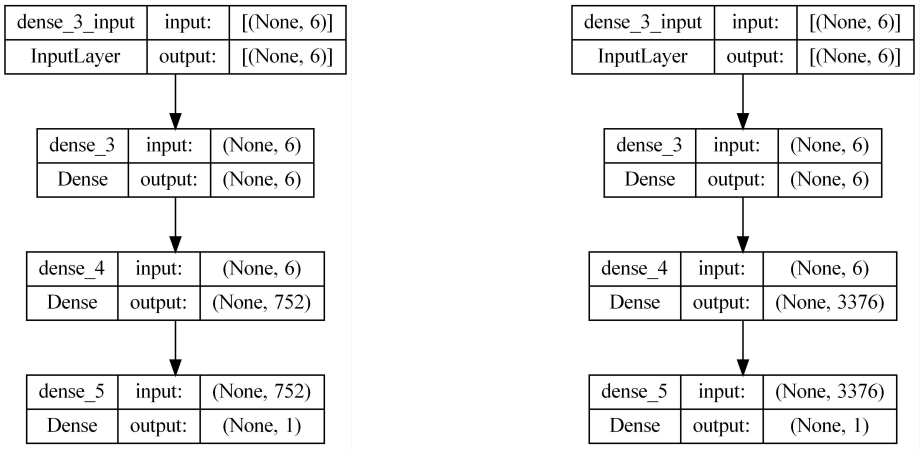

(a) (b)

Figure 3.123. The architectures of MLP models created for the displacement capacities of walls with a triangular-1 topology are as follows (a) model created using bias value, (b) model created without using bias value.

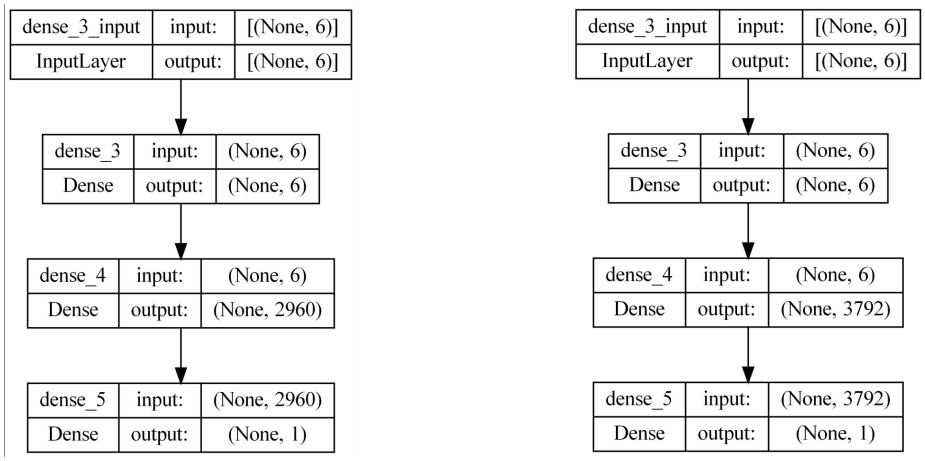

(a) (b)

Figure 3.124. The architectures of MLP models created for the shear capacities of walls with a triangular-1 topology are as follows (a) model created using bias value, (b) model created without using bias value.

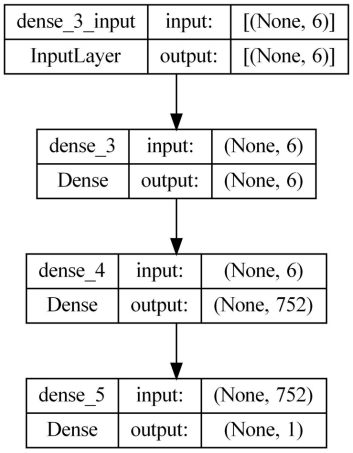

(a)

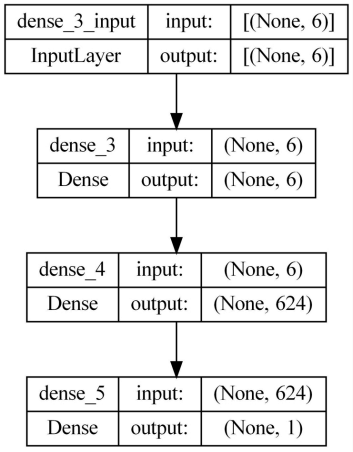

(b)

Figure 3.125. The architectures of MLP models created for the displacement capacities of walls with a triangular-2 topology are as follows (a) model created using bias value, (b) model created without using bias value.

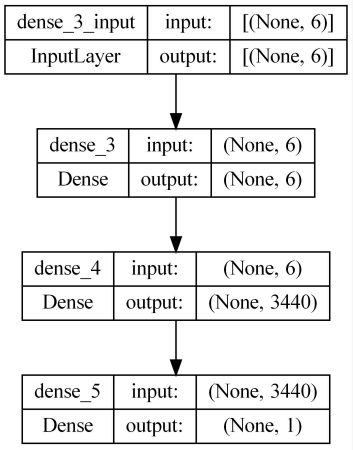

(a)

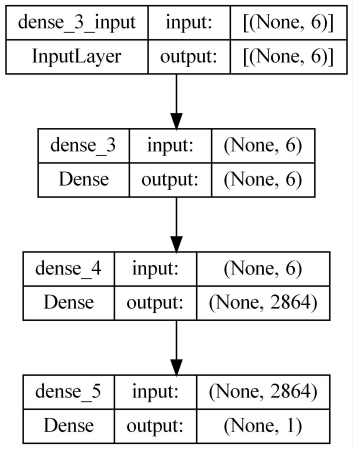

(b)

Figure 3.126. The architectures of MLP models created for the shear capacities of walls with a triangular-2 topology are as follows (a) model created using bias value, (b) model created without using bias value.

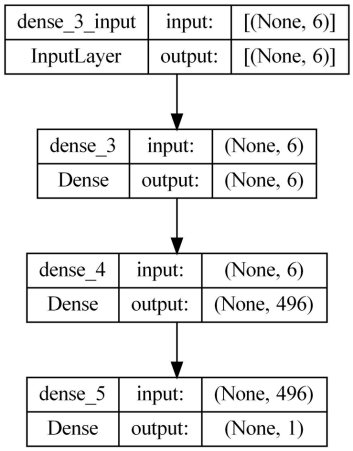

(a)

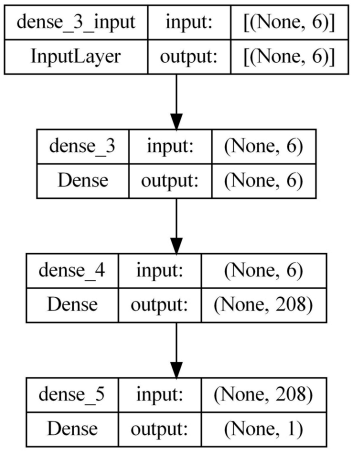

(b)

Figure 3.127. The architectures of MLP models created for the displacement capacities of walls with a truss topology are as follows (a) model created using bias value, (b) model created without using bias value.

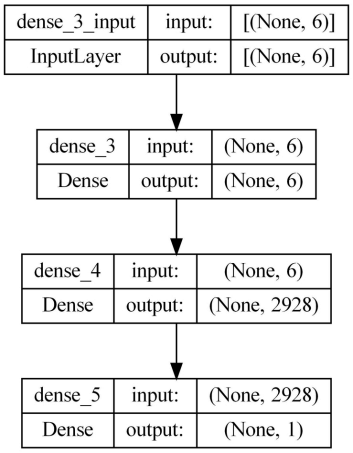

(a)

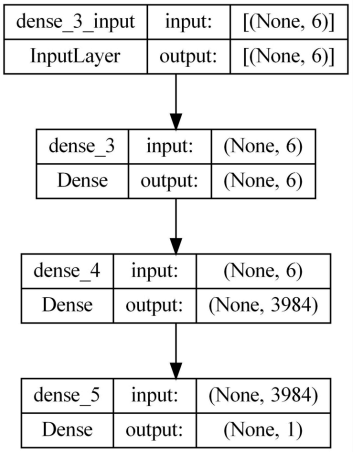

(b)

Figure 3.128. The architectures of MLP models created for the shear capacities of walls with a truss topology are as follows (a) model created using bias value, (b) model created without using bias value.

The learning curves of the MLP models created for the AI-based design tool are shown in Figures 3.129-3.146. As can be seen from these figures, the learning values obtained for the training and validation datasets are very close to each other, and the slopes of both learning curves almost do not change after 10000 epochs. This situation indicates that the

error convergence process has been largely completed, there is no underfitting or overfitting problem in the created models, and the created models are good fitted. The term "a good fit" refers to a training and validation loss corresponding to a stability point where there is a minimum difference between two final loss values.

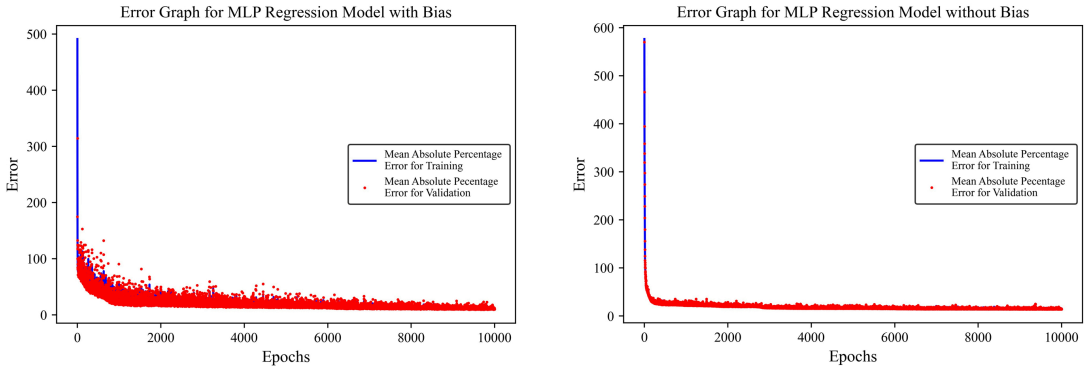

(a) (b)

Figure 3.129. The learning curves of the MLP models created for the displacement capacities of walls with an arch topology are as follows (a) plot for the model created using bias value, (b) plot for the model created without using bias value.

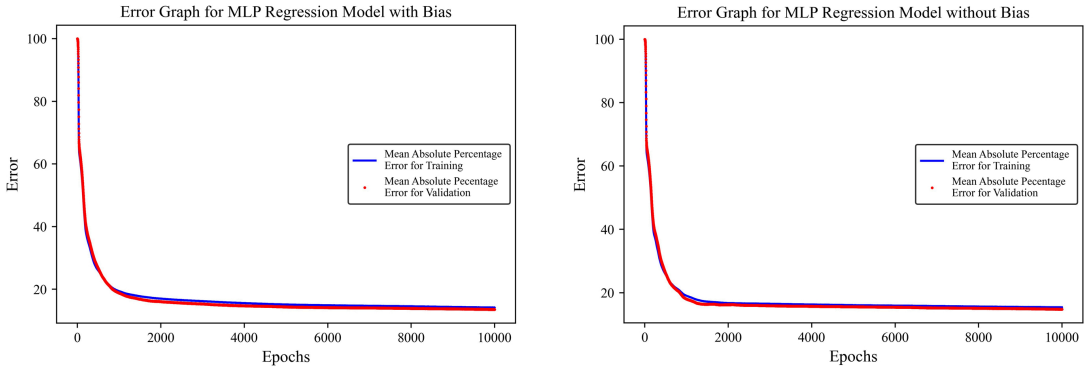

(a) (b)

Figure 3.130. The learning curves of the MLP models created for the shear capacities of walls with an arch topology are as follows (a) plot for the model created using bias value, (b) plot for the model created without using bias value.

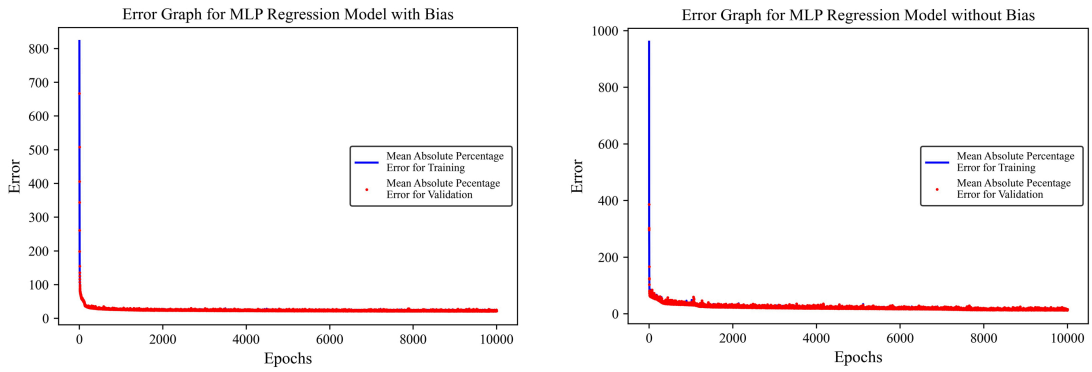

(a) (b)

Figure 3.131. The learning curves of the MLP models created for the displacement capacities of walls with a cellular topology are as follows (a) plot for the model created using bias value, (b) plot for the model created without using bias value.

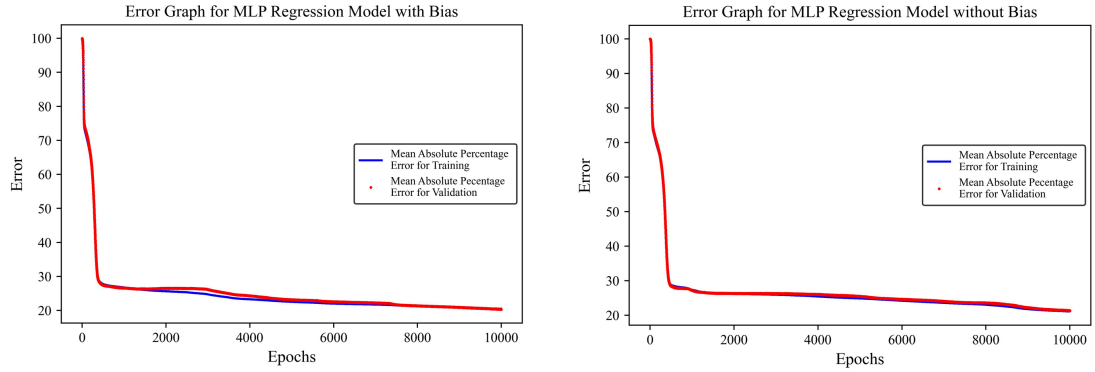

(a) (b)

Figure 3.132. The learning curves of the MLP models created for the shear capacities of walls with a cellular topology are as follows (a) plot for the model created using bias value, (b) plot for the model created without using bias value.

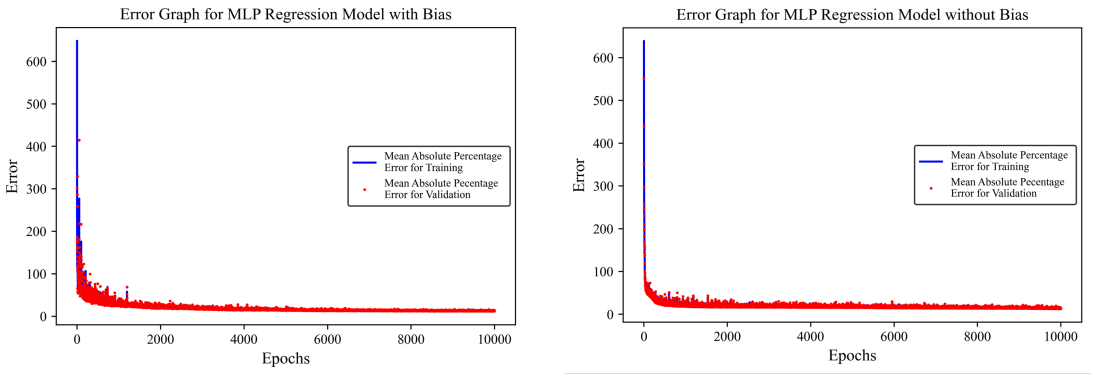

(a) (b)

Figure 3.133. The learning curves of the MLP models created for the displacement capacities of walls with an elliptic topology are as follows (a) plot for the model created using bias value, (b) plot for the model created without using bias value.

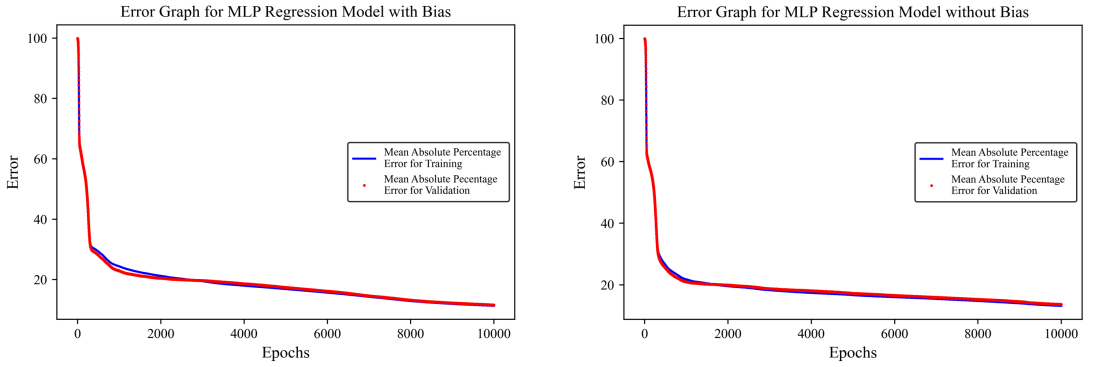

(a) (b)

Figure 3.134. The learning curves of the MLP models created for the shear capacities of walls with an elliptic topology are as follows (a) plot for the model created using bias value, (b) plot for the model created without using bias value.

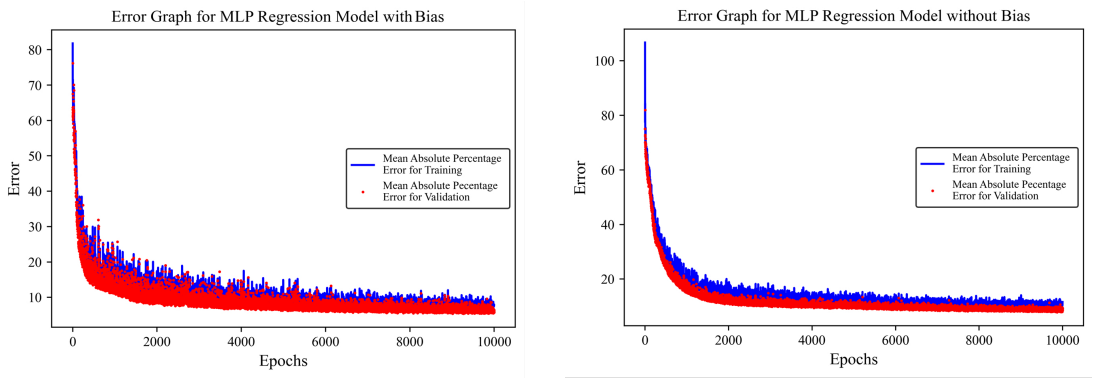

(a) (b)

Figure 3.135. The learning curves of the MLP models created for the displacement capacities of walls with a hollow topology are as follows (a) plot for the model created using bias value, (b) plot for the model created without using bias value.

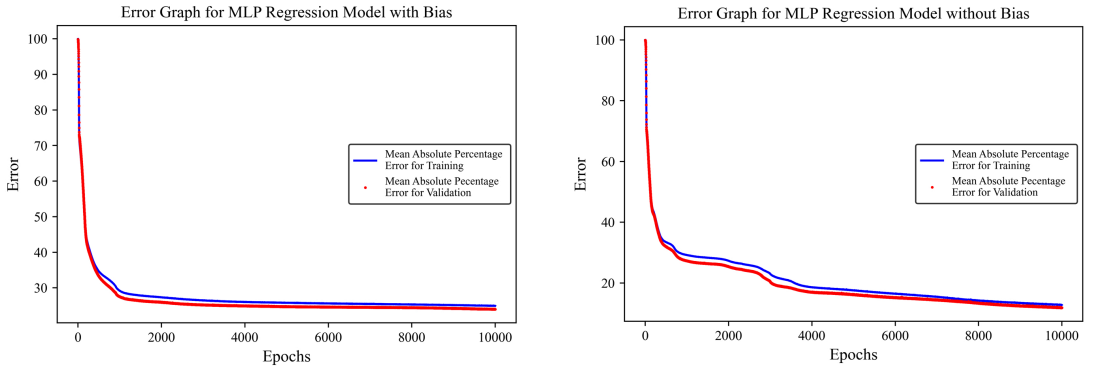

(a) (b)

Figure 3.136. The learning curves of the MLP models created for the shear capacities of walls with a hollow topology are as follows (a) plot for the model created using bias value, (b) plot for the model created without using bias value.

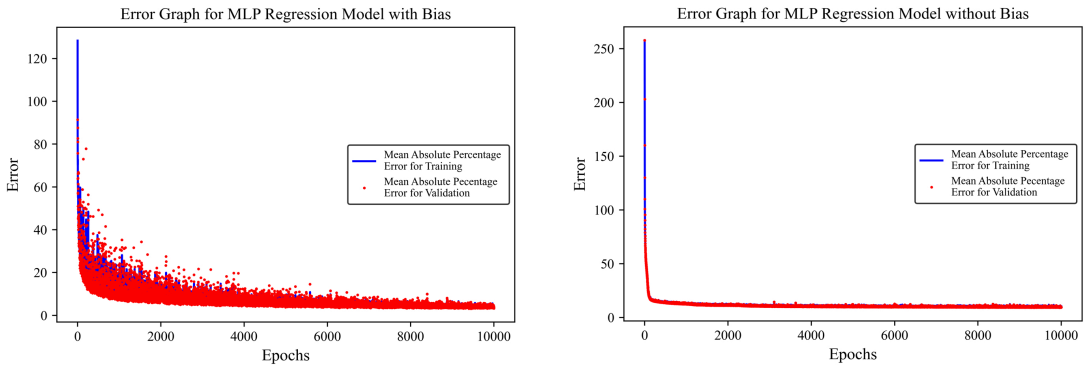

(a) (b)

Figure 3.137. The learning curves of the MLP models created for the displacement capacities of walls with a lattice topology are as follows (a) plot for the model created using bias value, (b) plot for the model created without using bias value.

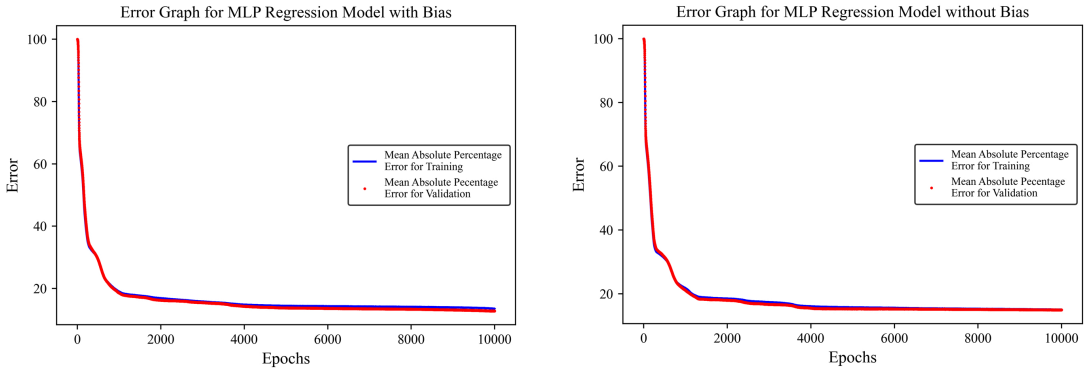

(a) (b)

Figure 3.138. The learning curves of the MLP models created for the shear capacities of walls with a lattice topology are as follows (a) plot for the model created using bias value, (b) plot for the model created without using bias value.

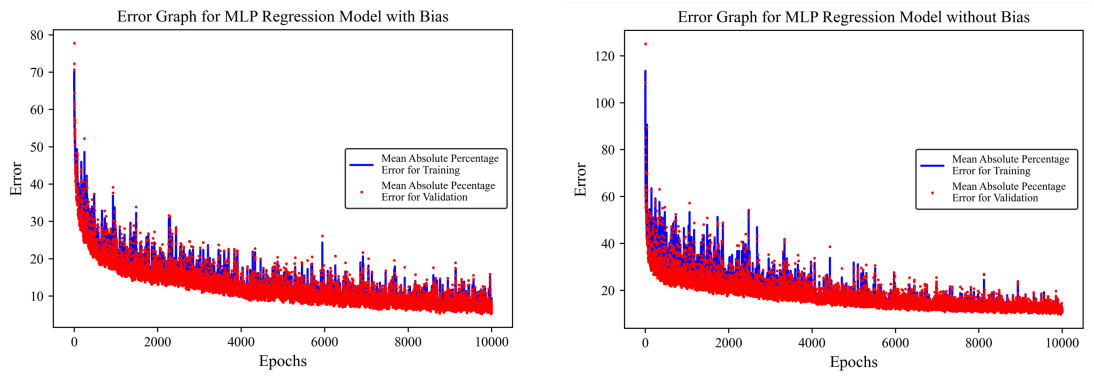

(a) (b)

Figure 3.139. The learning curves of the MLP models created for the displacement capacities of walls with a solid topology are as follows (a) plot for the model created using bias value, (b) plot for the model created without using bias value.

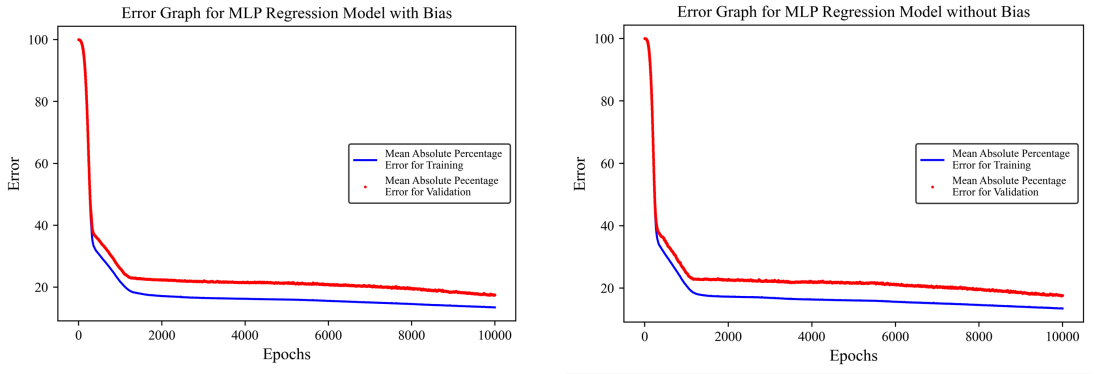

(a) (b)

Figure 3.140. The learning curves of the MLP models created for the shear capacities of walls with a solid topology are as follows (a) plot for the model created using bias value, (b) plot for the model created without using bias value.

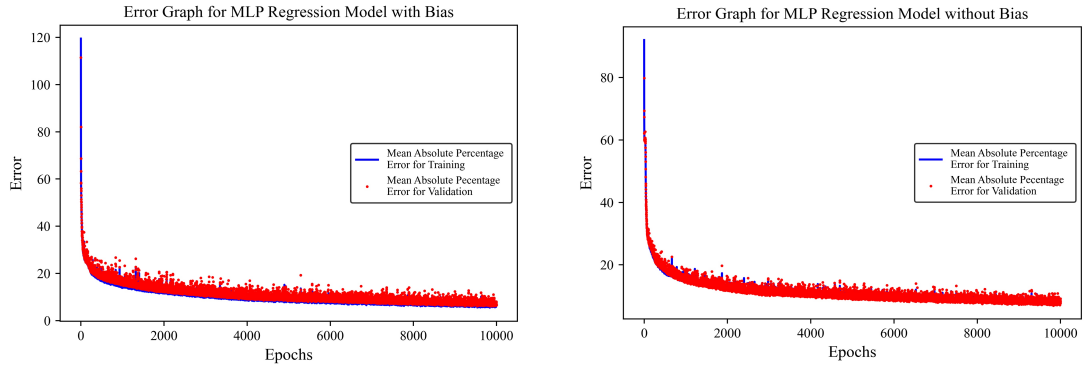

(a) (b)

Figure 3.141. The learning curves of the MLP models created for the displacement capacities of walls with a triangular-1 topology are as follows (a) plot for the model created using bias value, (b) plot for the model created without using bias value.

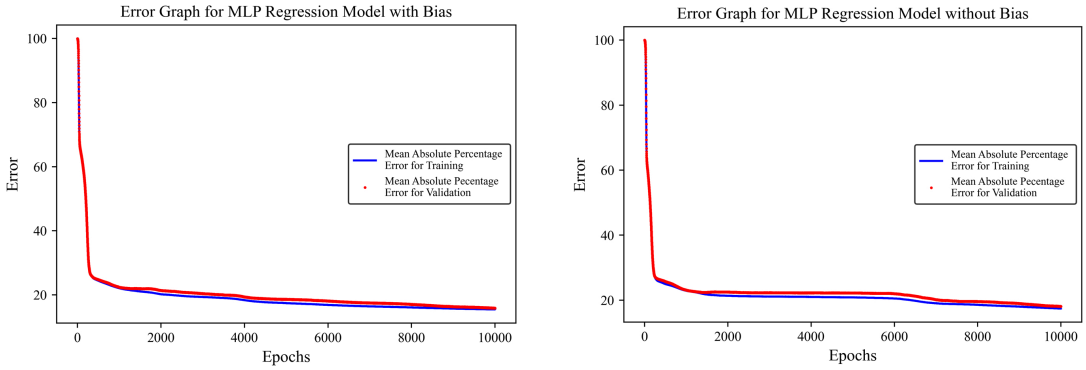

(a) (b)

Figure 3.142. The learning curves of the MLP models created for the shear capacities of walls with a triangular-1 topology are as follows (a) plot for the model created using bias value, (b) plot for the model created without using bias value.

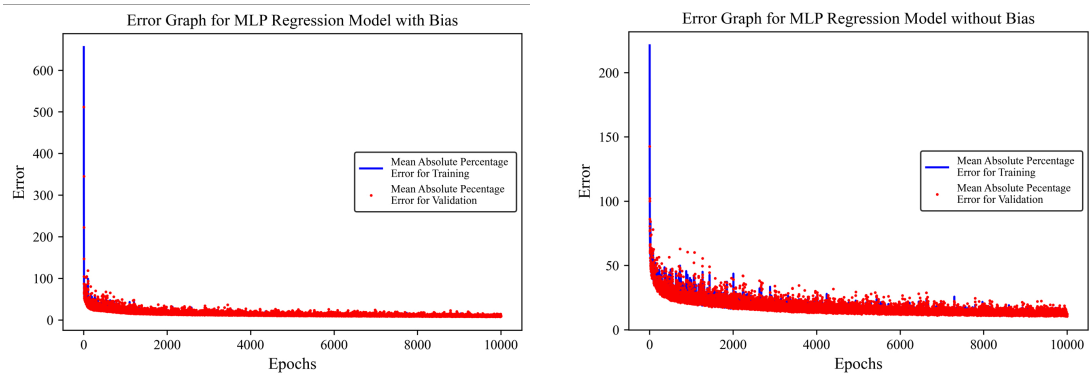

(a) (b)

Figure 3.143. The learning curves of the MLP models created for the displacement capacities of walls with a triangular-2 topology are as follows (a) plot for the model created using bias value, (b) plot for the model created without using bias value.

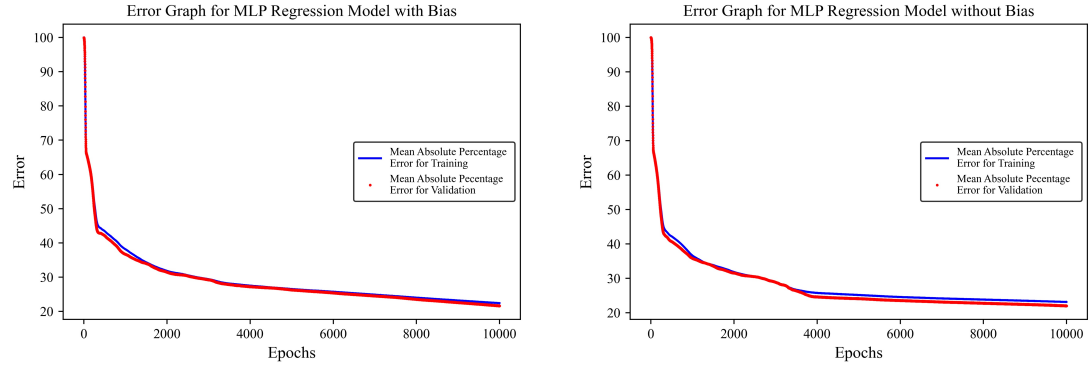

(a) (b)

Figure 3.144. The learning curves of the MLP models created for the shear capacities of walls with a triangular-2 topology are as follows (a) plot for the model created using bias value, (b) plot for the model created without using bias value.

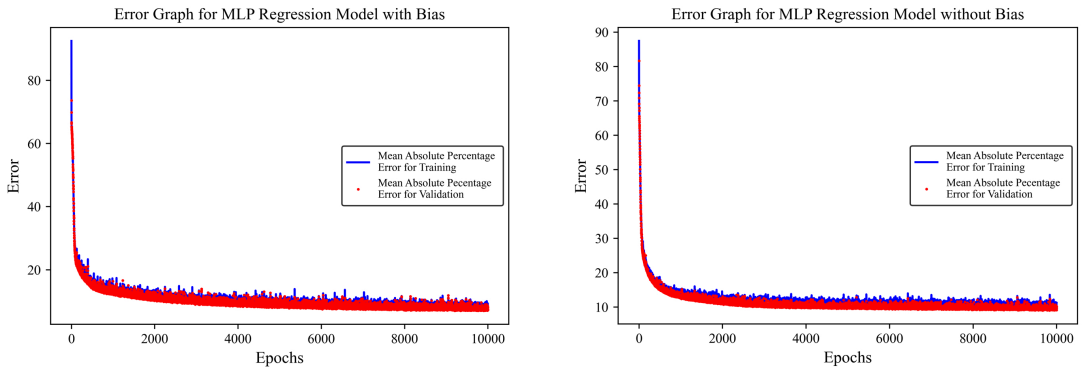

(a) (b)

Figure 3.145. The learning curves of the MLP models created for the displacement capacities of walls with a truss topology are as follows (a) plot for the model created using bias value, (b) plot for the model created without using bias value.

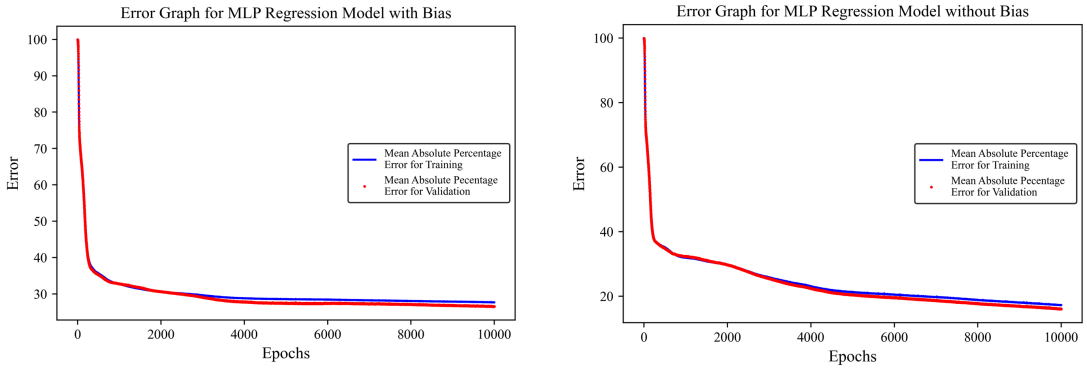

(a) (b)

Figure 3.146. The learning curves of the MLP models created for the shear capacities of walls with a truss topology are as follows (a) plot for the model created using bias value, (b) plot for the model created without using bias value.

The error values for the MLP models created within the scope of this study are provided in Table 3.7. Upon examining this table, it can be seen that the error values for the training, validation, and test datasets are quite close and that the validation errors are almost all lower than the training errors. This indicates that the created models are good fitted. However, in many of the created models, the error values exceed 10%, and for the MLP model with bias created for the shear capacity of walls with truss interior topology,

this value exceeds 25%. This indicates that the created MLP models do not provide sufficient accuracy, and therefore, these models are not efficient.

Table 3.7. Error values for MLP models.

Interior hollow topology	Data type	Model architecture	Mean absolute percentage error		
			Training	Validation	Test
Arch	Displacement Capacity	MLP with bias	10.32	9.97	10.88
		MLP without bias	15.33	14.29	14.97
	Shear Capacity	MLP with bias	14.15	13.55	13.56
		MLP without bias	15.38	14.77	14.77
Cellular	Displacement Capacity	MLP with bias	23.11	21.45	21.92
		MLP without bias	14.68	12.88	16.00
	Shear Capacity	MLP with bias	20.49	20.31	20.33
		MLP without bias	21.10	21.35	21.35
Elliptic	Displacement Capacity	MLP with bias	12.77	12.22	12.92
		MLP without bias	14.27	12.99	14.72
	Shear Capacity	MLP with bias	11.29	11.56	11.57
		MLP without bias	13.14	13.64	13.63
Hollow	Displacement Capacity	MLP with bias	7.22	5.52	5.73
		MLP without bias	9.69	8.08	9.11
	Shear Capacity	MLP with bias	24.95	23.99	24.00
		MLP without bias	12.78	11.85	11.88
Lattice	Displacement Capacity	MLP with bias	3.79	3.54	3.25
		MLP without bias	10.17	9.37	9.68
	Shear Capacity	MLP with bias	13.54	12.79	12.81
		MLP without bias	15.05	14.92	14.94
Solid	Displacement Capacity	MLP with bias	6.1	5.65	6.52
		MLP without bias	10.06	9.94	10.91
	Shear Capacity	MLP with bias	13.46	17.41	17.48
		MLP without bias	13.45	17.49	17.63
Triangular – 1		MLP with bias	5.64	6.23	6.7

	Displacement Capacity	MLP without bias	7.42	7.29	8.1
	Shear Capacity	MLP with bias	15.45	15.94	15.88
		MLP without bias	17.42	18.09	18.11
Triangular – 2	Displacement Capacity	MLP with bias	8.48	8.15	9.05
		MLP without bias	10.76	10.41	10.72
	Shear Capacity	MLP with bias	22.43	21.62	21.64
		MLP without bias	23.1	21.97	21.97
Truss	Displacement Capacity	MLP with bias	8.29	7.04	7.24
		MLP without bias	10.57	9.21	10.04
	Shear Capacity	MLP with bias	27.68	26.53	26.55
		MLP without bias	17.21	16.03	16.03

3.3.3. Creating CNN Models

In this study, CNN models with a single Conv layer were used to make a more reasonable comparison with MLP models and to investigate the efficiency of the Conv layer in learning more effectively. In addition to these parameters, the number of channels (filters or kernels) in the Conv layer was chosen as 512, 1024, 2048, and 4096 [43]. Since the input layer data were vectors of size 1x6, filter parameters of size 1x1, 1x2, 1x3, 1x4, 1x5, and 1x6 were selected in addition to other parameters. Since the outputs of the Conv layers in CNN are vectors of size 1x1, no pooling layer was used after these layers. In addition, for the same reasons mentioned above, the same data split ratio, data normalization method, activation function, regularization method, weight initializer, bias initializer, optimizer, error function, batch size, and number of epochs were used in CNN models as in MLP models. To train the CNN, the FFBP method, as used in MLP, was employed [52,56,58].

The optimum parameter values for the CNN models used are given in Table 3.8

Table 3.8. Optimum parameter values of CNN models.

	Parameter	Arch Wall		Cellular Wall		Elliptic Wall		Hollow Wall		Lattice Wall		Solid Wall		Triangular Wall - 1		Triangular Wall - 2		Truss Wall	
		MLP with bias	MLP without bias	MLP with bias	MLP without bias	MLP with bias	MLP without bias	MLP with bias	MLP without bias	MLP with bias	MLP without bias	MLP with bias	MLP without bias	MLP with bias	MLP without bias	MLP with bias	MLP without bias	MLP with bias	MLP without bias
Displacement capacity	Reg-1	0.00010	0.00001	0.00005	0.00005	0.00050	0.00005	0.00150	0.00000	0.00001	0.00001	0.00005	0.00010	0.00010	0.00005	0.00150	0.00010	0.00010	0.00005
	Reg-2	0.00001	0.00001	0.00100	0.00000	0.00000	0.00000	0.00001	0.00000	0.00000	0.00000	0.00000	0.00050	0.00005	0.00000	0.00100	0.00010	0.00005	0.00000
	Bias-1	0.500	-	0.025	-	0.200	-	0.150	-	0.150	-	0.000	-	0.025	-	0.025	-	0.200	-
	Bias-2	0.025	-	0.100	-	0.100	-	0.100	-	0.025	-	0.100	-	0.100	-	0.200	-	0.025	-
	Number of neurons in the hidden layer	3280	2832	1296	3056	3696	2480	2416	2992	624	272	1104	1360	1456	1008	1296	336	1456	2928
	Number of filters	48	1232	72	3216	272	3472	176	2032	208	2032	912	80	16	240	1424	48	16	400
	Filter size	1*6	1*6	1*6	1*4	1*6	1*6	1*6	1*5	1*5	1*5	1*5	1*5	1*2	1*6	1*6	1*3	1*2	1*2
	Learning rate	0.0050	0.0050	0.0100	0.0005	0.0050	0.0010	0.0050	0.0050	0.0050	0.0050	0.0050	0.0100	0.0050	0.0050	0.0050	0.0050	0.0050	0.0010
Shear Capacity	Reg-1	0.00001	0.00000	0.00000	0.00000	0.00000	0.00000	0.00000	0.00001	0.00000	0.00010	0.00005	0.00005	0.00000	0.00000	0.00000	0.00000	0.00010	0.00001
	Reg-2	0.00000	0.00000	0.00000	0.00000	0.00000	0.00000	0.00000	0.00000	0.00000	0.00000	0.00000	0.00000	0.00000	0.00000	0.00000	0.00000	0.00000	0.00000
	Bias-1	0.250	-	0.150	-	0.100	-	0.250	-	0.100	-	0.500	-	0.100	-	0.025	-	0.100	-
	Bias-2	0.150	-	0.150	-	0.250	-	0.250	-	0.250	-	0.200	-	0.025	-	0.500	-	0.250	-
	Number of neurons in the hidden layer	3120	3856	1520	1968	3280	3504	1968	3568	2608	1136	1296	2896	3248	2384	1968	3056	2896	3472
	Number of filters	3888	1392	2992	1776	3568	720	2288	2992	976	1072	3056	2864	3792	3536	1776	3024	1680	2352
	Filter size	1*2	1*6	1*2	1*5	1*4	1*2	1*5	1*5	1*2	1*1	1*2	1*1	1*1	1*3	1*5	1*2	1*4	1*2
	Learning rate	0.0100	0.0050	0.0200	0.0200	0.0050	0.0200	0.0100	0.0100	0.0100	0.0200	0.0200	0.0200	0.0100	0.0100	0.0200	0.0100	0.0500	0.0100

As can be seen from Table 3.8, different optimum parameter values are used for different models, and there is no definite ratio or relationship between these values. As mentioned earlier, this situation is mainly due to the fact that optimum artificial intelligence models generally vary depending on the dataset. The architectures of the convolutional neural network models created considering the parameters in Table 3.8 are shown in Figures 3.147-3.164.

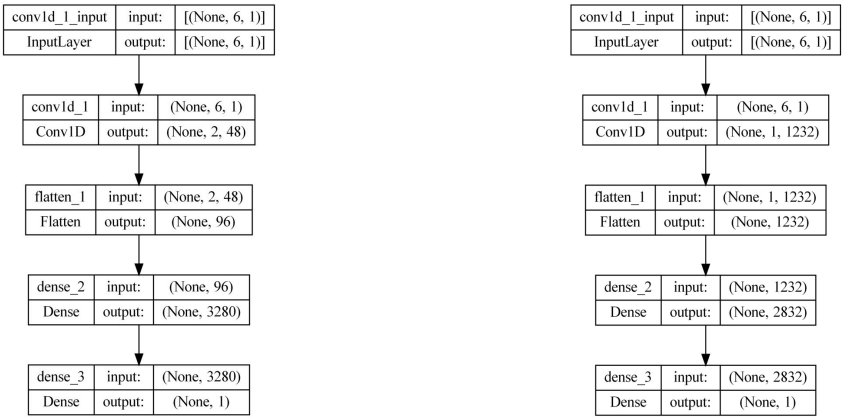

(a) (b)

Figure 3.147. The architectures of CNN models created for the displacement capacities of walls with an arch topology are as follows (a) model created using bias value, (b) model created without using bias value.

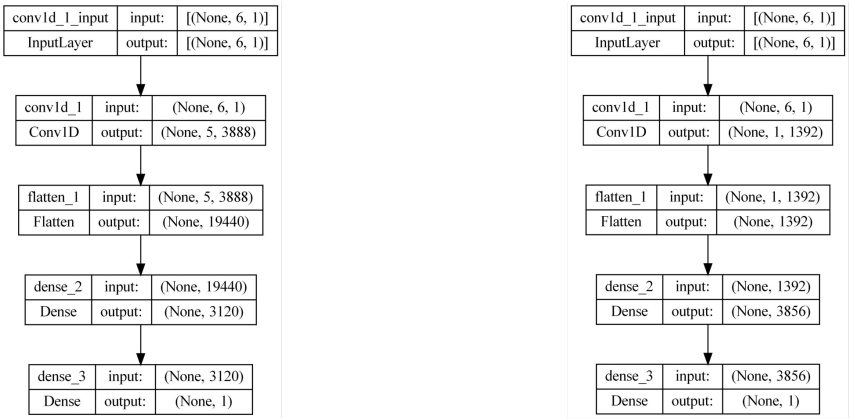

(a) (b)

Figure 3.148. The architectures of CNN models created for the shear capacities of walls with an arch topology are as follows (a) model created using bias value, (b) model created without using bias value.

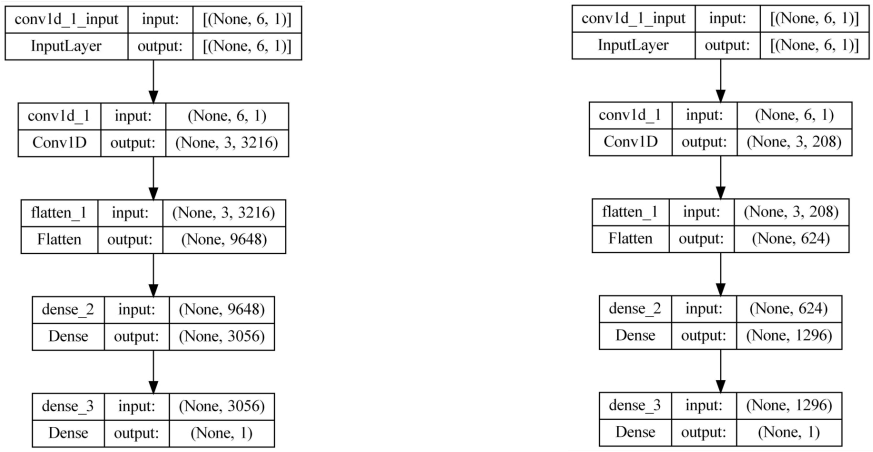

(a) (b)

Figure 3.149. The architectures of CNN models created for the displacement capacities of walls with a cellular topology are as follows (a) model created using bias value, (b) model created without using bias value.

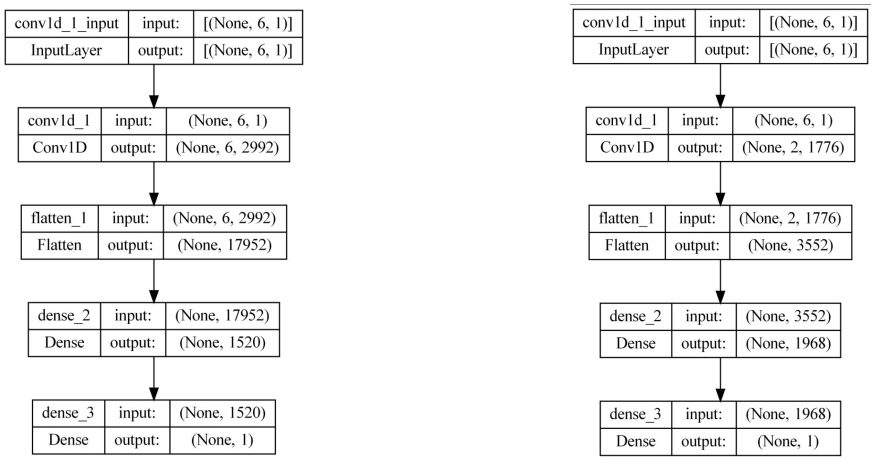

(a) (b)

Figure 3.150. The architectures of CNN models created for the shear capacities of walls with a cellular topology are as follows (a) model created using bias value, (b) model created without using bias value.

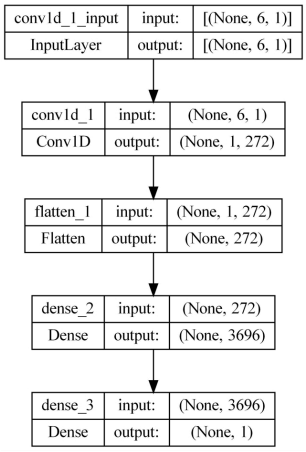

(a)

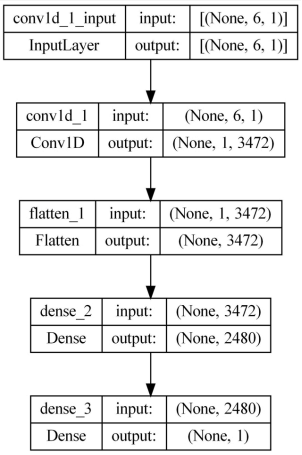

(b)

Figure 3.151. The architectures of CNN models created for the displacement capacities of walls with an elliptic topology are as follows (a) model created using bias value, (b) model created without using bias value.

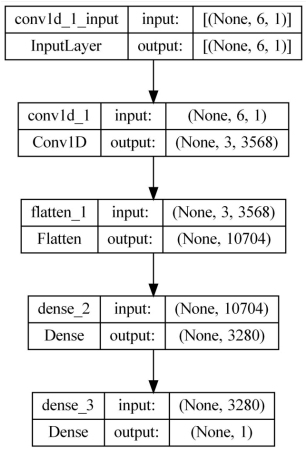

(a)

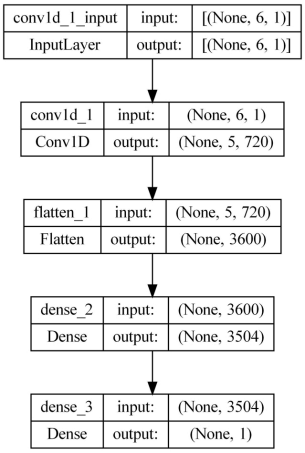

(b)

Figure 3.152. The architectures of CNN models created for the shear capacities of walls with an elliptic topology are as follows (a) model created using bias value, (b) model created without using bias value.

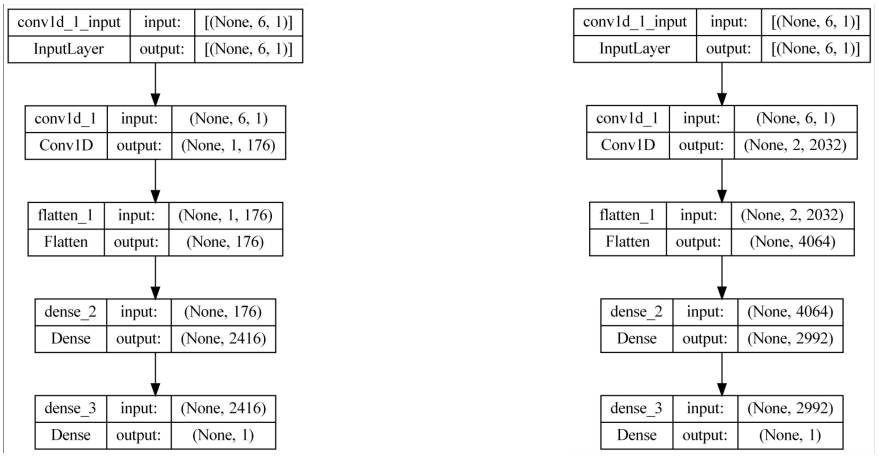

(a) (b)

Figure 3.153. The architectures of CNN models created for the displacement capacities of walls with a hollow topology are as follows (a) model created using bias value, (b) model created without using bias value.

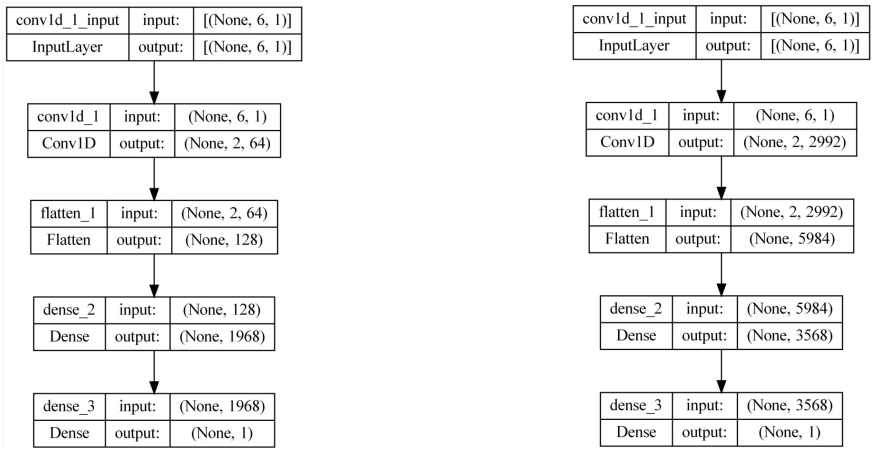

(a) (b)

Figure 3.154. The architectures of CNN models created for the displacement capacities of walls with a hollow topology are as follows (a) model created using bias value, (b) model created without using bias value.

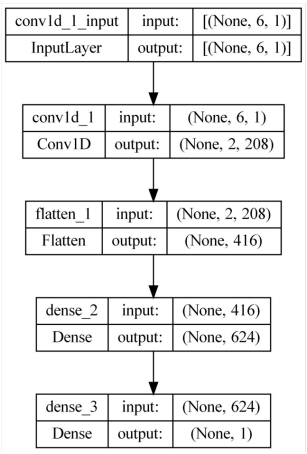

(a)

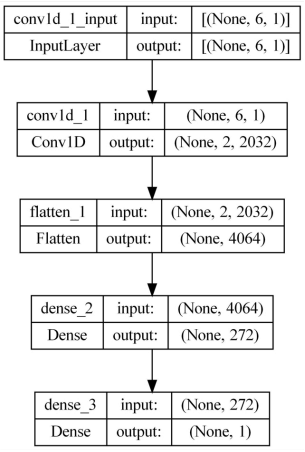

(b)

Figure 3.155. The architectures of CNN models created for the displacement capacities of walls with a lattice topology are as follows (a) model created using bias value, (b) model created without using bias value.

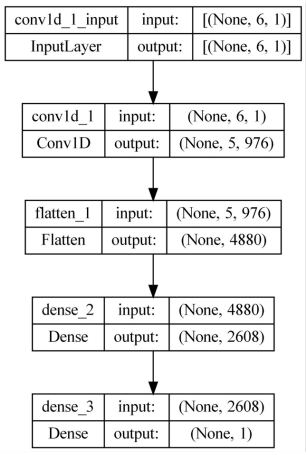

(a)

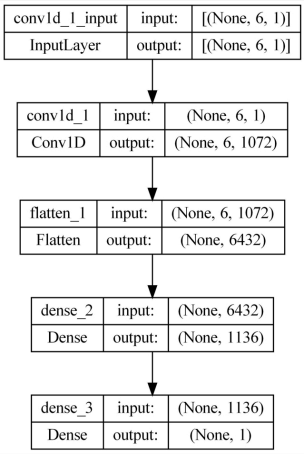

(b)

Figure 3.156. The architectures of CNN models created for the shear capacities of walls with a lattice topology are as follows (a) model created using bias value, (b) model created without using bias value.

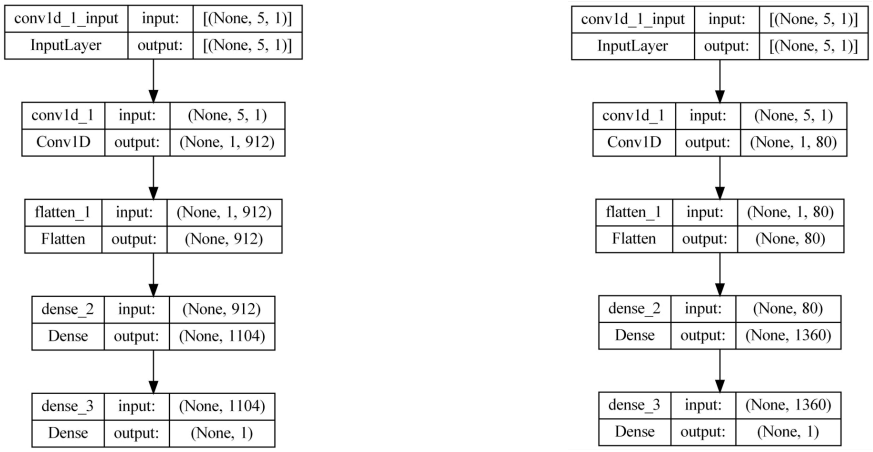

(a) (b)

Figure 3.157. The architectures of CNN models created for the displacement capacities of walls with a solid topology are as follows (a) model created using bias value, (b) model created without using bias value.

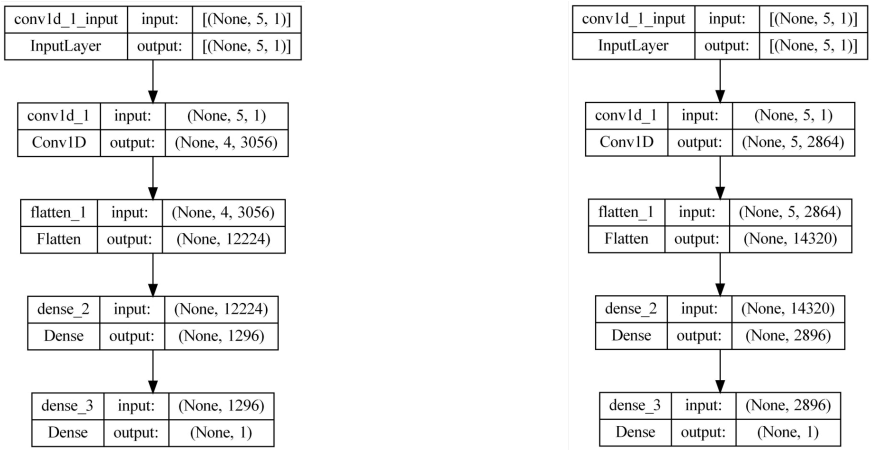

(a) (b)

Figure 3.158. The architectures of CNN models created for the shear capacities of walls with a solid topology are as follows (a) model created using bias value, (b) model created without using bias value.

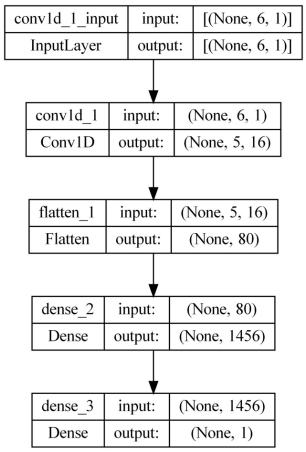

(a)

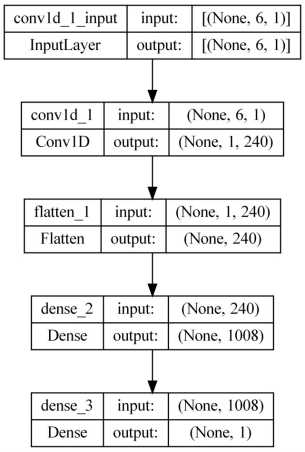

(b)

Figure 3.159. The architectures of CNN models created for the displacement capacities of walls with a triangular-1 topology are as follows (a) model created using bias value, (b) model created without using bias value.

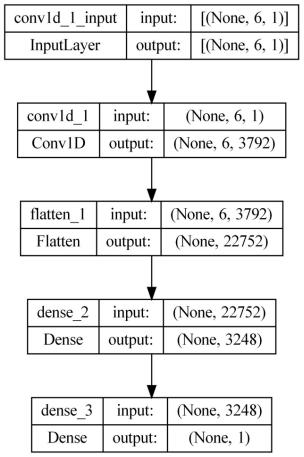

(a)

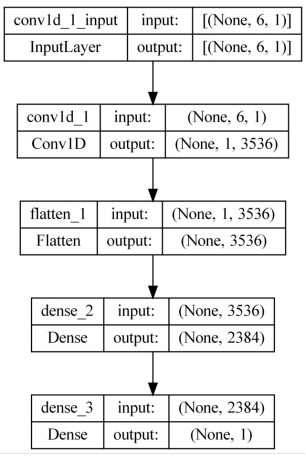

(b)

Figure 3.160. The architectures of CNN models created for the shear capacities of walls with a triangular-1 topology are as follows (a) model created using bias value, (b) model created without using bias value.

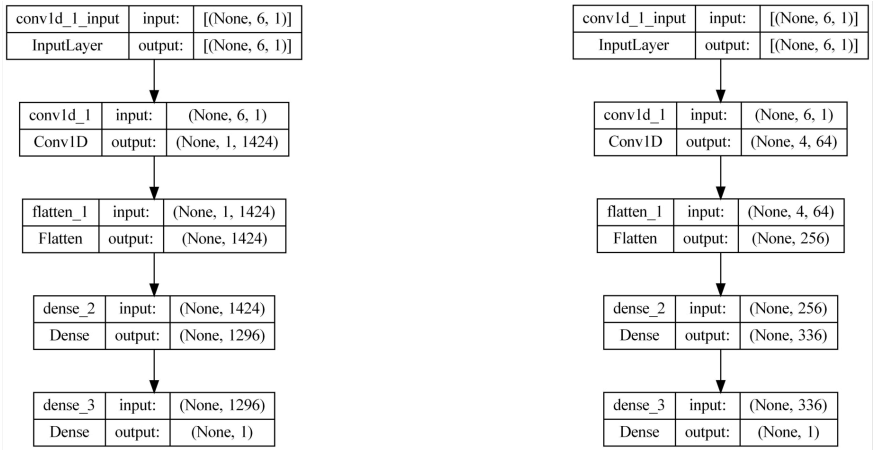

(a) (b)

Figure 3.161. The architectures of CNN models created for the displacement capacities of walls with a triangular-2 topology are as follows (a) model created using bias value, (b) model created without using bias value.

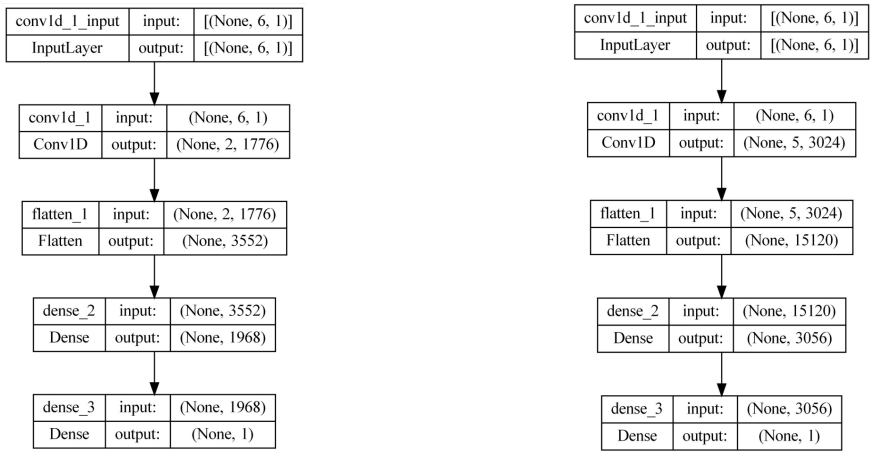

(a) (b)

Figure 3.162. The architectures of CNN models created for the shear capacities of walls with a triangular-2 topology are as follows (a) model created using bias value, (b) model created without using bias value.

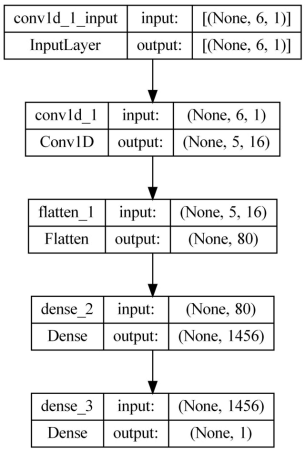

(a)

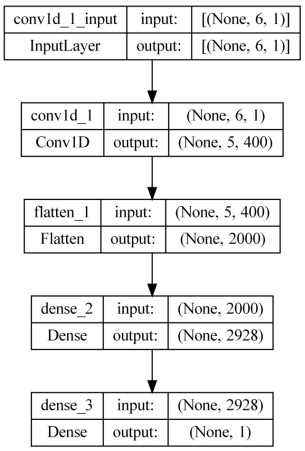

(b)

Figure 3.163. The architectures of CNN models created for the displacement capacities of walls with a truss topology are as follows (a) model created using bias value, (b) model created without using bias value.

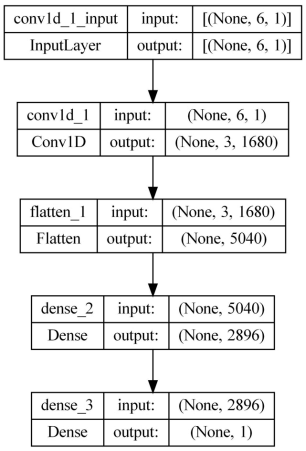

(a)

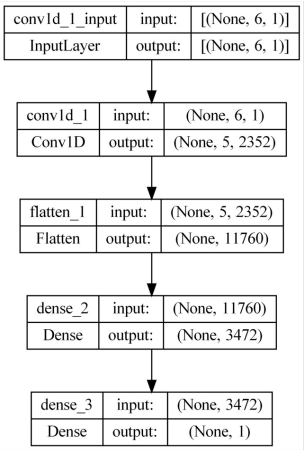

(b)

Figure 3.164. The architectures of CNN models created for the shear capacities of walls with a truss topology are as follows (a) model created using bias value, (b) model created without using bias value.

The learning curves of the used CNN models are shown in Figures 3.165-3.182. As can be seen from these figures, similar to the MLP models, the learning values obtained for the training and validation datasets are very close in CNN models as well, and the slopes of both learning curves hardly change after 10000 epochs. This situation indicates that

the error convergence process is largely completed, there is no underfitting or overfitting problem in the created models, and the created models are good fitted.

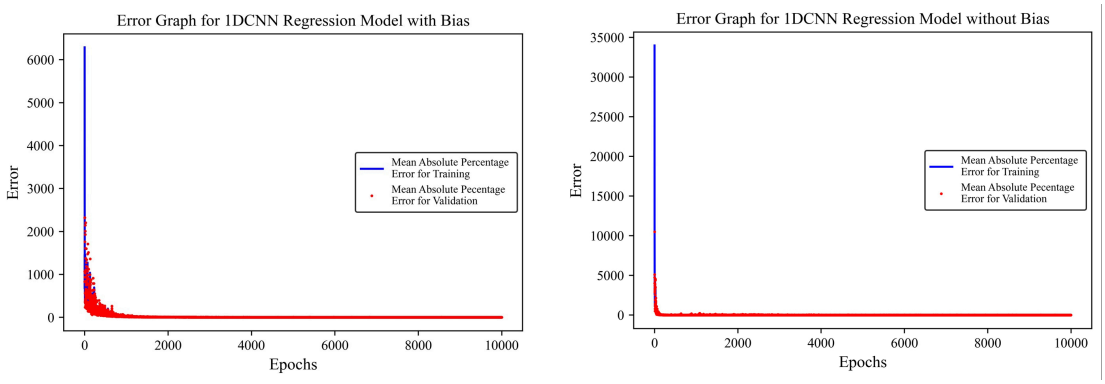

(a) (b)

Figure 3.165. The learning curves of the CNN models created for the displacement capacities of walls with an arch topology are as follows (a) plot for the model created using bias value, (b) plot for the model created without using bias value.

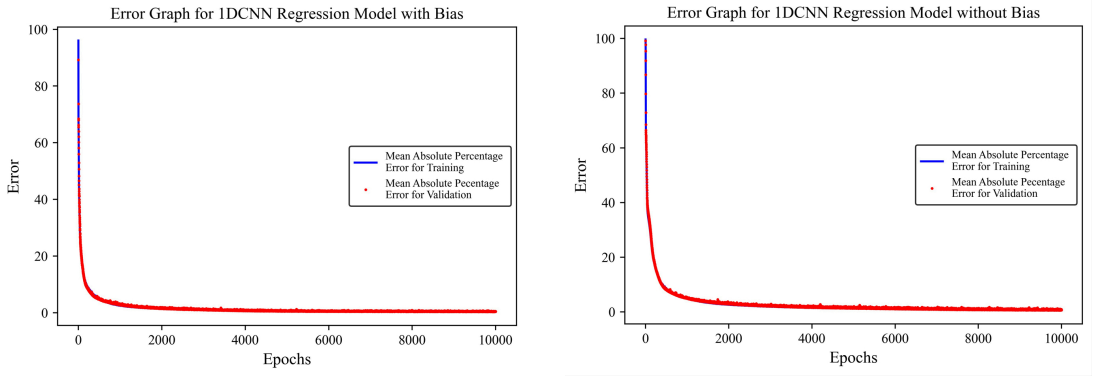

(a) (b)

Figure 3.166. The learning curves of the CNN models created for the shear capacities of walls with an arch topology are as follows (a) plot for the model created using bias value, (b) plot for the model created without using bias value.

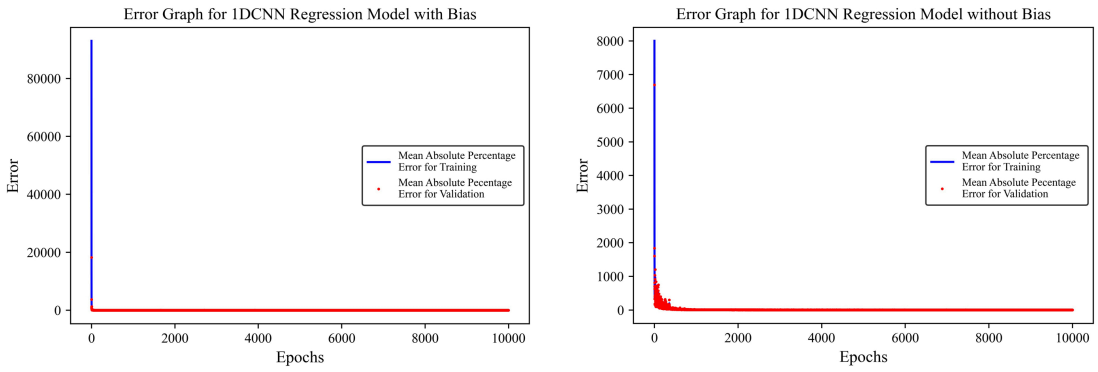

(a) (b)

Figure 3.167. The learning curves of the CNN models created for the displacement capacities of walls with a cellular topology are as follows (a) plot for the model created using bias value, (b) plot for the model created without using bias value.

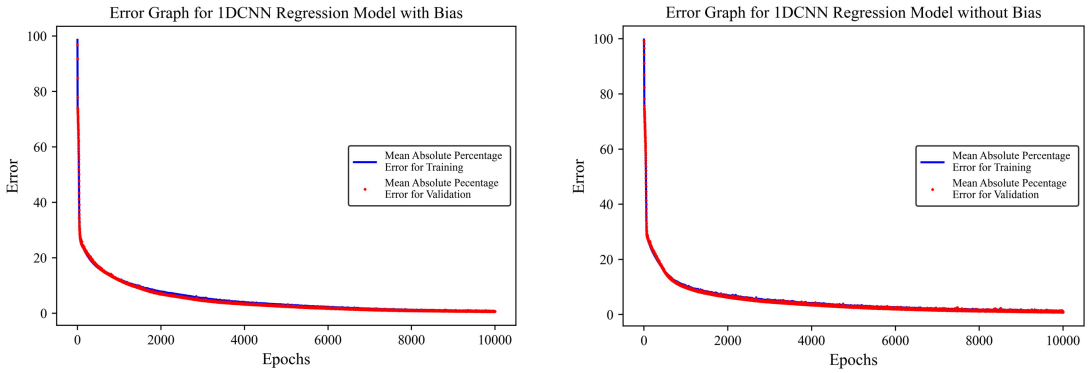

(a) (b)

Figure 3.168. The learning curves of the CNN models created for the shear capacities of walls with a cellular topology are as follows (a) plot for the model created using bias value, (b) plot for the model created without using bias value.

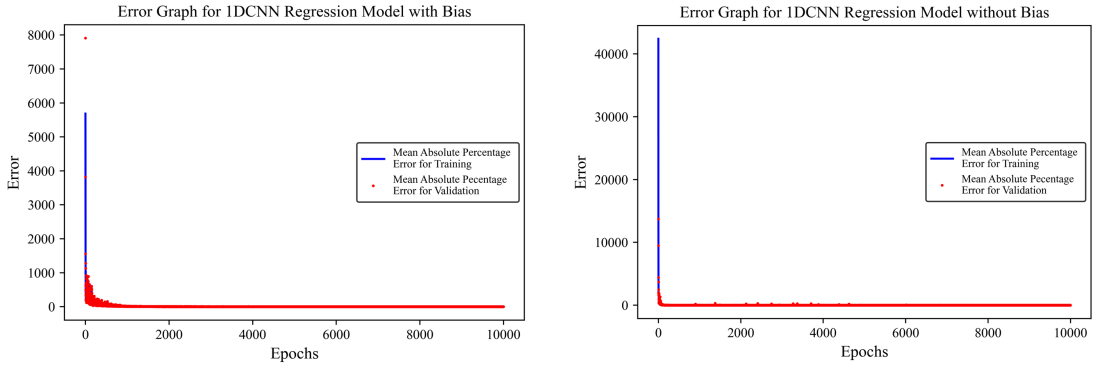

(a) (b)

Figure 3.169. The learning curves of the CNN models created for the displacement capacities of walls with an elliptic topology are as follows (a) plot for the model created using bias value, (b) plot for the model created without using bias value.

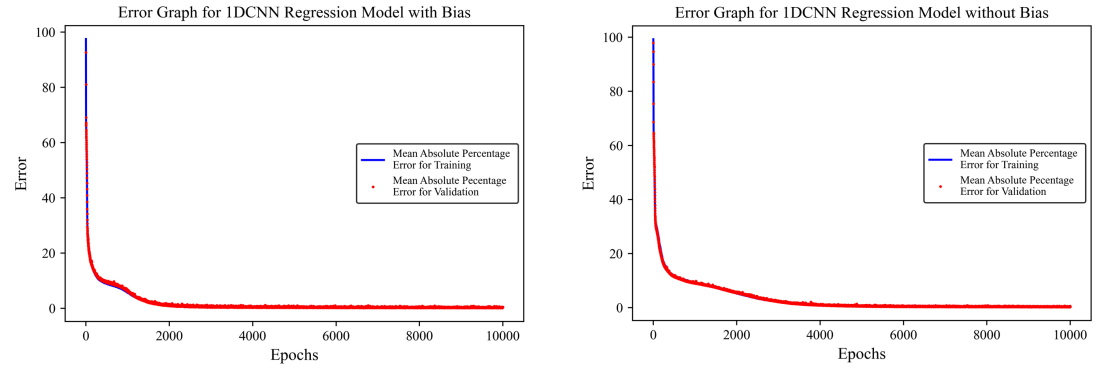

(a) (b)

Figure 3.170. The learning curves of the CNN models created for the shear capacities of walls with an elliptic topology are as follows (a) plot for the model created using bias value, (b) plot for the model created without using bias value.

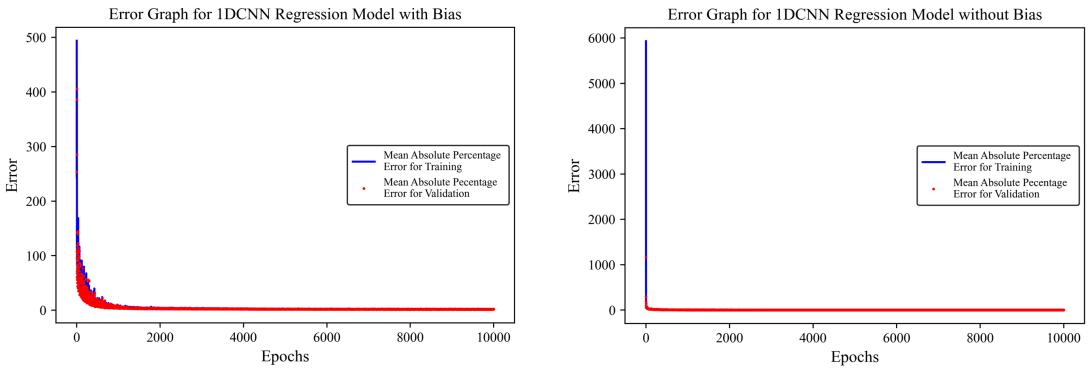

(a) (b)

Figure 3.171. The learning curves of the CNN models created for the displacement capacities of walls with a hollow topology are as follows (a) plot for the model created using bias value, (b) plot for the model created without using bias value.

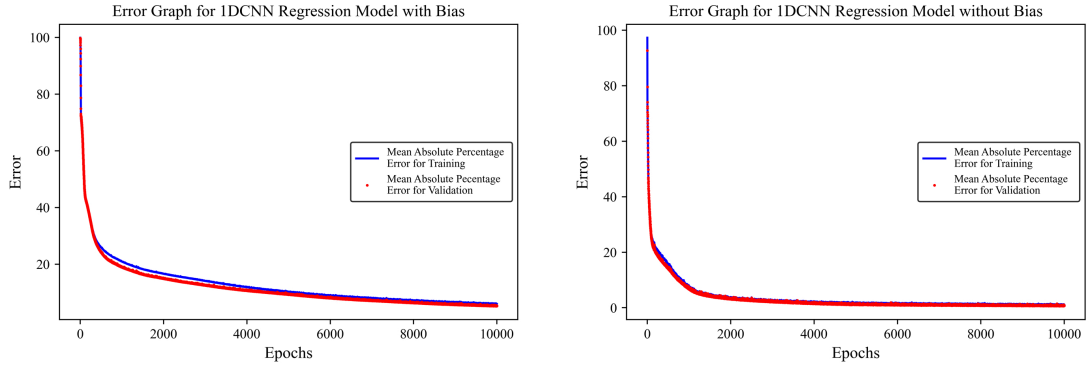

(a) (b)

Figure 3.172. The learning curves of the CNN models created for the shear capacities of walls with a hollow topology are as follows (a) plot for the model created using bias value, (b) plot for the model created without using bias value.

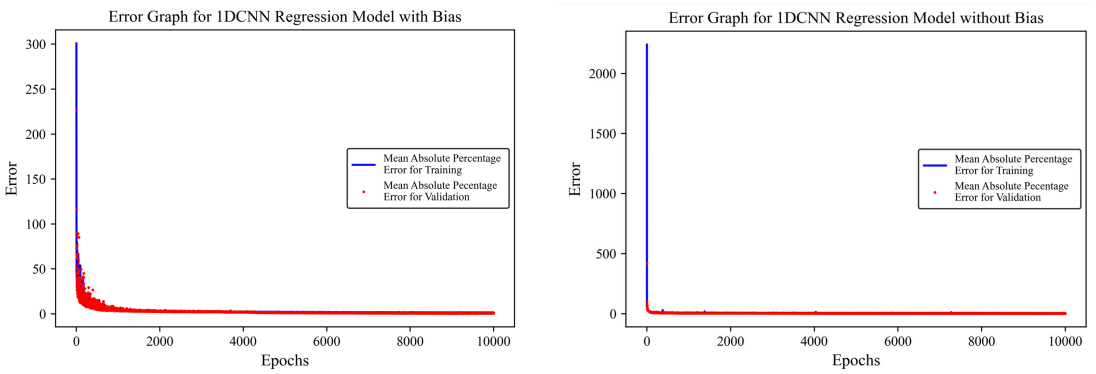

(a) (b)

Figure 3.173. The learning curves of the CNN models created for the displacement capacities of walls with a lattice topology are as follows (a) plot for the model created using bias value, (b) plot for the model created without using bias value.

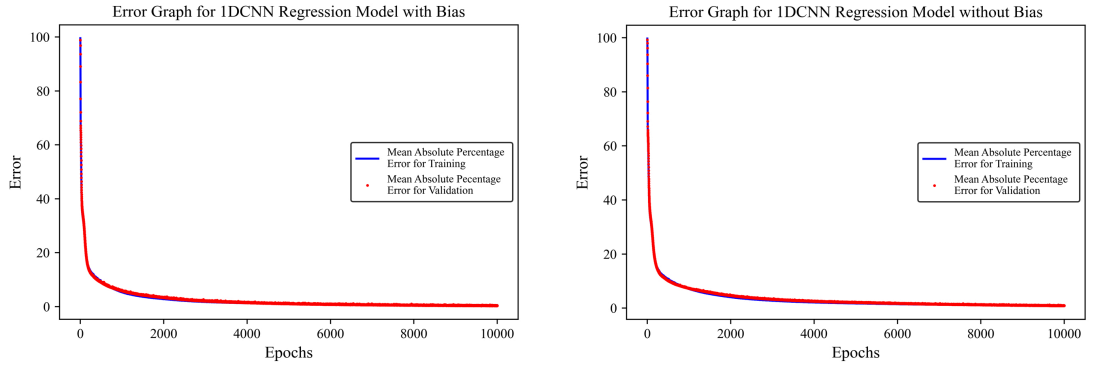

(a) (b)

Figure 3.174. The learning curves of the CNN models created for the shear capacities of walls with a lattice topology are as follows (a) plot for the model created using bias value, (b) plot for the model created without using bias value.

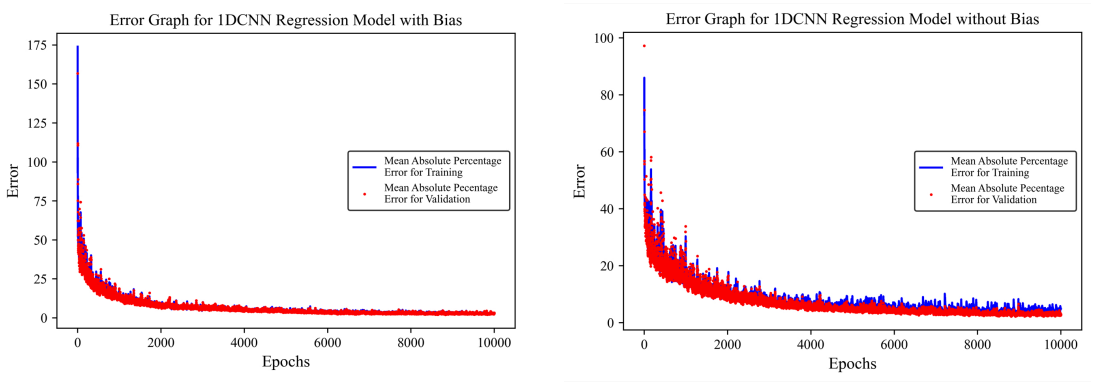

(a) (b)

Figure 3.175. The learning curves of the CNN models created for the displacement capacities of walls with a solid topology are as follows (a) plot for the model created using bias value, (b) plot for the model created without using bias value.

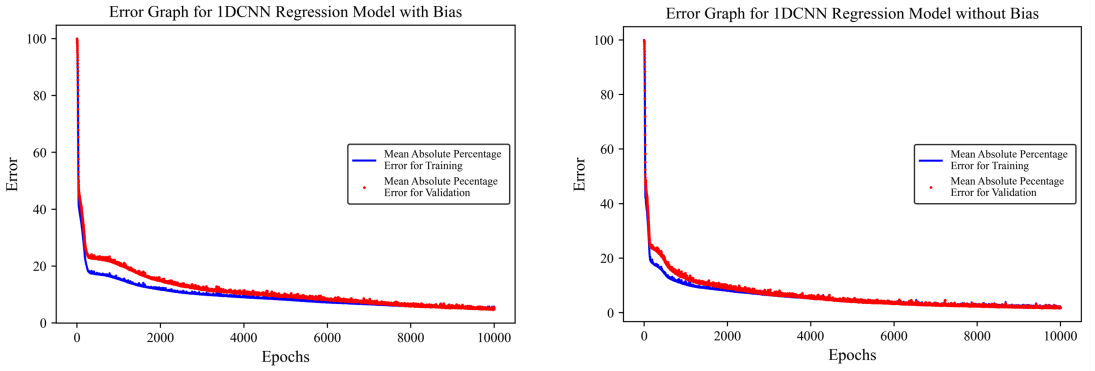

(a) (b)

Figure 3.176. The learning curves of the CNN models created for the shear capacities of walls with a solid topology are as follows (a) plot for the model created using bias value, (b) plot for the model created without using bias value.



(a) (b)

Figure 3.177. The learning curves of the CNN models created for the displacement capacities of walls with a triangular-1 topology are as follows (a) plot for the model created using bias value, (b) plot for the model created without using bias value.

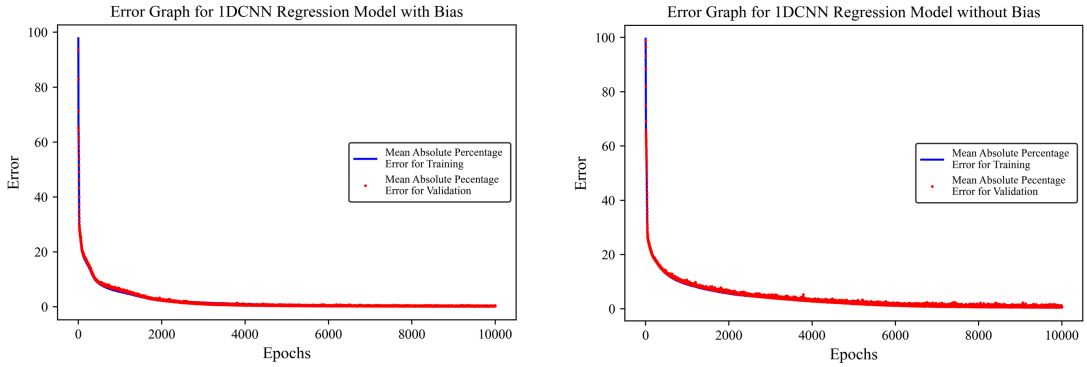

(a) (b)

Figure 3.178. The learning curves of the CNN models created for the shear capacities of walls with a triangular-1 topology are as follows (a) plot for the model created using bias value, (b) plot for the model created without using bias value.

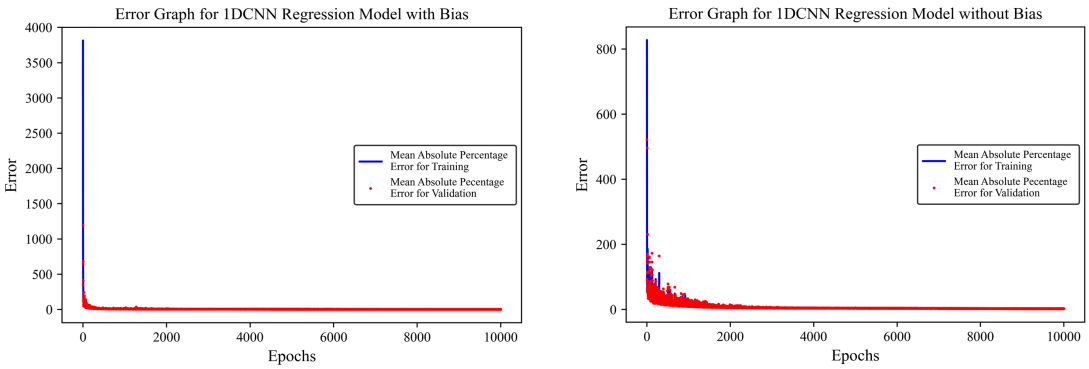

(a) (b)

Figure 3.179. The learning curves of the CNN models created for the displacement capacities of walls with a triangular-2 topology are as follows (a) plot for the model created using bias value, (b) plot for the model created without using bias value.

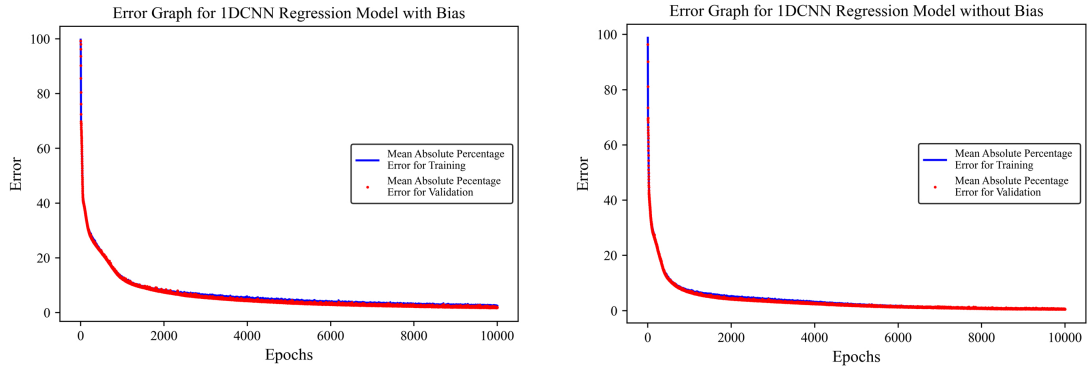

(a) (b)

Figure 3.180. The learning curves of the CNN models created for the shear capacities of walls with a triangular-2 topology are as follows (a) plot for the model created using bias value, (b) plot for the model created without using bias value.

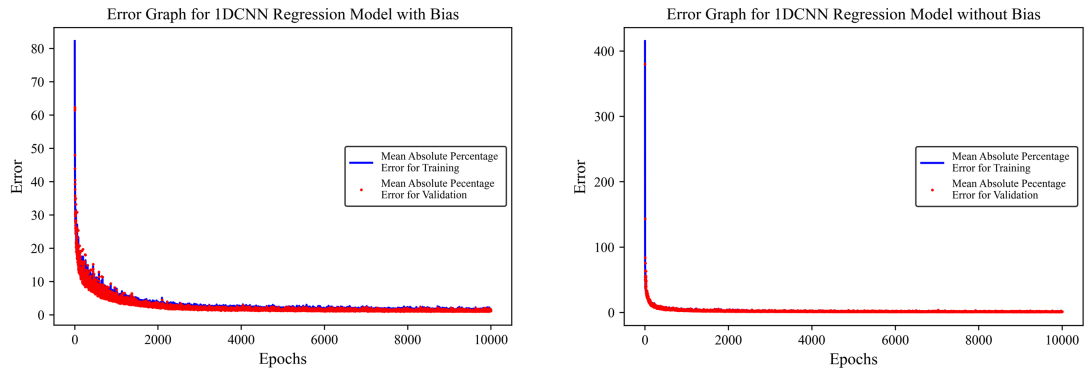

(a) (b)

Figure 3.181. The learning curves of the CNN models created for the displacement capacities of walls with a truss topology are as follows (a) plot for the model created using bias value, (b) plot for the model created without using bias value.

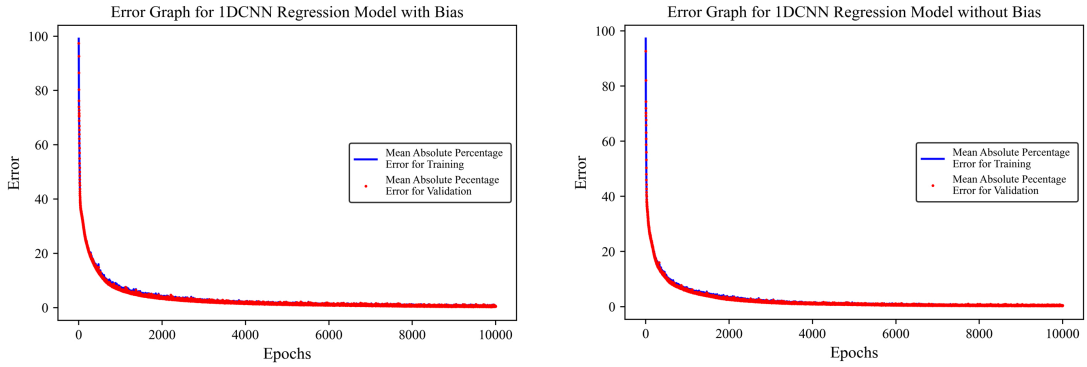

(a) (b)

Figure 3.182. The learning curves of the CNN models created for the shear capacities of walls with a truss topology are as follows (a) plot for the model created using bias value, (b) plot for the model created without using bias value.

Error values for the CNN models created in this study are given in Table 3.9. As can be seen from this table, the error values for the training, validation, and test datasets are quite close, and almost all validation errors are lower than training errors. This indicates that the created models are good fitted. Additionally, it is observed that error values are below 5% in almost all created models, and the highest error value is 7.75% (for test data) for the CNN model without bias created for the displacement capacity of walls with arc

interior hollow topology. This situation indicates that the created CNN models can provide sufficient accuracy, and therefore, these models are quite efficient.

Table 3.9. Error values for CNN models.

Interior hollow topology	Data type	Model architecture	Mean absolute percentage error		
			Training	Validation	Test
Arch	Displacement Capacity	1D CNN with bias	2.76	2.44	2.94
		1D CNN without bias	3.51	3.04	7.75
	Shear Capacity	1D CNN with bias	0.38	0.35	0.41
		1D CNN without bias	0.66	0.61	0.67
Cellular	Displacement Capacity	1D CNN with bias	6.38	6.18	6.62
		1D CNN without bias	4.30	3.56	4.05
	Shear Capacity	1D CNN with bias	0.71	0.56	0.66
		1D CNN without bias	1.15	0.83	0.86
Elliptic	Displacement Capacity	1D CNN with bias	3.24	1.79	2.75
		1D CNN without bias	5.16	3.36	4.31
	Shear Capacity	1D CNN with bias	0.18	0.17	0.40
		1D CNN without bias	0.25	0.23	0.29
Hollow	Displacement Capacity	1D CNN with bias	2.14	1.65	1.81
		1D CNN without bias	2.60	2.08	2.24
	Shear Capacity	1D CNN with bias	5.99	5.24	5.34
		1D CNN without bias	1.03	0.63	0.77
Lattice	Displacement Capacity	1D CNN with bias	1.45	0.67	0.93
		1D CNN without bias	3.96	3.36	3.44
	Shear Capacity	1D CNN with bias	0.39	0.29	0.39
		1D CNN without bias	0.84	0.87	0.90

Solid	Displacement Capacity	1D CNN with bias	2.48	2.08	3.29
		1D CNN without bias	3.34	2.5	2.98
	Shear Capacity	1D CNN with bias	5.08	4.75	5.01
		1D CNN without bias	2.03	1.68	1.82
Triangular – 1	Displacement Capacity	1D CNN with bias	1.45	1.09	1.19
		1D CNN without bias	0.9	0.46	0.47
	Shear Capacity	1D CNN with bias	0.25	0.19	0.28
		1D CNN without bias	0.7	0.54	0.8
Triangular – 2	Displacement Capacity	1D CNN with bias	3.33	3.72	3.8
		1D CNN without bias	2.82	2.6	2.75
	Shear Capacity	1D CNN with bias	2.37	1.73	1.98
		1D CNN without bias	0.57	0.51	0.55
Truss	Displacement Capacity	1D CNN with bias	1.4	1.03	1.24
		1D CNN without bias	1.44	1.05	1.25
	Shear Capacity	1D CNN with bias	0.55	0.3	0.4
		1D CNN without bias	0.39	0.31	0.35

3.4. Development of AI-Based Design Tools

In this study, two different design tools have been developed for predicting the shear strength and displacement capacity of walls with different interior topologies. While developing these AI-based tools, the CNN model with bias which has the highest accuracy created in the previous section was taken into consideration. Before the development of these tools, the AI models mentioned above were converted into pre-trained models. In this context, a total of 18 CNN models with bias, including nine shear strength prediction tools and nine displacement capacity prediction tools, were used for nine different wall internal topologies. After the pre-trained models were created, the source codes for the two different design tools were written in the Python programming language using the standard graphical user interface library called "Tkinter". Finally,

these source codes were packaged into executable programs by using the "PyInstaller" library to convert them into executable (.exe) files for various operating systems.

When the developed programs are running, the language selection screen is opened first. There are two language options available on this screen, Turkish and English. After the preferred language is selected on the language selection screen, the main screen containing nine different wall interior topologies is opened (Figure 3.183). Through this screen, the user can select the wall type for which they want to predict the shear capacity or displacement capacity.

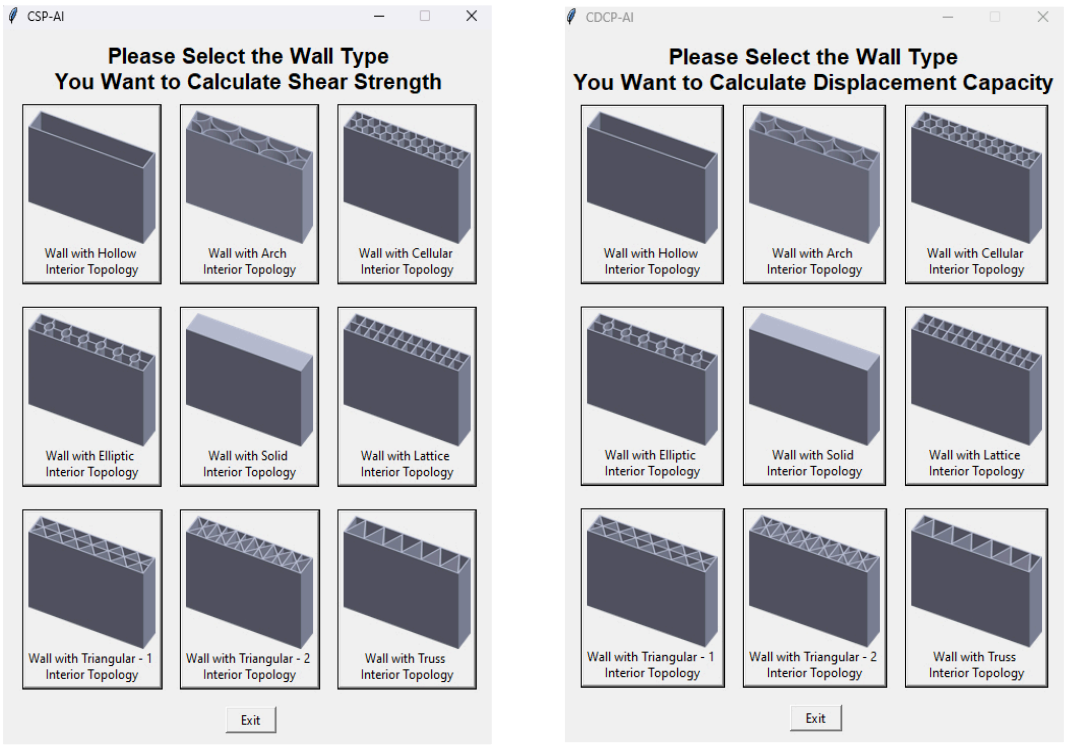

(a) (b)

Figure 3.183. The main screen includes different wall interior topologies (a) the main screen of the software developed for shear capacity prediction, (b) the main screen of the software developed for displacement capacity prediction.

After selecting the wall type on the main screen, the input screen containing the parameters of the wall type for which the shear capacity or displacement capacity will be estimated is opened (Figure 3.184).

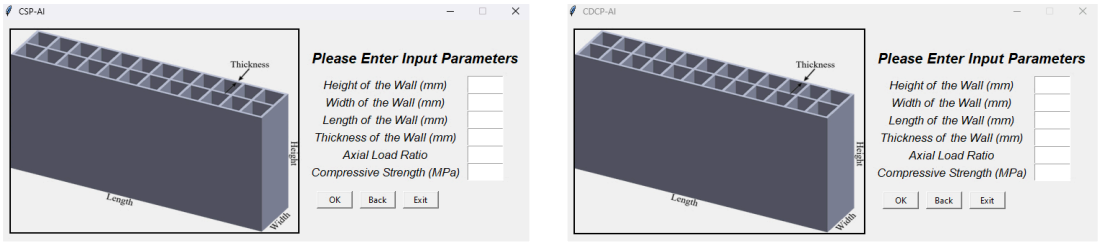

(a) (b)

Figure 3.184. The input screen includes the parameters of the wall for which capacity estimation will be performed (a) input screen of the software developed for shear capacity prediction, (b) input screen of the software developed for displacement capacity prediction.

After entering the necessary parameters on the input page, when the OK button is pressed, the developed program calculates the displacement or shear capacity for the selected wall type using the pre-trained AI models (Figure 3.185).

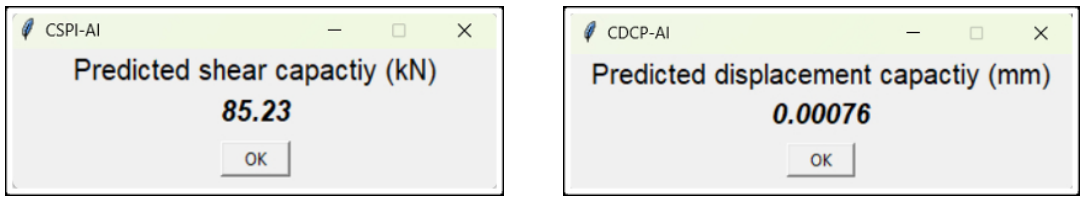

(a) (b)

Figure 3.185. The output screen displays the prediction made using pre-trained AI models (a) output screen of the program developed for shear capacity estimation, (b) output screen of the program developed for displacement capacity estimation.

3.5. Calculating the Shear Capacities According to Building Codes/Standards

In order to demonstrate the efficiency of the AI-based design tool developed for capacity prediction of walls produced through 3DCP in terms of practical application, the shear strength values predicted by the AI-based design tool should be compared with the strength values calculated through formulas in building codes/standards for unreinforced masonry structures. Therefore, in this study, shear capacity predictions made by AI-based design tool have been also compared with shear capacity values calculated by formulas given in building codes/standards to understand whether automated design tool is suitable to predict shear and displacement capacity of 3D printed concrete walls.

Unreinforced masonry structures have three main components: in-plane walls (walls parallel to the applied force), out-of-plane walls (walls perpendicular to the applied force), and flexible floor diaphragms (Figure 3.186) [88]. Horizontal loads affecting the unreinforced masonry structure are largely transmitted to the structure through in-plane walls because of their high stiffness [88]. In this research, since pushover analyses were conducted on unreinforced walls produced through 3DCP, failure modes of in-plane walls were considered.

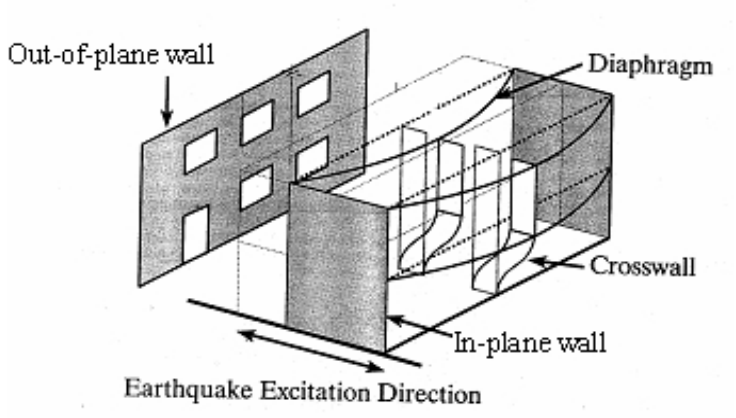

Figure 3.186. Schematic representation of a typical unreinforced masonry structure under earthquake load [88].

In-plane failures occur due to extremely high shear forces or flexural forces affecting the in-plane walls. The three basic failure modes occurring in unreinforced masonry structures are shown in Figure 3.187 [88,89].

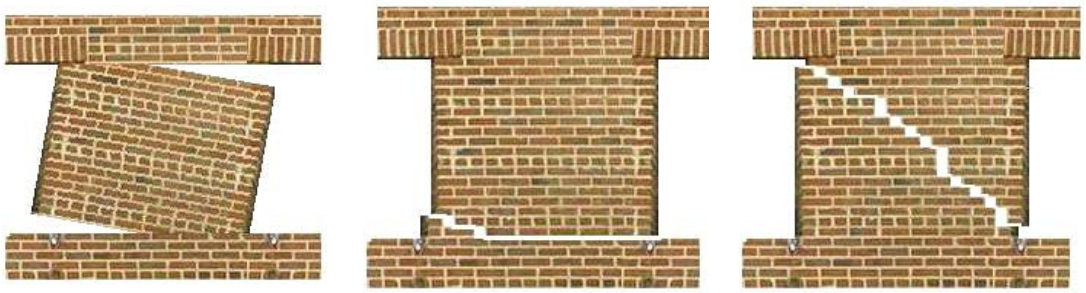

(a) (b) (c)

Figure 3.187. Failure modes of unreinforced in-plane masonry walls (a) rocking failure, (b) sliding failure, (c) diagonal tension failure [88].

Rocking failure occurs when significant flexural cracks develop at the top and bottom of a wall. In this scenario, as displacement increases, the wall behaves like a rigid body rotating about its base or supporting pier. Sliding failure is characterized by horizontal shear cracks at the wall's base or the bed joint, causing the wall to slide along the bed joint, with friction being the only source of resistance. Diagonal tension failure arises from diagonal cracks due to maximum principal tensile stress surpassing the tensile strength of the masonry. Depending on the strength of the mortar joints, the brick-mortar interface, and the bricks themselves, these cracks can appear in a stair-step pattern from the top to the bottom of the masonry wall, or they can cut through the bricks. The equations provided describe the strength calculations for these three failure types, where V_{be} denotes the shear capacity for rocking failure, β indicates a factor of 0.5 for a fixed-free cantilever wall or 1.0 for a fixed-fixed wall, L represents the wall's length, H_{eff} is the effective height, A is the wall's area, f_c is the concrete's compressive strength, P is the vertical load on the wall, κ is cohesion, γ is the friction coefficient, σ denotes the axial compressive strength, V_u is the shear capacity for sliding failure, f_t is the concrete's tensile strength, V_{dt} represents the shear capacity for diagonal tension and θ represents the capacity reduction factor depending on aspect ratio (Equation 3.33, 3.34, 3.35 and 3.36). These formulas are developed according to the FEMA 356 building code [88–90].

$$V_{be} = \beta P \frac{L}{H_{eff}} \left(1 - \frac{P}{0.8 f_c A}\right) \tag{3.33}$$

$$V_u = (\kappa + \gamma\sigma) * A \tag{3.34}$$

$$V_{dt} = f_t A \theta \sqrt{1 + \frac{\sigma}{f_t}} \tag{3.35}$$

$$\theta = \frac{L}{H_{eff}} \tag{3.36}$$

In Equation 3.34, cohesion value κ is calculated according to Equation 3.13, and friction coefficient value γ is determined as 0.5 according to TSC 2007 which is the Turkish Seismic Design Code for Buildings [91].

After calculating the shear capacity for three different failure modes using Equations 3.33, 3.34, and 3.35, correlation analyses were performed using actual data for each of the shear capacity values obtained for the three failure modes. Following these analyses, the minimum shear capacity values (governing shear capacity) for three failure modes were correlated with actual data. Finally, correlation analyses were conducted using predicted values from the AI-based design tool and actual values for the entire dataset.

4. RESULTS AND DISCUSSIONS

4.1. Comparison of the Values Predicted through the MLP Model and CNN Model

The scatter plots obtained as a result of regression and correlation analyses, considering the values predicted through AI models and the actual values, are given in Figures 4.1-4.36. It is observed from these plots that CNNs with bias have the highest correlation coefficient for shear capacities. In addition, it is seen that more than half of the CNN models without bias have a higher correlation coefficient than MLP models with bias. Moreover, it is also observed that all MLP models without bias have a lower correlation coefficient than MLP models with bias and all CNN models.

For displacement capacities, it was observed that CNN models without bias which were created for the test dataset of walls with lattice topology, and walls with triangular-2 topology, and for both the test and training dataset of walls with triangular-1 topology have a higher correlation coefficient than CNN models with bias. In the remaining 14 plots, CNN models with bias have had a higher correlation coefficient. Additionally, it is observed that all CNN models with bias and more than half of the CNN models without bias have a higher correlation coefficient than MLP models with bias. Furthermore, it is seen that MLP models without bias have a higher correlation coefficient than MLP models with bias for test datasets of walls with cellular topology and walls with solid topology and for both the training and test datasets of walls with triangular-1 topology. In the remaining 14 plots, MLP models with bias have had a higher correlation coefficient. However, in any case, it is also seen that MLP models without bias have a lower correlation coefficient than both the CNN models with and without bias.

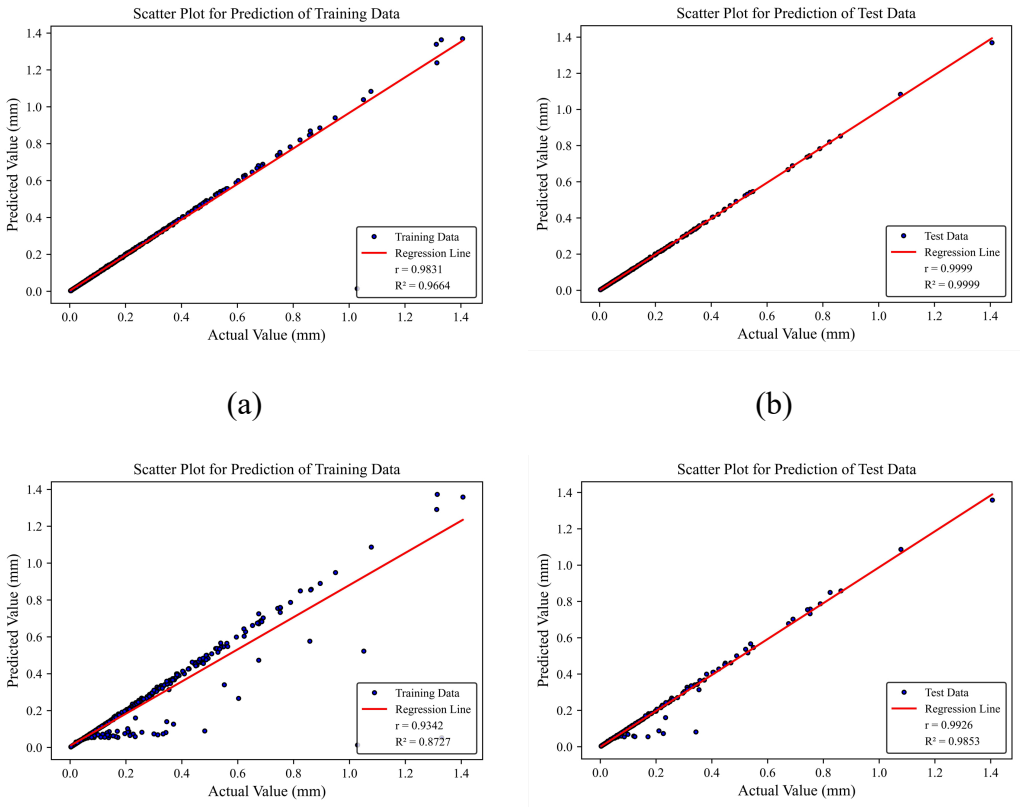

Figure 4.1. The scatter plots for the displacement capacity data of walls with arch topology are as follows (a) plot for the training dataset of the CNN model with bias, (b) plot for the test dataset of the CNN model with bias, (c) plot for the training dataset of the CNN model without bias, (d) plot for the test dataset of the CNN model without bias.

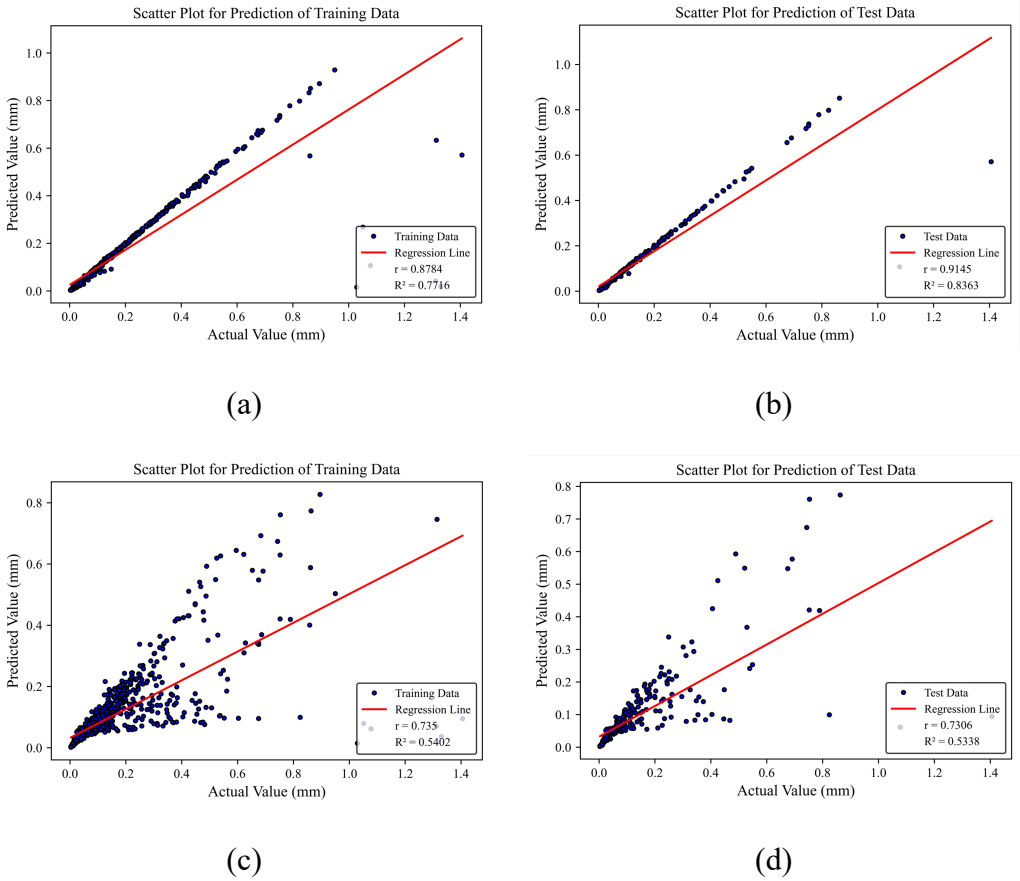

Figure 4.2. The scatter plots for the displacement capacity data of walls with arch topology are as follows (a) plot for the training dataset of the MLP model with bias, (b) plot for the test dataset of the MLP model with bias, (c) plot for the training dataset of the MLP model without bias, (d) plot for the test dataset of the MLP model without bias.

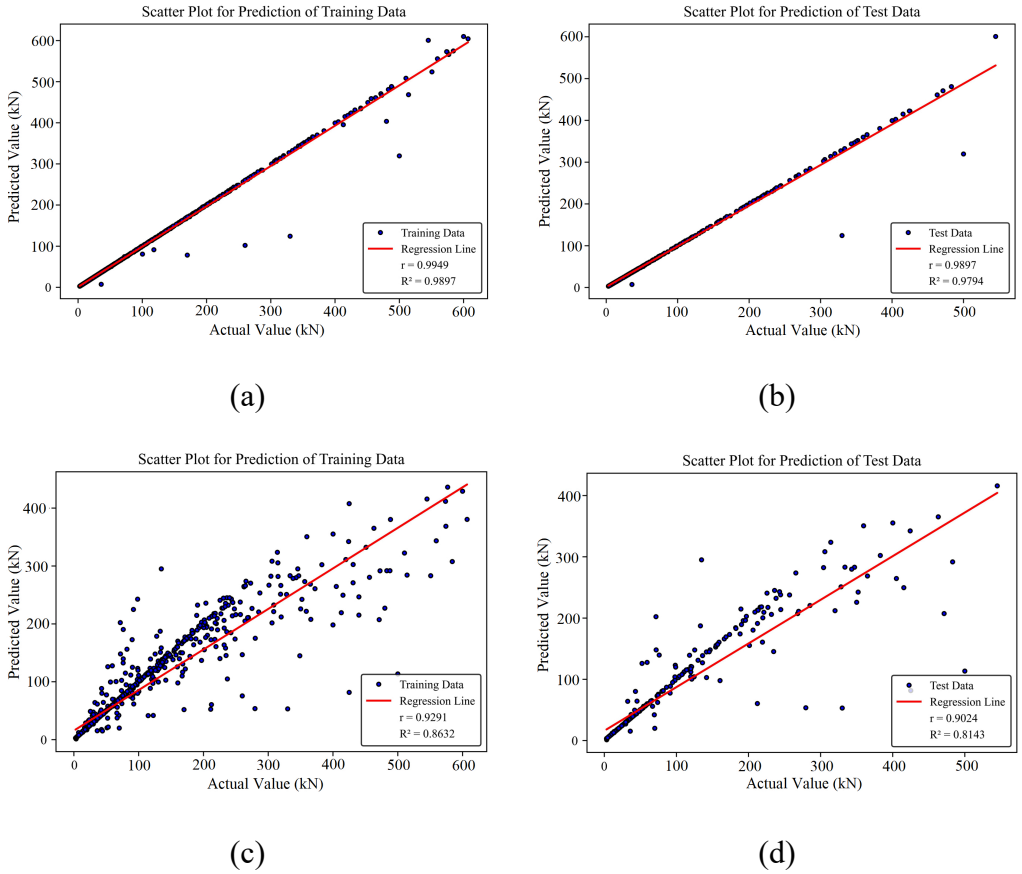

Figure 4.3. The scatter plots for the shear capacity data of walls with arch topology are as follows (a) plot for the training dataset of the CNN model with bias, (b) plot for the test dataset of the CNN model with bias, (c) plot for the training dataset of the CNN model without bias, (d) plot for the test dataset of the CNN model without bias.

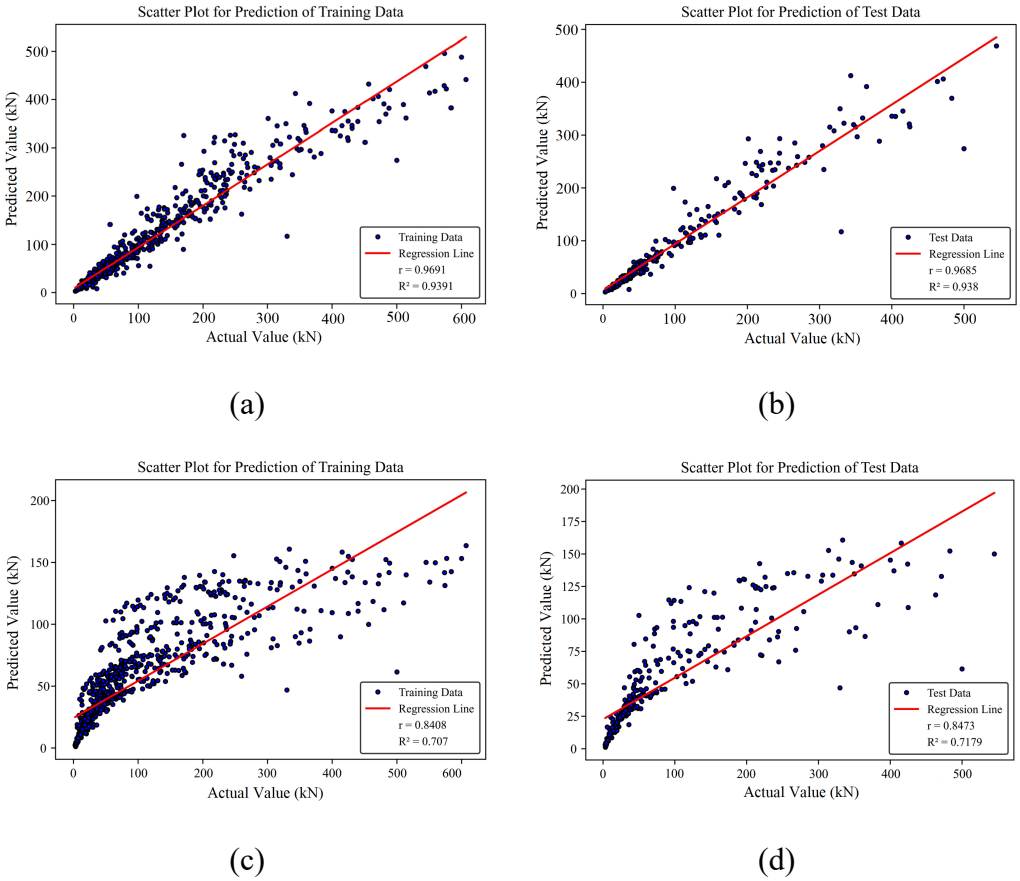

Figure 4.4. The scatter plots for the shear capacity data of walls with arch topology are as follows (a) plot for the training dataset of the MLP model with bias, (b) plot for the test dataset of the MLP model with bias, (c) plot for the training dataset of the MLP model without bias, (d) plot for the test dataset of the MLP model without bias.

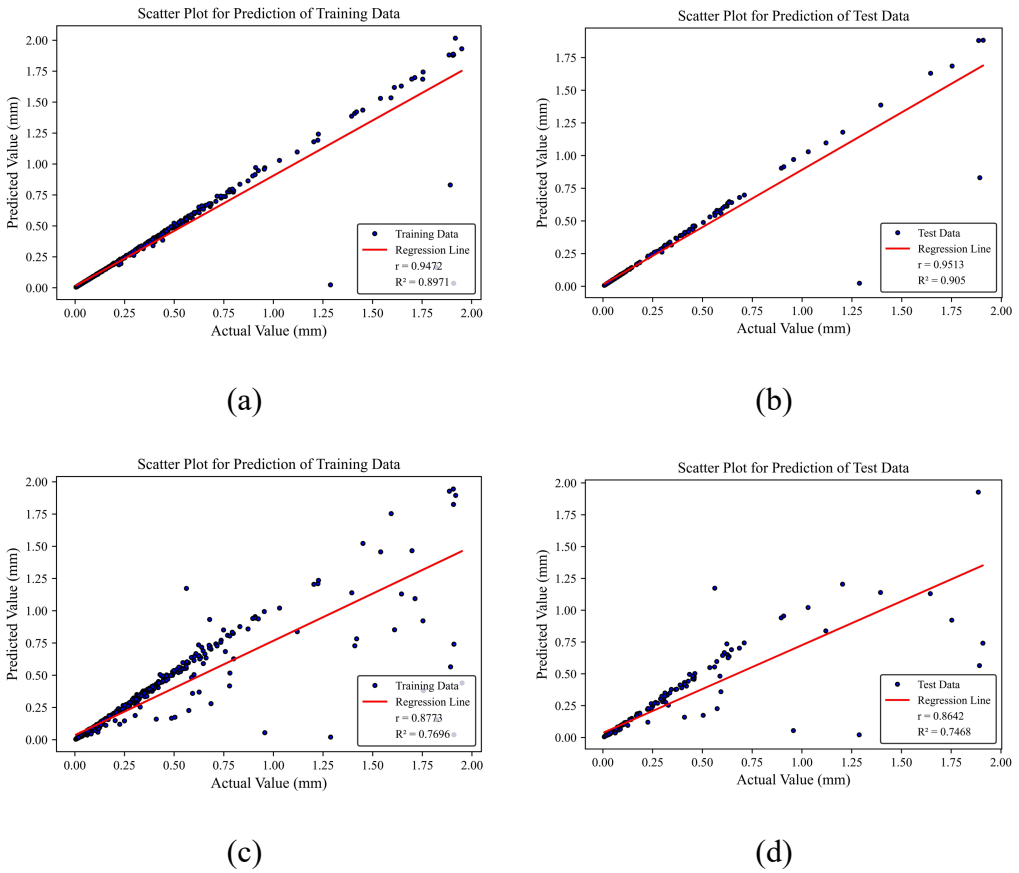

Figure 4.5. The scatter plots for the displacement capacity data of walls with cellular topology are as follows (a) plot for the training dataset of the CNN model with bias, (b) plot for the test dataset of the CNN model with bias, (c) plot for the training dataset of the CNN model without bias, (d) plot for the test dataset of the CNN model without bias.

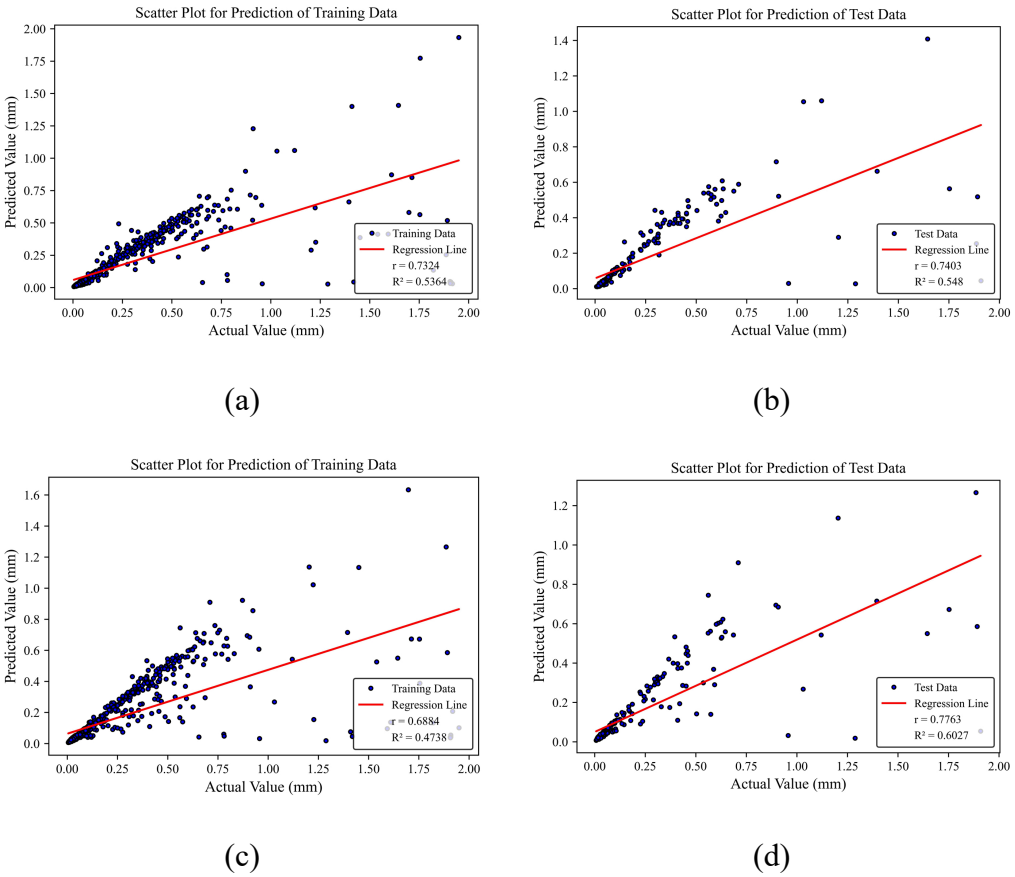

Figure 4.6. The scatter plots for the displacement capacity data of walls with cellular topology are as follows (a) plot for the training dataset of the MLP model with bias, (b) plot for the test dataset of the MLP model with bias, (c) plot for the training dataset of the MLP model without bias, (d) plot for the test dataset of the MLP model without bias.

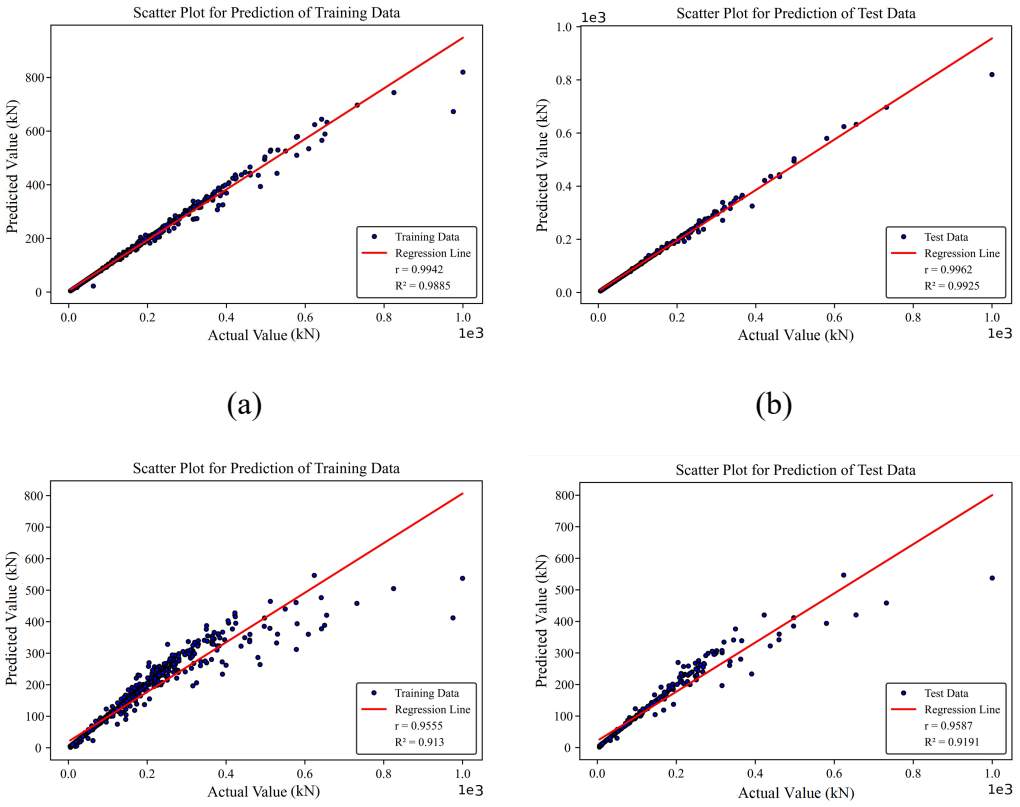

Figure 4.7. The scatter plots for the shear capacity data of walls with cellular topology are as follows (a) plot for the training dataset of the CNN model with bias, (b) plot for the test dataset of the CNN model with bias, (c) plot for the training dataset of the CNN model without bias, (d) plot for the test dataset of the CNN model without bias.

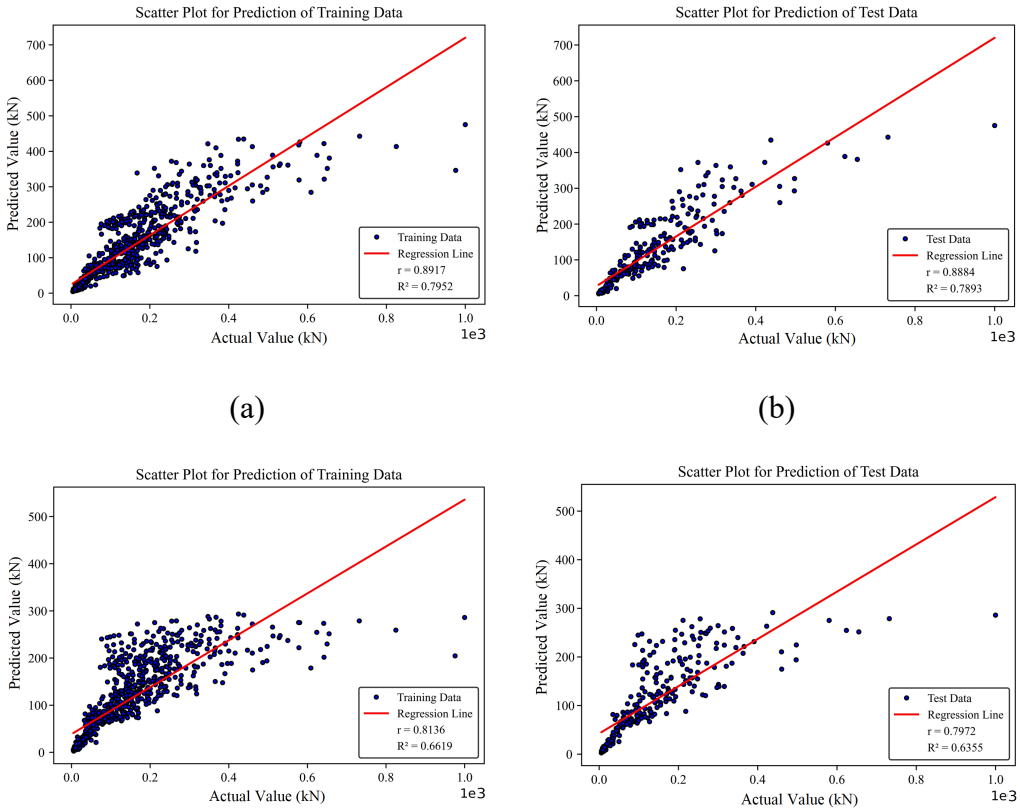

Figure 4.8. The scatter plots for the shear capacity data of walls with cellular topology are as follows (a) plot for the training dataset of the MLP model with bias, (b) plot for the test dataset of the MLP model with bias, (c) plot for the training dataset of the MLP model without bias, (d) plot for the test dataset of the MLP model without bias.

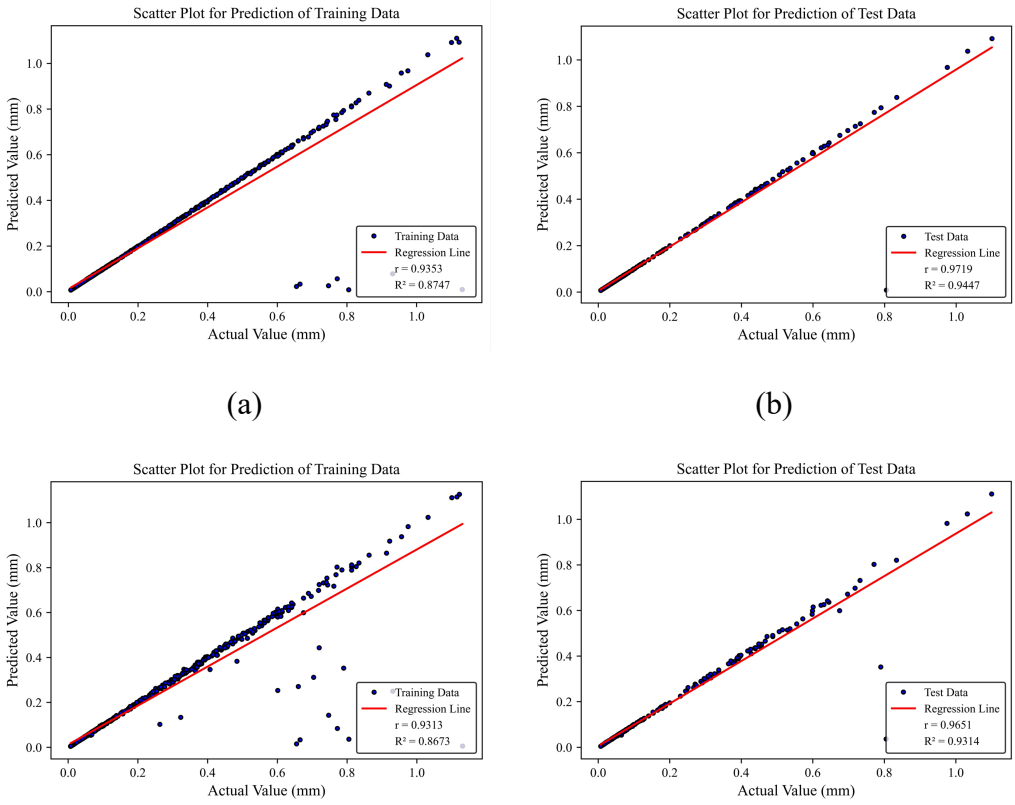

Figure 4.9. The scatter plots for the displacement capacity data of walls with elliptic topology are as follows (a) plot for the training dataset of the CNN model with bias, (b) plot for the test dataset of the CNN model with bias, (c) plot for the training dataset of the CNN model without bias, (d) plot for the test dataset of the CNN model without bias.

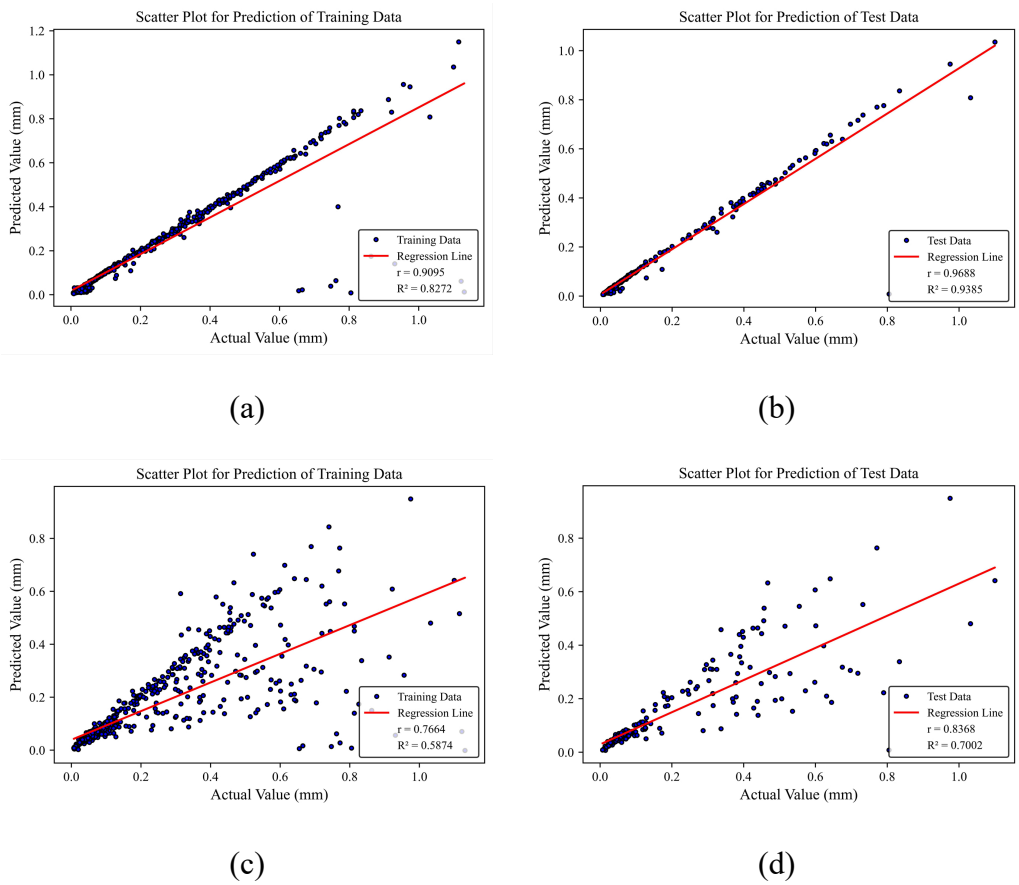

Figure 4.10. The scatter plots for the displacement capacity data of walls with elliptic topology are as follows (a) plot for the training dataset of the MLP model with bias, (b) plot for the test dataset of the MLP model with bias, (c) plot for the training dataset of the MLP model without bias, (d) plot for the test dataset of the MLP model without bias.

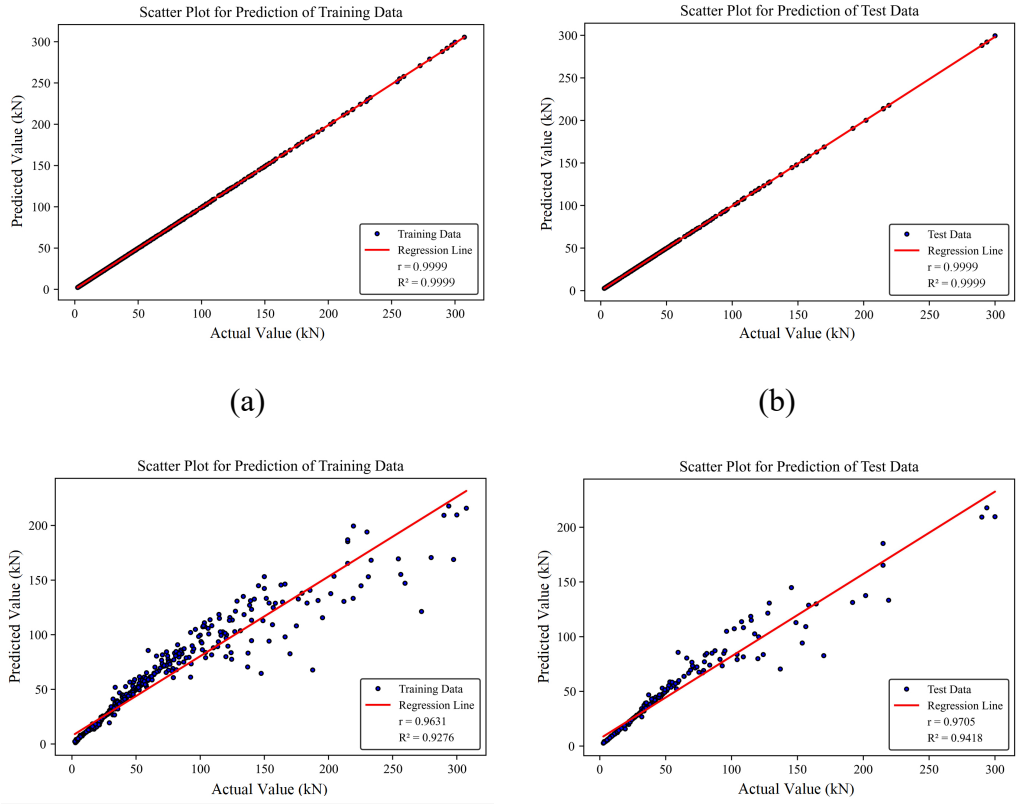

Figure 4.11. The scatter plots for the shear capacity data of walls with elliptic topology are as follows (a) plot for the training dataset of the CNN model with bias, (b) plot for the test dataset of the CNN model with bias, (c) plot for the training dataset of the CNN model without bias, (d) plot for the test dataset of the CNN model without bias.

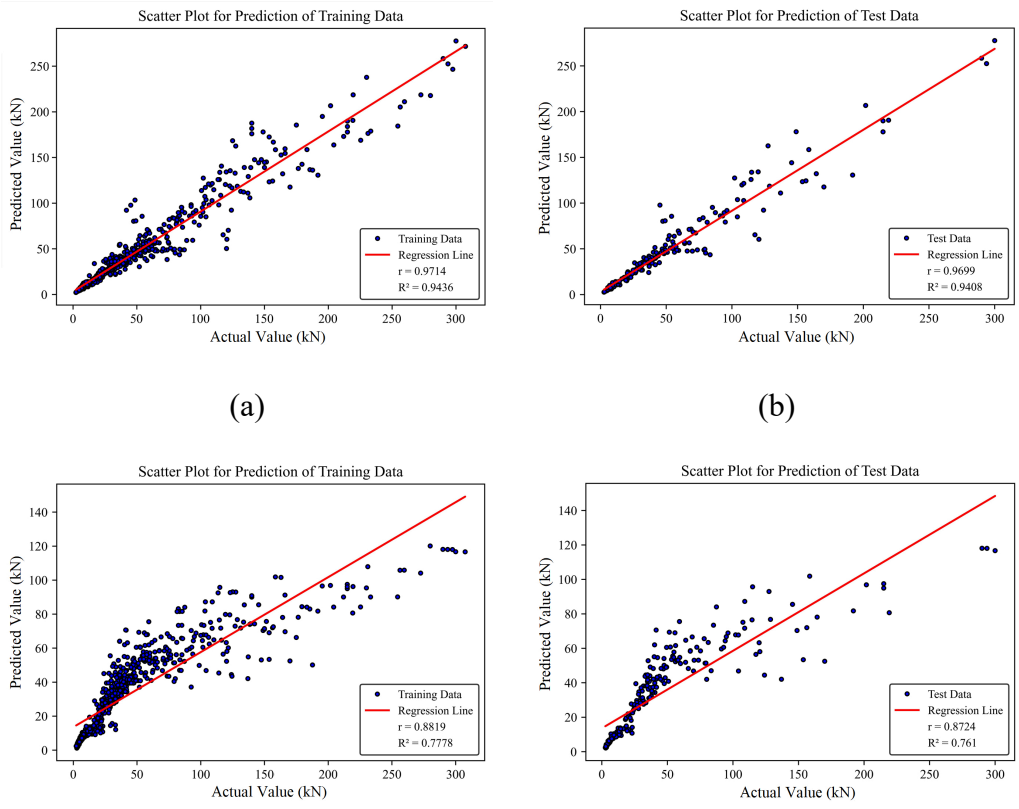

Figure 4.12. The scatter plots for the shear capacity data of walls with elliptic topology are as follows (a) plot for the training dataset of the MLP model with bias, (b) plot for the test dataset of the MLP model with bias, (c) plot for the training dataset of the MLP model without bias, (d) plot for the test dataset of the MLP model without bias.

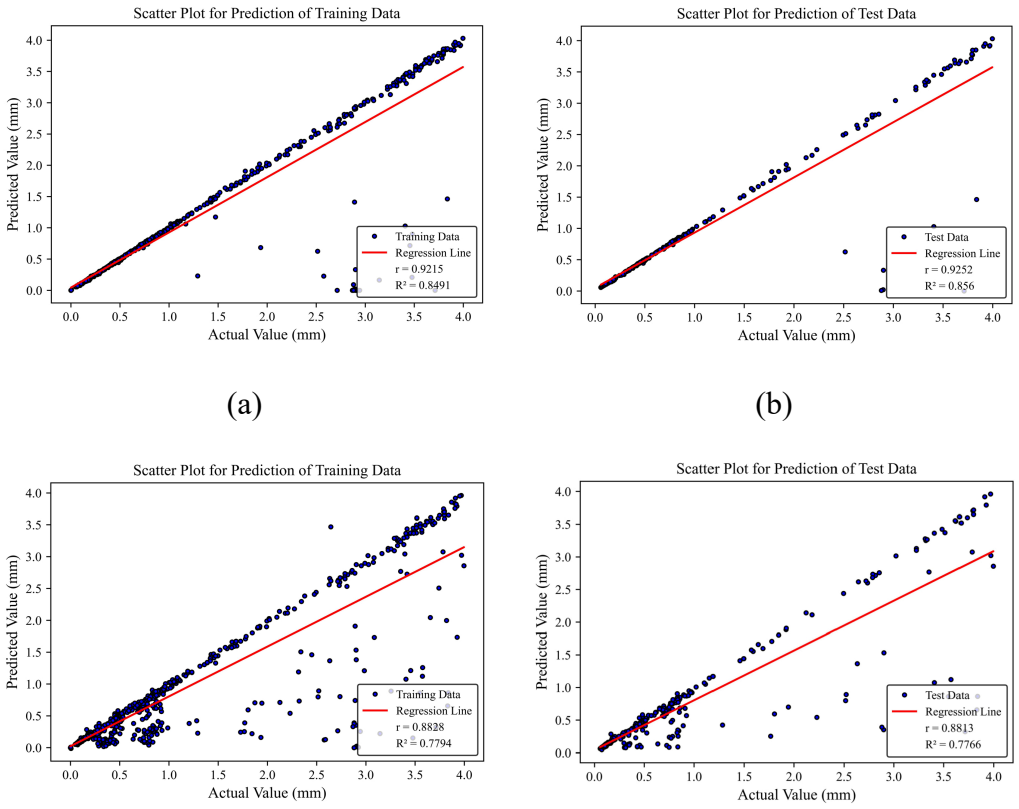

Figure 4.13. The scatter plots for the displacement capacity data of walls with hollow topology are as follows (a) plot for the training dataset of the CNN model with bias, (b) plot for the test dataset of the CNN model with bias, (c) plot for the training dataset of the CNN model without bias, (d) plot for the test dataset of the CNN model without bias.

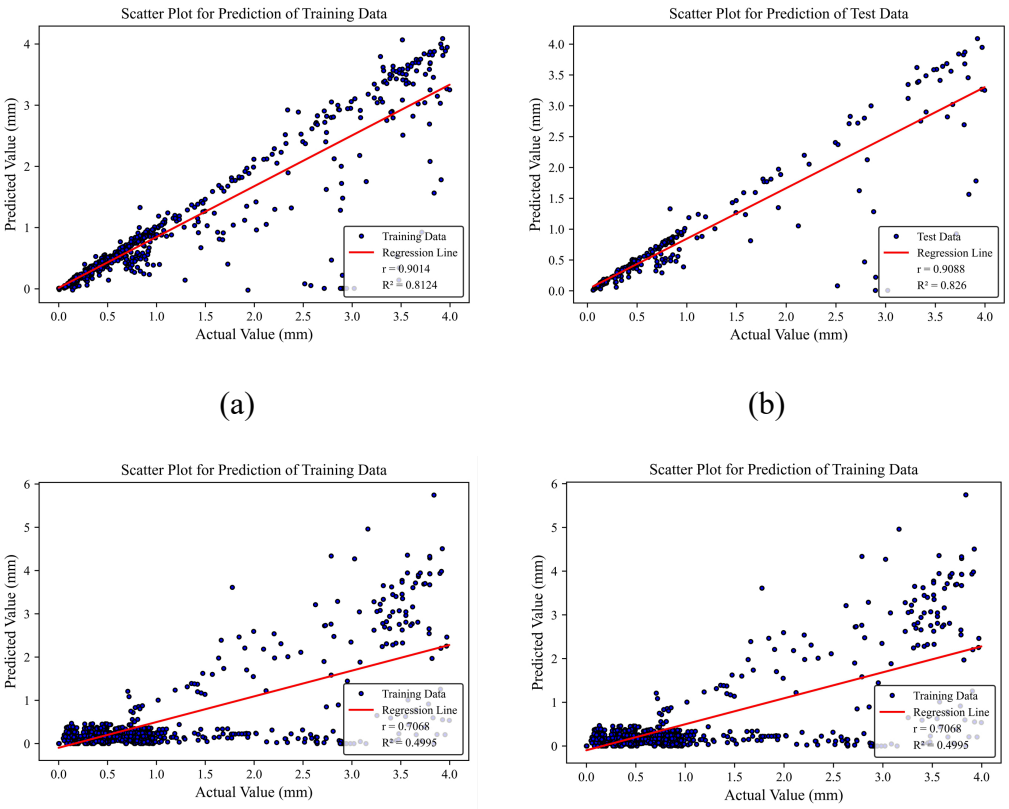

Figure 4.14. The scatter plots for the displacement capacity data of walls with hollow topology are as follows (a) plot for the training dataset of the MLP model with bias, (b) plot for the test dataset of the MLP model with bias, (c) plot for the training dataset of the MLP model without bias, (d) plot for the test dataset of the MLP model without bias.

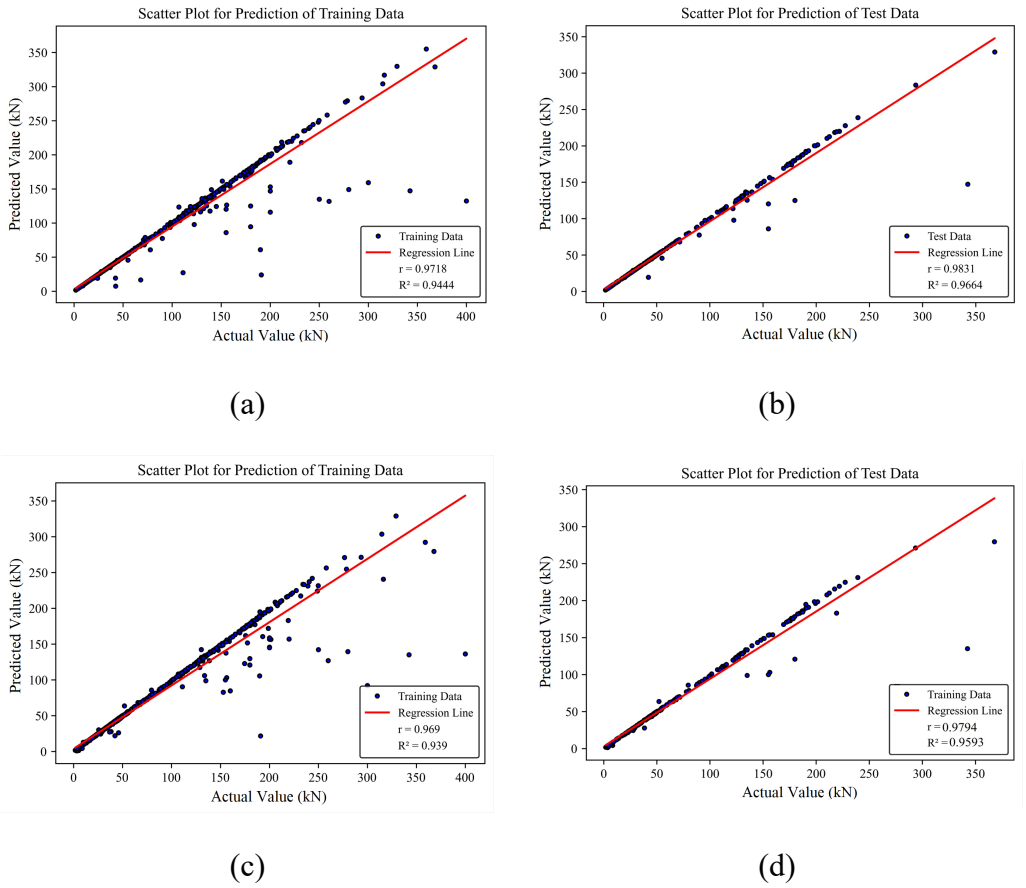

Figure 4.15. The scatter plots for the shear capacity data of walls with hollow topology are as follows (a) plot for the training dataset of the CNN model with bias, (b) plot for the test dataset of the CNN model with bias, (c) plot for the training dataset of the CNN model without bias, (d) plot for the test dataset of the CNN model without bias.

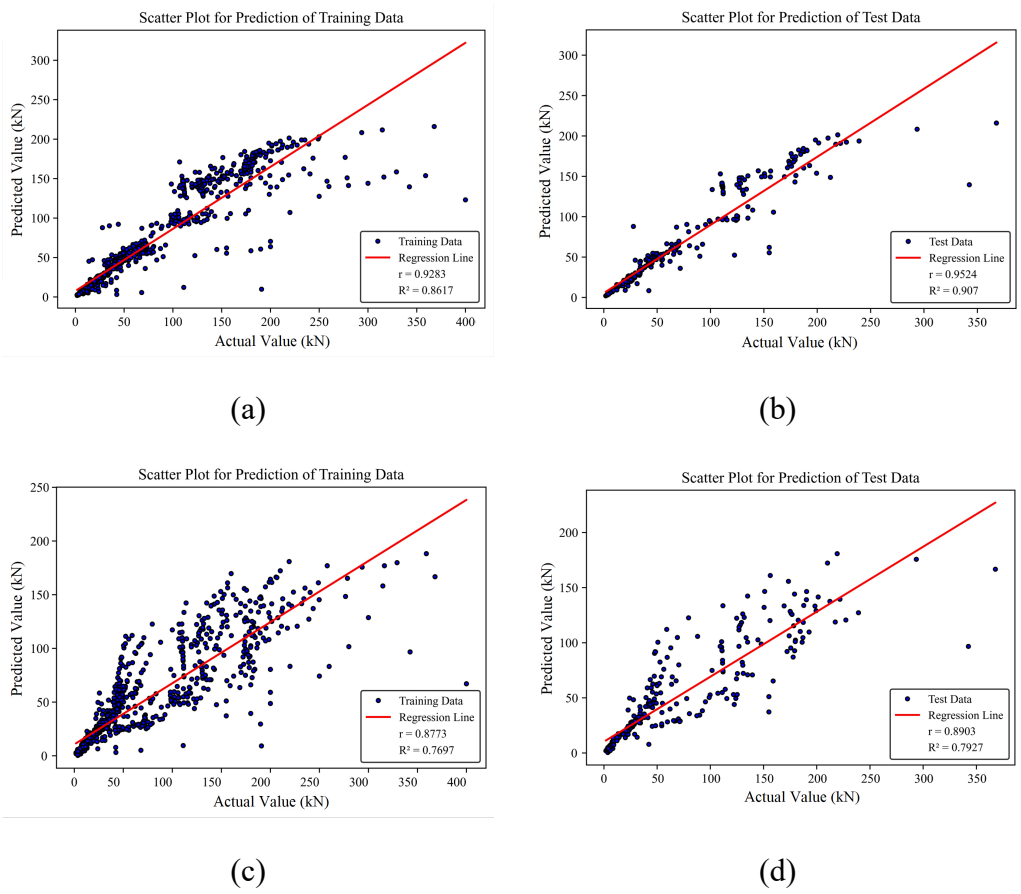

Figure 4.16. The scatter plots for the shear capacity data of walls with hollow topology are as follows (a) plot for the training dataset of the MLP model with bias, (b) plot for the test dataset of the MLP model with bias, (c) plot for the training dataset of the MLP model without bias, (d) plot for the test dataset of the MLP model without bias.

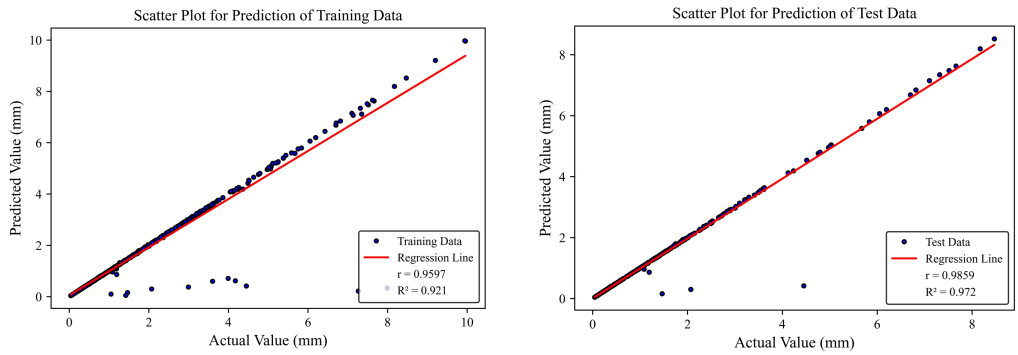

(a)

(b)

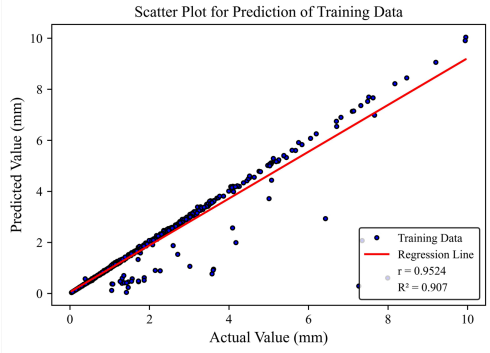

(c)

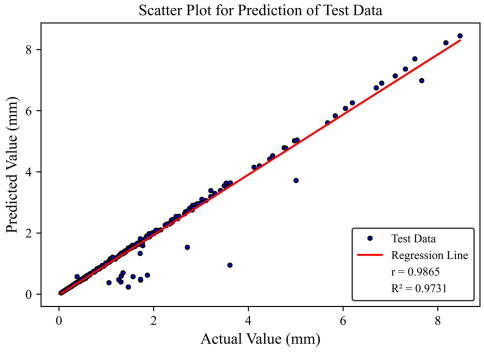

(d)

Figure 4.17. The scatter plots for the displacement capacity data of walls with lattice topology are as follows (a) plot for the training dataset of the CNN model with bias, (b) plot for the test dataset of the CNN model with bias, (c) plot for the training dataset of the CNN model without bias, (d) plot for the test dataset of the CNN model without bias.

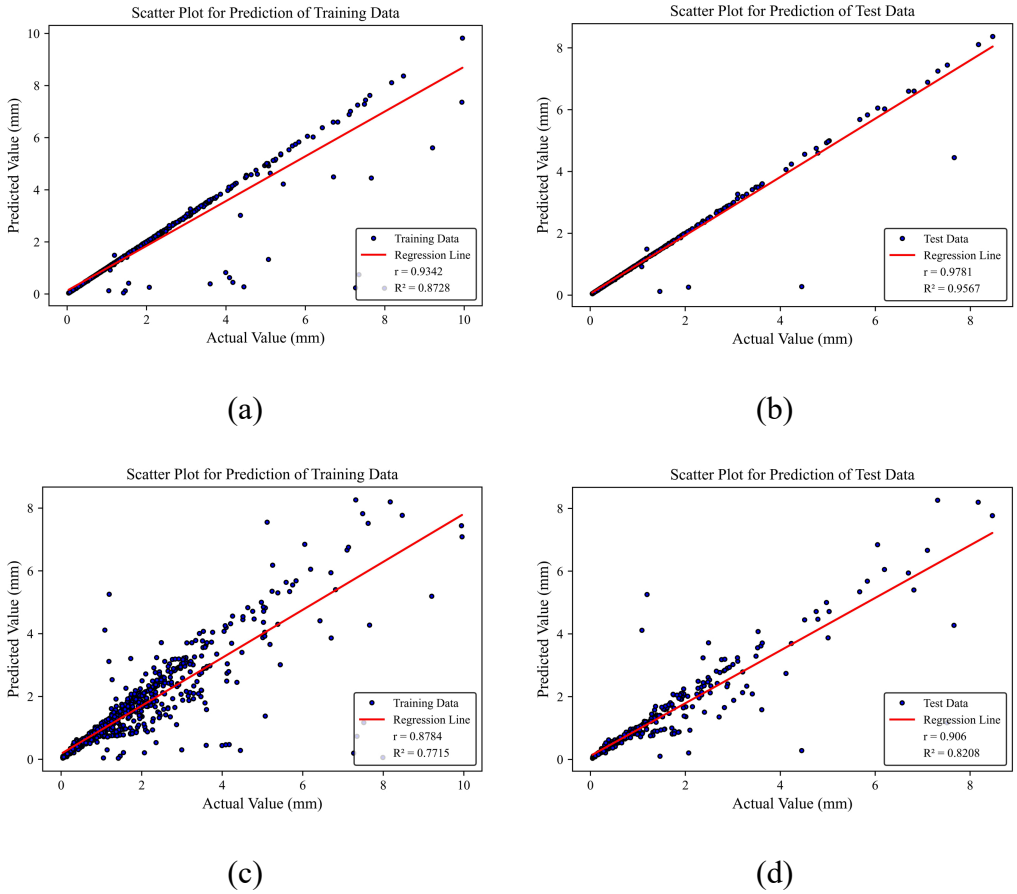

Figure 4.18. The scatter plots for the displacement capacity data of walls with lattice topology are as follows (a) plot for the training dataset of the MLP model with bias, (b) plot for the test dataset of the MLP model with bias, (c) plot for the training dataset of the MLP model without bias, (d) plot for the test dataset of the MLP model without bias.

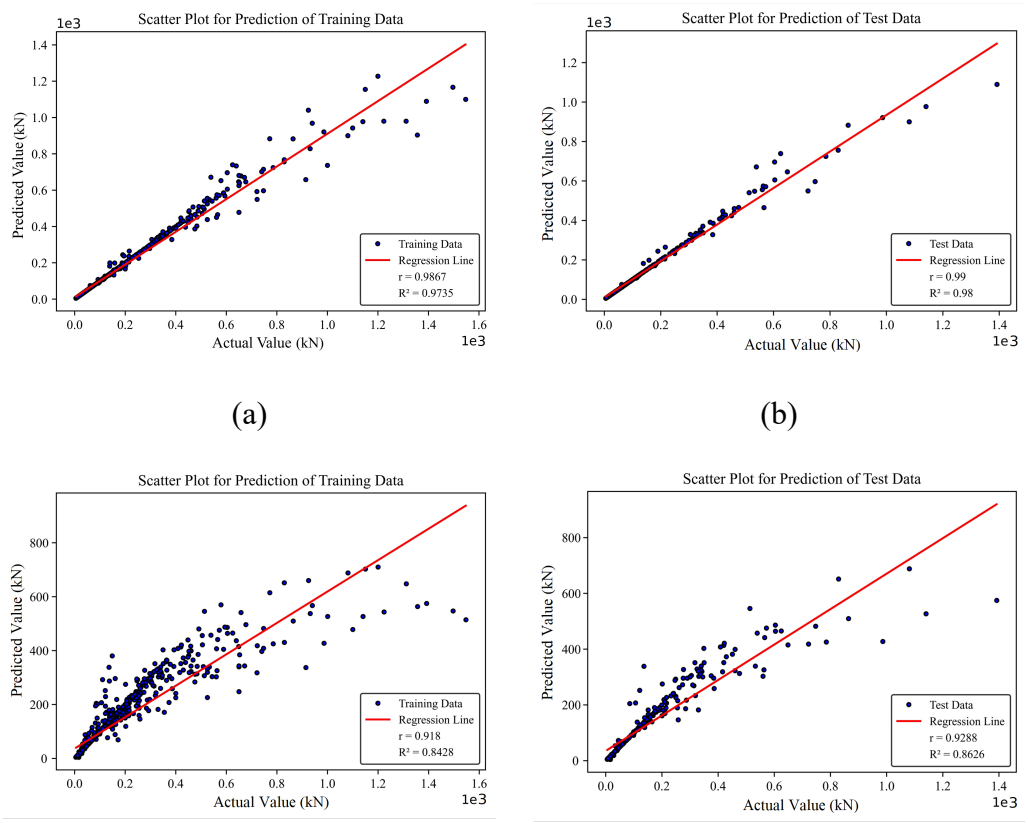

Figure 4.19. The scatter plots for the shear capacity data of walls with lattice topology are as follows (a) plot for the training dataset of the CNN model with bias, (b) plot for the test dataset of the CNN model with bias, (c) plot for the training dataset of the CNN model without bias, (d) plot for the test dataset of the CNN model without bias.

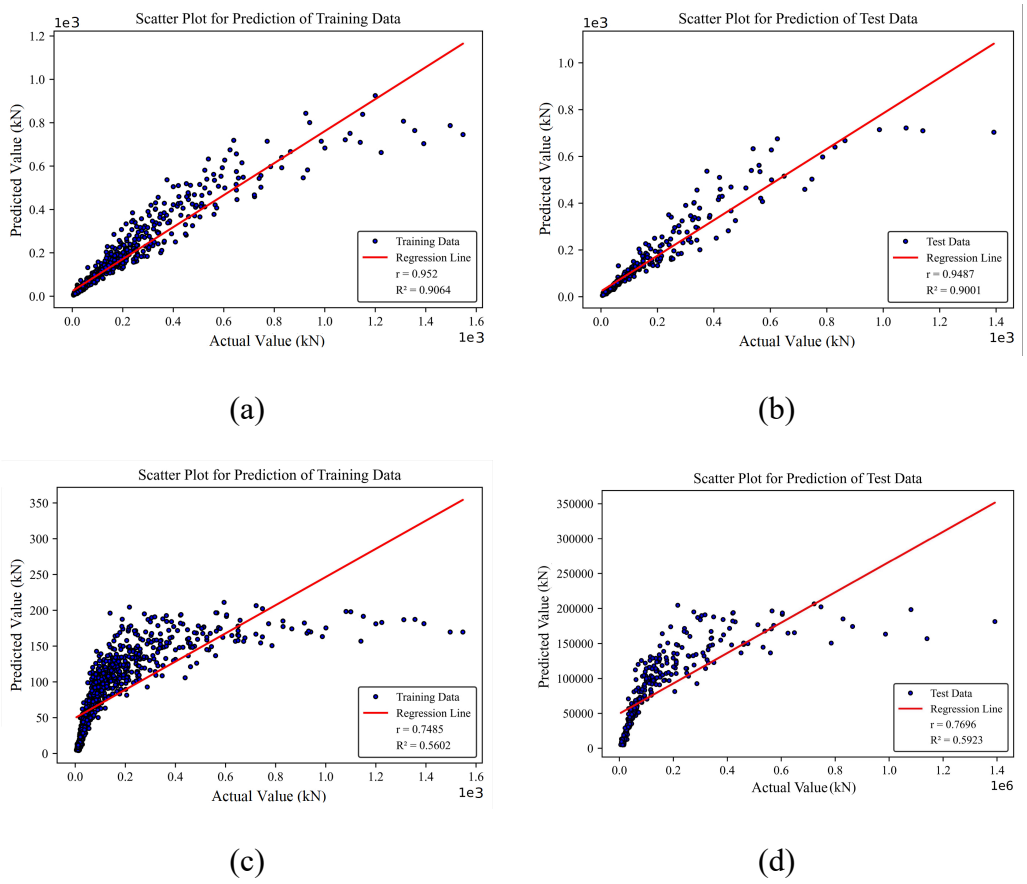

Figure 4.20. The scatter plots for the shear capacity data of walls with lattice topology are as follows (a) plot for the training dataset of the MLP model with bias, (b) plot for the test dataset of the MLP model with bias, (c) plot for the training dataset of the MLP model without bias, (d) plot for the test dataset of the MLP model without bias.

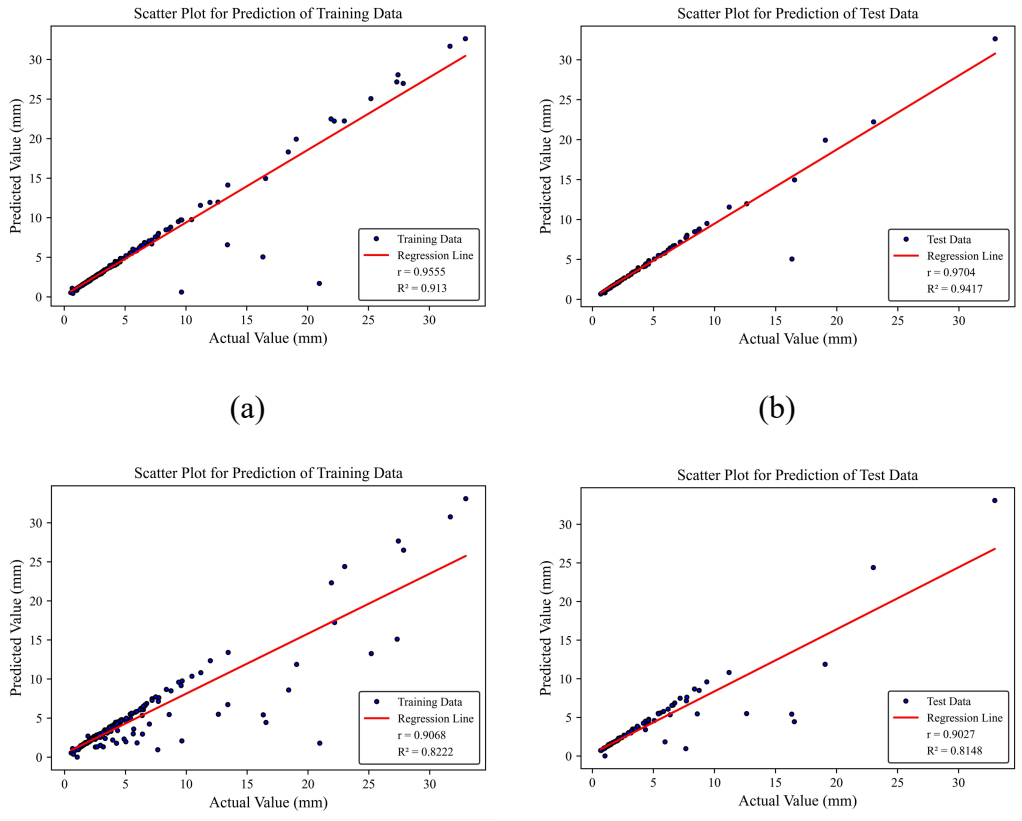

Figure 4.21. The scatter plots for the displacement capacity data of walls with solid topology are as follows (a) plot for the training dataset of the CNN model with bias, (b) plot for the test dataset of the CNN model with bias, (c) plot for the training dataset of the CNN model without bias, (d) plot for the test dataset of the CNN model without bias.

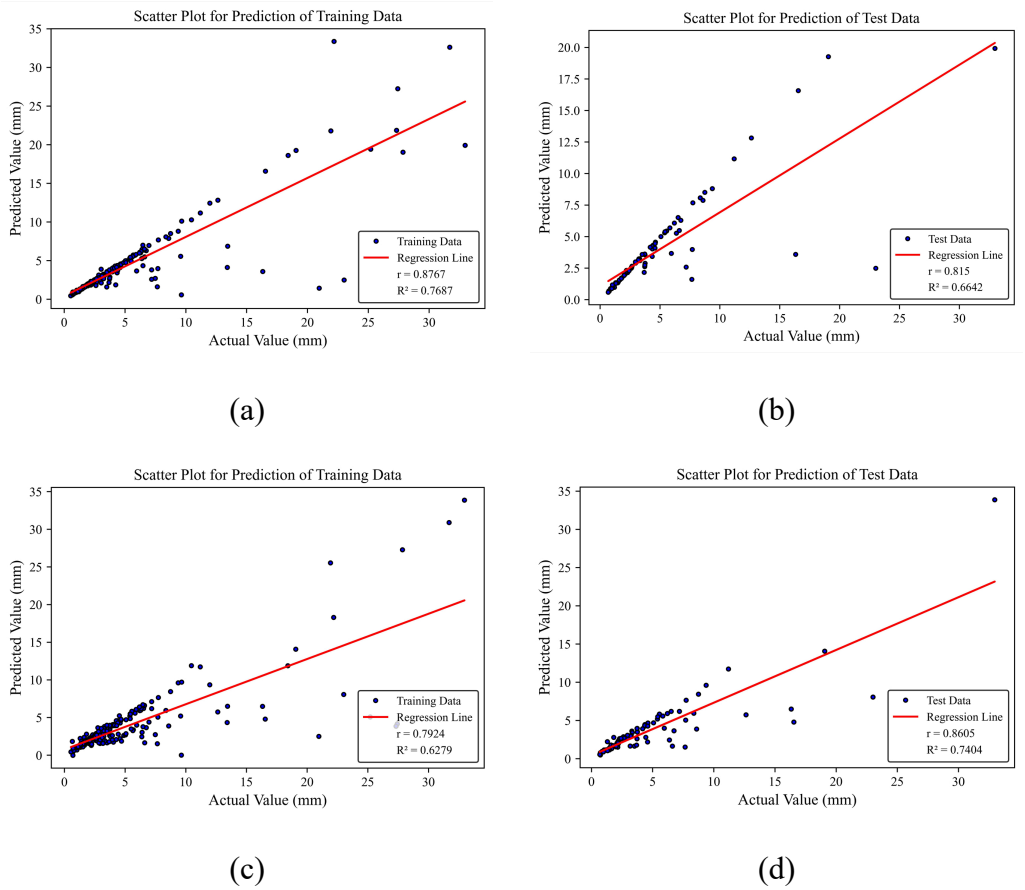

Figure 4.22. The scatter plots for the displacement capacity data of walls with solid topology are as follows (a) plot for the training dataset of the MLP model with bias, (b) plot for the test dataset of the MLP model with bias, (c) plot for the training dataset of the MLP model without bias, (d) plot for the test dataset of the MLP model without bias.

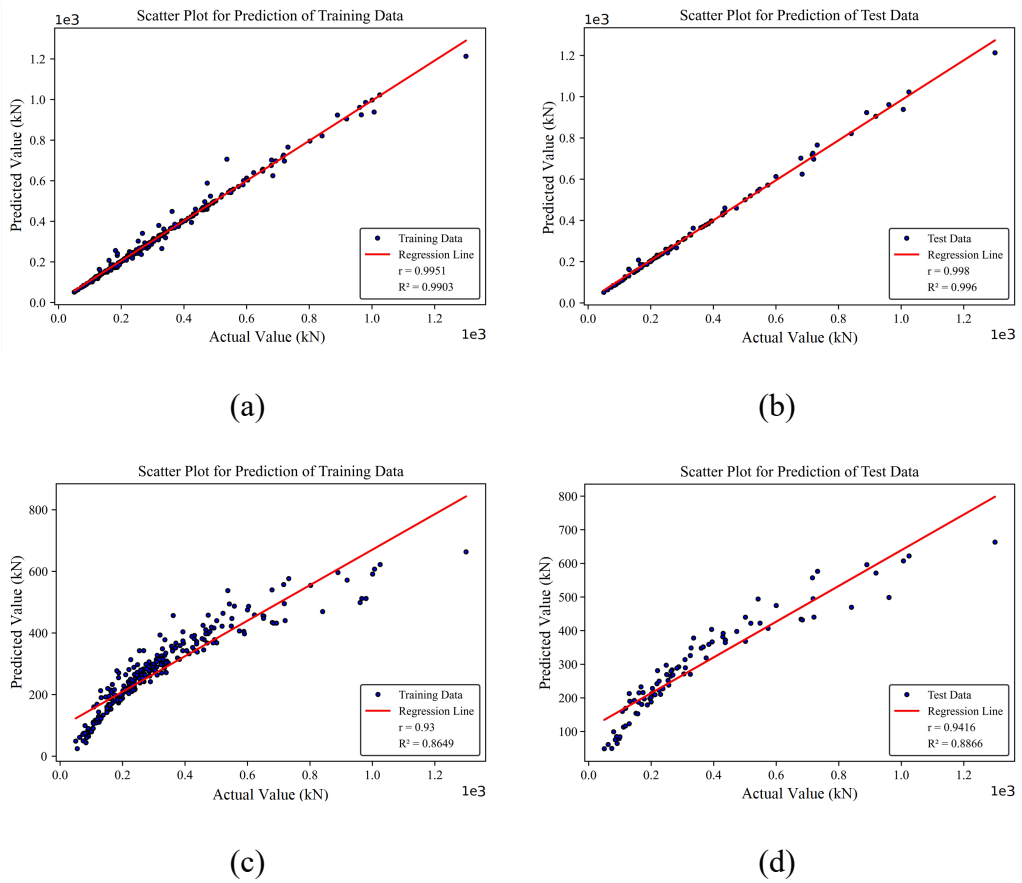

Figure 4.23. The scatter plots for the shear capacity data of walls with solid topology are as follows (a) plot for the training dataset of the CNN model with bias, (b) plot for the test dataset of the CNN model with bias, (c) plot for the training dataset of the CNN model without bias, (d) plot for the test dataset of the CNN model without bias.

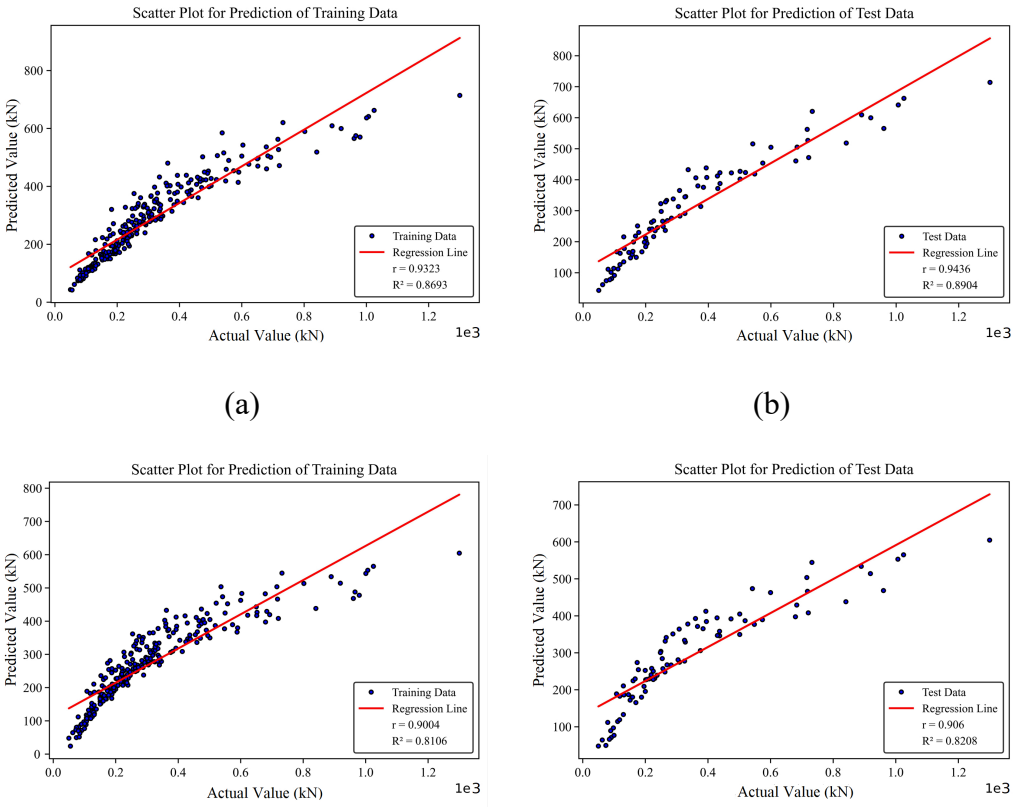

Figure 4.24. The scatter plots for the shear capacity data of walls with solid topology are as follows (a) plot for the training dataset of the MLP model with bias, (b) plot for the test dataset of the MLP model with bias, (c) plot for the training dataset of the MLP model without bias, (d) plot for the test dataset of the MLP model without bias.

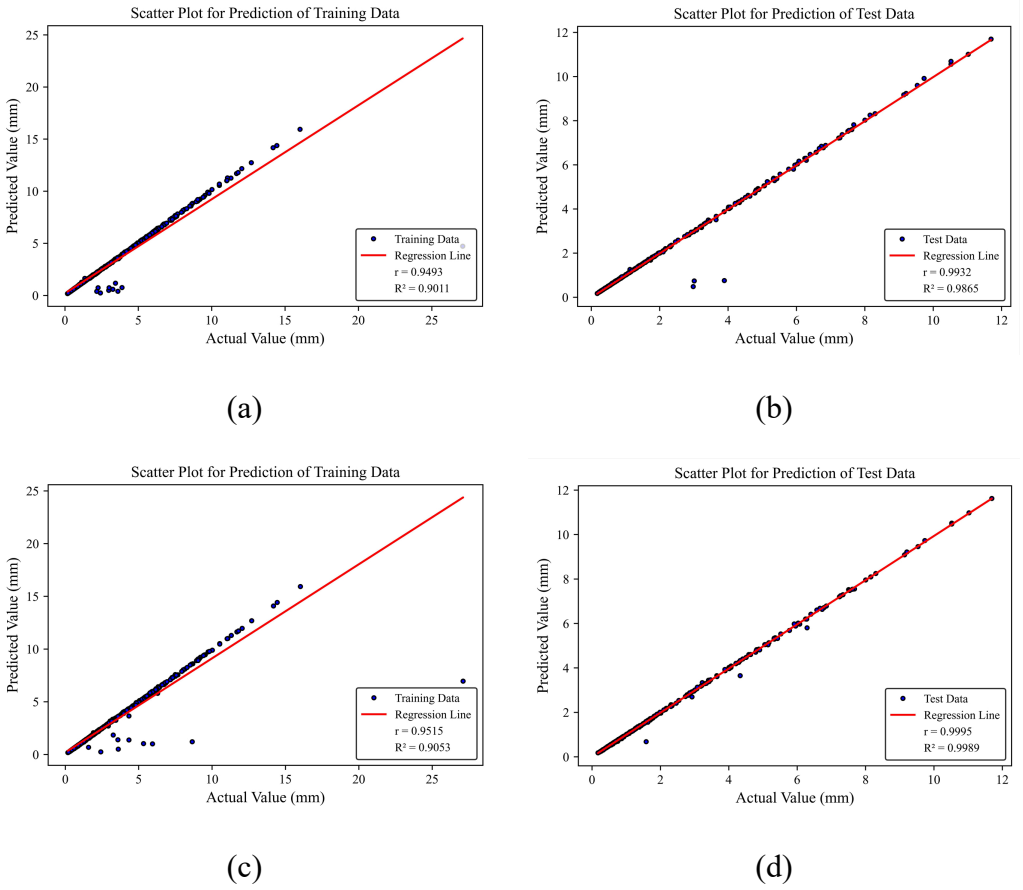

Figure 4.25. The scatter plots for the displacement capacity data of walls with triangular-1 topology are as follows (a) plot for the training dataset of the CNN model with bias, (b) plot for the test dataset of the CNN model with bias, (c) plot for the training dataset of the CNN model without bias, (d) plot for the test dataset of the CNN model without bias.

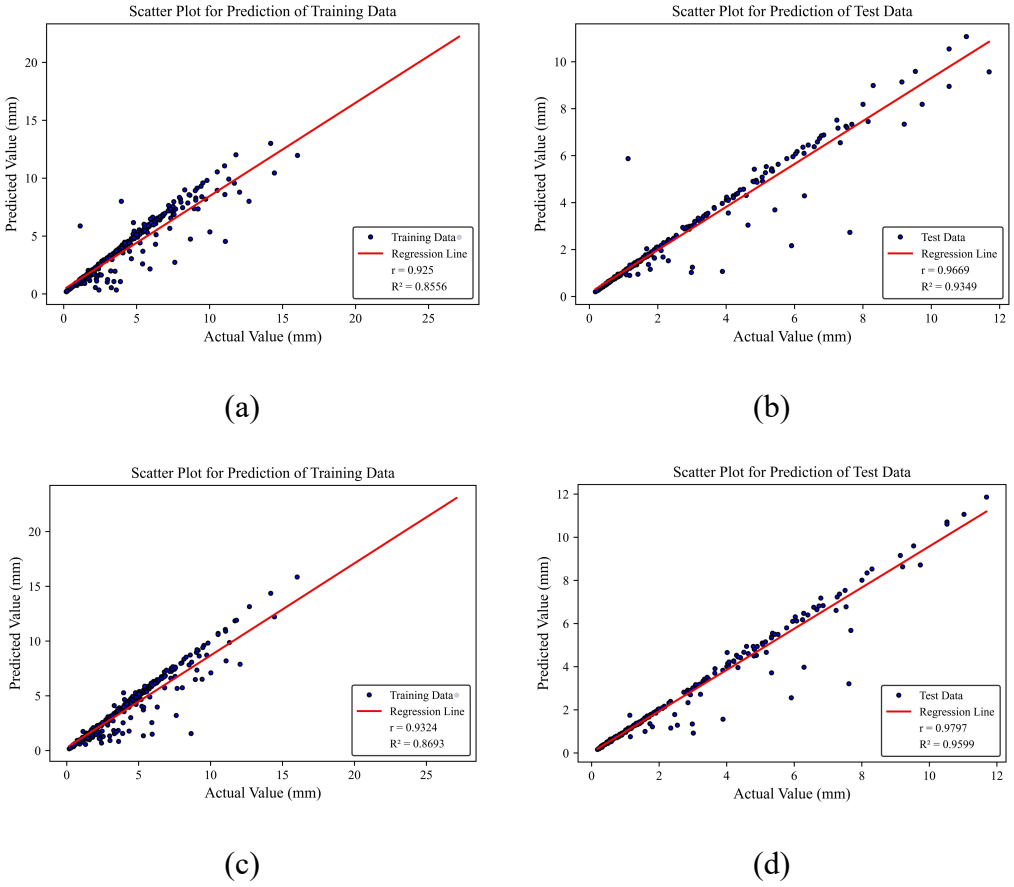

Figure 4.26. The scatter plots for the displacement capacity data of walls with triangular-1 topology are as follows (a) plot for the training dataset of the MLP model with bias, (b) plot for the test dataset of the MLP model with bias, (c) plot for the training dataset of the MLP model without bias, (d) plot for the test dataset of the MLP model without bias.

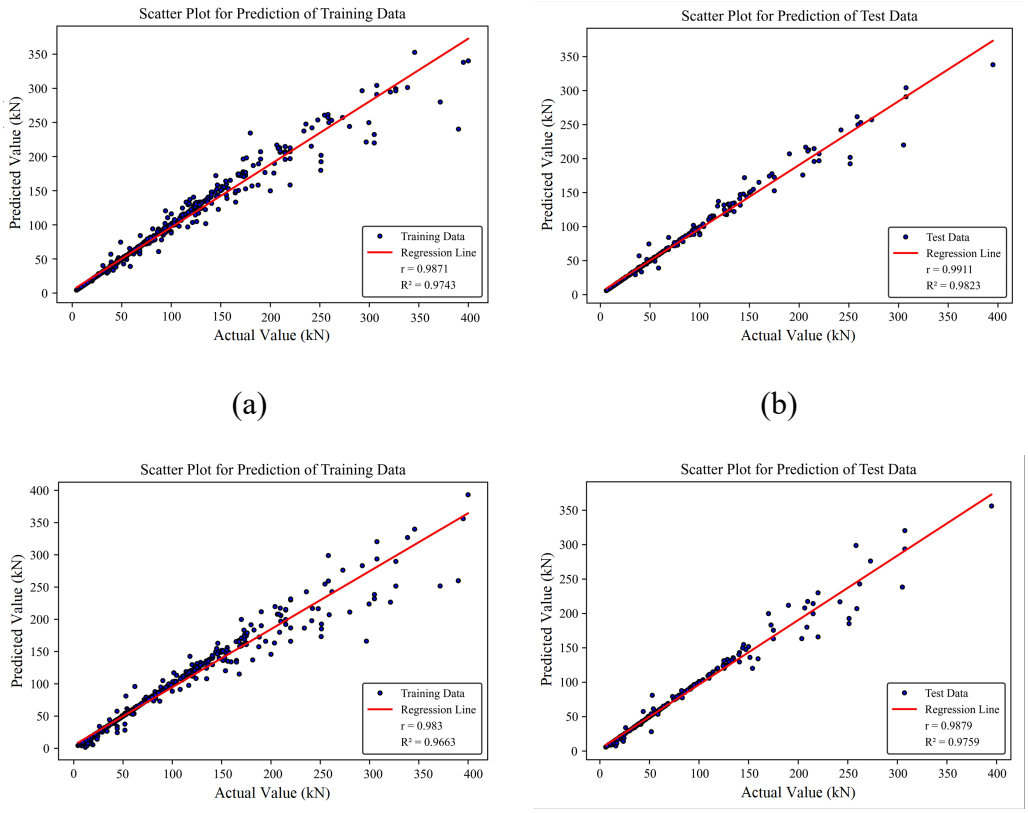

Figure 4.27. The scatter plots for the shear capacity data of walls with triangular-1 topology are as follows (a) plot for the training dataset of the CNN model with bias, (b) plot for the test dataset of the CNN model with bias, (c) plot for the training dataset of the CNN model without bias, (d) plot for the test dataset of the CNN model without bias.

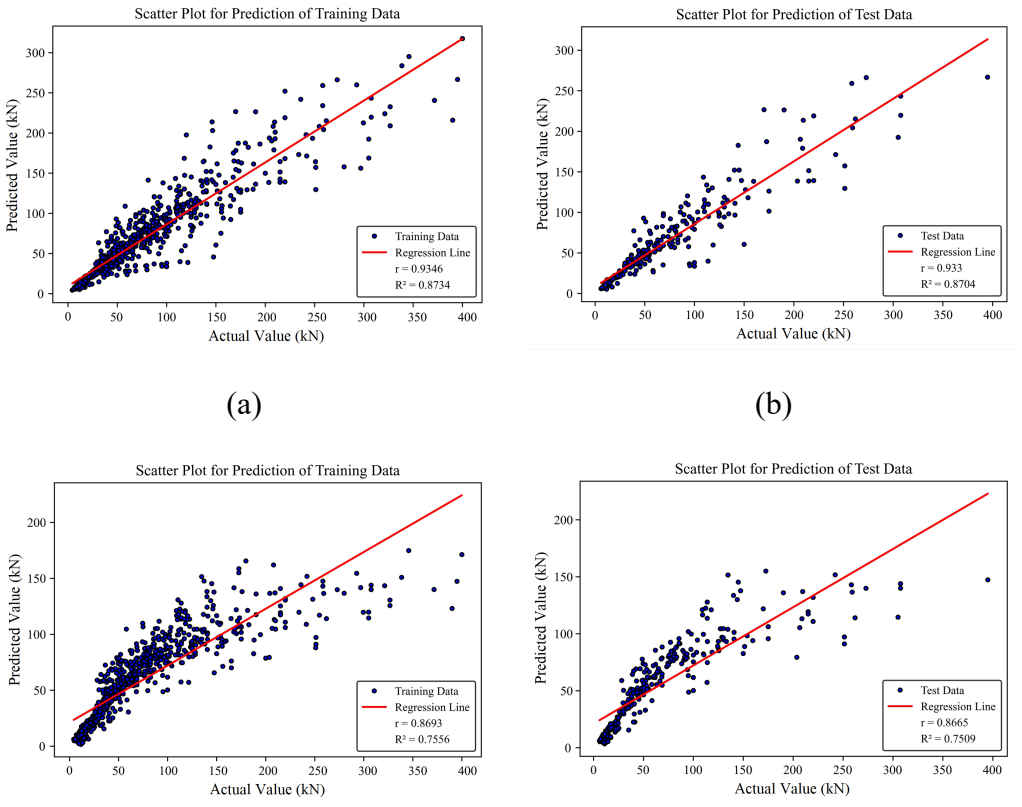

Figure 4.28. The scatter plots for the shear capacity data of walls with triangular-1 topology are as follows (a) plot for the training dataset of the MLP model with bias, (b) plot for the test dataset of the MLP model with bias, (c) plot for the training dataset of the MLP model without bias, (d) plot for the test dataset of the MLP model without bias.

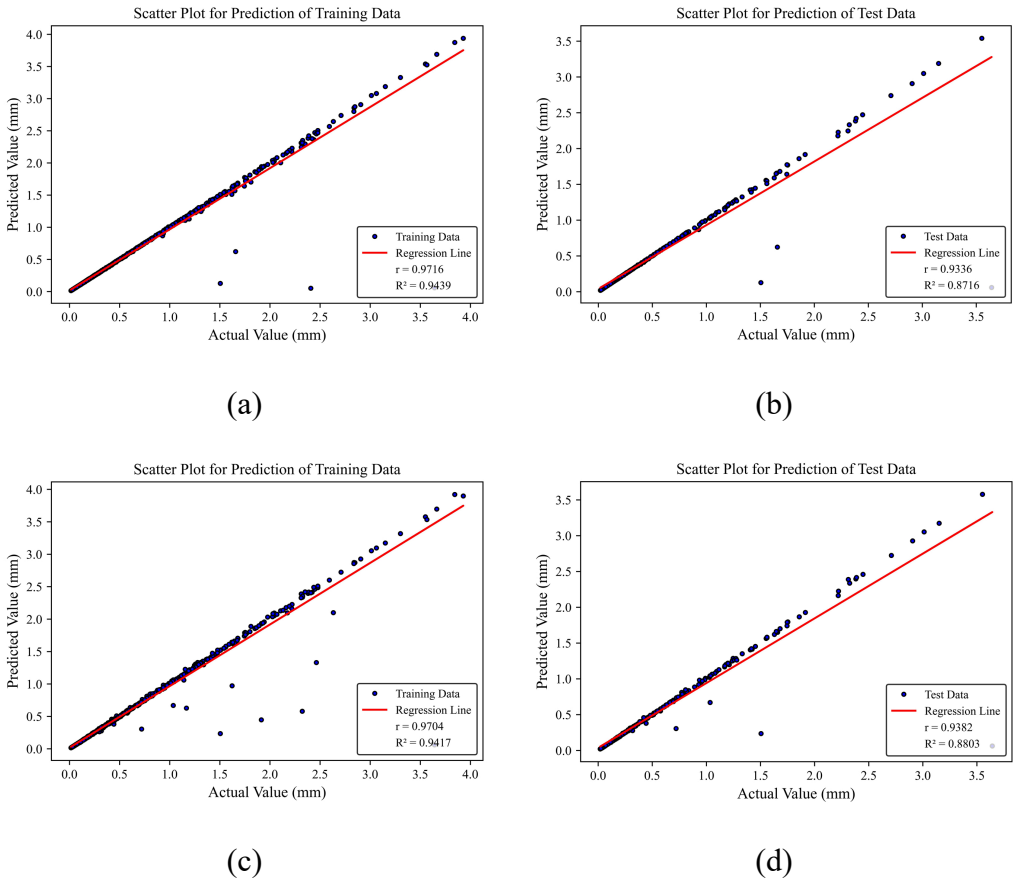

Figure 4.29. The scatter plots for the displacement capacity data of walls with triangular-2 topology are as follows (a) plot for the training dataset of the CNN model with bias, (b) plot for the test dataset of the CNN model with bias, (c) plot for the training dataset of the CNN model without bias, (d) plot for the test dataset of the CNN model without bias.

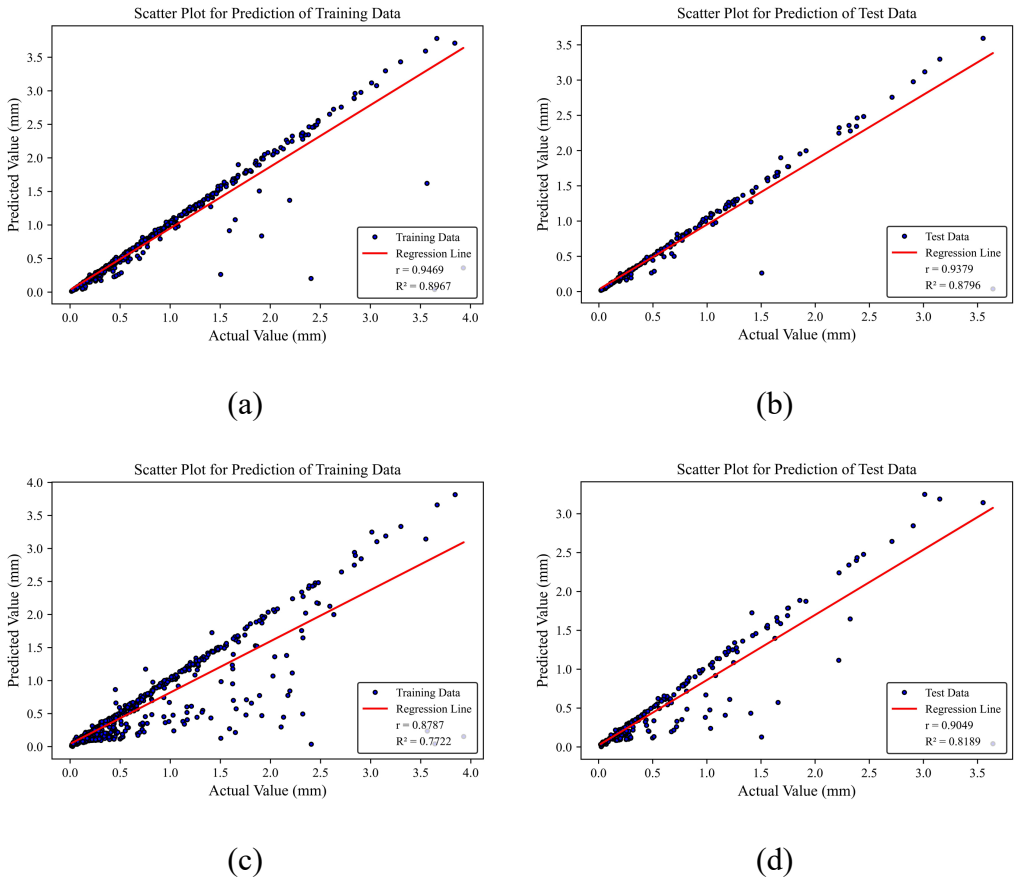

Figure 4.30. The scatter plots for the displacement capacity data of walls with triangular-2 topology are as follows (a) plot for the training dataset of the MLP model with bias, (b) plot for the test dataset of the MLP model with bias, (c) plot for the training dataset of the MLP model without bias, (d) plot for the test dataset of the MLP model without bias.

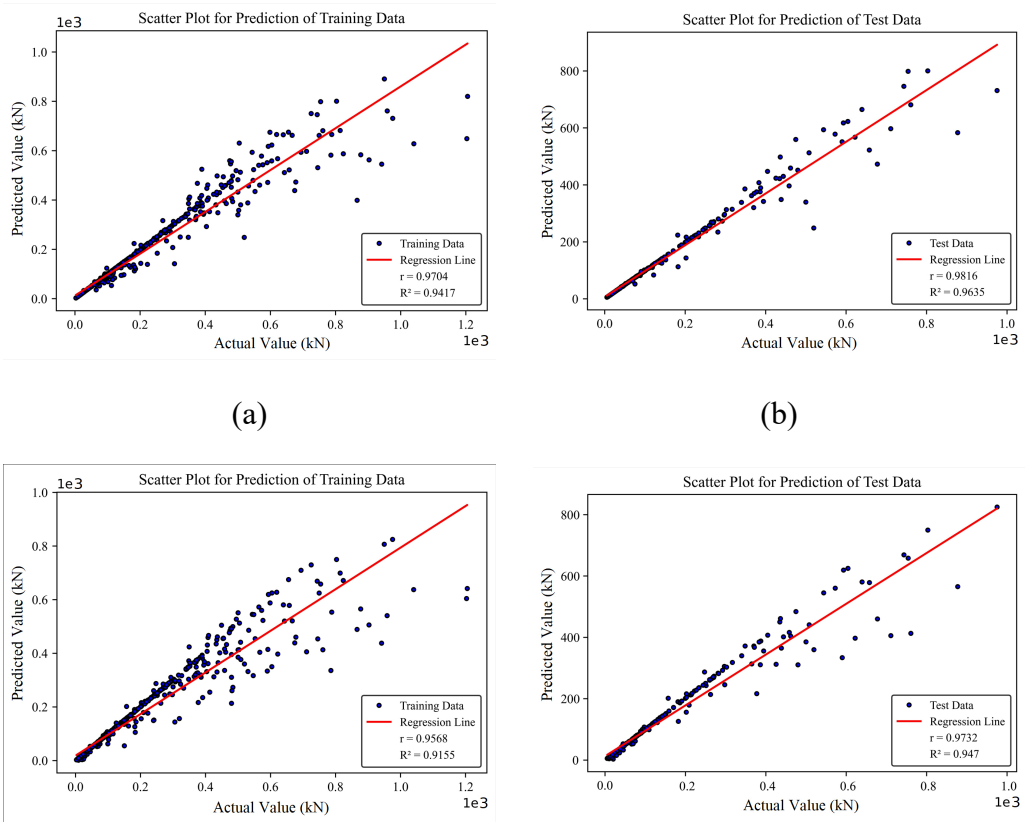

Figure 4.31. The scatter plots for the shear capacity data of walls with triangular-2 topology are as follows (a) plot for the training dataset of the CNN model with bias, (b) plot for the test dataset of the CNN model with bias, (c) plot for the training dataset of the CNN model without bias, (d) plot for the test dataset of the CNN model without bias.

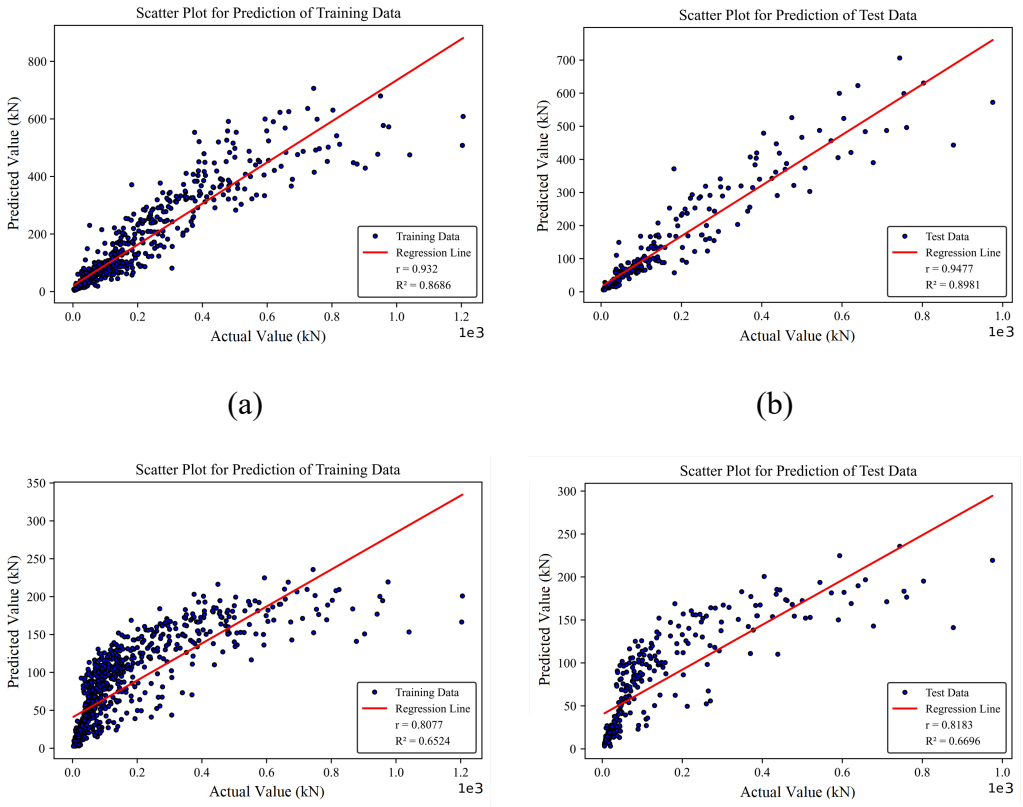

Figure 4.32. The scatter plots for the shear capacity data of walls with triangular-2 topology are as follows (a) plot for the training dataset of the MLP model with bias, (b) plot for the test dataset of the MLP model with bias, (c) plot for the training dataset of the MLP model without bias, (d) plot for the test dataset of the MLP model without bias.

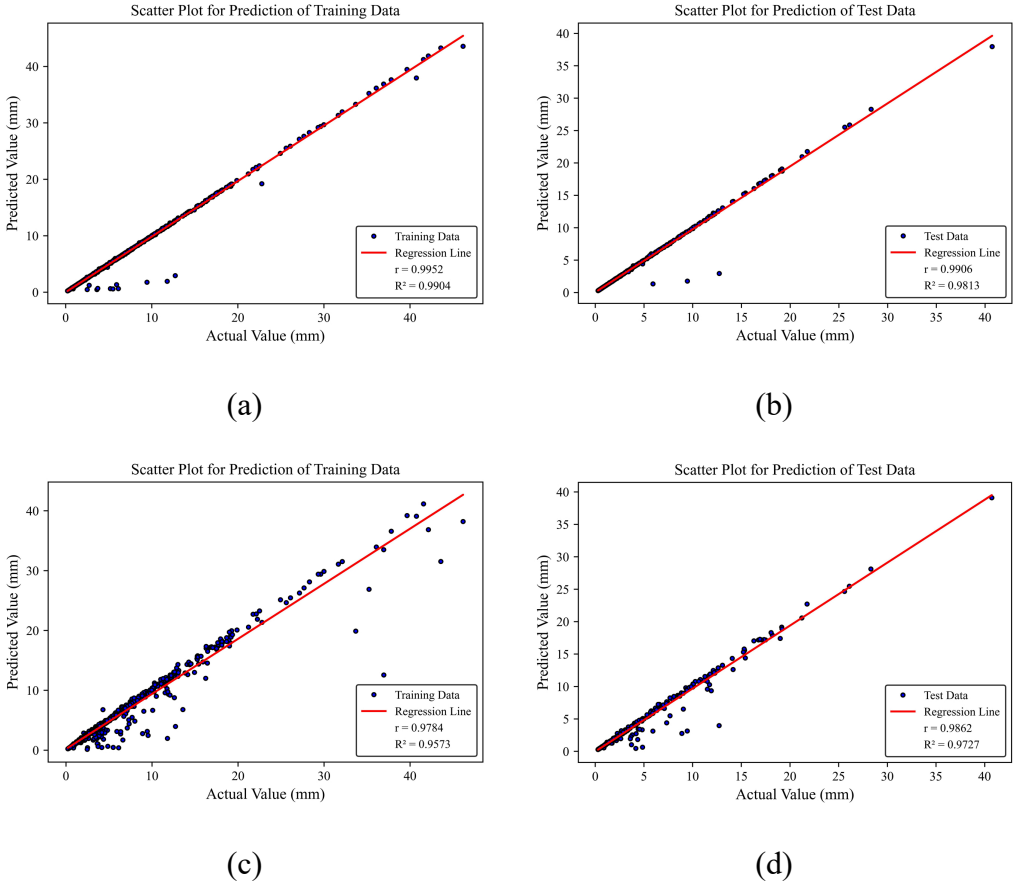

Figure 4.33. The scatter plots for the displacement capacity data of walls with truss topology are as follows (a) plot for the training dataset of the CNN model with bias, (b) plot for the test dataset of the CNN model with bias, (c) plot for the training dataset of the CNN model without bias, (d) plot for the test dataset of the CNN model without bias.

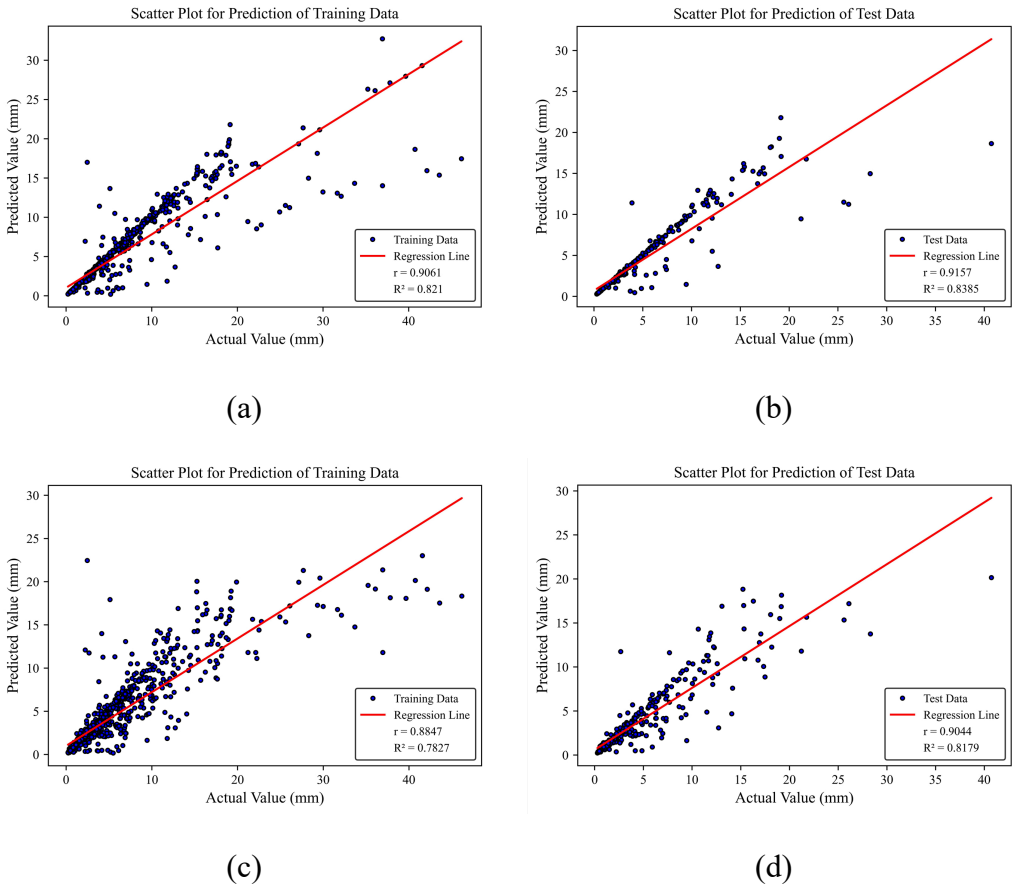

Figure 4.34. The scatter plots for the displacement capacity data of walls with truss topology are as follows (a) plot for the training dataset of the MLP model with bias, (b) plot for the test dataset of the MLP model with bias, (c) plot for the training dataset of the MLP model without bias, (d) plot for the test dataset of the MLP model without bias.

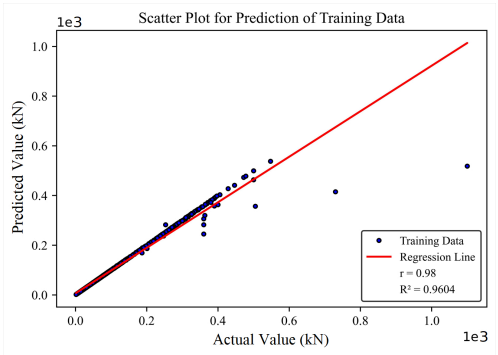

(a)

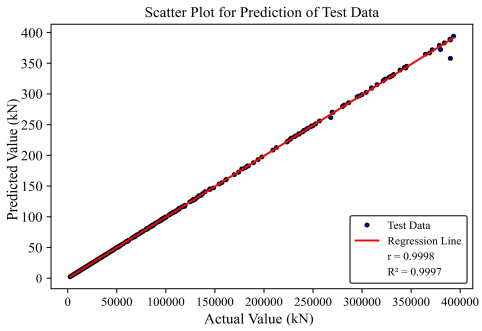

(b)

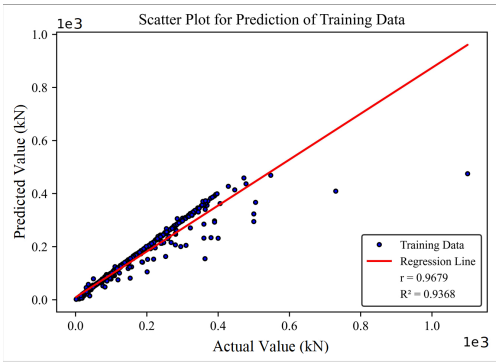

(c)

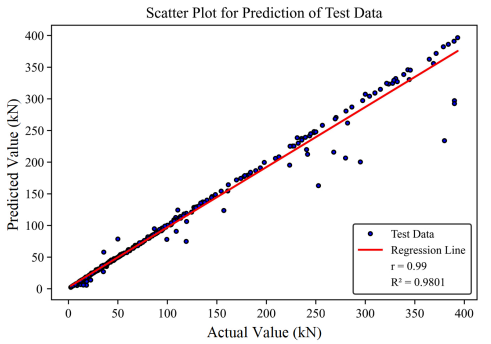

(d)

Figure 4.35. The scatter plots for the shear capacity data of walls with truss topology are as follows (a) plot for the training dataset of the CNN model with bias, (b) plot for the test dataset of the CNN model with bias, (c) plot for the training dataset of the CNN model without bias, (d) plot for the test dataset of the CNN model without bias.

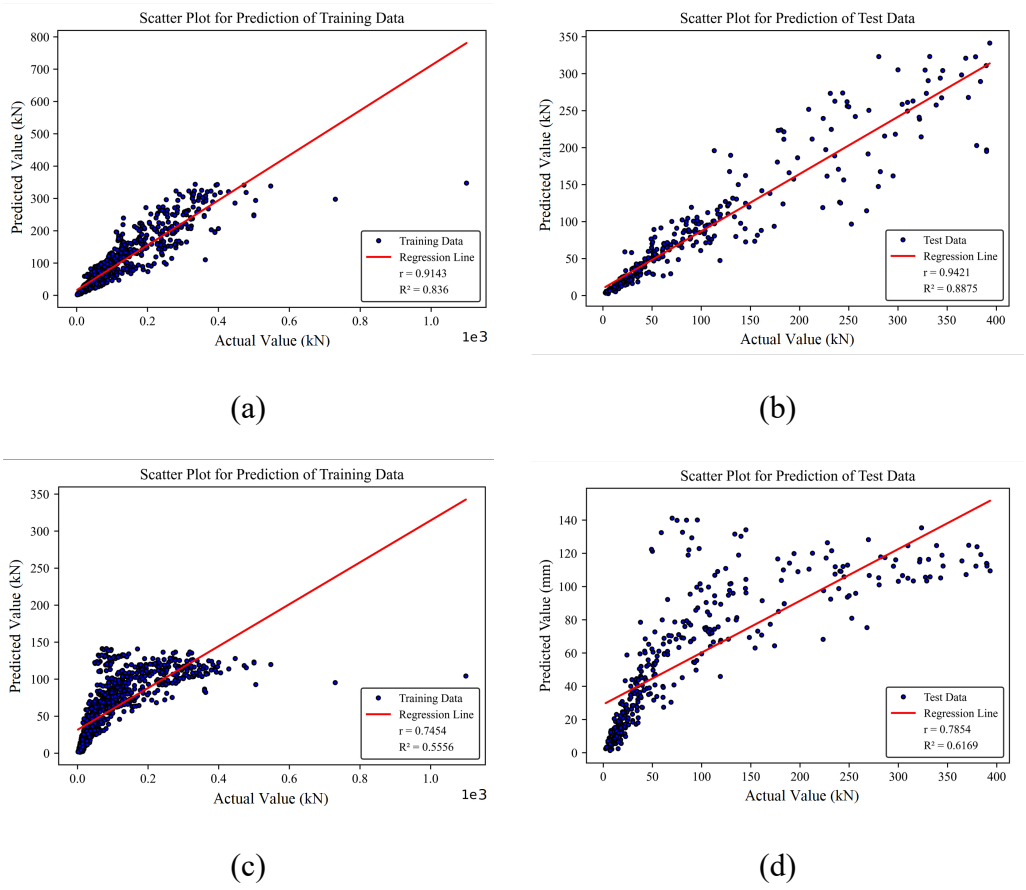

Figure 4.36. The scatter plots for the shear capacity data of walls with truss topology are as follows (a) plot for the training dataset of the MLP model with bias, (b) plot for the test dataset of the MLP model with bias, (c) plot for the training dataset of the MLP model without bias, (d) plot for the test dataset of the MLP model without bias.

The reason why AI algorithms that give the highest correlation coefficient and, therefore, the highest determination coefficient are different is because these ANN models are specific to the dataset. However, largely, both CNN models and models containing bias have higher correlation and determination coefficients for both displacement and shear capacities. Additionally, in some cases, the correlation coefficient of the test dataset has been higher than the correlation coefficient of the training dataset. However, the difference between these two values is very small, and it is thought to be due to the test dataset containing less data than the training dataset.

The correlation and determination coefficients obtained as a result of regression and correlation analyses considering the predicted values and the actual values through AI models are given in Tables 4.1 and 4.2. It is seen from the values in these tables that generally more successful results are obtained for shear capacities compared to displacement capacities. This is thought to be due to the output values in the dataset created for displacement capacities being very small. However, it has been observed that more than half of the CNN models with a bias for shear capacities and more than half of the CNN models with a bias for displacement capacities have correlation coefficients higher than 0.95 and determination coefficients higher than 0.90. This also indicates that the predictions made with these models are highly accurate and have a good distribution.

Table 4.1. Correlation coefficients obtained as a result of regression and correlation analyses.

Wall Type	Data Type	Correlation Coefficient							
		Training Dataset	Test Dataset	Training Dataset	Test Dataset	Training Dataset	Test Dataset	Training Dataset	Test Dataset
Arch Wall	Displacement Capacity	0.9831	0.9999	0.9342	0.9926	0.8784	0.9145	0.7350	0.7306
	Shear Capacity	0.9949	0.9897	0.9291	0.9024	0.9691	0.9685	0.8408	0.8473
Cellular Wall	Displacement Capacity	0.9472	0.9513	0.8783	0.8642	0.7324	0.7403	0.6884	0.7763
	Shear Capacity	0.9942	0.9962	0.9555	0.9587	0.8917	0.8884	0.8136	0.7972
Elliptic Wall	Displacement Capacity	0.9353	0.9719	0.9313	0.9651	0.9095	0.9688	0.7664	0.8368
	Shear Capacity	0.9999	0.9999	0.9631	0.9705	0.9714	0.9699	0.8819	0.8724
Hollow Wall	Displacement Capacity	0.9215	0.9252	0.8828	0.8813	0.9014	0.9088	0.7068	0.7068
	Shear Capacity	0.9718	0.9831	0.9690	0.9794	0.9283	0.9524	0.8773	0.8903

Lattice Wall	Displacement Capacity	0.9597	0.9859	0.9524	0.9865	0.9342	0.9781	0.8784	0.9060
	Shear Capacity	0.9867	0.9900	0.9180	0.9288	0.9520	0.9487	0.7485	0.7696
Solid Wall	Displacement Capacity	0.9555	0.9704	0.9068	0.9027	0.8767	0.8150	0.7924	0.8606
	Shear Capacity	0.9951	0.9980	0.9300	0.9416	0.9323	0.9436	0.9004	0.9060
Triangular - 1 Wall	Displacement Capacity	0.9493	0.9932	0.9515	0.9995	0.9250	0.9669	0.9324	0.9797
	Shear Capacity	0.9871	0.9911	0.9830	0.9879	0.9333	0.9346	0.8693	0.8665
Triangular - 2 Wall	Displacement Capacity	0.9716	0.9336	0.9704	0.9382	0.9469	0.9379	0.8727	0.9049
	Shear Capacity	0.9704	0.9816	0.9568	0.9732	0.9320	0.9477	0.8077	0.8183
Truss Wall	Displacement Capacity	0.9952	0.9906	0.9784	0.9862	0.9061	0.9157	0.8847	0.9044
	Shear Capacity	0.9800	0.9998	0.9679	0.9900	0.9143	0.9421	0.7454	0.7854

Table 4.2. Determination coefficients obtained as a result of regression and correlation analyses.

Wall Type	Data Type	Correlation Coefficient							
		Training Dataset	Test Dataset	Training Dataset	Test Dataset	Training Dataset	Test Dataset	Training Dataset	Test Dataset
Arch Wall	Displacement Capacity	0.9664	0.9999	0.8727	0.9853	0.7716	0.8363	0.5402	0.5338
	Shear Capacity	0.9897	0.9794	0.8632	0.8143	0.9391	0.9380	0.7070	0.7179
Cellular Wall	Displacement Capacity	0.8971	0.9050	0.7696	0.7468	0.5364	0.5480	0.4738	0.6027

	Shear Capacity	0.9885	0.9925	0.9130	0.9191	0.7952	0.7893	0.6619	0.6355
Elliptic Wall	Displacement Capacity	0.8747	0.9447	0.8673	0.9314	0.8272	0.9385	0.5874	0.7002
	Shear Capacity	0.9999	0.9999	0.9276	0.9418	0.9436	0.9408	0.7778	0.7610
Hollow Wall	Displacement Capacity	0.8491	0.8560	0.7794	0.7766	0.8124	0.8260	0.4995	0.4995
	Shear Capacity	0.9444	0.9664	0.9390	0.9593	0.8617	0.9070	0.7697	0.7927
Lattice Wall	Displacement Capacity	0.9210	0.9720	0.9070	0.9731	0.8728	0.9567	0.7715	0.8208
	Shear Capacity	0.9735	0.9800	0.8428	0.8626	0.9064	0.9001	0.5602	0.5923
Solid Wall	Displacement Capacity	0.9130	0.9417	0.8222	0.8148	0.7687	0.6642	0.6279	0.7404
	Shear Capacity	0.9903	0.9960	0.8649	0.8866	0.8693	0.8904	0.8106	0.8208
Triangular - 1 Wall	Displacement Capacity	0.9011	0.9865	0.9053	0.9989	0.8556	0.9349	0.8693	0.9599
	Shear Capacity	0.9743	0.9823	0.9663	0.9759	0.8704	0.8734	0.7556	0.7509
Triangular - 2 Wall	Displacement Capacity	0.9439	0.8716	0.9417	0.8803	0.8967	0.8796	0.7722	0.8189
	Shear Capacity	0.9417	0.9635	0.9155	0.9470	0.8686	0.8981	0.6524	0.6696
Truss Wall	Displacement Capacity	0.9904	0.9813	0.9573	0.9727	0.8210	0.8385	0.7827	0.8179
	Shear Capacity	0.9604	0.9997	0.9368	0.9801	0.8360	0.8875	0.5556	0.6169

For shear capacities, in MLP models with bias, the correlation coefficient is above 0.9 in all walls except the cellular wall, and the determination coefficient is above 0.8 in all walls except the cellular wall. Although these values are not perfect, they can be

considered successful. The same applies to the displacement capacities of almost all walls. However, in the displacement capacities of cellular walls, the correlation coefficient value for MLP models with bias is reduced to 0.7324, and the determination coefficient value is reduced to 0.5364. This means that the predictions for these walls have low accuracy and a poor distribution. A similar situation applies to walls with a solid topology in the test dataset. In most MLP models without bias, the correlation coefficient is below 0.85, and the determination coefficient is below 0.75. This indicates that MLP models without bias provide results with low accuracy and a poor distribution for the regression problem addressed in this study. Additionally, from Tables 4.1 and 4.2, it can be seen that predictions made with models including bias have higher accuracy and less deviation.

When selecting the optimum parameters for the created models, the number of parameters that the models have is given in Table 4.3. According to this table, for displacement capacities, the CNN model without bias has more parameters than the CNN model with bias for two out of nine different wall topologies. Similarly, for three out of nine different wall topologies, the MLP model without bias has more parameters than the MLP model with bias. It is also seen that all MLP models have fewer parameters than all CNN models.

Table 4.3. The number of parameters that the created models have, in case the optimum parameters are selected.

Wall Type	Model architecture	Mean absolute percentage error	
		Training	Validation
Arch	1D CNN with bias	164337	60670705
	1D CNN without bias	3499249	5379761
	MLP with bias	4779	28587
	MLP without bias	149	21429
Cellular	1D CNN with bias	96409	22751217
	1D CNN without bias	29500209	7001185
	MLP with bias	427	25003

	MLP without bias	1493	12021
Elliptic	1D CNN with bias	1014609	35133521
	1D CNN without bias	8633873	12619345
	MLP with bias	18603	30635
	MLP without bias	373	20309
Hollow	1D CNN with bias	431281	9023233
	1D CNN without bias	12172641	21369441
	MLP with bias	5291	30635
	MLP without bias	2837	27701
Lattice	1D CNN with bias	262081	12735185
	1D CNN without bias	1115841	7308961
	MLP with bias	18603	26795
	MLP without bias	373	28597
Solid	1D CNN with bias	2022145	19814641
	1D CNN without bias	219361	49770625
	MLP with bias	5803	24235
	MLP without bias	17845	22549
Triangular – 1	1D CNN with bias	119441	73912577
	1D CNN without bias	244369	33732289
	MLP with bias	6059	22723
	MLP without bias	23669	26581
Triangular – 2	1D CNN with bias	1858065	7004929
	1D CNN without bias	64993	46215825
	MLP with bias	6059	27563
	MLP without bias	4405	20085
Truss	1D CNN with bias	119441	14610033
	1D CNN without bias	5859724	40840017
	MLP with bias	4011	23467

MLP without bias	1493	27925

For shear capacities, the CNN model without a bias has more parameters than the CNN model with a bias for four out of nine different wall topologies. Similarly, out of nine different wall topologies, the MLP model without bias has more parameters than the MLP model with bias for three topologies. It has been observed that all MLP models have fewer parameters than all CNN models for shear capacities.

When considering all models, it is observed that the ratio of parameters in CNN models with bias to parameters in MLP models with bias ranges from 14 to 3500, while the ratio of parameters in CNN models without bias to parameters in MLP models with bias ranges from 10 to 23500. As can be understood from above, MLP models are much more advantageous in terms of computational cost compared to CNN models. However, as can be seen in Tables 3.6 and 3.8, CNN models provide much higher accuracy than MLP models, and MLP models cannot make predictions with sufficient accuracy. Therefore, it can be said that in terms of performance-computational cost, CNN models are more advantageous than MLP models.

Additionally, out of the 72 models created, only the CNN without bias created for the displacement capacity of the cellular wall has more parameters than the CNN without bias created for the shear capacity. In all other models, the models created for the shear capacity have more parameters than the models created for the displacement capacity. The ratio of the number of parameters in the models created for shear capacities to the number of parameters in the models created for displacement capacities ranges from 1.12 to 712. This situation is thought to be due to the fact that the output values in shear capacity datasets are larger than the output values in displacement capacity datasets, and they have different variances and standard deviation values because the input values in the datasets created for shear capacities are the same but only the output values are different for displacement capacities and shear capacities.

4.2. Comparison of the Shear Capacities Predicted by the AI-Based Design Tool with Shear Capacities Calculated through the Formulas in the FEMA 356

The scatter plots obtained as a result of regression and correlation analyses, considering the values calculated by Equation 3.33, 3.34, and 3.35, minimum shear capacity values for three failure modes, predicted values through AI models, and the actual values are shown in Figures 4.37-4.45, and the correlation and determination coefficients are presented in Table 4.4. These scatter plots were created to illustrate the deviation of the shear capacity values predicted by the AI-based design tool and those calculated using the formulas provided in FEMA 356 from the actual shear capacities. Additionally, they serve to compare the accuracy of the predicted shear capacities through AI-based design tool and calculated shear capacities using the FEMA 356 formulas in estimating the shear capacity of unreinforced 3D-printed concrete walls.

As can be seen from Figures 4.37-4.45 and Table 4.4, as the L/H_{eff} ratio of walls decreases, the governing failure mode for walls becomes a rocking failure. As this ratio increases, the governing failure mode for walls becomes diagonal tension failure. As the characteristic compressive strength of the concrete decreases, the governing failure mode for walls also becomes a rocking failure. As this ratio increases, the governing failure mode for walls becomes diagonal tension failure. In addition, it can be seen that sliding failure is not governing failure mode for any of the walls.

Upon examining the results, it can be observed that the correlation and determination coefficients for the calculated shear capacity values for the governing failure modes determined according to FEMA 356 are between 0.4514 - 0.91333 and 0.2037 - 0.8342 respectively, and the correlation and determination coefficients for the predicted shear capacity values obtained using the AI-based design tool are between 0.9747 - 0.9994 and 0.9501 - 0.9989 respectively. Additionally, it is observed that the correlation and determination coefficients for the shear capacity values determined according to FEMA 356 for walls with hollow topologies are below 0.80 and 0.65, respectively, and these values decrease to 0.4514 and 0.2037 for walls with hollow interior topology. This situation is thought to be because most of the failure in the walls with interior hollow topologies occurs in the local area located around the point where is pushover force

applied and formulas in FEMA 356 cannot simulate this condition properly. Therefore, it can be concluded that the AI-based design tool developed in this study for the shear capacity prediction of walls printed through 3DCP provides higher accuracy than the formulas for calculating the shear capacity of unreinforced masonry walls for in-plane failure modes according to FEMA 356 and AI-based design tool is more advantageous for practical application in the field of 3DCP.

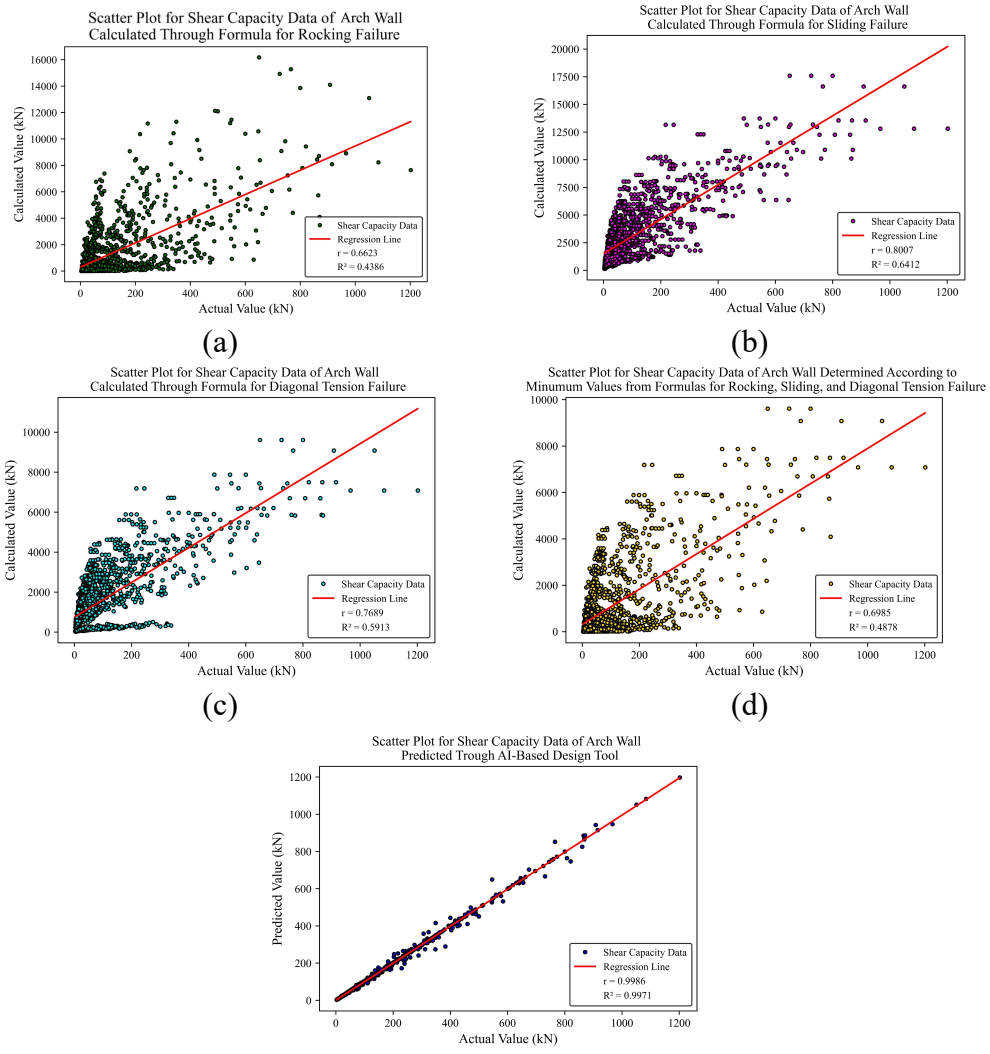

Figure 4.37. The scatter plots for the shear capacity of walls with arch topology are as follows (a) plot for the shear capacity in case of the rocking failure, (b) plot for the shear capacity in case of the sliding failure, (c) plot for the shear capacity in case of the diagonal tension failure, (d) plot for the minimum shear capacity of three failure modes, (e) plot for the shear capacity predicted through AI-based design tool.

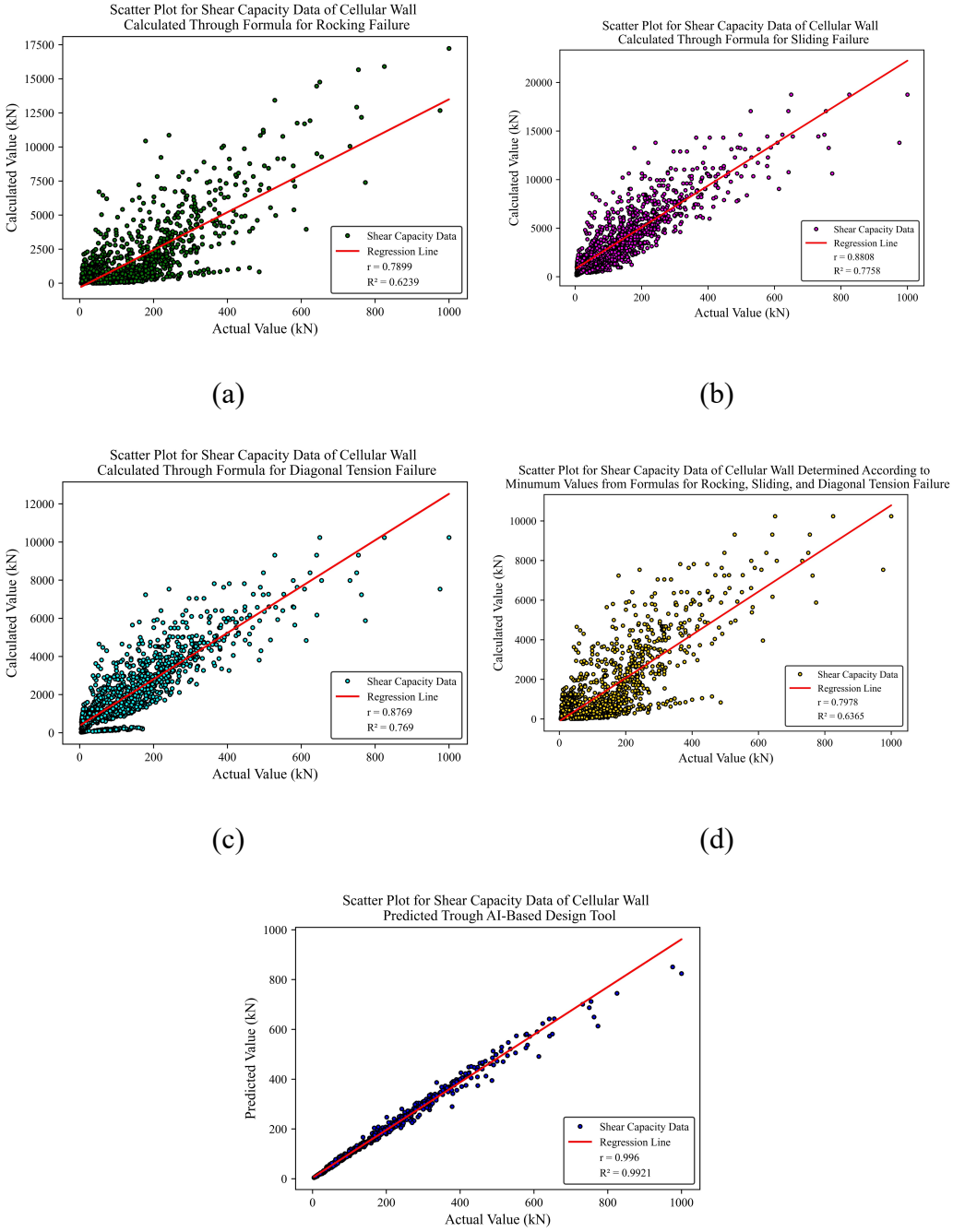

Figure 4.38. The scatter plots for the shear capacity of walls with cellular topology are as follows (a) plot for the shear capacity in case of the rocking failure, (b) plot for the shear capacity in case of the sliding failure, (c) plot for the shear capacity in case of the diagonal tension failure, (d) plot for the minimum shear capacity of three failure modes, (e) plot for the shear capacity predicted through AI-based design tool.

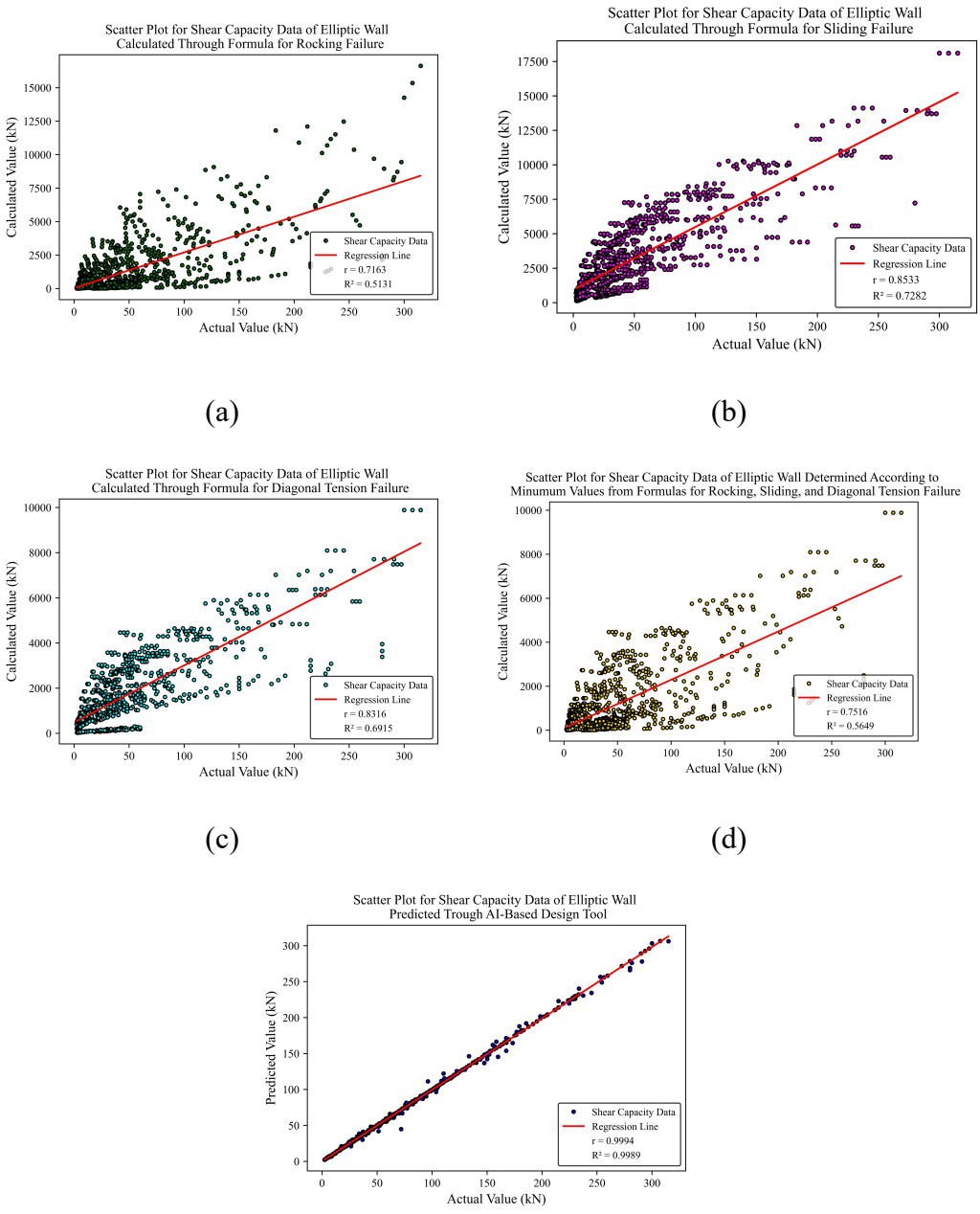

Figure 4.39. The scatter plots for the shear capacity of walls with elliptic topology are as follows (a) plot for the shear capacity in case of the rocking failure, (b) plot for the shear capacity in case of the sliding failure, (c) plot for the shear capacity in case of the diagonal tension failure, (d) plot for the minimum shear capacity of three failure modes, (e) plot for the shear capacity predicted through AI-based design tool.

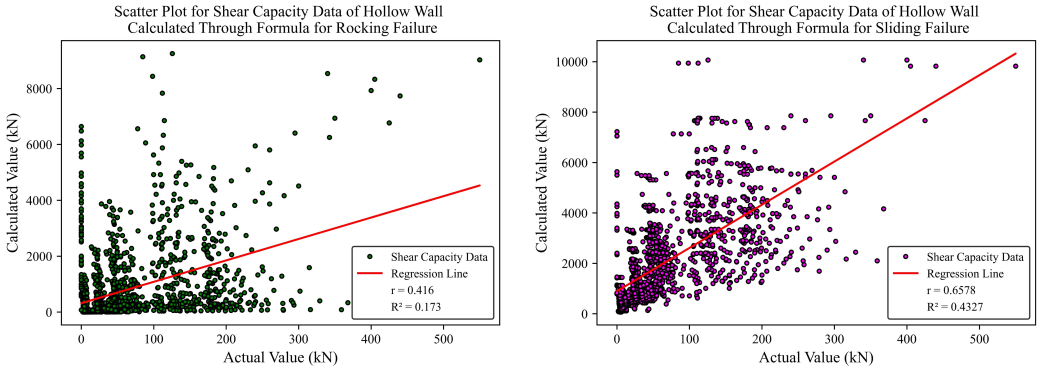

(a)

(b)

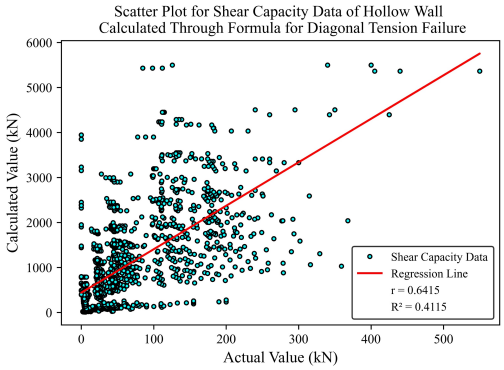

(c)

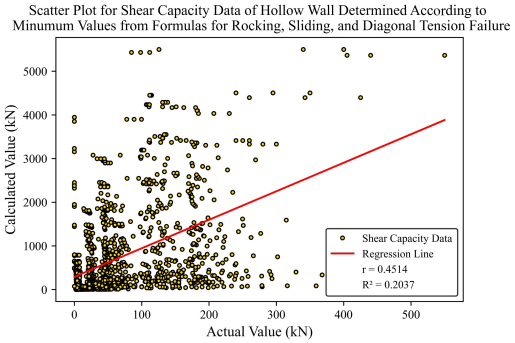

(d)

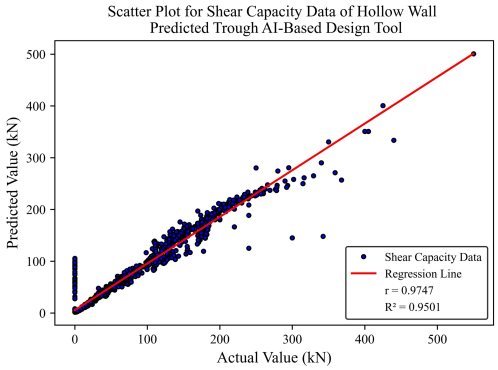

(e)

Figure 4.40. The scatter plots for the shear capacity of walls with hollow topology are as follows (a) plot for the shear capacity in case of the rocking failure, (b) plot for the shear capacity in case of the sliding failure, (c) plot for the shear capacity in case of the diagonal tension failure, (d) plot for the minimum shear capacity of three failure modes, (e) plot for the shear capacity predicted through AI-based design tool.

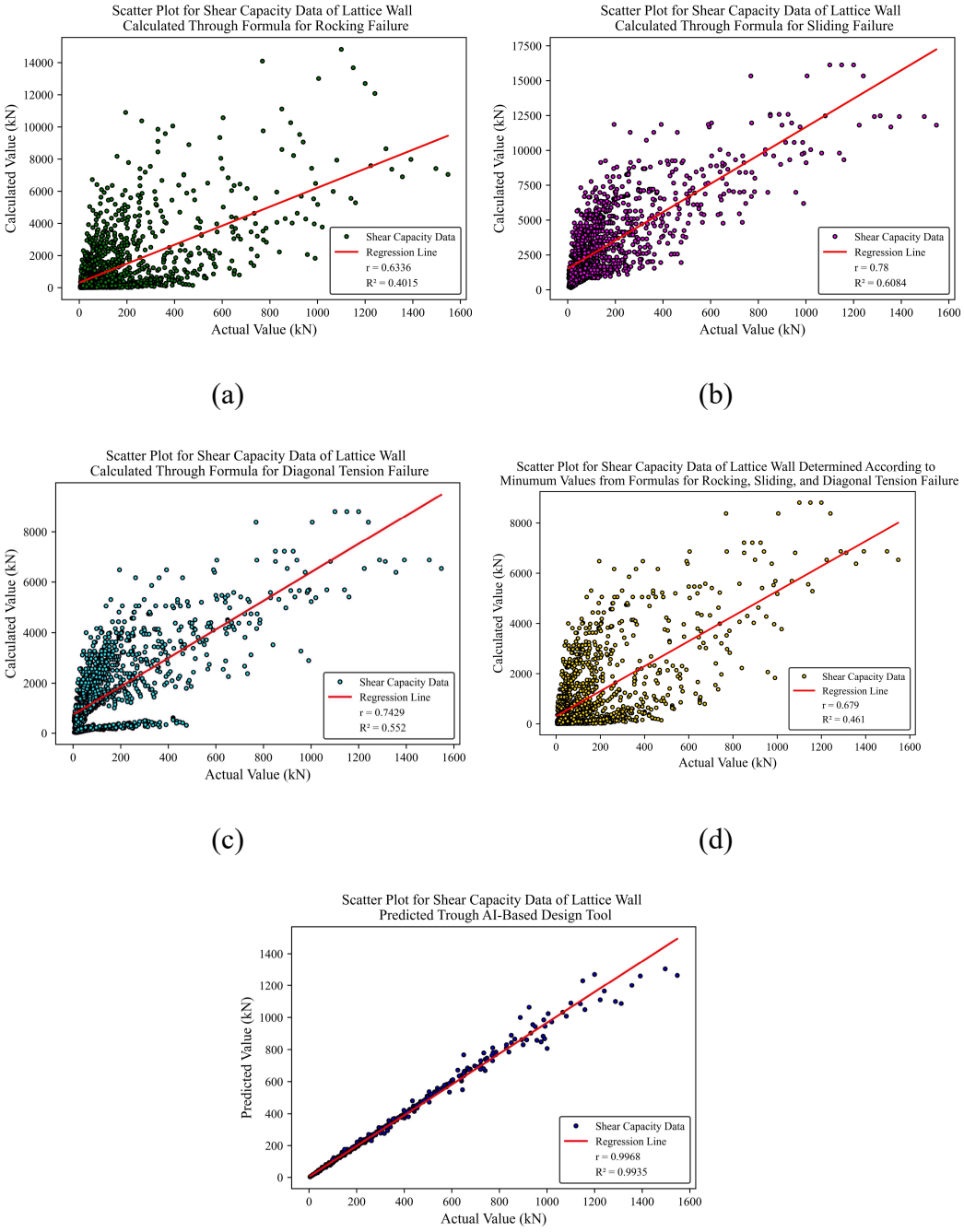

Figure 4.41. The scatter plots for the shear capacity of walls with lattice topology are as follows (a) plot for the shear capacity in case of the rocking failure, (b) plot for the shear capacity in case of the sliding failure, (c) plot for the shear capacity in case of the diagonal tension failure, (d) plot for the minimum shear capacity of three failure modes, (e) plot for the shear capacity predicted through AI-based design tool.

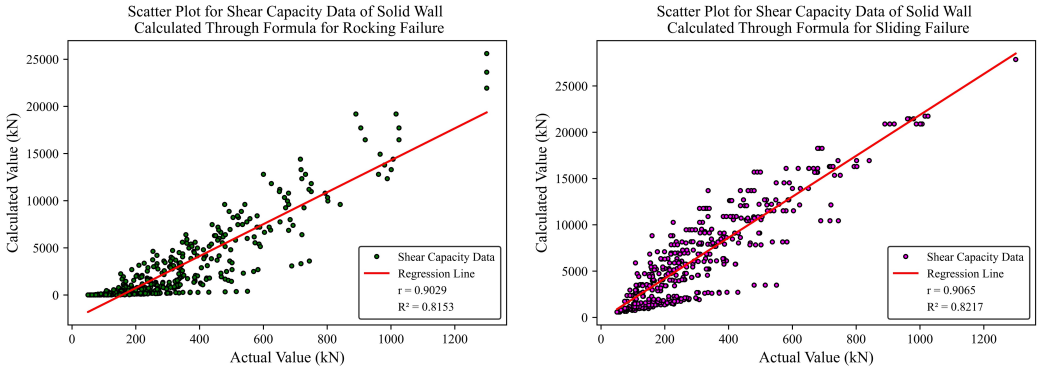

(a)

(b)

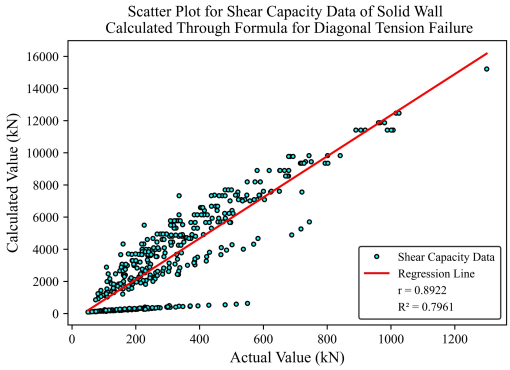

(c)

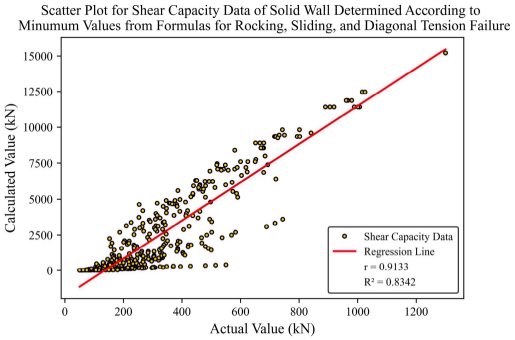

(d)

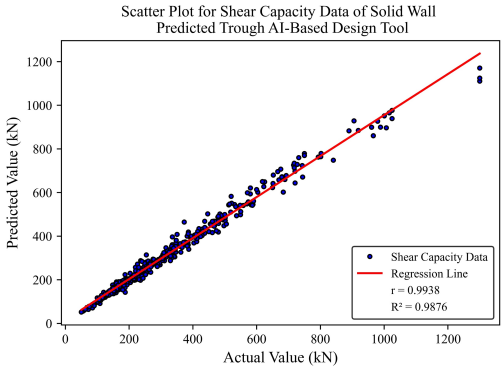

(e)

Figure 4.42. The scatter plots for the shear capacity of walls with solid topology are as follows (a) plot for the shear capacity in case of the rocking failure, (b) plot for the shear capacity in case of the sliding failure, (c) plot for the shear capacity in case of the diagonal tension failure, (d) plot for the minimum shear capacity of three failure modes, (e) plot for the shear capacity predicted through AI-based design tool.

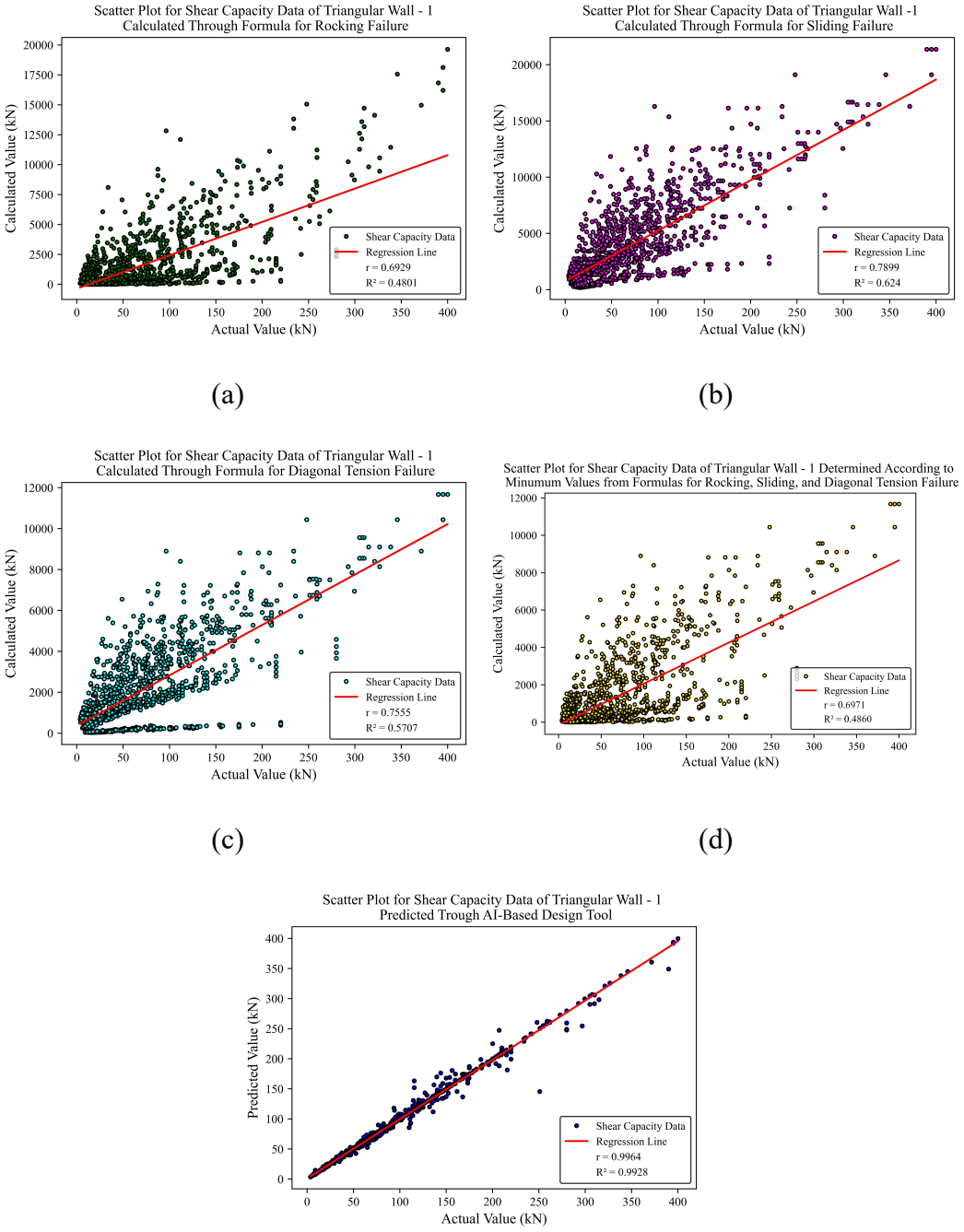

Figure 4.43. The scatter plots for the shear capacity of walls with triangular-1 topology are as follows (a) plot for the shear capacity in case of the rocking failure, (b) plot for the shear capacity in case of the sliding failure, (c) plot for the shear capacity in case of the diagonal tension failure, (d) plot for the minimum shear capacity of three failure modes, (e) plot for the shear capacity predicted through AI-based design tool.

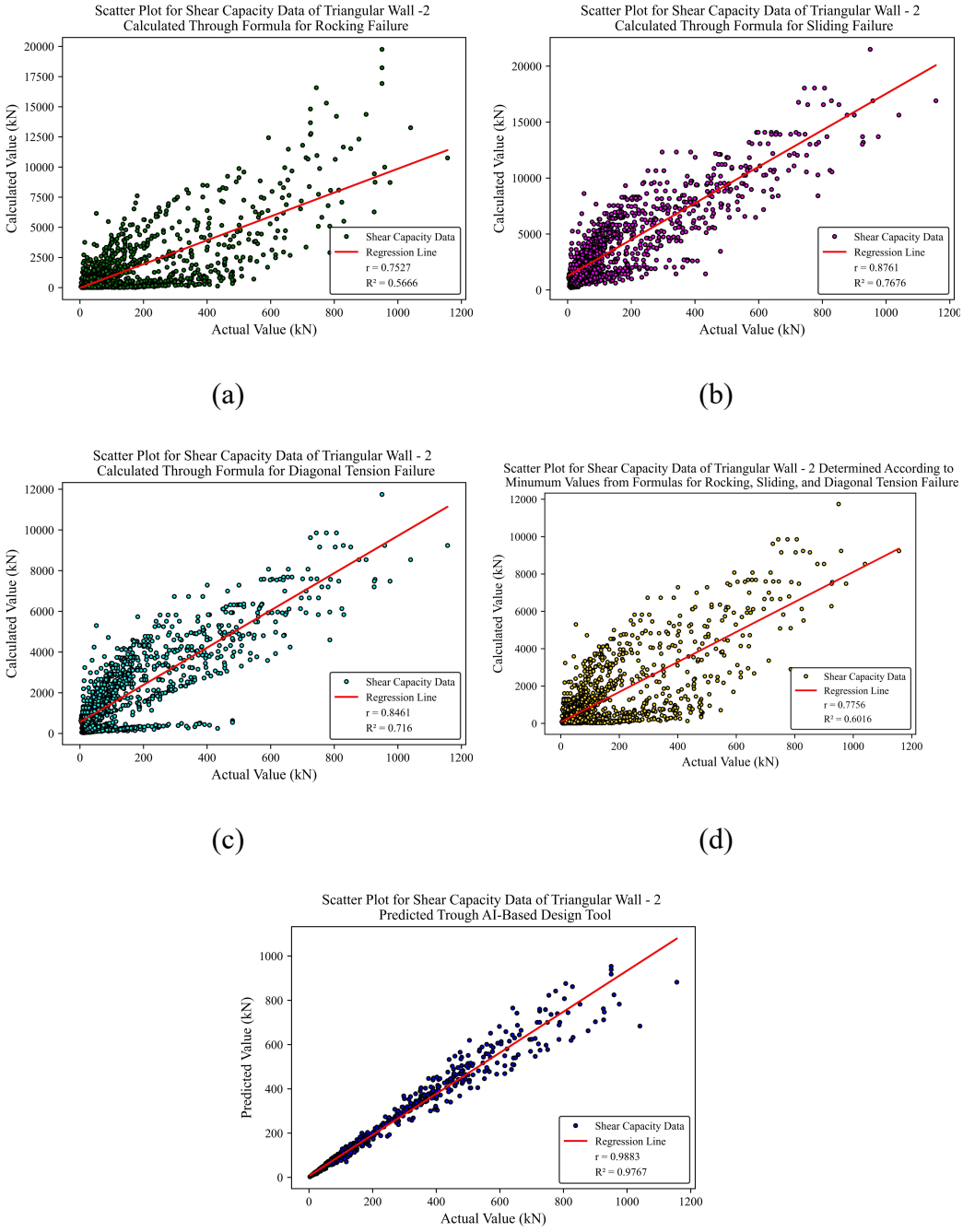

Figure 4.44. The scatter plots for the shear capacity of walls with triangular-2 topology are as follows (a) plot for the shear capacity in case of the rocking failure, (b) plot for the shear capacity in case of the sliding failure, (c) plot for the shear capacity in case of the diagonal tension failure, (d) plot for the minimum shear capacity of three failure modes, (e) plot for the shear capacity predicted through AI-based design tool.

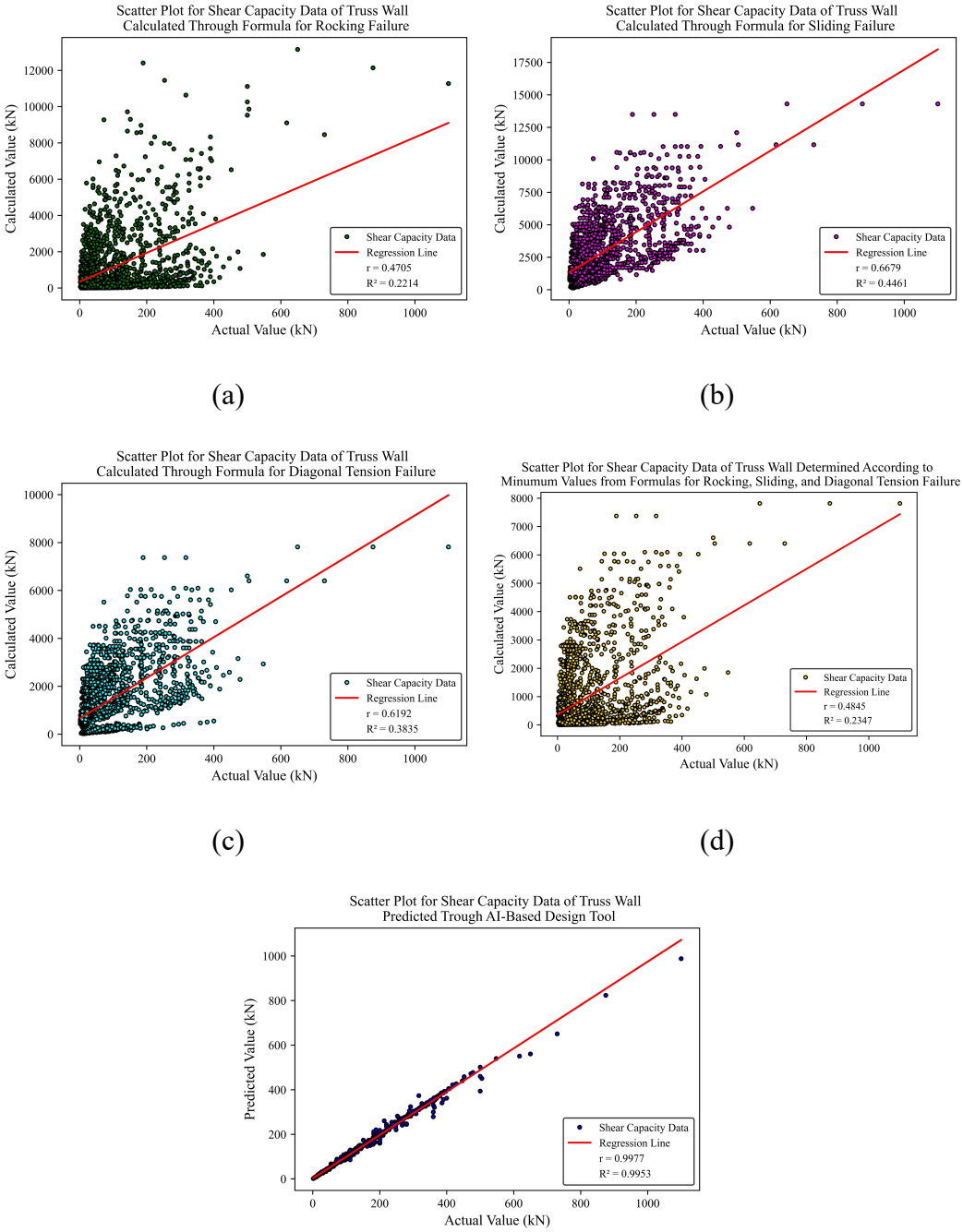

Figure 4.45. The scatter plots for the shear capacity of walls with truss topology are as follows (a) plot for the shear capacity in case of the rocking failure, (b) plot for the shear capacity in case of the sliding failure, (c) plot for the shear capacity in case of the diagonal tension failure, (d) plot for the minimum shear capacity of three failure modes, (e) plot for the shear capacity predicted through AI-based design tool.

Table 4.4. Correlation and determination coefficients obtained as a result of regression and correlation analyses.

Wall Type	Correlation coefficient					Determination coefficient				
	AI-based design tool	Rocking Failure	Sliding Failure	Diagonal Tension Failure	Minimum Value for Three Failure Mode	AI-based design tool	Rocking Failure	Sliding Failure	Diagonal Tension Failure	Minimum Value for Three Failure Mode
Arch Wall	0.9986	0.6623	0.8007	0.7689	0.6985	0.9971	0.4386	0.6412	0.5913	0.4878
Cellular Wall	0.9960	0.7899	0.8808	0.8769	0.7978	0.9921	0.6239	0.7758	0.7690	0.6365
Elliptic Wall	0.9994	0.7163	0.8533	0.8316	0.7516	0.9989	0.5131	0.7282	0.6915	0.5649
Hollow Wall	0.9747	0.4160	0.6578	0.6415	0.4514	0.9501	0.1730	0.4327	0.4115	0.2037
Lattice Wall	0.9968	0.6336	0.7800	0.7429	0.6790	0.9935	0.4015	0.6084	0.5520	0.4610
Solid Wall	0.9938	0.9029	0.9065	0.8922	0.9133	0.9876	0.8153	0.8217	0.7961	0.8342
Triangular Wall – 1	0.9964	0.6929	0.7899	0.7555	0.6971	0.9928	0.4801	0.6240	0.5707	0.4860
Triangular Wall – 2	0.9883	0.7527	0.8761	0.8461	0.7756	0.9767	0.5666	0.7676	0.7160	0.6016
Truss Wall	0.9977	0.4705	0.6679	0.6192	0.4845	0.9953	0.2214	0.4461	0.3835	0.2347

5. CONCLUSIONS AND RECOMMENDATIONS

The construction industry, due to its comprehensive nature and significant support to all other sectors, is a venture that carries great value in terms of creating facilities or assets. Cement-based materials are the primary choice for construction projects. In the construction field, the integration of Industry 4.0—representing a shift from conventional methods to self-sufficient smart systems using cutting-edge digital technologies—has not progressed as rapidly as in other industries regarding digital advancements and enhanced productivity. Digital technology applications such as 3D printers provide significant contributions to addressing the deficiencies in Construction 4.0 and offer new opportunities for the production of concrete structures. Structures with hollow topology produced through this technology will provide significant improvements in both the environmental and economic aspects of the construction sector. Physically based models developed to improve the properties of hollow printed elements require a deep understanding of the production process, which can be a very laborious process. Various AI methods that allow predictions to be made using only the obtained data can be used as an alternative to this method.

This study proposes new measures to achieve a fully automatic 3DCP method from the design stage to the construction stage. For this purpose, an AI-based design tool has been created to perform the on-site design of the necessary geometry of 3D printed structures to update the current state of the art in 3DCP technology. To develop this tool, AI methods were employed to optimize the wall structure in 3D-printed concrete construction, aiming to identify the most cost-effective and lightweight cross-section design that meets the required strength. Two different AI techniques were compared, and the most efficient model for the regression problem considered was determined. As a result, with the AI model, it was possible to design without trial and error, determining the most economical and lightest cross-section topology with the desired strength, without the need for human labor. As a result of the studies, it was observed that the proposed innovative wall interior topologies are more economical and robust than other wall interior topologies in the literature in some cases and that CNN created for them is quite efficient for the regression problems considered. Finally, the performance of the developed AI-based design tool was measured by comparing shear capacity predictions made through this tool with governing shear capacities calculated according to formulas for unreinforced masonry walls in the FEMA 356 building code. As a result of this comparison, it was observed that AI-based design tools

made much more accurate predictions compared to formulas in FEMA 356, especially for walls with interior hollow topologies. Therefore, it can be said that the developed AI-based design tool is more effective than formulas for shear capacity calculation of unreinforced masonry structures in FEMA 356 for shear capacity prediction of 3D printed concrete walls.

5.1. Conclusions

- For shear capacities, it has been observed that CNNs with bias have the highest correlation coefficients. Additionally, more than half of CNN models without bias have higher correlation coefficients than MLP models with bias. Furthermore, all MLP models without bias have lower correlation coefficients than MLP models with bias and all CNN models.
- For displacement capacities, it has been observed that in most of the generated models, CNNs with bias have higher correlation coefficients than CNNs without bias. Additionally, all CNN models with bias, and more than half of CNN models without bias, have higher correlation coefficients than MLP models with bias. Furthermore, in most of the generated models, MLP models with bias have higher correlation coefficients than MLP models without bias. It has also been observed that all MLP models without bias have lower correlation coefficients than both CNN models with bias and without bias. The reason for different AI algorithms yielding the highest correlation coefficients and therefore the highest determination coefficients is that these ANN models are specific to the dataset. However, it has been largely observed that both CNN models and bias-containing models have higher correlation and determination coefficients for both displacement and shear capacities.
- In terms of regression and correlation coefficients, generally, better results are obtained for shear capacities compared to displacement capacities. This is thought to be due to the output values in the dataset created for displacement capacities being very small. However, all CNN models with a bias for shear capacities and more than half of CNN models with a bias for displacement capacities have made predictions with high accuracy and good distribution.
- For shear capacities, predictions with a level of accuracy that can be considered successful, albeit not perfect, have been made with MLP models with bias. The same is true for almost all walls for displacement capacities. However, for displacement

capacities, predictions with low accuracy and a poor distribution have been made with very few MLP models with bias. In most MLP models without bias, predictions with low accuracy and a poor distribution have been made. For shear capacities, among the walls with nine different topologies, the CNN model without bias had more parameters than the CNN model with a bias for four topologies. Similarly, for nine different wall topologies, the MLP model without bias had more parameters than the MLP model with bias for three topologies. For shear capacities, it has been observed that all MLP models have fewer parameters than all CNN models.

- For both displacement and shear capacities, most CNN models with bias have more parameters than CNN models without bias, and most MLP models with bias have more parameters than MLP models without bias. Additionally, it has been observed that MLP models have fewer parameters than all CNN models. Therefore, it can be said that MLP models are much more advantageous in terms of computational cost. However, CNN models provide much higher accuracy than MLP models, and MLP models cannot make predictions with sufficient accuracy. Therefore, it can be said that in terms of performance-computational cost, CNN models are more advantageous than MLP models.
- Additionally, it has been observed in almost all generated models that models created for shear capacity have more parameter numbers than models created for displacement capacity. It is believed that this is due to the output values in the shear capacity datasets being larger than the output values in the displacement capacity datasets and having different variance and standard deviation values.
- Besides, it was observed that the created AI-based design tool can make predictions with higher accuracy than formulas for in-plane failure modes of unreinforced masonry structures in FEMA 356 building design code for shear capacity of 3D printed concrete walls, especially for walls with hollow interior topologies. This condition substantially may stem from that local failures occurring in the walls cannot be simulated properly in the formulas for shear capacity calculation of unreinforced masonry walls in FEMA 356. This situation reveals the importance of the need for a more accurate calculation method for the shear capacity of concrete walls printed through 3DCP and shows that the created AI-based design tool is quite advantageous in terms of practical application in the field of 3DCP.

5.2. Recommendations

5.2.1. Practical Recommendations

- The production of more robust and economical novel wall interior topologies, in addition to the novel wall interior topologies proposed in this study,
- Establishing standards/regulations for the design and analysis of members printed through 3DCP over time, or determining a standard procedure, minimizing assumptions as much as possible, and producing data sets in a healthier manner,

are recommended.

5.2.2. Future Academic Recommendations

- Addressing the performance of various analysis types when creating data sets,
- Working on more efficient and innovative AI models to reduce computational costs while increasing performance,
- Conducting TO studies for more 3D printed concrete structural members (columns, beams, etc.) or concrete structure types (houses, offices, bridges, etc.) to contribute more to the field of Construction 4.0,
- To conduct TO studies through AI for reinforced concrete elements and structures printed through 3DCP,

are recommended.

6. REFERENCES

[1] S.K. Baduge, S. Thilakarathna, J.S. Perera, M. Arashpour, P. Sharafi, B. Teodosio, A. Shringi, P. Mendis, Artificial intelligence and smart vision for building and construction 4.0: Machine and deep learning methods and applications, Autom Constr 141 (2022) 104440. https://doi.org/10.1016/J.AUTCON.2022.104440.

[2] M. Alabbasi, A. Agkathidis, H. Chen, Robotic 3D printing of concrete building components for residential buildings in Saudi Arabia, Autom Constr 148 (2023) 104751. https://doi.org/10.1016/J.AUTCON.2023.104751.

[3] Z. Chang, Y. Xu, Y. Chen, Y. Gan, E. Schlangen, B. Šavija, A discrete lattice model for assessment of buildability performance of 3D-printed concrete, Computer-Aided Civil and Infrastructure Engineering 36 (2021) 638–655. https://doi.org/10.1111/MICE.12700.

[4] T. Daungwilailuk, P. Pheinsusom, W. Pansuk, Uniaxial load testing of large-scale 3D-printed concrete wall and finite-element model analysis, Constr Build Mater 275 (2021) 122039. https://doi.org/10.1016/J.CONBUILDMAT.2020.122039.

[5] P. Kumar Mehta, Paulo J. M. Monteiro, Concrete: Microstructure, Properties, and Materials, McGraw-Hill Education, 2014. https://www.accessengineeringlibrary.com/content/book/9780071797870 (accessed May 4, 2023).

[6] T. Suntharalingam, I. Upasiri, P. Gatheeshgar, K. Poologanathan, B. Nagaratnam, P. Santos, H. Rajanayagam, Energy Performance of 3D-Printed Concrete Walls: A Numerical Study, Buildings 2021, Vol. 11, Page 432 11 (2021) 432. https://doi.org/10.3390/BUILDINGS11100432.

[7] J. Sun, J. Xiao, Z. Li, X. Feng, Experimental study on the thermal performance of a 3D printed concrete prototype building, Energy Build 241 (2021) 110965. https://doi.org/10.1016/J.ENBUILD.2021.110965.

[8] M. van den Heever, F. Bester, J. Kruger, G. van Zijl, Mechanical characterisation for numerical simulation of extrusion-based 3D concrete printing, Journal of Building Engineering 44 (2021) 102944. https://doi.org/10.1016/J.JOBE.2021.102944.

[9] J. Chandra, P. Pudjisuryadi, A. Antoni, H. Wibowo, Analytical modeling of 3D-printed reinforced concrete beams, IOP Conf Ser Mater Sci Eng 930 (2020) 012041. https://doi.org/10.1088/1757-899X/930/1/012041.

[10] S. Geng, Q. Luo, K. Liu, Y. Li, Y. Hou, W. Long, Research status and prospect of machine learning in construction 3D printing, Case Studies in Construction Materials 18 (2023) e01952. https://doi.org/10.1016/J.CSCM.2023.E01952.

[11] M. van den Heever, F. Bester, J. Kruger, G. van Zijl, Numerical modelling strategies for reinforced 3D concrete printed elements, Addit Manuf 50 (2022) 102569. https://doi.org/10.1016/J.ADDMA.2021.102569.

[12] D. Asprone, F. Auricchio, C. Menna, V. Mercuri, 3D printing of reinforced concrete elements: Technology and design approach, Constr Build Mater 165 (2018) 218–231. https://doi.org/10.1016/J.CONBUILDMAT.2018.01.018.

[13] R.J.M. Wolfs, F.P. Bos, T.A.M. Salet, Early age mechanical behaviour of 3D printed concrete: Numerical modelling and experimental testing, Cem Concr Res 106 (2018) 103–116. https://doi.org/10.1016/J.CEMCONRES.2018.02.001.

[14] G. Vantyghem, T. Ooms, W. De Corte, FEM modelling techniques for simulation of 3D concrete printing, Fib Symposium (2020) 964–972. https://arxiv.org/abs/2009.06907v1 (accessed March 29, 2023).

[15] P. Carneau, R. Mesnil, N. Roussel, O. Baverel, Additive manufacturing of cantilever - From masonry to concrete 3D printing, Autom Constr 116 (2020) 103184. https://doi.org/10.1016/J.AUTCON.2020.103184.

[16] Z. Chang, M. Liang, Y. Xu, E. Schlangen, B. Šavija, 3D concrete printing: Lattice modeling of structural failure considering damage and deformed geometry, Cem Concr Compos 133 (2022) 104719. https://doi.org/10.1016/J.CEMCONCOMP.2022.104719.

[17] M.S. Khan, F. Sanchez, H. Zhou, 3-D printing of concrete: Beyond horizons, Cem Concr Res 133 (2020) 106070. https://doi.org/10.1016/J.CEMCONRES.2020.106070.

[18] V. Nguyen-Van, S. Li, J. Liu, K. Nguyen, P. Tran, Modelling of 3D concrete printing process: A perspective on material and structural simulations, Addit Manuf 61 (2023) 103333. https://doi.org/10.1016/J.ADDMA.2022.103333.

[19] V. Nguyen-Van, H. Nguyen-Xuan, B. Panda, P. Tran, 3D concrete printing modelling of thin-walled structures, Structures 39 (2022) 496–511. https://doi.org/10.1016/J.ISTRUC.2022.03.049.

[20] S.A. Khan, M. Koç, Numerical modelling and simulation for extrusion-based 3D concrete printing: The underlying physics, potential, and challenges, Results in Materials 16 (2022) 100337. https://doi.org/10.1016/J.RINMA.2022.100337.

[21] W. Lao, M. Li, T.N. Wong, M.J. Tan, T. Tjahjowidodo, Improving surface finish quality in extrusion-based 3D concrete printing using machine learning-based extrudate geometry control, Virtual Phys Prototyp 15 (2020) 178–193. https://doi.org/10.1080/17452759.2020.1713580.

[22] F. Tahmasebinia, M. Niemelä, S.M.E. Sepasgozar, T.Y. Lai, W. Su, K.R. Reddy, S. Shirowzhan, S. Sepasgozar, F.A. Marroquin, Three-Dimensional Printing Using Recycled High-Density Polyethylene: Technological Challenges and Future Directions for Construction, Buildings 2018, Vol. 8, Page 165 8 (2018) 165. https://doi.org/10.3390/BUILDINGS8110165.

[23] J. Xiao, H. Liu, T. Ding, Finite element analysis on the anisotropic behavior of 3D printed concrete under compression and flexure, Addit Manuf 39 (2021) 101712. https://doi.org/10.1016/J.ADDMA.2020.101712.

[24] T. Ooms, G. Vantyghem, R. Van Coile, W. De Corte, A parametric modelling strategy for the numerical simulation of 3D concrete printing with complex geometries, Addit Manuf 38 (2021) 101743. https://doi.org/10.1016/J.ADDMA.2020.101743.

[25] F. Tahmasebinia, S. M.E. Sepasgozar, S. Shirowzhan, M. Niemela, A. Tripp, S. Nagabhyrava, ko ko, Z. Mansuri, F. Alonso-Marroquin, Criteria development for sustainable construction manufacturing in Construction Industry 4.0: Theoretical and laboratory investigations, Construction Innovation 20 (2020) 379–400. https://doi.org/10.1108/CI-10-2019-0103/FULL/XML.

[26] A.S.J. Suiker, Mechanical performance of wall structures in 3D printing processes: Theory, design tools and experiments, Int J Mech Sci 137 (2018) 145–170. https://doi.org/10.1016/J.IJMECSCI.2018.01.010.

[27] K. Tan, Predicting Compressive Strength of Recycled Concrete for Construction 3D Printing Based on Statistical Analysis of Various Neural Networks, Journal of Building Construction and Planning Research 6 (2018) 71–89. https://doi.org/10.4236/JBCPR.2018.62005.

[28] G. Vantyghem, V. Boel, W. De Corte, M. Steeman, Compliance, stress-based and multi-physics topology optimization for 3D-printed concrete structures, RILEM Bookseries 19 (2019) 323–332. https://doi.org/10.1007/978-3-319-99519-9_30/COVER.

[29] G. Vantyghem, W. De Corte, E. Shakour, O. Amir, 3D printing of a post-tensioned concrete girder designed by topology optimization, Autom Constr 112 (2020) 103084. https://doi.org/10.1016/J.AUTCON.2020.103084.

[30] M. Bi, P. Tran, L. Xia, G. Ma, Y.M. Xie, Topology optimization for 3D concrete printing with various manufacturing constraints, Addit Manuf 57 (2022) 102982. https://doi.org/10.1016/J.ADDMA.2022.102982.

[31] G.H. Ahmed, A review of "3D concrete printing": Materials and process characterization, economic considerations and environmental sustainability, Journal of Building Engineering 66 (2023) 105863. https://doi.org/10.1016/J.JOBE.2023.105863.

[32] A. Aramburu, I. Calderon-Uriszar-Aldaca, I. Puente, Parametric modelling of 3D printed concrete segmented beams with rebars under bending moments, Case Studies in Construction Materials 18 (2023) e01910. https://doi.org/10.1016/J.CSCM.2023.E01910.

[33] V. Nguyen-Van, B. Panda, G. Zhang, H. Nguyen-Xuan, P. Tran, Digital design computing and modelling for 3-D concrete printing, Autom Constr 123 (2021) 103529. https://doi.org/10.1016/J.AUTCON.2020.103529.

[34] J. Reinold, V.N. Nerella, V. Mechtcherine, G. Meschke, Extrusion process simulation and layer shape prediction during 3D-concrete-printing using the Particle Finite Element Method, Autom Constr 136 (2022) 104173. https://doi.org/10.1016/J.AUTCON.2022.104173.

[35] J. Kruger, S. Zeranka, G. van Zijl, A rheology-based quasi-static shape retention model for digitally fabricated concrete, Constr Build Mater 254 (2020) 119241. https://doi.org/10.1016/J.CONBUILDMAT.2020.119241.

[36] H. Liu, T. Ding, J. Xiao, V. Mechtcherine, Buildability prediction of 3D–printed concrete at early-ages: A numerical study with Drucker–Prager model, Addit Manuf 55 (2022) 102821. https://doi.org/10.1016/J.ADDMA.2022.102821.

[37] V. Nguyen-Van, J. Liu, S. Li, G. Zhang, H. Nguyen-Xuan, P. Tran, Modelling of 3D-printed bio-inspired Bouligand cementitious structures reinforced with steel fibres, Eng Struct 274 (2023) 115123. https://doi.org/10.1016/J.ENGSTRUCT.2022.115123.

[38] V. Ekanayaka, L. Lachmayer, A. Raatz, A. Hürkamp, Approach to optimize the interlayer waiting time in additive manufacturing with concrete utilizing FEM modeling, Procedia CIRP 109 (2022) 562–567. https://doi.org/10.1016/J.PROCIR.2022.05.295.

[39] L. Lachmayer, V. Ekanayaka, A. Hürkamp, A. Raatz, Approach to an optimized printing path for additive manufacturing in construction utilizing FEM modeling, Procedia CIRP 104 (2021) 600–605. https://doi.org/10.1016/J.PROCIR.2021.11.101.

[40] X. Yao, X. Lyu, J. Sun, B. Wang, Y. Wang, M. Yang, Y. Wei, M. Elchalakani, D. Li, X. Wang, AI-based performance prediction for 3D-printed concrete considering anisotropy and steam curing condition, Constr Build Mater 375 (2023) 130898. https://doi.org/10.1016/J.CONBUILDMAT.2023.130898.

[41] R.J.M. Wolfs, F.P. Bos, T.A.M. Salet, Triaxial compression testing on early age concrete for numerical analysis of 3D concrete printing, Cem Concr Compos 104 (2019) 103344. https://doi.org/10.1016/J.CEMCONCOMP.2019.103344.

[42] H. Liu, K.J.I. Egbe, H. Wang, A.M. Nazar, P. Jiao, R. Zhu, A Numerical Study on 3D Printed Cementitious Composites Mixes Subjected to Axial Compression, Materials 2021, Vol. 14, Page 6882 14 (2021) 6882. https://doi.org/10.3390/MA14226882.

[43] H. Bolandi, X. Li, T. Salem, V.N. Boddeti, N. Lajnef, Bridging finite element and deep learning: High-resolution stress distribution prediction in structural components, Frontiers of Structural and Civil Engineering 16 (2022) 1365–1377. https://doi.org/10.1007/S11709-022-0882-5/METRICS.

[44] N. Roussel, J. Spangenberg, J. Wallevik, R. Wolfs, Numerical simulations of concrete processing: From standard formative casting to additive manufacturing, Cem Concr Res 135 (2020) 106075. https://doi.org/10.1016/J.CEMCONRES.2020.106075.

[45] M.A. Mahmood, A.I. Visan, C. Ristoscu, I.N. Mihailescu, Artificial Neural Network Algorithms for 3D Printing, Materials 2021, Vol. 14, Page 163 14 (2020) 163. https://doi.org/10.3390/MA14010163.

[46] B. Panda, M. Leite, B.B. Biswal, X. Niu, A. Garg, Experimental and numerical modelling of mechanical properties of 3D printed honeycomb structures, Measurement 116 (2018) 495–506. https://doi.org/10.1016/J.MEASUREMENT.2017.11.037.

[47] K.M. Dolatshahi, M.T. Nikoukalam, K. Beyer, Numerical study on factors that influence the in-plane drift capacity of unreinforced masonry walls, Earthq Eng Struct Dyn 47 (2018) 1440–1459. https://doi.org/10.1002/EQE.3024.

[48] B.V. Wilding, K. Beyer, The effective stiffness of modern unreinforced masonry walls, Earthq Eng Struct Dyn 47 (2018) 1683–1705. https://doi.org/10.1002/EQE.3035.

[49] J.S. Kuang, Y.P. Yuen, Ductility design of reinforced concrete shear walls with the consideration of axial compression ratio, HKIE Transactions 22 (2015) 123–133. https://doi.org/10.1080/1023697X.2015.1071027.

[50] L. Wang, H. Jiang, Z. Li, G. Ma, Mechanical behaviors of 3D printed lightweight concrete structure with hollow section, Archives of Civil and Mechanical Engineering 20 (2020) 1–17. https://doi.org/10.1007/S43452-020-00017-1/METRICS.

[51] G.D. Goh, S.L. Sing, W.Y. Yeong, A review on machine learning in 3D printing: applications, potential, and challenges, Artif Intell Rev 54 (2021) 63–94. https://doi.org/10.1007/S10462-020-09876-9/METRICS.

[52] Vasileios Sergis, C. M. Ouellet-Plamondon, Automating mix design for 3D concrete printing using optimization methods, Digital Discovery 1 (2022) 645–657. https://doi.org/10.1039/D2DD00040G.

[53] Z. Chang, Z. Wan, Y. Xu, E. Schlangen, B. Šavija, Convolutional neural network for predicting crack pattern and stress-crack width curve of air-void structure in 3D printed concrete, Eng Fract Mech 271 (2022) 108624. https://doi.org/10.1016/J.ENGFRACMECH.2022.108624.

[54] Y. Pan, L. Zhang, Roles of artificial intelligence in construction engineering and management: A critical review and future trends, Autom Constr 122 (2021) 103517. https://doi.org/10.1016/J.AUTCON.2020.103517.

[55] A. Raza, K.M. Deen, R. Jaafreh, K. Hamad, A. Haider, W. Haider, Incorporation of machine learning in additive manufacturing: a review, International Journal of Advanced Manufacturing Technology 122 (2022) 1143–1166. https://doi.org/10.1007/S00170-022-09916-4/METRICS.

[56] H. Izadgoshasb, A. Kandiri, P. Shakor, V. Laghi, G. Gasparini, Predicting Compressive Strength of 3D Printed Mortar in Structural Members Using Machine Learning, Applied

Sciences 2021, Vol. 11, Page 10826 11 (2021) 10826. https://doi.org/10.3390/APP112210826.

[57] K. Tan, The Framework of Combining Artificial Intelligence and Construction 3D Printing in Civil Engineering, MATEC Web of Conferences 206 (2018) 01008. https://doi.org/10.1051/MATECCONF/201820601008.

[58] I. Rojek, D. Mikołajewski, P. Kotlarz, K. Tyburek, J. Kopowski, E. Dostatni, Traditional artificial neural networks versus deep learning in optimization of material aspects of 3d printing, Materials 14 (2021) 7625. https://doi.org/10.3390/MA14247625/S1.

[59] B. Nedjar, On a geometrically nonlinear incremental formulation for the modeling of 3D concrete printing, Mech Res Commun 116 (2021) 103748. https://doi.org/10.1016/J.MECHRESCOM.2021.103748.

[60] L. He, W.T. Chow, H. Li, Effects of interlayer notch and shear stress on interlayer strength of 3D printed cement paste, Addit Manuf 36 (2020) 101390. https://doi.org/10.1016/J.ADDMA.2020.101390.

[61] A. Perrot, A. Pierre, V.N. Nerella, R.J.M. Wolfs, E. Keita, S.A.O. Nair, N. Neithalath, N. Roussel, V. Mechtcherine, From analytical methods to numerical simulations: A process engineering toolbox for 3D concrete printing, Cem Concr Compos 122 (2021) 104164. https://doi.org/10.1016/J.CEMCONCOMP.2021.104164.

[62] O. Zienkiewicz, R. Taylor, J.Z. Zhu, The Finite Element Method: its Basis and Fundamentals: Seventh Edition, Butterworth-Heinemann Seventh Edition (2013). https://doi.org/10.1016/C2009-0-24909-9.

[63] F. Bester, M. van den Heever, J. Kruger, S. Zeranka, G. van Zijl, BENCHMARK STRUCTURES FOR 3D CONCRETE PRINTING, in: Fib Symposium Krakow Innovations in Materials, Design and Structures, Krakow, 2019. https://www.researchgate.net/publication/333419075_BENCHMARK_STRUCTURES_FOR_3D_CONCRETE_PRINTING (accessed March 29, 2023).

[64] A.N. Attiyah, H. Gesund, M. Mohammed, H. Rasool, FINITE ELEMENT MODELLING OF CONCRETE SHRINKAGE CRACKING IN WALLS, Kufa Journal of Engineering 5 (2013) 127–140. https://journal.uokufa.edu.iq/index.php/kje/article/view/1233 (accessed March 20, 2023).

[65] K.F. Abdulla, L.S. Cunningham, M. Gillie, Simulating masonry wall behaviour using a simplified micro-model approach, Eng Struct 151 (2017) 349–365. https://doi.org/10.1016/J.ENGSTRUCT.2017.08.021.

[66] G. Baloevic, J. Radnic, D. Matesan, N. Grgic, I. Banovic, Comparison of Developed Numerical Macro and Micro Masonry Models for Static and Dynamic Analysis of Masonry-infilled Steel Frames, Latin American Journal of Solids and Structures 13 (2016) 2251–2265. https://doi.org/10.1590/1679-78252520.

[67] M.F. Funari, L.C. Silva, N. Savalle, P.B. Lourenço, A CONCURRENT MICRO/MACRO FE-MODEL OPTIMIZED WITH A LIMIT ANALYSIS TOOL FOR THE ASSESSMENT OF DRY-JOINT MASONRY STRUCTURES, Int J Multiscale Comput Eng 20 (2022) 65–85. https://doi.org/10.1615/INTJMULTCOMPENG.2021040212.

[68] M.Z. Naser, R.A. Hawileh, J. Abdalla, Modeling Strategies of Finite Element Simulation of Reinforced Concrete Beams Strengthened with FRP: A Review, Journal of Composites Science 2021, Vol. 5, Page 19 5 (2021) 19. https://doi.org/10.3390/JCS5010019.

[69] P.I. Kattan, MATLAB guide to finite elements: An interactive approach, Springer Berlin Heidelberg, 2008. https://doi.org/10.1007/978-3-540-70698-4.

[70] L.R. Alejano, A. Bobet, Drucker-Prager criterion, Rock Mech Rock Eng 45 (2012) 995–999. https://doi.org/10.1007/S00603-012-0278-2/FIGURES/2.

[71] İ. Kazaz, Dynamic characteristics and performance assessment of reinforced concrete structural walls, Middle East Technical University, 2010. https://open.metu.edu.tr/handle/11511/19443 (accessed April 22, 2024).

[72] Turkish Standards Institution, TS 500 Requirements for Design and Construction of Reinforced Concrete Structures, Turkish Standards Institution February (2000). https://intweb.tse.org.tr/Standard/Standard/Standard.aspx?081118051115108051104119110104055047105102120088111043113104073101043079047073050100084114050099 (accessed May 10, 2023).

[73] Uri. Kirsch, Reanalysis of Structures : A Unified Approach for Linear, Nonlinear, Static, and Dynamic Systems, Springer, 2008.

[74] W.D.R. Astre, I. Hidayat, Andryan, Comparison of thickness shear wall against drift floor using pushover method, IOP Conf Ser Earth Environ Sci 998 (2022) 012021. https://doi.org/10.1088/1755-1315/998/1/012021.

[75] M.R. Maheri, M.K. Khajeheian, F. Vatanpour, In-plane seismic retrofitting of hollow concrete block masonry walls with RC layers, Structures 20 (2019) 425–436. https://doi.org/10.1016/J.ISTRUC.2019.05.008.

[76] M.A. Rahman, M. Teguh, F. Saleh, G. Rendi, R. Wibowo, R. Kholilur, S.D. Cahyono, Comparison of thickness shear wall against drift floor using pushover method, IOP Conf Ser Earth Environ Sci 998 (2022) 012021. https://doi.org/10.1088/1755-1315/998/1/012021.

[77] N. Valoroso, F. Marmo, S. Sessa, A novel shell element for nonlinear pushover analysis of reinforced concrete shear walls, Bulletin of Earthquake Engineering 13 (2015) 2367–2388. https://doi.org/10.1007/S10518-015-9724-3/METRICS.

[78] B.V. Wilding, K. Beyer, Effective Stiffness and drift capacity of modern unreinforced masonry walls, 16th European Conference on Earthquake Engineering (2018). https://infoscience.epfl.ch/record/256845 (accessed April 3, 2023).

[79] A.H. Salmanpour, N. Mojsilovic, J. Schwartz, Deformation capacity of unreinforced masonry walls subjected to in-plane loading: a state-of-the-art review, International Journal of Advanced Structural Engineering 5 (2013) 1–12. https://doi.org/10.1186/2008-6695-5-22/FIGURES/9.

[80] Cohen, Applied Multiple Regression/Correlation Analysis for the Behavioral Sciences, Applied Multiple Regression/Correlation Analysis for the Behavioral Sciences (2013). https://doi.org/10.4324/9780203774441.

[81] K. Nefs, V. Menkovski, F.P. Bos, A.S.J. Suiker, T.A.M. Salet, Automated image segmentation of 3D printed fibrous composite micro-structures using a neural network, Constr Build Mater 365 (2023) 130099. https://doi.org/10.1016/J.CONBUILDMAT.2022.130099.

[82] I. Goodfellow, Y. Bengio, A. Courville, Deep Learning, The MIT Press, Massachusetts, 2016. https://mitpress.mit.edu/9780262035613/deep-learning/ (accessed April 3, 2023).

[83] K. He, X. Zhang, S. Ren, J. Sun, Delving deep into rectifiers: Surpassing human-level performance on imagenet classification, Proceedings of the IEEE International Conference on Computer Vision ICCV 2015 (2015) 1026–1034. https://doi.org/10.1109/ICCV.2015.123.

[84] Z. Teng, S. Teng, J. Zhang, G. Chen, F. Cui, Structural Damage Detection Based on Real-Time Vibration Signal and Convolutional Neural Network, Applied Sciences 2020, Vol. 10, Page 4720 10 (2020) 4720. https://doi.org/10.3390/APP10144720.

[85] X. Glorot, A. Bordes, Y. Bengio, Deep Sparse Rectifier Neural Networks, in: Proceedings of the Fourteenth International Conference on Artificial Intelligence and Statistics, JMLR Workshop and Conference Proceedings, Florida, 2011: pp. 315–323. https://proceedings.mlr.press/v15/glorot11a.html (accessed April 3, 2023).

[86] S. Bock, J. Goppold, M. Weiß, An improvement of the convergence proof of the ADAM-Optimizer, in: OTH CLUSTERKONFERENZ, 2018. https://arxiv.org/abs/1804.10587v1 (accessed May 16, 2023).

[87] P. Ramachandran, B. Zoph, Q. V Le Google Brain, Searching for Activation Functions, 6th International Conference on Learning Representations, ICLR 2018 - Workshop Track Proceedings (2017). https://arxiv.org/abs/1710.05941v2 (accessed April 3, 2023).

[88] F.L. Moon, Seismic Strengthening of Low-Rise Unreinforced Masonry Structures with Flexible Diaphragms, Georgia Institute of Technology, 2004. http://hdl.handle.net/1853/5128 (accessed April 22, 2024).

[89] A. Aldemir, B. Binici, E. Canbay, A. Yakut, Lateral load testing of an existing two story masonry building up to near collapse, Bulletin of Earthquake Engineering 15 (2017) 3365–3383. https://doi.org/10.1007/S10518-015-9821-3/METRICS.

[90] Federal Emergency Management Agency, American Society of Civil Engineers, FEMA 356 Prestandard and Commentary for the Seismic Rehabilitation of Buildings, US Federal Emergency Management Agency Publication No. 356 (2000).

[91] Ministry of Public Works and Resettlement, TSC 2007 Turkish Seismic Design Code for Buildings, Official Journal of Turkish Republic March (2007). https://www.resmigazete.gov.tr/eskiler/2007/03/20070306-3.htm (accessed April 24, 2024).

APPENDICIES

APPENDIX 1 – Articles Derived from Thesis Work

[1] A. Ozalp and A. Aldemir, Artificial intelligence-based displacement capacity prediction tool for three-dimensional printed concrete walls, Structural Concrete. https://doi.org/10.1002/suco.70039. (printed)

[2] A. Ozalp and A. Aldemir, Engineering the Future: AI-Driven Design Tool for 3D-Printed Concrete Buildings, Archives of Computational Methods in Engineering. (under review)